CRACK ARREST METHODOLOGY AND APPLICATIONS

Hahn/Kanninen, *editors*

ASTM STP 711

AMERICAN SOCIETY FOR TESTING AND MATERIALS

CRACK ARREST METHODOLOGY AND APPLICATIONS

A symposium
sponsored by ASTM
Committee E-24 on
Fracture Testing of Metals
AMERICAN SOCIETY FOR
TESTING AND MATERIALS
Philadelphia, Pa., 6–7 Nov. 1978

ASTM SPECIAL TECHNICAL PUBLICATION 711
G. T. Hahn, Vanderbilt University, and
M. F. Kanninen, Battelle Columbus
Laboratories, editors

List price $44.75
04-711000-30

AMERICAN SOCIETY FOR TESTING AND MATERIALS
1916 Race Street, Philadelphia, Pa. 19103

Library of Congress Catalog Card Number: 79-56317

NOTE

The Society is not responsible, as a body,
for the statements and opinions
advanced in this publication.

Printed in Baltimore, Md.
June 1980

Foreword

The symposium on Crack Arrest Methodology and Applications was presented at Philadelphia, Pa., 6-7 Nov. 1978. ASTM Committee E-24 on Fracture Testing of Metals sponsored the symposium. G. T. Hahn, Vanderbilt University, presided as symposium chairman. G. T. Hahn and M. F. Kanninen, Battelle Columbus Laboratories, are editors of this publication.

Related ASTM Publications

Fracture Mechanisms Applied to Brittle Materials, STP 678 (1979), $25.00, 04-678000-30

Fracture Mechanics, STP 677 (1979), $60.00, 04-677000-30

Fast Fracture and Crack Arrest, STP 627 (1977), $42.50, 04-627000-30

Cracks and Fracture, STP 601 (1976), $51.75, 04-601000-30

Fractography—Microscopic Cracking Process, STP 600 (1976), $27.50, 04-600000-30

Mechanics of Crack Growth, STP 590 (1976), $45.25, 04-590000-30

A Note of Appreciation to Reviewers

This publication is made possible by the authors and, also, the unheralded efforts of the reviewers. This body of technical experts whose dedication, sacrifice of time and effort, and collective wisdom in reviewing the papers must be acknowledged. The quality level of ASTM publications is a direct function of their respected opinions. On behalf of ASTM we acknowledge with appreciation their contribution.

ASTM Committee on Publications

Editorial Staff

Jane B. Wheeler, *Managing Editor*
Helen M. Hoersch, *Associate Editor*
Helen Mahy, *Assistant Editor*

Contents

Introduction

This symposium volume takes stock of the progress toward a procedure for measuring the crack arrest toughness—a property that expresses a material's resistance to penetration by a running crack. Values of the arrest toughness are needed to assess the risk of a long fracture in a structure. These values enter into the ongoing safety assessment of nuclear vessels under emergency core cooling conditions and other situations where fracture could have severe consequences. In the long term, the availability of reliable measurements can be expected to improve fracture safety and structural efficiency of a wide range of welded structures such as ship hulls, bridges, storage tanks, and pressurized containers.

The development of a standardized crack arrest test procedure is a current goal of ASTM Committee E-24 on Fracture Testing of Metals. It is also a topic of world-wide interest. Investigators from eleven foreign countries have participated in the cooperative evaluation of test procedures described in this volume. The proceedings of the 1976 symposium on arrest toughness, *STP 627: Fast Fracture and Crack Arrest*, have received wide distribution and are being translated for publication in the Soviet Union. This symposium attracted even greater interest.

The most direct approach to the evaluation of the crack arrest toughness is based on the measurements of the instantaneous dynamic stress field close to the propagating crack tip. Such measurements are generally difficult, particularly in the opaque structural steels that are of most practical interest, in the short-time durations that are involved. For this reason, the development of a crack arrest test has called for advances in both testing and analysis capabilities. Efforts have been focused on a procedure for initiating and arresting a fracture in a laboratory specimen under conditions that can be controlled, reproduced, and analyzed. These efforts have been coupled with work to define and validate relations between the arrest toughness and features of the specimen remote from the crack tip that can be measured before and after the arrest event, rather than concurrent with it. The second task has required more detailed fracture mechanics analyses of the running crack and its arrest, the development of numerical procedures, and experimentation with photoelastic transparent materials which permit comparisons between direct and indirect methods of evaluation.

The present symposium was sponsored by Committee E-24 to provide a forum for discussing the emerging crack arrest test methods. The symposium attracted 22 papers and engaged an attentive audience of 86 specialists. The papers show that substantial progress was made in the 2 ½ year period between the 1976 symposium and the meeting at which the contents of this volume were presented. Two new test methods have been developed and descriptions of these can be found in this volume. The two methods have been evaluated in 30 laboratories in the U.S. and eleven foreign countries by way of a Cooperative Test Program organized by E-24.03.04. The results of the tests—data for 300 large compact-type crack arrest test specimens (typically 0.2 by 0.2 by 0.05 m) are previewed in this volume. They represent one of the largest bodies of toughness data collected from one plate of a pressure vessel steel.

Other papers in this volume examine the validity of static and dynamic fracture mechanics analyses for interpreting the laboratory test. New and extensive sets of crack arrest toughness measurements of the nuclear pressure vessel steels A533B and A508 are reported. Finally, the application of current arrest concepts to thermally stressed cylinders, pipes, and nuclear vessels are described. Brief descriptions of these results together with discussions of the unsettled issues are discussed further in the Summary section of this volume.

The present symposium was organized by a committee drawn principally from the E-24: G. T. Hahn, Vanderbilt University (Chairman); H. T. Corten, The University of Illinois; P. B. Crosley, Materials Research Laboratory; L. B. Freund, Brown University; G. R. Irwin, University of Maryland; M. F. Kanninen, Battelle Columbus Laboratories (Secretary); A. S. Kobayashi, University of Washington; and G. T. Smith and J. McGowan, University of Alabama. Two other individuals played key roles: T. U. Marston, Electric Power Research Institute and the late E. K. Lynn, U.S. Nuclear Regulatory Commission. Marston and Lynn were instrumental in attracting financial support, both for the various research activities and the cooperative test program described in this volume, as well as for the symposium itself. The editors would like to express their sincere appreciation to these men and also to J. Gallagan, United States Steel Company, who served as the technical consultant. The task of converting 22 lightly edited manuscripts into a finely honed Special Technical Publication, requiring much patience, persistence, and expertise, was performed by Jane Wheeler, Kathy Green, and Helen Hoersch of the ASTM staff.

G. T. Hahn

Vanderbilt University, Nashville, Tenn. 37235; editor.

M. F. Kanninen

Battelle Memorial Institute, Columbus Laboratories, Columbus, Ohio; 43201; editor.

Computational and Experimental Methods for the Analysis of Dynamic Crack Propagation and Arrest

C.H. Popelar[1] and M.F. Kanninen[2]

A Dynamic Viscoelastic Analysis of Crack Propagation and Crack Arrest in a Double Cantilever Beam Test Specimen

REFERENCE: Popelar, C. H. and Kanninen, M. F., "**A Dynamic Viscoelastic Analysis of Crack Propagation and Crack Arrest in a Double Cantilever Beam Test Specimen,**" *Crack Arrest Methodology and Applications, ASTM STP 711*, G. T. Hahn and M. F. Kanninen, Eds., American Society for Testing and Materials, 1980, pp. 5–23.

ABSTRACT: Studies of dynamic crack propagation and arrest in polymeric materials are generally interpreted using rate-independent elastic analyses. To ascertain the importance of the viscoelastic constitutive behavior exhibited by polymers that is neglected in these approaches, a simple mathematical model for dynamic viscoelastic crack propagation in wedge-loaded double cantilever beam (DCB) test specimens has been developed. Computational results have been obtained for four different polymers using a three-parameter solid linear viscoelastic constitutive representation. In comparing these results with rate-independent elastic behavior, it is found that significant differences in the crack propagation/arrest process do exist. However, close correlations can nevertheless be obtained if, in displaying experimental results, proper account is taken of the viscoelastic properties.

KEY WORDS: double cantilever beam specimen, viscoelastic, crack propagation, crack arrest, dynamic viscoelasticity, Araldite B, Homalite, PMMA, Clearcast

Research aimed at establishing a sound fundamental basis for crack arrest calculations has proceeded in two different ways. Work by Hahn et al [*1-3*][3] combined crack propagation/arrest experiments with results obtained from dynamic fracture analysis models. By matching the observed crack growth-time results with calculations using assumed dynamic fracture toughness

[1] Professor, Department of Engineering Mechanics, The Ohio State University, Columbus, Ohio 43210.

[2] Senior research scientist, Applied Solid Mechanics Section, Battelle Memorial Institute, Columbus Laboratories, Columbus, Ohio 43201.

[3] The italic numbers in brackets refer to the list of references appended to this paper.

values, the latter properties have been obtained for nuclear steels and other engineering materials on a trial-and-error basis. Investigators such as Kobayashi et al [*4*], Kobayashi and Dally [5], and Kalthoff et al [*6*], in contrast, have employed optical experimentation to deduce the toughness properties more directly. The disadvantage of the latter approach is that optical techniques are generally applied using polymeric materials.

Unlike steel, which has essentially rate- and time-independent mechanical properties, polymers are viscoelastic materials. Hence, the tacit assumption that the crack arrest process in such materials is basically the same as in steel is questionable. Indeed, Kalthoff [*7*] has observed that the behavior of the stress-intensity factor following arrest is significantly affected by the degree of viscoelasticity exhibited by the test specimen material. However, because a viscoelastic-dynamic fracture solution procedure has not been previously available, it has not been possible to systematically assess these differences.

This paper provides preliminary calculations showing the differences to be expected in crack propagation/arrest experiments in viscoelastic materials from those in elastic materials. The work focuses on the double cantilever beam (DCB) fracture specimen, adopting the one-dimensional analysis model which has proven to be quite successful in earlier dynamic fracture analyses for the DCB specimen. The essential refinement introduced in this work is to replace the elastic constitutive behavior used in the previous model by the relations corresponding to a three-parameter linear viscoelastic solid. It is recognized that this formulation is highly specialized. Nevertheless, it is felt that the results obtained from this approach offer some important new insights into the effects of viscoelasticity in dynamic crack propagation.

The Computational Model

The double cantilever beam (DCB) test specimen illustrated in Fig. 1 has been found to be very useful in studying crack propagation and arrest events. With quasi-static wedge loading and a blunted initial crack tip, this configuration offers a number of significant advantages over tests conducted in other specimen types. Of primary usefulness, crack propagation occurs at very high speeds (controllable by the degree of crack-tip blunting). Yet, because the load point displacement is essentially unchanged while the crack is in motion, crack arrest can occur within the specimen. Also of importance, the crack travels at an ostensibly constant speed during a large portion of the event. This simplifies the task of extracting experimental crack speed-dependent fracture toughness values. At the same time, it offers a decisive test of analysis procedures which, in fact, reveals the inadequacy of a quasi-static treatment of rapid crack propagation in the DCB specimen.

Recent work has shown that the DCB specimen is the most "dynamic" of the test specimens that have been used [*7*]. Whether this is an advantage or a

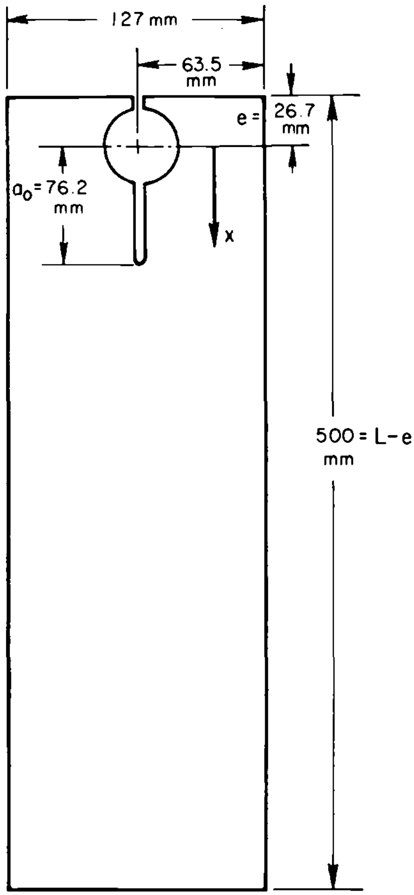

FIG. 1—*Dimensions of transverse wedge-loaded DCB test specimen used in the computations given in this paper.*

disadvantage, it is clear that dynamic effects are most strongly brought out in experiments using the DCB specimen. It follows that dynamic analyses are generally required for this configuration. Fortunately, the DCB specimen lends itself to a simplified treatment that allows the essential features of the crack propagation/arrest event to be taken into account. The computational method that has been evolved was known initially as a "beam-on-elastic-foundation" model [*8*] but is perhaps more aptly termed a one-dimensional model [*9,10*].

Details of the derivation of the governing equations of the one-dimensional DCB model are given in Ref *9*. It will suffice here to say that the equations of motion, kinematic equations, and constitutive equations of the two-dimensional (planar) theory of elasticity are operated on by integral operators that produce "beam-like" variables in a manner similar to that used initially by Cowper [*11*]. The resulting equations of motion become[4]

$$\frac{\partial M}{\partial x} - S = \rho I \frac{\partial^2 \psi}{\partial t^2} \tag{1}$$

$$\frac{\partial S}{\partial x} - pH(x - \mathcal{a}) = \rho A \frac{\partial^2 w}{\partial t^2} \tag{2}$$

where

A = cross sectional area,
I = moment of inertia,
ρ = mass density,
H = Heaviside step function,
$\mathcal{a}$ = crack length, and
M, S, p, w, ψ = beam variables.

The latter are defined as follows

$$M = \int_A z\sigma_x dA \text{ (bending moment)} \tag{3}$$

$$S = \kappa \int_A \sigma_{xz} dA \text{ (shear force)} \tag{4}$$

$$p = b\sigma_{zz}(z = -h/2) \text{ (crack plane tension)} \tag{5}$$

$$w = \frac{1}{A} \int_A u_z dA \text{ (displacement)} \tag{6}$$

$$\psi = \frac{1}{I} \int_A z u_x dA \text{ (rotation)} \tag{7}$$

where

κ = shear coefficient,
b = specimen thickness, and
h = specimen height.

Like the equations of motion, the kinematic relations to be used here are

[4] Here, and throughout this work, the deformation is taken to be relative to a plane of symmetry coinciding with the crack plane. Hence, the parameters refer to onc half of the specimen.

unchanged from the previous (elastic) formulation. These relations express the relevant strain components as functions of the beam variables in the following manner

$$\epsilon_{xx} = -z \frac{\partial \psi}{\partial z} \tag{8}$$

$$\epsilon_{xz} = \frac{1}{2}\left(\frac{\partial w}{\partial x} - \psi\right) \tag{9}$$

$$\epsilon_{zz} = \frac{2w}{h} H(-z)\, H(x - \mathfrak{a}) \tag{10}$$

Viscoelastic constitutive behavior can be introduced at this point to relate the strains to the stresses. In particular, a three-parameter linear viscoelastic solid representation will be used. This can be generally expressed as

$$\left(\frac{\partial}{\partial t} + \frac{1}{\tau}\frac{E_0}{E_\infty}\right)\sigma_{ij} = 2\left(\frac{\partial}{\partial t} + \frac{1}{\tau}\right)\left(G_0\epsilon_{ij} + \frac{\nu}{1-2\nu} G_0 \epsilon_{kk}\delta_{ij}\right) \tag{11}$$

where

$G_0 = E_0/2\,(1 + \nu)$,
E_0 = short-time modulus,
E_∞ = long-time modulus,
τ = relaxation time, and
ν = Poisson's ratio.

Note that if Eq 11 is applied to a uniaxial tension test—see, for example, Flügge [12]—the relaxation modulus $E = E(t)$ can be written as

$$E(t) = E_\infty + (E_0 - E_\infty)\exp\left(-\frac{E_0}{E_\infty}\frac{t}{\tau}\right) \tag{12}$$

which more clearly demonstrates the significance of the three viscoelastic material properties E_0, E_∞, and τ.

Omitting the details, combination of the kinematic relations, Eqs 8-10, with the viscoelastic constitutive relation, Eq 11, gives

$$\left(\frac{\partial}{\partial t} + \frac{1}{\tau}\frac{E_0}{E_\infty}\right)M = -E_0 I\left(\frac{\partial}{\partial t} + \frac{1}{\tau}\right)\frac{\partial \psi}{\partial x} \tag{13}$$

$$\left(\frac{\partial}{\partial t} + \frac{1}{\tau}\frac{E_0}{E_\infty}\right)S = \kappa G_0 A\left(\frac{\partial}{\partial t} + \frac{1}{\tau}\right)\left(\frac{\partial w}{\partial x} - \psi\right) \tag{14}$$

$$\left(\frac{\partial}{\partial t} + \frac{1}{\tau}\frac{E_0}{E_\infty}\right)p = \frac{2E_0 b}{h}\left(\frac{\partial}{\partial t} + \frac{1}{\tau}\right)wH(x - \mathfrak{a}) \tag{15}$$

These three equations together with Eqs 1 and 2 comprise a set of five equations for the determination of the five dependent variables M, S, p, w, and ψ as functions of x and t.

To complete the formulation of the problem, a crack growth criterion must be provided. This is done by generalizing the energy release rate (or crack driving force) parameter for dynamic viscoelastic crack propagation. The basis for this is the energy-balance expression

$$G = \frac{1}{\dot{\mathfrak{a}}B}\left\{\frac{dW}{dt} - \frac{dU}{dt} - \frac{dT}{dt} - \frac{dD}{dt}\right\} \tag{16}$$

where

W = work done by external forces,
U = internal stored or free energy,
T = kinetic energy,
D = viscous energy dissipation,
$\dot{\mathfrak{a}}$ = crack speed, and
B = width of specimen at crack plane.

Omitting some rather lengthly algebraic manipulations, Eq 16 can be recast in terms of the beam variables. The result is

$$G = \frac{1}{B}\left\{2pw - \frac{2E_0 B}{h}w^2 + \frac{h}{2b(E_0 - E_\infty)}\left[p - \frac{2E_0 b}{h}w\right]^2\right\}_{x=\mathfrak{a}(t)} \tag{17}$$

which indicates that G is a local criterion that can be evaluated at the crack tip, that is, the axial position $x = \mathfrak{a}(t)$.

It is instructive to note that the limiting form of Eq 17 as $E_0 \to E_\infty$ is

$$G = \frac{2Eb}{B}\left[\frac{w^2}{h}\right]_{x=\mathfrak{a}(t)} \tag{18}$$

which is just the same as derived previously for linear elastic behavior. Both of these results are consistent with the interpretation of the energy release rate as the amount of stored energy in the mechanical spring-dashpot element that holds the crack faces together; compare Bland [*13*]. This may well be of importance for future work using more complex viscoelastic models.

The equations that have been given here are equally valid for both rectangular DCB specimens where h is a constant and for contoured specimens where $h = h(x)$. But, application of these results in this paper is exclusively for rectangular DCB specimens. In this special case, $I = 1/12\ bh^3$, $A = bh$, and, as shown in Ref *10*, $\kappa = 5/6$. Solution of the field equations—Eqs 1, 2 and 13-15—is done by a finite-difference method [*14*]. At each time step, Eq 17 is evaluated. The crack is allowed to extend when G becomes equal to R, the fracture toughness, a prescribed critical value of the energy release rate taken as a material constant. In this way, the crack length can be computed as a function of time from the onset of unstable crack propagation in some prescribed initial configuration, the crack arrest point can be determined, and, if desired, conditions after arrest examined.

Computational Results

The computations given herein are based on the assumption that the specimens are wedge-loaded and that the wedge is inserted infinitely slowly. Then, the appropriate initial conditions are those for an equilibrium elastic configuration using the long-time elastic modulus E_∞. Crack growth commences from a state specified by an initial load point displacement or, equivalently, by an initial strain energy release rate. Material properties used for the analysis are given in Table 1. Note first that the material designated as "elastic" is one having the properties of A533B nuclear pressure vessel steel but with no rate- or time-dependence. The viscoelastic properties appropriate for a three-parameter solid representation for the four polymers included in Table 1 were provided by Rosenfield [*15*] on the basis of tests performed at moderate strain rates. The fracture toughness values are representative values taken from the literature [*2,5,6,16*].

While it is quite clear that all of the materials listed in Table 1 exhibit crack speed-dependent fracture toughness, one of the objectives of this analysis was to determine the extent to which such a dependence could be a result of ignoring the viscoelastic nature of the material behavior. If fracture toughness values obtained in this way were used to perform the computations, it would be difficult to judge this point. Accordingly, R denotes herein a single speed-independent toughness value (corresponding roughly to the initiation value) for each material considered.

Just as for computations performed with the linear elastic DCB crack propagation model, very nearly linear crack length-time results are obtained for dynamic viscoelastic crack propagation.[5] Hence, two key parameters can be associated with the results of each computation: the average crack speed

[5]Like the experimental observations, the computed crack length values typically increase with time in an approximately linear manner over a substantial portion of the rapid propagation event (for example, 80 percent), then increase less and less rapidly as the crack arrest point is approached. It should be recognized that these crack speed predictions are not forced upon the model (for example, by assuming constant speed) but instead result from satisfying the equations of motion and the specified fracture criterion. Consequently, qualitative agreement with the experimental results provides a check on the validity of the analysis.

TABLE 1—*Properties used for three-parameter solid linear viscoelastic representation of constitutive behavior in dynamic crack propagation computations.*

Material	E_0, MN/(mm)^2	E_∞, MN/(mm)^2	τ, s	ν (dimensionless)	$(E_0/\rho)^{1/2}$, m/s	R, J/m^2
Elastic	0.207	0.207	0	0.29	5000	12 100
Araldite B	0.00552	0.00480	345	0.40	2150	130
Clearcast	0.00519	0.00201	0.73	0.31	2080	320
Homalite 100	0.00476	0.00386	1460	0.30	1990	51
PMMA[a]	0.00453	0.00265	17	0.35	1940	500

[a] PMMA = Polymethyl methacrylate.

and the crack jump distance (the difference between crack length at arrest and initial crack length). Results computed for these two quantities for each of the five materials given in Table 1, using the configuration shown in Fig. 1, are given in Figs. 2 and 3.

Note that in the abscissa of Figs. 2 and 3 (and in the two which follow), the parameter G_Q denotes the strain energy release rate at the onset of crack propagation. It is possible for this number to be greater than R because the initial crack tip is blunted in the type of experiment being simulated by the computations. In fact, G_Q can be varied arbitrarily by increasing the radius of the initial blunted region. Because G_Q is a parameter which directly enters the computational model, it is the most convenient parameter with which to display the computational results.

One negative feature of the one-dimensional computational model is that

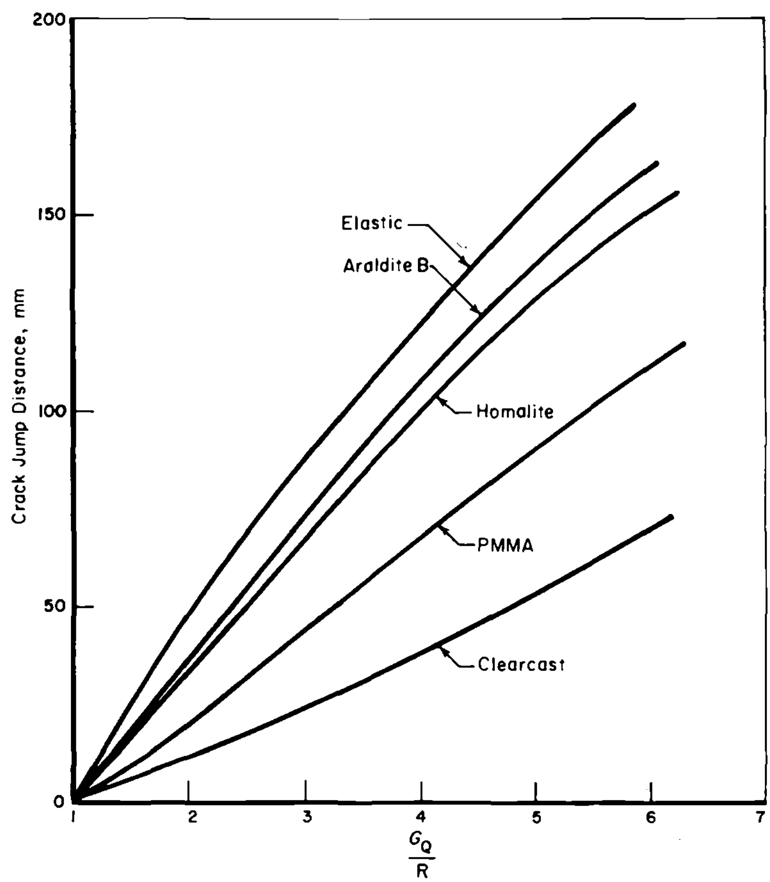

FIG. 2—*Computed values of crack jump distance in the DCB test specimen for various polymers.*

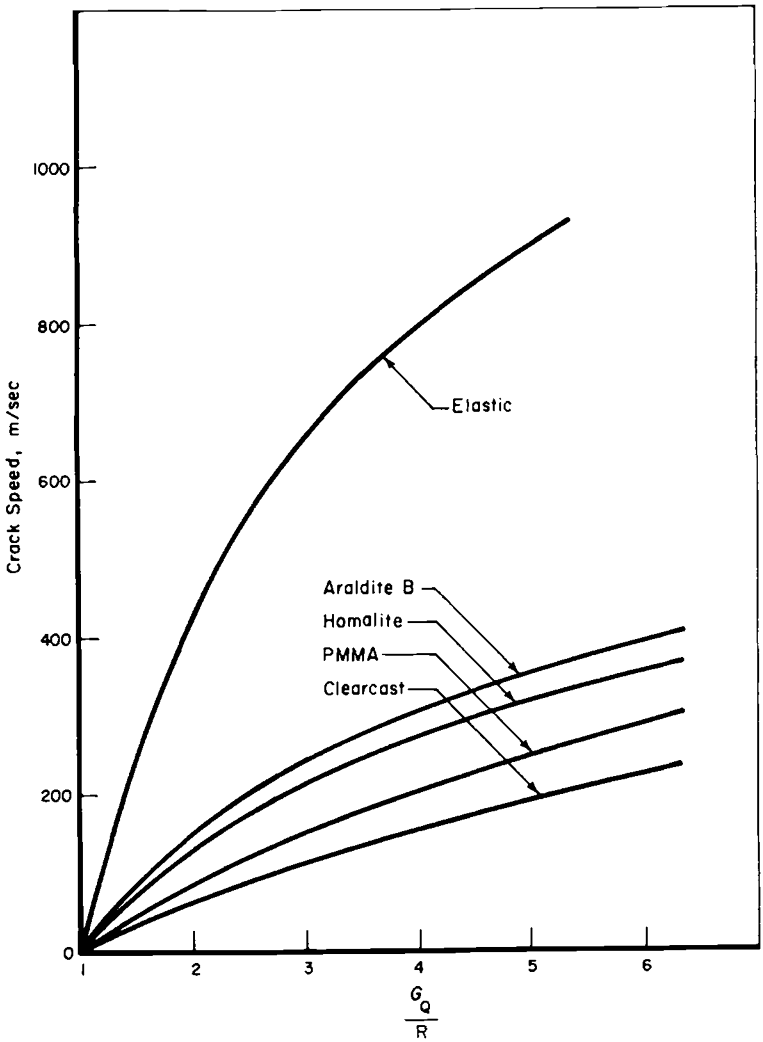

FIG. 3—*Computed values of the crack speed in the essentially constant crack speed portion of the unstable propagation event.*

it does not offer a direct calculation of the stress-intensity factor K. In linear elastic conditions, this is no particular drawback because the Freund-Nilsson equation, which expresses the equivalence between K and G, can be used to deduce one from the other. For plane-strain conditions, this equation is

$$K^2 = \frac{E}{1 - \nu^2} A(\dot{a}) G \tag{19}$$

where A denotes a universal function of the crack speed which, for speeds of interest here, is very nearly equal to unity; compare Kanninen [17]. For steady-state crack propagation in a brittle viscoelastic material, Kostrov and Nikitin [18] have shown that Eq 19 also holds if the short-time modulus is used. Therefore, since $K = K_D$ during crack propagation,

$$K_D{}^2 = \frac{E_0}{1 - \nu^2} R \tag{20}$$

where the crack speeds are assumed to be small enough that $A(\dot{\alpha})$ can be taken as unity.

It is of interest to examine the "dynamic" effect—the difference between the dynamic value of the stress-intensity factor at the instant of crack arrest and the corresponding static value. Because a crack speed-independent fracture toughness is used in this work, the dynamic stress intensity value at arrest is simply equal a priori to K_D. From Eq 19, the static value can be expressed as

$$K_a{}^2 = \frac{E_\infty}{1 - \nu^2} G_a \tag{21}$$

where G_a is the statically computed energy release rate for the crack length and load point displacement existing at the time of crack arrest. Hence, an expression of the "dynamic" effect can be made in terms of a parameter obtained by combining Eqs 20 and 21. This is

$$\frac{K_D}{K_a} = \left[\frac{E_0}{E_\infty} \frac{R}{G_a}\right]^{1/2} \tag{22}$$

Computational results illustrating the behavior of this parameter for the five different materials are shown in Fig. 4.

The relaxation times given in Table 1 are very large in comparison with the duration of a crack propagation event (typically a few hundred microseconds). This fact, taken together with the results showing the miniscule amounts of viscous energy dissipation during crack propagation in Fig. 5, suggests that the τ-parameter is not too significant. (In Fig. 5 the viscous energy dissipation D_a has been normalized by the initial stored energy U_0). Indeed, all of the results given in Figs. 2-5 can be ordered with respect to the ratio E_0/E_∞. Figures 6-8 show further correlations that can be achieved from the point of view that the short-term modulus governs dynamic crack propagation even though the long-term modulus was used to set the initial conditions.

Figure 6 shows a crossplot of results taken from Figs. 2 and 3 with the

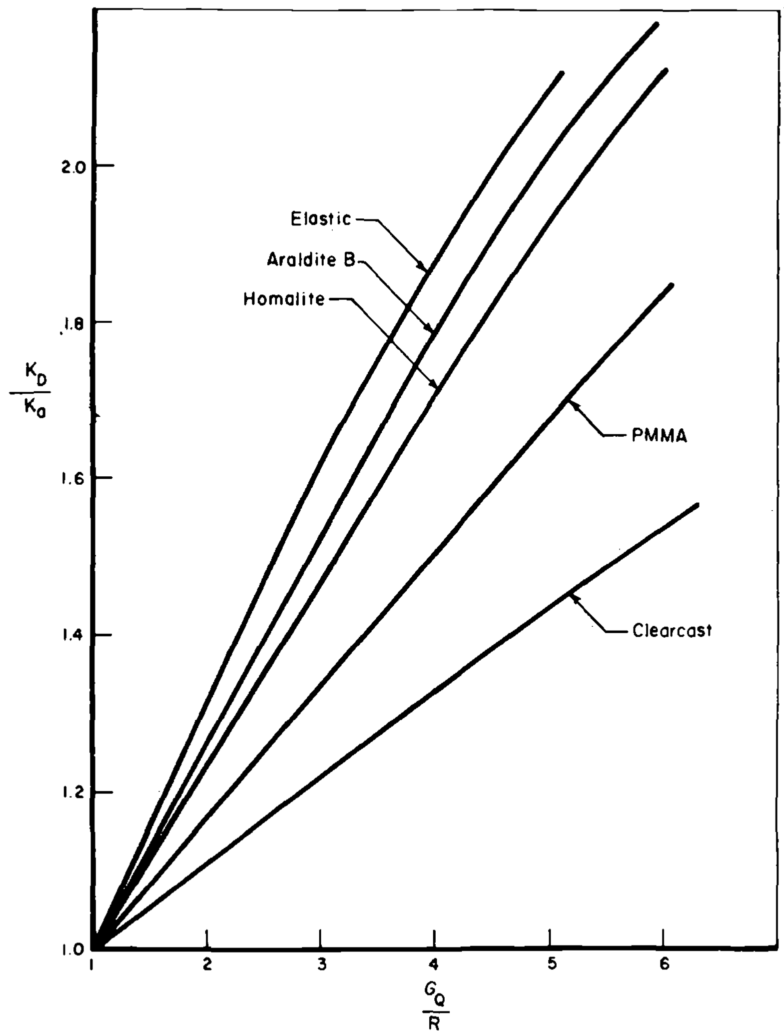

FIG. 4—*Computed values at crack arrest in the DCB test specimen for various polymers.*

crack speeds made dimensionless by introducing the dynamic bar wave speed, $(E_0/\rho)^{1/2}$. It can be seen that the previously disparate results now collapse onto virtually a single line.[6] Note that this kind of representation therefore offers a very convenient way of obtaining crack speeds for use in a crack arrest methodology because no direct measurement would be required. At the same time it should also be noticed that, in general, the G_Q/R values for the various materials at each point on a curve like that of Fig. 6 are dif-

[6]The fact that the order of the materials has changed in Fig. 6 is not believed to be significant inasmuch as the differences are comparable to the computational accuracy.

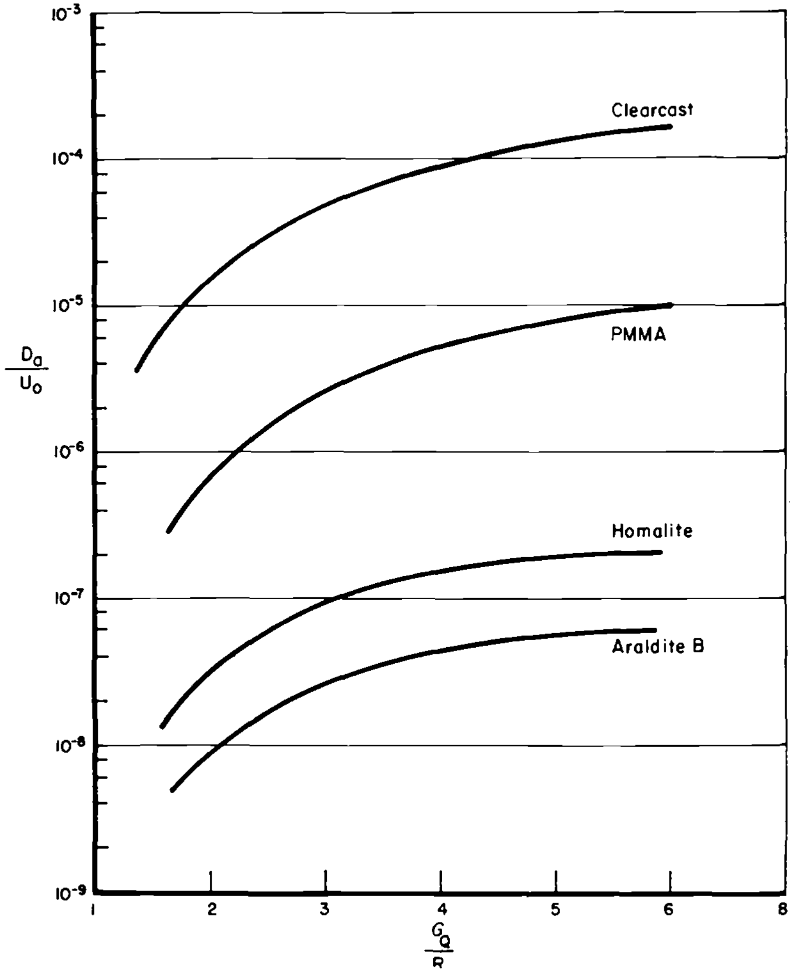

FIG. 5—*Fraction of initial strain energy dissipated viscously during unstable crack propagation.*

ferent. Consequently, the apparent agreement between the results of tests under different conditions, presented in terms of crack speed and crack jump distance, can be somewhat misleading.

The key curve in the crack arrest methodology approach suggested by Hahn et al [*1,2*] is one for the parameter K_D/K_Q as a function of the crack jump length. This quantity can be extracted approximately from the results obtained here in terms of the parameter

$$\frac{K_D}{K_Q} = \left[\frac{E_0}{E_\infty}\frac{R}{G_Q}\right]^{1/2} \tag{23}$$

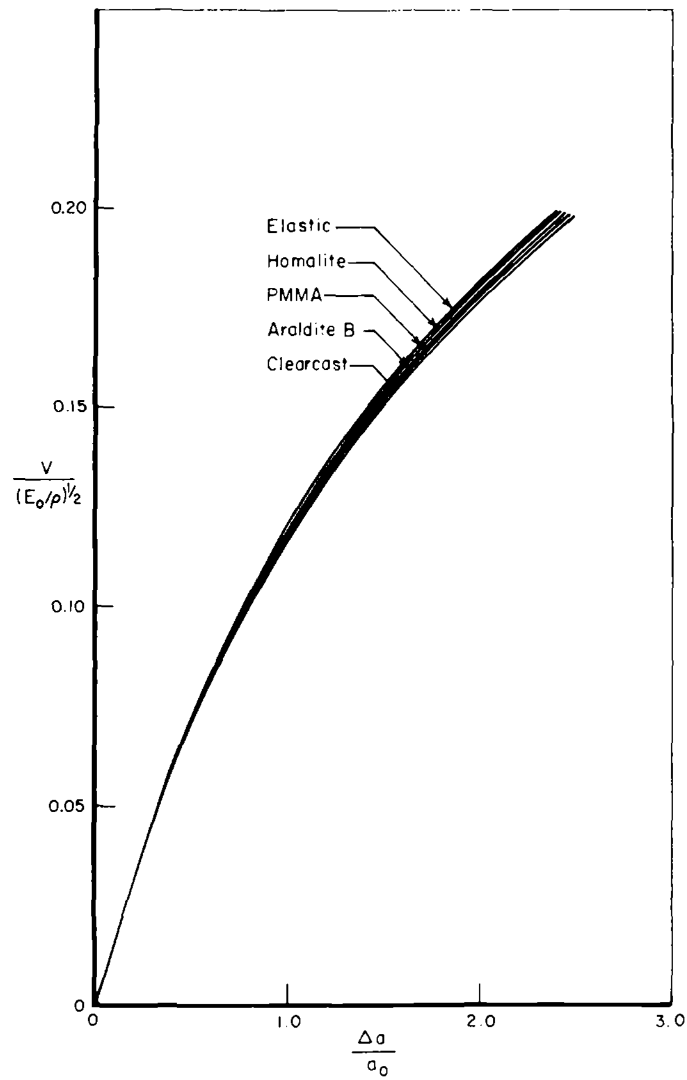

FIG. 6—*Computed values of the dimensionless crack speed versus crack jump distance.*

Such results (taken from Fig. 2) are shown in Fig. 7. It can be seen that, while a considerable degree of consolidation is achieved by this representation, viscoelastic effects have not been eliminated altogether. In fact, an ordering of material response in accord with the ratio E_0/E_∞ is still evident.

Finally, for completeness, results illustrating the dynamic effect at crack arrest are shown in Fig. 8. (These have been obtained by cross plotting the results given in Figs. 2 and 4.) It can again be seen that the spread is considerably reduced, but, unlike the crack speeds, not to the point where the viscoelastic efforts are completely eliminated.

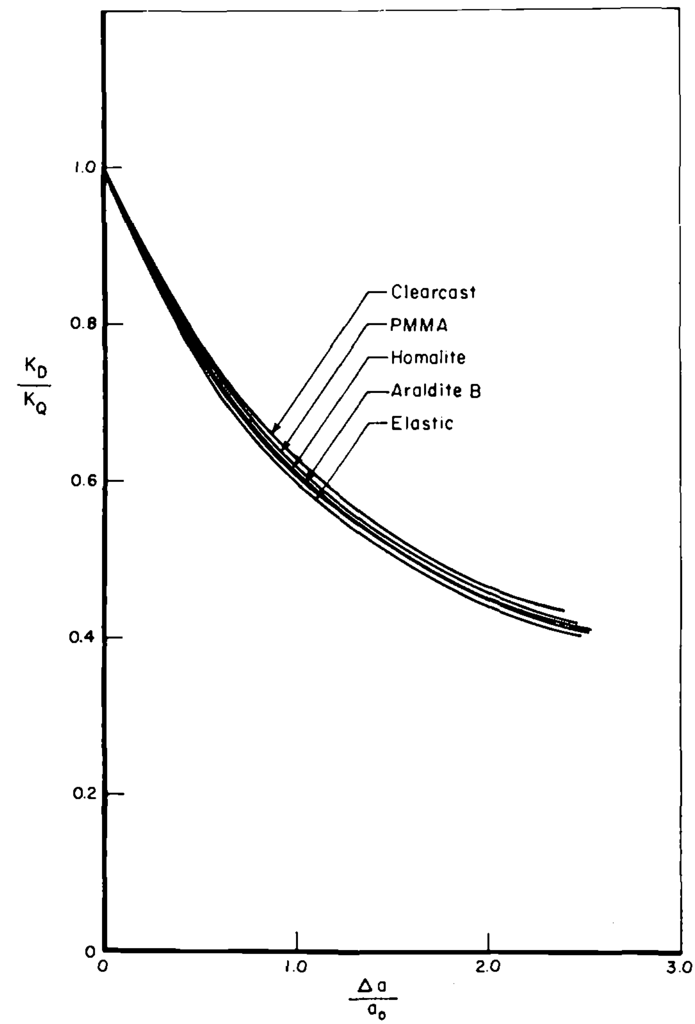

FIG. 7—*Computed relation between the crack jump distance and the ratio of the dynamic fracture toughness to the initial stress-intensity factor.*

Discussion of Results

The mathematical model described in this paper is simple in three respects. First, it allows the DCB specimen to have only one spatial degree of freedom. Second, it represents the viscoelastic constitutive behavior as a three-parameter solid with properties determined at moderate strain rates. Third, crack speed-independent fracture toughness values have been used exclusively. In defense of these, it can be said that the approach is intended only as a first step to explore the importance of combined dynamic and viscoelastic effects. And, despite the geometric and constitutive restrictions

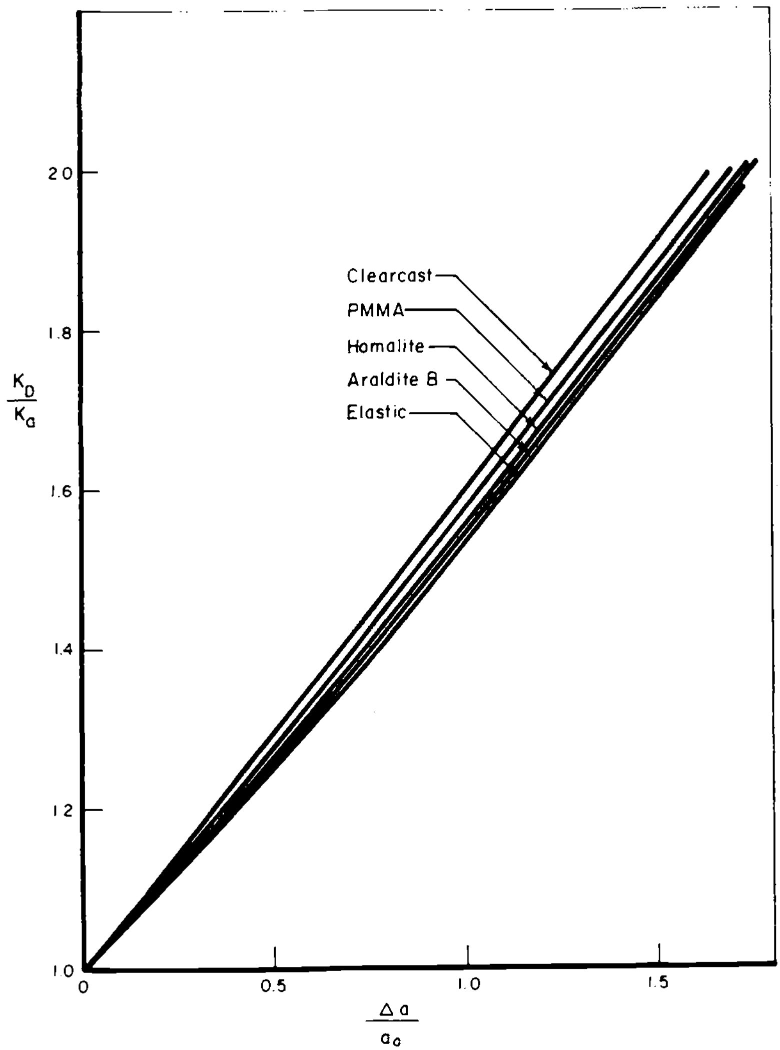

FIG. 8—*Computed relation between the crack jump distance and the ratio of the dynamic fracture toughness and the static stress-intensity factor corresponding to the point of crack arrest.*

on the applicability of the model, this has been accomplished. At the same time, it is clear that the results presented herein pertain only to one phase of the complete process—unstable crack propagation. Further work is needed to examine viscoelastic effects, both during loading prior to unstable growth and following the arrest of rapid crack propagation. It is also clear that the material parameters to be used in the viscoelastic model (a five-parameter solid model is now being developed) must be more representative of the strain rates occurring in dynamic crack propagation than are those that have been used in this paper.

These limitations aside, the computational approach presented here can begin to shed some light on the two prime controversial aspects of the subject that now exist. One of these is the possibility that the dynamic fracture toughness values—conventionally denoted as $K_D = K_D(\dot{a})$ where $\dot{a}$ is the crack speed—are not unique material property values as they must be. The second involves the connection, if any, that exists between the dynamic arrest event and the static conditions that exist sometime after arrest. The work described in this paper was motivated by the concern that many important experimental observations are being made on polymers and, because the interpretation of these experiments has generally ignored the viscoelastic nature of the materials, such observations may, to some extent, be hindering the resolution of these controversies.

The results presented show that, while the crack is in motion, the deformation is controlled by the short-time viscoelastic modulus and, at least to the point of crack arrest, the viscous energy dissipation is negligible. This suggests that the use of a linear elastic analysis to extract fracture parameters from tests on polymeric materials is not inappropriate. Indeed, as Figs. 6 and 7 show, crack speeds and stress-intensity factors relative to suitable reference values for the polymeric materials are not greatly different from the elastic material values. Caution must be exercised, however, to choose proper nondimensional forms. Clearly, these will depend on the initial conditions, the type of applied loading, and possibly other aspects of the test.

In observations of the dynamic stress-intensity factor after the arrest of rapid crack propagation, Kalthoff et al [19] have found qualitatively the same behavior in Araldite B and in Homalite 100. In both materials, the dynamic stress-intensity factor inferred from the caustic size at the instant of arrest is larger than the corresponding static stress-intensity factor. Following crack arrest, the dynamic stress-intensity factor oscillates with damped amplitude around the static value. However, the initial amplitude differs quite markedly in the two materials. Specifically, the initial amplitude—a value now often termed the "dynamic effect"—is a factor of 2 to 3 lower in Homalite 100 than in Araldite B. Kalthoff concludes that, because of the stronger viscoelastic behavior of Homalite 100, dynamic effects show up less clearly in it than in Araldite B and much less clearly than in steel.

The results for K_D/K_a, shown in Figs. 4 and 8, qualitatively show the same dynamic effect as observed by Kalthoff. This is, of the three materials addressed by Kalthoff, Homalite shows the least dynamic effect, Araldite B is somewhat greater, while the elastic material having the properties of steel shows the greatest. Quantitatively, however, the differences are substantially less than those observed. A plausible explanation for this deficiency of the computations likely lies in the use of speed-independent fracture toughnesses for the computations reported here. If more realistic fracture toughness-crack speed relations had been used (that is, monotonically increasing functions), the dynamic stress-intensity factor at arrest would be lower and, hence, nearer to the static value. The differences between the K_D/K_a values for the different materials might be expected to remain about the same, whereupon the relative differences would become much greater, consistent with Kalthoff's observations.

Conclusions

A preliminary assessment of dynamic crack propagation in a wedge-loaded DCB test specimen of a linear viscoelastic material (taken as a three-parameter solid) has been made. It has been found that, during the unstable crack propagation event itself, viscous energy dissipation is quite small. The differences that exist between the viscoelastic results and those for a rate-independent elastic material are therefore attributable to the rate-dependence of the modulus in viscoelastic behavior. Specifically, for a specimen loaded slowly enough that an equilibrium configuration corresponding to the long-time viscoelastic modulus characterizes the conditions at the initiation of rapid growth, it is shown in this paper first that the short-time viscoelastic modulus dominates during dynamic crack propagation, and second that correlations between elastic dynamic events and viscoelastic dynamic crack propagation/arrest can be made using only the short-time and long-time viscoelastic moduli.

The work has also reaffirmed a finding of earlier work that, for long crack jump lengths, no connection exists between the dynamic value of the crack driving force at the instant of crack arrest and the static value corresponding to the arrest state. Consequently, it seems clear that ascribing a material property to the static value of the stress-intensity factor long after arrest in steel, as suggested by Crosley and Ripling [*20*], on the basis of experiments done on Homalite or other highly viscoelastic materials, has doubtful validity.

Finally, it might be noted that dynamic viscoelastic analyses are but one way to generalize the more conventional fracture mechanics approaches to crack arrest determinations. Work by Achenbach and Kanninen [*21*] has addressed another generalization, dynamic plastic crack propagation, to treat propagation/arrest events in highly ductile materials where large-scale yielding accompanies crack growth. It is likely true that only by developing more realistic material models for viscoelastic and for plastic behavior can the limits of linear elastic dynamic behavior be properly determined and, perhaps, the present controversies completely resolved.

Acknowledgments

This paper is based directly upon research work supported by the U.S. Nuclear Regulatory Commission under Contract NRC-04-76-293-06, and has also drawn upon results obtained in research supported by the Army Research Office under ARO Project 11691-MS. The authors would like to thank J. F. Kalthoff of the Institut für Festkörpermechanik, for providing specimens of the optical polymers and A. R. Rosenfield of Battelle's Columbus Laboratories for obtaining the viscoelastic characterizations of these materials and of the other polymers used in our computations. The authors would also like to acknowledge the useful discussions on this subject that were held with G. T. Hahn, J. F. Kalthoff, and A. S. Kobayashi.

References

[*1*] Hahn, G. T. et al, "Critical Experiments, Measurements and Analyses to Establish a Crack-Arrest Methodology for Nuclear Pressure Vessel Steels," Report to the U.S. Nuclear Regulatory Commission, Battelle's Columbus Laboratories, Columbus, Ohio, 1974-1978.

[*2*] Hoagland, R. G., Rosenfield, A. R., Gehlen, P. C., and Hahn, G. T. in *Fast Fracture and Crack Arrest, ASTM STP 627,* American Society for Testing and Materials, 1977, p. 177.

[*3*] Hahn, G. T., Rosenfield, A. R., Marshall, C. W., Hoagland, R. G., Gehlen, P. C., and Kanninen, M. F. in *Fracture Mechanics,* N. Perrone et al, Eds., University of Virginia Press, Charlottesville, Va., 1978, p. 205.

[*4*] Kobayashi, A. S., Emery, A. F., and Mall, S. in *Fast Fracture and Crack Arrest, ASTM STP 627,* American Society for Testing and Materials, 1977, p. 95.

[*5*] Kobayashi, T. and Dally, J. W. in *Fast Fracture and Crack Arrest, ASTM STP 627,* American Society for Testing and Materials, 1977, p. 257.

[*6*] Kalthoff, J. F., Beinert, J., and Winkler, S. in *Fast Fracture and Crack Arrest, ASTM STP 627,* American Society for Testing and Materials, 1977, p. 161.

[*7*] Kalthoff, J. F., private communication, 1978.

[*8*] Kanninen, M. F., *International Journal of Fracture,* Vol. 10, 1974, p. 415.

[*9*] Kanninen, M. F., Popelar, C., and Gehlen, P. C. in *Fast Fracture and Crack Arrest, ASTM STP 627,* American Society for Testing and Materials, 1977, p. 19.

[*10*] Gehlen, P. C., Popelar, C. H., and Kanninen, M. F., *International Journal of Fracture,* Vol. 15, 1979, p. 281.

[*11*] Cowper, G. R., *Journal of Applied Mechanics,* Vol. 33, 1966, p. 335.

[*12*] Flügge, W., *Viscoelasticity,* Blaisdell, Waltham, Mass., 1967, pp. 16-17.

[*13*] Bland, D. R., *The Theory of Linear Viscoelasticity,* Pergammon, London, 1960, p. 49.

[*14*] Forsythe, G. E. and Wasow, W. R., *Finite-Difference Methods for Partial Differential Equations,* Wiley, New York, 1960, pp. 125-127.

[*15*] Rosenfield, A. R., private communication, 1978.

[*16*] Andrews, E. H. and Stevenson, A., *Journal of Materials Science,* Vol. 13, 1978, p. 1680.

[*17*] Kanninen, M. F. in *Numerical Methods in Fracture Mechanics,* A. R. Luxmoore and D. R. J. Owen, Eds., University College of Swansea Press, Swansea, U.K., 1978, p. 612.

[*18*] Kostrov, B. V. and Nikitin, L. V., *Archiwum Mechaniki Stosowanij,* Vol. 6, 1970, p. 749.

[*19*] Kalthoff, J. F., "Influence of Dynamic Effects on Crack Arrest," Institut für Festkörpermechanik reports to the Electric Power Research Institute, Freiburg, Germany, 1977-78.

[*20*] Crosley, P. B. and Ripling, E. J., *Fast Fracture and Crack Arrest, ASTM STP 627,* American Society for Testing and Materials, 1977, p. 372.

[*21*] Achenbach, J. D. and Kanninen, M. F. in *Fracture Mechanics,* N. Perrone, et al, Eds., University of Virginia Press, Charlottesville, Va., 1978, p. 649.

C.H. Popelar[1]

A Model for Dynamic Crack Propagation in a Double-Torsion Fracture Specimen

REFERENCE: Popelar, C. H., "**A Model for Dynamic Crack Propagation in a Double-Torsion Fracture Specimen,**" *Crack Arrest Methodology and Applications, ASTM STP 711*, G. T. Hahn and M. F. Kanninen, Eds., American Society for Testing and Materials, 1980, pp. 24-37.

ABSTRACT: A simple one-dimensional mathematical model for rapid fracture and crack arrest in a double-torsion fracture specimen is developed. The model indicates that the crack speed is limited by the torsional wave speed, which depends upon the shear wave speed and the cross-sectional geometry. By appropriate design of the specimen, it appears that some control can be exercised over the portion of the fracture toughness-crack speed relation that the crack tip samples. Analyses are performed for both speed-independent and speed-dependent fracture toughnesses. Qualitatively the predicted crack history for this specimen has many of the characteristics predicted and measured in the more traditional specimens.

KEY WORDS: double-torsion fracture specimen, fracture toughness, dynamic crack propagation

As shown in Fig. 1, the double-torsion (DT) fracture specimen consists of a rectangular plate with a starter notch or precrack. A four-point loading subjects the two halves of the specimen to equal and opposite torques. These specimens have been used, for example, to study the fracture of glass [*1*],[2] and polymers [*2,3*] and the stress corrosion cracking of steels [*4*].

While the mode of fracture is somewhat complicated, it is usually approximated as Mode I. A further approximation which is made in the static analysis of this specimen is that the crack front is straight and normal to the plane of the plate. Within these approximations an elastic analysis based upon the theory of torsion of thin rectangular sections yields a stress-intensity factor

[1] Professor, Department of Engineering Mechanics, The Ohio State University, Columbus, Ohio 43210.

[2] The italic numbers in brackets refer to the list of references appended to this paper.

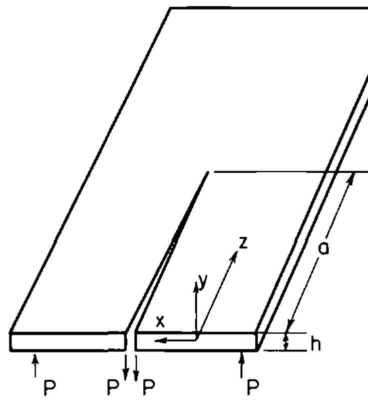

FIG. 1—*Double torsion fracture specimen.*

which is independent of the length of the crack. From an experimental viewpoint this feature of a fracture specimen is attractive.

The DT fracture specimen has been used primarily in studies of quasi-static stable crack growth. It seems reasonable that it could also be used to characterize the fracture toughness of rapidly propagating cracks. The specimen's relatively simple geometry and loading lends itself to analysis, which is an essential ingredient for interpreting experimental results.

The purpose here is to present a dynamic analysis of fracture and crack arrest in a DT specimen under fixed rotation loading. When approximations equivalent to those made in the static analysis of this specimen are invoked, the dynamic event is modeled by a one-dimensional torsional wave equation. There is a close analogy between portions of this analysis and Freund's [5] analysis of a very simple shear model for a running crack in a double cantilever beam beam (DCB) specimen. Since the latter is governed by a one-dimensional shear-wave equation, some of the mathematics, while couched in different terms, is necessarily similar. Nevertheless the DT specimen and its modeling are sufficiently different to warrant some repetition. Furthermore, in the present paper, an analysis is performed for a fracture toughness-crack speed dependency that closely approximates that found for polymers. In addition, the DT specimen is shown to exhibit a feature not found heretofore in more commonly used dynamic fracture specimens.

Governing Equations

Let the origin of the triad xyz be located at the loaded end of the specimen (see Fig. 1) with the z-axis directed along the centroidal axis of an arm of the specimen. The position of the crack tip at time t is defined by $z = a(t)$. Initially the crack is of length a_0 and its tip is blunted, which permits a supercritical condition to exist. The end $z = 0$ is twisted until the blunted tip is transformed into a sharp one and rapid fracture commences. During the subsequent motion the rotation of the cross section about the centroidal axis remains fixed; that is, a fixed grip loading is assumed.

The development of a mathematically tractable model for rapid fracture and crack arrest is guided by the assumptions inherent in previous static analyses. They are

1. The crack front is straight and normal to the plane of the plate.
2. The deformation of the arms of the specimen is described by the elastic theory of torsion of thin rectangular sections.
3. The stiffness of the plate ahead of the crack tip is sufficiently great that deformations there can be neglected.

The last approximation can be shown to be acceptable if the length of the ligament is greater than the width of the specimen's arm.

Experience indicates that for a brittle material the tension side of the crack will lead its compression side by as much as one or two plate thicknesses. The same phenomenon is also observed in quasi-static fracture of this specimen. After the initiation phase of propagation the crack tends to propagate in a self-similar manner. Therefore, after the initial transient, the exact shape of the crack front will have little influence upon the subsequent events for envisioned crack extensions exceeding several plate thicknesses. The curved crack front also yields a variable torsional rigidity in this region. This effect is minimal if the crack length is much greater than the length of the crack front. In this instance, therefore, the consequence of the first assumption is the neglect of the initial transient and the variable torsional rigidity.

The motion is governed by the torsional wave equation

$$GK\beta'' = \rho I\ddot{\beta} \qquad 0 < z < a(t) \tag{1}$$

where β is the rotation of the cross section about the z-axis (the primes and dots are used to denote differentiation with respect to z and t), respectively, and GK and ρI are the torsional rigidity and mass moment of inertia. It is convenient to introduce the twist gradient $\alpha(z, t) \equiv \beta'$ and angular velocity $\omega(z, t) \equiv \dot{\beta}$ and write Eq 1 and the compatibility condition as

$$\left.\begin{aligned} c^2\alpha' - \dot{\omega} &= 0 \\ \dot{\alpha} - \omega' &= 0 \end{aligned}\right\} \qquad 0 < z < a(t) \tag{2}$$

where $c = (GK/\rho I)^{1/2}$ is the torsional wave speed. In contrast to Freund's simple shear model of the DCB, the wave speed here depends upon the geometric properties of the specimen as well as on the material properties. The implications of this are discussed later. Upon differentiating with respect to t, the boundary conditions $\beta(0, t) = \beta_0$ and $\beta[a(t), t] = 0$ become

$$\begin{aligned} \omega &= 0 \qquad \text{at } z = 0 \\ \omega + \dot{a}\alpha &= 0 \qquad \text{at } z = a(t) \end{aligned} \tag{3}$$

At $t = 0$

$$\alpha = -\beta_0/a_0 \equiv \alpha_0, \qquad \omega = 0 \tag{4}$$

The fracture criterion is based upon a balance between the energy release rate or crack driving force, $\mathcal{G}$, and the dynamic fracture energy $\mathcal{R}$, which is a material property and may depend upon crack speed. That is

$$\begin{aligned} \mathcal{G} &= \mathcal{R}(\dot{a}), \qquad \dot{a} > 0 \\ \mathcal{G} &< \mathcal{R}, \qquad \dot{a} = 0 \end{aligned} \tag{5}$$

For fixed grip loading

$$\mathcal{G} = -(\dot{U} + \dot{T})/\dot{a}h \tag{6}$$

where h is the thickness of the specimen at the crack plane

$$U = Gk \int_0^a \alpha^2 \, dz \tag{7}$$

is the strain energy, and

$$T = \rho I \int_0^a \omega^2 dz \tag{8}$$

is the kinetic energy of the specimen. After the introduction of Eqs 7 and 8 into Eq 6, a subsequent integration by parts and employment of Eqs 2 and 3, then

$$\mathcal{G} = \frac{GK}{h}(1 - \dot{a}^2/c^2)\alpha^2(a, t), \qquad \dot{a} < c \tag{9}$$

It follows that at incipient crack growth the static energy release rate is

$$\mathcal{G}_Q = GK\alpha_0{}^2/h \tag{10}$$

There are two distinct but related problems that are of interest. In both cases the solution to Eq 2 satisfying Eqs 3 and 4 is required. In the first case the crack history is prescribed; for example, $a(t)$ is experimentally measured, and the dynamic fracture energy as a function of crack speed is desired. With $a(t)$ known, $\mathcal{G}$ is determined explicitly by Eq 9 and $\mathcal{R}$ is given by Eq 5. In the second problem the fracture energy is prescribed and the crack history is required. When Eq 9 is introduced into Eq 5, the resulting equation governs the crack history. In the following, both problems are investigated.

Prescribed Crack History

It is assumed here that $a(t)$ is prescribed. The method of characteristics provides a rather straightforward solution. The characteristics, depicted in Fig. 2, are $z \pm ct =$ constant, and on them $\omega \pm c\alpha =$ constant. At $t = 0$ the crack tip abruptly changes from a blunt to a sharp one and it commences propagating at the speed $\dot{a}_0$. An unloading wave emanating from A, the initial position of the crack tip, propagates with the speed c along the characteristic AB toward the end $z = 0$ (B). There it is reflected and propagates along BC and overtakes the crack tip at C. Associated with C is a further unloading which propagates along CD, and the process is repeated.

Along the arc AC the method of characteristics yields

$$\alpha_N = \alpha_0/(1 + \dot{a}_N/c), \qquad \omega_N = -\dot{a}_N\alpha_0/(1 + \dot{a}_N/c) \tag{11}$$

where the subscript denotes the point in the solution domain at which the variable is evaluated. Between Points C and E where the wave front overtakes the crack tip for the second time

$$\alpha_R = \frac{\alpha_0(1 - \dot{a}_N/c)}{(1 + \dot{a}_N/c)(1 + \dot{a}_R/c)}, \qquad \omega_R = -\frac{\dot{a}_R\alpha_0(1 - \dot{a}_N/c)}{(1 + \dot{a}_N/c)(1 + \dot{a}_R/c)} \tag{12}$$

Further values of these variables along $z = a(t)$ can be obtained by induction.

The solution procedure can be used to determine α and ω for other points.

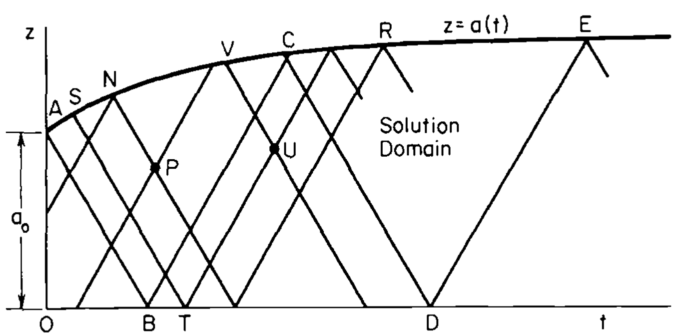

FIG. 2—*Family of characteristics.*

Of course for a point in the region AOB, $\omega = 0$ and $\alpha = \alpha_0$. At Point P within the region ABC

$$\alpha_P = \alpha_0/(1 + \dot{a}_N/c) \qquad \omega_P = -\dot{a}_N\alpha_0/(1 + \dot{a}_N/c) \tag{13}$$

and for point U in region BCD

$$\alpha_U = \frac{\alpha_0(1 - \dot{a}_S\dot{a}_V/c^2)}{(1 + \dot{a}_V/c)(1 + \dot{a}_S/c)}, \qquad \omega_U = \frac{\alpha_0(\dot{a}_S - \dot{a}_V)}{(1 + \dot{a}_V/c)(1 + \dot{a}_S/c)} \tag{14}$$

and so on.

When Eq 9 is introduced into Eq 5, it follows for Eqs 11 and 12 that

$$\begin{aligned} \mathcal{R}(\dot{a}_N) &= \mathcal{G}_Q \frac{1 - \dot{a}_N/c}{1 + \dot{a}_N/c}, \qquad N \text{ on } AC \\ \mathcal{R}(\dot{a}_R) &= \mathcal{G}_Q \frac{(1 - \dot{a}_R/c)(1 - \dot{a}_N/c)^2}{(1 + \dot{a}_R/c)(1 + \dot{a}_N/c)^2}, \qquad R \text{ on } CE \end{aligned} \tag{15}$$

and so on. Equation 15 implies that at initiation the energy release rate decreases precipitously from $\mathcal{G}_Q$ to $\mathcal{G}_Q(1 - \dot{a}_0/c)/(1 + \dot{a}_0/c)$.

Constant Crack Speed

Assume that the crack propagates at the constant speed $\dot{a} = \dot{a}_0$. In the time t_C that it takes the crack tip to advance to C, the wave front will have traveled the distance $a_0 + a_C$. It follows that

$$a_C = a_0 \frac{1 + \dot{a}_0/c}{1 - \dot{a}_0/c}, \qquad t_C = \frac{2a_0/c}{1 - \dot{a}_0/c} \tag{16}$$

A similar deduction yields

$$a_E = a_0 \frac{(1 + \dot{a}_0/c)^2}{(1 - \dot{a}_0/c)^2}, \qquad t_E = \frac{4a_0/c}{(1 - \dot{a}_0/c)^2} \tag{17}$$

and so on.

Assuming that the crack continues propagating at the speed $\dot{a}_0$ after the wave front overtakes the crack tip, then it follows from Eq 15 that

$$\begin{aligned} \mathcal{R}(\dot{a}_0) &= \mathcal{G}_Q \frac{1 - \dot{a}_0/c}{1 + \dot{a}_0/c}, \qquad a_0 < a < a_C \\ \mathcal{R}(\dot{a}_0) &= \mathcal{G}_Q \left(\frac{1 - \dot{a}_0/c}{1 + \dot{a}_0/c}\right)^3, \qquad a_C < a < a_E \end{aligned} \tag{18}$$

and so on. It is apparent from Eq 18 that each time a wave front overtakes the constant-speed crack tip there is a discontinuous decrease of the energy release rate. For this to occur $\mathcal{R}(\dot{a})$ must have a vertical slope at $\dot{a} = \dot{a}_0$. Several polymers seem to exhibit this characteristic; for example, see Kobayashi and Mall [*6*].

Prescribed Fracture Toughness

Speed-Independent Toughness

Consider a material whose fracture toughness is independent of crack speed; that is

$$\mathcal{R}(\dot{a}) = \mathcal{R}_m \leq \mathcal{G}_Q \tag{19}$$

It follows from combining Eqs 18 and 19 that the crack advances at the constant speed

$$\frac{\dot{a}_0}{c} = \frac{\mathcal{G}_Q/\mathcal{R}_m - 1}{\mathcal{G}_Q/\mathcal{R}_m + 1} \quad , \; a_0 < a < a_C \tag{20}$$

In the regions *ABC* and *BCD* of the solution domain, Eqs 13 and 14 yield, respectively

$$\alpha = \alpha_0/(1 + \dot{a}_0/c) \qquad \omega = -\dot{a}_0\alpha_0/(1 + \dot{a}_0/c) \tag{21}$$

and

$$\alpha = \alpha_0(1 - \dot{a}_0/c)/(1 + \dot{a}_0/c) \qquad \omega = 0 \tag{22}$$

Equations 21 and 22 indicate that behind the reflected wave front the specimen is at rest and, in particular, a discontinuous decrease in α occurs as this wave front advances. Consequently, when the wave front overtakes the crack tip, $\mathcal{G} < \mathcal{R}_m$, the crack arrests, and all motion ceases. The rate of twist is given by Eq 22 for all subsequent time. Furthermore, Eqs 16 and 20 yield for the crack length at arrest

$$a_C = \mathcal{G}_Q a_0/\mathcal{R}_m \tag{23}$$

For a speed-independent toughness, Eq 23 suggests that for this test specimen the dynamic fracture toughness can be inferred from the initial and final crack lengths and the initial twist suffered by the specimen. The speed of the crack tip is given by Eq 20.

The introduction of Eqs 20 and 22 into Eq 9 yields for the energy release rate after arrest

$$\mathcal{G}_a = \mathcal{R}_m{}^2/\mathcal{G}_Q \tag{24}$$

whereas prior to arrest $\mathcal{G} = \mathcal{R}_m$. Irwin and Wells [7] hypothesized that crack arrest may be viewed as the reversal of crack initiation. By this reasoning the energy release rate after crack arrest is a material property in much the same way that the energy release rate at initiation for a sharp crack is a material property. This concept of crack arrest has been the subject of much controversy. It is now generally recognized, however, that the energy release rate after crack arrest is not a material property as Eq 24 demonstrates. Furthermore, depending upon the degree of initial bluntness, $\mathcal{G}_a$ can significantly underestimate $\mathcal{R}_m$.

A Speed-Dependent Fracture Toughness

Many polymers have a dynamic fracture energy-crack speed dependence similar to that illustrated in Fig. 3*a*. Limited data indicate that a similar dependence may exist for some steels. The shear wave speed is c_2, and $\dot{a}_l$ is the limiting crack speed at which the toughness becomes virtually unbounded. This limiting speed for polymers is of the order of $c_2/3$. It has been suggested that this toughness relation can be approximated by the dashed lines. This idealization is shown in Fig. 3*b* for the DT fracture specimen. Because the torsional wave speed depends upon the specimen's cross section, then $\dot{a}_l/c$ can be greater than or less than unity. Immediate consideration will be given to $r \equiv \dot{a}_l/c < 1$.

For the idealized fracture toughness, the crack speed will be a piecewise constant with possible discontinuities occurring whenever a wave front overtakes the crack tip. In the following it will be assumed that

$$\mathcal{R}_m/\mathcal{G}_Q < (1 - r)/(1 + r) \tag{25}$$

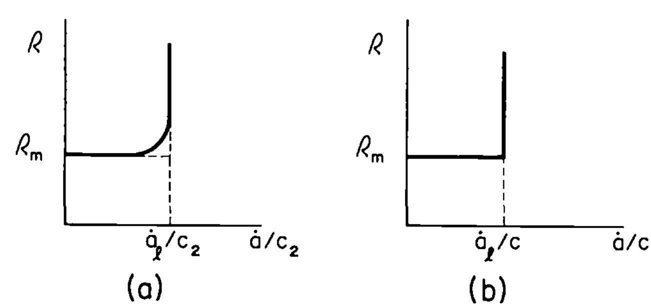

FIG. 3—*Real and idealized fracture energies.*

In this way the event is initially governed by the vertical branch of $\mathcal{R}(\dot{a})$. Otherwise the crack history is governed by the horizontal branch and is identical to that for a speed-independent toughness.

If

$$\left(\frac{1-r}{1+r}\right) > \frac{\mathcal{R}_m}{\mathcal{G}_Q} > \left(\frac{1-r}{1+r}\right)^2 \tag{26}$$

the crack arrests as soon as the first torsional wave overtakes the crack tip. While the tip is advancing

$$\mathcal{R}(\dot{a}_l) = \mathcal{G} = \mathcal{G}_Q(1-r)/(1+r) \tag{27}$$

At the instant $t_1 = 2a_0/(c - \dot{a}_l)$ of crack arrest

$$a_1 \equiv a(t_1) = a_0(1+r)/(1-r) \tag{28}$$

and afterwards

$$\mathcal{G}_a = \mathcal{G}_Q\left(\frac{1-r}{1+r}\right)^2 \tag{29}$$

For yet smaller values of $\mathcal{R}_m/\mathcal{G}_Q$, the number of times a reflected wave overtakes the crack tip is $n + 1$ where n satisfies

$$\left(\frac{1-r}{1+r}\right)^{2n} > \frac{\mathcal{R}_m}{\mathcal{G}_Q} > \left(\frac{1-r}{1+r}\right)^{2n+1}; \qquad n \geq 1 \tag{30}$$

The crack speed during the first n traverses of the torsional waves is $\dot{a}_l$. At the instant

$$t_n = t_{n-1} + 2a_{n-1}/(c - \dot{a}_l)$$

that the crack tip is overtaken for the nth time

$$a_n \equiv a(t_n) = a_0\left(\frac{1+r}{1-r}\right)^n \tag{31}$$

During the subsequent motion the horizontal branch $\mathcal{R} = \mathcal{R}_m$ governs. Consequently this final segment of the event is identical to that for a speed-independent toughness if a_0 and α_0 are replaced, respectively, by a_n and $\alpha_0 a_0/a_n$. The crack speed for this interval is determined from

$$\frac{\mathcal{R}_m}{\mathcal{G}_Q} = \left(\frac{1-s}{1+s}\right)\left(\frac{1-r}{1+r}\right)^{2n}; \qquad s \equiv \dot{a}/c \tag{32}$$

At the time $t = t_n + 2a_n/(c - \dot{a})$ of crack arrest

$$\frac{a}{a_0} = \frac{\mathcal{G}_Q}{\mathcal{R}_m}\left(\frac{1-r}{1+r}\right)^{n} \tag{33}$$

and after arrest

$$\frac{\mathcal{G}_a}{\mathcal{R}_m} = \frac{\mathcal{R}_m}{\mathcal{G}_Q}\left(\frac{1+r}{1-r}\right)^{2n} \tag{34}$$

For purposes of illustration and without a great deal of loss of generality, assume in the sequel that $n = 1$. In this case the crack history is governed by the vertical branch of Fig. 3 during the first traversing of the unloading wave, while the horizontal branch governs the event during the second and final passage of the unloading wave.

In addition to the fracture energy F, considerable insight into the dynamic fracture process is afforded by the strain and kinetic energies and their contributions to the crack driving force. With Eqs 11 and 12, these energies can be computed in a straightforward manner. After some manipulations and normalizing with respect to the initial strain energy

$$U_0 = GKa_0\alpha_0^2 \tag{35}$$

they can be written as follows

For $a_0 \leq a \leq a_0(1 + r)$:

$$\begin{aligned} U/U_0 &= 1 - (a/a_0 - 1)/(1 + r) \\ T/U_0 &= r(a/a_0 - 1)/(1 + r) \\ F/U_0 &= (a/a_0 - 1)(1 - r)/(1 + r) \end{aligned} \tag{36}$$

For $a_0(1 + r) \leq a \leq a_0(1 + r)/(1 - r)$:

$$\begin{aligned} \frac{U}{U_0} &= \frac{2 - (1-r)^2 - (a/a_0 - 1)(1 - r)}{(1 + r)^2} \\ \frac{T}{U_0} &= \frac{2r^2 - r(a/a_0 - 1)(1 - r)}{(1 + r)^2} \\ \frac{F}{U_0} &= \frac{(a/a_0 - 1)(1 - r)}{1 + r} \end{aligned} \tag{37}$$

For $a_0\left(\frac{1+r}{1-r}\right) \leq a \leq a_0(1+s)\left(\frac{1+r}{1-r}\right)$:

$$\frac{U}{U_0} = \frac{(1-r)(1+3r+s+rs) - (a/a_0 - 1)(1-r)^2}{(1+s)(1+r)^2}$$

$$\frac{T}{U_0} = \frac{s(a/a_0 - 1)(1-r)^2 - 2rs(1-r)}{(1+s)(1+r)^2} \tag{38}$$

$$\frac{F}{U_0} = \frac{4r(r+s) + (1-s)(a/a_0 - 1)(1-r)^2}{(1+s)(1+r)^2}$$

And for $a_0(1+s)\left(\frac{1+r}{1-r}\right) \leq a \leq a_0\left(\frac{1+s}{1-s}\right)\left(\frac{1+r}{1-r}\right)$:

$$\frac{U}{U_0} = \frac{(1-r)[1+3r+2s-s^2-s^2r-(1-r)(1-s)(a/a_0-1)]}{(1+r)^2(1+s)^2}$$

$$\frac{T}{U_0} = \frac{s(1-r)[2(r+s)-(1-r)(1-s)(a/a_0-1)]}{(1+r)^2(1+s)^2} \tag{39}$$

$$\frac{F}{U_0} = \frac{(1-s)(1-r)^2(a/a_0-1) + 4r(r+s)}{(1+s)(1+r)^2}$$

The limits of the foregoing regions represent the crack's length at A, B, C, D, and E in Fig. 2.

For $\mathcal{G}_Q/\mathcal{R}_m = 12$ and $\dot{a}_l/c = 1/2$, the variation of the energies with crack extension is shown in Fig. 4. The initial coincidence of the fracture energy and the kinetic energy is fortuitous. For purposes of comparison the static solution is given by the dashed curves.

The crack tip emerges from the notch with a speed $\dot{a}_l$. Simultaneously the rate of twist at the crack tip decreases abruptly from α_0 to $2\alpha_0/3$ (compare Eq 10) and $\mathcal{G}$ drops from $\mathcal{G}_Q$ to $\mathcal{G}_Q/3$ (Eq 27). Because of this sudden decrease in α, the specimen is no longer in equilibrium and an unloading torsional wave commences propagating at a speed c toward the loaded end. This unloading wave produces a reduction of strain energy and an increase in the kinetic energy as more of the specimen gathers momentum. The difference between the rate of decrease of the strain energy and the rate of increase of kinetic energy is the rate at which energy is absorbed at the crack tip. These rates remain constant until the wave front reaches the loaded end and is reflected. As the reflected wave propagates toward the crack tip, it brings to rest the material behind its front and further reduces α, but to a lesser degree

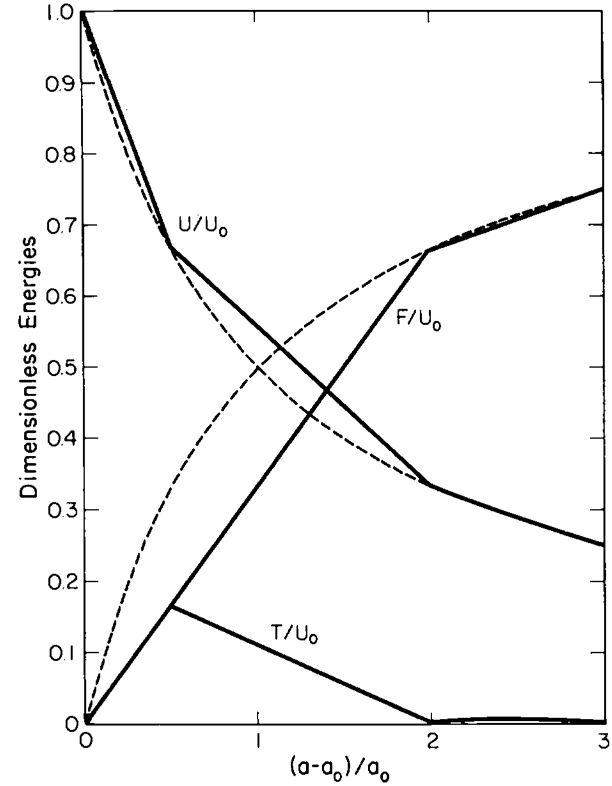

FIG. 4—*Variation of strain, kinetic, and fracture energies with crack growth for* $\mathcal{G}_Q/\mathcal{R}_m$ = 12 *and* $\dot{a}_I/c = 1/2$.

than the initial wave. Consequently, both the kinetic and strain energies decrease. It is obvious that initially ($a < \sqrt{3}\ a_0$) the static solution overestimates the crack driving force and then underestimates it during the latter stages of this portion of the event.

At the instant the wave front overtakes the crack tip, the specimen is momentarily at rest, but the crack driving force is greater than the minimum value required to sustain growth. Consequently, a second unloading wave begins propagating toward the loaded end and crack growth continues. In this case, however, the crack advances at the slower speed $\dot{a}/c = 1/7$ as determined by Eq 32 with $n = 1$. Moreover, the magnitude of this second unloading is smaller than the first one and produces less-dramatic changes in the strain and kinetic energies. The preceding events are repeated with the exception that $\mathcal{G}$ decreases from $\mathcal{R}_m$ to $\mathcal{G}_a$, Eq 34, when the second reflected wave overtakes the crack tip. Consequently, the crack arrests, the specimen is quiescent, and the final crack length is given by Eq 33. The crack history for this example is shown in Fig. 5. The crack history and variations of strain, kinetic, and fracture energies are reminiscent of their predicted counterparts for the DCB fracture specimen; for example, see Gehlen et al [8].

If $\dot{a}_l > c$, then the horizontal branch of Fig. 3*b* governs the event and the effect is as if the fracture toughness were speed-independent. The crack speed is given by Eq 20. Furthermore, the crack arrests at the instant the first reflected wave overtakes the crack tip. The strain, kinetic, and fracture energies are given by Eqs 37 and 38 if $\dot{a}_l$ is replaced by $\dot{a}_0$.

Figure 6 is a plot of the stress-intensity factor K_a at arrest versus the stress-intensity factor K_Q at initiation normalized with respect to the minimum dynamic fracture toughness K_m for the material depicted in Fig. 3*b* and $\dot{a}_l/c = 1/2$. Except for isolated values of K_Q, K_a always underestimates K_m and is only an adequate approximation of K_m for limited values of K_Q.

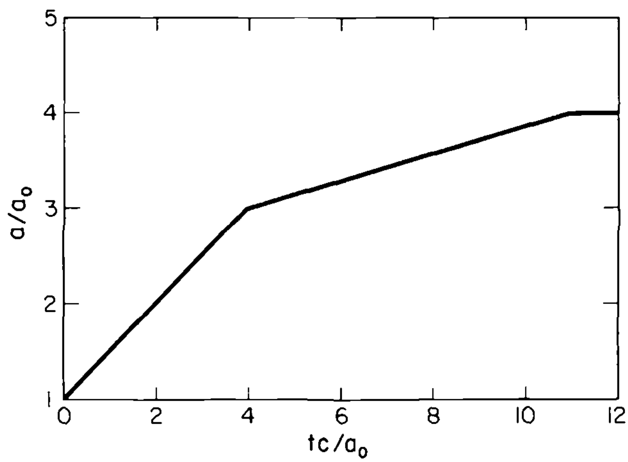

FIG. 5—*Crack history for* $\mathcal{G}_Q/\mathcal{R}_m = 12$ *and* $\dot{a}_l/c = 1/2$.

Discussion

One of the principal material parameters of interest is $\mathcal{R}_m$. The present model of dynamic crack propagation in a DT specimen suggests a potentially simple means of determining $\mathcal{R}_m$ for materials possessing a dynamic fracture toughness-crack speed dependency depicted in Fig. 3. Since the torsional wave speed c depends upon the specimen's cross-sectional geometry, then by appropriate design of the specimen it is possible to insure $c < \dot{a}_l$. Consequently, only the horizontal branch of the idealized fracture toughness of Fig. 3*b* or a limited portion of the real toughness of Fig. 3*a* is sampled irrespective of the value of $\mathcal{G}_Q$. It follows from Eq 23 that

$$\mathcal{R}_m = \mathcal{G}_Q a_0/a_c \tag{40}$$

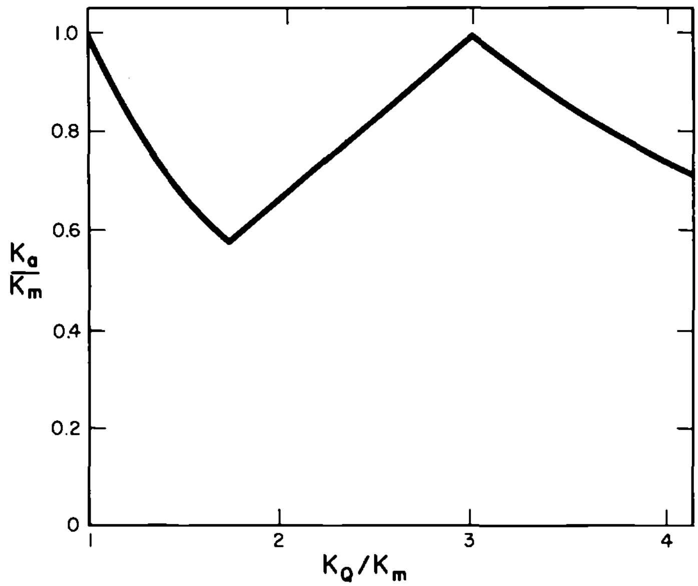

FIG. 6—K_a/K_m *versus* K_Q/K_m *for the material of Fig. 3*b *with* $\dot{a}_1/c = 1/2$.

Moreover, Eq 40 is valid for speed-independent fracture toughnesses. Since all the parameters on the right side of Eq 40 can be easily measured, then $\mathcal{R}_m$ is readily determined.

The present model should furnish sufficient quantitative results and understanding of rapid fracture and crack arrest in the double-torsion specimen to provide a rational basis for its design and to aid in the interpretation of experimental results.

References

[1] Kies, J. A. and Clark, A. B. J. in *Fracture 1969*, P. L. Pratt, Ed., Chapman and Hall, London, p. 483.
[2] Knauss, W. G. in *The Mechanics of Fracture*, F. Erdogan, Ed., AMD, Vol. 19, American Society of Mechanical Engineers, 1976, p. 69.
[3] Beaumont, P. W. R. and Young, R. J., *Journal of Materials Science*, Vol. 10, 1975, p. 1334.
[4] Beachem, C. D., Kies, J. A., and Brown, B. F., *Materials Research and Standards*, Vol. 11, 1971, p. 30.
[5] Freund, L. B., *Journal of the Mechanics and Physics of Solids*, Vol. 25, 1977, p. 69.
[6] Kobayashi, A. S. and Mall, S., *Experimental Mechanics*, Vol. 18, 1978, p. 11.
[7] Irwin, G. R. and Wells, A. A., *Metallurgical Reviews*, Vol. 10, 1965, p. 223.
[8] Gehlen, P. C., Popelar, C. H., and Kanninen, M. F., *International Journal of Fracture*, Vol. 15, 1979, p. 281.

J.F. Malluck[1] *and W.W. King*[2]

Fast Fracture Simulated by Conventional Finite Elements: A Comparison of Two Energy-Release Algorithms

REFERENCE: Malluck, J. F. and King, W. W., **"Fast Fracture Simulated by Conventional Finite Elements: A Comparison of Two Energy-Release Algorithms,"** *Crack Arrest Methodology and Applications, ASTM STP 711*, G. T. Hahn and M. F. Kanninen, Eds., American Society for Testing and Materials, 1980, pp. 38–53.

ABSTRACT: Three problems of constant-speed fast fracture have been simulated by finite-element analyses. The mechanism for the release of mechanical energy was the gradual relaxation of the restraining reaction at a node adjacent to the crack tip. The numerical results are used to compare the performances of two recently proposed methods for prescribing the manner in which the relaxing force depends upon the crack-tip location between nodes in the finite-element model. Energy-release rates generated from the algorithm proposed by Rydholm et al are found to be in slightly better accord with continuum elastodynamics than are those produced by the algorithm previously proposed by the authors.

KEY WORDS: crack propagation, fast fracture, finite elements, energy dissipation

The results of a number of two-dimensional finite-element analyses of rapid opening-mode crack propagation in linearly elastic isotropic bodies have been published during the past three years [*1*-*9*].[3] With two exceptions [*8*, *9*], these studies have had in common the simulation of crack propagation by the sequential release of nodes along one edge of a finite-element model which takes advantage of elastodynamic symmetry about the crack-tip trajectory and which is composed of regular elements; that is, the elements have

[1]Senior aircraft structures engineer, Aeronautical Research Department, Lockheed-Georgia Co., Marietta, Ga.

[2]Professor, School of Engineering Science and Mechanics, Georgia Institute of Technology, Atlanta, Ga. 30332; also, consultant, Lockheed-Georgia Co., Marietta, Ga.

[3]The italic numbers in brackets refer to the list of references appended to this paper.

stiffness and inertia properties which do not vary with crack-tip location, and the crack-tip stress singularity is not represented in the finite-element model. Under these conditions it is not evident what mechanism should be provided for the release of mechanical energy that accompanies crack extension. Several authors [*1,3,4,6*] have proposed algorithms by which, as the crack tip is imagined to pass, the condition of a crack-trajectory node is smoothly altered from that of zero displacement to that of zero external nodal force normal to the crack plane. The negative work done by the diminishing force restraining the crack-trajectory node is the energy-release mechanism. The relative merits of the different algorithms are difficult to assess because of the absence of benchmark analytical solutions to problems of fast fracture in finite bodies and because of the different finite elements (typically constant-strain triangles or isoparametric quadrilaterals), mass distribution schemes (lumped or consistent), and time-integration algorithms (usually central difference or Newmark-β) employed by the several investigators. The present paper is concerned with comparisons of results obtained from the closely related algorithms proposed by the authors [*3*] and by Rydholm, Fredriksson, and Nilsson [*4*]. A common finite-element model has been employed for the simulation of three problems of extension, at a constant rate, of a central crack in a square sheet.

The Near-Tip Nodal Force

Figure 1 depicts a near neighborhood of the simulated crack tip in a finite-element model for a problem exhibiting elastodynamic symmetry about the crack plane, the base of the model coinciding with the crack-tip trajectory. During the time interval in which the crack tip would pass the location of Node A and proceed to the location of Node B in the finite-element model, the restraining force, F, is prescribed to decay from the reaction F_0, computed at the instant prior to release of node A, to zero when the crack tip

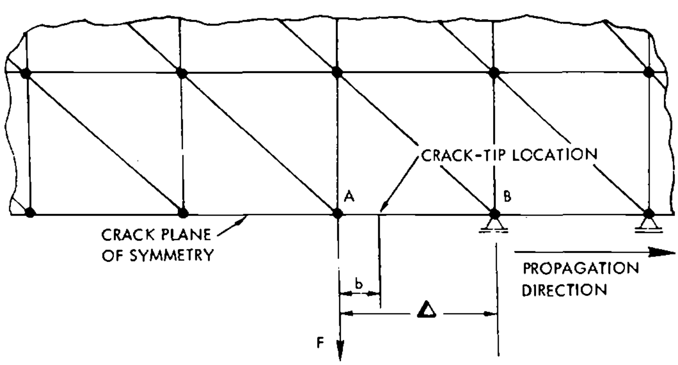

FIG. 1—*Crack-tip neighborhood of finite-element model.*

reaches Node B. It is in the manner by which F is prescribed to decay (or the restraint is relaxed) that the algorithms proposed in Ref *3* and in Ref *4* differ.

The algorithm advanced in Ref *3* by the authors, and hereinafter designated MK, assigns, F in accord with the virtual-work-consistent nodal force appropriate to a singular external traction field traveling in advance of the crack tip. By assuming a constant "stress-intensity factor" while the crack tip traverses the distance between Nodes A and B and by assuming that displacements vary linearly between the nodes, there results

$$F/F_0 = [1 - b/\Delta]^{3/2} \tag{1}$$

where b is the distance from Node A to the crack tip and Δ is the distance between the nodes.

The algorithm proposed by Rydholm, Fredriksson, and Nilsson [*4*], and hereinafter designated RFN, prescribes F to decay in the manner that yields a constant energy-release rate in the finite-element model for quasi-static crack extension between Nodes A and B while prescribed remote loads or displacements are held constant. The result is

$$F/F_0 = [1 - b/\Delta]^{1/2} \tag{2}$$

The variations of nodal force with crack-tip location given by Eq 1 and 2 are shown in Fig. 2, the pertinent difference being that the one (MK) decays more rapidly at the beginning of the interval of extension and the other (RFN) decays more rapidly at the end of the interval. Between these two lies the uniform rate of decay suggested by Ref *5*.

The Finite-Element Model

All of the numerical results presented in this paper have been obtained using the finite-element model depicted in Fig. 3. The model represents one

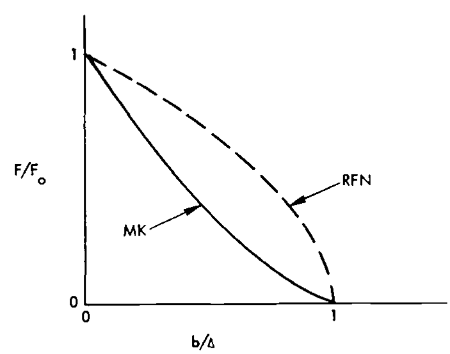

FIG. 2—*Variation of nodal force with crack-tip location.*

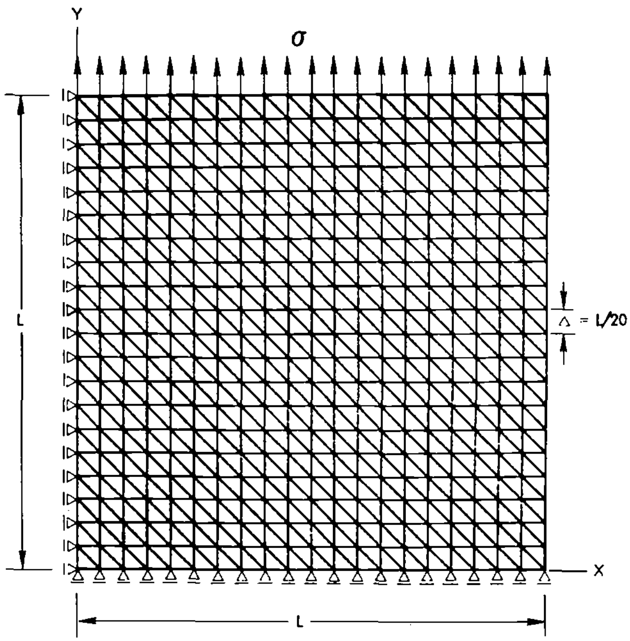

FIG. 3—*Finite-element model of one quadrant of a square sheet.*

quadrant of a centrally cracked square region in plane strain and subjected to uniform tension, σ, on the edges parallel to the crack trajectory (x-axis). The model is composed of 800 constant-strain triangles and has 441 nodes and was chosen to duplicate the uniform mesh ($\Delta = 0.05L$) of Rydholm et al in Ref *4* where square bilinear elements were employed. A second motivation for the choice of a uniform mesh was the desire to compare results so obtained with those reported in Ref *3*, where elements differing in size by an order of magnitude were used in an attempt to simulate propagation in an infinite sheet. That previous work had left unresolved the question as to what extent some oscillations in nodal displacements might be associated more with the nonuniformity of mesh than with the process of simulating crack extension.

Calculations have been carried out for a material having a Poisson's ratio $\nu = 1/3$ so that the ratio of longitudinal (c_1) and shear (c_2) wave speeds was $c_1/c_2 = 2$. The central-difference method of time integration [*10*] and the lumped-mass characterization of inertia have been employed. In each simulation of fast fracture, 20 time steps of numerical integration have been used for the interval between the releases of adjacent nodes. The average energy-release rate, $\mathcal{G}$, for each increment (nodal spacing) of crack extension was computed from the work of remote loads and changes in strain and kinetic energies; thus, if t_1 and t_2 were the times of successive releases of nodes

$$\begin{aligned} \tfrac{1}{2}\, \mathcal{G}\, \Delta &= \tfrac{1}{2}\,[\dot{\mathbf{u}}^T(t_1)\mathbf{M}\dot{\mathbf{u}}(t_1) - \dot{\mathbf{u}}^T(t_2)\mathbf{M}\dot{\mathbf{u}}(t_2)] \\ &+ \tfrac{1}{2}\,[\mathbf{u}^T(t_1)\mathbf{K}\mathbf{u}(t_1) - \mathbf{u}^T(t_2)\mathbf{K}\mathbf{u}(t_2)] \\ &+ [\mathbf{u}^T(t_2) - \mathbf{u}^T(t_1)]\mathbf{P} \end{aligned} \tag{3}$$

where

$\mathbf{u}$ = vector of nodal displacements and $\mathbf{u}^T$ its transpose,
$\mathbf{M}$ = mass matrix,
$\mathbf{K}$ = stiffness matrix,
$\mathbf{P}$ = vector of external forces (constant), excluding the relaxing force F, and
$\dot{\mathbf{u}}$ = vector of nodal velocities computed from

$$\mathrm{h}\mathbf{M}\dot{\mathbf{u}}(t_2) = \mathbf{M}[\mathbf{u}(t_2) - \mathbf{u}(t_2 - h)] + [P - \mathbf{K}\mathbf{u}(t_2)]h^2/2 \tag{4}$$

where h is the time step in the numerical integration; F does not appear in Eq 4 since it vanishes at t_2. Throughout this paper the average energy-release rates from Eq 3 are depicted in the figures at the midpoints of nodal spacings.

An indication of the performance that might be expected of the finite-element model in applications to fracture mechanics can be gleaned from the static energy-release rates (Fig. 4) which have been normalized to the static value appropriate to a crack of length $2a$ in an infinite sheet; that is,

$$\mathcal{G}_{s\infty} = (1 - \nu)\pi a \sigma^2/2\mu$$

where μ is the shear modulus. For $a > 0.3L$, the energy-release rates, deduced from finite-element analyses of the appropriate sequence of equilibrium problems, differ from those reported by Isida [11] by less than 10 percent. For shorter cracks the finite-element model produces significant errors in the static energy-release rates.

Static Loading and Extension from Zero Initial Length

The first problem to be discussed is the extension at constant rate $2c$ of a crack having zero initial length, the square region being initially in equilibrium with the prescribed uniaxial stress σ and the edges perpendicular to the crack trajectory being free of stress. This is a problem simulated by Rydholm et al [4], and for sufficiently small time the near-tip behavior of the

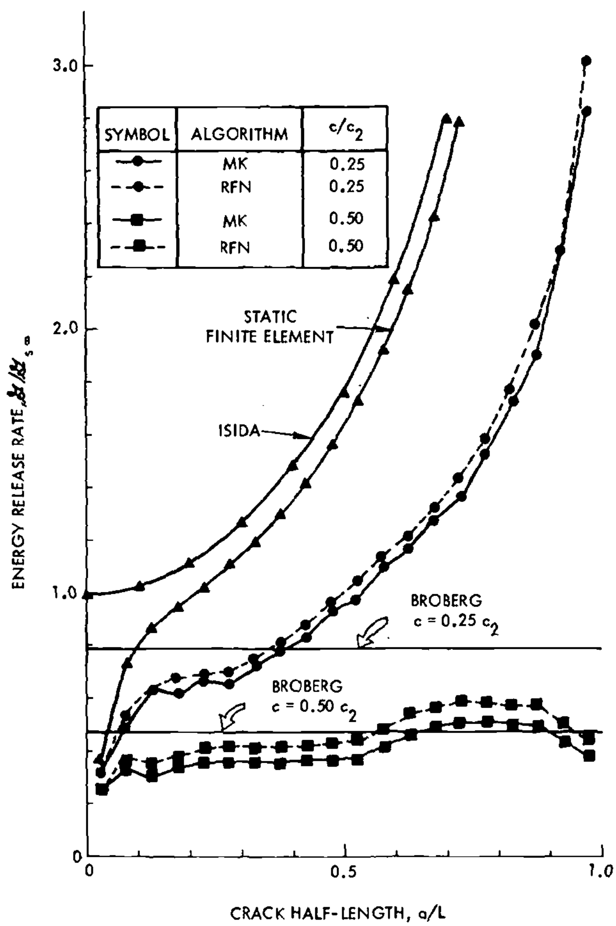

FIG. 4—*Static loading and extension from zero length: energy release rates.*

sheet is given by Broberg's solution [*12*] to the corresponding infinite-sheet problem. Energy-release rates calculated from finite-element simulations using the MK and RFN algorithms are shown in Fig. 4 for two propagation speeds, $c = 0.25c_2$ and $c = 0.5c_2$. Broberg's solution is applicable for comparisons before boundary effects are felt at the crack tip, that is, for $a \leq 0.22L$ at $c = 0.25c_2$ and $a \leq 0.4L$ at $c = 0.5c_2$. Although the RFN algorithm produced energy-release rates consistently higher than those from the MK algorithm, the differences in the finite-element results were significant only at the higher crack speed. Each of the finite-element simulations yielded energy-release rates substantially lower than those of Broberg during the time intervals prior to the arrivals of signals from boundaries. For plane-stress conditions, Rydholm et al [*4*] reported substantially better agreement with the Broberg solution when bilinear elements and the consistent-mass characterization of inertia were employed.

The y-component, v, of a nodal displacement on the crack face (at $x = 0.3L$), displayed in Figs. 5 and 6, exhibits the mild oscillations characteristic of those reported in Ref *3*, indicating that this feature is a consequence of spatial discretization along the crack-tip trajectory rather than of the nonuniformity of the finite elements employed by the authors in the earlier study. As might be anticipated from the relative rates of nodal-force relaxation, the crack-face displacements generated by the RFN algorithms lag those generated by the MK scheme, which can be expected to produce near-tip displacements significantly lower than those appropriate to continum elastodynamics (Fig. 5).

Shown in Fig. 7 are nodal forces occurring on a crack-trajectory node at the instant of release of the node. Keegstra has proposed [*1*] a calibration by which this force is assumed to be proportional to the stress-intensity factor in the corresponding continuous body problem, and the use of a critical value of this force as a crack-extension criterion for problems in which the crack extension speed is not prescribed in advance. Thus, it is of interest to note that the nodal force at release, according to either algorithm, was smaller at the

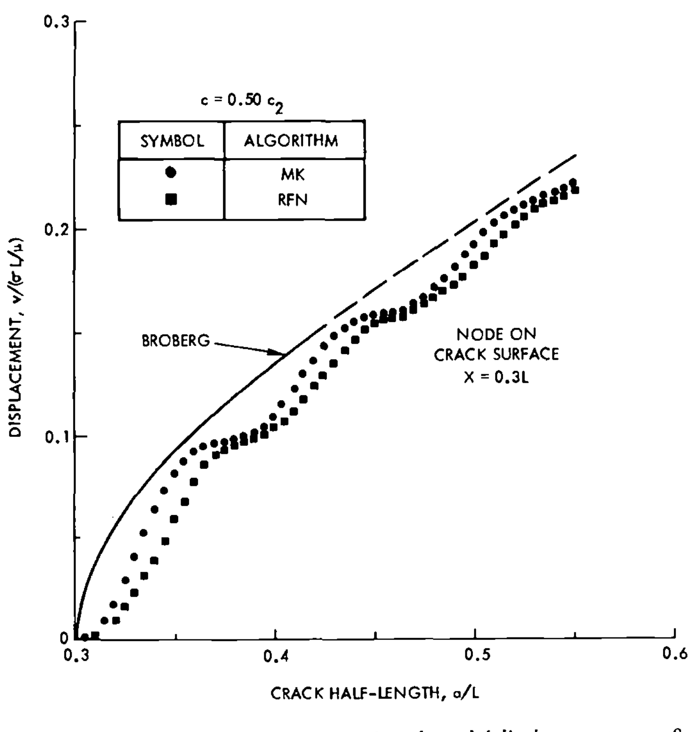

FIG. 5—*Static loading and extension from zero length: nodal displacements,* c = $0.50c_2$.

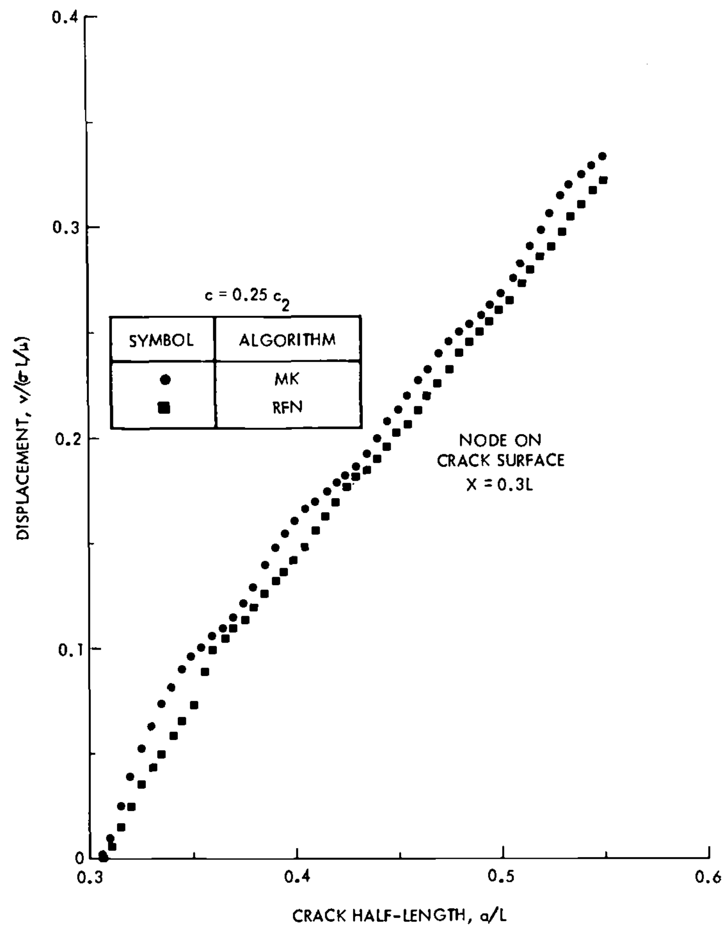

FIG. 6—*Static loading and extension from zero length: nodal displacements,* $c = 0.25c_2$.

higher speed of propagation than at the lower speed, which is consistent with the speed dependence of the stress-intensity factor in the continuum. It also should be noted that the RFN algorithm generated nodal forces smaller and, at least at the lower speed, more smoothly varying with crack-tip location than those generated by the MK algorithm.

It should be realized that, while this problem is a useful vehicle for contrasting the performances of the two algorithms, it is impossible to assess the extent to which the inability of the finite-element model to simulate the short-crack-length conditions is felt at later times. The other two problems treated in this study have been chosen so as to remove that uncertainty; that is, a crack of nonzero initial length has been considered.

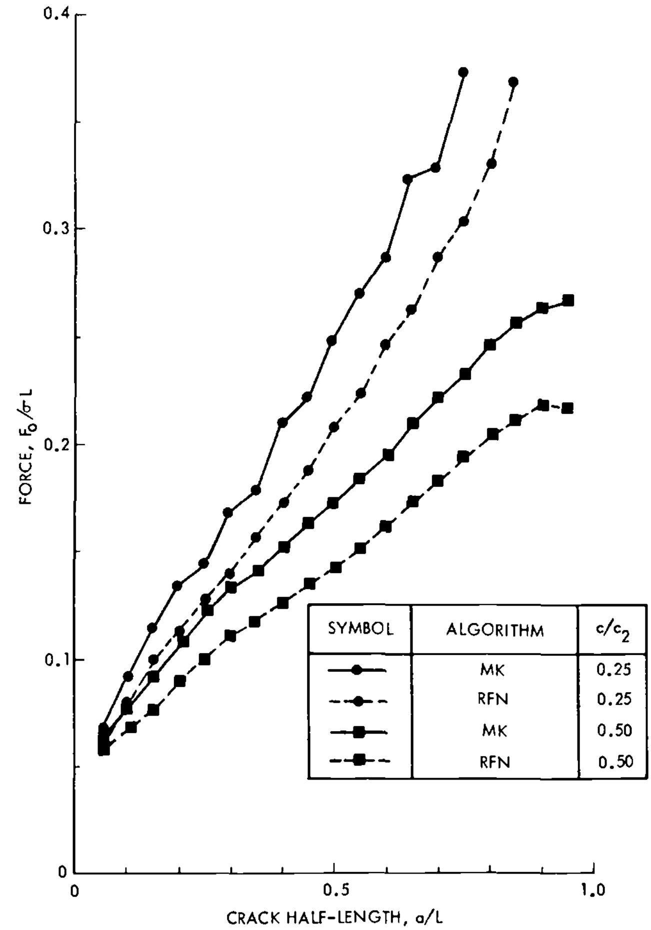

FIG. 7—*Static loading and extension from zero length: nodal force at release.*

Stress-Wave Loading and Extension from Nonzero Initial Length

The second problem considered is that of sudden application of the remote stress σ to the initially unstressed sheet. If the edges paralleling the y-axis are constrained against a normal component of displacement, this loading induces plane longitudinal step-stress waves approaching the crack trajectory from opposite sides. By applications of superposition principles [*13*] the ensuing stress-intensity factor is twice the value resulting from sudden pressurization of the crack faces. Thus, if the crack is prescribed to extend at constant speed beginning at the instant of impingement of the stress waves, then, for sufficiently small times, the stress-intensity factor is twice that given by Baker's analysis [*14*] for sudden appearance and propagation of a semi-infinite crack. The artificial feature of this problem is, of course, the initiation of crack propagation at zero stress-intensity factor.

The finite-element analysis was carried out for only one crack speed ($c = 0.5c_2$) and only five releases of crack-trajectory nodes, starting with an initial crack $a_0 = 0.4L$. At the crack tip in the corresponding continuum, neither signals from the other tip nor reflections from boundaries are received during this time. Energy-release rates (Fig. 8) determined from each algorithm are in remarkable agreement with those predicted by Baker, when consideration is given to how severe a test case this is for approximate methods which involve spatial discretization. Again the finite-element simulations have produced release rates generally lower than from a continuum analysis, and of the two algorithms the RFN has produced the higher values.

Displacements, v, of the first ($x = 0.4L$) and third ($x = 0.5L$) nodes released are shown in Fig. 9. There is little difference in the displacements, but again those generated by the RFN algorithm lag those generated by the MK method. Also shown in Fig. 9 are displacements at a point ($x = 0.5L$) on the loaded surface and at a point ($x = 0.1L$) on the face of the initial crack. At these locations the two algorithms produced displacements which cannot

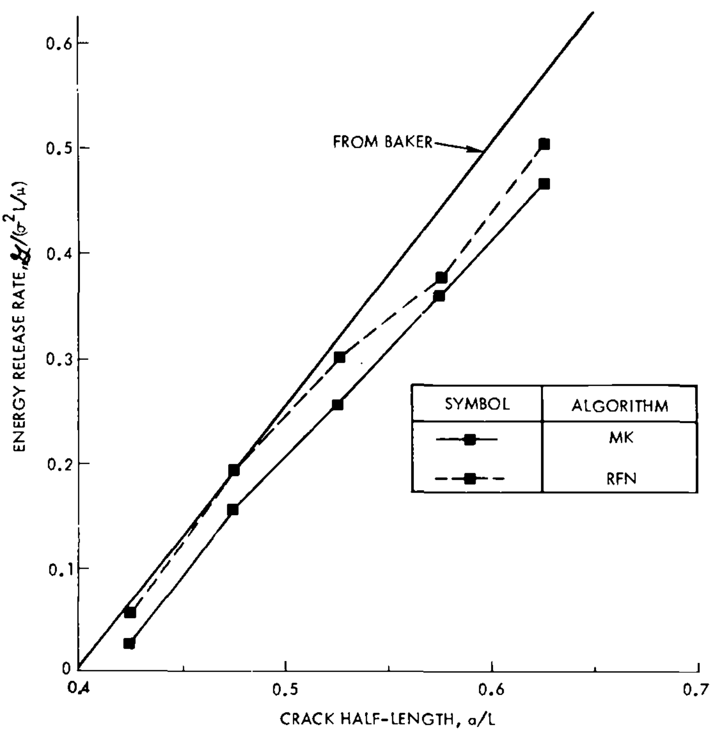

FIG. 8—*Stress wave loading and extension from nonzero length: energy release rates.*

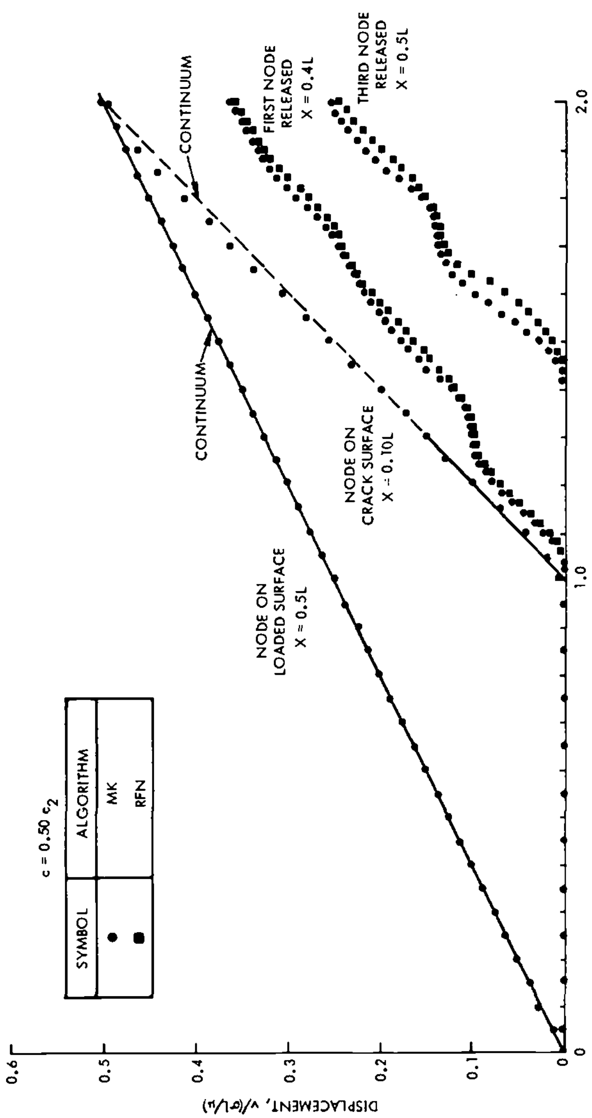

FIG. 9—*Stress wave loading and extension from nonzero length: nodal displacements.*

be distinguished on the figure, and they are in very close agreement with the predictions (solid straigth lines) of continuum elastodynamics for one-dimensional wave propagation.

As in the preceding problem, the nodal reactions (Fig. 10) at the instants before releases produced by the RFN simulation were consistently lower than those produced by the MK scheme. The fact that the reactions are essentially equal prior to the release of the second node is apparently a consequence of the very small force associated with the instant of release of the first node.

Static Loading and Extension from Nonzero Initial Length

The final problem considered is, of the three, the most representative of potential practical applications of a finite-element analysis. Conditions are taken to be the same as in the preceding problem except that, instead of stress-wave loading, the body with initial crack half-length $a_0 = 0.4L$ is taken to be in equilibrium prior to the onset of constant-speed extension.

Energy-release rates computed from finite-element simulations, each of five nodal releases, for speeds $c = 0.25c_2$ and $c = 0.5c_2$ are shown in Fig. 11. While there is not an analytical solution against which the results can be

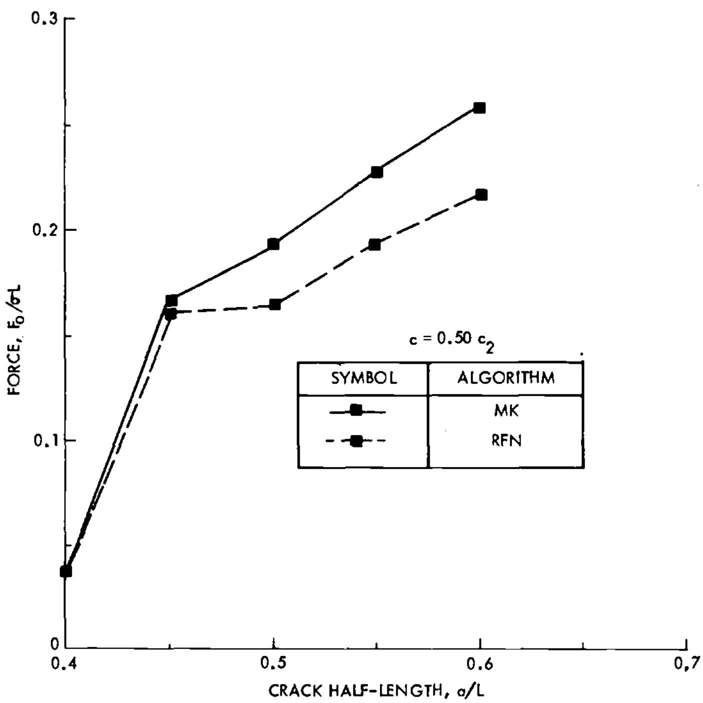

FIG. 10—*Stress wave loading and extension from nonzero length: nodal forces at release.*

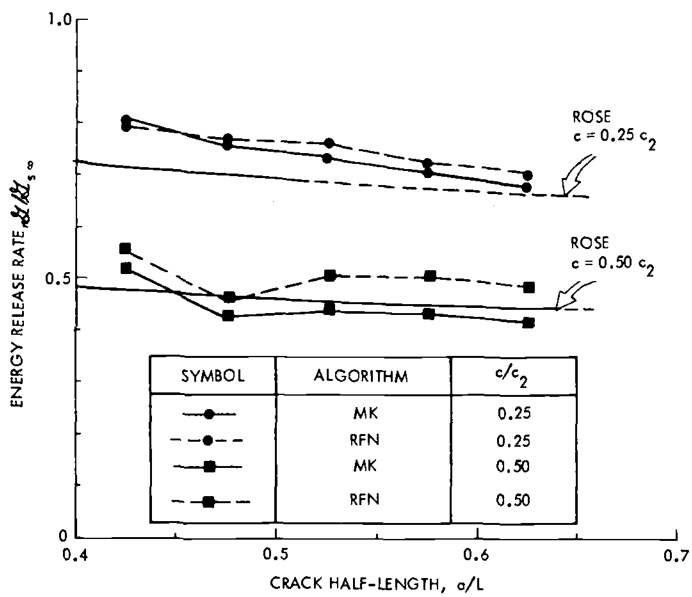

FIG. 11—*Static loading and extension from nonzero length: energy release rates.*

compared, because of the finite width of the sheet, Rose's results [15], valid until a longitudinal wave traverses the full crack length, for the corresponding infinite-sheet problem are also shown. It is to be expected that a continuum analysis would yield slightly higher release rates than those of Rose due to the finite width of the plate. The two algorithms yielded similar energy-release rates at each propagation speed, the higher values arising from the RFN method and the differences being insignificant at the lower speed.

Crack-face displacements (at $x = 0$ and $x = 0.4L$) shown in Fig. 12 for $c = 0.25c_2$ are similar to those observed from the results of the first problem. The RFN algorithm yielded lower and somewhat more smoothly varying displacements than did the MK algorithm.

Crack-trajectory nodal forces at the instants before releases (Fig. 13) also follow the patterns observed before; namely, the RFN algorithm yielded the smaller forces, and smaller forces were generated at the higher speed than at the lower speed.

Conclusions

The results of finite-element simulations of three problems of constant-speed rapid fracture have exhibited the following common features:

1. Crack-face displacements produced by the MK algorithm were slightly lower than those generated by the RFN method.

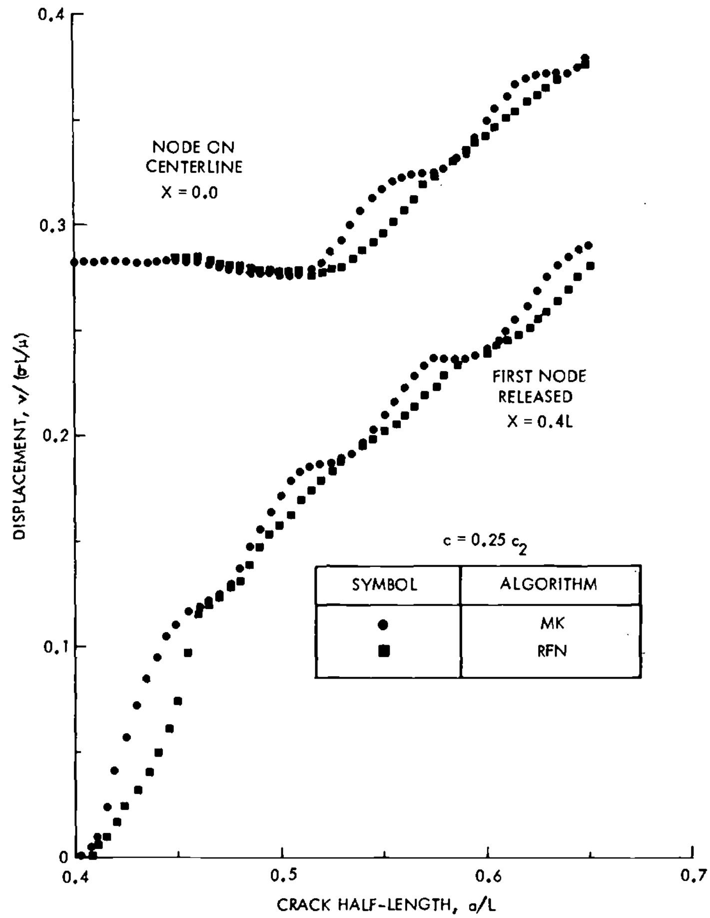

FIG. 12—*Static loading and extension from nonzero length: nodal displacements.*

2. There were significant differences in the nodal-reaction-at-release forces produced by the two algorithms, the RFN method yielding the smaller forces.
3. At lower crack speed ($c = 0.25c_2$) there were only slight differences in the energy-release rates predicted by use of the two schemes. At the higher speed ($c = 0.5c_2$) the RFN method produced the higher release rates, and at both speeds the finite-element results were generally lower than to be expected from continuum elastodynamics. This is consistent with the quasi-static performance of the model, which produced static energy-release rates slightly lower than those reported by Isida.

All of the calculated displacements and energy-release rates appear to be consistent with the accuracy that reasonably could be expected from such a

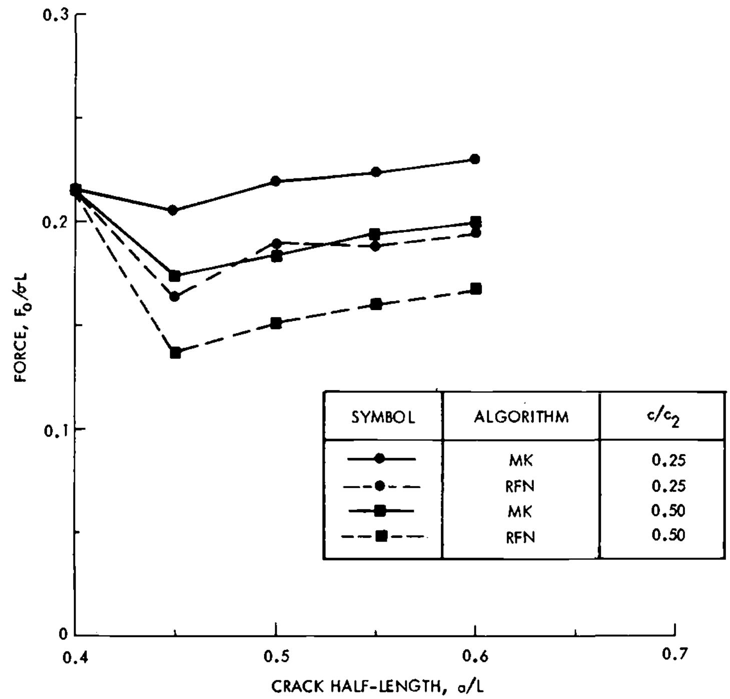

FIG. 13—*Static loading and extension from nonzero lenght: nodal forces at release.*

coarse spatial discretization along the crack-tip trajectory, and it is to be expected that similar results for these responses would be obtained from an analysis based upon a linear decay of the near-tip nodal force. However, the algorithm proposed by Rydholm, Fredriksson, and Nilsson seems to have particular merit, since it has produced the better energy-release rates at the higher crack speed considered here, and it also has a strong analytical basis for the limiting case of quasi-static crack extension.

The present investigation has but scratched the surface of numerical experiments which might shed light on the utility of this approach to the finite-element simulation of fast fracture. Sensitivities of the results to the type of finite element, mass distribution, and time-integration algorithm employed have not been explored here. Neither is it clear what response of the finite-element model should be employed as a crack extension criterion for applications in which the propagation rates are not prescribed; the observed sensitivity of the nodal-reaction-at-release forces to the manner in which the crack trajectory nodal forces are prescribed to decay seems to preclude a universal calibration of nodal force with continuum stress-intensity factor such as the one proposed by Keegstra. In addition, and most importantly, the energy-release mechanism is necessarily linked to the near-tip behavior of the finite-element model, the region most poorly represented in the present approach. The recent work of Aoki et al [9] portends a resolution of this difficulty through the development of finite-element codes employing an element, or elements, which incorporates the proper stress singularity and in which an embedded crack tip can move continuously.

Acknowledgments

The authors are grateful for financial support provided by the Lockheed-Georgia Co. Independent Research and Development Program. The second author was supported in part by National Science Foundation Grant NSF ENG 77-12948 to the Georgia Institute of Technology.

References

[1] Keegstra, P. N. R., *Journal of the Institution of Nuclear Engineers*, Vol. 17, No. 4, 1976, pp. 89-96.
[2] Keegstra, P. N. R., Head, J. L., and Turner, C. E. in *Numerical Methods in Fracture Mechanics*, A. R. Luxmoore and D. R. J. Owen, Eds., University College of Swansea, Swansea, Wales, Jan. 1978, pp. 634-647.
[3] Malluck, J. F. and King, W. W. in *Numerical Methods in Fracture Mechanics*, A. R. Luxmoore and D. R. J. Owen, Eds., University College of Swansea, Swansea, Wales, Jan. 1978, pp. 648-659.
[4] Rydholm, G., Fredriksson, B., and Nilsson, F., *Numerical Methods in Fracture Mechanics*, A. R. Luxmoore and D. R. J. Owen, Eds., University College of Swansea, Swansea, Wales, Jan. 1978, pp. 660-672.
[5] Kobayashi, A. S., Mall, S., Urabe, Y., and Emery, A. F. in *Numerical Methods in Fracture Mechanics*, A. R. Luxmoore and D. R. J. Owen, Eds., University College of Swansea, Swansea, Wales, Jan. 1978, pp. 673-684.
[6] Yagawa, G., Sakai, Y., and Ando, Y. in *Fast Fracture and Crack Arrest, ASTM STP 627*, G. T. Hahn and M. F. Kanninen, Eds., American Society for Testing and Materials, 1977, pp. 109-122.
[7] Owen, D. R. J. and Shantaram, D., *International Journal of Fracture*, Vol. 13, No. 6, Dec. 1977, pp. 821-837.
[8] Bažant, Z. P., Glazik, J. L., Jr., and Achenbach, J. D., *Computers and Structures*, Vol. 8, 1978, pp. 193-198.
[9] Aoki, S., Kishimoto, K., Kondo, H., and Sakata, M., *International Journal of Fracture*, Vol. 14, No. 1, Feb. 1978, pp. 59-68.
[10] Bathe, K.-J. and Wilson, E. L., *Numerical Methods in Finite-Element Analysis*, Prentice-Hall, Englewood Cliffs, N.J., 1976, p. 310.
[11] Isida, M., *International Journal of Fracture Mechanics*, Vol. 7, No. 3, Sept. 1971, pp. 301-316.
[12] Broberg, K. B., *Arkiv för Fysik*, Vol. 18, 1960, pp. 159-192.
[13] Achenbach, J. D. and Nuismer, R., *International Journal of Fracture Mechanics*, Vol. 7, No. 1, March 1971, pp. 77-88.
[14] Baker, B. R., *Journal of Applied Mechanics*, Vol. 29, No. 3, Sept. 1962, pp. 449-458.
[15] Rose, L. R. F., *International Journal of Fracture*, Vol. 12, No. 6, Dec. 1976, pp. 829-841.

M. Shmuely[1] *and M. Perl*[1]

The SMF2D Code for Proper Simulation of Crack Propagation

REFERENCE: Shmuely, M. and Perl, M., "**The SMF2D Code for Proper Simulation of Crack Propagation,**" *Crack Arrest Methodology and Applications, ASTM STP 711,* G. T. Hahn and M. F. Kanninen, Eds., American Society for Testing and Materials, 1980, pp. 54-69.

ABSTRACT: An improved two-dimensional finite-difference code for simulating crack initiation, fast crack propagation, and arrest is presented. Compared with the previously available numerical codes, the present one simulates crack processes much more accurately, yielding results which have been found to be in excellent agreement with analytical and experimental findings. The code is applied to the single edge notch and double cantilever beam specimens and preliminary numerical results are discussed.

KEY WORDS: crack propagation, fracture properties, numerical analysis, finite differences

Rapid crack propagation, dynamic toughness, and crack arrest are currently receiving much attention. The available analytical solutions are limited to infinite [*1-3*][2] and semi-infinite [*4*] body configurations and to linearly elastic materials. Thus it becomes essential that numerical dynamic fracture analysis techniques such as finite differences and finite elements be developed. In this paper, an improved finite-difference code (the SMF2D Code) is presented.

Finite-element simulations of rapid crack propagation have been developed. Efforts have been made to extend the singular element which, so far, has been successfully applied to the static case [*5*]. Yet the main difficulty encountered has been an intermittent crack extension caused by the jumps of the crack tip from one nodal point to another. Rydhalm, Nilson et al [*6*] tried to avoid such discontinuities by using a relaxation technique which could not be physically justified, as they themselves mentioned. The finite-difference method, as applied by Shmuely [*7,8*], Kanazawa [*9*],

[1] Associate professor, Faculty of Mechanical Engineering and instructor, Faculty of Aeronautical Engineering, respectively, Technion-Israel Institute of Technology, Haifa, Israel.
[2] The italic numbers in brackets refer to the list of references appended to this paper.

Stöckl [10], and others, encountered the same difficulties, and remedies of the same nature were employed.

The SMF2D code overcomes most of the aforementioned difficulties. The use of a semimoving grid results in smoother crack extension. Hence, a more reliable fast crack propagation simulation is achieved and a higher degree of resolution for the various parameters is reached.

In the following sections, the field equations and the numerical scheme are described. Preliminary static and dynamic results for the SEN (single edge notch) and DCB (double cantilever beam) specimens are presented. The numerical results are compared with experimental findings and discussed.

The Field Equations

The SMF2D code was constructed by adding a moving element (Fig. 1) to the previously developed finite-difference code [7]. There is a stationary domain grid *Ds*. It has a coordinate system (x, y) based at the initial crack tip. Its boundaries, *Bs* (including the free surfaces of the crack), overlap the boundaries of the body being solved. In addition, there is a moving domain grid, *Dm*, which has boundaries *Bm*. It also has a coordinate system (ξ, η) which has its origin at the moving crack tip. The only boundary of the moving domain which coincides with one of the body's boundaries is the boundary $(-\beta \leq \xi \leq 0, \eta = 0)$ which coincides with the free crack surface. The rest of *Bm* represent internal points in the body.

The purpose of using the stationary grid system is to be able to readily accommodate boundary conditions of specimens of finite dimensions. Difficulties in satisfying such conditions arise when attempting to use just the moving grid system [17].

The Displacement Field

The displacement field **U** in the stationary domain *Ds* is governed by the following equations of motion.

$$(\lambda + \mu)U_{k,ki} + \mu U_{i,kk} = \rho U_{i,tt} \qquad i, k = 1, 2 \tag{1}$$

where

λ, μ = Lamé constants, N/m^2,
ρ = density, kg/m^3, and
t = time, s.

The summation convention is used. The normalized version of Eq 1 is

$$\frac{1}{2(1-\nu)}[U_{k,ki} + (1-2\nu)U_{i,kk}] = U_{i,\tau\tau} + \psi U_{i,\tau} \qquad i, k = 1, 2 \tag{2}$$

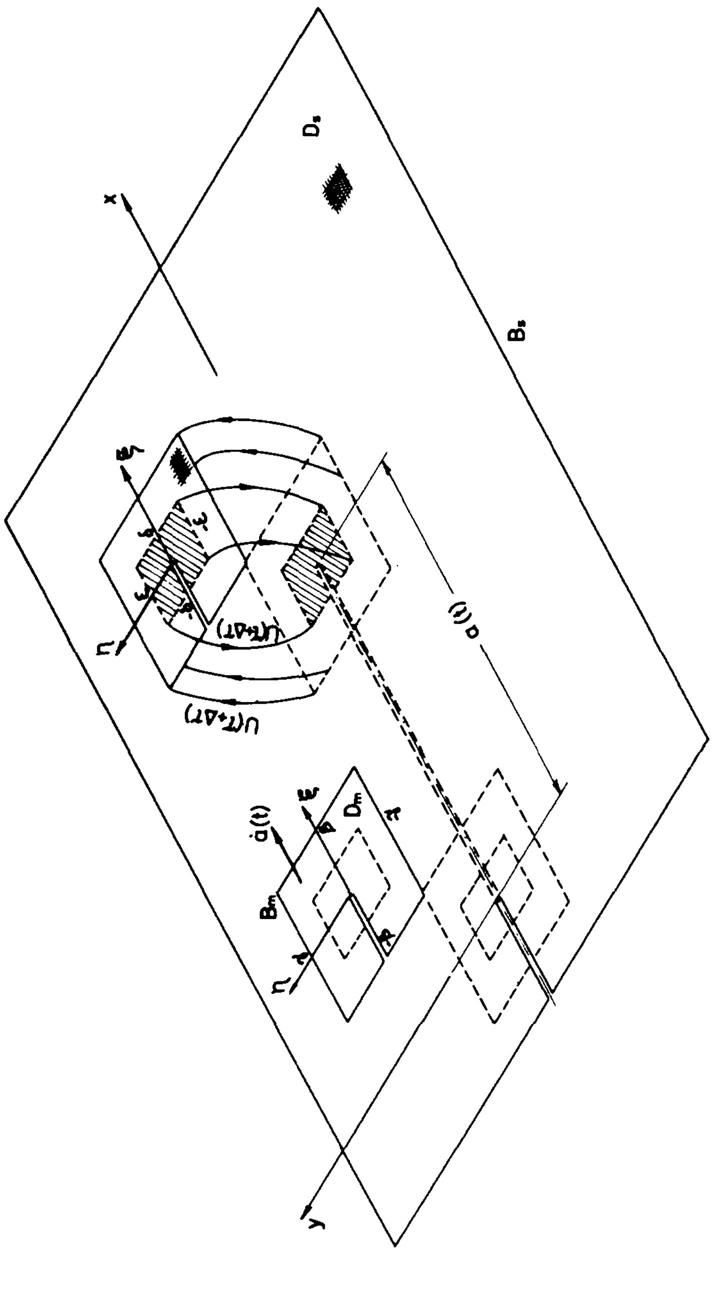

FIG. 1—*Stationary and moving grids.*

The normalization was carried out as follows. Lengths are normalized to an arbitrarily chosen unit of length, H; say, for convenience, the height of the specimen investigated. Time is normalized to H/C_1 where C_1 is the dilatational or the plate wave velocity, depending upon whether plane-strain or plane-stress conditions prevail. ν is the Poisson ratio of the material investigated, but it is replaced by the apparent Poisson ratio $\nu^* = \nu/1 + \nu$ in plane-stress conditions. The last term in Eqs 2 has been added for solving the static case using dynamic relaxation [*11*]. ψ is a parameter by which the code is switched from the static case ($\psi > 0$) to the dynamic one ($\psi = 0$). Equations 2 together with the appropriate boundary conditions for the particular problem being solved (for example, Ref *8*) completely define the problem in the stationary domain.

The Moving Element

The coordinate system moves together with the crack tip so that

$$\begin{aligned} \xi &= x - a(t) \\ \eta &= y \end{aligned} \tag{3}$$

where $a(t)$ is the time-dependent crack length.

Expressing the nondimensional equations of motion (2) in terms of ξ and η, we obtain

$$\frac{1}{2(1-\nu)}[U_{k,ki} + (1-2\nu)U_{i,kk}] = U_{i,\tau\tau} - 2\dot{\alpha}(\tau)U_{i,1\tau} + [\dot{\alpha}(\tau)]^2 U_{i,11}$$

$$- \ddot{\alpha}(\tau)U_{i,1} + \psi U_{i,\tau} \qquad i, k = 1, 2 \quad (4)$$

where $\alpha(\tau)$ is the nondimensional time-dependent crack length and the dot denotes derivation with respect to time. As mentioned before, the traction-free surface of the crack is subjected to the boundary condition

$$\sigma_{\eta\eta} = \sigma_{\xi\eta} = 0 \quad \text{on} \quad \eta = 0 \quad \text{for} \quad -\beta \leq \xi < 0 \tag{4a}$$

where σ_{ij} is the stress tensor component.

The Numerical Scheme

Equations 2 subjected to the appropriate boundary conditions are solved by the finite-difference method. Equations 2 are approximated by central finite differences which, together with the proper boundary conditions, yield an explicit time-step algorithm for solving both static and dynamic displacement fields [12]. The central finite-difference form of Eqs 2 is

$$U_i(x,y,\tau+k)=\frac{1}{1+\psi}\Big\{2U_i(x,y,\tau)-(1-\psi)U_i(x,y,\tau-k)+A_i\left(\frac{k}{h}\right)^2$$

$$\cdot[U_i(x+h,y,\tau)-2U_i(x,y,\tau)+U_i(x-h,y,\tau)]+\frac{1}{2(1-\nu)}$$

$$\cdot\left(\frac{k}{h}\right)^2\cdot[U_j(x+h,y+h,\tau)-U_j(x+h,y-h,\tau)$$

$$-U_j(x-h,y+h,\tau)+U_j(x-h,y-h,\tau)]+A_j\cdot\left(\frac{k}{h}\right)^2$$

$$\cdot[U_i(x,y+h,\tau)-2U_i(x,y,\tau)+U_i(x,y-h,\tau)]\Big\}\qquad i,j=1,2 \quad (5)$$

where

k = dimensionless time increment ($\Delta\tau$),
h = dimensionless mesh size,
A_1 = 1, and
$A_2 = (1-2\nu)/2(1-\nu)$.

This scheme is explicit and it seems to be of a three-order type, so that the displacements at $(\tau + \Delta\tau)$ can be computed whenever their values are known at two previous time steps: τ and $\tau - \Delta\tau$. We also express Eqs 4 in finite-difference form

$$U_i(\xi,\eta,\tau+k)=\frac{1}{1+\psi}\Big\{(2U_i(\xi,\eta,\tau)-(1-\psi)U_i(\xi,\eta,\tau-k)+(A_i-\dot{\alpha}^2)$$

$$\cdot\left(\frac{k}{h}\right)^2\cdot[U_i(\xi+h,\eta,\tau)-2U_i(\xi,\eta,\tau)$$

$$+U_i(\xi-h,\eta,\tau)]+\frac{1}{2(1-\nu)}$$

$$\cdot\left(\frac{k}{h}\right)^2\cdot[U_j(\xi+h,\eta+h,\tau)-U_j(\xi+h,\eta-h,\tau)$$

$$-U_j(\xi-h,\eta+h,\tau)+U_j(\xi-h,\eta-h,\tau)]+A_j$$

$$\cdot \left(\frac{k}{h}\right)^2 \cdot [U_i(\xi,\eta+h,\tau)-2U_i(\xi,\eta,\tau)+U_i(\xi,\eta-h,\tau)] + \frac{\ddot{\alpha}\cdot k}{2}$$

$$\cdot [U_i(\xi+h,\eta,\tau)-U_i(\xi-h,\eta,\tau)] + \frac{\dot{\alpha}k}{h}$$

$$\cdot [U_i(\xi+h,\eta,\tau)-U_i(\xi-h,\eta,\tau)-U_i(\xi+h,\eta,\tau-k)$$

$$\left.+U_i(\xi-h,\eta,\tau-k)]\right\} \qquad i,j=1,2 \tag{6}$$

These are in second-order central difference form except for the term $-2\dot{\alpha}(\tau)U_{i'1\tau}$, which has been approximated by a first-order difference form. The reason for this is that if it is transferred into a second-order form, the scheme becomes implicit. An alternative could be to express it as a second-order backward difference scheme (in place of a central difference scheme), but then a four-level type of scheme would result. In order to achieve second-order accuracy, the following procedure is used. The displacement field $\mathbf{U}$ is solved for the time level $\tau + \Delta\tau$ using Eqs 6 in their present form. Then the last line of Eqs 6 is changed to

$$\frac{\dot{\alpha}k}{h}[U_i(\xi + h, \eta, \tau + k) - U_i(\xi - h, \eta, \tau + k)$$

$$- U_i(\xi + h, \eta, \tau - k) + U_i(\xi - h, \eta, \tau - k)] \qquad i, j = 1, 2 \tag{6a}$$

The modified equations are then solved again explicitly for $\mathbf{U}(\tau + \Delta\tau)$, with the implicit $\mathbf{U}(\tau + \Delta\tau)$ expressions in Eq 6*a* being given the values obtained in the first solutions of Eqs 6. This whole procedure is repeated iteratively until the variation of $\mathbf{U}(\tau + \Delta\tau)$ between two successive iterations is less than a prescribed value.

The Crack Propagation Simulation

The crack propagation simulation runs as follows. We are given $\mathbf{U}$ in the closed domains *Ds* and *Dm* at time levels $\tau - \Delta\tau$ and τ ($\Delta\tau$ being the time increment) and also $\alpha(\tau)$, as measured experimentally. Then Eqs 2 are solved subjected to the boundary conditions on *Bs*, and $\mathbf{U}(\tau + \Delta\tau)$ on *Ds* is found. With the actual crack length extended to $\alpha(\tau + \Delta\tau)$, the relative position of the moving and stationary grids is determined. Special attention was given to the location of the images of the mesh points along *Bm*, as reflected on *Ds* [that is, along the lines intersecting at $x = \alpha(\tau + \Delta\tau) \pm \beta; y = \pm\gamma$]. These images hardly ever coincide with mesh points on *Ds*. Hence, $\mathbf{U}(\tau + \Delta\tau)$ values at the image points are calculated by a four-point Lagrangian interpolation procedure and are then transferred to the original mesh points on *Bm*. At this point, Eqs 6 subjected to the boundary conditions (4*a*) are solved within the open domain *Dm*. This solution is further elaborated on by the iteration procedure previously described. Finally, the values of $\mathbf{U}(\tau + \Delta\tau)$, just obtained in *Dm*, are fed back by the same Lagrangian interpolation into all mesh points enclosed in the rectangle $x = \alpha(\tau + \Delta\tau) \pm \delta$, $y = \pm\epsilon$, and override the previously obtained $\mathbf{U}(\tau + \Delta\tau)$. The space between the rectangle $x = \alpha(\tau + \Delta\tau) \pm \delta$, $y = \pm\epsilon$, and the projection of *Bm* on *Ds* was deliberately left untouched to avoid undesirable close-loop interaction between *Dm* and *Ds* grids.

Essentially the same procedure applies to the static case (effected by letting ψ be > 0 and $\dot{\alpha} = \ddot{\alpha} = 0$). In that case, however, successive changes in $\mathbf{U}$ with time correspond to successive iterative cycles, which finally converge to the static solution, which in turn serves as initial values for the dynamic case.

The two main variables evaluated during dynamic as well as during static simulations are the stress-intensity factor, $K_{\mathrm{I}}^{\mathrm{dyn}}$ or $K_{\mathrm{I}}^{\mathrm{stat}}$, and the energy release rate, $G_{\mathrm{I}}^{\mathrm{dyn}}$ or $G_{\mathrm{I}}^{\mathrm{stat}}$, calculated from the $\mathbf{U}$ field on *Dm*. The cleavage stress $\sigma_{\eta\eta}(\tau)$ at the mesh point lying on $\eta = 0$ next to the crack tip normalized to $\sigma_{\eta\eta}(0)$ at initiation is assumed to be a measure of the dynamic stress-intensity factor $K_{\mathrm{I}}^{\mathrm{dyn}}$ as compared with its static value $K_{\mathrm{I}}^{\mathrm{stat}}$

$$\frac{\sigma_{\eta\eta}(\tau)}{\sigma_{\eta\eta}(0)} = \frac{K_{\mathrm{I}}^{\mathrm{dyn}}}{K_{\mathrm{I}}^{\mathrm{stat}}} \tag{7}$$

Results described later seem to corroborate this relation. The instantaneous energy release rate was evaluated by the relation

$$G_{\mathrm{I}}^{\mathrm{dyn}}(\tau) = \frac{1}{\dot{\alpha}(\tau)}\left[-\frac{\partial}{\partial\tau}\int_{Dm}(e_s + e_k)\,d\xi\,d\eta + \oint_{Bm}\mathbf{T}\frac{\partial\mathbf{U}}{\partial\tau}\,dS\right] + \oint_{Bm}(e_s + e_k)\,d\eta - \oint_{Bm}\mathbf{T}\frac{\partial\mathbf{U}}{\partial\xi}\,dS \tag{8}$$

where

e_s = strain energy,
e_k = kinetic energy,
$\mathbf{T}$ = traction vector, and
S = curve length along *Bm*.

Note that in the static case, ($e_k = \partial/\partial\tau = 0$) the right-hand side of Eq 8 reduces to the path-independent J-integral.

Static and Dynamic Solutions and Results

The Static Case

In order to evaluate the accuracy and to present the advantages of the SMF2D code, two static configurations were solved, the SEN and the DCB.

The SEN specimen was $2h$ high, $b = h$ wide, having an edge crack of length a, and being subjected to uniform normal displacement $U_y =$ const, $U_x = 0$, with no rotation (see Ref *13*, pp. 88–89). It was solved for several crack lengths, most of which were not multiple integers of the mesh size Δx. Numerical and analytical results are presented in Table 1.

As can be seen from Table 1, the numerical results are in excellent agreement with those obtained from an approximated analytical solution, and are within the accuracy range of the latter. Furthermore, the SMF2D code has the advantage of being very sensitive to even very small changes in crack length of the order of $\Delta x \times 10^{-5}$. Thus, problems concerning any crack length can be practically solved without changing the mesh size due to such sensitivity. Very small differences of less than 0.5 percent were found between the stress-intensity factor obtained numerically by using the J-integral in the *Ds* and the one evaluated from the energy release rate (Eq 8).

The convergency of the SMF2D code is approximately twice as fast as that of the previous codes, using the same mesh size. This also reduces computation time by the same amount.

In order to add information to the DCB dynamic problem, static stress-intensity factors K_1^{stat} were computed for different crack lengths. The static numerical results (dashed lines in Fig. 3) are in excellent agreement with the experimental findings reported in Ref *14*. The isochromatic fringe

TABLE 1—*Comparison of results of present work with corresponding results from Ref* 13 *in terms of the dimensionless stress-intensity factor* K_I/K_0.

a/b	$a/\Delta x$	K_I/K_0[a]	K_I/K_0(Ref 13)[b]
0.13333	9.99975	1.110	1.16
0.19333	14.49975	1.136	1.17
0.19800	14.85	1.144	1.17
0.2	15	1.149	1.17
0.20666	15.4995	1.154	1.18
0.22	16.5	1.167	1.18
0.3	22.5	1.175	1.22
0.35	26.25	1.209	1.26
0.4	30	1.244	1.30
0.45	33.75	1.292	1.36
0.5	37.5	1.327	1.41

[a] Where $K_0 = \sigma\sqrt{\pi a}$ and σ denotes the average stress on the ends of the sheet.
[b] These values were interpolated for $h/b = 1$ from Ref *13*.

pattern of the DCB specimen shown in Fig. 2 illustrates the good matching obtained between experimental and numerical results at initiation (static case).

The Dynamic Case

The SMF2D code was applied to four of Kalthoff et al's [*14*] DCB test cases (those having maximum crack velocities of 295, 272, 207, 108 m/s). With the objective of comparing the numerical solution with the experimental study, the specimen geometry for the analysis was chosen so as to correspond to the one used in experiments. The actual dimensions of the experimental specimens were $H/L/a_0 = 63.5/321.0/68.0$ ($2H$ and L being the specimen's height and length, respectively, and a_0 the initial crack length). $H/L/a_0 = 1.0/5.06/1.07$ were accordingly used for the analysis (the mesh size used was $h = H/31.0$). The simulation was run under both fixed-grip and plane-stress conditions as prevailed in the experiments, and with a Poisson ratio $\nu = 0.392$ (for Araldite B).

The experimentally measured crack velocity/time history served as input to the simulation. Unfortunately, the accelerating stage was not measured. Some forms of accelerating functions were tried, all of which were obviously restricted to yield the experimentally measured maximum velocities at the appropriate crack lengths. It was found that numerical results for

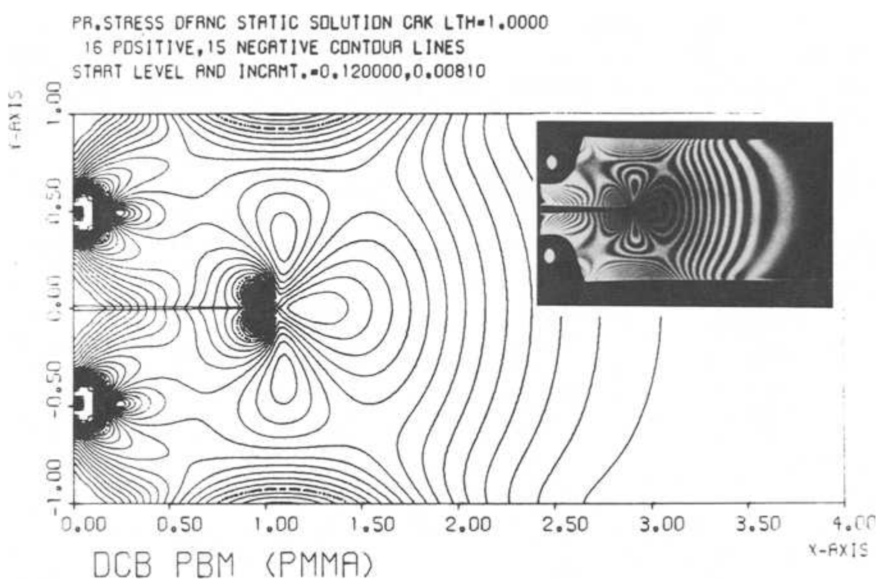

FIG. 2—*Analytical principal stress difference field compared with the fringe pattern observed in a circular polariscope.*

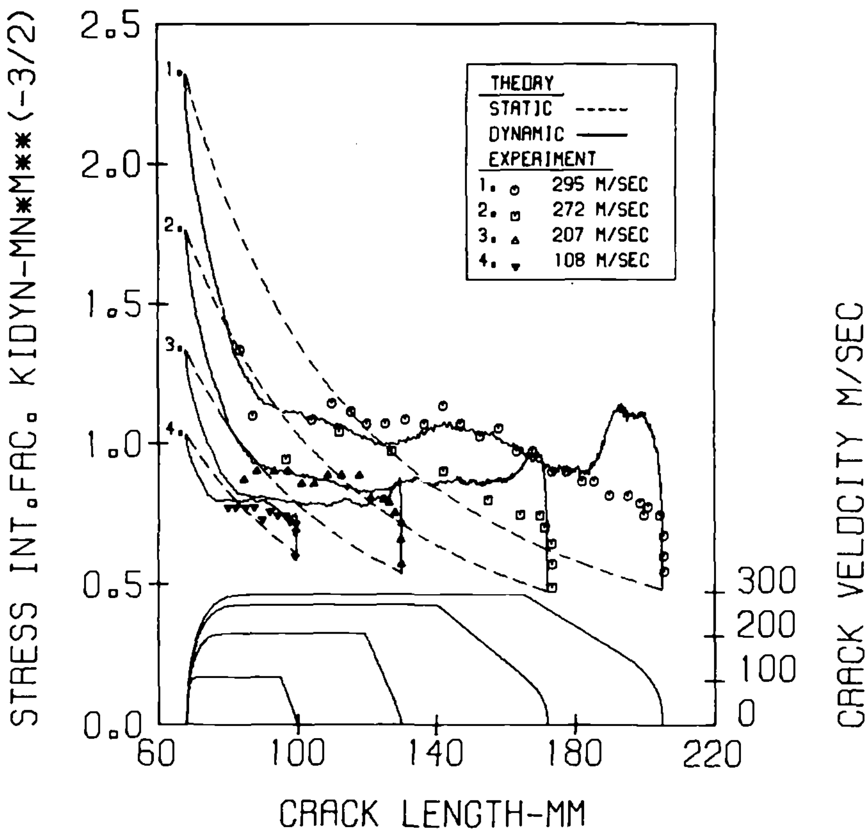

FIG. 3—*Dynamic and static stress-intensity factors* $(MN \cdot m^{-3/2})$.

the periods following the accelerating stage were quite insensitive to the specific function chosen. The accelerating stages described in Fig. 3, however, correspond to a time-dependent velocity of the form

$$V = V_{max}\left\{1 - \left(\frac{\tau_1 - \tau}{\tau_1}\right)^3\right\}$$

(τ_1 being the rise time).

The *dynamic stress field* obtained at some point during crack propagation is given in terms of an isochromatic fringe pattern in Fig. 4. This pattern seems to be in very good agreement with the experimental one given in Fig. 5 [*15*]. Figure 6 shows a parallel pattern to the one shown in Fig. 4 obtained by the old code [*15*], which emphasizes the improvement in describing the dynamic stress field achieved by the new code.

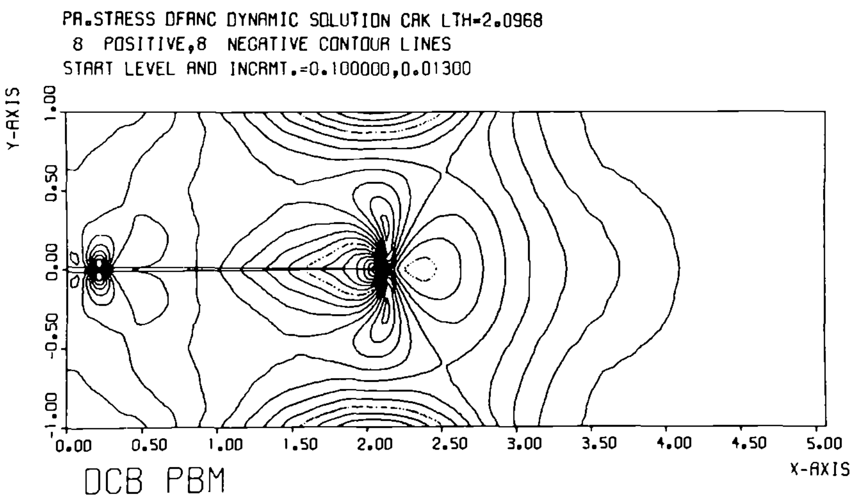

FIG. 4—*Analytical dynamic principal stress difference field of the DCB.*

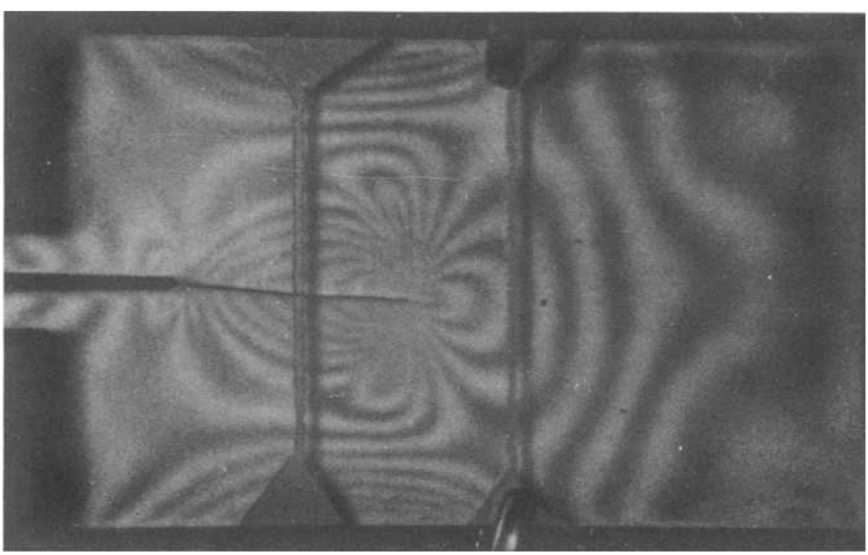

FIG. 5—*Dynamic fringe pattern as observed in a circular polariscope (exposure time was 1 μs).*

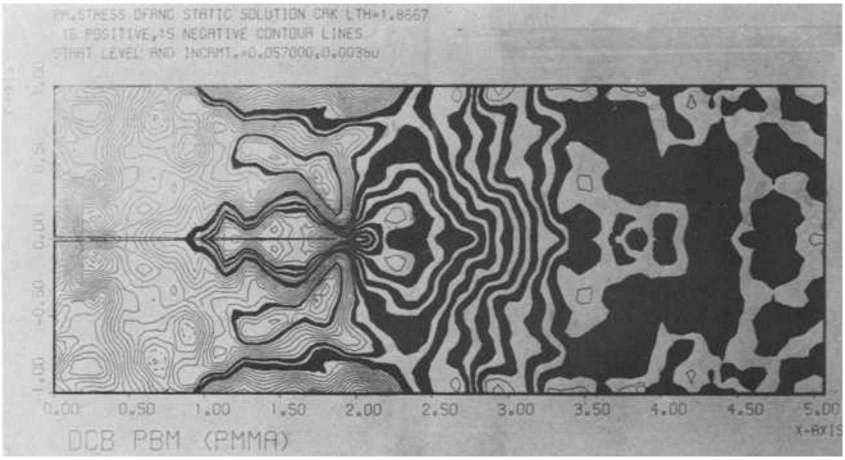

FIG. 6—*Analytical dynamic principal stress difference field of the DCB obtained by the old code.*

Dynamic Stress-Intensity Factors

Numerical results for the dynamic stress-intensity factors $K_I{}^{dyn}$ for the various cases studied are shown in Fig. 3 as a function of crack length. $K_I{}^{dyn}$ was evaluated at each time step using Eq 7. The experimental points of Ref *14* are also shown in this figure. For comparison purposes, $K_I{}^{stat}$ numerically evaluated curves are presented as dashed lines in the same figure. These static curves overlap the experimental ones given in Ref *14*.

The numerical results for $K_I{}^{dyn}$ are in good agreement with the experimental findings in the accelerating and constant-velocity stages of the propagating cracks. The numerical results seem to fall within the accuracy range of the experimental data. The results for the decelerating stage are still unsatisfactory. This may be due to wave reflections, appearing at the crack tip during this part of the simulation, which have no counterpart in experiments. Improvement of this stage is currently being worked on by the authors.

The Energy Release Rate

Numerical results for the dynamic energy release rate $G_I{}^{dyn}$ as a function of crack length are given in Fig. 7. $G_I{}^{dyn}$ was evaluated at each time step using Eq 8. For comparison, a numerically evaluated curve for $G_I{}^{stat}$ is shown by a dashed line in the same figure.

Experimental verification of the numerical findings is still impossible as no experimental data for $G_I{}^{dyn}$ exist. However, an additional corroboration of the SMF2D code is found in comparing Freund's [*16*] analytically de-

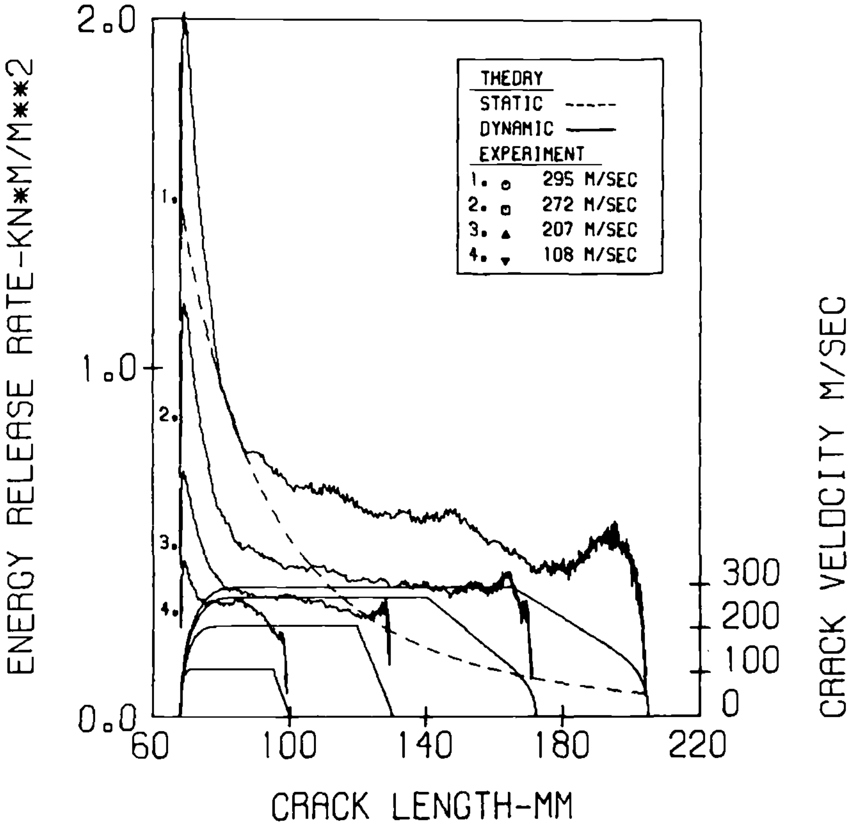

FIG. 7—*Dynamic and static energy release rates* $(KN \cdot m/m^2)$.

rived crack-velocity-dependent $F(\dot{\alpha})$ function, relating G_I^{dyn} to $K_I^{2\ \text{dyn}}$, with its numerical counterpart

$$G(\dot{\alpha}) = \left(\frac{J}{K_I^{2\ \text{stat}}}\right)\left(\frac{G_I^{\text{dyn}}(\tau)}{J}\right)\left[\frac{\sigma_{\eta\eta}(\tau)}{\sigma_{\eta\eta}(0)}\right]^2 \tag{9}$$

where, for $J/K_I^{2\ \text{stat}}$ we substitute $(1 - \nu^2)/E$ in the plane-strain case and $1/E$ in the plane-stress case with E designating Young's modulus.

The ratio of $G(\dot{\alpha})/F(\dot{\alpha})$ is given in Fig. 8, showing that during the constant-velocity stage the numerical results are in excellent agreement with the analytical ones.

Since the relation between G_I^{dyn} and K_I^{dyn}, as was found in the simulation, is in good agreement with the one predicted by the analytical solu-

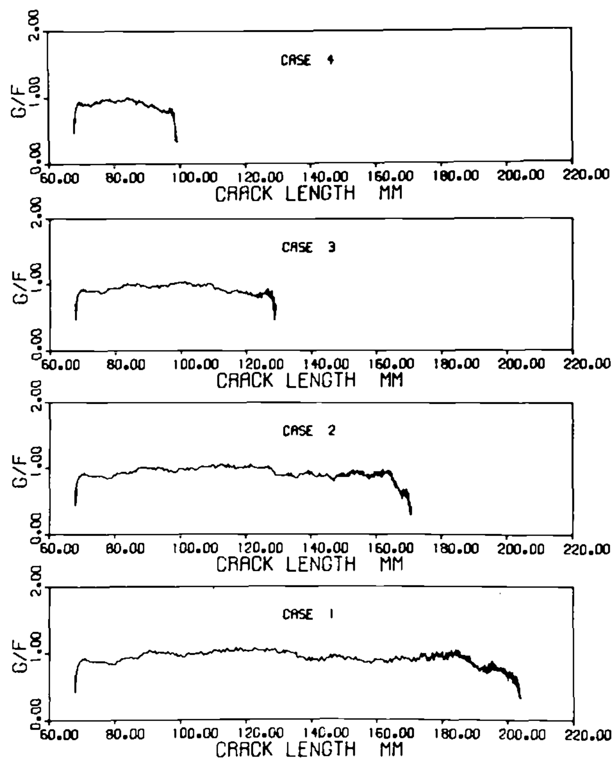

FIG. 8—*Ratio between the numerical and analytical values of the crack-velocity-dependent function.*

tion, and since the K_I^{dyn} is in good agreement with its experimental values, one may assume that the numerical values obtained for G_I^{dyn} are correct.

Conclusions

An improved finite-difference code for simulation of dynamic crack propagation was presented. Preliminary results for static and dynamic cases were given, most of which are in very good agreement with experimental and analytical findings. Compared with the previous codes, the SMF2D code has the following advantages:

In the Static Case

1. A convergency, which is approximately twice as fast for the same mesh sizes.
2. Crack lengths must not be a multiple integer of the mesh size.

In the Dynamic Case

1. Crack growth is not simulated any more by intermittent one-mesh-size extensions, which in the past implied the solution of a sequence of transient problems, each separately contributing to a disturbing noise which has no counterpart in practice. Instead, while choosing any desirable mesh size, the crack may now be smoothly extended—each time step by a fraction of a grid interval—yielding consequently much more reliable results.

2. The degree of resolution depends solely on the time increment, the shortening of which has obviously no impact on the numerical stability.

3. $G_I{}^{dyn}$, the most significant variable in fracture mechanics, is readily derived.

In Both Static and Dynamic Cases

The local accuracy at the vicinity of the crack tip can be readily improved with no significant expenditure on either the computer's memory or its time consumption.

Acknowledgment

The work of the first author was carried out in the course of research sponsored by the U.S. Army Research Office under Grant DAAG29-78-G-0086.

References

[1] Broberg, K. B., *Arkiv für Physik*, Vol. 18, 1960, pp. 159-192.
[2] Baker, B. R., *Journal of Applied Mechanics*, Vol. 29, 1962, pp. 449-458.
[3] Freund, L. B., *Journal of the Mechanics and Physics of Solids*, Vol. 22, 1974, pp. 137-146.
[4] Nilson, F., *International Journal of Fracture*, Vol. 8, 1972, pp. 403-411.
[5] Aberson, J. A., Anderson, J. M., and King, W. W. in *Fast Fracture and Crack Arrest*, *ASTM STP 627*, G. T. Hahn and M. F. Kanninen, Eds., American Society for Testing and Materials, 1976, pp. 123-134.
[6] Rydholm, G., Fredriksson, B., and Nilson, F. in *Numerical Methods in Fracture Mechanics*, A. R. Luxmoore and D. R. J. Owens, Eds., University of Swansea, Swansea, Wales, Jan. 1978, pp. 9-13.
[7] Shmuely, M., *International Journal of Fracture*, Vol. 10, 1974, pp. 596-598.
[8] Shmuely, M. and Peretz, D., *International Journal of Solids and Structures*, Vol. 12, 1976, pp. 67-79.
[9] Kanazawa, T. and Machida, S. in *Proceedings*, 4th International Conference on Fracture, D. M. R. Taplin, Ed., Waterloo, Ont., Canada, 1977, pp. 223-232.
[10] Stöckl, H. and Auer, F., *International Journal of Fracture*, Vol. 12, 1976, pp. 345-358.
[11] Day, A. S., *The Engineer*, Jan. 1965, pp. 218-221.
[12] Shmuely, M. and Alterman, Z. S., *Journal of Applied Mechanics*, Vol. 40, No. 4, Dec. 1973, pp. 902-908.
[13] Roake, D. P. and Cartwright, D. J., *Compendium of Stress Intensity Factors*, Her Majesty's Stationery Office, London, England, 1977, pp. 88-89.

[14] Kalthoff, J. F., Beinert, J., and Winkler, S. in *Fast Fracture and Crack Arrest, ASTM STP 627*, G. T. Hahn and M. F. Kanninen, Eds., American Society for Testing and Materials, 1976, pp. 161-176.
[15] Peretz, D. and Shmuely, M., *International Journal of Fracture*, Vol. 13, 1977, pp. 231-235.
[16] Freund, L. B. in *The Mechanics of Fracture*, F. Erdogan, Ed., ASME-AMD, American Society of Mechanical Engineers, Vol. 19, 1976, pp. 105-134.
[17] Bazant, Z. P., Glazik, J. L., and Achenbach, J. D., *Computer & Structures*, Vol. 8, 1978, pp. 193-198.

S. Mall,[1] *A. S. Kobayashi,*[2] *and F. J. Loss*[3]

Dynamic Fracture Analysis of Notched Bend Specimens

REFERENCE: Mall, S., Kobayashi, A. S. and Loss, F. J., **"Dynamic Fracture Analysis of Notched Bend Specimens,"** *Crack Arrest Methodology and Applications, ASTM STP 711,* G. T. Hahn and M. F. Kanninen, Eds., American Society for Testing and Materials, 1980, pp. 70-85.

ABSTRACT: A dynamic finite-element code was used to determine dynamic initiation fracture toughness, K_{Id}, in 25.4-mm-thick (1 in.) notched bend specimens of A533B steel and a 15.9-mm-thick (5/8 in.) dynamic tear specimen of 6061 aluminum alloy. These specimen types can reflect varying dynamic fracture response due to differences in test temperature, specimen geometry, and material as well as notch tip sharpness. Measured load-time histories were applied to the tup as modeled by finite elements, and the dynamic stress-intensity factor was computed by a calibrated crack opening displacement procedure. Dynamic stress-intensity factors were also computed by the ASTM Test for Plane-Strain Fracture Toughness of Metallic Materials (E 399-74) using a load based on local dynamic strain measurements and a static K calibration.

Reasonable agreements between measured and computed dynamic strains in the vicinity of the crack tip verified the accuracy of the dynamic finite-element model. The attendant agreement between measured versus computed time-varying dynamic stress-intensity factors also verified, for the first time, the applicability of ASTM E 399-74 for computing dynamic initiation fracture toughness, K_{Id}, on the basis of local dynamic strain measurements.

KEY WORDS: dynamic initiation fracture toughness, notch bend specimen, dynamic finite-element analysis

The dynamic tear (DT) specimen is a simple dynamically loaded three-point bend specimen which was developed by the Naval Research Laboratory (NRL) [*1-3*][4] to characterize the fracture resistance of ductile material by

[1]Assistant professor, University of Maine-Orono, Mechanical Engineering, Orono, Maine 04473.

[2]Professor, University of Washington, Department of Mechanical Engineering, Seattle, Wash. 98195.

[3]Head, High Temperature System Criterion Section, Thermostructural Materials Branch, Material Science and Technology Division, Naval Research Laboratory, Washington, D. C. 20375.

[4]The italic numbers in brackets refer to the list of references appended to this paper.

an energy criterion. As a result of extensive experimental investigation, empirical correlations were made between the DT energy (DTE) and the static fracture toughness, K_{Ic}, for high-strength steels that are not strain-rate sensitive [4]. Research is also underway to establish a correlation between the DTE and dynamic initiation fracture toughness, K_{Id}. In this regard, an empirical correlation between DTE and K_{Id} at the nil-ductility transition (NDT) temperature has been obtained and the size effect on DTE has been established [3]. In a parallel research effort to the preceding, theoretical and experimental analyses were made on the dynamic responses of a DT specimen and the associated loading system [5] in order to establish the relationship between hammer force and specimen bending moment during impact. With these studies as a basis, later NRL research [6] focused on an analysis of forces and bending moments in an ASTM Test for Plane-Strain Fracture Toughness of Metallic Materials (E 399-74) type bend specimen. The objective of the latter program was to establish an experimental method for K_{Id} measurements. The results of the preceding programs showed that the instantaneous tup load at fracture cannot be directly related to the K_{Id} of the material. Furthermore, it was concluded that the measurement of K_{Id} required that the specimen be instrumented to determine the local dynamic state of stress surrounding the crack tip at the time of fracture.

As another parallel effort in analyzing the dynamic response of a DT specimen, one of the authors and his colleague initiated a dynamic photoelastic study [7] of the DT specimen [ASTM Test for Dynamic Tear Energy of Metallic Materials (E 604-77)]. More recently, two of the authors extended this study and used a combined experimental and numerical procedure, that is, dynamic photoelasticity and dynamic finite-element analysis, to determine the dynamic fracture responses of DT specimens machined from brittle and ductile photoelastic polymers, namely, 9.5-mm-thick (3/8 in.) Homalite-100 plates [8] and 3.2-mm-thick (1/8 in.) polycarbonate plates [9], respectively. Despite their thinness and pronounced ductility under static loading, the polycarbonate DT specimens exhibited cleavage fracture, thus providing a phenomenological model of the dynamic response in a low-carbon steel notched bend specimen in the linear elastic regime, that is, near the NDT temperature. The results of the aforementioned combined dynamic photoelastic and finite-element analyses showed the following.

1. K_{Id} is approximately equal to K_{Ic} of the brittle Homalite-100 specimens.

2. K_{Id} is approximately equal to 65 percent of the pop-in K_{Ic} of the ductile polycarbonate specimens.

3. The kinetic energy at complete specimen fracture represents a significant portion of the total external work imparted to both brittle and ductile specimens.

4. K_{Id} can be determined from the dynamic strain measured near the crack tip for both brittle and ductile specimens.

The fourth conclusion resulted from a comparison of K_{Id} obtained directly from dynamic photoelasticity and dynamic finite-element analysis with that obtained by a dynamic finite-element modeling of the experimental procedure where K_{Id} is computed, following Loss [6], from a local dynamic strain value using a static calibration of the three-point bend specimen. The success of Loss's procedure in determining K_{Id} in photoelastic DT specimens led to the present investigation for verifying this approach when used to determine K_{Id} in actual steel and aluminum bend specimens. In our analysis of these opaque specimens, photoelasticity was replaced by dynamic finite-element analysis. The latter was used to determine the local transient state of stress surrounding the crack tip as well as to determine K_{Id} directly. Results of this investigation are summarized here.

Loss's Procedure

With the objective to develop a procedure to determine the dynamic initiation fracture toughness, K_{Id}, without any dynamic analysis, Loss [6] conducted a series of drop-weight impact tests of notched bend specimens. These specimens were instrumented with the strain gage near the crack tip as shown in Fig. 1. Before the impact testing, a static calibration between this strain gage near the crack tip and tup load is established. During the impact test, the dynamic strain of the same gage is measured. This measured dynamic strain in conjunction with static calibration yields the dynamic bending moment or equivalent midspan load on the specimen. The dynamic stress-intensity factor is, then, computed from this equivalent mid-span load using the expression of K_I for the three-point bend specimen given in ASTM E 399-74.

The primary assumption in this procedure is that the ASTM E 399-74 relationship for the stress-intensity factor, K_I, which has been derived for static loading, is also applicable to dynamic impact loading provided the correct value for dynamic specimen load is employed. A calibrated strain gage close to the crack tip is believed to be an accurate indicator of mid-span load that does not, however, reflect the confusing inertial loads that would be sensed by a transducer mounted on the tup.

The experimental method relies on a sudden (pop-in) crack extension that enables K_{Id} to be readily computed from the strain gage-versus-time record. The pop-in is accompanied by a region of cleavage on the fracture surface. A test is therefore considered meaningful by this method only if a macroscopic examination of the fracture surface indicates the absence of ductile crack extension adjoining the fatigue precrack of the specimen. In other words, any ductile tearing that precedes the cleavage pop-in would indicate that crack initiation began in a stable manner, that is, with rising

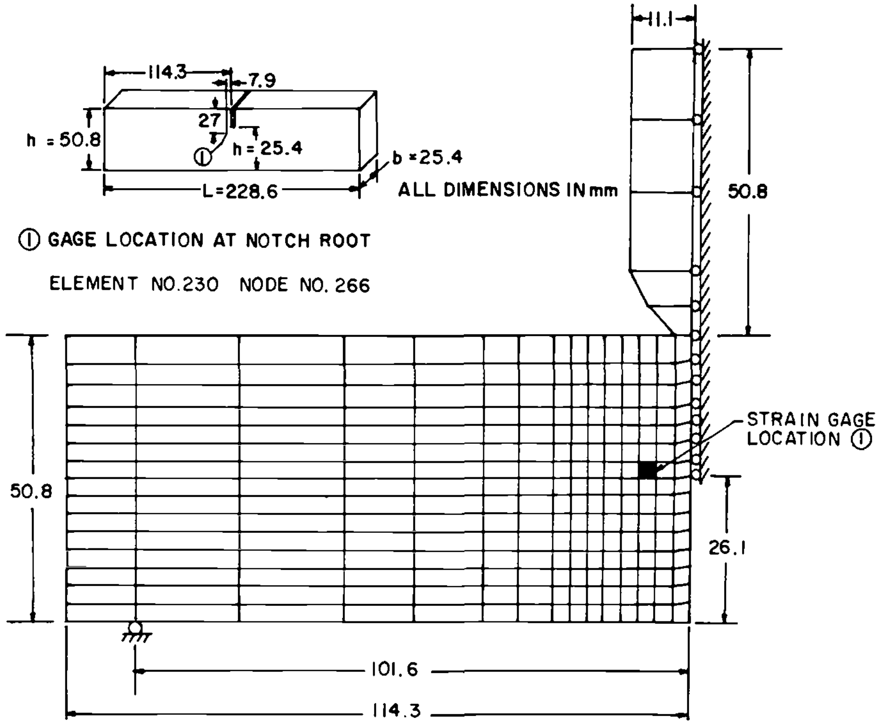

FIG. 1—*A533B steel three-point bend specimen No. 2.*

load. Thus, the occurrence of a pop-in later in time can no longer be equated with the initiation of crack extension.

The foregoing procedure is empirical and therefore requires a firm analytical basis before it can be accepted as a viable experimental tool. For example, if the strain gage is not properly located, its output may sense strains due to inertial effects or reflected stress waves that preclude accurate measurement of K_I. Consequently, a dynamic finite-element analysis was performed to validate the procedure. In the finite-element analysis, K_I was computed as a function of time on the basis of an input loading taken from the measured record of tup load versus time. The validity of the experimental procedure is assessed by the degree of its correspondence with the finite-element calculation of K_I as a function of time.

Dynamic Finite-Element Analysis

The procedure used is a two-dimensional dynamic finite-element code, HONDO [*10*], which was updated and modified for dynamic fracture analysis. The basic modifications consisted of algorithms for start-up and for computing dynamic stress-intensity factor, dynamic energy release rate, fracture energy, kinetic energy, and strain energy at each increment of crack advance.

In the start-up procedure, the initial static stress distribution in a preloaded structure prior to dynamic crack propagation is computed. This initial stress distribution must be in complete static equilibrium prior to the initiation of a dynamic event. The finite-element breakdown and hence the initial stiffness matrix used in this preliminary static analysis should be identical to those at the initiation or at the instant of time $t = 0+$ in the dynamic analysis. Close attention must be given to computational details such as matching the 2×2 Gaussian integration points in the preliminary static and subsequent dynamic analyses in order to avoid any small differences between the finite-element algorithms which will be sensed as unequilibrated residual stresses and thus set off parasitic stress wave propagation in the dynamic analysis.

The dynamic stress-intensity factor can then be computed from the dynamic energy release rate using Freund's relation [*11*]. Alternatively, the near-field dynamic stress field as derived by King et al [*12*] can be used to calculate the dynamic stress-intensity factor directly from the numerically obtained stresses either at the closest Gaussian integration point or at the crack opening displacements (COD's). The appropriateness of these procedures for computing a dynamic stress-intensity factor was checked by analyzing the Broberg problem [*13*] and is discussed in detail in Ref [*14*].

Since the primary concern in this paper is the increase in dynamic stress-intensity factor prior to crack extension, the COD at the second node (not the closest node) adjacent to the crack tip node was used for computing the dynamic stress-intensity factor. While the accuracy of K_{Id} determination using the computed COD of the second node adjacent to the crack-tip node was within $\pm$ 5 percent of the theoretical value of a Broberg crack, no comparable accuracy assessment of the authors' dynamic finite-element algorithm for a dynamically loaded stationary crack was made in the past. Thus, Chen's problem [*15*], which is a centrally cracked strip with step-loaded edge tension, was used for this accuracy assessment. The dynamic stress-intensity factors thus obtained by the authors and those of Chen are shown in Fig. 2. Although some minor deviations between the fine-grid results and Chen's results are noted, the former are in good agreement with similar finite-element results by Anderson et al [*16*] and Glazik [*17*].

Test Specimens

The two steel and one aluminum specimens analyzed in this paper are the standard ASTM specimens of the 25.4-mm-thick (1 in.) bend type (ASTM 399-74) and the 15.9-mm-thick (5/8 in.) DT type (ASTM E 64-77),

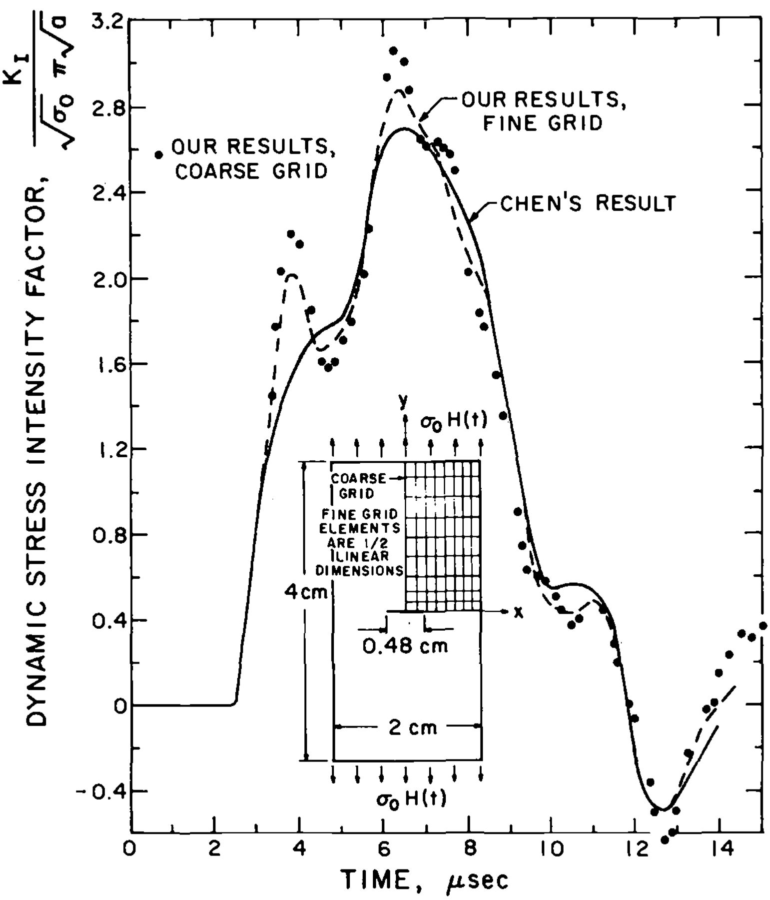

FIG. 2.—*Dynamic stress-intensity factor for a centrally cracked strip subjected to step-loaded edge tension.*

respectively. The legends in Figs. 1 and 3 show the geometries of these specimens as well as the finite-element breakdowns used in the dynamic analysis. The finite-element breakdown used in the first A533B steel specimen had 156 elements and was slightly coarser than that shown in Fig. 1. Since the load transducer on the tup was mounted away from the impact point with the specimen, a portion of the tup was also incorporated into the finite-element model in order to reduce the ambiguity in dynamic loads transmitted to the specimen [*16*].

The two steel specimens were machined from A533B steel and were fatigue-precracked to a nominal 1.5-mm (0.060 in.) crack length beyond the machined notch. These specimens were instrumented with a 3 by 3-mm (1/8 by 1/8 in.) strain gage near the notch tip. The strain-gage output versus time was recorded on a transient recorder and the time of fracture was assessed

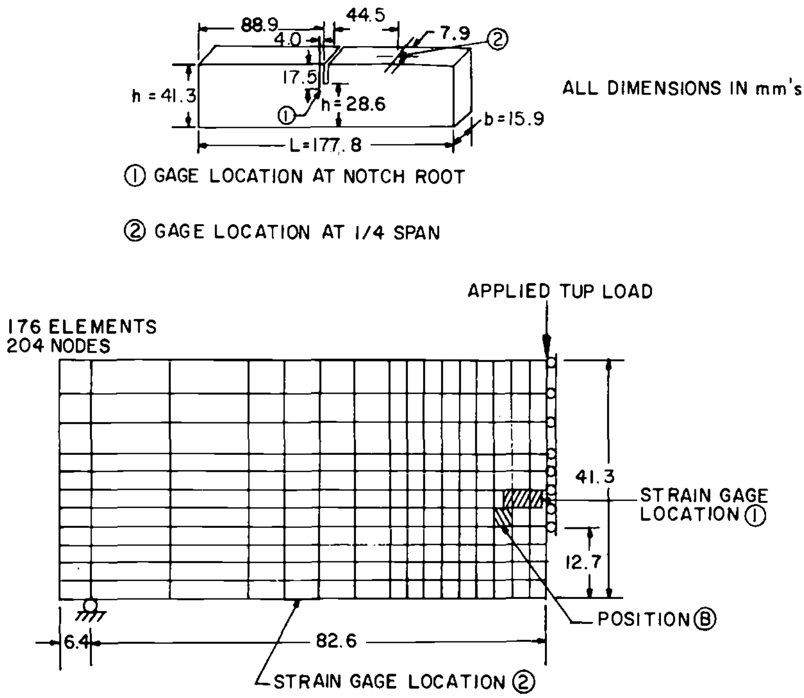

FIG. 3—*6061 aluminum dynamic tear specimen.*

by the discontinuity in strain-gage traces as related to a cleavage pop-in of the specimen. Strain gages were also placed approximately 50 mm (2 in.) from the tup tip on the centerline of the tup to monitor the transient loading condition. These steel specimens were tested in a drop-weight testing machine at NRL [*6*].

The experimental results for the 15.9-mm-thick (5/8 in.) aluminum 6061 DT specimen were taken from Ref *18*. The tup configuration and loading machine for this test differed substantially from that of the drop-weight machine used for the steel specimens and this made it difficult to model with our two-dimensional finite-element code. As a result, the precalibrated transient tup load as provided in Ref *18* was prescribed directly onto the impact point of the specimen without the finite-element model of the tup. The aluminum specimen was instrumented with two 3 by 6-mm (1/8 by 1/4 in.) strain gages at the locations shown in Fig. 3 and the transient strain signals were recorded on a dual-beam oscilloscope. Unlike the notch in the fatigue-precracked steel specimens, the notch in this aluminum specimen was mechanically sharpened to a tip radius of less than 0.025-mm (0.001 in.) radius and was tested in a double-pendulum impact machine.

Results of Dynamic Finite-Element Analysis

The first steel specimen was tested at 10°C (50°F) and the second steel specimen at −18°C (0°F). The NDT for this A533B steel was −18°C (0°F). These specimens were impacted with the same loading rate of 2.9×10^5 MPa$\sqrt{m}$/s, and impact velocity was about 2.5 m/s.

Figure 4 shows the tup load computed from the measured dynamic strains in the tup during this test and the idealized tup load used in the dynamic finite-element analysis. The idealized tup-load time history was input uniformly as a time-dependent boundary condition across the end section of the tup shown in Fig. 1. The modeled portion of the tup along with the specimen in the dynamic finite-element analysis was assumed initially to be at rest. Figure 5 shows the reasonable agreement between the measured and computed dynamic strains at the strain-gage location which is also shown in the legend of Fig. 1. The surface strain was evaluated from the computed dynamic state of stress using a plane-stress assumption. The sharp drop in measured dynamic strain signifies the onset of dynamic crack propagation, which was not modeled in the dynamic finite-element analysis. Thus the computed dynamic strain associated with the assumed stationary crack continues to increase after this crack propagation.

After the accuracy of the computed dynamic strain at a specific location near the crack tip had been verified, the computed dynamic strain was

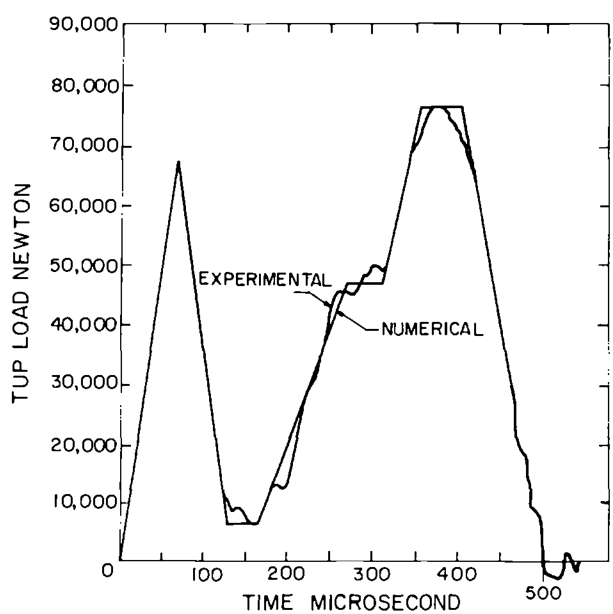

FIG. 4—*Tup load for A533B steel bend specimen No. 1. Test temperature 10°C (50°F).*

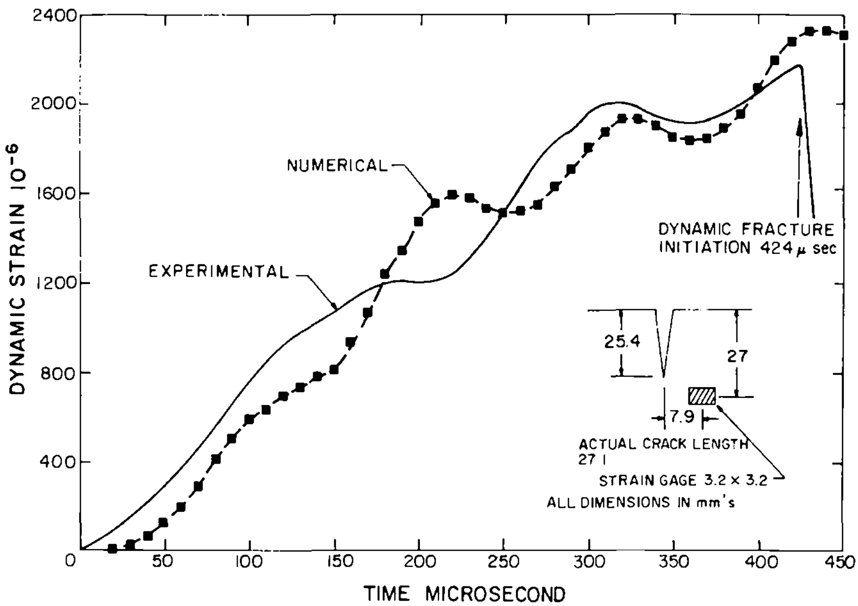

FIG. 5—*Dynamic strain at Location 1, A533B steel bend specimen No. 1.*

then used to compute the dynamic stress-intensity factor using Loss's procedure [*6*]. Figure 6 shows the excellent agreement between the dynamic stress-intensity factor computed directly from the COD and that computed from the numerically determined dynamic strain. The lack of precipitous drop after dynamic fracture initiation in the two dynamic stress-intensity factors is due to the fact that the crack remained stationary in the finite-element model since the objective of this investigation was to study only the dynamic response up to dynamic fracture initiation.

Figure 7 shows the measured and the idealized tup loads during the DT test at −17.7°C (0°F) for the second steel specimen. The loading rate was the same as for the first steel specimen, but fracture initiated 232 μs after impact and is about half of the loading period of the first steel specimen. Figure 8 shows the computed and measured dynamic strains at the strain-gage location shown in Fig. 1. Figure 9 shows again the excellent agreement between the dynamic stress-intensity factors computed directly from COD and by Loss's procedure.

Figure 10 shows the measured and idealized tup loads during the DT test at presumably room temperature for the 6061 aluminum specimen. This specimen was impact-loaded at a velocity of 8.6m/s, which was more than three times the impact velocity for the steel specimens. Figure 11 shows the computed and measured dynamic strains at the two strain-gage locations shown in Fig. 2. Note that these strain gages were not located at

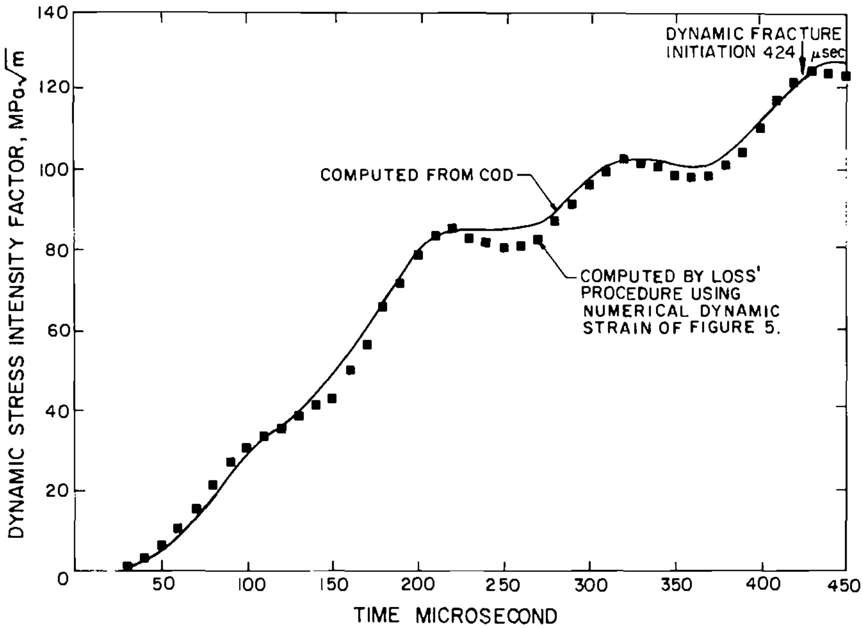

FIG. 6—*Dynamic stress-intensity factor, A533B steel specimen No. 1.*

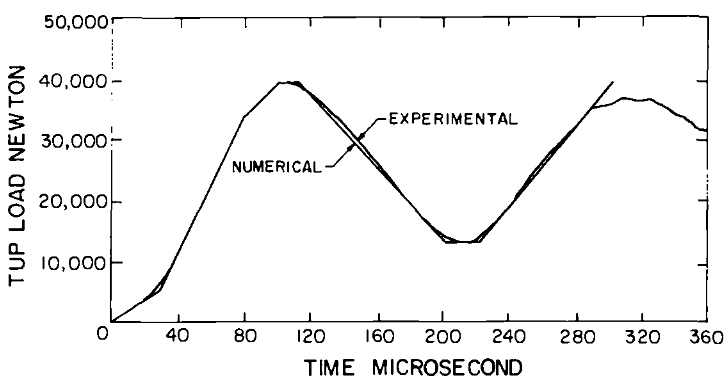

FIG. 7—*Tup load, A533B steel bend specimen No. 2. Test temperature −17.70°C (0°F).*

the geometrically similar position of the previously discussed steel specimens. The lack of strain oscillations, which is prominent in the measured dynamic strains, in the computed dynamic strain at Gage Location 2, as well as the lack of agreement between the two dynamic strains at Gage Location 1, is noted. Despite these discrepancies in computed and experimentally determined dynamic strains, good agreement between the dynamic stress-intensity factors computed directly by COD and by Loss'

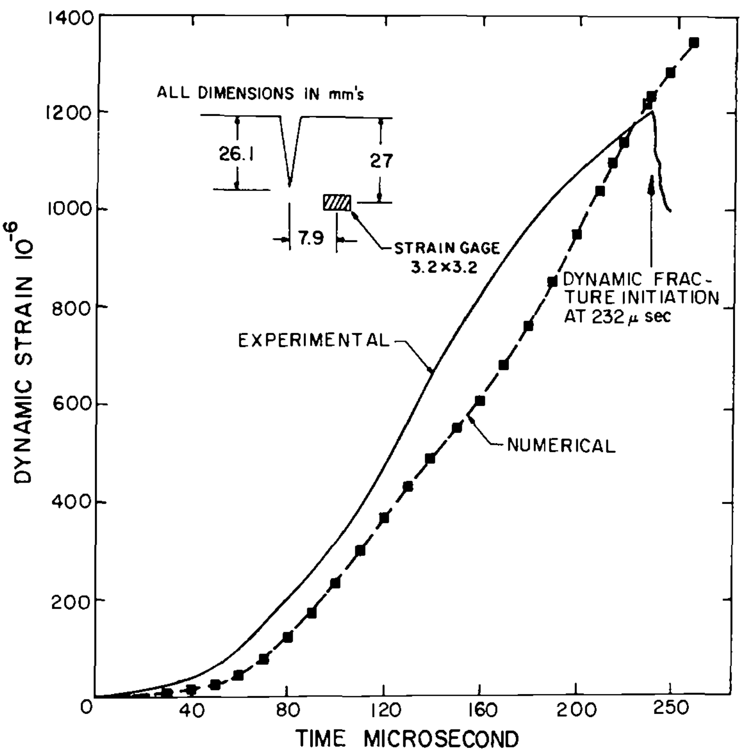

FIG. 8—*Dynamic strain at Location 1, A533B bend specimen No. 2.*

procedure is noted, as shown in Fig. 12. The dynamic stress-intensity factor was also computed by Loss's procedure using the numerically determined dynamic strain at the equivalent gage location considered in the two steel specimens, that is, Location 3 in Fig. 11. This dynamic stress-intensity factor is also in good agreement with the other dynamic stress-intensity factors (Fig. 12).

Discussion

While excellent agreement between the measured and computed dynamic strains in the steel specimens was noted, this comparison differed considerably in the aluminum specimen. This discrepancy could possibly be generated by the dynamic interaction between the compliant specimen support system of the double-pendulum impact machine, which is not modeled in the finite-element model. Another source of error could be the development of a significant plastic yield zone, at the blunt notch tip, which also is not modeled in this elastodynamic finite-element analysis.

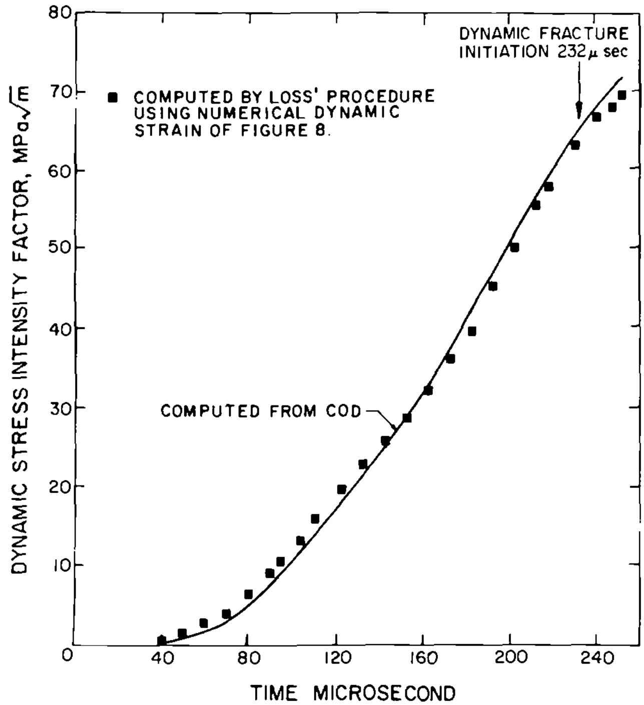

FIG. 9—*Dynamic stress-intensity factor, A533B steel bend specimen No. 2.*

Such an elastoplastic dynamic analysis should be a natural follow-on to this paper.

In using Loss's procedure to determine K_{Id} in bend specimens of different proportions, one should note that the stress wave velocity and nominally the dynamic initiation stress-intensity factor, K_{Id}, are presumably material properties and thus are invariant with specimen size. Since the plastic zone size at the crack tip in somewhat brittle materials is proportional to β, given by the following equation

$$\beta = \frac{1}{B}\left(\frac{K_I}{\sigma_{ys}}\right)^2$$

where B is the specimen thickness and σ_{ys} the static yield strength, it is also independent of specimen size. The reasonable agreement between K_{Id} obtained directly by COD and by Loss's procedure thus suggests that, for larger A533B steel specimens tested at the same temperature, the dynamic strains for K_{Id} calculation, regardless of specimen size, could be measured approximately at the same location from the crack tip, as shown in Fig. 1. For smaller specimens also tested at the same temperature,

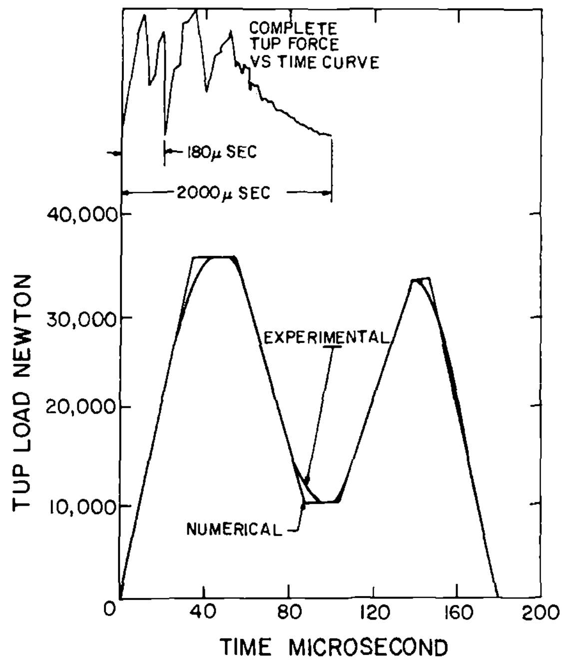

FIG. 10.—*Tup load, 6061 aluminum DT specimen. Test temperature: room temperature.*

the dynamic strains should be measured closer to the crack tip but sufficiently away from the crack-tip plastic zone in order to avoid superposed nonlinear effects in the otherwise elastic analysis.

When the notched bend specimens are used to measure higher K_{Id} at higher test temperature, larger test specimens may be required for valid K_{Id} data. The accompanying increase in plastic zone size with increasing toughness may thus require a shift away from the crack tip of the monitoring strain gage in order to avoid the larger plastic zone. In any event, further detailed elastoplastic dynamic finite-element analyses of such tougher materials as well as of the smaller specimen described in the foregoing should provide the necessary information regarding the optimum positioning of the strain gage.

It is well recognized that hammer (tup) force versus time behavior during impact loading cannot be employed directly to compute K_{Id}. The impact loading introduces inertial effects which cause a disparity between the recorded tup load and the actual load experienced by the specimen. Electronic filters have been used to attenuate the tup-load oscillations [*19*], but such filtering must be coupled with the minimum time to fracture, which is also unknown. More important is the lack of coincidence between the peak of the hammer (tup) force versus time history and the hammer load at crack initiation. Thus, Loss's present procedure for computing

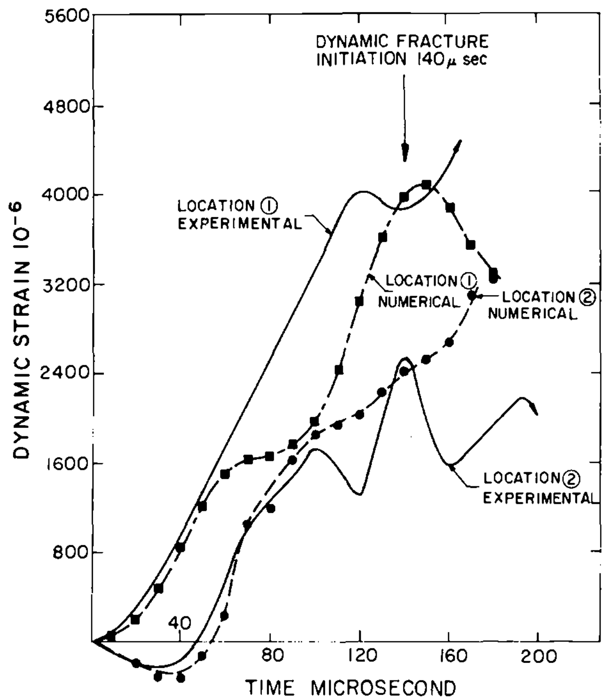

FIG. 11—*Dynamic strains at Locations 1 and 2, 6061 aluminum specimen.*

dynamic initiation fracture toughness, K_{Id}, from the dynamic strain near the crack tip in conjunction, without any dynamic analysis, has a great potential application in the instrumented impact tests.

Conclusions

1. Limited comparisons between measured and calculated dynamic strains near the crack tip indicate that the dynamic finite-element model in this paper is a good representation of the three-point bend test under the impact test conditions considered herein.

2. Loss's procedure of computing the dynamic stress-intensity factor up to dynamic fracture initiation is accurate and simple.

Acknowledgments

The dynamic finite-element analysis of a DT specimen was initiated at the University of Washington under the Office of Naval Research Contract No. 00014-76-C-0600 NR 064-478. Subsequent numerical computations were conducted at the University of Maine, Orono, under institutional funding. The experimental results were generated at the Naval Research

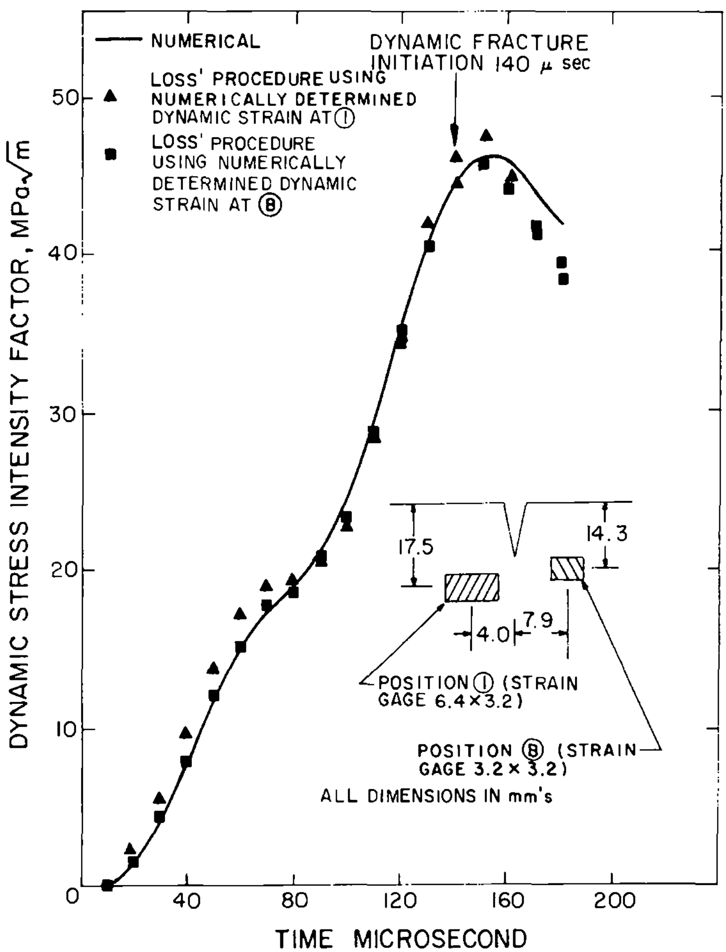

FIG. 12—*Dynamic stress-intensity factor, 6061 aluminum DT specimen.*

Laboratory under the support of the Nuclear Regulatory Commission and the Office of Naval Research. The authors gratefully acknowledge the support received from these multiple sources.

References

[1] Lange, E. A., Puzak, P. P., and Cooley, L. A., "Standard Method for the 5/8 Inch Dynamic Tear Test," Naval Research Laboratory Report 7159, 27 Aug. 1970.

[2] Hawthorne, J. R. and Loss, F. J., "Fracture Toughness Characterizations of Shipbuilding Steel," Naval Research Laboratory Report 7701, 10 July 1974.

[3] Lange, E. A., "Dynamic Fracture Resistance Testing and Methods for Structural Analysis," Naval Research Laboratory Report 7979, 27 April 1976.

[4] Pellini, W. S., "Evolution of Engineering Principles for Fracture-Safe Design of Steel Structures," Naval Research Laboratory Report 6957, 23 Sept. 1969.

[5] Nash, G. E., "An Analysis of the Forces and Bending Moments Generated During the NRL Dynamic Tear Test," Naval Research Laboratory Report 6864, 30 Jan. 1969.
[6] "Structural Integrity of Water Reactor Pressure Boundary Components," Progress Report ending Feb. 1976, F. J. Loss, Ed., Naval Research Laboratory Report 8006 (also NRL NUREG 1), 26 Aug. 1976.
[7] Kobayashi, A. S. and Chan, C. F., *Experimental Mechanics*, Vol. 16, No. 5, May 1976, pp. 176-181.
[8] Mall, S., Kobayashi, A. S., and Urabe, Y., *Experimental Mechanics*, Vol. 18, No. 12, Dec. 1978, 449-456.
[9] Mall, S., Kobayashi, A. S., and Urabe, Y. in *Fracture Mechanics, ASTM STP 677*, American Society for Testing and Materials, 1979, pp. 498-510.
[10] Key, S. W., "HONDO, A Finite Element Computer Program for the Large Deformation Dynamic Responses of Axisymmetric Solid," Sandia Laboratories, SLA-74-0039, Albuquerque, N. Mex., April 1974.
[11] Freund, L. B., *Journal of Mechanics and Physics of Solids*, Vol. 20, 1972, pp. 141-152.
[12] King, W. W., Malluck J. F., Aberson, J. A., and Anderson, J. M., *Mechanics Research Communication*, Vol. 3, No. 3, 1976, pp. 197-202.
[13] Broberg, K. B., *Arkir fur Fysik*, Vol. 18, 1960, pp. 159-198.
[14] Kobayashi, A. S., Mall, S., Urabe, Y., and Emery, A. F. in *Numerical Methods in Fracture Mechanics*, A. R. Luxmoore and D. R. J. Owens, Eds., University College of Swansea, Swansea, Wales, 9-13 Jan. 1978, pp. 673-684.
[15] Chen, Y. M., *Engineering Fracture Mechanics*, Vol. 7, 1975, pp. 653-660.
[16] Anderson, J. M., Aberson, J. A., and King, W. W. in *Computational Fracture Mechanics*, E. F. Rybicki and S. E. Benzley, Eds., American Society of Mechanical Engineers, 1975, pp. 173-184.
[17] Glazik, J. L., Jr., "Dynamic Finite Element Analysis of Cracked Bodies," ASME Preprint 78-PVP-94, American Society of Mechanical Engineers, 1978.
[18] Nash, G. E. and Lange, E. A., *Journal of Basic Engineering, Transactions*, American Society of Mechanical Engineers, Vol. 91, Series D, Sept. 1969, pp. 535-543.
[19] Ireland, D. R. in *Proceedings*, International Conference on Dynamic Fracture Toughness, London, England, 5-7 July 1976, pp. 47-62.

Fundamental Issues in Dynamic Crack Propagation and Crack Arrest Analysis

L. Dahlberg,[1] *F. Nilsson,*[1] *and B. Brickstad*[1]

Influence of Specimen Geometry on Crack Propagation and Arrest Toughness

REFERENCE: Dahlberg, L., Nilsson, F., and Brickstad, B., "**Influence of Specimen Geometry on Crack Propagation and Arrest Toughness,**" *Crack Arrest Methodology and Applications, ASTM STP 711,* G. T. Hahn and M. F. Kanninen, Eds., American Society for Testing and Materials, 1980, pp. 89–108.

ABSTRACT: A number of crack propagation experiments on four different specimen geometries were performed in order to investigate the existence of a unique relationship between crack propagation toughness and crack-tip velocity. For one geometry, dynamic finite-element method (FEM) calculations were found to be necessary in order to obtain proper stress-intensity factors, whereas quasi-static FEM-calculations were found to be sufficient for the other geometries. Crack-tip velocities were determined from continuous recordings of crack length versus time, which was measured by an impedance method. The stress-intensity factor and the instantaneous crack-tip velocity were obtained for a number of crack lengths for each experiment. The experimental results do not contradict the hypothesis of a unique relationship between these two quantities at low load levels; neither do they contradict the hypothesis of a geometry-independent crack arrest toughness. At high load levels a deviation from the uniqueness was observed. The height of the specimens was found to influence the crack propagation toughness level at the beginning of deviation from the unique relationship.

KEY WORDS: arrest toughness, crack arrest, crack propagation, crack propagation toughness, dynamic fracturing, dynamic finite-element solutions, dynamic linear fracture mechanics, dynamic toughness, fracture properties, nonlinear behavior

In recent years there has been a growing interest in crack arrest problems. It has been recognized that in order to predict arrest of rapidly moving cracks, a description of the crack growth preceding arrest is needed [*1,2*].[2] Most of the work done in this area has been based on the assumption of linear elastic fracture mechanics (LEFM); that is, the state at the crack tip

[1] Research assistant, research associate, and research assistant, respectively, Department of Strength of Materials and Solid Mechanics, The Royal Institute of Technology, S-100 44 Stockholm, Sweden.

[2] The italic numbers in brackets refer to the list of references appended to this paper.

is assumed to be characterized by one linear elastic parameter, usually the stress-intensity factor.

The theoretical foundation of dynamic LEFM appears to be good. The existing empirical knowledge is, however, not yet sufficient in order to judge whether the linear theory really is valid or, rather, if it gives the desired accuracy level in a certain situation.

In linear theory it is implied that for a given material a unique relationship exists between crack propagation toughness and instantaneous crack-tip velocity. By unique relationship is meant in this context a one-to-one unique relationship. Previous investigations indicate, however, a certain dependence of crack propagation toughness on the geometry of the body and on crack-tip acceleration. From crack propagation experiments at high load levels on two geometries of steel foil, Nilsson [3] reported a pronounced geometry dependence. Kalthoff et al [4] experimented on three different specimen geometries made of a polymeric material, namely, two different double cantilever beam geometries and one crack line loaded, single-edge notched geometry, and also found geometry dependence. Hahn et al [5], on the other hand, found good agreement between crack propagation toughness data obtained from compact tension and double cantilever beam specimens made of the same heat of A533B steel. Investigations by Kobayashi and Dally [6] as well as an earlier reported part of this investigation, Brickstad and Nilsson [7], showed a dependence of crack propagation toughness on crack-tip acceleration, especially in the low-velocity region.

In the present investigation, results from dynamic crack propagation experiments performed on a number of geometries are reported and compared in order to shed some light on the important question of geometry dependence. Some observations concerning the dependence of crack-tip acceleration are also reported.

General Background

A definition of what is here meant by dynamic LEFM is that during crack growth the following equation shall be satisfied to some desired degree of accuracy

$$\begin{aligned} K(t) &= K_{pc}(\dot{a}) \qquad \dot{a} > 0 \\ K(t) &< K_{pc}(\dot{a} = 0) \qquad \dot{a} = 0 \end{aligned} \tag{1}$$

where

K = stress-intensity factor,
t = time,
K_{pc} = crack propagation toughness, and
$\dot{a}$ = crack-tip velocity.

For a given material, K_{pc} is assumed to be a unique function only of the instantaneous crack-tip velocity; however, K_{pc} may well also vary with the thickness of the plane body as is the case in static LEFM. Experimental results by Hahn et al [8] as well as unpublished results by the authors indicate, however, independence of thickness at considerably smaller thicknesses than in the static case. A possible explanation is that deformation in the thickness direction is hindered by inertia effects and thereby a state of plane strain is developed at a smaller thickness than in the static case.

It has been shown by several authors [9-12] that for a linear elastic body there exists a universal displacement and stress distribution in the vicinity of an arbitrarily propagating crack tip only dependent on the instantaneous crack-tip velocity

$$u_i \rightarrow \frac{K(t)}{\mu} \sqrt{2\pi r}\, f_i(\varphi, \dot{a}) \qquad \text{as } r \rightarrow 0 \tag{2}$$

$$\sigma_{ij} \rightarrow \frac{K(t)}{\sqrt{2\pi r}} g_{ij}(\varphi, \dot{a}) \qquad \text{as } r \rightarrow 0 \tag{3}$$

where

u_i = displacement vector,
σ_{ij} = stress tensor,
r, φ = moving coordinate system attached to crack tip,
μ = shear modulus, and
f_i, g_{ij} = universal functions of φ, $\dot{a}$, and the elastic properties.

A description of crack growth based on the linear elastic parameter K can be successful only if the nonelastic deformation occurring in the body is associated with crack growth and concentrated to such a small region in the vicinity of the crack tip that it is dominated by the elastic singularity, Eqs 2 and 3. A dependence of K_{pc} on higher-order time derivatives of crack length cannot, however, be excluded even if the nonelastic deformation is dominated by the elastic singularity, as is indicated by earlier experimental results.

A theoretical investigation of the dependence of K_{pc} on body geometry and on higher-order time derivatives of crack length would require a fully nonlinear dynamic analysis. Today, we have no methods to solve such complicated problems. Instead, an empirical procedure seems to be the best way.

By carefully performed experiments it should be possible to observe any significant dependence of K_{pc} on body geometry and on higher-order time derivatives of crack length or at least on crack-tip acceleration.

The ultimate goal is to formulate empirical conditions for the limit of dynamic linear fracture mechanics as has been done for static linear fracture mechanics. The number of conditions will, however, be larger in the dynamic case. The following conditions derived by Dahlberg and Nilsson [13] have, for instance, no counterpart in the static case

$$\frac{R_p}{K \cdot \dot{a}} \cdot \left| \frac{\partial K}{\partial t} \right| \ll 1 \tag{4}$$

$$\frac{R_p}{\dot{a}^2} \cdot \left| \frac{\partial^2 a}{\partial t^2} \right| \ll 1 \tag{5}$$

where R_p is the radius of the nonelastic zone and a is the crack length.

A considerable influence on K_{pc} of body geometry as well as of higher-order time derivatives of crack length must probably be accepted within the frame-work of dynamic linear fracture mechanics. The alternative in the case of geometry dependence is a fully nonlinear dynamic analysis, and how a dependence of higher-order time derivatives of crack length shall be explicitly involved in the linear theory is at present not clear.

The purpose of this study is to investigate the limit of linear theory for a cold-rolled and hardened carbon steel, and to increase the knowledge necessary for formulating relevant empirical conditions of general validity.

Experimental Procedure

The experiments were performed on four different specimen geometries. The specimens were made of sheets of a cold-rolled and hardened carbon steel with a thickness of 0.5 mm, thus giving plane-stress conditions. The mechanical properties of the material are given in Table 1. The static fracture toughness given in the table is the value at initiation of slow, stable crack growth.

All four specimen geometries were rectangular, with a width w of 406 mm, and are shown in Fig. 1. The following heights and loading conditions were used.

1. Specimens A, B, and C: total height $2h$ between grips was 200, 400, and 600 mm, respectively. The specimens were given a uniform displacement v_0 in a special testing machine where fixed grip conditions can be realized. The boundary displacement v_0 was slowly increased until fracture

TABLE 1—*Mechanical properties of the material.*

Density	$\rho = 7870$ kg/m^3
Poisson's ratio	$\nu = 0.3$
Young's modulus	$E = 2.1 \times 10^5$ MN/m^2
Yield strength	$\sigma_{ys} = 1500$ MN/m^2
Shear wave velocity	$C_2 = 3200$ m/s
Static fracture toughness	$K_c = 125$ MN/m$^{3/2}$

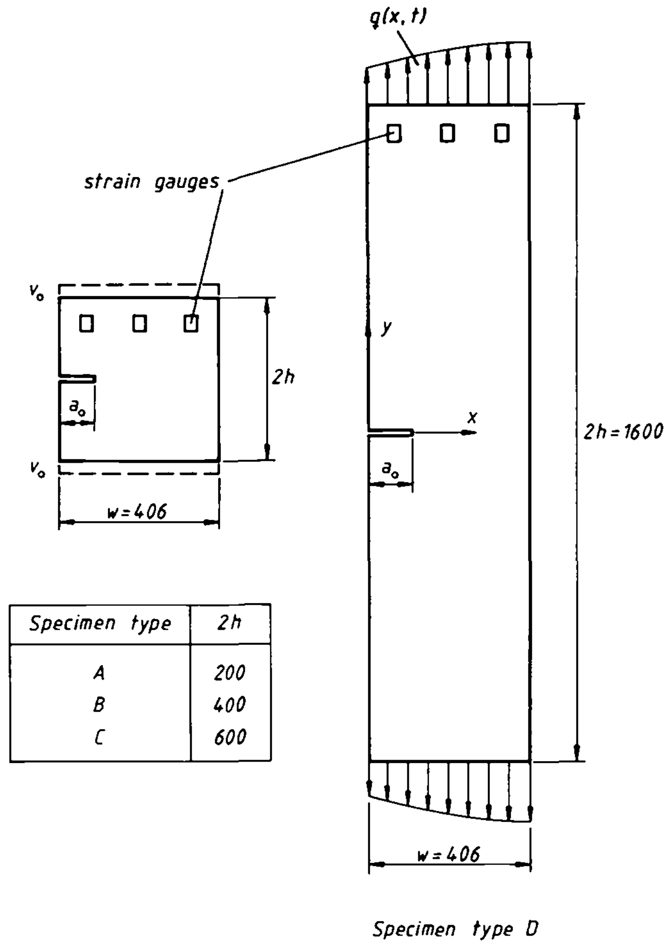

Specimen type	2h
A	200
B	400
C	600

FIG. 1—*Specimen geometries and loading conditions.*

occurred. For a detailed description of the testing machine, see Ref *14*. The actual displacement v_0 at the boundaries was determined by three strain gages glued to the specimen; see Fig. 1. The deflection of the machine was in all cases less than 12 percent of the total displacement of the specimen $2v_0$. Measurement of the strain in the specimen during a rapid crack propagation event shows, however, that the fixed grip conditions are much better fulfilled in a crack propagation experiment. This is due to inertia effects of the large masses of the machine.

2. Specimen D: total height $2h$ between grips was 1600 mm. The specimens were loaded in a hydraulic testing machine where the load could be slowly increased until fracture occurred. Each end of the specimen was clamped in a jointed grip to avoid unsymmetric loading. During the whole

propagation event, the strains in the vicinity of one specimen end were measured by three strain gages; see Fig. 1. In Ref *7*, more-detailed information concerning the experimental procedure and the evaluation of the experiments on Specimen D is given.

All specimens were edge notched. The notch root was sharpened by a specially prepared saw blade giving a root radius of about 0.1 mm. In order to initiate fracture at different load levels, the initial crack length a_0 was varied between 2 and 100 mm. A continuous recording of crack length as a function of time was made by use of an impedance method developed by Carlsson [*15*]. The crack length signal and the signals from the three strain gages were recorded on a data tape recorder. The information could afterwards be visualized on a storage oscilloscope and obtained for any time point of the crack propagation event.

Evaluation Procedure

The stress-intensity factor was calculated using a method developed and implemented into the finite-element method (FEM) program system NONSAP [*16,17*] by Rydholm et al [*18*]. The method consists of a particular way of gradual node relaxation in order to simulate a continuous crack growth.

The computations were performed under the assumption of plane-stress conditions and isotropic, linearly elastic material behavior.

The FEM mesh used contained 342 elements and 651 degrees of freedom for Specimens A, B, and C and 429 elements and 841 degrees of freedom for Specimen D; see Fig. 2. In the mesh for Specimen D, a row of long, very stiff and almost massless elements was added to the end of the actual specimen geometry to ensure that the specimen end maintained its straightness and underwent a rigid-body rotation around the joint.

With this method the energy released during crack growth from one nodal point to the subsequent one is calculated. An average of the energy release rate G during crack growth between two neighboring nodal points is then obtained by dividing the released energy by the length of the element side, provided the plate has unit thickness. The corresponding stress-intensity factor K is obtained from the following relationship between K and G, which is a consequence of the results about the crack-tip singularity Eqs 2 and 3

$$K = \left[2\mu G \frac{C_2^2 [4(1 - \dot{a}^2/C_1^2)^{1/2} (1 - \dot{a}^2/C_2^2)^{1/2} - (2 - \dot{a}^2/C_2^2)^2]}{\dot{a}^2 (1 - \dot{a}^2/C_1^2)^{1/2}} \right]^{1/2} \tag{6}$$

where C_1 is the velocity of irrotational waves and C_2 is the velocity of equivoluminal waves.

As input to the FEM-program, the times and the actual loads when the

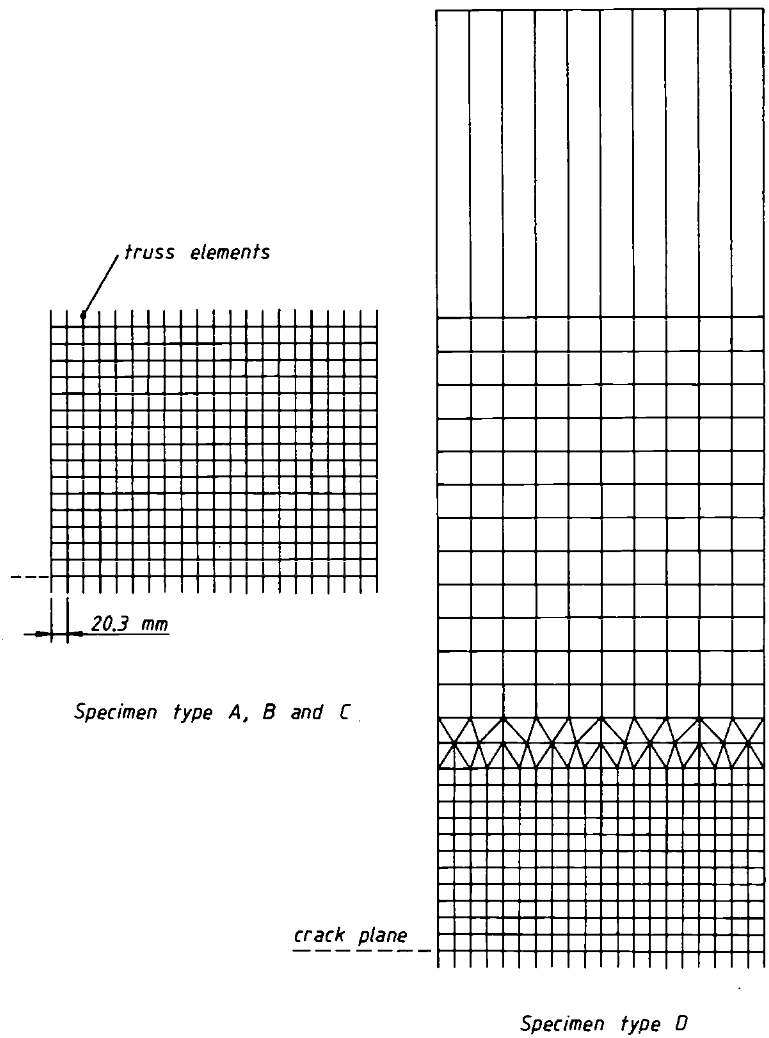

FIG. 2—*FEM-mesh used in the calculations.*

crack tip passes the nodal points along the crack plane are required. The program then assumes a constant crack-tip velocity between neighboring nodal points and makes a linear interpolation of the load.

The passing times were obtained from the crack length versus time recordings. These recordings showed small oscillations of high frequency which probably are due partly to the fact that the crack front does not advance uniformly over the specimen thickness and partly to noise in the electrical measuring equipment. The oscillations were, however, smoothed out before the passing times were determined.

For Specimens A, B, and C, the load was given to the FEM-program in the form of constant boundary displacement v_o as measured at initiation of crack growth. This displacement was kept constant during the whole FEM-simulation of the experiment. Since nonzero displacements cannot be directly prescribed in NONSAP, the recommended arrangement with very stiff truss elements at the boundary loaded to give the desired displacements was used; see Fig. 2. For Specimen D a time-dependent stress distribution in the specimen ends was calculated from the signals of the three strain gages. A second-degree polynomial was fitted to the three signals at every desired time instant. The stress distribution was then converted into consistent nodal forces.

The other quantity needed to establish a $K_{pc} - \dot{a}$ relationship is the instantaneous crack-tip velocity $\dot{a}$. The calculated average of the stress-intensity factor between two neighboring nodal points is referred to the midpoint of the interjacent element side and the same is done for the velocity $\dot{a}$ and the acceleration $\ddot{a}$. To obtain these quantities in a certain midpoint, a third-degree polynomial was fitted to the passing times of four neighboring nodal points, two on each side of the midpoint. Successive time derivations of this interpolation polynomial then gave the velocity $\dot{a}$ and the acceleration $\ddot{a}$ at the considered midpoint.

Figure 3 shows the results from an experiment on Specimen C. Among all experiments on Specimens A, B, and C, this is one of the experiments where the highest velocity was reached. For comparison, the results from an experiment on Specimen D, where approximately the same velocity level was reached, is shown in Fig. 4. In these figures the squares show the crack-tip velocity evaluated in the manner described previously. The triangles show the dynamically calculated stress-intensity factor (K^d) and the circles the corresponding statically calculated stress-intensity factor (K^s). The K^s-values in the experiments on Specimen D were calculated from known static solutions of the stress-intensity factor using the instantaneous values of applied mean stress and bending moment, as estimated from the recordings of the strain gages. Since no standard solution was found for the geometry and loading conditions of Specimen C, the K^s-values for this specimen were determined from quasi-static FEM-calculations where the previously described energy method for calculation of K^d-values was used.

As is seen in the figures, no significant difference was obtained between K^d and K^s in the experiment on Specimen C, whereas K^s was substantially larger than K^d in the experiment on Specimen D. This difference in behavior between the two experiments depends to some degree on the different specimen geometries, but mainly on the different boundary conditions. In the experiment on Specimen C the same amount of energy is supplied to the specimen from the surroundings during the crack propagation event both in the dynamic and in the quasi-static case, that is, no energy. In the experiment on Specimen D, where the specimen is supplied

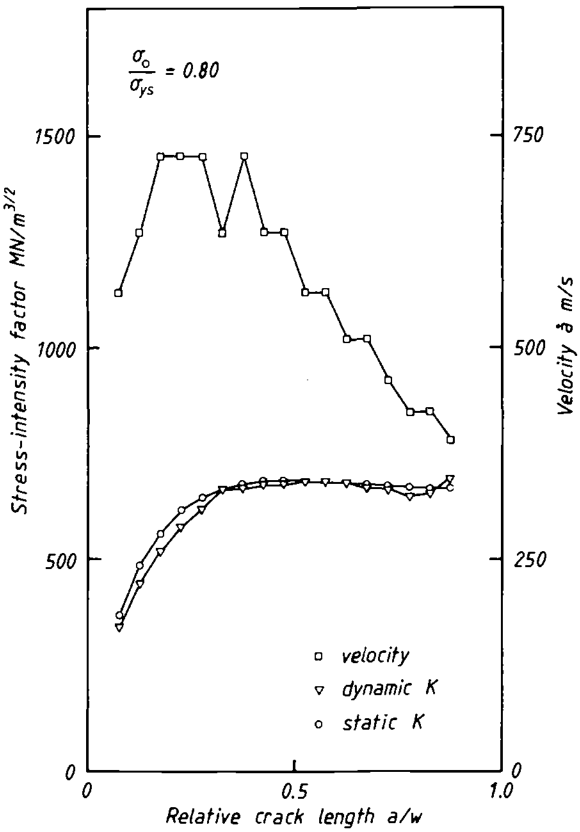

FIG. 3—*Stress-intensity factors and crack-tip velocity as a function of crack length for an experiment on Specimen C.*

by energy during the crack propagation event, less energy is supplied to the specimen in the dynamic case than in the quasi-static case, due to inertia effects in the specimen. This difference in energy supply is clearly reflected in the stress-intensity factor.

These results indicate that a quasi-static treatment is improper for a body exchanging energy with the surroundings during the crack propagation event, that is, for a body with force-controlled boundary conditions. It is especially so if there is energy exchange only in the quasi-static case and not in the dynamic case. For a body without energy exchange with the surroundings, that is, a body with displacement-controlled boundary conditions, a quasi-static treatment can obviously be fully satisfactory even at fairly high propagation velocities. Since the results in Fig. 3 originate from one of the experiments on specimens A, B, and C where the highest velocity was reached, a quasi-static calculation of all stress-intensity factors

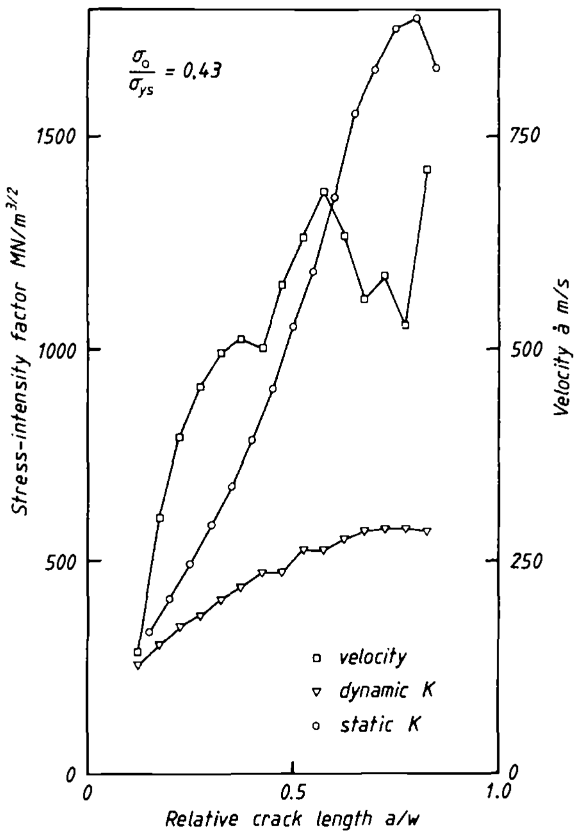

FIG. 4—*Stress-intensity factors and crack-tip velocity as a function of crack length for an experiment on Specimen D.*

in the experiments on these specimens was judged to give satisfactory accuracy. The discrepancy between K^s and K^d for the first evaluated experiment on Specimen D was so large that a dynamic calculation of the stress-intensity factors was considered necessary for each experiment on this specimen type. An extensive presentation and discussion of the eight experiments on Specimen D is found in Ref 7.

In Fig. 5 the statically calculated values of the stress-intensity factor for Specimens A, B, and C are shown as a function of relative crack length. In the figure, K^s is normalized with respect to the stress-intensity factor of the corresponding infinite strip geometry ($K_\infty{}^s$). Disregarding the edges of the specimen, K^s for all three specimen geometries almost reaches the value of the corresponding infinite strip. As can be expected, a slight decrease can be observed in the ratio $K^s/K_\infty{}^s$ as the relative height h/w of the specimen increases.

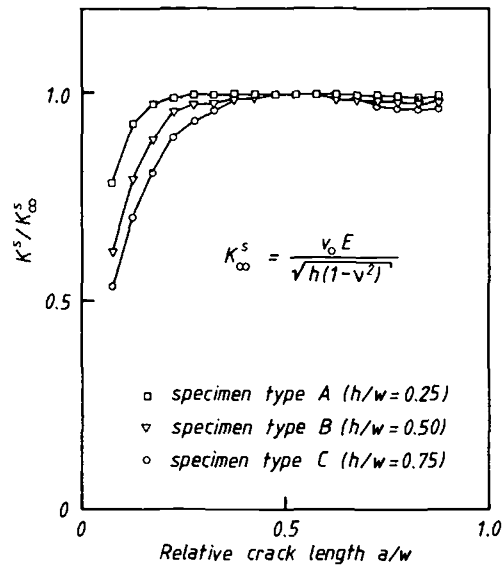

FIG. 5—*Quasi-statically calculated stress-intensity factors for Specimens A, B, and C as a function of crack length.*

The inaccuracy in the FEM-calculations and in the crack length measurements increases at very short crack lengths and very short remaining ligaments between the crack tip and the edge of the specimen. Accordingly, the experiments on Specimens A, B and C were evaluated only within the interval $0.075 \leq a/w \leq 0.875$ and the experiments on Specimen D only within the interval $0.075 \leq a/w \leq 0.825$.

One cause of inaccuracy in the results is the uncertainty in the boundary conditions, that is, the boundary displacement and the calculated stress distribution, respectively. This uncertainty in the boundary conditions has been estimated to be less than 5 percent. The uncertainty in the times when the crack tip passes the nodal points along the crack plane depends on the accuracy of the oscilloscope tracings and is increased by the small oscillations occurring in the signal. The maximum relative error in these data is estimated to be at most 10 percent. Because of this, the inaccuracy in the crack-tip velocity can be estimated to be less than 20 percent. Nothing definite can be said about the inaccuracy of the calculated stress-intensity factors, which depends on both the uncertainty in the input (that is, the boundary conditions and, for experiments on Specimen D, the passing times of the nodal points) and on the accuracy of the numerical technique. However, the inaccuracy in the stress-intensity factors is probably less than the inaccuracy in the velocity data.

Results and Discussion

The initial crack length of the specimens was varied to give fracture in as wide a range of load level as possible. In Table 2 the range of nominal stress reached at initiation of crack growth and the number of successful experiments are given. As can be noted from the table, general yield almost occurred in the highest loaded specimens, A, B, and C.

If a unique $K_{pc} - \dot{a}$ relationship exists, a nearly constant velocity should be reached in the experiments on Specimens A, B, and C, where the stress-intensity factor is almost constant during the main part of crack growth; see Figs. 3 and 5. This is also the case at low load levels, whereas at higher load levels a considerable variation in the velocity is obtained in the experiments on all three specimen types. Figure 6 shows two recordings of velocity versus crack length. The velocity signal is obtained from an electrical derivation of the crack length versus time signal. Both recordings originate from experiments on Specimen B, one where the load level is quite low ($\sigma_0/\sigma_{ys} = 0.45$) and one at a high load level ($\sigma_0/\sigma_{ys} = 0.91$). As can be seen, the velocity is fairly constant in the experiment at low load level, disregarding the small oscillations that were commented on in a previous chapter. In the experiment at high load level the velocity first reaches a high value and then successively decreases to a fairly constant level in the last part of the specimen. The same main feature can be observed in Fig. 3 from an experiment on a highly loaded Specimen C. This behavior cannot be explained by deviations from the prescribed constant boundary displacement during the crack propagation event, since the boundary displacement afterwards can be checked from the recordings of the strain gage signals during the event. The same principal feature can also be observed in experiments on Specimen D at high load levels. In Fig. 4, for instance, the velocity is decreasing in the last part of the specimen, despite a slight increase in the stress-intensity factor. Since this observed deviation from a unique $K_{pc} - \dot{a}$ relationship is obtained at higher load levels, it is believed to be due to extensive nonelastic deformation during the crack growth. This is supported by the fact that the specimens exposed to high loads are buckled after the completed fracture, whereas the low-loaded specimens show no noticable buckling. A simple measurement of the resi-

TABLE 2—*Experimental data.*

Specimen Type	h/w	Number of Experiments	Maximum Nominal Stress, σ_0/σ_{ys}	Minimum Nominal Stress, σ_0/σ_{ys}
A	0.25	12	0.97	0.49
B	0.50	11	0.91	0.36
C	0.75	9	0.84	0.27
D	2.00	8	0.54	0.12

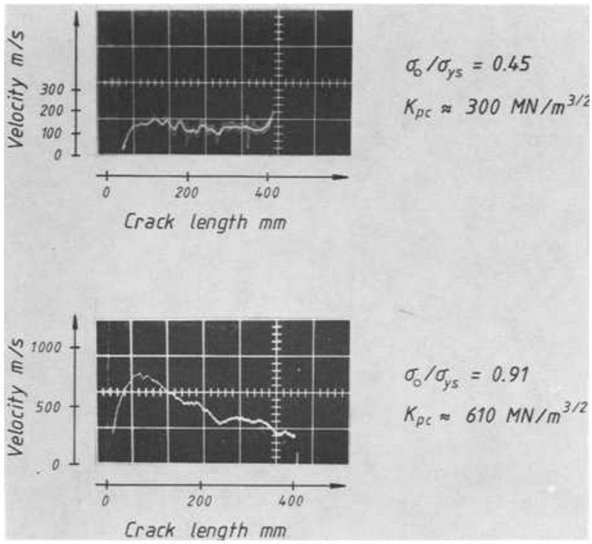

FIG. 6—*Oscilloscope recordings of crack velocity versus crack length from two experiments on Specimen B at different load levels.*

dual stresses in a highly loaded specimen after fracture showed substantial tensile stresses near and parallel to the crack plane.

In Figs. 7-10 the obtained crack propagation toughness values are plotted versus the crack-tip velocity for Geometries A, B, C, and D, respectively. Points where the crack tip is accelerating are marked with squares, where it has constant velocity with triangles, and where it is decelerating with circles. In order to compare the results for the different geometries, second-degree polynomials were fitted to the points for each geometry by the method of least squares. Since the uncertainty is thought to be larger in the determination of the velocities than in the determination of the stress-intensity factor, we chose to minimize the residual with respect to the velocity.

As can be seen in the Figs. 7-10 at low velocities, there is a very good fit between the points and the curves for Geometries A, B, and C, whereas the fitted curve is somewhat below the major part of the points for Geometry D. This discrepancy depends on larger scatter at low velocities for Geometry D than for the other geometries and especially on two points which fall markedly lower than the others. As is discussed in Ref 7, these particular points are found to be no less significant than the others and cannot be rejected.

At higher load levels where the scatter is substantially increased, the curves tend to show a maximum of velocity and turn backwards. It shall be

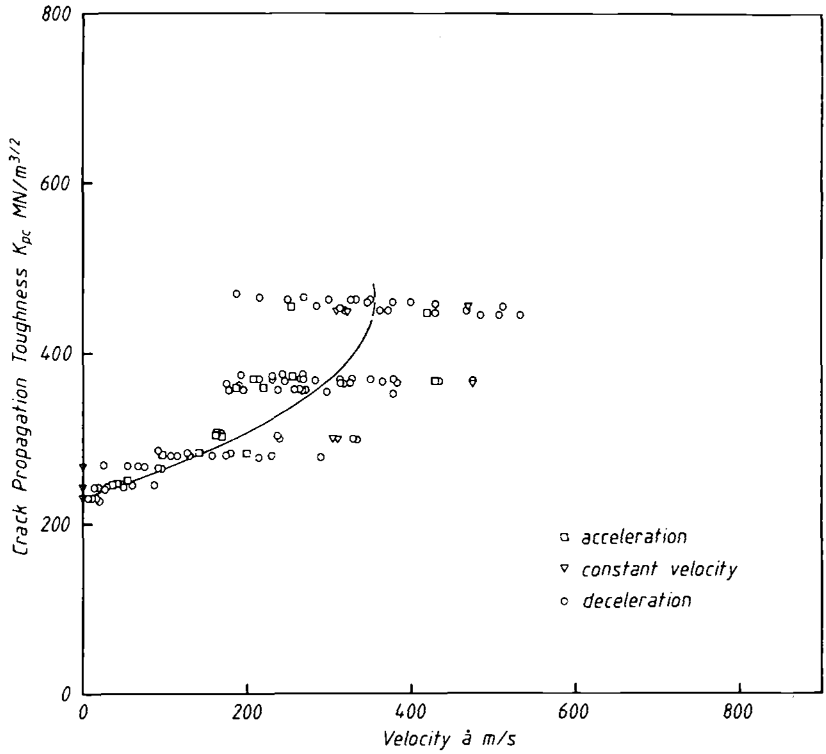

FIG. 7—*Crack propagation toughness as a function of crack-tip velocity obtained from experiments on Specimen A.*

pointed out that this behavior is not significant but rather a consequence of the large scatter in this region and of the arbitrarily chosen method for adapting the curves. What it actually indicates is that a description of crack growth in the considered specimen based on the linear elastic parameter K is improper in this region. This is not surprising in view of the high nominal stresses involved in this region; see Table 2.

In Fig. 11 the regression curves for the different geometries are compared. For low velocities the curves for Geomtries A, B, and C are very close. The curve for Geometry D is somewhat lower and intersects the K_{pc}-axis at a value of 85 percent of the intersection value for A, B, and C. This difference is due mainly to the poor fit between the points and the curve for Geometry D in this region. If the points from the four geometries were compiled in one plot, the major parts of the points from each experiment would fall together surprisingly well in the low-velocity region. Therefore, in our opinion the obtained results do not invalidate the hypothesis of a unique crack propagation toughness versus crack-tip velocity relationship, nor do

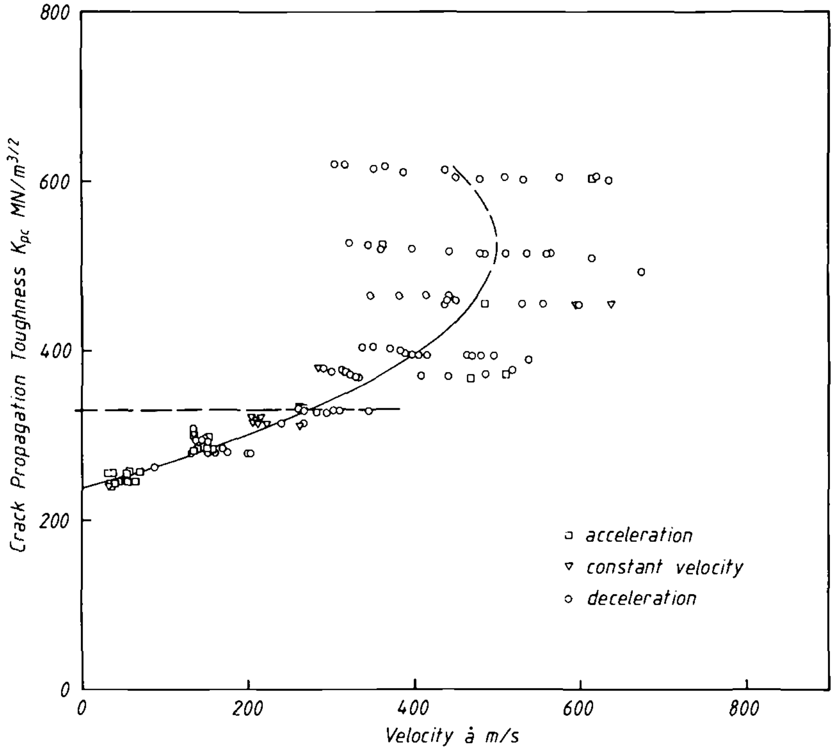

FIG. 8—*Crack propagation toughness as a function of crack-tip velocity obtained from experiments on Specimen B.*

they invalidate the hypothesis of a geometry-independent crack arrest toughness.

At higher velocities the difference between the curves gradually increases and, for a given value of velocity, the crack propagation toughness increases with decreasing height of the specimen. This is consistent with the assumption that nonuniqueness in the $K_{pc} - \dot{a}$ relationship is connected with nonelastic deformation in the specimen. Since the four geometries have the same characteristic horizontal dimensions, such as crack length and ligament width, the vertical dimension seems to be of greater importance and to be the cause of the difference in the results of the four geometries.

Now we turn to the question of deviations from the unique $K_{pc} - \dot{a}$ relationship caused by the rate of the stress-intensity factor and by the crack-tip acceleration, that is, the question if the conditions Eqs 4 and 5 are fulfilled. In the experiments on Specimens A, B, and C, the stress-intensity factor is almost constant in the main part of the specimen (see Figs. 3 and 5) and the velocity, as a consequence, should also be nearly

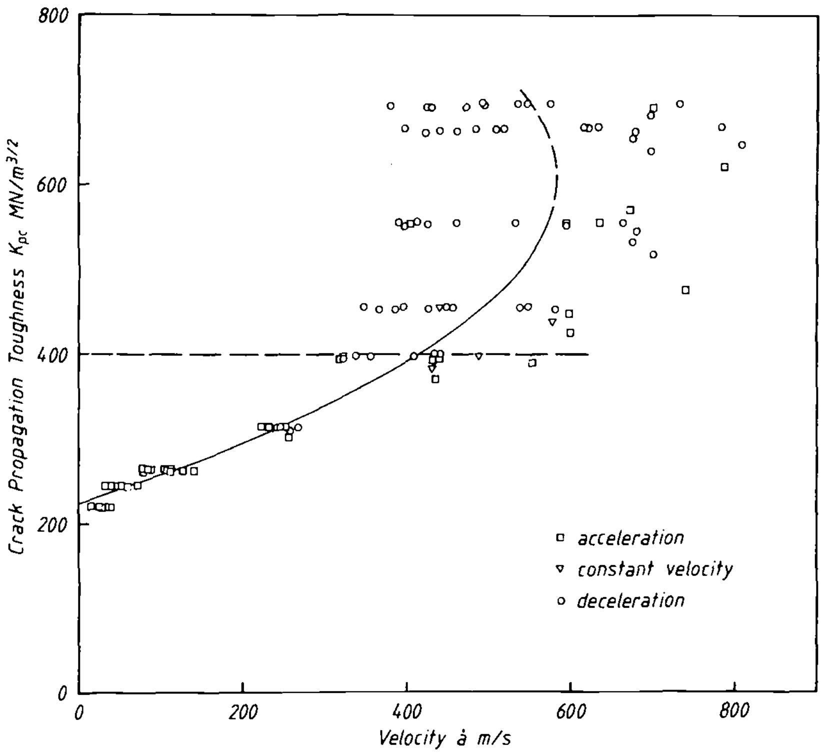

FIG. 9—*Crack propagation toughness as a function of crack-tip velocity obtained from experiments on Specimen C.*

constant if a unique $K_{pc} - \dot{a}$ relationship exists. The nonconstant velocity obtained at high load levels in these experiments is then rather caused by nonuniqueness in the $K_{pc} - \dot{a}$ relationship than causing it. In the experiments on Specimen D, the stress-intensity factor is also quite constant, whereas substantial accelerations occur even in the low-velocity region. A rough estimate of the radius of the nonelastic zone indicates, however, that the condition Eq 5 is fulfilled in these experiments, except possibly at very low velocities. This can be an explanation of the quite large scatter in the low-velocity region of the $K_{pc} - \dot{a}$ plot for this geometry; see Fig. 10.

In Table 3, the crack propagation toughness level, the corresponding velocity from the regression line, and the nominal stress at initiation of crack growth are given for the lowest loaded specimen of each type where a significant deviation from a unique $K_{pc} - \dot{a}$ relationship was observed. In all the experiments on Specimen A, a pronounced nonconstant velocity was obtained; that is, no unique $K_{pc} - \dot{a}$ relationship was obtained for this specimen geometry. The values of K_{pc} at the beginning of a significant deviation from a unique $K_{pc} - \dot{a}$ relationship, as given in Table 3, are

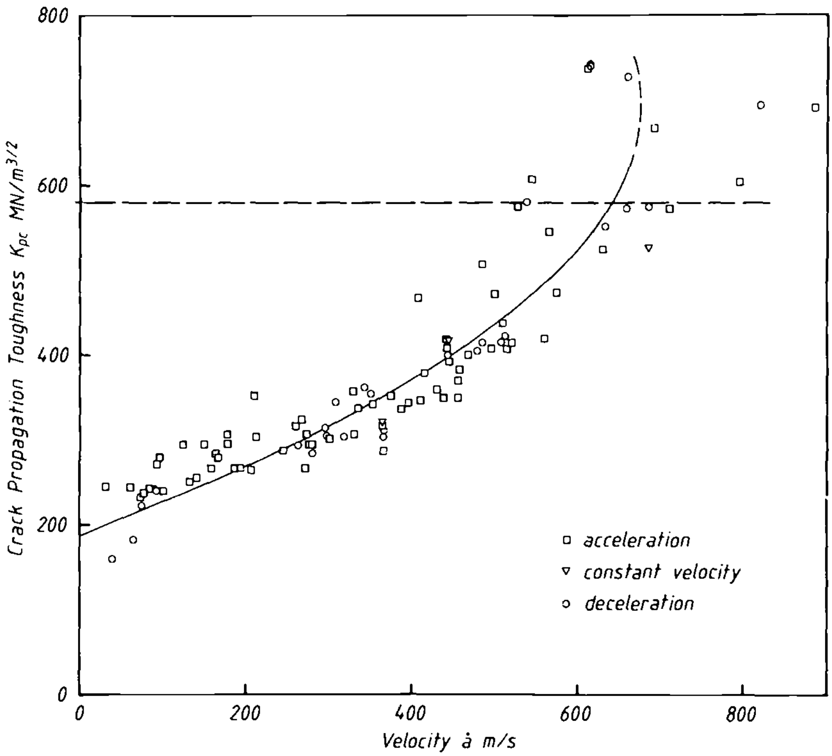

FIG. 10—*Crack propagation toughness as a function of crack-tip velocity obtained from experiments on Specimen D.*

shown as dotted lines in Figs. 8-11. As is seen in Figs. 8-10, the values coincide with a pronounced increase of the scatter.

The values of K_{pc} given in Table 3 increase with increasing height of the specimen. This is consistent with the assumption that nonuniqueness in the $K_{pc} - \dot{a}$ relationship is connected with nonelastic deformation in the specimen. The ratio h/K_{pc}^2 given in Table 3 is surprisingly constant for the different geometries. The differences occurring are not significant in view of the uncertainties involved. This constancy of the ratio h/K_{pc}^2 indicates that a condition similar to the well-known limit, ASTM Test for Plane-Strain Fracture Toughness of Metallic Materials (E 399-74), for static linear fracture mechanics may be of significance. The ASTM limit is applicable to a plane-strain situation and states that the maximum plastic zone size must be much smaller than some characteristic dimension of the specimen

$$l_{\text{char}} > 2.5 \left(\frac{K_{\text{Ic}}}{\sigma_{ys}}\right)^2 \tag{7}$$

where K_{Ic} is the plane-strain fracture toughness.

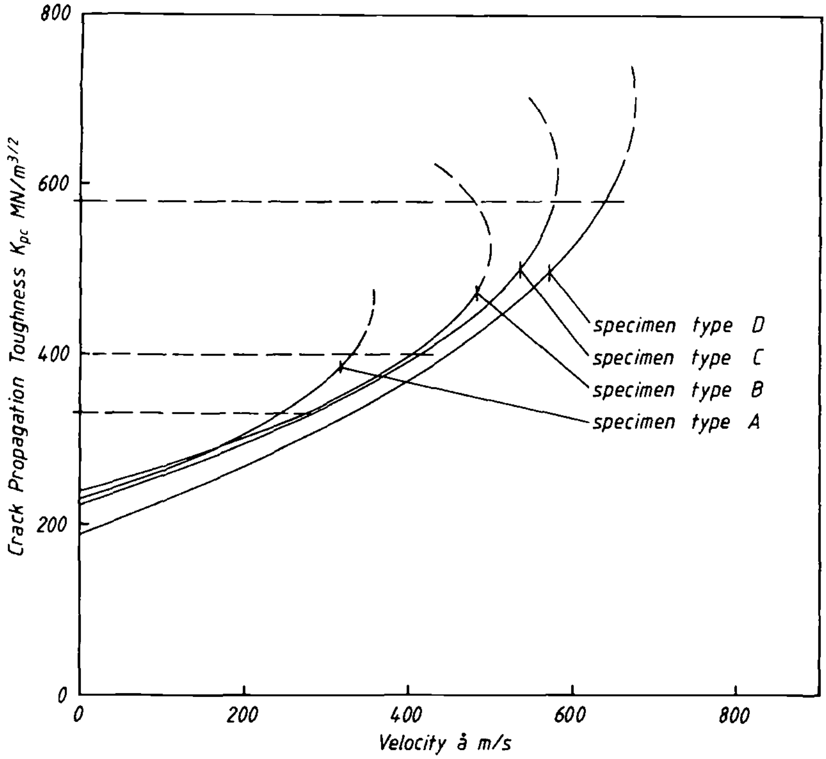

FIG. 11—*A comparison of the regression curves in Figs. 7-10.*

TABLE 3—*Experimental data for the lowest loaded specimen of each type where a significant deviation from a unique* K_{pc} — $\dot{a}$ *relationship was observed.*

Specimen Type	h, m	σ_0/σ_{ys}	K_{pc}, MN/m$^{3/2}$	$\dot{a}$, m/s	h/K_{pc}^2, m^4/MN^2
A	0.1	<0.49	<230	...	$>1.9 \times 10^{-6}$
B	0.2	0.49	330	270	1.8×10^{-6}
C	0.3	0.48	400	415	1.9×10^{-6}
D	0.8	0.43	580	640	2.4×10^{-6}

The condition for the limit of dynamic linear fracture mechanics with respect to extensive nonelastic deformation is then presumably also best expressed in terms of a toughness-strength ratio, but, because of rate and heat effects near the crack tip, an appropriate value of the strength is very difficult to select. If we instead choose the largest value of the ratio h/K_{pc}^2 in Table 3, $h/K_{pc}^2 = 2.4 \times 10^{-6}$, which gives the strongest restriction on the height of the specimen for a given value of K_{pc}, and rearrange this relation and arbitrarily normalize the right-hand side with respect to the square of the static yield strength, we arrive at the relation $h = 5.4$ (K_{pc}/

$\sigma_{ys})^2$. The condition on the height of the specimen geometries for the limit of dynamic linear fracture mechanics in the material and in the crack-tip velocity region investigated can then be formulated

$$h > 5.4 \left(\frac{K_{pc}}{\sigma_{ys}}\right)^2 \tag{8}$$

The condition on the height of these geometries is then found about twice as restrictive as the ASTM limit, Eq 7. Admittedly, the comparison is questionable since the ASTM limit is applicable to a plane-strain situation, whereas the fracture mode in this case was shearing on 45-deg planes, that is, a typical plane-stress fracture appearance.

No systematic dependence of K_{pc} on crack-tip acceleration was found, disregarding the previously reported [7] dependence observed in the low-velocity region of the $K_{pc} - \dot{a}$ plot for Specimen D, Fig. 10.

Conclusions

1. In displacement-controlled systems a quasi-static analysis of dynamic crack propagation may give sufficient results, whereas in force-controlled systems a fully dynamic analysis is needed in general.
2. The experimental results do not contradict the hypothesis of a unique relationship between crack propagation toughness and crack-tip velocity at low load levels, nor do they contradict the hypothesis of a geometry-independent crack arrest toughness.
3. It appears that a geometry condition for the limit of dynamic LEFM of the same structure as the well-known ASTM condition for static LEFM can be applied. For the material, the geometries, and the crack-tip velocity range investigated, the geometry condition is found to be more restrictive than the ASTM condition.

Acknowledgment

This work is part of a project on crack arrest studies supported by the Swedish Board for Technical Development (STU). The authors want to express their gratitude for this support. We also want to thank Mr. H. Öberg for invaluable assistance in the experimental work and Mr. S. Wästberg for reading through the manuscript very carefully and giving valuable suggestions for improvements.

References

[1] Kanninen, M. F., *International Journal of Fracture*, Vol. 10, 1974, pp. 415–430.
[2] Bergkvist, H., *Journal of the Mechanics and Physics of Solids*, Vol. 22, 1974, pp. 491–502.
[3] Nilsson, F., *Engineering Fracture Mechanics*, Vol. 6, 1974, pp. 397–403.

[4] Kalthoff, J. F., Beinert, J., and Winkler, S., "Effect of Specimen Geometry on Crack Arrest Toughness," presented at ASME/CSME Pressure Vessels and Pipings Conference, Montreal, Que., Canada, June 1978, to appear in *Journal of Engineering Materials and Technology.*

[5] Hahn, G. T. et al., "Critical Experiments, Measurements, and Analyses to Establish a Crack Arrest Methodology for Nuclear Pressure Vessel Steels," Quarterly Report for Jan.-March 1977, Battelle Columbus Laboratories, Columbus, Ohio, 1978.

[6] Kobayashi, T. and Dally, J. W. in *Fast Fracture and Crack Arrest, ASTM STP 627,* American Society for Testing and Materials, 1977, pp. 257-273.

[7] Brickstad, B. and Nilsson, F., "Numerical Evaluation by FEM of Crack Propagation Experiments," *International Journal of Fracture,* Vol. 16, 1980.

[8] Hahn, G. T. et al., "Critical Experiments, Measurements, and Analyses to Establish a Crack Arrest Methodology for Nuclear Pressure Vessel Steels," Report No. BMI-1937, Battelle Columbus Laboratories, Columbus, Ohio, 1975.

[9] Cherepanov, G. P., *International Journal of Solids and Structures,* Vol. 5, 1969, pp. 863-871.

[10] Nilsson, F., *Journal of Elasticity,* Vol. 4, 1974, pp. 73-75.

[11] Freund, L. B. and Clifton, R. J., *Journal of Elasticity,* Vol. 4, 1974, pp. 293-299.

[12] Achenbach, J. D. and Bazant, Z. P., *Journal of Applied Mechanics,* Vol. 42, 1975, pp. 183-189.

[13] Dahlberg, L. and Milsson, F. in *Proceedings,* International Conference on Dynamic Fracture Toughness, The Welding Institute, Abington, Cambridge, England, 1976, pp. 281-291.

[14] Dahlberg, L., "A Testing Equipment for Fixed Boundary Displacement Conditions," Publication No. 202, Department of Strength of Materials, Royal Institute of Technology, Stockholm, Sweden, 1978.

[15] Carlsson, A. J., *Transactions,* Royal Institute of Technology, Stockholm, Sweden, No. 189, 1962.

[16] Bathe, K.-J., Ozdmir, H., and Wilson, E. L., "Static and Dynamic Geometric and Material Nonlinear Analysis," Report No. UCSESM 74-4, Structural Engineering Laboratories, University of California, Berkeley, Calif., 1974.

[17] Bathe, K.-J., Wilson, E. L., and Iding, R. H., "NONSAP," Report No. UCSESM 74-3, Structural Engineering Laboratories, University of California, Berkeley, Calif., 1974.

[18] Rydholm, G., Fredriksson, B., and Nilsson, F. in *Proceedings,* Conference on Numerical Methods in Fracture Mechanics, Swansea, England, 1978, pp. 660-672.

J.F. Kalthoff,[1] *J. Beinert,*[1] *S. Winkler,*[1] *and W. Klemm*[1]

Experimental Analysis of Dynamic Effects in Different Crack Arrest Test Specimens

REFERENCE: Kalthoff, J. F., Beinert, J., Winkler, S., and Klemm, W., "**Experimental Analysis of Dynamic Effects in Different Crack Arrest Test Specimens,**" *Crack Arrest Methodology and Applications, ASTM STP 711,* G. T. Hahn and M. F. Kanninen, Eds., American Society for Testing and Materials, 1980, pp. 109–127.

ABSTRACT: For different crack arrest test specimens, the influence of dynamic effects on the crack arrest process is investigated. Utilizing the shadow optical method of caustics, actual dynamic stress-intensity factors directly before, at, and after arrest were measured. In the first part of the investigation, specimens made from the model material Araldite B were analyzed. It was found that the dynamic effects, that is, the difference between statically and dynamically determined crack arrest stress-intensity factors, are largest for longitudinal wedge-loaded rectangular double cantilever beam specimens, considerably smaller for machine-loaded tapered double cantilever beam specimens, and smallest for transverse wedge-loaded compact specimens. In the second part of the paper, the behavior of arresting cracks in high-strength steel specimens was investigated. The overall dynamic effects on the crack arrest process were found to be similar to those in Araldite B, but in steel the oscillation of the dynamic stress-intensity factor after arrest shows higher-frequency disturbances and is damped out only after much longer times.

KEY WORDS: stress analysis, photoelasticity, crack propagation, crack arrest, dynamic stress intensity, fracture criterion, fracture properties, dynamic fracture toughness

Nomenclature

K_I^{stat}	Statically determined stress-intensity factor
K_I^{dyn}	Dynamically determined stress-intensity factor
K_{Ic}	Fracture (initiation) toughness
K_{Iq}	Crack initiation stress-intensity factor for blunted notches
K_{ID}	Fracture toughness for propagating cracks

[1]Physicists, Fraunhofer-Institut für Werkstoffmechanik (formerly IFKM), Freiburg, Germany.

K_{Ia} Crack arrest toughness
K_{Im} Minimum fracture toughness [min $K_{ID}(v)$]
K_{Ia}^{stat} Statically determined crack arrest toughness (equivalent to K_{Ia})
K_{Ia}^{dyn} Dynamically determined crack arrest toughness (equivalent to K_{Im})

In order to establish a crack arrest methodology for nuclear pressure vessel steels, different measuring procedures and test specimens have been used.

Crosley and Ripling [*1-3*][2] propose to measure a fracture toughness value K_{Ia}. The procedure for measuring this quantity is based on a static analysis of the crack arrest process. It is assumed that the static situation for the time after arrest (about 1 ms in steel) provides an adequate description of the actual crack arrest condition. Accordingly, by utilizing conventional static stress-intensity factor formulas, the crack arrest toughness K_{Ia} is determined from the arrest crack length a_a and the critical load P_a (or displacement δ_a) measured a short time after arrest.

Hahn et al [*4*], Kanninen et al [*5*], and Hoagland et al [*6*] developed a procedure for measuring the minimum fracture toughness K_{Im}, that is, the lowest value of the dynamic fracture toughness $K_{ID}(v)$ for propagating cracks, where v is the crack velocity. This approach is based on a dynamic analysis of the crack arrest process. According to energy balance calculations performed by these investigators, the crack in its initial phase of propagation builds up kinetic energy in the specimen which is subsequently available to contribute to the actual dynamic stress-intensity factor at arrest. They conclude, therefore, that a statically determined crack arrest toughness K_{Ia} would be smaller than the true material resistance and, in general, would not represent a material property. The minimum fracture toughness K_{Im} is determined as the lowest K_{ID}-value measured in a series of experiments with different steady-state crack velocities v. The dynamic fracture toughness value K_{ID} for each experiment is derived from measurements of the crack initiation stress-intensity factor K_{Iq} and the arrest crack length a_a utilizing so-called reference curves which have been established by these investigators on a theoretical basis.

During the course of the development of these two measuring procedures, different test specimens have been used, primarily the machine-loaded tapered double cantilever beam (TDCB) specimen with the static concept and the longitudinal wedge-loaded rectangular double cantilever beam (RDCB) specimen with the dynamic concept. Both measuring procedures are now applied to the transverse wedge-loaded compact (C) specimen.

In this paper, the differences between the two measuring procedures are examined for the three different types of crack arrest test specimens. Utilizing shadow optical techniques of stress analysis, the influence of dynamic effects on the crack arrest process is investigated. The results obtained for

[2]The italic numbers in brackets refer to the list of references appended to this paper.

specimens made from the model material Araldite B are discussed, and a comparison is made with equivalent data obtained in high-strength steel specimens.

Crack Arrest Behavior in General

The principal influence of dynamic effects on the crack arrest process has already been analyzed by the authors in previous investigations [*9-11*]. The dynamic stress-intensity factors at the tip of propagating and subsequently arresting cracks have been measured by means of the shadow optical method of caustics. These dynamic stress-intensity factor results have been compared with equivalent data for the static stress-intensity factor determined from measurements of the load (or displacement) using conventional static stress-intensity factor formulas. The general behavior found is shown schematically in Fig. 1.

1. The dynamic stress intensity factor at the beginning of the crack propagation phase is smaller; however, at the end and directly at arrest it is larger than the equivalent static stress-intensity factor (see stress-intensity factor-crack length plane of Fig. 1). Consequently, the dynamically determined crack arrest stress-intensity factor $K_{Ia}{}^{dyn}$ (equivalent to the minimum

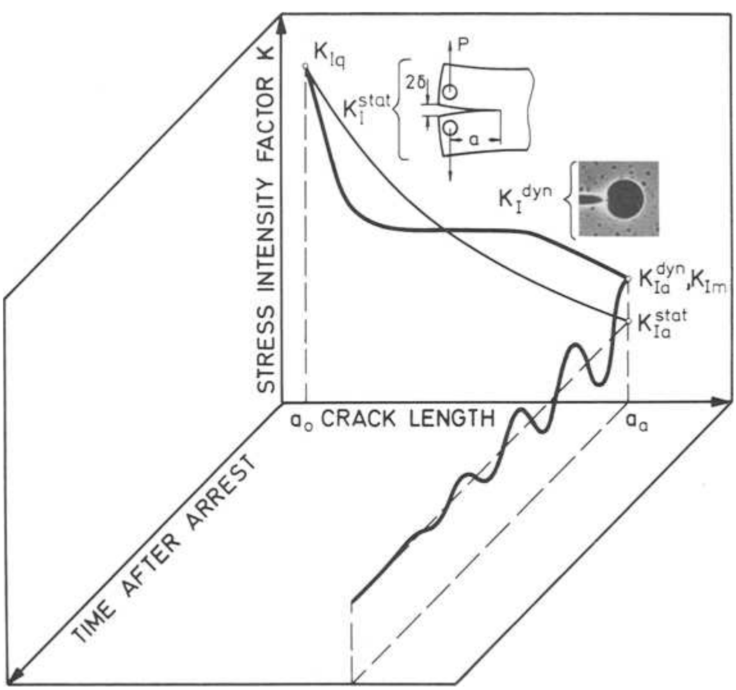

FIG. 1—*Schematic representation of stress-intensity factors for arresting cracks.*

fracture toughness K_{Im} according to the dynamic crack arrest concept) is larger than the statically determined crack arrest stress-intensity factor K_{Ia}^{stat} (equivalent to the crack arrest toughness K_{Ia} according to the static crack arrest concept). The differences between K_{Ia}^{dyn} and K_{Ia}^{stat} increase with increasing crack jump distances, $\Delta a = a_a - a_0$.

2. After arrest, the dynamic stress-intensity factor approaches the static stress-intensity factor value at arrest, K_{Ia}^{stat}, via an oscillation with a damped amplitude (see stress-intensity factor–time plane of Fig. 1). The initial amplitude of the dynamic stress-intensity factor oscillation after arrest, $(K_{Ia}^{dyn} - K_{Ia}^{stat})/K_{Ia}^{stat}$, is a measure of the influence of the dynamic effects on the crack arrest process. The K_I^{dyn} -oscillation after arrest, therefore, is analyzed in detail in the following sections.

The Shadow Optical Method of Caustics

Stress-intensity factors for stationary as well as for fast-running cracks can be measured by means of the shadow optical method of caustics which was introduced by Manogg [7].

The physical principle of this method is sketched in Fig. 2. In the upper part of the figure, a transparent specimen is considered and in the lower part a nontransparent specimen. Due to the stress concentration at the crack tip, the thickness of the specimens is reduced, and for the transparent material the refractive index is also altered. As a consequence, in the transmission case, the light passing through the specimen is deflected outward. On an image plane at any distance z_0 behind the specimen, therefore, a dark shadow spot bounded by a bright light concentration (the caustic) is formed. For optically isotropic materials a single caustic results, while for optically anisotropic materials a double caustic is obtained. In the lower part of Fig. 2 (reflection case), it is illustrated that for nontransparent materials the light being reflected from the mirrored surface of the specimen forms qualitatively the same shadow pattern as obtained in transmission, when observed in a virtual image plane positioned behind the specimen. In both arrangements, transmission and reflection, the shadow patterns for propagating and subsequently arresting cracks are photographed by a Cranz Schardin 24-spark high-speed camera, which is focused on the respective image plane. Figure 3 shows experimentally observed shadow patterns for running cracks in the epoxy resin Araldite B, photographed in transmission, and in the high-strength steel HFX 760, photographed in reflection. From the diameter D of the caustic, the stress-intensity factor K_I for the crack is derived utilizing the relation

$$K_I = F(v)\, MD^{5/2}$$

The factor M is determined by the elasto-optical constants of the material

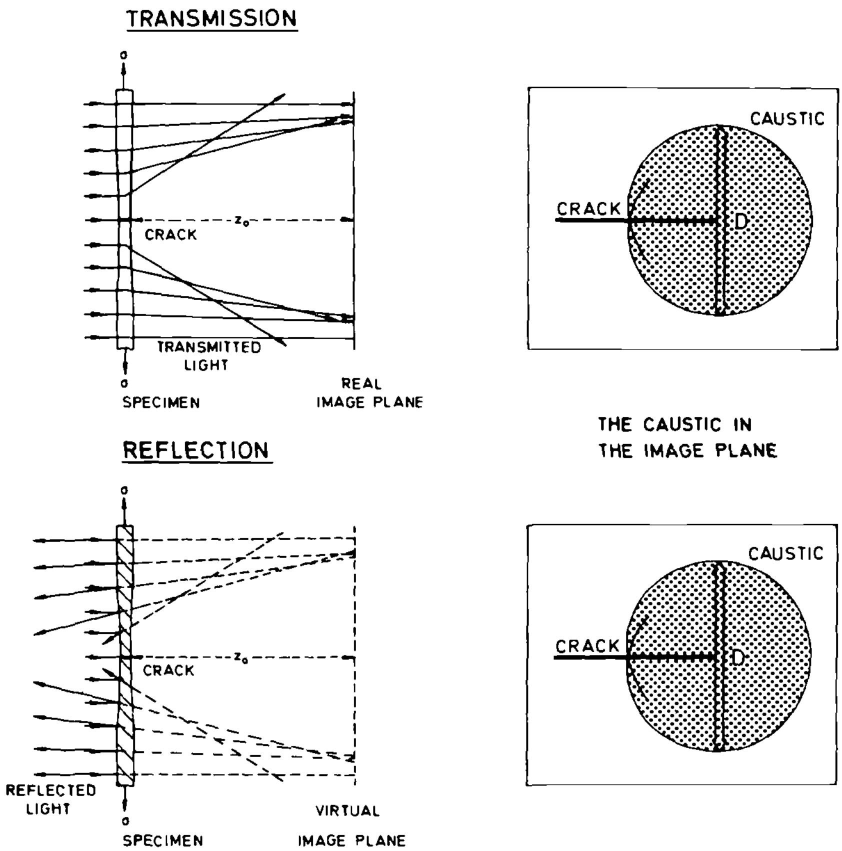

FIG. 2—*The shadow optical method of caustics for transmission and reflection.*

and the geometrical arrangement of the experimental setup. The term $F(v)$ accounts for the crack velocity dependence of the shadow pattern. For the velocities usually attained in crack arrest experiments, $F(v) \approx 1$. Detailed information on the values for M and $F(v)$ for shadow optial arrangements in transmission and reflection is given by Beinert et al [*8*].

Dynamic Effects on the Crack Arrest Process in Test Specimens of Different Geometries

In order to quantify the influence of dynamic effects on the crack arrest process in test specimens of different geometries, shadow optical measurements of the dynamic stress-intensity factor directly before, at, and after arrest have been carried out. The specimens considered, shown in Fig. 4, are the longitudinal wedge-loaded RDCB-specimen, the machine-loaded TDCB-specimen, and the transverse wedge-loaded C-specimen.

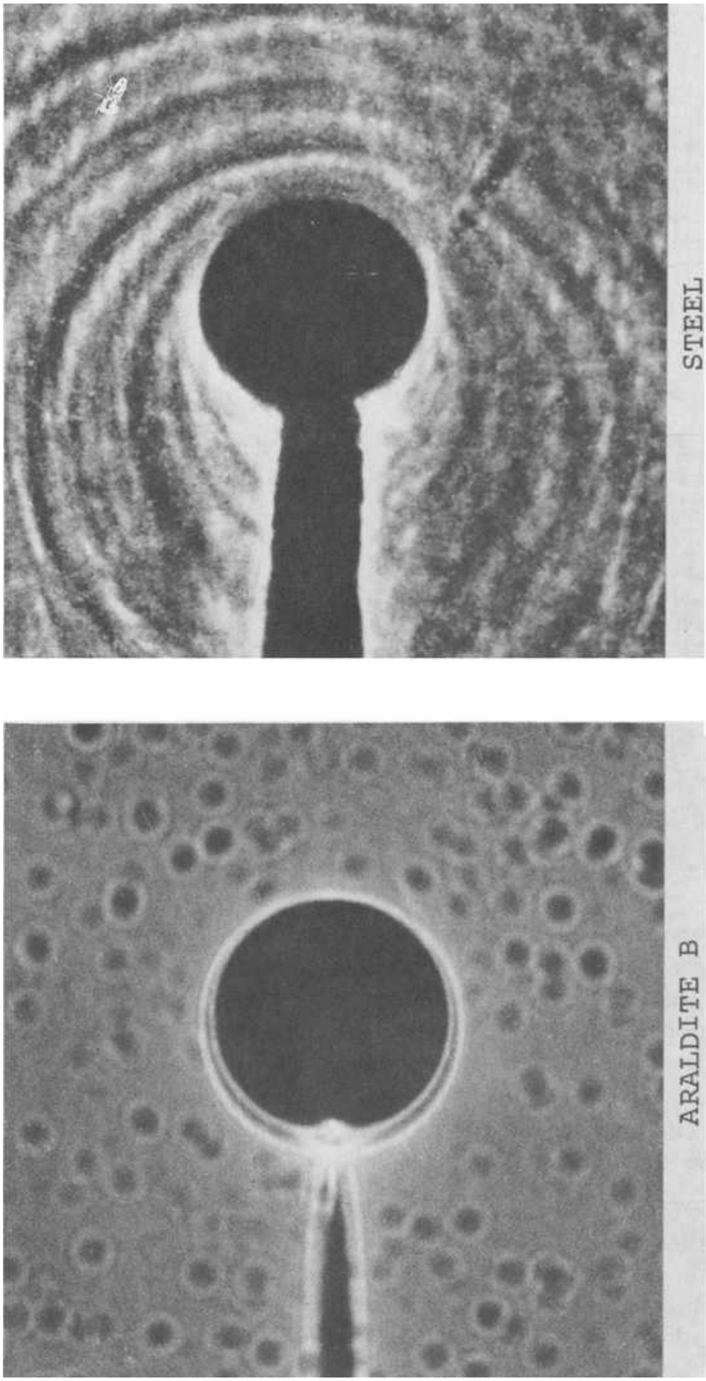

FIG. 3—*Shadow patterns for propagating cracks.*

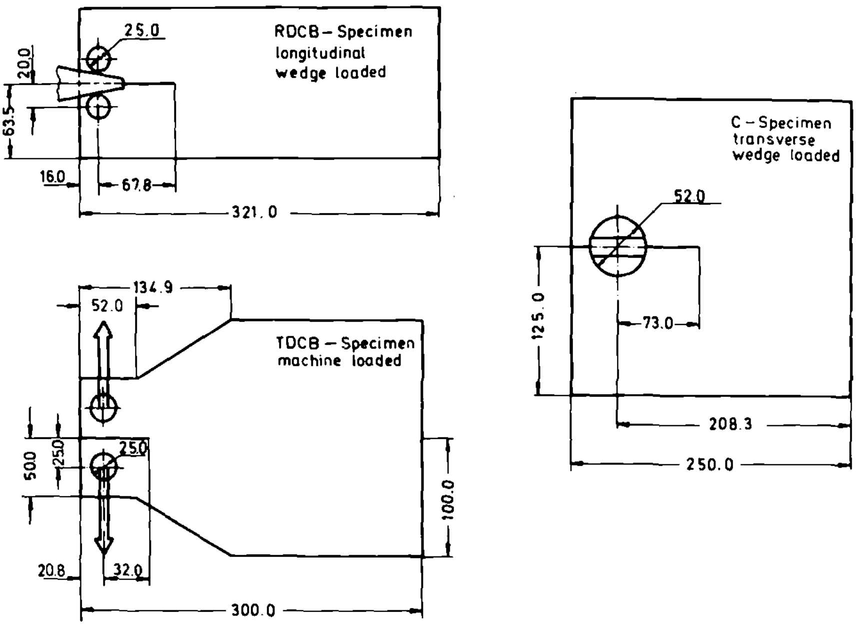

FIG. 4—*Crack arrest test specimens.*

Experimental Procedure

The test specimens were machined from the epoxy resin Araldite B. The sizes of the specimens were chosen according to the measurements given in Fig. 4. The specimen thickness was 10 mm for all specimens. No side grooves were used. Steel fixtures were employed to load the specimens. The cracks were started from blunted tips of the initial notches prepared by specially modified jeweler's saws of different thicknesses. During the test, the load (compressive force for wedge loading, tensile force for machine loading) was recorded versus time or crack-opening displacement or both. For the propagating and subsequently arresting cracks, shadow patterns were recorded with a Cranz Schardin 24-spark high-speed camera. The picture interval times were chosen to specifically analyze the dynamic stress-intensity factor behavior directly before and after arrest. The high-speed camera was triggered by the starting crack, which interrupts a laser beam traversing the specimen directly ahead of the initial notch.

Experimental Results

Experimental results on the crack arrest behavior in the three different types of test specimens are shown in Figs. 5-7. (The data on RDCB-specimens were taken from Ref *9*.) In each figure the crack length *a* and the

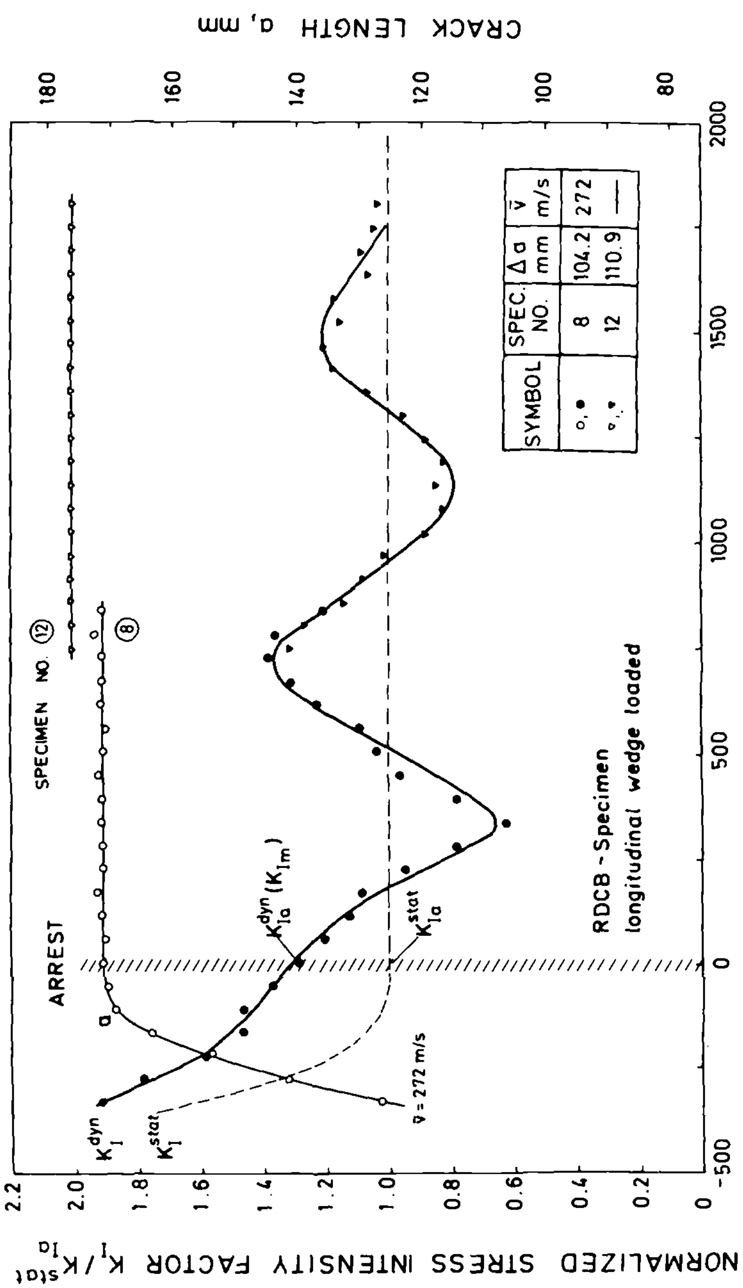

FIG. 5—*Crack arrest behavior in longitudinal wedge-loaded RDCB-specimens.*

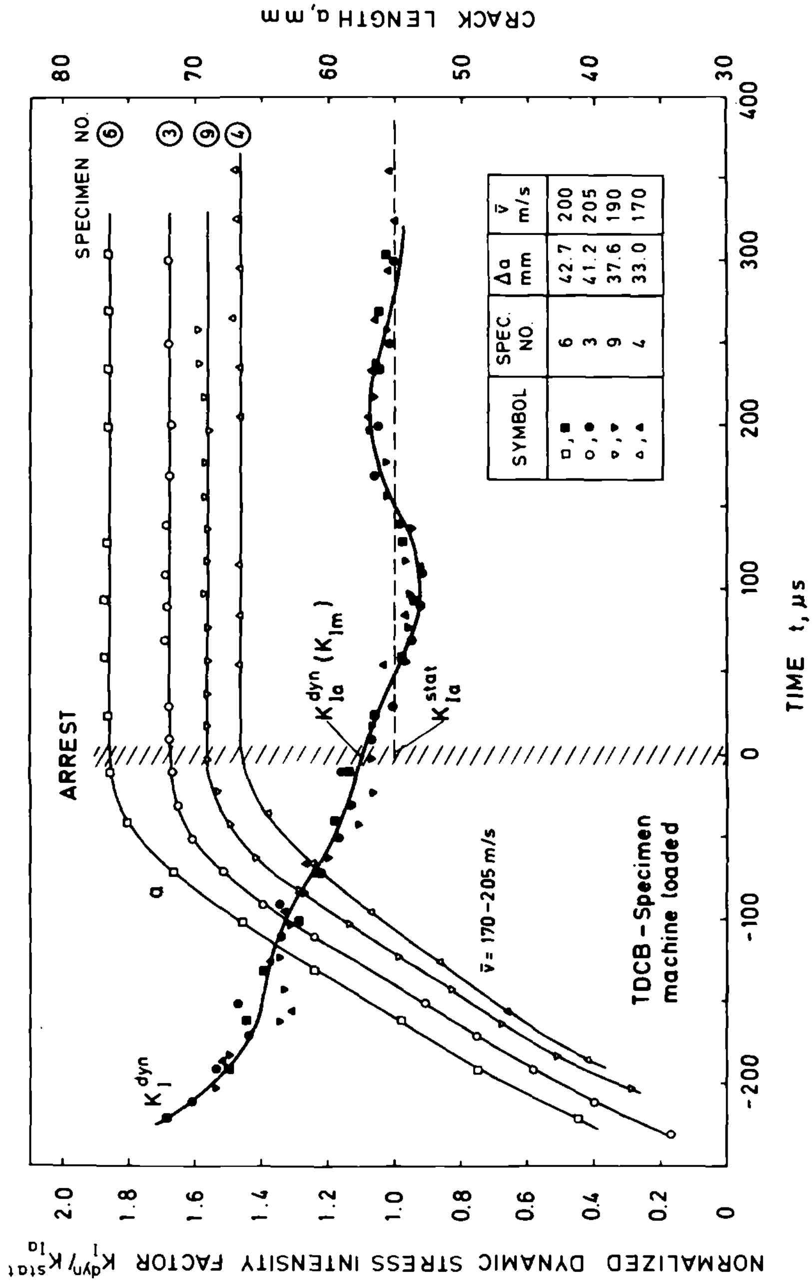

FIG. 6—*Crack arrest behavior in machine-loaded TDCB-specimens.*

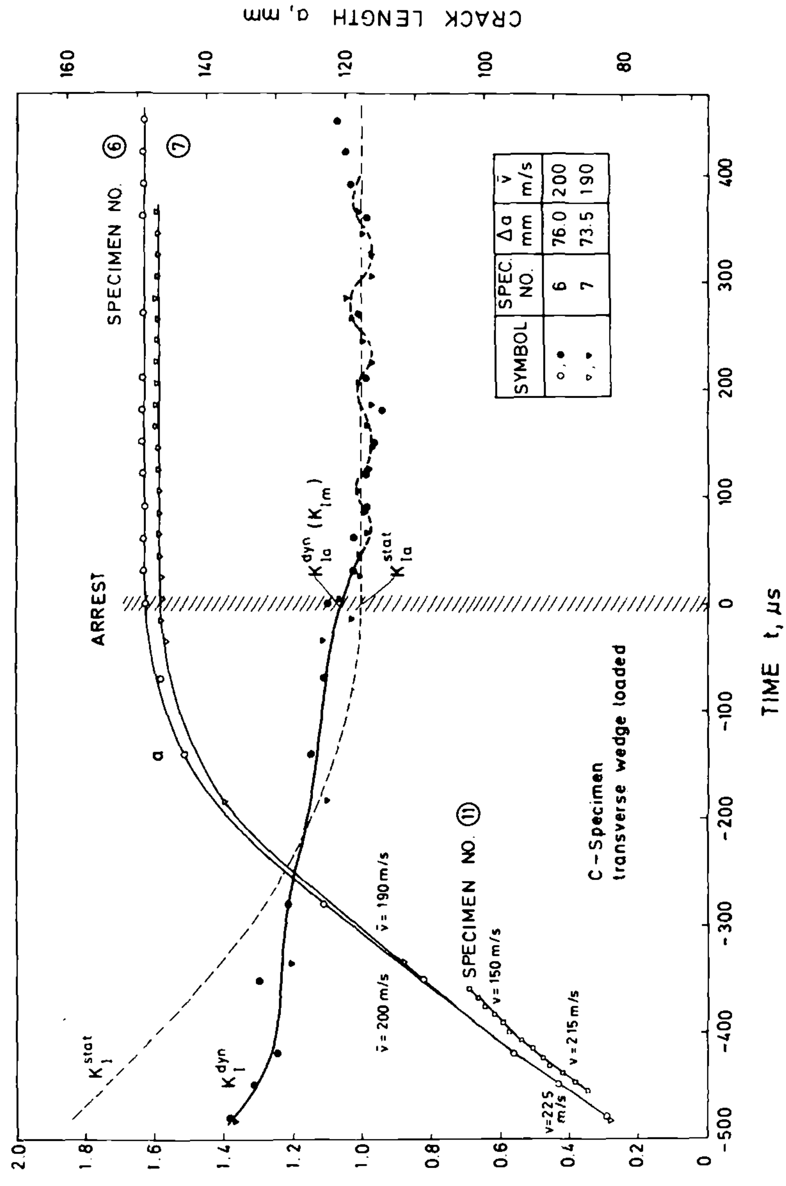

FIG. 7—*Crack arrest behavior in transverse wedge-loaded C-specimens.*

dynamic stress-intensity factor K_I^{dyn} are plotted as functions of time t. The time at which arrest occurs has been set equal to zero for each experiment. In order to emphasize the general trend in the results, the data of different experiments, showing a similar arrest behavior, have been combined in one graph, and the dynamic stress-intensity factors K_I^{dyn} have been normalized by the static stress-intensity factor at arrest K_{Ia}^{stat}, where K_{Ia}^{stat} is the mean value of the K_I^{dyn} -oscillation after arrest. Thus, the increased number of measuring points—despite the scatter in the data and despite the limited number (24) of data points for one experiment—give a reliable picture of the stress-intensity factor behavior.

Crack Propagation and Arrest—For all types of specimens the crack length-time curves (Figs. 5-7) indicate a gradual decrease of the crack velocity prior to the actual arrest event. Because of this behavior the exact time of crack arrest can be determined only with some uncertainty (see shaded time intervals in Figs. 5-7). Reinitiation of crack propagation after the first arrest event—as was often observed in prior experiments with longitudinal wedge-loaded single-edge notch (SEN) specimens [*11*]—occurred very seldom and only after longer times. The stability of the crack propagation direction in the machine-loaded TDCB-specimens and especially in the transverse wedge-loaded C-specimens was found to be much better than for the longitudinal-wedge loaded RDCB-specimens. Therefore, in practice, less-deep side grooves can be used with C-specimens. A constant steady-state crack velocity $\bar{v}$ for the whole crack propagation event, except for the deceleration phase prior to arrest, was observed only for the RDCB-specimens [*9*]. In the TDCB- and the C-specimens at the very beginning of crack propagation, a slightly larger crack velocity was observed than for the intermediate crack propagation range (see Figs. 6 and 7). For C-specimens, this behavior is also demonstrated by the crack length-time curve for Experiment 11 (Fig. 7), for which the early phase of crack propagation was photographed with a higher time resolution. (In this context it should also be mentioned that in longitudinal wedge-loaded SEN-specimens this effect is even more pronounced, with two clearly separated steady-state velocities observed [*11*].)

Oscillation of the Dynamic Stress Intensity Factor After Arrest—For all three types of specimens the dynamic stress-intensity factor K_I^{dyn} after arrest shows an oscillatory behavior. The amplitude and the frequency of these oscillations vary from specimen type to specimen type. In all cases the frequency of the K_I^{dyn} -oscillation can be roughly correlated to the frequency of the vibration of a beam corresponding to one half of the cracked specimen. The amplitude of the K_I^{dyn} -oscillation is very large in the longitudinal wedge-loaded RDCB-specimen (see Fig. 5), considerably smaller in the machine-loaded TDCB-specimen (see Fig. 6), and very low (almost within the range of experimental scatter) in the transverse wedge-loaded C-specimen (see thicker dashed line in Fig. 7). The initial amplitudes of the K_I^{dyn}-

oscillation after arrest, $(K_{Ia}^{dyn} - K_{Ia}^{stat})/K_{Ia}^{stat}$, when considered for the same averaged crack propagation velocity, indicate the following quantitative result. The influence of the dynamic effects on the crack arrest process in the machine-loaded TDCB-specimens is smaller by a factor of more than two, and in the transverse wedge-loaded C-specimens smaller by a factor of almost four, when compared with the longitudinal wedge-loaded RDCB-specimens.

This result indicates that in machine-loaded TDCB-specimens and in transverse wedge-loaded C-specimens smaller amounts of kinetic energy are recovered during the crack arrest process than in wedge-loaded RDCB-specimens. Obviously, in TDCB- and C-specimens, elastic waves emanating from the tip of the propagating crack at the beginning of the crack propagating phase, after being reflected at the finite boundaries of the specimen, do interfere with the arresting crack but to a lesser extent. Due to the larger dimensions or different configurations of these two kinds of specimens, the waves are attenuated more strongly or are reflected differently so that the smaller interaction with the crack results.

The data obtained from the model experiments show that the crack arrest process in wedge-loaded RDCB-specimens can be described properly by a dynamic analysis only, whereas the errors in applying a static analysis for arrest processes in machine-loaded TDCB-specimens would be considerably smaller. Also, in transverse wedge-loaded C-specimens smaller discrepancies between the results of the two crack arrest concepts are anticipated.

Dynamic Effects on the Crack Arrest Process in High-Strength Steel Specimens

Conclusions on the influence of dynamic effects on the crack arrest process in reactor pressure vessel steels, based on results from model experiments in plastic materials (as Araldite B or Homalite 100), can be made only with restrictions. The material behavior of steels is very different from that of plastics. In particular, the wave propagation properties—which obviously influence the dynamic effects associated with crack arrest (see previous section)—are different; for example, the attenuation of the elastic waves in steels is considerably smaller than in plastics. Therefore, the crack arrest process in steels has been analyzed directly, utilizing the shadow optical method of caustics in reflection.

Experimental Procedure

In order to apply the method of shadow patterns for steels and to determine a stress-intensity factor from the stress-strain field in the vicinity of the tip of the crack, a steel with a sufficiently small plastic zone at the crack tip had to be utilized. The high-strength maraging steel HFX 760, Stahlwerke

Südwestfalen (heat treatment: 480°C/4 h/ air), was chosen. The steel has a yield strength of $\sigma_Y = 2100$ MN/m^2 and a crack initiation toughness K_{Ic} in the range of 70 to 100 MN/m$^{3/2}$.

From this steel, RDCB-specimens of the size as given in Fig. 4 and a thickness of about 9 mm were machined. One side of the specimens was specially prepared by grinding, lapping, and final hand-polishing in order to achieve a completely straight and mirrored surface. The cracks were started from a sawed-in chevron notch which, at the tip of the chevron, had an additional very fine saw cut machined with a specially modified jeweler's saw. The specimens were loaded by a longitudinal wedge, as were the Araldite B specimens. The high-speed camera was triggered by the starting crack through a signal recorded by a strain gage positioned very near the initial notch tip. In a reflection arrangement, the camera was focused on a virtual image plane behind the specimen (see Fig. 2).

Experimental Results

A typical shadow optical picture of a crack propagating at a velocity of 1000 m/s in a high-strength steel specimen is given in Fig. 8. In addition to the shadow spot at the tip of the crack, elastic waves are visible. These waves radiate outward from the tip of the propagating crack into the specimen, are reflected at the finite boundaries of the specimen, and then interfere with the crack tip again. The generation of these waves immediately ceases when the crack arrests, thus giving additional information on the crack arrest time. This shadow optical photograph of Fig. 8 gives visible evidence of the influence of dynamic effects on the crack arrest process.

Quantitative data on the dynamic stress-intensity factors for propagating and arresting cracks from such shadow optical photographs are given in Figs. 9 and 10.

Dynamic Stress-Intensity Factors for Propagating Cracks—For a fast-running crack (Experiment 13), the measured dynamic stress-intensity factor K_I^{dyn}, the equivalent static stress-intensity factor K_I^{stat}, and the crack velocity v are plotted as functions of the crack length a in Fig. 9*b*. The results are compared with those for propagating cracks in Araldite B (RDCB) specimens, which are shown in Fig. 9*a* (the Araldite B data are taken from Ref 9). A dimensionless plot of the data was chosen for this comparison. The (dynamic and static) stress-intensity factors are normalized by the initiation stress-intensity factor K_{Iq}, and the crack velocity v by the bar wave speed c_0. Because the main specimen dimensions were identical in both cases, the crack length a is plotted in absolute values.

It is recognized that the crack velocity history in both materials is similar. For the largest part of the crack propagation phase, the crack velocity is constant and only prior to arrest the velocity gradually decreases from its steady-state value. In the high-strength steel experiments, however, more often than

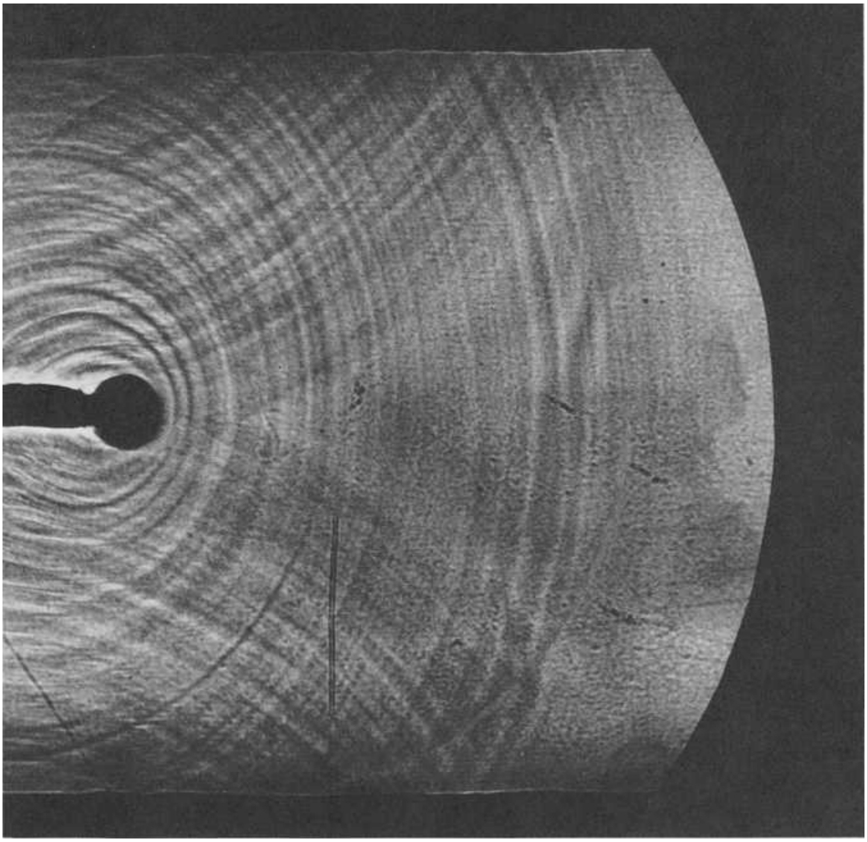

FIG. 8—*Shadow optical picture of a propagating crack in a high-strength steel RDCB-specimen.*

in the Araldite B experiments, a stop-and-go arrest behavior (which does not show up in Fig. 9*b*) was observed. For both materials the decrease in the crack velocity is preceded by a decrease in the dynamic stress-intensity factor values (this effect was observed also by Bradley and Kobayashi [*12*]). Since the relative steady-state crack velocity v/c_0 in the high-strength steel specimen was larger than in the Araldite B specimens, a larger crack jump distance results for the high-strength steel specimen. (In this case the crack came to arrest only a few millimetres before the far edge of the specimen. The crack arrest process itself was not photographed.)

The K_I^{dyn} -curves for the two materials, however, exhibit a characteristic difference. Although similar in nature (K_I^{dyn} at the beginning of crack propagation is smaller and at the end is larger than K_I^{stat}), the K_I^{dyn} -values in the high-strength steel specimen show large variations, whereas the data for

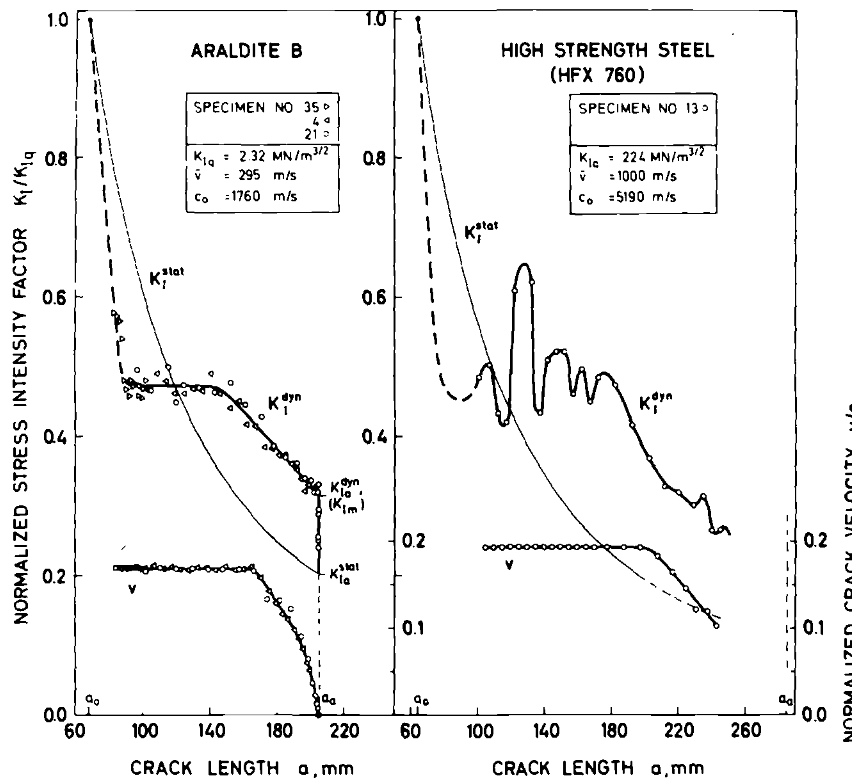

FIG. 9—*Stress-intensity factors for propagating cracks in Araldite B and the high-strength steel HFX 760.*

the Araldite B specimens can be represented by a rather smooth curve. These large variations of the dynamic stress-intensity factor values in the high-strength steel specimen are not due to experimental scatter, but rather due to higher-frequency vibrations or higher-frequency stress waves interacting with the crack. In Araldite B, very likely because of the larger attenuation and because of the characteristics of the shadow optical arrangement in transmission (which is less sensitive to surface deformations), these higher-frequency effects practically are not noticeable.

Oscillation of the Dynamic Stress-Intensity Factor After Arrest—Data on the dynamic stress-intensity factor behavior directly before, at, and after arrest are shown in Fig. 10. The dynamic stress-intensity factors, normalized as in Figs. 5-7 by the static stress-intensity factor values at arrest, K_{Ia}^{stat}, are plotted as functions of time t for different crack jump distances Δa. The crack jump distance increases from the upper to the lower curves. In order to illustrate graphically the crack jump distances obtained, shaded bars, the lengths of which were chosen proportional to Δa, are given in each diagram.

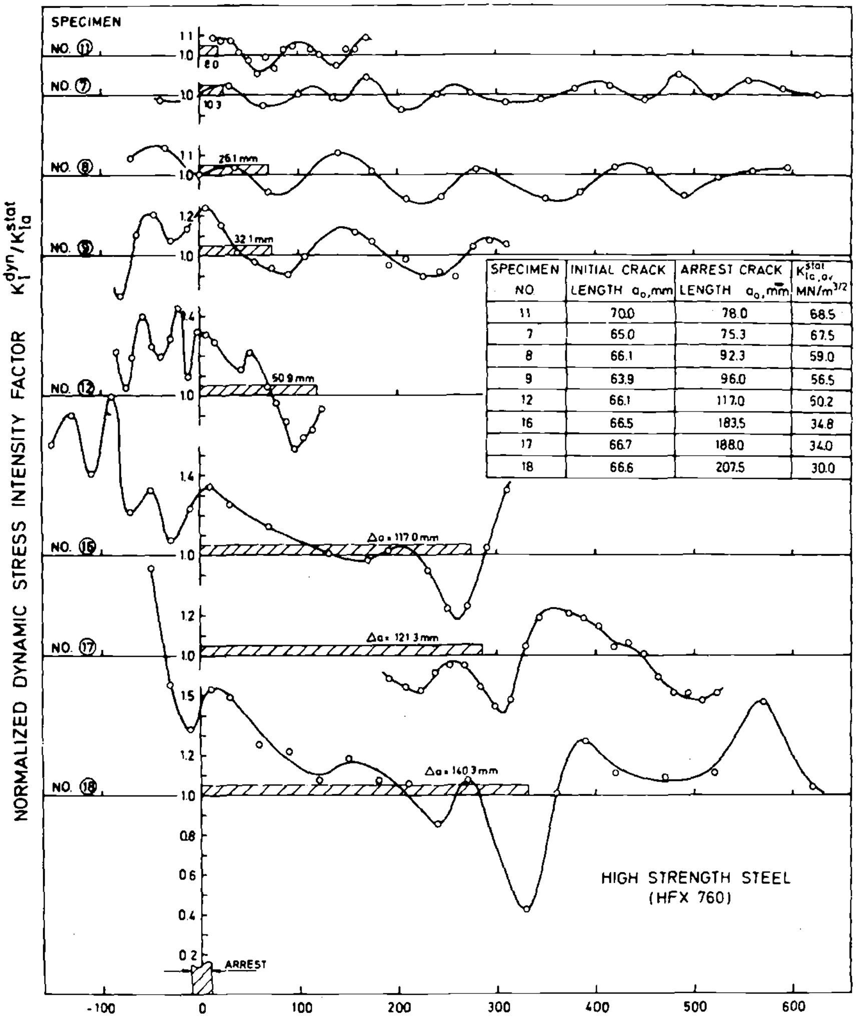

SPECIMEN NO	INITIAL CRACK LENGTH a_0, mm	ARREST CRACK LENGTH $\bar{a}_0$, mm	$K_{Ic,a}^{stat}$ $MN/m^{3/2}$
11	70.0	78.0	68.5
7	65.0	75.3	67.5
8	66.1	92.3	59.0
9	63.9	96.0	56.5
12	66.1	117.0	50.2
16	66.5	183.5	34.8
17	66.7	188.0	34.0
18	66.6	207.5	30.0

FIG. 10—*Oscillation of the dynamic stress-intensity factor after arrest in the high-strength steel HFX 760.*

It can be recognized that the dynamic stress-intensity factor–time curves for the high-strength steel experiments in general do not show a simple harmonic oscillation as did the Araldite B experiments (see Fig. 5). From the few data obtained so far, however, special characteristics in the K_I^{dyn} -behavior are apparent:

For Specimens 11 and 7 with the lowest (8.0 and 10.3 mm) crack jump distance, oscillations of similar period, phase, and amplitude are observed. The higher time resolution in the data of Experiment 11 justifies considering the variations in the scarce data points of Experiment 7 as a real oscillation and not as a scatter.

Experiments 8 and 9 with a somewhat larger (26.2 and 32.1 mm) crack jump distance are again similar to each other. In comparison with Experiments 11 and 7, the period and the amplitude of the oscillation now are larger, as one might expect due to the larger crack jump distances.

In Experiments 12 and 16–18 with larger crack jump distances (varying from 50.9 mm up to 140.9 mm) harmonic oscillations are no longer observed. However, a distinct minimum in the dynamic stress-intensity factor curve is recognized which corresponds to the first minimum in the K_I^{dyn} -t-curve for Experiments 8 and 9. The minimum is steadily shifted to larger times for increasing crack jump distances (compare the Δa-bars with the times at which the minimum appears). This lower-frequency behavior is disturbed by high frequency oscillations. These disturbances again are not experimental scatter, as can be seen from special characteristics of the K_I^{dyn} -t-curves (for example, the distinct minimum is preceded by a small hump and followed by a steep increase) which show up for all experiments (Nos 9, 12, and 16–18) and which are also clearly documented by the data with the higher time resolution of Experiments 12 and 17. In accordance with the results of Experiments 11 and 7 and Experiments 8 and 9, the amplitude of the oscillation for Experiments 12 and 16–18 steadily increases with increasing crack jump distance.

The actual dynamic stress-intensity factors at arrest, K_{Ia}^{dyn}, are difficult to determine from the K_I^{dyn} -t-plots. Due to the strong variation of K_I^{dyn} during the crack arrest event and also due to the inexactly defined time of arrest, some uncertainties result. However, a comparison of the results obtained for the high-strength steel (RDCB) specimen, No. 16 (Fig. 10), with those of the Araldite B (RDCB) specimens, Nos. 8 and 12 (Fig. 5) (having almost the same crack jump distance), shows that the initial amplitudes of the K_I^{dyn}-oscillation, $(K_{Ia}^{dyn} - K_{Ia}^{stat})/K_{Ia}^{stat}$, are practically the same for both materials. This finding is supported also by a comparison of the other high-strength steel data in Fig. 10 with the Araldite B results of Ref *9*. Therefore, the overall general influence of dynamic effects on the crack arrest process in the Araldite B and the high-strength steel specimens seems to be similar. The K_I^{dyn} -oscillation after arrest in high-strength steel specimens, however, is disturbed by higher-frequency effects (see especially Experiments 12 and 16–18), whereas the Araldite B specimens in general show a harmonic dynamic stress-intensity factor–time behavior. In addition, the K_I^{dyn} -oscillation in high-strength steel specimens is considerably less attenuated than in Araldite B specimens (see especially Experiments 7 and 8). A static loading condition at the tip of the arrested crack will be established only for times considerably longer than 1 ms (see Ref *2*) after the arrest event.

Preliminary findings of the first 18 experiments, carried out with high-strength steel specimens, have been presented. Additional experiments and further evaluation of the data are necessary and will be performed in order to better quantify the results obtained to date.

Summary and Conclusions

Utilizing the shadow optical method of caustics, the influence of dynamic effects on the crack arrest process has been analyzed for different crack arrest test specimens made from different materials. In the first part of the investigation, model experiments were performed with specimens made from the epoxy resin Araldite B. The dynamic effects were found to be very large for longitudinal wedge-loaded RDCB-specimens, considerably smaller for machine-loaded TDCB-specimens, and smallest for transverse wedge-loaded C-specimens. In the second part, the crack propagation and arrest behavior in high-strength steel (RDCB) specimens was investigated and compared with the behavior in Araldite B (RDCB) specimens. The results obtained to date indicate that the overall dynamic effects on the difference of the dynamically and the statically determined crack arrest stress-intensity factors are practically the same for both materials. In steel, however, the oscillation of the dynamic stress-intensity factor after arrest shows higher-frequency disturbances, which are also apparent in the crack propagation phase. In addition, the K_I^{dyn} -oscillation after arrest in steel is damped out only after much longer times than in Araldite B.

The results presented in this paper show that dynamic effects, in principle, have an influence on the crack arrest process and must be taken into account when establishing a physically correct, generally applicable measuring procedure to quantify the crack arrest capability of materials. The magnitude of these dynamic effects varies for different crack arrest test specimens. Among the specimen types investigated, the differences between statically and dynamically determined crack arrest stress-intensity factor values are smallest for the transverse wedge-loaded C-specimen.

Acknowledgment

The work reported in this paper is sponsored by the Electric Power Research Institute under Contract No. RP 1022-1. The authors wish to thank Dr. K. E. Stahlkopf and Dr. T. U. Marston of the Electric Power Research Institute for their encouragement to pursue these studies. The authors would like to acknowledge also the skillful laboratory assistance of A. Wolf and the help of B. Hübner, M. Hug, and S. Kunzelmann in performing the experiments.

References

[1] Crosley, P. B. and Ripling, E. J., *Nuclear Engineering and Design*, Vol. 17, No. 1, Aug. 1971, pp. 32–45.

[2] Crosley, P. B. and Ripling, E. J. in *Fast Fracture and Crack Arrest, ASTM STP 627,* American Society for Testing and Materials, 1977, pp. 203-227.
[3] Crosley, P. B. and Ripling, E. J. in *Fast Fracture and Crack Arrest, ASTM STP 627,* American Society for Testing and Materials, 1977, pp. 372-391.
[4] Hahn, G. T., Gehlen, P. C., Hoagland, R. G., Kanninen, M. F., Rosenfield, A. R. et al., "Critical Experiments, Measurements and Analyses to Establish a Crack Arrest Methodology for Nuclear Pressure Vessel Steels," BMI-1937, 1959, 1995, Battelle Colombus Laboratories, Columbus, Ohio, Aug. 1975, Oct. 1976, May 1978.
[5] Kanninen, M. F., Popelar, C., and Gehlen, P. C. in *Fast Fracture and Crack Arrest, ASTM STP 627,* American Society for Testing and Materials, 1977, pp. 19-38.
[6] Hoagland, R. G., Rosenfield, A. R., Gehlen, P. C., and Hahn, G. T. in *Fast Fracture and Crack Arrest, ASTM STP 627,* American Society for Testing and Materials, 1977, pp. 177-202.
[7] Manogg, P. in *Proceedings,* International Conference on the Physics of Non-Crystalline Solids, Delft, The Netherlands, 1964, pp. 481-490.
[8] Beinert, J., Kalthoff, J. F., and Maier, M. in *Proceedings,* 6th International Conference on Experimental Stress Analysis, Munich, Germany, VDI-Report No. 313, VDI-Verlag, Düsseldorf, Germany, 1978, pp. 791-798.
[9] Kalthoff, J. F., Beinert, J., and Winkler, S. in *Fast Fracture and Crack Arrest, ASTM STP 627.* American Society for Testing and Materials, 1977, pp. 161-176.
[10] Kalthoff, J. F., Beinert, J., Winkler, S., and Blauel, J. G. in *Proceedings,* 4th International Conference on Fracture, Waterloo, Ont., Canada, 1977, Vol. 3, pp. 751-756.
[11] Kalthoff, J. F., Beinert, J., and Winkler, S., "Influence of Dynamic Effects on Crack Arrest," IFKM-Report V9/78 prepared for EPRI, Institut für Festkörpermechanik, Freiburg, Germany.
[12] Bradley, W. B. and Kobayashi, A. S., *Experimental Mechanics,* Vol. 10, No. 3, March 1970, pp. 106-113.

J. T. Metcalf[1] *and Takao Kobayashi*[1]

Comparison of Crack Behavior in Homalite 100 and Araldite B

REFERENCE: Metcalf, J. T. and Kobayashi, Takao, "**Comparison of Crack Behavior in Homalite 100 and Araldite B,**" *Crack Arrest Methodology and Applications, ASTM STP 711*, G. T. Hahn and M. F. Kanninen, Eds., American Society for Testing and Materials, 1980, pp. 128–145.

ABSTRACT: Currently, two polymeric materials, Homalite 100 and Araldite B, are extensively utilized in the study of dynamic fracture. Homalite 100 is employed in the dynamic photoelastic studies of Dally et al of the University of Maryland, and Kobayashi et al of the University of Washington. They have determined the instantaneous stress-intensity factor from the isochromatic fringe loops and have studied the influence of specimen geometry on crack propagation and arrest, postarrest oscillations, and K-versus-$\dot{a}$ relationships.

Araldite B is employed by Kalthoff et al of the Institüt für Festköpermechanik of the Federal Republic of Germany. In their study of dynamic fracture with Araldite B, however, the instantaneous stress-intensity factor is determined by the method of shadow patterns (caustics). The results of photoelastic studies with Homalite 100 and caustic studies with Araldite B show good agreement in some areas, but disagreement in other areas. Since dynamic fracture behavior is studied with two different materials and two different methods, it is difficult to determine whether the points of disagreement are due to material properties or experimental method.

This paper presents the results of a characterization of the physical and mechanical properties and photoelastic observations of dynamic crack behavior of Homalite 100 and Araldite B. Also presented are detailed observations of the differences in fracture surface features of the two materials, and a discussion of the effect of material properties and specimen geometry on crack propagation, crack arrest, and postarrest oscillation.

KEY WORDS: photoelasticity, crack propagation, crack initiation, fracturing, crazing, dynamic properties, mechanical properties, physical properties, viscoelastic properties, stress-intensity factor, polymers

Two polymeric materials are extensively utilized in current studies of dynamic fracture. The first, Homalite 100, is employed in the dynamic photoelastic studies of Dally et al [*1*][2] of the University of Maryland, and

[1]Assistant professor and professor, respectively, Mechanical Engineering Department, University of Maryland, College Park, Md. 20742.

[2]The italic numbers in brackets refer to the list of references appended to this paper.

Kobayashi, A. et al [2] of the University of Washington. They have determined the stress-intensity factor from isochromatic fringe loops and have studied the influence of specimen geometry on crack propagation and arrest, postarrest oscillations, and K-versus-$\dot{a}$ relationships.

The second polymer, Araldite B, is employed by Kalthoff et al [3] of the Institüt für Festköpermechanik of the Federal Republic of Germany. In their studies of dynamic fracture using Araldite B, however, the instantaneous stress-intensity factor is determined by the method of shadow patterns (caustics). The results of photoelastic studies with Homalite 100 and caustic studies with Araldite B show good agreement in some areas, disagreement in other areas. Since dynamic fracture behavior is studied with two different materials and two different methods, it is difficult to determine whether the points of disagreement are due to material properties or experimental method. The photomechanics laboratory at the University of Maryland has performed a series of experiments with Araldite B to establish static and dynamic properties, and to study crack propagation, crack arrest, and postarrest phenomena. The results of these experiments and those of previous experiments using Homalite 100 are used to evaluate the effect of material properties and specimen geometry on crack propagation, crack arrest, and postarrest oscillation.

Experimental Procedure

Static Properties

The static physical and mechanical properties of interest for photoelastic observations are modulus of elasticity (E), material fringe valves ($f\sigma$ and $f\epsilon$), Poisson's ratio (ν), and density (ρ). The material fringe value was determined using a 76.2-mm (3 in.) disk, edge loaded in a polariscope. Over a 24-h period, readings were taken using the Tardy compensation method, and the fringe value was calculated.

Three tension specimen experiments were conducted to determine the static modulus of elasticity under various conditions and to check the fringe value previously obtained. The first experiment used a standard tension specimen of Araldite B with two rectangular strain-gage rosettes attached, one on each side of the specimen, at the center of the gage length. The specimen was loaded in an Instron tension test machine and axial and transverse strain were measured by the strain rosettes through two arm bridges in a BAM-1 bridge amp meter, and plotted on an X-Y recorder. These plots gave static values for the modulus of elasticity and Poisson's ratio. Also as part of this experiment the test machine was fitted with a polarizer and analyzer, a helium-neon (He-Ne) laser shining through the specimen between the strain gages for a light source, and a photodiode to observe the photoelastic fringe orders. The specimen was again loaded and the load versus light intensity (photodiode output) diagram was plotted on the X-Y recorder. From this plot and the specimen geometry, the static fringe values were calculated.

Two additional tension experiments were conducted using Tuckerman optical strain gages mounted on the specimen, front and back, to measure strain. The first of these experiments was to determine the effect of temperature and the second to determine the effect of loading time on the modulus of elasticity. The laboratory air-conditioning was adjusted to vary specimen temperature between tests, and the modulus of elasticity was calculated from load and strain readings. Homalite 100 (second shipment) was selected for comparison with Araldite B in this experiment. The final tension experiment was conducted at constant temperature; full load was applied and the strain gages read over a 24-h period. The resulting data were used to calculate modulus of elasticity for each loading time interval.

The density of Araldite B is needed to calculate dynamic properties. A Kraus Jolly Balance was used to measure specimen weight in air and loss of weight in water. The ratio of these two weights gives specific gravity, which, when combined with the density of water at laboratory temperature, gives the density of Araldite B.

Dynamic Properties

The dynamic properties desired for Araldite B are modulus of elasticity (E_D), Poisson's ratio (ν), and the material fringe value ($f_{\sigma D}$). All of these quantities were measured using the dynamic bar test. The bar specimen was machined to 9.5 by 9.5 by 510 mm (0.375 by 0.375 by 20 in.) from Araldite B, and strain gages were mounted at two locations 127 mm (5 in.) apart in the gage length. The gages were connected in two arm bridges, with calibration resistance included, to measure axial and transverse strain separately. The bar was fitted with a soft attenuator at the point of impact of a sharp projectile from an air gun, and a throw-off bar absorbed energy at the other end. A polariscope was set up using a He-Ne laser shining through the specimen between the strain gages as light source, and a photodiode to receive the monochromatic light and measure fringe orders. The data were recorded on three oscilloscopes. The first oscilloscope recorded axial strain at the two gage locations to measure bar wave velocity. The second was a digital oscilloscope which recorded the photodiode output (fringe orders) and axial strain at the same location. The third oscilloscope recorded axial and transverse strain at one location for determination of Poisson's ratio. All oscilloscopes were triggered by the projectile as it passed a switching mechanism just prior to impact. From the data and specimen dimensions, the bar wave velocity, dynamic modulus of elasticity, Poisson's ratio, and dynamic fringe values were calculated.

Viscoelastic Properties

Polymeric materials exhibit viscoelastic behavior; that is, there is a phase lag or phase angle δ between stress application and strain response. The tendency for a material to behave in this manner is time- and temperature-dependent. To evaluate this behavior and its effect on crack propagation experiments, a series of experiments was conducted using specimens of Araldite B and Homalite 100 in a dynamic viscoelastometer, Rheovibron DDV-III-C. Specimens were machined to approximately 1 by 6 by 70 mm (0.04 by 0.25 by 2.8 in.) of Araldite B and Homalite 100 (first and fourth shipments) and were cycled in the Rheovibron at frequencies of 3.5 and 110 Hz, with a temperature range of from −120 to +125°C (−184 to +257°F). The low temperatures were achieved in a liquid nitrogen-cooled chamber, and the high temperatures with electric heaters. The extreme temperatures are of academic interest only. The temperature range of interest for this series of experiments is the seasonal temperature range of the laboratory—approximately 18 to 26°C (64 to 79°F).

The Rheovibron measures the energy loss factor, tangent δ, directly. It also measures specimen extension and from this, the instrument constants, and the specimen geometry the complex (dynamic) modulus E^* may be calculated. Both tangent δ and E^* are plotted as a function of temperature to produce a diagram typical of the viscoelastic behavior of polymeric materials.

K-*Versus*-$\dot{a}$-*Relationship*

The stress-intensity factor (K) versus crack-tip velocity ($\dot{a}$) relationship is believed to be a material property and therefore is considered in this comparison of crack behavior of Araldite B and Homalite 100. To characterize the complete K-versus-$\dot{a}$ relationship, crack propagation at all possible velocities must be induced in photoelastic specimens and the corresponding stress-intensity factors calculated from the photoelastic data recorded. Three specimen geometries were selected for this purpose: modified compact tension (M-CT), center pin loaded single edge notched specimens (SEN), and rectangular double cantilever beam (R-DCB) specimens.

The photoelastic specimens of Araldite B were prepared and tested following the same laboratory procedure as was used for previous Homalite 100 experiments, reported in Refs *1* and *4*. The specimens were loaded to a predetermined $K_Q > K_{Ic}$ value and the crack initiated by drawing a sharp knife across the starter crack.

The apparatus used for this series of experiments was a polariscope using a Cranz-Schardin multiple-spark-gap camera as a light source and a photographic plate for recording data. The effective wavelength of this light is 4920 Å and the timing of the camera can be adjusted so that four banks of four spark gaps each fire in succession over a period of about 500 to 1500 μs, which can measure crack velocity of over 380 m/s (15 000 in./s). The data recorded from the specimen are load and displacement; the camera timing is sensed by a photodiode and recorded by an oscilloscope. The photoelastic data are recorded on the photographic plate. The camera is triggered when a conductive line in the crack path is severed, and all data are recorded subsequent to this triggering signal.

The modified compact tension specimens gave a wide range of crack velocities, the SEN specimens gave intermediate to high-velocity crack propagation, and the R-DCB specimens gave low to intermediate crack velocity. For each velocity there are corresponding values of stress-intensity factor which are calculated from the photoelastic data recorded.

Each experiment yielded 16 photographs of isochromatic fringe loops at the crack tip. On each of these photographs the crack tip is located and the crack length measured. These values combined with the spark-gap timing were plotted to determine crack velocity. The stress-intensity factor was calculated using the method and computer program according to Dally and Sanford [5]. The parameters r and θ identify points on the fringe loops in polar coordinates where the crack tip is the origin, and are measured either by hand or by X-Y scanner. The manual method uses a radial grid overlay which is lined up with the crack line, centered at the crack tip, and secured in place. Proportional dividers are used to measure r at predetermined values of θ. For best accuracy, fringe loops of maximum radius 2 to 5 mm (0.0787 to 0.1968 in.) are used and five measurements are taken per loop. The median value of r should be close to r_{max} and the two on either side smaller. For best accuracy the loops are taken in pairs, one on each side of the crack tip, 10 or 20 readings per photograph, 16 photographs per specimen. The resulting data are entered into the computer program and the stress-intensity factor is retrieved.

Postarrest Experiments

Two postarrest experiments were successfully conducted using R-DCB specimens of Araldite B in the Cranz-Schardin camera polariscope. The camera timing was extended to cover approximately 1200 μs, the specimens loaded to a low value of $K_Q < K_{Ic}$, and the crack initiated. The resulting crack velocity was low and arrest was achieved at about 500 μs. Crack velocity and stress-intensity factor were calculated as previously.

Surface Features

The energy released at the tip of a running crack must be absorbed by the specimen material. As the energy increases with increased values of stress-intensity factor, the effect on the fracture surface becomes more pronounced. This can be observed with the naked eye; however, a more thorough examination was made using a microscope. Specimen fracture surfaces were chosen to give a variety of crack velocity and stress-intensity factor values both for Homalite 100 and Araldite B. A high magnification was not necessary to view the fracture surface, and photographs were taken to record the surface appearance, at 50-diameter magnification.

Results

Mechanical and Physical Properties

The results of all measurements of static and dynamic mechanical and physical properties of Araldite B are given in Table 1. Similar properties for Homalite 100 taken from Ref *4* are included in Table 1 for comparison.

Temperature and Rate Sensitivity

The static modulus of elasticity as a function of temperature for Homalite 100 (second shipment) and Araldite B is shown in Fig. 1 and, as a function of time of load application, in Fig. 2. Also, with regard to rate sensitivity, it can be noted that over four time decades Araldite B exhibited a decrease in static fringe value of approximately 10 percent, while Homalite 100 (first shipment) showed approximately 2 percent change over the same time span.

TABLE 1—*Mechanical and physical properties.*

	Homalite 100 (First Shipment)	Araldite "B" (First Shipment)
C_1 (m/s): (in./s)	2150: 84 700	2004: 78 900
C_2 (m/s): (in./s)	1230: 48 600	1156: 45 100
E_s (GPa): (lb/in.^{2})	3.86: 560 000	3.34: 485 000
E_D (GPa): (lb/in.^{2})	4.83: 700 000	3.65: 530 000
μ_D (GPa): (lb/in.^{2})	1.84: 267 000	1.16: 233 000
ν	0.31	0.37
ρ(KG-s^2/m^4): (lb-s^2/in.^{4})	122: 0.000112	125: 0.0001145
K_{IM} (MPa$\sqrt{m}$): (lb/in.$^2\sqrt{in.}$)	0.42: 380	0.67: 606
f_{σ_s} (MPa-mm/fringe): (lb/in.^{2}-in./fringe)		
@ 6328 Å	25.1: 143	12.6: 72.2
@ 5893 Å	23.2: 132	11.8: 67.2
@ 4920 Å	19.3: 110	9.82: 56.1
f_{σ_D} (MPa-mm/fringe): (lb/in.^{2}-in./fringe)		
@ 6328 Å	28.2: 161	12.7: 72.5
@ 5893 Å	26.3: 150	11.8: 67.5
@ 4920 Å	21.9: 125	9.9: 56.4

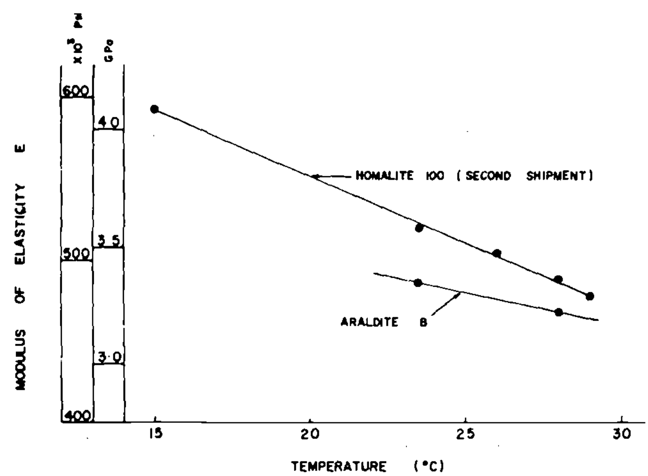

FIG. 1—*Modulus of elasticity as a function of temperature for Araldite B and Homalite 100 (second shipment).*

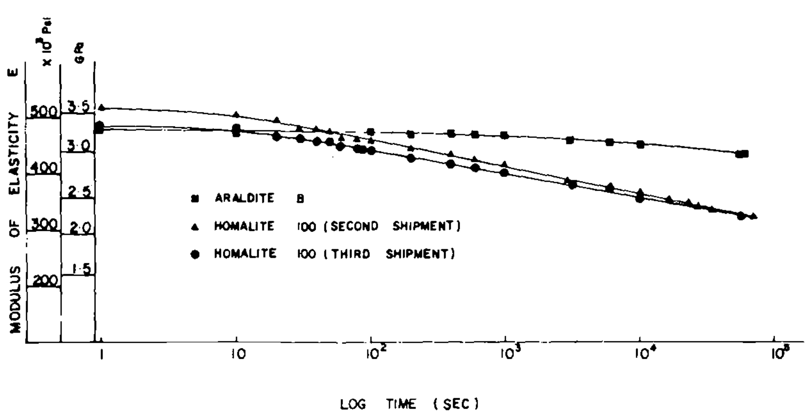

FIG. 2—*Elastic modulus as a function of time for Araldite B and Homalite 100.*

Viscoelastic Behavior

As polymeric materials, both Homalite 100 and Araldite B behave in a viscoelastic manner as was shown by the results of the viscoelastic experiments. Typical results of the experiments performed are shown in Fig. 3. This is a composite plot of the three materials tested, Homalite 100 (first and fourth shipments) and Araldite B, showing the tangent δ and complex modulus (E^*) as a function of temperature over a wide temperature range. The data used for Fig. 3 were taken at a frequency of 110 Hz, which simulates more closely the dynamic loading time.

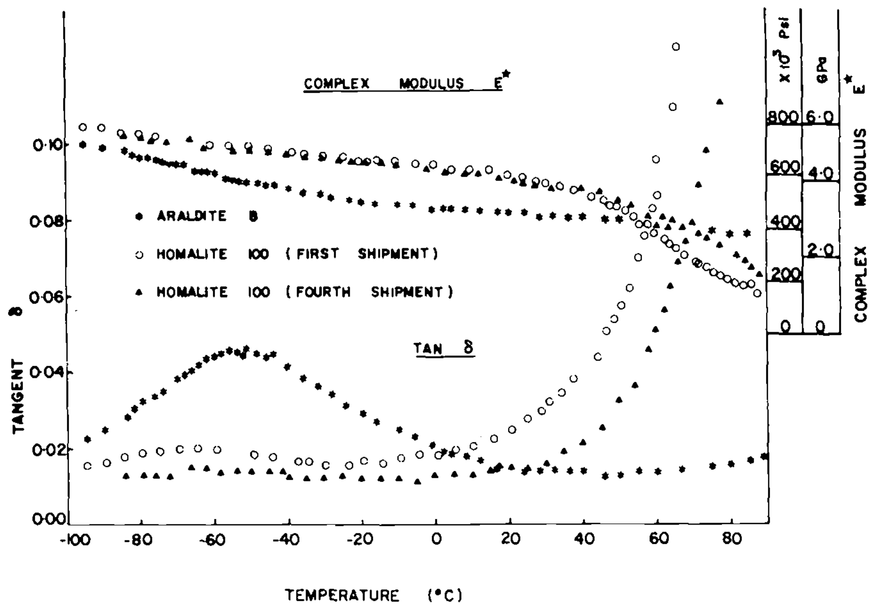

FIG. 3—*Tangent δ and complex modulus* E* *as a function of temperature for Araldite B and Homalite 100 (first and fourth shipments).*

K-*Versus*-$\dot{a}$-*Relationship*

The results of all of the crack propagation experiments reported herein are shown in the K-versus-$\dot{a}$ plot, Fig. 4. All data points are included and identified as to specimen geometry. In order to compare relationships typical of each material, Homalite 100 and Araldite B, the data values were normalized, crack velocity $\dot{a}$ being normalized with shear wave velocity C_2 and stress-intensity factor being normalized with K_{Im}. The normalized values are plotted in Fig. 5.

Postarrest Oscillations

The results of the postarrest experiments for Aldrite B can be compared with the results of experiments conducted with Homalite 100, previously reported in Ref *4*. This comparison, Fig. 6, shows typical results for both materials. Both crack-tip position and stress-intensity factor are shown as a function of time in such a way that the time of arrest, reinitiation, and rearrest are obvious. It should be noted that the time base for the experiment using Model No. 6, Homalite 100, was extended using time delays. These gaps in time are represented in Fig. 6 by dashed lines.

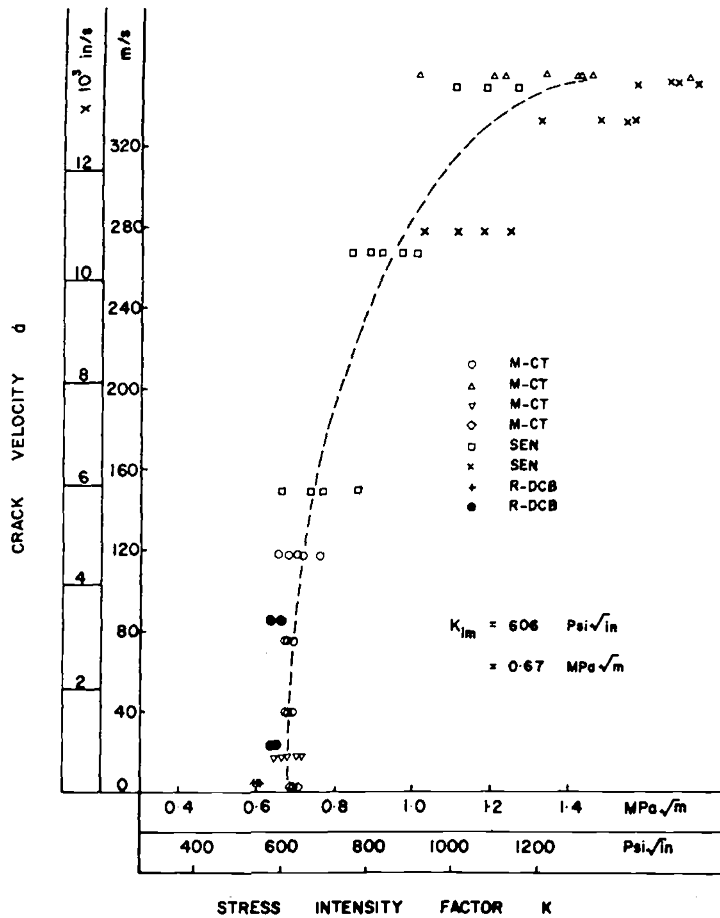

FIG. 4—*Crack velocity as a function of stress-intensity factor for Araldite B.*

Surface Features

Typical photographs taken during the microscopic examination of fracture surfaces are presented in Fig. 7 for Homalite 100 and in Fig. 8 for Araldite B. All photographs were taken on polaroid film at a magnification of 50 diameters. Each photograph is identified by the magnitude of crack velocity and instantaneous stress-intensity factor for each material. In all photographs the crack travel is left to right, with increasing crack velocity and stress-intensity fact or also left to right.

Discussion

The physical and mechanical properties of Araldite B determined by experiments described in the foregoing and listed in Table 1 are, in general,

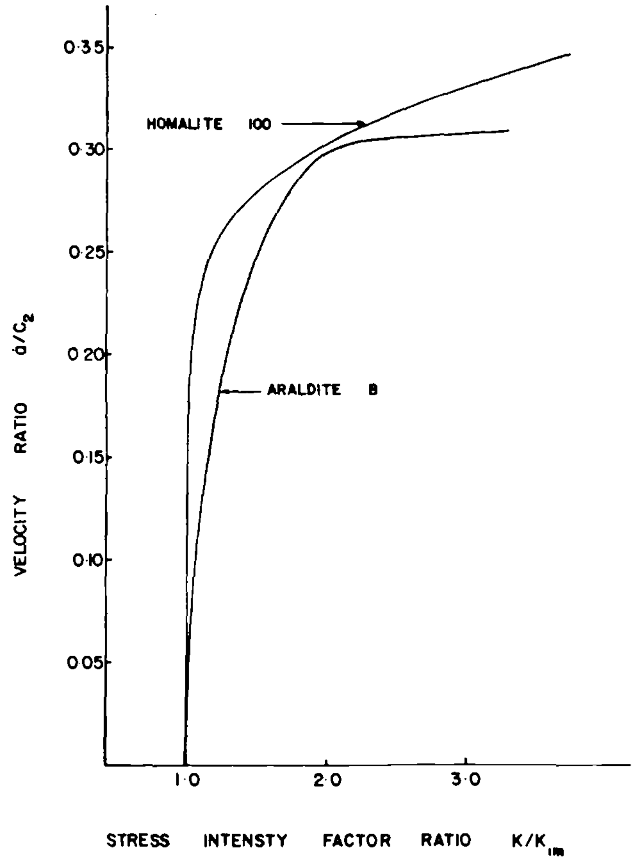

FIG. 5—*Normalized* K*-versus-*ȧ *relationship for Homalite 100 and Araldite B.*

in good agreement with available published data [*1,6*]. The properties for Homalite 100 listed in Table 1 were taken from Ref *4*. Photoelastically, Araldite B is more sensitive than Homalite 100, and the static and dynamic fringe values show little change. Homalite 100 is more sensitive to changes in temperature and its modulus of elasticity is more rate-sensitive than Araldite B. It is concluded on the basis of this comparison of properties that both materials are satisfactory for photoelastic experiments.

The viscoelastic behavior of both materials, Homalite 100 and Araldite B, as shown in Fig. 3, is typical of that expected for polymers. The plot of complex modulus, E^*, as a function of temperature shows that for both materials E^* is sensitive to temperature, but not markedly so at laboratory temperature—Homalite slightly more so than Araldite B. Also it is of interest to note the steep positive slope of the plot of tangent δ as a function of temperature for Homalite 100 (especially the first shipment) at close to laboratory temperature. Tangent δ is an energy loss factor, and is a

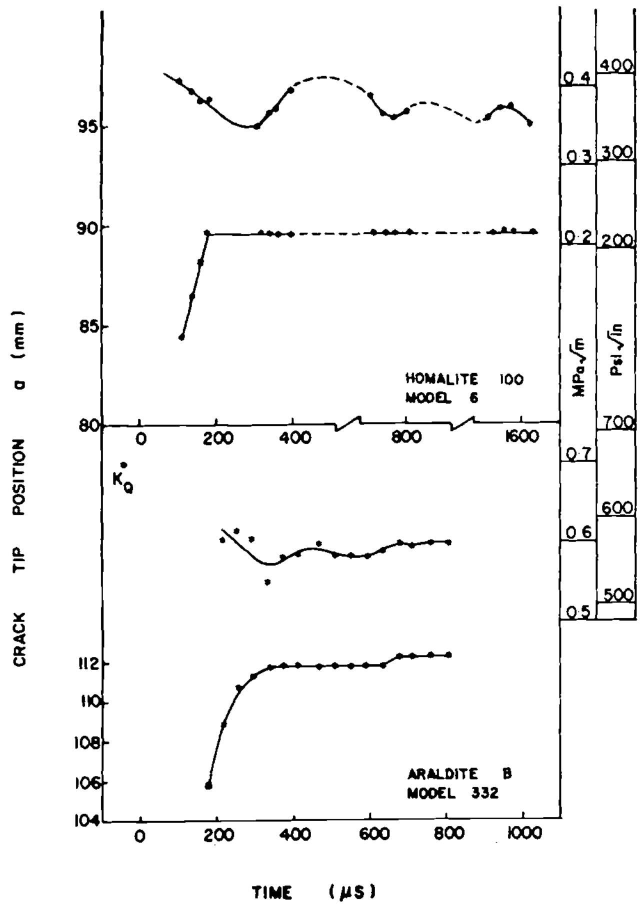

FIG. 6—*Postarrest oscillation in stress-intensity factor: R-DCB, Araldite B.*

measure of the amount of energy that a material is capable of dissipating. This relates to damping properties, and it can be seen that Homalite 100 potentially could show much stronger damping capabilities than Araldite B.

The K-versus-$\dot{a}$ relationship for Araldite B is shown in Fig. 4. This plot shows a characteristic vertical or near-vertical stem at low crack velocity, and a horizontal tail at high crack velocity. All data points are shown, and, while there is some scatter, it is not beyond the bounds of experimental error. The data points shown in Fig. 4 are from experiments using three specimen geometries: M-CT, SEN, and R-DCB. The stress-intensity factor measured by R-DCB specimens was 6 to 10 percent lower than corresponding values achieved from M-CT specimens. This is within expected experimental accuracy; therefore there is no strong evidence to indicate that a separate K-versus-$\dot{a}$ relationship exists for each specimen geometry.

A point of interest in the K-versus-$\dot{a}$ relationship for Araldite B is that it shows a positive slope at the lower values of crack velocity and this slope decreases rapidly as crack velocity increases. To compare the K-versus-$\dot{a}$ relationship of Araldite B with that of Homalite 100, a normalized form of the relationship was used, as shown in Fig. 5. Here the difference in slope of the near-vertical stem shows up clearly. With Homalite 100 the stress-intensity factor is virtually constant over half the crack velocity range, while for Araldite B the stress-intensity factor increases by 13 percent in the same portion of the crack velocity range. The reason for this difference is not readily apparent, and a study of material properties would not be complete without an attempt to explain it. As a crack runs through a specimen under the influence of a stress field, energy must be dissipated at the crack tip, and, as crack velocity and stress-intensity factors increase, the amount of energy required to be absorbed increases as well. One mechanism for absorbing energy may be found in the study of the fracture zone. Examination of the fracture surface shows, even to the naked eye, that striations and crazing appear in varying amounts on the fracture surface. Closer examination under a microscope (×50 is satisfactory magnification) reveals all features of the fracture surface. Striations were observed in all fracture surfaces studied from low to high crack velocity. The density of the striations increased with crack velocity. Crazing was observed in both Homalite 100 and Araldite B specimens at the higher values of crack velocity and stress-intensity factor. Also observed in specimens of Araldite B but not in Homalite 100 were points of stress intensity and crack nucleation. The density of these nucleation points increases with crack velocity and stress-intensity factor to the point that they become dense enough to be called crazing. It is believed that it is these nucleation points which provide the energy sinks needed to allow the stress-intensity factor to increase at a faster rate for Araldite B than for Homalite 100 at the middle crack-velocity range. Figures 7 and 8 show photographs of the fracture surface under a magnification of 50 diameters. The photographs showing the surface features influenced by the lowest crack velocity are upper left, and highest velocity are lower right. It can be seen that all photographs show striations until obscured by crazing. It also can be seen that there are more crack nucleation points in the photographs for Araldite B than for Homalite 100.

Postarrest oscillations in stress-intensity factor were observed in postarrest experiments using R-DCB specimens of Homalite 100 and Araldite B. Typical results are shown for comparison in Fig. 6. The oscillations in stress-intensity factor are small, on the order of 5 percent in magnitude, which is the same order of magnitude as the experimental accuracy considered valid for these experiements. Therefore, quantitative conclusions on postarrest oscillations are not valid. It is interesting to note, however, that similar oscillations appear in all prearrest and postarrest experiments,

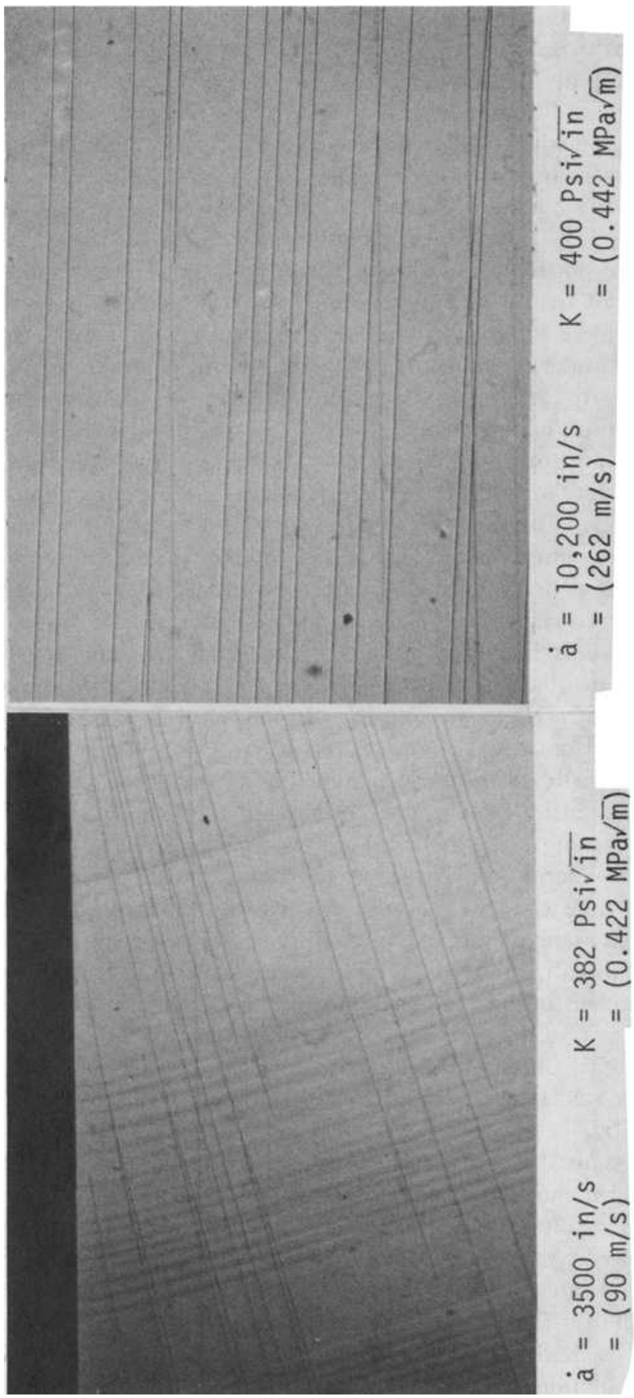

ȧ = 3500 in/s
= (90 m/s)
K = 382 Psi√in
= (0.422 MPa√m)
ȧ = 10,200 in/s
= (262 m/s)
K = 400 Psi√in
= (0.442 MPa√m)

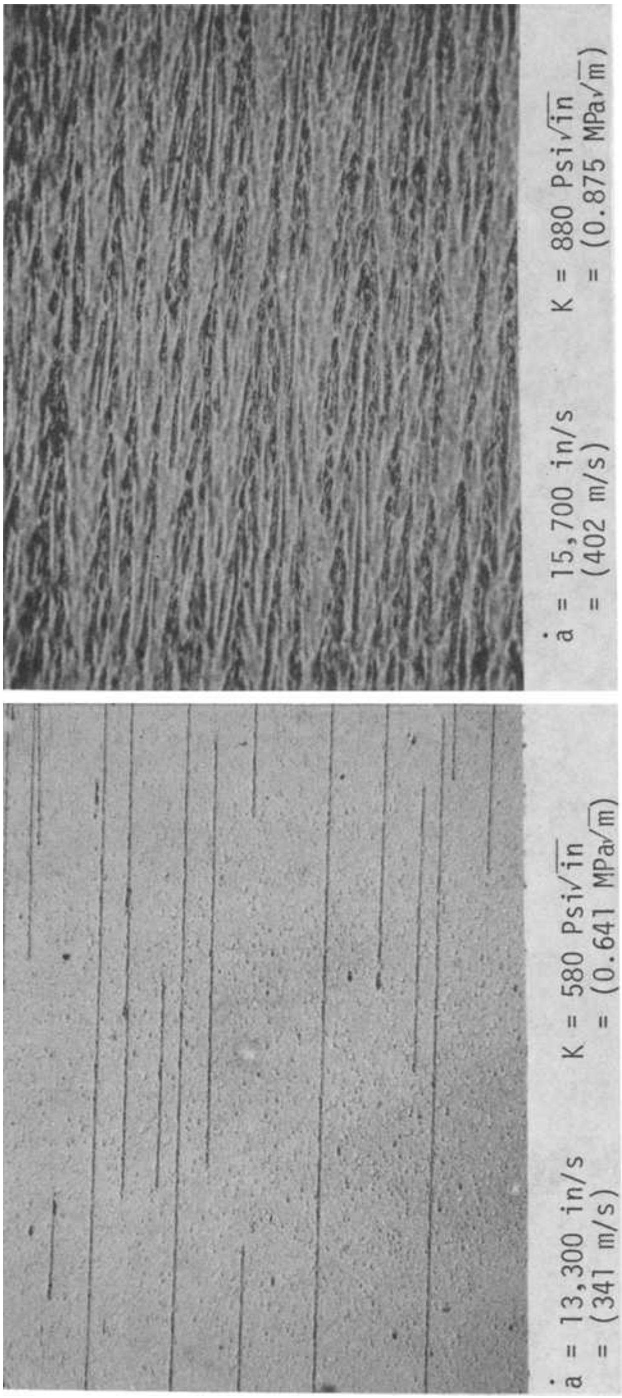

FIG. 7—*Surface features of Homalite 100 (×50).*

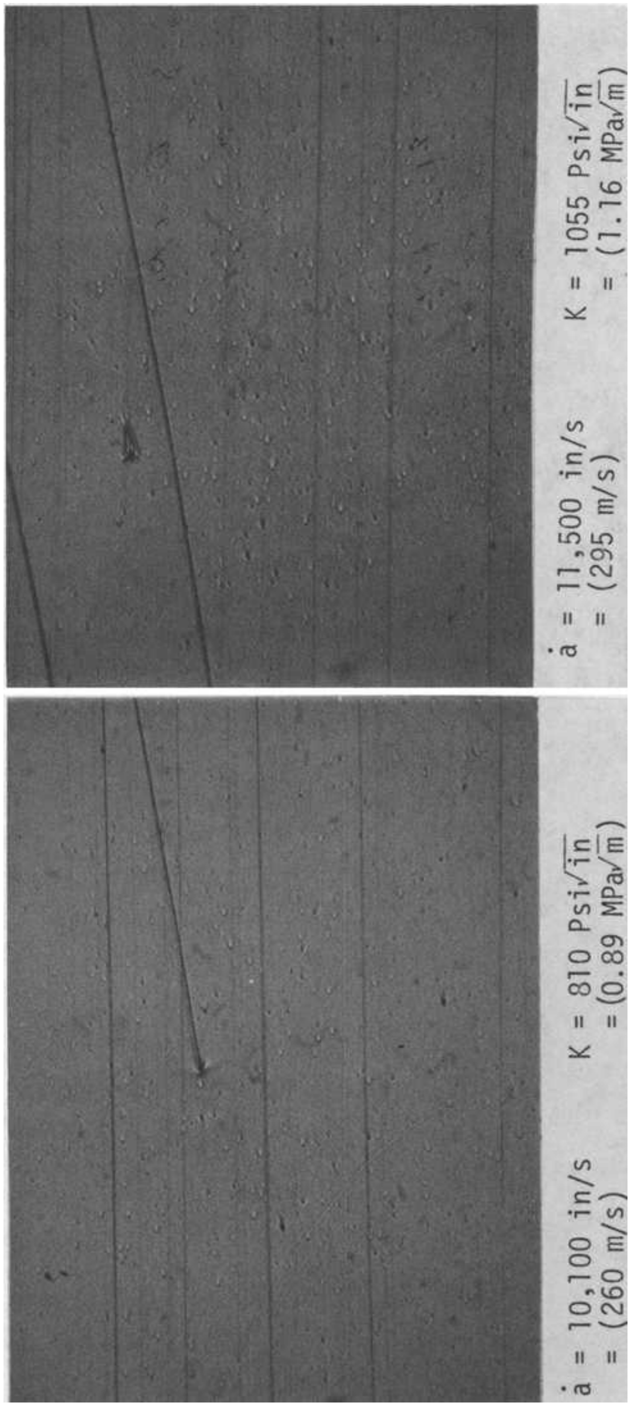
$\dot{a}$ = 11,500 in/s
= (295 m/s)
K = 1055 Psi$\sqrt{\text{in}}$
= (1.16 MPa$\sqrt{\text{m}}$)
$\dot{a}$ = 10,100 in/s
= (260 m/s)
K = 810 Psi$\sqrt{\text{in}}$
= (0.89 MPa$\sqrt{\text{m}}$)

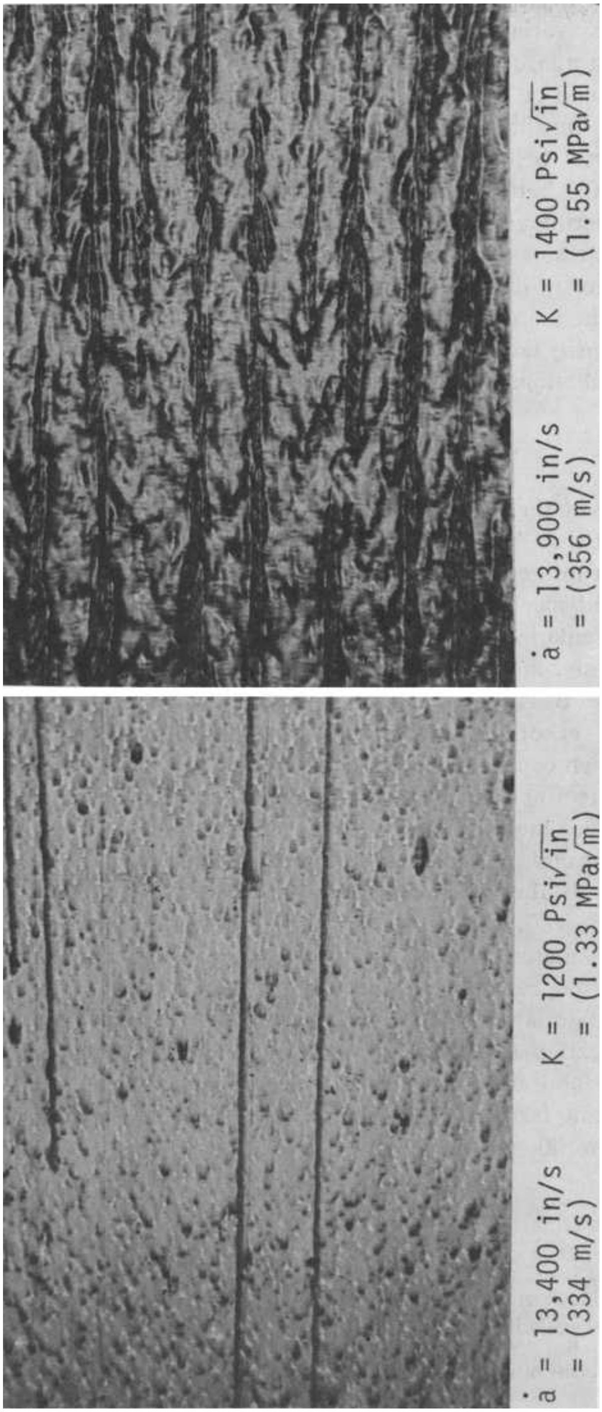

FIG. 8—*Surface features of Araldite B* (×100).

and, from the dynamic nature of the experiments, it is reasonable to expect that prearrest variations in stress-intensity factor would carry over into the postarrest phase, with the test specimen providing a medium for damping. This should be more true after abrupt crack arrest than after gradual crack arrest. On this premise it is possible to draw qualitative conclusions from postarrest behavior as related to specimen material. Homalite 100 was judged the better damping material based on the results of the viscoelastic experiments, and that appears also to be true from the results of the postarrest experiments. Figure 6 shows more damping of stress-intensity factor in the case of Homalite 100 than in the case of Araldite B. Also, it can be seen from Fig. 6 that reinitiation is accompanied by a rise in stress-intensity factor. Finally, it can be seen that abrupt arrest is followed by larger oscillations than those following gradual arrest.

Conclusions

This study of the mechanical and physical properties of Araldite B and Homalite 100 has been an attempt to determine these properties and to evaluate their influence on dynamic fracture response. The effect of material properties and specimen geometry on crack propagation, crack arrest, and postarrest oscillations has been discussed and conclusions drawn where possible. These conclusions are summarized as follows:

1. Araldite B is more sensitive photoelastically than Homalite 100. Investigation of other physical and mechanical properties revealed no problems which could not be overcome by good laboratory techniques.

2. Homalite 100 has stronger damping characteristics than Araldite B. A quantitative analysis of the effect of damping on dynamic fracture response is beyond the scope of this investigation.

3. Araldite B absorbs more energy near the tip of a running crack than does Homalite 100. This is evidenced by the unique K-versus-$\dot{a}$ relationship for each material. Also, Araldite B can sustain a low crack velocity and shows strong resistance to crack branching.

4. Both materials exhibit similar dynamic fracture responses during crack propagation and crack arrest and in the postarrest period, within the limits of laboratory experimental accuracy. It is concluded that satisfactory dynamic fracture experimental results can be achieved using either specimen material.

References

[1] Dally, J. W., Irwin, G. R., Kobayashi, T., and Etheridge, J. M., "A Photoelastic Study of the Dynamic Fracture Behavior of Homalite 100," U.S. Nuclear Regulatory Commission Report NUREG-75/107, Sept. 1975.

[2] Bradley, W. B., "A Photoelastic Investigation of Dynamic Brittle Fracture," Ph.D. Thesis, University of Washington, Seattle, Wash., 1969 (A. S. Kobayashi, Thesis Advisor).

[3] Kalthoff, J. F., Beinert, J., and Winkler, S. in *Fast Fracture and Crack Arrest, ASTM STP 627,* American Society for Testing and Materials, 1977, pp. 161-176.
[4] Irwin, G. R., Dally, J. W., Kobayashi, T., Fourney, W. L., and Etheridge, J. M., "A Photoelastic Characterization of Dynamic Fracture," U.S. Nuclear Regulatory Commission Report NUREG-0072, Dec. 1976.
[5] Sanford, R. J. and Dally, J. W., *Engineering Fracture Mechanics Journal,* Vol. 11, 1979, pp. 621-633.
[6] Clark, A. B. J. and Sanford, R. J., *Proceedings,* Society for Experimented Stress Analysis, Vol. 20, No. 2, 1963, p. 148.

R.S. Gates [1]

Some Effects of Specimen Geometry on Crack Propagation and Arrest

REFERENCE: Gates, R. S., "**Some Effects of Specimen Geometry on Crack Propagation and Arrest,**" *Crack Arrest Methodology and Applications, ASTM STP 711,* G. T. Hahn and M. F. Kanninen, Eds., American Society for Testing and Materials, 1980, pp. 146-160.

ABSTRACT: Fast crack propagation and arrest have been studied in steel specimens of the double cantilever beam type using three different geometries and either a fixed grip or compliant loading system. A finite-difference computer program was used to measure values of the dynamic stress-intensity factor K_D. The relationship between values of K_D and K_S, the stress-intensity factor for a quasi-statically growing crack depended on the specimen geometry and loading system used.

Stable crack arrest was easier to obtain in the specimens loaded with fixed grips. This probably resulted from the rigidity of the loading system, which produced specimen oscillations after arrest of insufficient magnitude to reinitiate crack growth. An examination of the energy associated with a moving crack suggests that kinetic energy may be reabsorbed to aid further crack propagation but is not all reabsorbed at arrest. The remaining fraction causes oscillations of the cracked specimen halves which may reinitiate the crack, or be damped out as the stress intensity rings down to its static value. Examination of the data suggests that intermediate arrests, characterized by a minimum in the crack length velocity curve, were a common feature of all tests. The stress intensity for crack arrest appeared to depend on specimen geometry.

KEY WORDS: crack propagation, crack arrest, cantilever beams, dynamic stress intensity, fracture properties, finite difference, steel

Many crack arrest studies use specimens of the double cantilever beam (DCB) type with a blunt starting notch to guarantee fast propagation [*1-3*].[2] A common assumption has been that, due to loading system inertia, the grips do not move during the propagation event. This has been shown to be incorrect [*4-6*], at least when the loading system compliance is comparable to that of the specimen. The effect of an error in this assumption on the analysis is to alter both the elastic strain energy input to the speci-

[1]Research officer, Materials Division, Central Electricity Research Laboratories, Leatherhead, Surrey KT22 7SE, U. K.

[2]The italic numbers in brackets refer to the list of references appended to this paper.

men and the kinetic energy distribution since the massive grips and pull rods are no longer fixed.

In order to help quantify some of the effects resulting from the variation in load train compliance, sets of tests have been performed using apparatus where, first, the compliance was well characterized and, second, where it was negligible. Two specimen geometries with sharp starting notches were used with the first system so that values of K_{Ic} could be determined in addition to the dynamic parameters. The second system used blunt notched specimens.

The specimens were instrumented and the data analyzed to give values of the crack velocity, the stress-intensity factor for the propagating crack, K_D, the stress intensity for a quasi-statically growing crack at the same instantaneous length, K_S, and the strain and kinetic energies during propagation. The various results are presented and their implications for the interpretation of both crack propagation and crack arrest data are discussed.

Specimens and Experimental Apparatus

The three specimen designs, machined from a tool steel of 1.0C-1.3Mn-0.5Cr-0.5W-0.2V-0.3Si approximate composition, are shown in Fig. 1. All specimens were given the same nominal heat treatment of 1½ h at 875°C

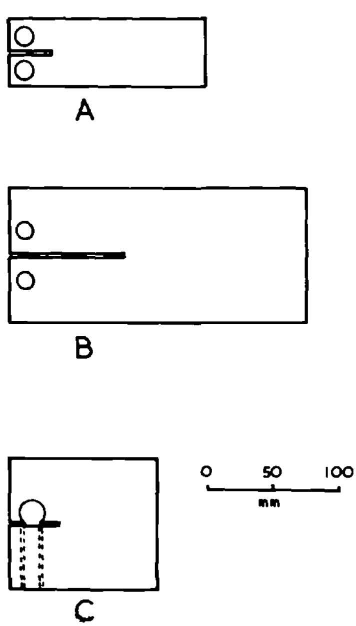

FIG. 1—*Specimen geometries.*

with an air-cool to produce a toughness of about 30 to 40 $\text{MNm}^{-3/2}$ in Specimen A and about 55 $\text{MNm}^{-3/2}$ in Specimen B. The toughness was not determined in Specimen C. Toughness was sensitive to cooling rate in this steel so that the variation along a specimen was probably less than that between specimens. Both A and B had prefatigued starting notches while C had a blunt starting notch produced by spark machining. Specimen A had a single side groove to a depth of 20 percent of the specimen thickness while B and C were ungrooved. All specimens had a series of conducting aluminium strips vapor-deposited on the ungrooved face over a thin layer of epoxy resin. These were connected to a resistance network whose output altered as the strips were broken by the advancing crack and which could be interpreted to give the crack position and hence the crack length/time history. The first conducting strip was approximately 5 mm from the crack tip so that errors were minimized when extrapolating the crack length/time history back to the initiation point. Further details of the technique used here have been given previously [*6*].

Specimens A and B were tested in apparatus described previously [*6*] and consisted of a set of compliant loading rods pin-jointed to the specimen and loading machine so that the value of K_S would rise and then fall below the value of K_{Ic} in a controlled manner as the crack extended. A set of strain gages was applied to the load rods, whose output was proportional to the instantaneous applied load during propagation. This could then be used to calculate the specimen pin movement during propagation by using the following formula

$$W_g = W_o + [P_o - P(t)]\, C_K$$

where

W_g = time dependent pin displacement,
W_0 = initial, static, pin displacement calculated from the initial load and specimen compliance,
$P(t)$ = time dependent load indicated by the strain gage,
P_0 = initial load recorded on the machine, and
C_K = compliance of the loading system.

It was found that despite using compliant loading rods, the value of C_K was dominated by that of the machine and had a value of approximately 37 mm/MN. It was thus impossible to simulate fixed grips by using a conventional loading machine with pull rods to load the specimen. The following system was thus devised where a good approximation to fixed grips could be closely attained.

Specimen C (Fig. 1) was loaded by means of a bolt-threaded through the lower specimen half acting against a tup in the upper half. The failure load was determined by calibrating, for each specimen, the output of a clip gage placed across the mouth of the specimen when the specimen was loaded in a conventional testing machine below the failure load. The test was then carried out by clamping the specimen in a vise and tightening the bolt with a large torque wrench.

Analysis

Values of the stress intensity at initiation (K_{Ic} for Specimens A and B) and values of K_S were determined by using the beam on an elastic foundation model of Kanninen [7] with a subsequent modification [8] that gave more accurate solutions for both shallow and deep notches. The final expression used involved complex trigonometric functions and so is not reproduced here. The appropriate value of the load, P, used to evaluate K_S is given by

$$P = \frac{P_o\,[C_s(a_o) + C_K]}{C_s(a) + C_K}$$

where

P_o = initiation load,
$C_s(x)$ = specimen compliance at crack length x,
C_K = loading system compliance, and
a_o, a = initial and instantaneous crack length, respectively.

Values of C_s were also determined from the beam on the elastic foundation model.

Instantaneous values of K_D were determined by means of a one-dimensional dynamic finite-difference computer program. This was a modification [9] of the program described by Kanninen [10], calculating K_D directly from successive values of crack and grip displacement at successive time steps. This inverts the more usual procedure of computing the crack speed and arrest length using selecting values of K_D until the computed parameters agree with the experimental ones [10,11].

Fourth-order polynomials were fitted to both the load/time and crack length/time data so that fitted values of the grip displacement and crack length could be used by the program at any time value. Since the recording equipment triggered when the first conducting strip broke, the time interval between crack initiation and triggering was determined by extrapolating the crack length/time data back to the initial crack length. The polynomial fit tended to smooth out and hence reduce random experimental errors in the input data while still faithfully reproducing the overall trend. Values of the strain and kinetic energies were computed by summing their values for each element of the finite-difference grid.

A comparison between the stress intensity factors determined from the static version of the dynamic equations used in this analysis and experimentally determined values [8] showed good agreement for uncracked ligaments greater than $h/2$ where $2h$ is the specimen dimension perpendicular to the crack plane. It was thus assumed that the one-dimensional dynamic analysis had the same limit of applicability.

Values of the stress-intensity factor at the instant of arrest K_{Ia} were determined from the corresponding value of K_D while that a short time after arrest, K_{Ia}^+, was determined from the value of K_S at the arrested crack length.

Results

The results are summarized in Table 1 and Figs. 2-4 with the essential features described in the following.

Stress-Intensity Factors

Each series of specimens exhibited a characteristic but different relationship between K_S and K_D. In Type A specimens illustrated in Fig. 1*a*, values of K_S initially rose above and then decreased toward the K_{Ic} value

TABLE 1—*Crack velocities and initiation and arrest stress-intensity factors.*

Specimen No.	Average Velocity, m/s	K_{Ic}, K_q, $MNm^{-3/2}$	K_{Ia}, $MNm^{-3/2}$	K_{Ia}^+	K_{Ia}/K_{Ic}	K_{Ia}^+/K_{Ic}
A16	212	43.4	47.8	42.0	1.10	0.97
A20	134	33.0	56.1	42.0	1.70	1.27
A21	195	38.6	51.4	47.0	1.33	1.22
A22	267	36.1	74.9	39.0	2.07	1.08
A23	153	31.2	48.4	40.0	1.55	1.28
...	...	...	44.8	43.0	1.44	1.38
A24	294	41.8	63.7	56.0	1.52	1.34
A25	262	40.3	61.3	49.5	1.52	1.23
A26	200	33.5	55.0	31.0	1.64	0.93
B1	15	57.7	53.8	52.5	0.93	0.91
B2/1	58	52.5	50.3	51.0	0.96	0.97
B2/2	58	54.2	52.9	52.4	0.98	0.97
B3	142	57.4	46.8	55.6	0.82	0.97
C1	629	109.8[a]	41.3	20.3	1.13[b]	0.55[b]
C2	575	107.1[a]	52.5	42.0	1.43[b]	1.15[b]
	...	...	27.2	27.2	0.89[b]	0.74[b]
C3	474	71.5[a]	35.7	33.5	0.97[b]	0.92[b]
	...	...	24.8	19.8	0.68[b]	0.54[b]
C4	598	70.8[a]	49.2	41.0	1.34[b]	1.12[b]
	...	...	31.2	33.0	0.85[b]	0.90[b]
C6	439	76.3[a]	46.0	42.5	1.26[b]	1.16[b]
	...	...	31.5	35.4	0.86[b]	0.97[b]

[a]Since a blunt starting notch was used, these are marked K_q, not K_{Ic}.
[b]These values are based on the mean value of K_{Ic} for Series A of 36.6 $MNm^{-3/2}$.

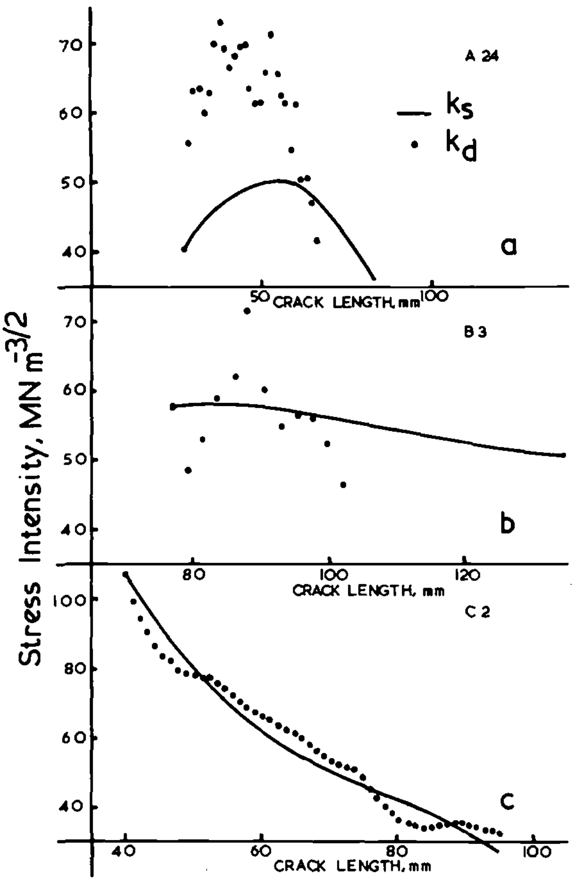

FIG. 2—*Comparative values of* K_S *and* K_D *for* (a) *Series A,* (b) *Series B, and* (c) *Series C specimens. Values of* K_S *start at the initiation stress intensity.*

as the crack length increased, Fig. 2*a*. Values of K_D were computed up to a predetermined crack length. This was generally where the crack had started to run out of the central crack plane, except for Specimen A23, which arrested in the crack plane. However, there was no obvious difference between the computed results of this and the other specimens. Values of K_D exceeded those of K_S, their difference being least when computation was discontinued.

The general behavior of specimens of Design B is illustrated in Fig. 2*b*. The behavior for K_S was similar to that just described although the peak was a lot flatter as a result of the change in the relative specimens compliance to that of the loading system. The K_D values oscillated about K_{Ic}. Computations were again generally stopped because the crack plane changed direction, although the crack arrested in Specimen B2 again with

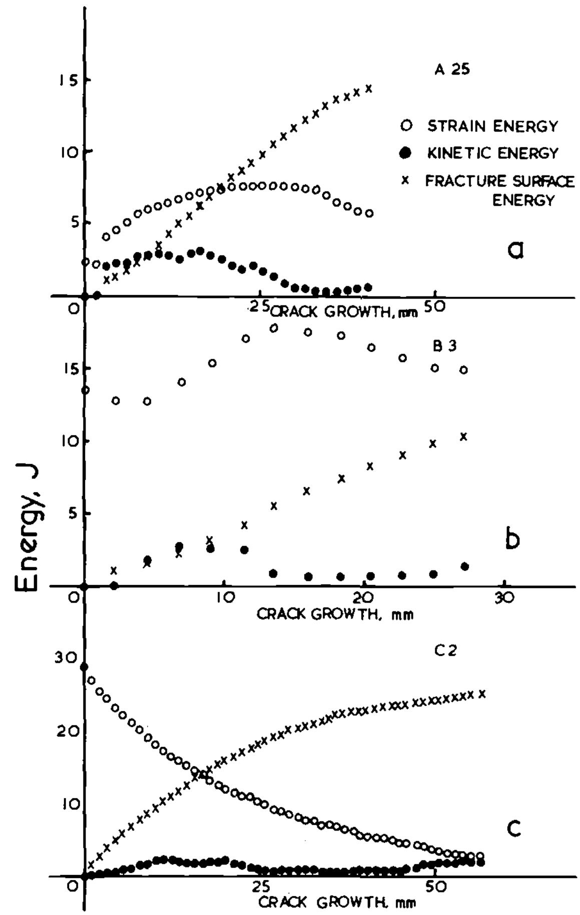

FIG. 3—*Energy of the fast crack propagation in* (a) *Series A,* (b) *Series B, and* (c) *Series C specimens.*

no obvious difference between the computed results from this specimen and the others of the series.

Specimens C were tested with fixed grips and the values K_S dropped steadily from the initiation value, Fig. 2*c*. Values of K_D were initially below K_S and then oscillated about it. Stable arrest always occurred within the specimen although in Specimens C1 and C3 this was sufficiently close to the uncracked face that the analysis was no longer accurate.

Distribution of Energy

Values of the kinetic, strain, and absorbed surface energies (T, U, and S, respectively) were calculated as described in the previous section. The value of T, and hence dT/da, depends on the unknown mass of the moving

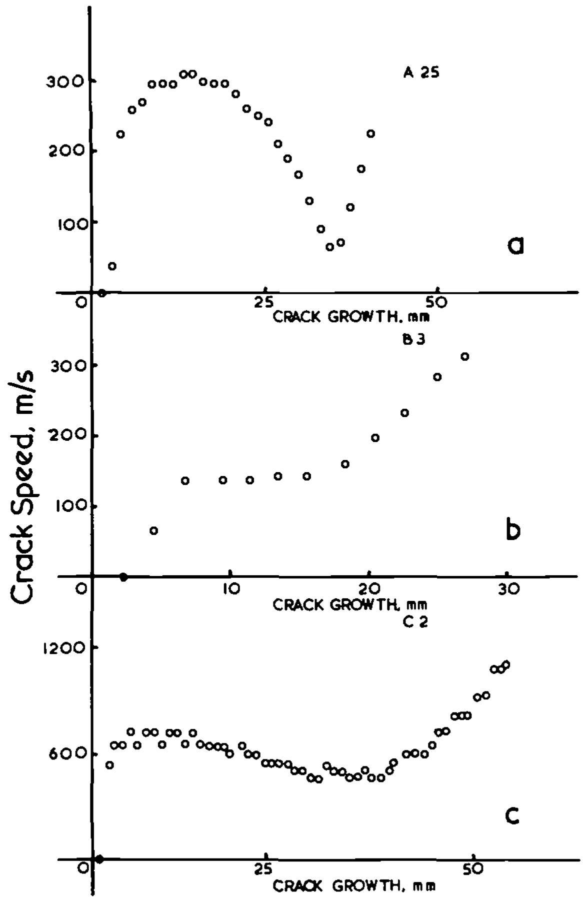

FIG. 4—*Crack Velocity variation for* (a) *Series A*, (b) *Series B, and* (c) *Series C specimens.*

grips, M, since the whole system must move in sympathy. This may also significantly alter the values of K_D through the following relationship

$$\frac{K_D{}^2}{E(1-\nu)} A\,(\mathrm{v}) = G_D = \frac{dU}{da} + \frac{dT}{da} \tag{1}$$

where

E = Young's modulus,
ν = Poisson's ratio,
A (v) = function of velocity, v, given by Freund [*12*], and
a = crack length.

In the analysis, the sensitivity of K_D to the choice of M was determined by augmenting the mass of the first beam element by an amount ranging from 0 to 1 kg. Although the values of T increased markedly, the resultant values of K_D changed only slightly. It was thus concluded that a reasonable rather than an exact value for M could be used in the computations and a value of 500 g was used subsequently.

The distribution of the various energy forms was similar in Specimens A and B loaded with compliant pull rods and is illustrated in Fig. 3*a* for Specimen A and in Fib. 3*b* for Specimen B. The specimen strain energy rose as the rapid energy flow from the loading system fed the specimen, and then fell. The integrated fracture surface energy ($= \int G_D da$) rose at a steady rate, its slight nonlinearity reflecting the variation in G_D (Fig. 2). The kinetic energy rose and fell with a small superimposed oscillation, but was not zero when computation was terminated. This behavior was similar in all specimens, including A23, where the crack arrested stably.

The energy distribution for C-type specimens is illustrated in Fig. 3*c*. The strain energy fell steadily from initiation while the integrated fracture surface energy rose steadily, showing more pronounced nonlinearity. The kinetic energy again showed oscillations and was nonzero at stable arrest.

Crack Velocities

Crack velocities were calculated in two ways. First, an average value was determined from a least-squares linear regression fit to the "steady" part of the propagation phase. These values are given in Table 1. Those from Specimen A were in the range 130 to 300 m/s. Those from Type B were low, in the range 15 to 140 m/s, while those for Type C were highest, in the range 470 to 630 m/s.

A second approach to the calculation of crack velocities was to fit a fourth-order polynomial by least squares to the crack length/time data, which when differentiated showed velocity variations about the average value. Whether such variations were physically rather than mathematically meaningful was tested by comparing the polynomial fits with the original data. Satisfactory agreement was found. An additional check was that the behavior in each series of tests was similar whereas a doubtful procedure might not have indicated a consistent trend.

The crack velocities in Type A specimens increased from the sharp starting notch and then decreased, although in many specimens this was followed by a second increase (Fig. 4*a*) as the crack started to depart from the centerplane in most specimens, or arrested in Specimen A23. In Type C specimens, the initial velocity was constant before decreasing to a minimum and then accelerating toward arrest (Fig. 4*c*).

Discussion

Relationship Between K_S *and* K_D

When there is no net energy flow across the system boundaries, Eq 1 is frequently written in the form

$$G_S - G_D = dT/da \qquad (2)$$

where G_S is the static strain energy release rate calculated at the instantaneous crack length. Thus the sign of dT/da determines whether G_D is greater or less than G_S and similarly whether K_D is greater or less than K_S. Since dT/da changed sign many times (Fig. 3), then Eq 2 suggests that K_D should oscillate about K_S, although experimentally K_D was greater than K_S for most of the propagated length (Fig. 2*a*) and did not oscillate about K_D with the change in sign of dT/da. Since Eq 1 is simply a statement of conservation of energy, this suggests that the interpretation of it in the form of Eq 2 is incorrect. Indeed, Eqs 1 and 2 are only equivalent, if the strain energy distribution for the dynamic specimen is identical to the static case, which is unlikely. This artificial introduction of G_S should not therefore be used to suggest any predetermined relationship between G_S and G_D (for example, $G_S > G_D$).

The data from Specimens *C* (Fig. 2*c*) are qualitatively similar to those reported for a similar loading system by Kalthoff et al [*3*] using photoelasticity. Initially K_D fell below K_S but then oscillated about it. An examination of the computed specimen displacements during propagation in the present study showed that this behavior resulted from the oscillation of the cracked specimen halves relative to the static position, similar to that reported by Kalthoff et al [*3*] after arrest. If the crack opening angle is considered to be an indication of K_D, then specimen inertia causes K_D to fall below K_S initially. The accumulated difference between the static and dynamic displacements results in the specimen halves oscillating about the static configuration, giving rise to an apparent short plateau in K_D. The plateau was less extensive than reported by Kalthoff et al [*3*], presumably because of the specimen dimensions used, which were shorter in the present tests.

Velocity Dependence of K_D

Determination of the velocity dependence of K_D is necessary when predicting the arrest point from computer programs [*13,14*]. Since in the present tests both the instantaneous values of K_D and the crack velocity v varied during the course of a single test, such a relationship might be obtained from a minimal number of specimens. A typical set of data from one specimen of Type A is shown in Fig. 5. While the overall trends for both K_D and v are considered accurate, individual points are prone to experimental and computational error. The individual errors in K_D and v are compounded when cross-plotting these parameters, so that any possible acceleration dependence for K_D would be impossible to quantify. The data do suggest, however, that K_D may not be a single valued function of v and that K_D may be a function of higher time derivatives of crack length than just the first.

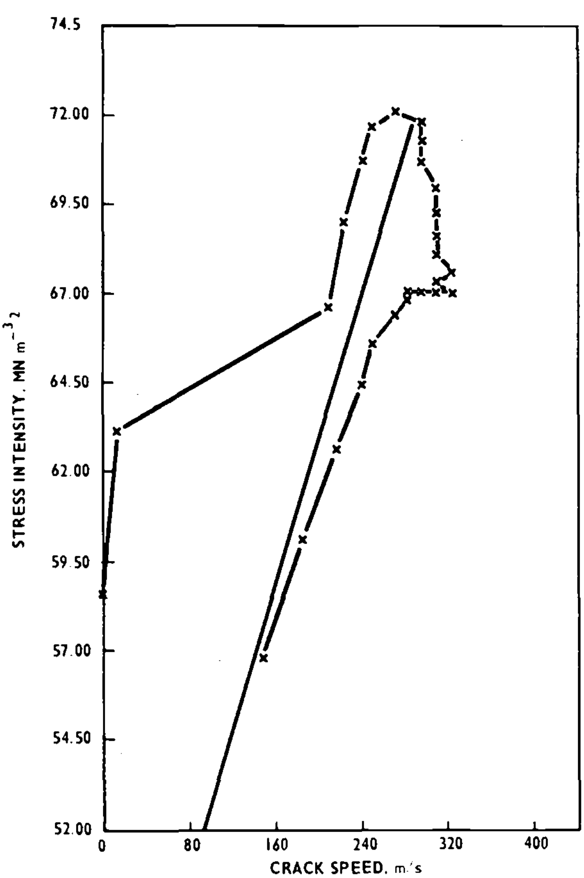

FIG. 5—*Variation of* K_D *with crack speed. The straight solid line is a suggested, single-valued function relating these parameters.*

An acceleration dependence for K_D is different from that assumed by Hahn et al [*15*] and Kanninen et al [*13*] for steels, and observed by Kobayashi and Dally [*16*] for polymers, where K_D and v have a single valued relationship. There are many effects which can result in a velocity dependence of K_D. First, the surface appearance of the propagated crack was considerably rougher than the fatigue precracked surface and the resultant increase in surface area per unit increase in crack length would have increased G_D and hence K_D. Second, there are dynamic effects on the shape and content of the elastic and plastic strain fields surrounding the moving crack tip. The shape of the elastic strain field is probably not strongly dependent on velocity since the relative strain effects are small at the present experimental velocities [*17-18*]. However, there is plenty of scope for dynamic effects on the shape and content of the plastic strain field. Also, since the dislocations forming the plastic zone must move at a speed in excess of the crack speed, they would be subject to viscous drag mechanisms [*19*] and to a resultant increase in yield stress which may be partially counteracted by a heating effect from the propagating crack. These effects do not exclude a K_D dependence on higher time derivatives of crack length. On the contrary, it would seem improbable if higher derivatives did not exist.

From a practical viewpoint, Hahn et al [*15*] have shown that the computation of crack speeds is not strongly dependent on the shape of the K_D velocity curve chosen. The computation would thus be even less dependent on higher derivatives, so that practically these may be ignored and a single line placed through the data in Fig. 5. Such data from Specimens A and C, shown in Fig. 6, demonstrate a strong velocity dependence for K_D which increases with increasing velocity.

Crack Arrest

Specimens A and B with the compliant loading system were not conducive to stable crack arrest, only one example being recorded in each specimen type, whereas Specimens C always produced stable crack arrest. In Speci-

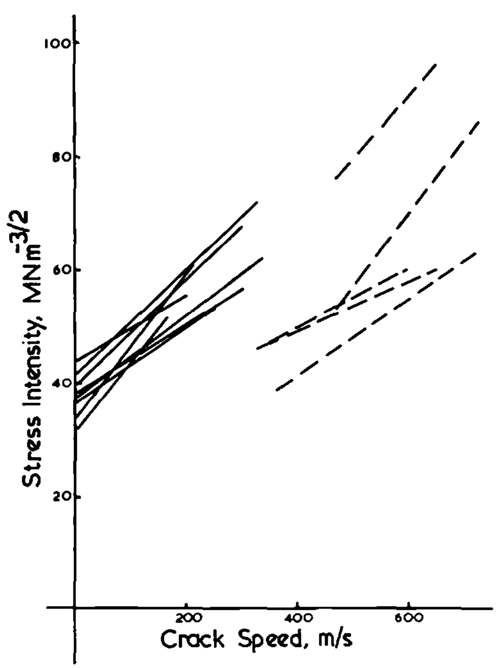

FIG. 6—*Dependence of* K_D *with crack speed for all specimens tested.*

mens A and B it was noted that, after arrest, the load recorded by the strain-gaged loading system oscillated, with the first peak similar to the arrest load. Such oscillations could have easily reinitiated the crack in the remaining specimens, particularly with the compliant loading system, where energy is continuously fed into the specimen and may thus enhance following oscillations. This effect would not be so pronounced with the fixed loading system, where the oscillation would damp down as noted by Kalthoff et al [3]. The observation that the kinetic energy was never zero at arrest is also consistent, since this would be dissipated as the stress intensity rings down to the static value $K_{Ia}{}^{+}$.

Crack velocities usually exhibited a minimum (Fig. 4) just before the crack left the centerplane in Specimen Types A and B, or final arrest in Specimens *C*.[3] It is suggested that the velocity minima corresponded to an intermediate arrest and that the change of crack plane in Specimens A and B is a consequence of reinitiation. The stress intensities at these points were determined and are given in Table 1. Since a reinitiation would depend more on specimen geometry and loading system than on material properties, these arrests could thus well have been stable had the loading system been suitable. Reinitiation and arrest cycles have been observed directly as a result of oscillating stress waves by Theocaris and Katsamanis [23].

These intermediate arrests, marked K_{Ia} in Table 1, are in the range 0.8 to 2.1 K_{Ic}. The arrest was stable in Specimen A23 and showed no significant difference from this trend. Static reinitiation was achieved in this specimen by reloading up to a stress intensity of 49.0 $MNm^{-3/2}$. This high value originated from the roughness of the arrested crack front. In general, the surface roughness of the arrested crack front would be expected to exceed that of a fatigue precrack used in the measurement of K_{Ic}. Without quantifying this roughness, the value of a comparison between K_{Ic} and K_{Ia} would appear to be decreased somewhat.

In the Series A specimens the value of K_{Ia} was higher than that of K_{Ic} (1.1 to 2.1, Table 1), while in the B specimens the K_{Ic} and K_{Ia} values were similar (0.82 to 0.98, Table 1). For the C-type specimens, two values of K_{Ia} are given. The first corresponded to a local crack velocity minimum and the second to the final stable arrest (Fig. 4*c*); the former values were generally slightly higher than the latter. It was also noted that the crack surface became progressively smoother following initiation, which may be sufficient to account for the different values. The data in Table 1 suggest therefore that values of K_{Ia} may depend on both the specimen geometry and the loading system.

Values of $K_{Ia}{}^{+}$, the static stress intensity that the crack tip would ring down to after arrest [3], are also given in Table 1. This ringing would also

[3]Specimen A23 exhibited a velocity minimum before final arrest while Specimen C1 did not.

dissipate any remaining kinetic energy. In a few cases, $K_{Ia}{}^{+}$ is slightly lower than K_{Ia} and the stress intensity would have to ring up to the static value. Physically this creates no problems, since if the stress intensity oscillates about the mean static value after arrest, it simply indicates that the oscillations start from the bottom of the cycle rather than from the top.

Conclusions

The crack initiation, propagation, and arrest cycle have been studied using three specimen geometries and two loading systems. A comparison of data obtained from the different systems led to the following conclusions.

1. If the loading system compliance is comparable to that of the specimen, then the crack will initially accelerate from a sharp starting notch, and stable crack arrest will be difficult. With a rigid loading system, initially the crack speed will be steady and arrest easy to obtain.

2. In general, the following relationship between static and dynamic strain energy release rate (G_S and G_D, respectively) and the rate of change of kinetic energy with crack length (dT/da) is incorrect: $G_S - G_D = dT/da$.

3. The dynamic stress intensity K_D was found to be strongly dependent on the crack speed v, and possibly on higher time derivates as well. For practical purposes, however, higher derivatives may be ignored.

4. Kinetic energy can be absorbed by a moving crack to aid further propagation. However, a fraction remains at arrest, to be dissipated as the arrest stress intensity rings down to its static value. The stress intensity at arrest is probably dependent on both specimen geometry and loading system.

Acknowledgments

The author is grateful to the Battelle Columbus Laboratories for supplying copies of their computer programs, which were the basis for the one used here. This work was carried out at the Central Electricity Research Laboratories and is published by permission of the C.E.G.B.

References

[1] Hoagland, R. G., Rosenfield, A. R., and Hahn, G. T., *Metallurgical Transactions*, Vol. 3, 1972, pp. 123-236.
[2] Kobayashi, A. S., Emery, A. F., and Mall, S., *Experimental Mechanics*, Vol. 16, No. 9, 1976, pp. 321-328.
[3] Kalthoff, J. F., Beinert, J., and Winkler, S. in *Fast Fracture and Crack Arrest, ASTM STP 627*, American Society for Testing Materials, 1977, pp. 161-176.
[4] Hahn, G. T., Gehlen, P. C., Hoagland, R. G., Kanninen, M. F., Popelar, C., and Rosenfield, A. R., "Critical Experiments, Measurements and Analyses to Establish a Crack Arrest Methodology for Nuclear Pressure Vessel Steels," Second Quarterly

Progress Report, Task Agreement 62, BMI-1934, Battelle Columbus Laboratories, Columbus, Ohio, May 1975.

[5] Crosley, P. B. and Ripling, E. J. in *Fast Fracture and Crack Arrest, ASTM STP 627,* American Society for Testing and Materials, 1977, pp. 203-227.

[6] Gates, R. S. in *Proceedings,* Symposium on Dynamic Fracture Toughness, The Welding Institute, Abingdon, Cambridge, England, 1976, p. 293.

[7] Kanninen, M. F., *International Journal of Fracture,* Vol. 9, No. 1, 1973, pp. 83-92.

[8] Gates, R. S., *International Journal of Fracture,* Vol. 13, 1977, pp. 710-713.

[9] Gates, R. S. in *Proceedings,* Symposium on Numerical Methods in Fracture Mechanics, University College, Swansea, U.K., 9-13 Jan. 1978, pp. 834-836.

[10] Kanninen, M. F., *International Journal of Fracture,* Vol. 10, No. 3, 1974, pp. 415-430.

[11] Shmuely, M. and Peretz, D., *International Journal of Solids and Structures,* Vol. 12, 1976, pp. 67-78.

[12] Freund, L. B., *Journal of the Mechanics and Physics of Solids,* Vol. 20, No. 3, 1972, pp. 141-52.

[13] Kanninen, M. F., Popelar, C., and Gehlen, P. C. in *Fast Fracture and Crack Arrest, ASTM STP 627,* American Society for Testing and Materials, 1977, pp. 19-38.

[14] Hoagland, R. G., Rosenfield, A. R., Gehlen, P. C., and Hahn, G. T. in *Fast Fracture and Crack Arrest, ASTM STP 627,* American Society for Testing and Materials, 1977, pp. 177-202.

[15] Hahn, G. T., Gehlen, P. C., Hoagland, R. G., Kanninen, M. F., Popelar, C., Rosenfield, A. R., and de Campos, V. S., "Critical Experiments. Measurements and Analyses to Establish a Crack Arrest Methodology for Nuclear Pressure Vessel Steels," First Annual Progress Report, Task 62, BMI-1937, Battelle Columbus Laboratories, Columbus Laboratories, Columbus, Ohio, Aug. 1975.

[16] Kobayashi, T. and Dally, J. W. in *Fast Fracture and Crack Arrest, ASTM STP 627,* American Society for Testing and Materials, 1977, pp. 257-273.

[17] Yoffe, E. H., *Philosophical Magazine,* Vol. 42, 1961, pp. 739-750.

[18] Baker, B. R., *Journal of Applied Mechanics,* Vol. 29, 1962, pp. 449-458.

[19] Lothe, J., *Journal of Applied Physics,* Vol. 33, 1962, pp. 2116-2125.

[20] Campbell, J. D. and Harding, J., *Response of Metals to High Velocity Deformation,* Interscience Publishers, New York, 1961, p. 51.

[21] Döll, W., *Engineering Fracture Mechanics,* Vol. 5, 1973, pp. 259-268.

[22] Döll, W., *International Journal of Fracture,* Vol. 12, 1976, pp. 595-605.

[23] Theocaris, P. S. and Katsamanis, F., *Engineering Fracture Mechanics,* Vol. 10, 1978, pp. 197-210.

J. W. Dally,[1] *A. Shukla,*[2] *and Takao Kobayashi*[2]

A Dynamic Photoelastic Study of Crack Propagation in a Ring Specimen

REFERENCE: Dally, J. W., Shukla, A., and Kobayashi, Takao, "**A Dynamic Photoelastic Study of Crack Propagation in a Ring Specimen,**" *Crack Arrest Methodology and Applications, ASTM STP 711,* G. T. Hahn and M. F. Kanninen, Eds., American Society for Testing and Materials, 1980, pp. 161-177.

ABSTRACT: Crack propagation in a thick-walled ring specimen subjected to a mechanically simulated thermal stress was investigated by employing dynamic photoelasticity. Ring models fabricated from Homalite 100 were loaded with a specially designed mechanical deformeter which separated and rotated a slit cut into the ring to produce a combination of tension and bending that simulated a steady-state thermal stress.

Short starter cracks were machined into a series of ring models and the deformeter adjusted to give K_Q/K_{Im} ranging from 1.2 to 3.0. The crack was initiated and high-speed photographs of the isochromatic fringe loops at the tip of the running crack were recorded. The data were analyzed to obtain the instantaneous stress-intensity factor K, the normalized crack position a/w, and the crack velocity $\dot{a}$.

The relation between K and $\dot{a}$ was established for Homalite 100 using the ring specimen. It was noted that this K-$\dot{a}$ relation compared well with those determined previously using single edge notch, rectangular double cantilever beam, contoured double cantilever beam, and modified compact tension specimens.

A comparison of K, as a function of position a/w, was made between static and dynamic crack growth. A marked difference was noted. For static crack growth, K increases with a/w until $a/w = 0.2$ and then decreases with further crack extension. For dynamic crack growth, K decreased monotonically with increasing a/w.

KEY WORDS: dynamic photoelasticity, fracture, thermal stresses, mechanical deformeter, ring specimen, high-speed camera, stress-intensity factor, dynamic crack propagation

This investigation examines the behavior of a crack propagating in a ring specimen subjected to a mechanically simulated thermal stress field. Particular emphasis was placed on the arrest behavior of the crack as it propa-

[1] Dean, College of Engineering, University of Rhode Island, Kingston, R.I. 02881.

[2] Research assistant and associate professor, respectively, Photomechanics Laboratory, Mechanical Engineering Department, University of Maryland, College Park, Md. 20742.

gated from the tension into the compression region of this self-equilibrated stress field.

The study is motivated by the possibility of crack initiation and propagation in pressure vessels due to thermal stresses produced by a loss-of-coolant accident (LOCA). Previous work at Oak Ridge National Laboratory (ORNL) by Cheverton et al [*1*][2] has shown the applicability of linear elastic fracture mechanics in predicting crack initiation in cylindrical pressure vessels subjected to thermal stress fields. The behavior of the crack after initiation has not been explored, however, and questions arise regarding the arrest of the crack as it propagates from the high tensile stress region near the inside wall of the pressure vessel into the compressive region in the central region of the wall.

Some insight can be gained regarding crack propagation into self-equilibrated thermal stress fields by performing a dynamic photoelastic analysis. Photoelasticity provides whole field data during the propagation period which contain the instantaneous stress-intensity factor, the crack-tip position, and the change in the state of the stress across the section due to crack movement.

The model selected for the study was a ring with an inside radius r_i = 101.6 mm and an outside radius r_o = 228.6 mm (r_o/r_i = 2.25). The thermal stresses were mechanically simulated by using a mechanical deformeter following a procedure introduced by Durelli and Barriage [*2*]. Dynamic isochromatic fringe patterns were recorded with a Cranz-Schardin high-speed camera. The results obtained show energy lost during propagation, the arrest of the crack, oscillations of the stress-intensity factor after arrest, and reinitiation of the crack. The numerical results obtained should provide a data base for verifying computer codes which are currently being developed to treat problems of crack propagation in a stress field composed of tensile and compressive zones similar to those found in thermally stressed cylinders.

Experimental Procedure

Mechanical Simulation of a Thermal Stress Field

In 1935, Biot [*3*] considered the thermal stresses produced in a multiply connected cylinder due to steady-state heat flow. Biot used the Cauchy-Riemann equations to show that the thermal strain ϵ was related to the rotation ω by

$$\omega = \int \left(\frac{\partial \epsilon}{\partial y}\, dx + \frac{\partial \epsilon}{\partial x}\, dy\right) \tag{1}$$

[2]The italic numbers in brackets refer to the list of references appended to this paper.

For a state of plane strain, the thermal strain in the direction of heat flow is given by

$$\epsilon = (1 + \nu)\,\alpha\,\Delta T \tag{2}$$

where

ν = Poisson's ratio,
α = coefficient of thermal expansion, and
ΔT = temperature difference.

Since both $\partial\epsilon/\partial x$ and $\partial\epsilon/\partial y$ are proportional to the temperature gradient, the rotation ω is linearly related to the heat transmitted across the section.

If the multiply connected cylinder is cut between the inner and outer boundaries, the body becomes simply connected and the thermal stresses are relieved. The displacements u and v at the free edge of the cut are

$$u + iv = \int (\epsilon + i\omega)\,(dx + idy) \tag{3}$$

The integral in Eq 3 is evaluated to give the values of displacements u and v which correspond to a prescribed steady-state temperature distribution.

If the radial cut is machined into the photoelastic model and the displacements u and v are imposed on the model with a mechanical deformeter, then the stress field introduced in the model simulates the thermal stresses due to steady-state temperature gradients. This procedure, known as Biot's analogy, has been used in the present investigation to produce simulated thermal stresses in photoelastic models of thick-walled pressure vessels.

Mechanical Deformeter

The mechanical deformeter consists of two pairs of aluminum plates which are attached to a segment of a ring specimen as shown in Fig. 1. The opening between the plates represents the radial cut in Biot's analogy. The displacements u and v which are imposed on the model are controlled by two pairs of pins which extend through the aluminum plates. Each pair of pins is connected to a set of adjusting screws. The screws are rotated to open the radial cut and impose the displacements corresponding to a simulated thermal stress field on the photoelastic model.

The deformeter was massive and rigid compared with the relatively flexible photoelastic model. The aluminum plates were large and 13 mm (0.51 in.) thick and the screws were 6.35 mm (0.25 in.) in diameter with 20 threads per 25.4 mm (1 in.). The ring specimen defined in Fig. 2 was fabricated from Homalite 100 with a thickness of 12.7 mm (0.5 in.).

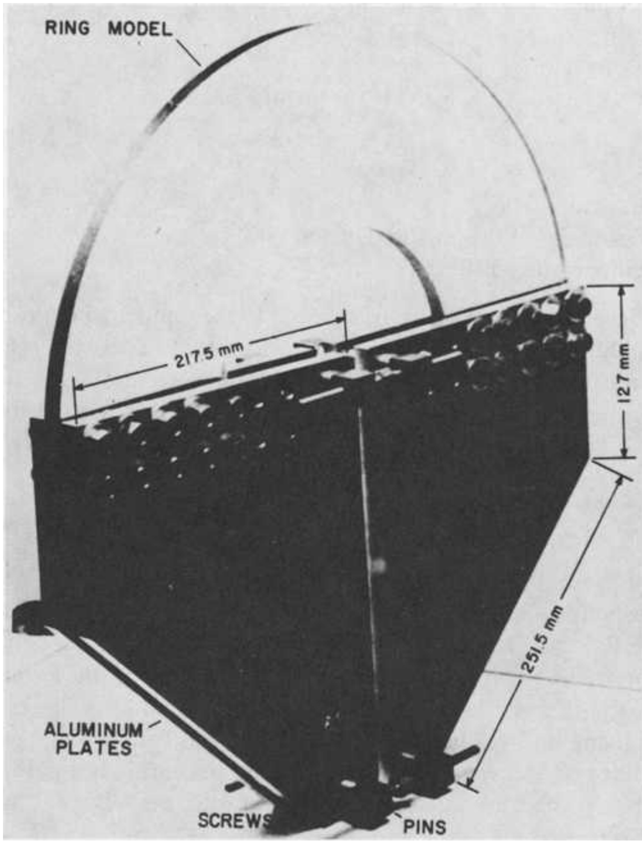

FIG. 1—*Loading fixture attached to the ring specimen.*

Calibration of the Loading System

The loading system and the model were calibrated to obtain a relation between the stress-intensity factor K_Q associated with the blunt crack tip and the pin displacement. The loading system was also evaluated by using a ring specimen without a crack.

In the evaluation of the ring specimen without the crack, the screws on the deformeter were adjusted to place the neutral axis at the position y/w = 0.38. The slit opening was then increased to produce an increase in the magnitude of the stresses while maintaining the same position of the neutral axis. It was noted that the ratio of the outer and inner pin displacements d_o/d_i and the ratio of the fringe orders N_o/N_i at the outer and inner boundaries were constant ($d_o/d_i = 2.5$, $N_o/N_i = 0.53$ for $y/w = 0.38$) as the slit opening was varied. It was also observed that the central region of the ring specimen was not affected by the clamping action of the grips. Based on

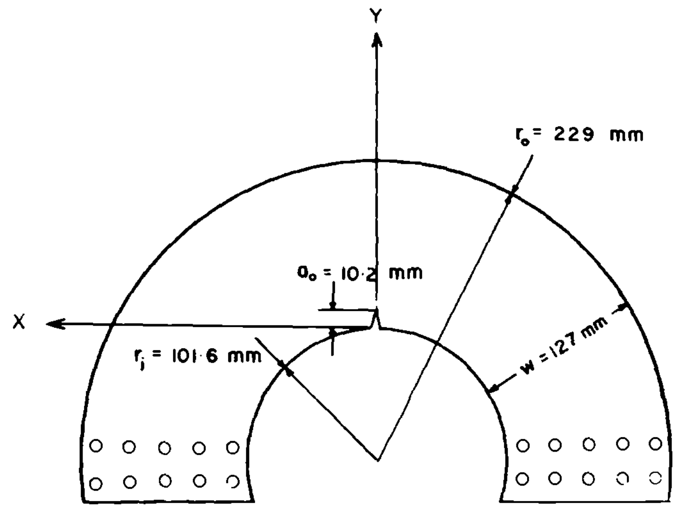

FIG. 2—*Dimensions of the ring specimen and definition of the coordinate system.*

these findings the deformeter was considered adequate to simulate steady-state thermal stresses in the ring specimens.

A short crack of $a_o/w = 0.08$ was then saw-cut into the specimen and its effect on the stress distribution studied. Fringe patterns showing the stress distribution across the ring specimen before and after introduction of the crack are shown in Fig. 3. Comparison of the two patterns indicates that the crack relieves the stresses on the inner boundary and shifts the neutral axis towards the outer boundary. The stresses on the outer boundary are not affected to a significant degree if a_o/w is sufficiently small.

A calibration curve for the specimen deformeter combination giving the value of stress-intensity factor K_Q associated with the blunt crack tip was then established. The fringe loops at the crack tip were evaluated to give K by using the simplified three-parameter method due to Etheridge [*4*]

$$K = K_n \frac{Nf_\sigma}{h} \sqrt{2\pi r_m} \tag{4}$$

where

K_n = f_n of θ_m defined in Ref *4*,
N = fringe order,
f_σ = material fringe value,
h = thickness of model, and
r_m = maximum radius of loop measured from crack tip.

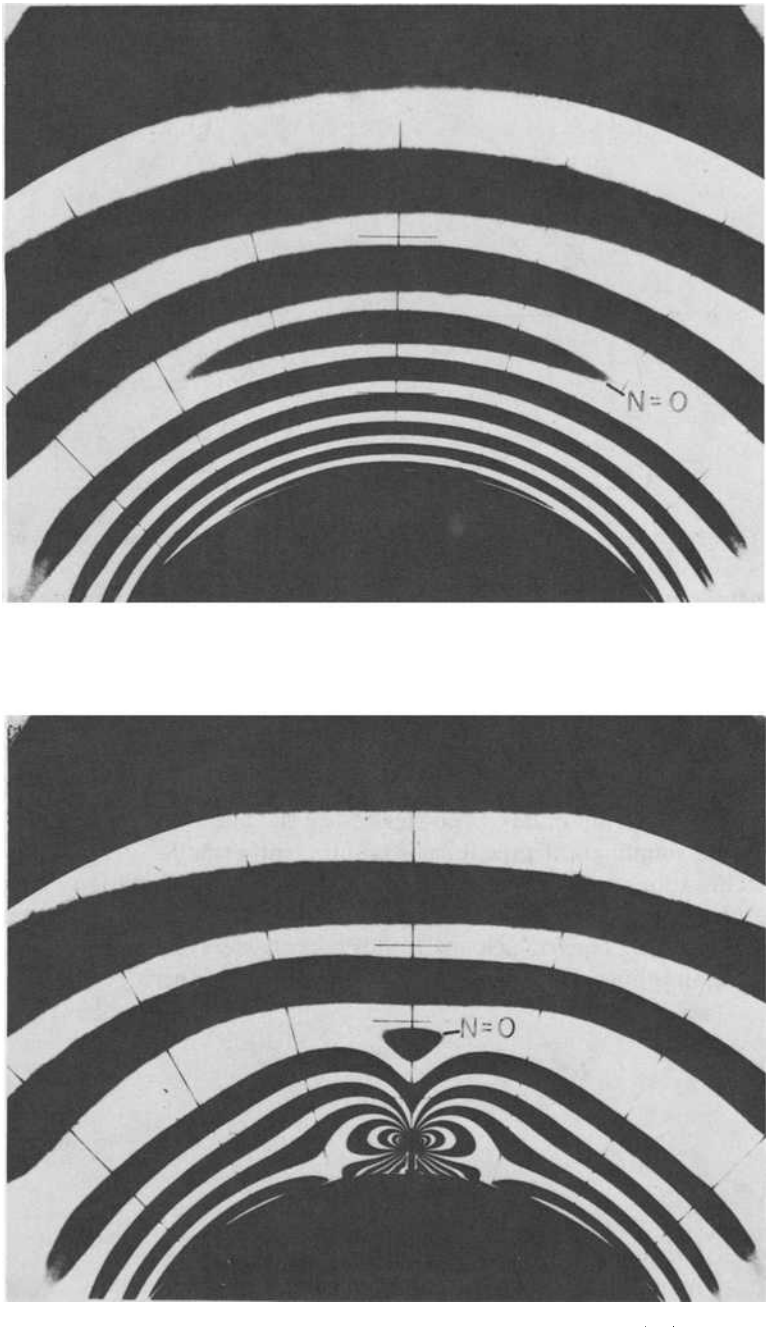

FIG. 3—*Fringe pattern with and without the starter crack.*

The inner and outer pin displacements d_i and d_o were increased in steps while maintaining a constant d_o/d_i, and K was determined for each displacement set. It was found that the value of K increased linearly with the pin displacement as shown in Fig. 4. This curve was used later in estimating the value of K_Q associated with the blunt crack tip in the dynamic experiments.

Determination of the Static K *as a Function of Crack Length*

The influence of the crack length on the stress-intensity factor K was determined. Static experiments were conducted where the crack length was increased in increments and K was measured for the blunt crack from isochromatic fringe loops. As the crack was extended, the pin displacements were held fixed by using spacers between the pins. The determination of K-a was made with four different sets of pin displacement and the results obtained are shown in Fig. 5. It was observed that K increases with a until $a/w = 0.2$. For $a/w > 0.2$, K decreases monotonically, tending to zero as the crack tip approaches the outer boundary.

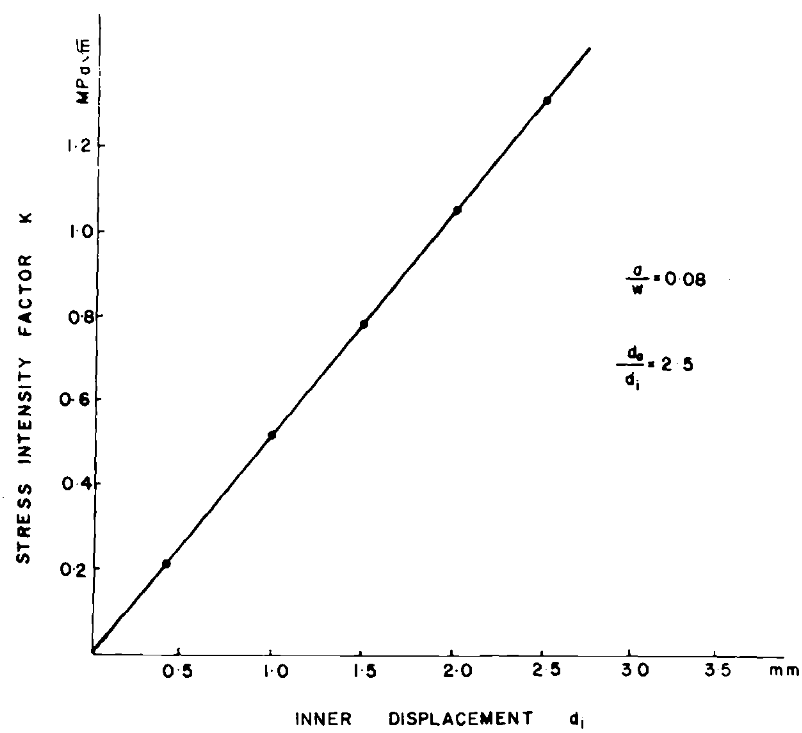

FIG. 4—*Stress-intensity factor* K *as a function of inner pin displacement* d_i (*third shipment of Homalite 100*).

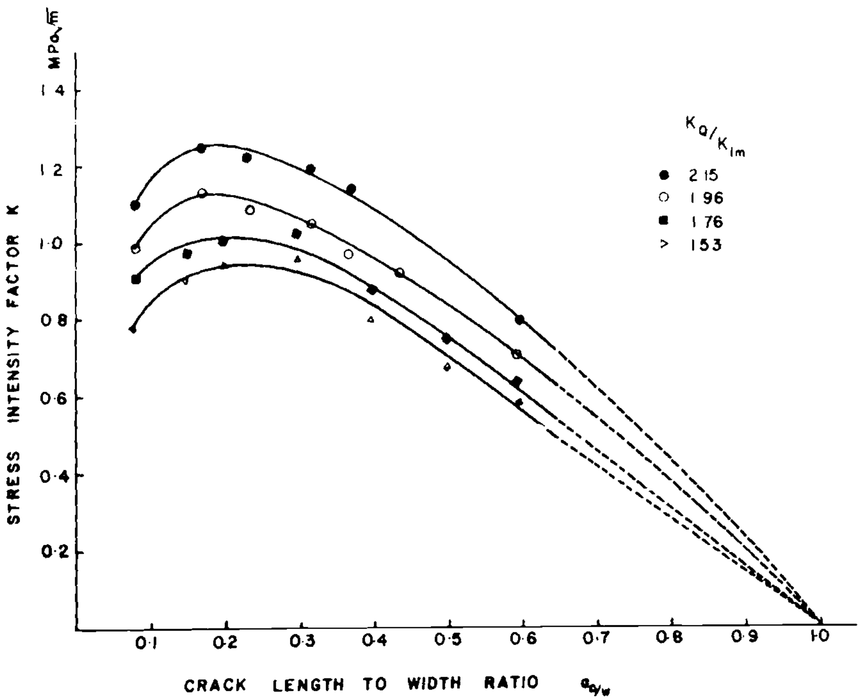

FIG. 5—*Stress-intensity factor* K *as a function of starter crack length-to-width ratio* a_0/w.

Dynamic Crack Propagation in Monolithic Ring Specimens

Ring specimens were used to study crack propagation in a two-dimensional, self-equilibrated, thermal stress field. A precut crack in a ring specimen was initiated and the stress-intensity factor K was determined as a function of time and crack length. A relation between the crack jump distance and the stress-intensity ratio K_Q/K_{Im} was established. Finally, a curve showing the stress-intensity factor K and crack velocity $\dot{a}$ was determined from data taken from the ring specimen.

The ring-type fracture specimens were loaded to a specified value of K_Q by applying a predetermined displacement to the pins of the mechanical deformeter. The pin displacement was converted to K_Q by using the calibration procedure described previously. The ratio K_Q/K_{Im} was varied between 1.2 and 3.0 in the series of experiments to cover the range of crack behavior of interest.

The starter crack was saw-cut into the specimen and the crack tip rounded to inhibit premature initiation at high values of K_Q. The crack was then initiated by drawing a sharp blade across the tip. As the crack propagated, it interrupted a silver conductive paint line on the model and triggered the multiple-spark Cranz-Schardin camera. High-speed records of the dynamic isochromatic fringe patterns showing the crack propagation in the ring specimen are shown in Fig. 6. A cursory inspection of the size of the fringe loops at the crack tip shows that K decreases monotonically throughout the propagation interval until the crack is arrested in the compression zone.

Analysis and Results of Dynamic Photoelastic Experiments

Five dynamic photoelastic experiments, identified here as R-1 through R-5, were performed with monolithic ring specimens. The isochromatic fringe loops associated with the crack tip were analyzed using a simplified version of Etheridge's three-parameter method. A dynamic correction due to Irwin and Rossmanith [5] was made in the determination to account for the effect of the crack velocity on K.

A high value of K_Q was used in Experiment R-1 to provide data for high-velocity crack propagation and complete fracture of the ring specimen. The other four experiments were performed with lower values of K_Q and crack arrest was obtained in each case.

High-Velocity Crack Propagation

A high value of $K_Q/K_{1m} = 3.12$ used in R-1 caused the crack to propagate completely through the model without arrest. The results indicate that the crack initially propagated at a constant $\dot{a} = 356$ m/s for a distance of 61.5 mm (2.42 in.) and then $\dot{a}$ decreased monotonically. As the crack tip approached the outer boundary, $\dot{a}$ had decreased to 77 m/s.

The isochromatic fringe patterns from Model R-1 were analyzed to obtain the values of K. The results shown in Fig. 7 indicate that K decreases monotonically from 0.935 to 0.365 MPa$\sqrt{m}$ in a period of 378 μs. The decrease in K is quite rapid for the first 200 μs; then K decreases more slowly and approaches K_{1m}.

These photoelastic results provided data for a relatively complete K-versus-$\dot{a}$ relation presented in Fig. 8. It is noted that the crack achieves a maximum velocity of 356 m/s and the arrest toughness of Homalite 100 is 0.36 MPa$\sqrt{m}$. These results compare well with the K-versus-$\dot{a}$ relations obtained for rectangular double cantilever beam (R-DCB), contoured double cantilever beam (C-DCB), and single edge notch (SEN) specimens fabricated from the same shipment of Homalite 100 [*6*].

Crack Arrest

In Experiments R-2 to R-5, the value of K_Q/K_{1m} was varied between 1.29 and 1.54 (where $K_{1m} = 0.52$ MPa$\sqrt{m}$). The photoelastic results obtained showed the behavior of the crack as its velocity decreased and the crack arrested.

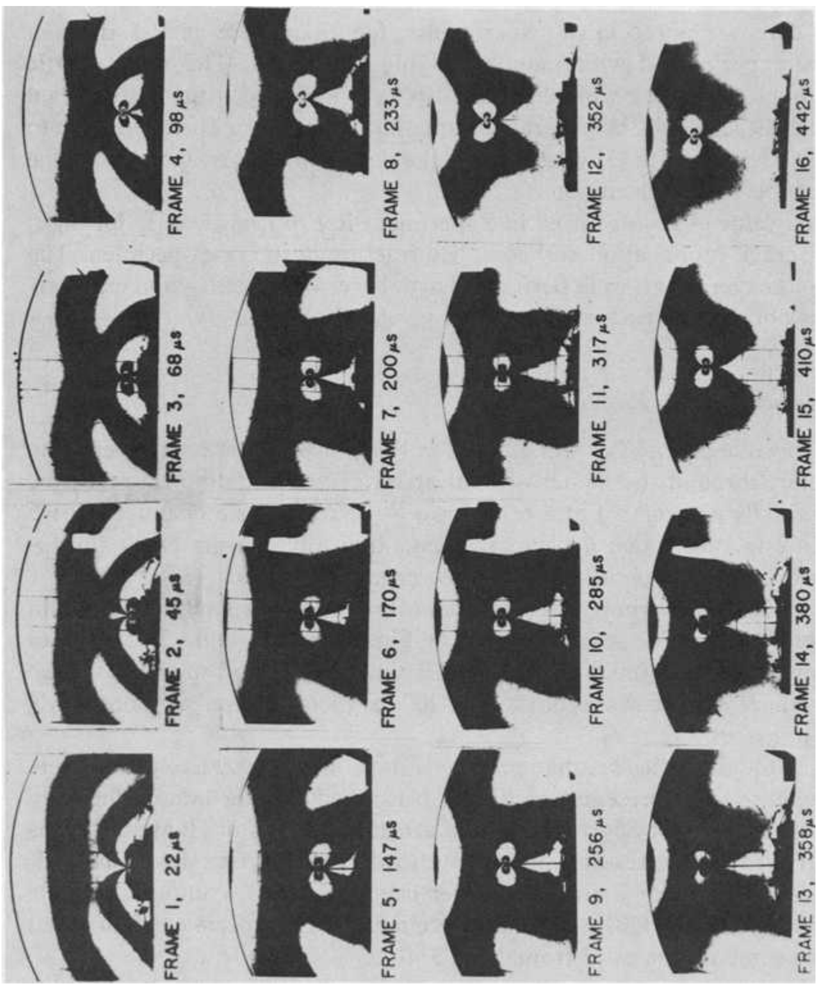

FIG. 6—*Typical dynamic isochromatic fringe patterns as the crack propagates in the ring specimen.*

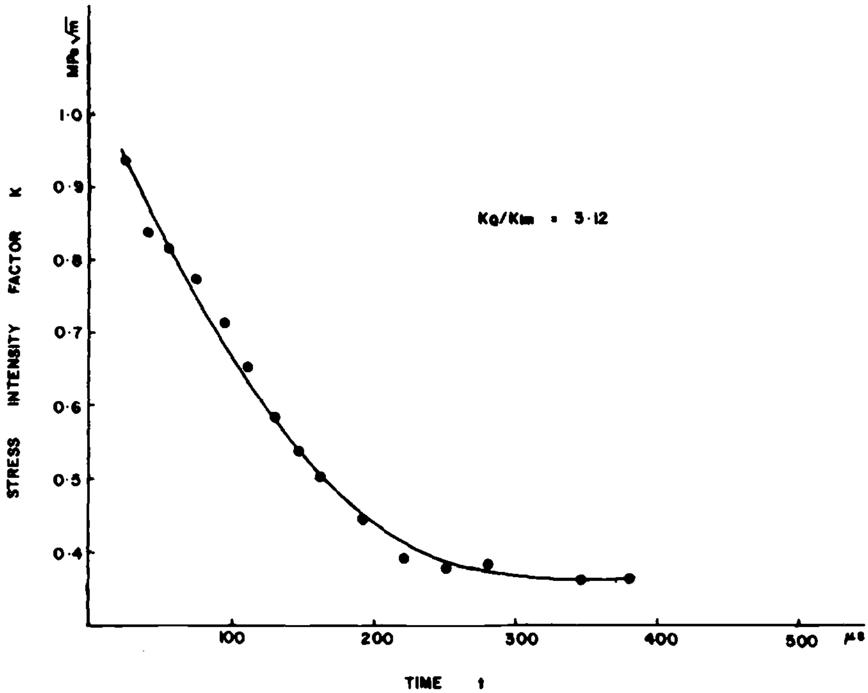

FIG. 7—*Stress-intensity factor* K *as a function of time* t *for Model R-1 with* $K_Q/K_{Im} = 3.12$.

In Experiment R-2, where $K_Q/K_{Im} = 1.29$, the crack propagated at a constant velocity of 169 m/s for the first 200 μs. Due to misfiring of the camera, data were not available for the last 200 μs. However, the crack arrested at $a/w = 0.57$.

In Experiment R-3 where $K_Q/K_{Im} = 1.36$, the crack velocity decreased from 179 to 12 m/s in 435 μs, prior to arrest. The crack first arrested at $a/w = 0.60$, then reinitiated twice before finally arresting at $a/w = 0.84$.

A higher value of K_Q ($K_Q/K_{Im} = 1.54$) was used in Experiment R-4. Immediately after initiation, the crack propagated at a velocity of 231 m/s then progressively decreased to 75 m/s in 440 μs. The crack was first arrested at $a/w = 0.73$, and final arrest occurred at $a/w = 0.95$.

In the final experiment, R-5, $K_Q/K_{Im} = 1.48$ was used and photographs of the arrest were obtained. The crack velocity decreased from 170 to 10 m/s prior to arrest, in 340 μs. Initial crack arrest occurred at $a/w = 0.70$ and final arrest at $a/w = 0.86$.

The fracture surfaces as illustrated in Fig. 9 showed striations the shape of a thumbnail, indicating the positions of crack arrest.

The distance from the inner boundary to the location of the striation was measured for each specimen to give the crack jump distance as a function of

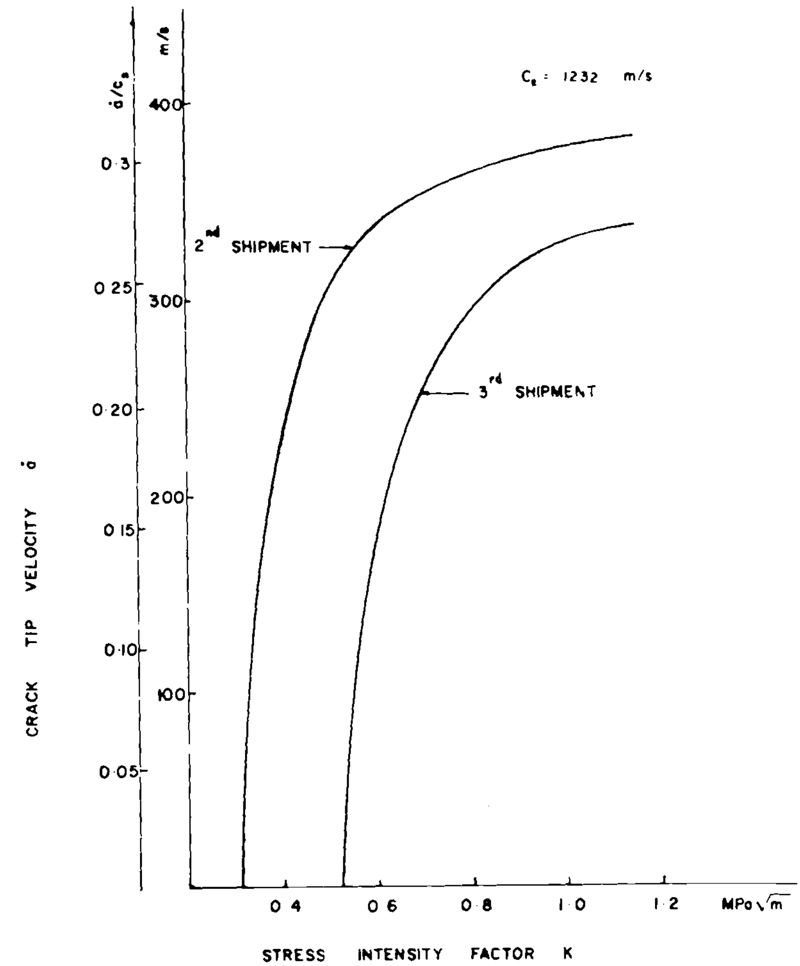

FIG. 8—*Stress-intensity factor as a function of crack velocity—Homalite 100—second and thrid shipments.*

K_Q/K_{Im}. The results shown in Fig. 10 indicate that it becomes increasingly difficult to drive the crack into the ring as a/w becomes large.

The photoelastic data from these experiments were analyzed to obtain the values of K, a, and $\dot{a}$ as a function of time. The results obtained are shown in Figs. 11 and 12. Inspection of Fig. 11 indicates that K decreased monotonically until the crack arrested. After the arrest, K increased as the available kinetic energy was converted to strain energy. When K increased to K_{Id} the crack reinitiated. The curve for Model R-5, in Fig. 11, shows the increase in K after arrest; however, the experiment was terminated prior to reinitiation.

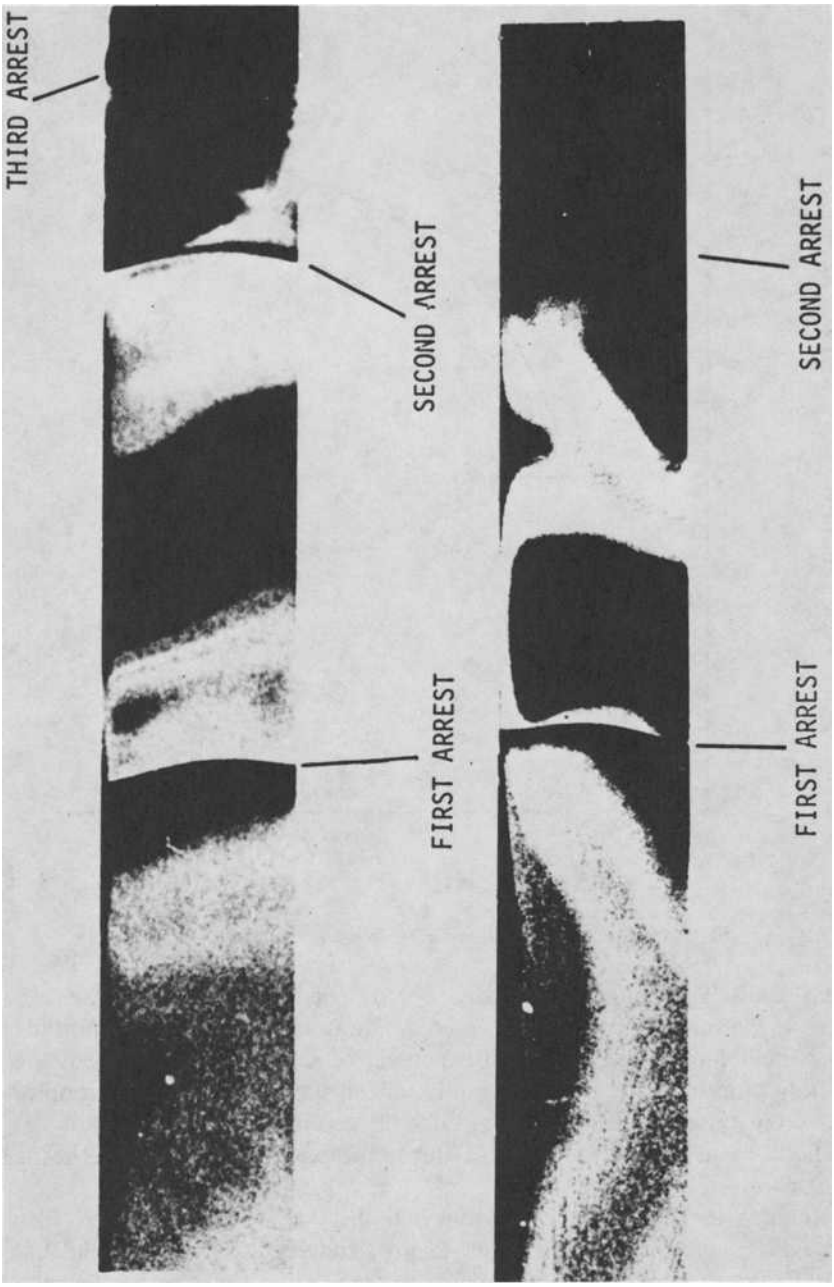

FIG. 9—*Fracture surfaces showing the markings due to crack arrest.*

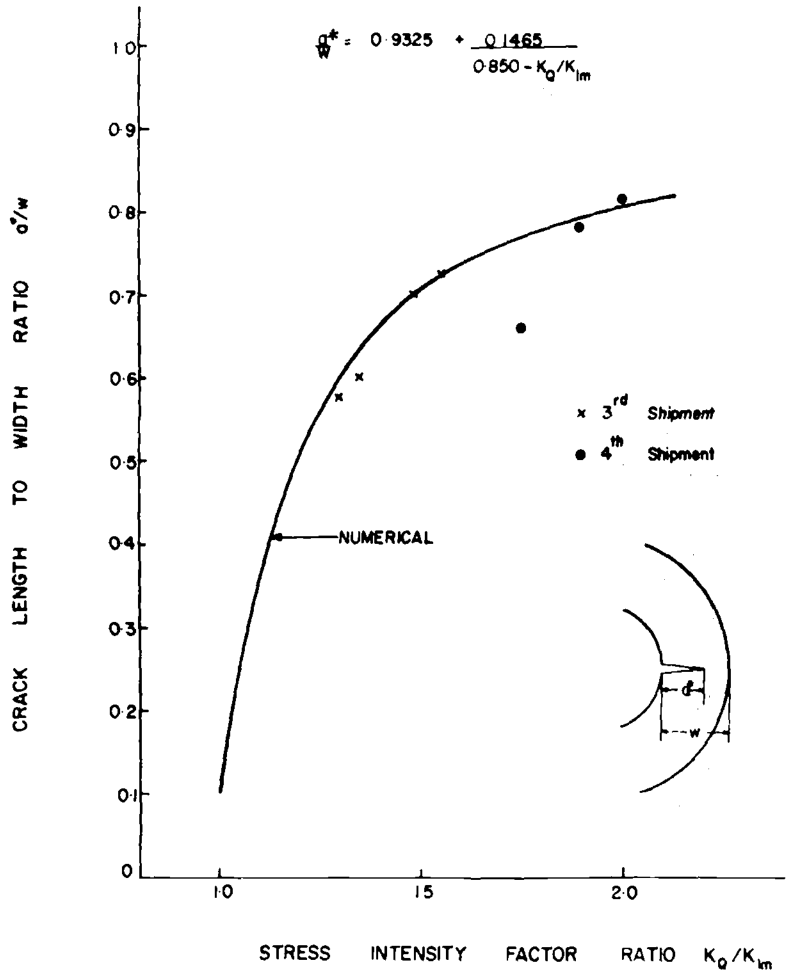

FIG. 10—*Crack jump distance* a^*/w *as a function of* K_Q/K_{Im}.

The results show that K increased about 16 percent after the crack arrested. If the variations in K are treated as vibratory behavior, the amplitude of the oscillations would be about 8 percent of K_{Im}. These oscillations are probably produced due to the dynamics of the specimen and interaction of the loading system. The exact magnitude of the amplitude of the oscillation is difficult to measure because the scatter in the experimental results is of the same order.

Reference to the K-a/w data shown in Fig. 12 indicates that K also decreases monotonically with crack length. Indeed, it is remarkable that results from all four experiments coincide, indicating that the K-a/w relationship appears to be nearly independent of K_Q/K_{Im}.

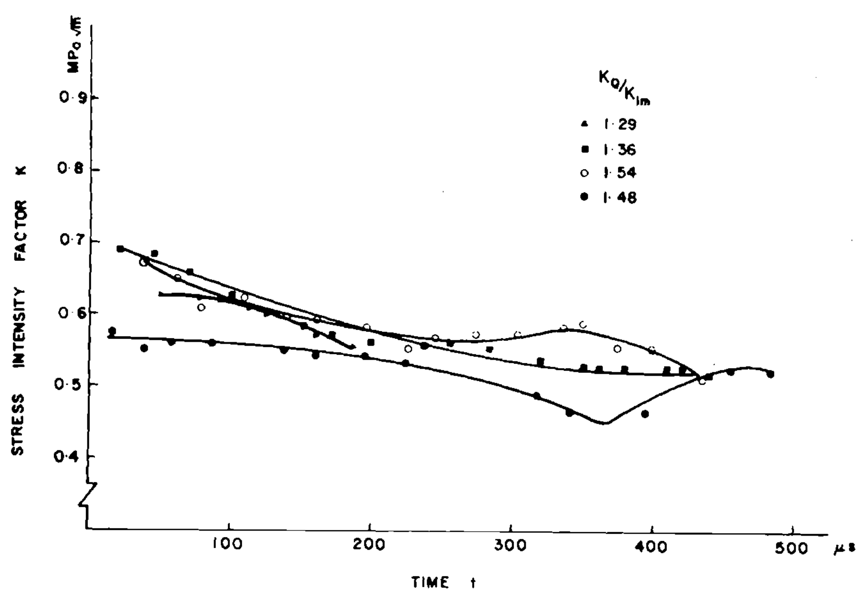

FIG. 11—*Stress-intensity factor* K *as a function of time t for models R-2 through R-5.*

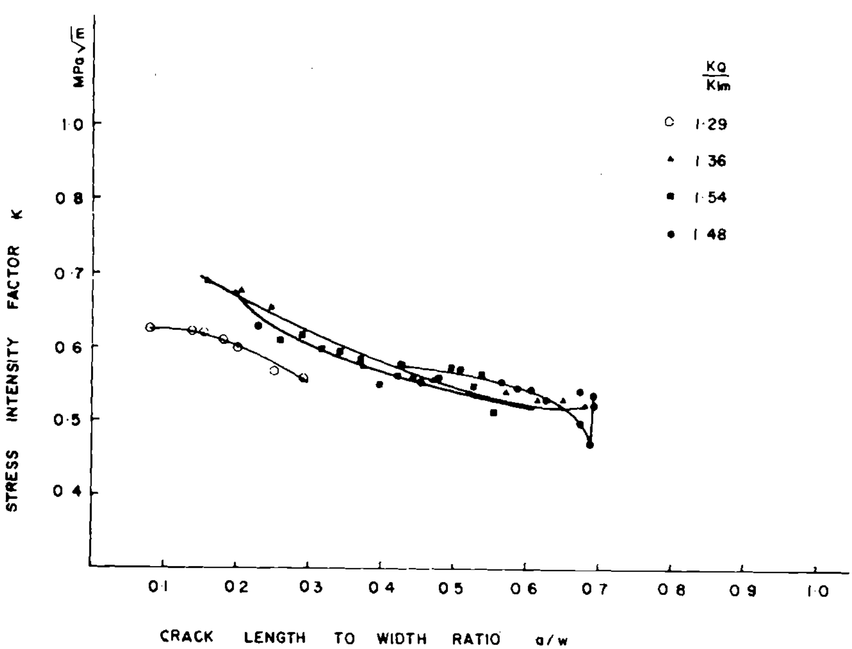

FIG. 12—*Stress-intensity factor* K *as a function of crack length* a *for models R-2 through R-5.*

A comparison of the K-a/w relation for statically extended cracks and dynamically running cracks is shown in Fig. 13. It is evident from this comparison that considerable difference exists between the stress-intensity factor associated with a statically positioned crack and a crack which achieves the same position by dynamic propagation.

Finally, the data permitted a relation between the crack velocity $\dot{a}$ and stress-intensity factor K to be established (see Fig. 8). The results (for the third shipment of Homalite 100) showed a terminal velocity of $\dot{a}_T/c_2 = 0.264$ and $K_{\mathrm{Im}} = 0.52$ MPa$\sqrt{\mathrm{m}}$. The comparison of the K-versus-$\dot{a}$ relations presented in Fig. 8 indicates a higher value of K_{Im} and a lower value of $\dot{a}_T$ for the third shipment of Homalite 100 than for the second shipment of Homalite 100.

Conclusion and Discussion

A dynamic photoelastic study of crack propagation in ring specimens subjected to mechanically simulated thermal stresses showed that the instantaneous stress-intensity factor decreased monotonically with both crack extension and time until crack arrests. This behavior was quite different from that of the static crack extension, where K increased with increasing crack length until $a/w = 0.2$, and then decreased monotonically toward zero for

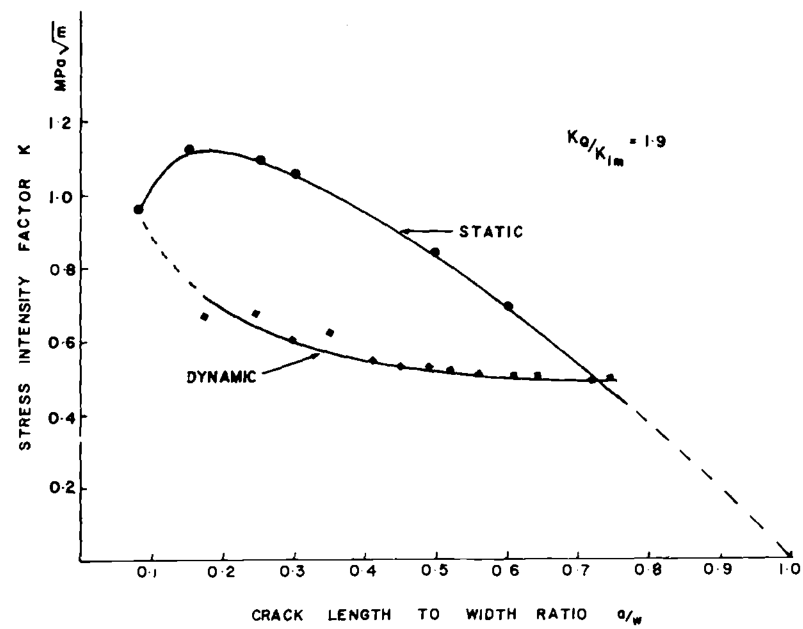

FIG. 13—*Static and dynamic stress-intensity factor as a function of* a/w *for the same pin displacement.*

$a/w > 0.2$. This significant difference gives a clear indication that static stress analyses will not be applicable in determining K associated with a crack which is propagating in a dynamic stress field.

Oscillations in K during the propagation phase were not observed in the ring specimen. Oscillations did occur after crack arrest with a peak-to-peak amplitude of about 16 percent.

The K-$\dot{a}$ relation was determined from the ring specimen for two different shipments of Homalite 100. The results obtained for $K_{\text{Im}} = 0.37$ MPa$\sqrt{\text{m}}$ and $\dot{a}_T/c_2 = 0.29$ compared favorably with results obtained from R-DCB, C-DCB, modified compact tension, and SEN specimens fabricated from the same shipment (second) of Homalite 100. Results from the third shipment of Homalite 100 with the ring specimen gave $K_{\text{Im}} = 0.52$ MPa$\sqrt{\text{m}}$ and $\dot{a}_T/c_2 = 0.26$. Thus, it is evident that the fracture characteristics of Homalite 100 depend upon the manufacturing process.

The crack jump distance from initiation to the first arrest is a function of K_Q/K_{Im} which can be approximated by

$$\frac{a}{w} = 0.9325 + \frac{0.1465}{0.85 - K_Q/K_{\text{Im}}}$$

for $1 < K_Q/K_{\text{Im}} \leq 2$. It appears that $K_Q/K_{\text{Im}} \simeq 3$ will be required to completely drive the crack across the ring if the initial crack length is $a/w = 0.08$.

Acknowledgments

The authors wish to thank the Nuclear Regulatory Commission for its support under Grant No. AT(49-24)-0172. They would also like to thank Dr. George R. Irwin for his keen advice throughout this study.

References

[1] Cheverton, R. D., "Pressure Vessel Fracture Studies Pertaining to a PWR LOCA-ECC Thermal Shock, Experiments TSE1 and TSE2," Oak Ridge National Laboratory, Oak Ridge, Tenn., September 1976.

[2] Barriage, J. B. and Durelli, A. J. in *Proceedings*, Society for Experimental Stress Analysis, Iowa State Press, Ames, Iowa, Vol. 13, No. 2, 1956, pp. 97-106.

[3] Biot, M. A., *Philisophical Magazine*, Vol. 19, Series 7, 1935.

[4] Etheridge, J. M., "Determination of the Stress Intensity Factor from Isochromatic Fringe Loops," Ph.D. Dissertation, University of Maryland, College Park, Md., 1976 (J. W. Dally, Thesis Advisor).

[5] Rossmanith, H. P. and Irwin, G., "The Dynamic Correction for the K Determination," Interim Report to the Nuclear Regulatory Commission, March 1978.

[6] Kobayashi, T. and Dally, J. W. in *Fast Fracture and Crack Arrest, ASTM STP 672*, G. T. Hahn and M. F. Kanninen, Eds., American Society for Testing and Materials, 1977, pp. 257-273.

S. J. Burns[1]

Fast Fracture: An Adiabatic Restriction on Thermally Activated Crack Propagation

REFERENCE: Burns, S. J., "**Fast Fracture: An Adiabatic Restriction on Thermally Activated Crack Propagation,**" *Crack Arrest Methodology and Applications, ASTM STP 711*, G. T. Hahn and M. F. Kanninen, Eds., American Society for Testing and Materials, 1980, pp. 178–185.

ABSTRACT: Slow, isothermal crack propagation is widely suspected to be rate-controlled by thermally activated plastic deformation in the crack-tip region. Adiabatic conditions are generally established in the fracture-modified material at the tip of a crack during fast fracture. The temperature of this material is not the temperature of the specimen and is generally not measured during fast fracture. Thus, a complete thermodynamic description of adiabatic crack propagation data cannot be made. When the slow, isothermal crack propagation mechanisms are assumed to be operative during adiabatic crack propagation, then certain predictions can be made. For example: the changes in $\mathcal{G}$ due to temperature and rate are always in the opposite sense; there is no minimum in $\mathcal{G}$ versus crack velocity without a change in mechanism; the temperature rise in the crack-tip fracture-modified material is determined mainly by the activation enthalpy for crack propagation; the interpretation of fast fracture structural steel data from simple plastic models is suspect since these materials have dissimilar isothermal temperature dependencies.

KEY WORDS: fast fracture, adiabatic fracture, dynamic fracture, fracture thermodynamics

There have been many observations of the dependence of the crack velocity on the strain energy release rate (or the equivalent stress-intensity factor) and the test temperature. Very slow, stable, isothermal crack propagation has been reproducably measured and reported [*1*-*5*][2]; more recently, attention has been focused on fast fracture [*6*]. There are, however, very few analyses that predict the behavior of the crack velocity as a function of the strain energy release rate and the temperature. Kinetic models of slow,

[1] Professor, Department of Mechanical and Aerospace Sciences and the Materials Science Program, University of Rochester, Rochester, N.Y. 14627.

[2] The italic numbers in brackets refer to the list of references appended to this paper.

isothermal crack propagation have been relatively successful in interpreting slow crack growth [7-10]. The objective of this paper is to restrict the isothermal, kinetic, thermally activated crack propagation expressions to adiabatic conditions. The rate-controlling processes that occur in the crack-tip region in fast fracture are assumed to be the same processes that occur in slow, isothermal crack propagation. In fast fracture the crack is moving rapidly and in the irreversible process zone, at the crack tip, there is insufficient time for the heat generated to be dissipated to the surrounding material. The process zone is therefore restricted to an adiabatic condition and the temperature of the process zone is different from the temperature of the bulk material surrounding it.

Thermally Activated Crack Propagation

Figure 1 is a schematic of a crack in a solid. The crack propagates in the solid at a macroscopic velocity v, under the action of the driving force, $\mathcal{G}$. It is assumed that the crack velocity v is controlled by thermally rate-controlled processes near the crack tip. The material in the crack tip region undergoes a transition from the original material to fracture-modified material at the crack tip. The crack element of the crack tip is considered

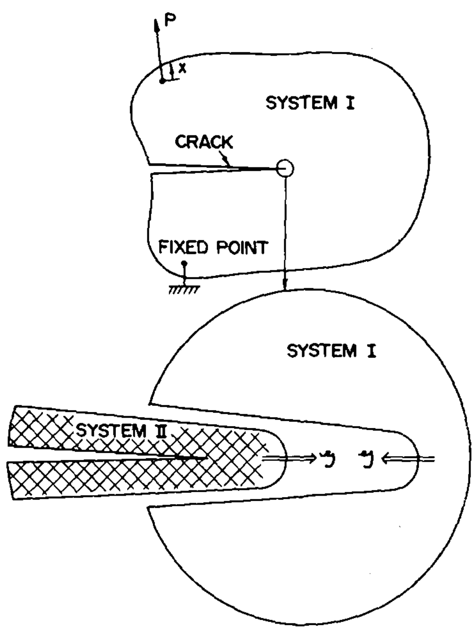

FIG. 1—*A schematic representation of an elastic body containing a crack. It is assumed that $\mathcal{G}$ is known. System II contains a thermally activated process that controls the rate of crack propagation.*

small enough that a single energy barrier is overcome at a time. The energy barriers are the rate-controlling mechanism and will, in general, be unspecified. If plastic deformation, in the crack-tip region, is the rate-controlling process and if it is thermally activated, then the crack motion is thermally activated.

With the assumption of thermally activated barriers, the average crack velocity can be written as an Arrhenius-type equation

$$\nu = \nu_0 e^{-\Delta G/kT} \tag{1}$$

where

ν = crack velocity,
ν_0 = maximum obtainable crack velocity,
ΔG = Gibbs free energy of activation,
k = Boltzman's constant, and
T = temperature in the process zone.

T is assumed to be uniform throughout the process zone and is of course not necessarily the temperature of the bulk specimen.

The Gibbs free energy of the cracked element will in general depend on two independent-state variables of the crack system; choosing $\mathcal{G}$, the strain energy release rate (the crack driving force) and T as the independent variables, with A the crack area and S the entropy as the dependent variables, it follows from Eq 1 that

$$\ln \nu = f(\mathcal{G}, T) \tag{2}$$

where $f(\mathcal{G}, T)$ is a function yet to be specified. Equation 2 may be considered as a steady-state equation. The crack is assumed to have grown long enough so that under the crack driving force, $\mathcal{G}$, it has achieved a steady-state velocity ν and a temperature T in the process zone.

It follows from Eq 2 that

$$\left.\frac{\partial \mathcal{G}}{\partial \ln \nu}\right|_T = -\left(\left.\frac{\partial \mathcal{G}}{\partial T}\right|_{\ln \nu}\right)\left(\left.\frac{\partial T}{\partial \ln \nu}\right|_{\mathcal{G}}\right) \tag{3}$$

The left-hand side of Eq 3 is the isothermal rate dependence of $\mathcal{G}$. The first term on the right-hand side is the temperature dependence of $\mathcal{G}$ at a constant rate. The second term on the right is $kT^2/\Delta H_+$ for any thermally activated process [*9*]. ΔH_+ is the forward activation enthalpy for the process. Since ΔH_+ must be positive, it follows that the isothermal rate dependence and the temperature dependence at constant rate have opposite signs. In steels there are many reports of $\mathcal{G}$ increasing with test temperature; it follows that $\mathcal{G}$ decreases with rate. In polymers, $\mathcal{G}$ often (although not always) decreases with increasing temperature; it follows that $\mathcal{G}$ increases with rate.

If in Eq 2, $\mathcal{G}$ were replaced by the stress and ν by the strain-rate, then tensile rather than fracture properties would be described. The condition of negative strain-rate sensitivity or serrated yielding, in a tension test, is always accompanied by the yield stress increasing with temperature [*11-13*]. Materials that deform by twinning also show serrated stress versus strain curves; the stress level in these materials increases with increasing temperature [*14*].

A schematic activation barrier is shown in Fig. 2. The Helmholtz free energy, ΔF, is plotted versus crack area in Fig. 2*a*. The isothermal derivative of the Helmholtz free energy with respect to the crack area is the crack driving force, $\mathcal{G}$, and this value is also shown in Fig. 1 (System II). In System I, $\mathcal{G}$ is the strain energy release rate. Thermal fluctuations are assumed to provide the energy for the barriers to be overcome by the crack.

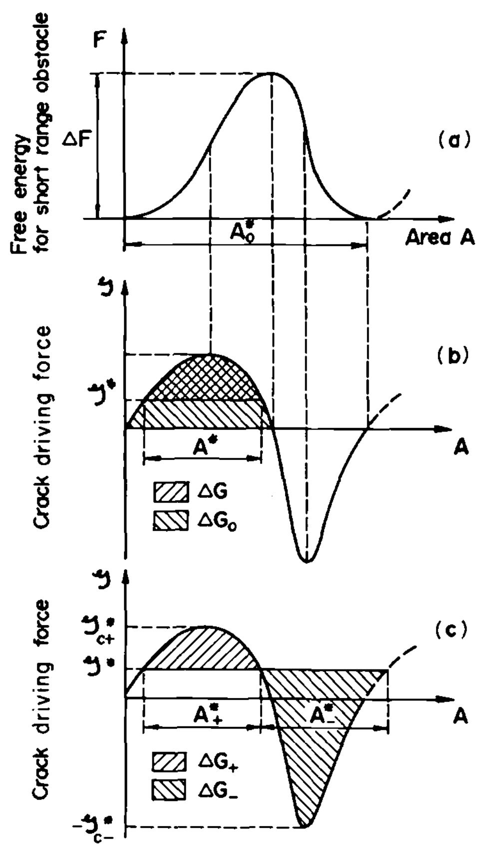

FIG. 2—(a) *Helmholtz free energy versus crack area in System II;* (b) $\mathcal{G}$ *versus* A *for the barrier in* (a); (c) $\Delta G_{\pm}$ *for forward crack propagation.*

Now, restricting the crack system to large driving forces and therefore only forward crack motion, Eq 1 is

$$\nu = \nu_0 e^{-\Delta G_0/kT} e^{\int_0^{\mathcal{G}} A_+^* d\mathcal{G}/kT} \tag{4}$$

The geometry of Fig. 2 has been used in developing Eq 4. In the general case, the functional relation between A_+^* and $\mathcal{G}$ is unknown and therefore an explicit relationship between ν and $\mathcal{G}$ at a constant T is unknown.

The derivatives of the internal energy ΔU_+, the enthalpy ΔH_+, the Gibbs free energy ΔG_+, and the Helmholtz free energy ΔF_+ for forward crack motion are given in Table 1. The Jacobian entries follow from Eq 4

TABLE 1—*Jacobian table for System II for forward crack propagation.*

f	$\partial f/\partial T\|_{\mathcal{G}}$	$\partial f/\partial \mathcal{G}\|_T$
T	1	0
$\mathcal{G}$	0	1
$\ln \nu_+$	$\Delta H_+/kT^2$	A_+^*/kT
ΔG_+	$-\Delta S_+$	$-A_+^*$
ΔH_+	C_+	$T\gamma_+ - A_+^*$
A_+^*	γ_+	θ_+
S	C_+/T	γ_+
ΔF_+	$-\Delta S_+ + \mathcal{G}\gamma_+$	$\mathcal{G}\theta_+$
ΔU_+	$C_+ + \mathcal{G}\gamma_+$	$T\gamma_+ + \mathcal{G}\theta_+$

or by definition. The Jacobian table is the same table given in Ref *9* and it permits derivatives of energy or state variables to be systematically calculated [*15*]. Figure 3 shows schematically an adiabatic and an isothermal rate slope. The adiabatic rate slope calculated from the Jacobian entries $J(\ln \nu, S)$ and $J(\mathcal{G}, S)$ in Table 1 is

$$\frac{J(\ln \nu, S)}{J(\mathcal{G}, S)} = \left.\frac{\partial \ln \nu}{\partial \mathcal{G}}\right|_S = \frac{A_+^*}{kT} - \frac{\Delta H_+ \gamma_+}{kT\,C_+} \tag{5}$$

Two other derivatives from Table 1 are

$$\left.\frac{\partial T}{\partial \mathcal{G}}\right|_S = -\frac{T\gamma_+}{C_+} \tag{6}$$

and

$$\left.\frac{\partial \ln v}{\partial \mathcal{G}}\right|_T = \frac{A_+^*}{kT}$$

Combining Eqs 3, 5, and 6 gives

$$\left.\frac{\partial \ln v}{\partial \mathcal{G}}\right|_S = \frac{\Delta H_+}{kT^2}\left\{\left.\frac{\partial T}{\partial \mathcal{G}}\right|_S - \left.\frac{\partial T}{\partial \mathcal{G}}\right|_{\ln v}\right\} \tag{7}$$

Equation 7 has several interesting features: the fast fracture rate dependence is on the left-hand side and the fast fracture temperature dependence is on the right-hand side, as is the constant rate temperature dependence of $\mathcal{G}$. When $\partial T/\partial \mathcal{G}|_S = \partial T/\partial \mathcal{G}|_{\ln v}$, then $\partial \mathcal{G}/ \ln v|_S \rightarrow \infty$; that is, $\mathcal{G}$ is discontinuous with rate in a fast fracture experiment. Some polymers seem to show such a sharply rising curve [*16,17*]. In some commercial steels at the brittle-to-ductile transition, $\partial T/\partial \mathcal{G}|_{\ln v} \rightarrow 0$. It follows for this restriction that the sign of the adiabatic heating coefficient $\partial T/\partial \mathcal{G}|_S$ will determine the sign of $\partial \ln v/\partial \mathcal{G}|_S$ since ΔH_+ is always positive. On the other hand, when $\partial T/\partial \mathcal{G}|_S \rightarrow 0$, then the adiabatic rate dependence is of the opposite sign to the constant rate temperature dependence. In most metals, near room temperature, $\partial T/\partial \mathcal{G}|_{\ln v}$ is positive. In most polymers $\partial T/\partial \mathcal{G}|_{\ln v}$ is negative. Thus, there is reason to suspect that crack propagation behavior in a structural alloy will have substitutive differences from crack propagation behavior in a "model" polymetric material.

The last point to make from Eq 7 is that it also shows that when

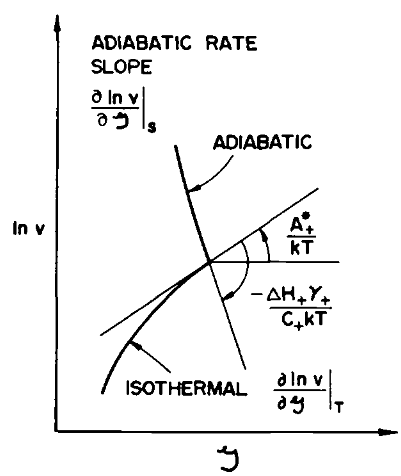

FIG. 3—*The ln of the crack velocity versus the crack driving force, $\mathcal{G}$. The lower part of the curve is assumed isothermal, the upper part adiabatic.*

$\partial \mathcal{G}/\partial \ln v|_S \rightarrow 0$; that is, when fast fracture has a minimum $\mathcal{G}$ versus rate, $\partial T/\partial \mathcal{G}|_S$ or $\partial T/\partial \mathcal{G}|_{\ln v}$ must $\rightarrow \infty$. The consequences of having $\partial \mathcal{G}/\partial \ln v|_S \rightarrow 0$ because $\partial T/\partial \mathcal{G}|_{\ln v} \rightarrow \infty$ are particularly disturbing; $\mathcal{G}$ decreases very strongly with increasing temperature at constant rate.

Conclusions

Crack propagation was assumed to be a thermal rate activated process. The rate-controlling mechanism in the irreversible process zone at the crack tip is, in general, unspecified. A complete comparison of rapid fracture data with the thermal model is not possible since T, $\mathcal{G}$, and v are not all measured during rapid fracture. Several derivatives, restricted to adiabatic conditions that apply during fast fracture and that are the most frequently measured quantities in fast fracture experiments, were found. It was shown that a complete description of the activation enthalpy for crack propagation is an important aspect of rapid fracture.

Acknowledgments

This work was supported by the U.S. Department of Energy through Contract EY-76-S-02-2422 at the University of Rochester.

References

[1] Wiederhorn, S. M. in *Fracture Mechanics of Ceramics*, Vol. 4, R. C. Bradt, D. P. H. Hasselman, and F. F. Lange, Eds., Plenum Press, New York, 1978, p. 549.
[2] Swain, M. V. and Lawn, B. R., *International Journal of Fracture Mechanics*, Vol. 9, 1973, p. 481.
[3] Atkins, A. G., Lee, C. S., and Caddell, R. M., *Journal of Materials Science*, Vol. 10, 1975, p. 1381.
[4] Floreen, S., *Metallurgical Transactions*, Vol. 6A, 1975, p. 1741.
[5] Evans, A. G., Russell, L. R., and Richerson, D. W., *Metallurgical Transactions*, Vol. 6A, 1975, p. 707.
[6] *Fast Fracture and Crack Arrest*, *ASTM STP 627*, G. T. Hahn and M. F. Kanninen, Eds., American Society for Testing Materials, 1976.
[7] Charles, R. J. and Hillig, W. B. in *Proceedings* Symposium on Mechanical Strength of Glass and Ways of Improving It, Florence, Italy, Sept. 1961; Union Scientifique Continental du Verre, Charlerai, Belgium, 1962.
[8] Lawn, B. R., *Journal of Materials Science*, Vol. 10, 1975, p. 469.
[9] Pollet, J-C. and Burns, S. J., *International Journal of Fracture*, Vol. 13, 1977, p. 667.
[10] Pollet, J-C. and Burns, S. J., *International Journal of Fracture*, Vol. 13, 1977, p. 775.
[11] Mulford, R. A. and Kocks, U. F., "New Observations on the Mechanisms of Dynamic Strain Aging and of Jerky Flow," *Acta Metallurgica*, Vol. 27, 1979, p. 1125.
[12] Brindley, B. J. and Worthington, P. J., *Metallurgical Review*, No. 145, *Metals and Materials*, Vol. 4, 1970, p. 101.
[13] Baird, J. D. in *The Inhomogeneity of Plastic Deformation*, American Society for Metals, Park, Ohio, 1973, p. 210.

[*14*] Bolling, G. F. and Richman, R. H., *Acta Metallurgica*, Vol. 13, 1965, pp. 709, 723, 745.
[*15*] Crawford, F. H., *American Journal of Physics*, Vol. 17, 1949, p. 1.
[*16*] Kalthoff, J. F., Beinert, J., and Winkler, S. in *Fast Fracture and Crack Arrest, ASTM STP 627*, American Society for Testing and Materials, 1977, p. 161.
[*17*] Kobayashi, T. and Dally, J. W. in *Fast Fracture and Crack Arrest, ASTM STP 627*, American Society for Testing and Materials, 1977, p. 257.

Test Methods for Measuring Dynamic Fracture Properties for Use in a Crack Arrest Methodology

Takao Kobayashi[1] *and J. W. Dally*[2]

Dynamic Photoelastic Determination of the $\dot{a}$-K Relation for 4340 Alloy Steel

REFERENCE: Kobayashi, Takao and Dally, J. W., "**Dynamic Photoelastic Determination of the $\dot{a}$-K Relation for 4340 Alloy Steel,**" *Crack Arrest Methodology and Applications, ASTM STP 711,* G. T. Hahn and M. F. Kanninen, Eds., American Society for Testing and Materials, 1980, pp. 189–210.

ABSTRACT: A method of direct determination of the instantaneous stress-intensity factor associated with running and arrested cracks in steels has been developed at the University of Maryland. Birefringent coatings have been applied to the proposed ASTM standard crack arrest compact specimens of oil-quenched and tempered 4340 steel. Isochromatic fringe patterns during crack propagation and crack arrest have been photographed successfully with an ultrahigh-speed Cordin camera and specially designed high-intensity and short-duration Xenon lamp system.

In this paper a detailed description of the experimental apparatus, the method of isochromatic fringe analysis technique, and an examination of behavior of the stress-intensity factor during crack propagation and after arrest are presented.

KEY WORDS: dynamic photoelasticity, birefringent coating, crack propagation, crack arrest, stress intensity factor and crack velocity.

In recent years brittle birefringent polymers and dynamic photoelasticity have been extensively utilized to study crack propagation and crack arrest, and to aid in the development of test specimens and procedures for standard crack arrest toughness measurements [*1-6*].[3]

The means for characterizing dynamic fracture, which has been explored at the University of Maryland, is to establish the relationship between crack velocity ($\dot{a}$) and the instantaneous stress-intensity factor (K). Dynamic photoelasticity has been used with brittle birefringent polymers such as Homalite 100 to obtain isochromatic fringe loops associated with the run-arrest event.

[1] Associate professor, Mechanical Engineering Department, University of Maryland, College Park, Md. 20742.

[2] Dean College of Engineering, University of Rhode Island, Kingston, R.I. 02881.

[3] The italic numbers in brackets refer to the list of references appended to this paper.

A typical example of the $\dot{a}$-versus-K curve determined from these data for Homalite 100 is shown in Fig. 1.

The minimum K-value (K_{Im}) on the $\dot{a}$-versus-K curve is the crack arrest toughness. It was found that the minimum K-value occurred at zero crack velocity. Three characteristic features were observed in the $\dot{a}$-versus-K curves. In the low-velocity region, K is almost independent of crack velocity, and small increases in K above K_{Im} result in very sharp increases in crack velocity. In the high-velocity region, crack velocity is not sensitive to the K-value, and significant increases in K are required to produce a small increase in crack velocity. Finally, there is a transition region between these two regions where changes in the stress-intensity factor result in significant changes in the crack velocity. Extensive investigations have shown that the K-$\dot{a}$ relation is independent of specimen size and shape [7].

It has been noted that the available information on crack speed as a function of K for brittle fracturing of structural steel includes features which are generally similar to those shown in Fig. 1 [8]. The behavior and properties of brittle polymers are, however, quite different from those of metals in some respects. Properties of polymeric materials are much more strain-rate sensi-

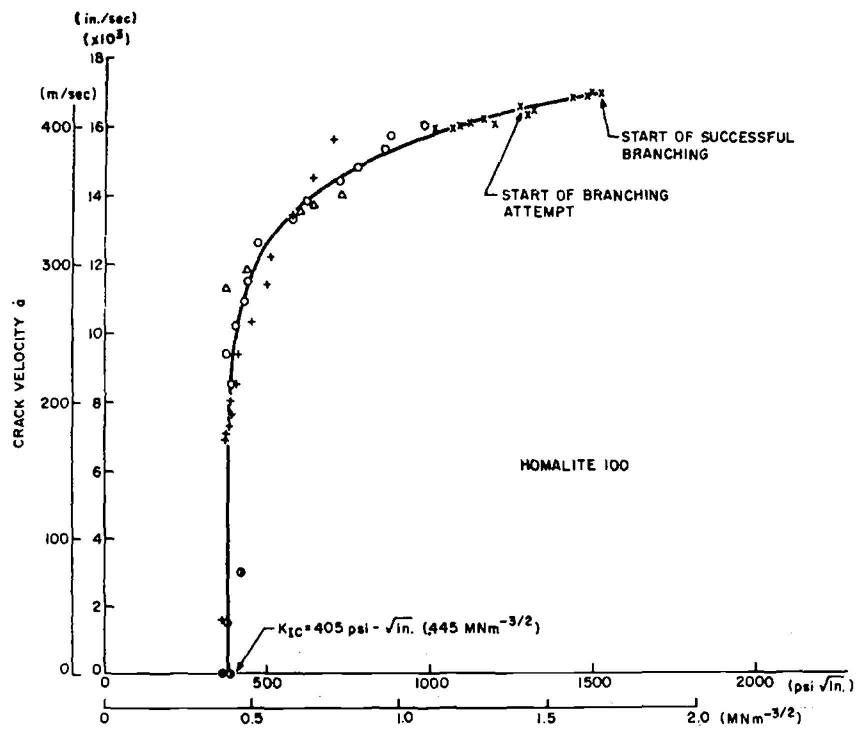

FIG. 1—*Crack velocity* $\dot{a}$ *as a function of stress-intensity factor* K *for Homalite 100.*

tive than those of steel, and the energy loss due to damping of polymers is much higher than that of steel. Also, the fracture zone size in steel may be larger than that in brittle polymers since steel is an aggregate of randomly oriented grains. Considering these differences, it is of interest to develop methods to observe dynamic crack behavior directly and to determine the instantaneous stress-intensity factor associated with a propagating crack. It is also important to examine the proposed ASTM crack arrest procedures with steel specimens.

An application of birefringent coating to steel specimens to measure the dynamic stress-intensity factor has been developed at the University of Maryland. The use of birefringent coatings in the study of dynamic fracture has been attempted previously [*9,10*]. In these investigations, however, a continuous sheet of birefringent coating material was used over the specimen surface and this procedure caused uncertainty as to whether the observed response in the coating is dominated by the fracture of the base material or by the fracture of the coating itself [*11*]. A split birefringent coating technique—a separate sheet of birefringent coating on either side of the anticipated crack path—has been developed which alleviates problems encountered by previous investigators. The method has been applied to the proposed ASTM compact specimen proposed by Materials Research Laboratory (MRL) [*12*]. This paper describes the experiments and presents the first results showing the $\dot{a}$-K relationship for 4340 steel.

Experimental Procedure

The experimental apparatus, shown in Fig. 2, includes an ultrahigh-speed camera, flash lamp system, loading fixture, and specimen. Details pertaining to the experimental apparatus and the method of data analysis are presented in the following subsections.

High-Speed Camera

The camera employed in this experiment was a Cordin Model 330A continuous-writing, simultaneous streak and framing camera. When used in the framing mode, the camera is capable of recording 80 frames with an image size of 15 by 21 mm on 35-mm film at a framing rate up to 2×10^6 frames per second (fps). The selection of framing rate depends upon the crack behavior (that is, high-speed propagation, crack arrest, or postarrest) and the duration of the flash lamp system, since the test is conducted with an open shutter. For the results reported here, the framing rate was approximately 330 000 fps.

The exposure time for the Cordin camera is a function of frame rate and the width of the framing stop. For these experiments the exposure time is about 1 μs. The film employed was Kodak 2495 RAR high-speed negative

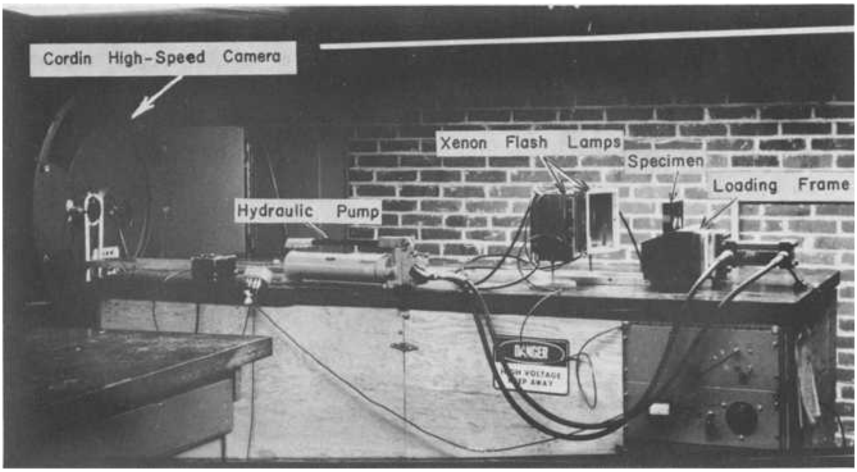

FIG. 2—*Experimental apparatus.*

35-mm film. This film is medium grained with an orthochromatic emulsion and has good resolving power. As it is sensitive only to light of wavelengths below 580 nm, a Kodak No. 8 filter was used to block the light with wavelengths below 500 mm. Thus, the wavelength of the light used to record the fringe patterns peaked at 540 nm with a band of about ±40 nm.

Flash Lamp System

Photographing dynamic isochromatic fringe patterns in the birefringent coatings with the Cordin Model 330A framing camera required a high-intensity, short-duration light. A special Xenon flash lamp circuit was designed to accommodate this requirement. The circuit diagram of the flash lamp, Fig. 3, shows three capacitors (121 μF-5 kV d-c each) connected with inductive coils (5.7 μH). The capacitors are charged to 3.4 kV with a 5-kV d-c power supply. Two 101.6-mm-long (4 in.) Xenon flash lamps (Model EG & G FX81C-4) are connected in series to the capacitor bank. The firing of the lamps is initiated by applying a 25-kV trigger pulse produced by an EG & G TM11-A trigger module. The flash lamp system develops sufficient light to expose the film (Kodak 2495 RAR) within 15 to 20 μs after receiving a trigger signal, and the duration of this intensity is about 200 μs.

Synchronization between the firing of the flash lamps and initiation of crack propagation was achieved with a conductive paint line placed at the tip of the machined initial crack and by a pulse-forming circuit. When the conductive paint line was broken by the crack propagation, a 20-V d-c pulse of 50-ns duration was produced which triggered the EG & G TM11-A for firing of the lamps. A detailed examination of the response of the conductive line

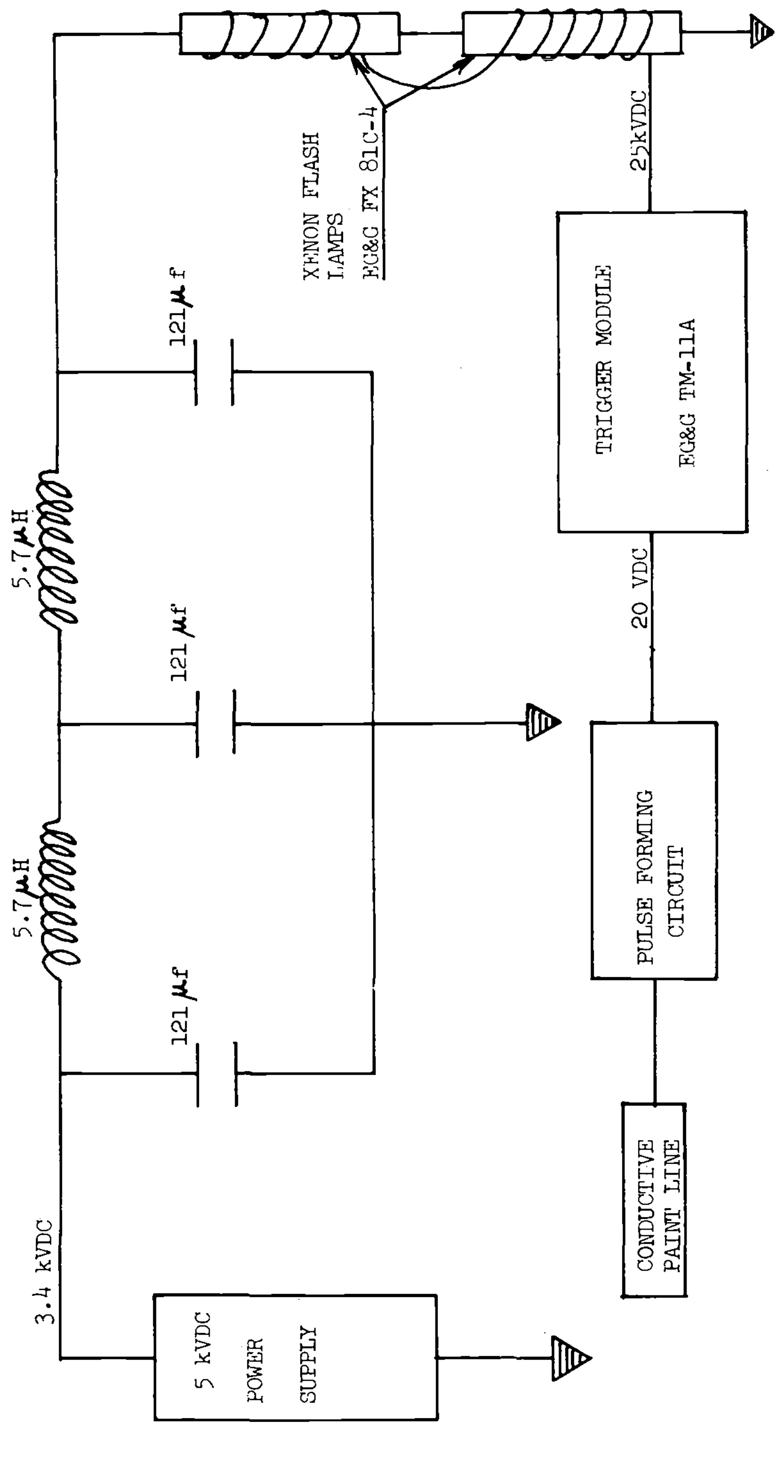

FIG. 3—*Diagram showing flash tube power supply and synchronization circuits.*

circuit, pulse forming, and firing of flash lamps indicated that the time delay between the initiation of crack propagation and firing of the lamps was always less than 10 μs.

Specimen and Loading Fixture

The specimen material used was hot-rolled, annealed, vacuum degassed, aircraft-quality 4340 steel. A specimen, Fig. 4, was machined from a 27 by 210 by 210-mm plate. The geometry of the specimen was in accordance with the MRL specification in the cooperative test program. A machined specimen was then subjected to the following heat treatment: 1 h at 900°C, oil-quenching, and tempering at 370°C. One face of the heat-treated specimen was sanded and cleaned for bonding with a birefringent coating.

The birefringent coating material selected was a 2-mm-thick polycarbonate sheet (PS-1) with reflective backing, manufactured by Photoelastic, Inc. Two pieces of coating, 75 by 110 mm in size, were prepared. The edges of the coating which were to be placed along the face groove of the specimen were machined to have the same slope as the groove face as shown in Fig. 5. The coating was bonded to the specimen with Hysol EA 9810 structural high-strength epoxy adhesive.

The specimen was loaded by a transverse wedge and a split pin in the specially designed loading fixture as illustrated in Fig. 6. The wedge was forced between the two halves of the split pin with a hydraulic cylinder until crack initiation occurred. The crack-opening displacement during thc test period was monitored with an eddy current displacement transducer (Kaman Model KD-2300-2S) mounted at a position 0.25 W away from the load line as specified by the MRL procedure. The signal from the displacement transducer was recorded with a digital memory oscilloscope (Nicolets, Inc., Model Explorer III). The crack-opening displacement was utilized to calculate the crack initiation stress-intensity factor, K_Q, and the stress-intensity factor after crack arrest, K_{Ia}, following the MRL procedure [*12*].

Method for Determination of the Stress-Intensity Factor

A typical high-speed photograph of isochromatic fringe patterns observed in the birefringent coated face-grooved 4340 steel specimen is presented in Fig. 7. It is evident that the fringe loops are relatively large and some inaccuracy in the determination of K by a three-parameter method may occur. Nevertheless, direct measurements of $K(t)$ in steel are extremely difficult and some error in analyzing the data may have to be tolerated.

The stress-intensity factor was determined from the isochromatic loops with a three-step method of analysis. First, an overdeterministic method developed by Sanford and Dally [*13*] was used to compute the stress-intensity factor in the coating. This technique involves a numerical method of least-

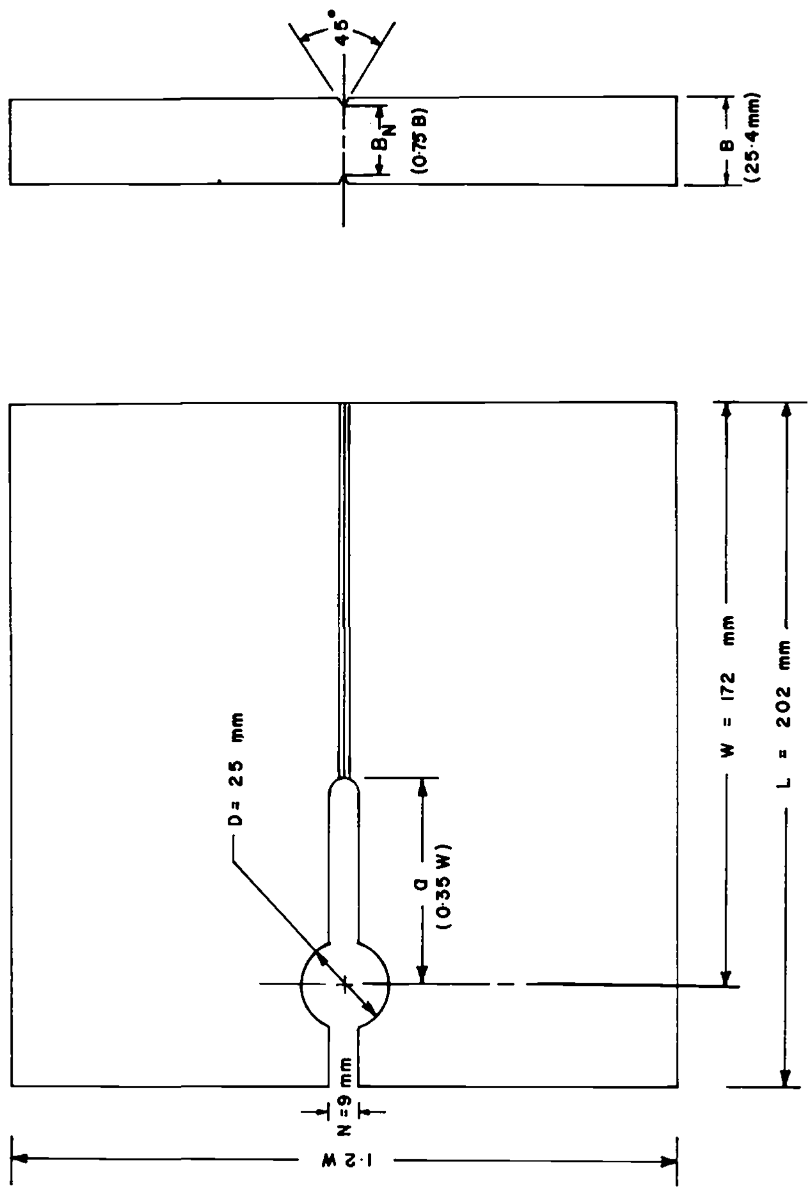

FIG. 4—*Modified compact tension specimen.*

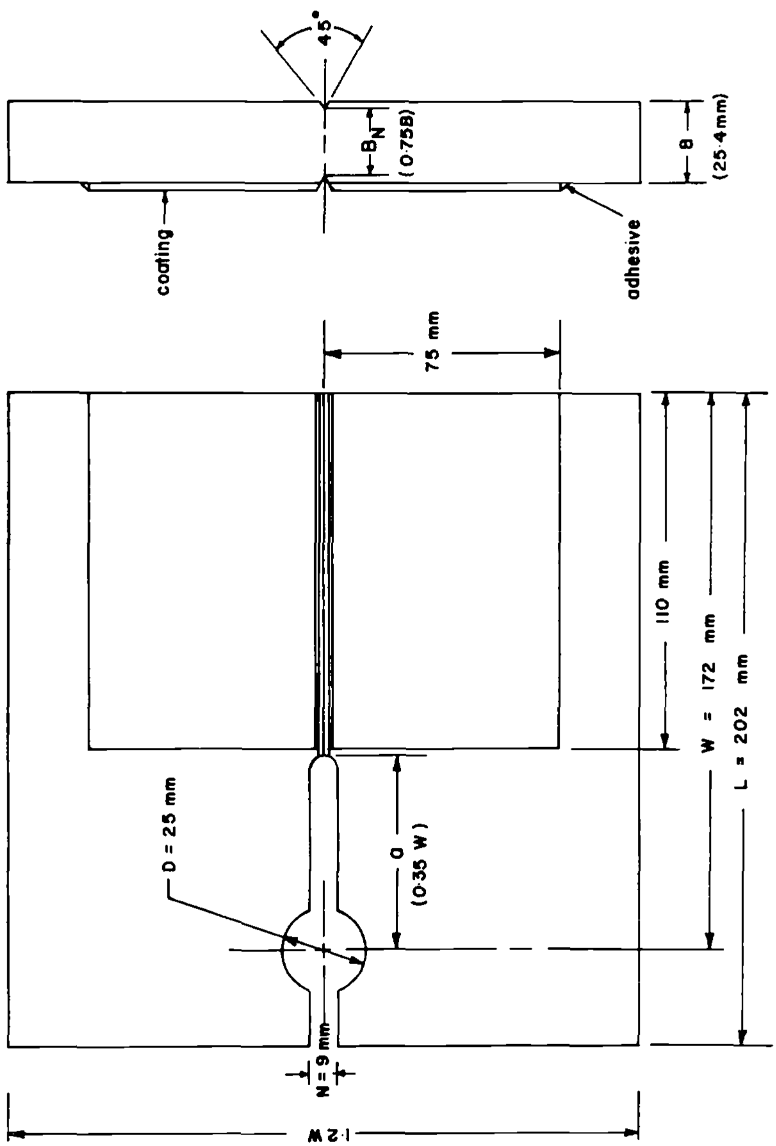

FIG. 5—*Birefringent coating on the compact tension specimen.*

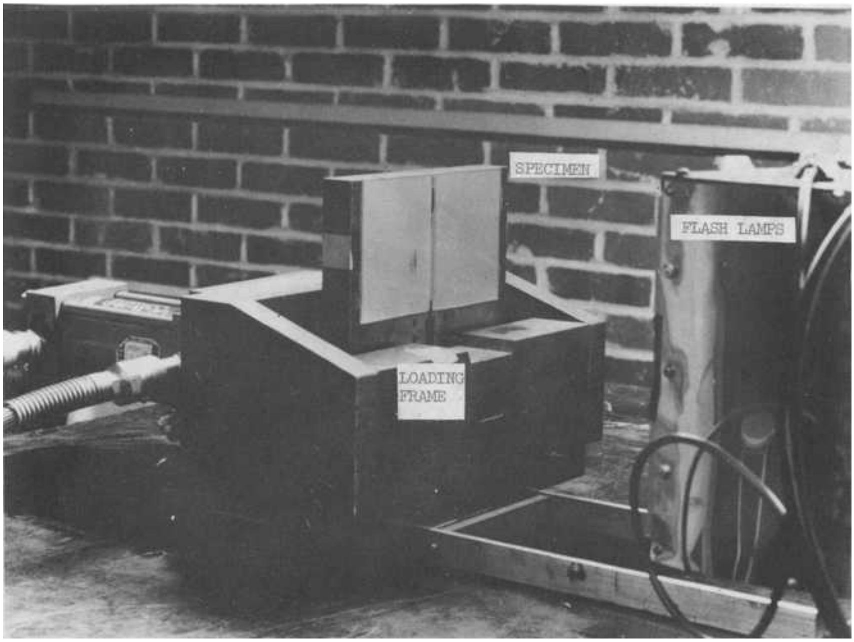

FIG. 6—*Close-up view of specimen with coating in the loading frame.*

squares fitting of a theoretical solution which includes K_{I}, K_{II}, and σ_{ox} to field data taken from isochromatic loops. Ten sets of data (N_i, r_i, and θ_i) were taken from the isochromatic loops as shown schematically in Fig. 8. In measuring r_i and θ_i, the points were selected on the outer arc of the fringe so that small deviations in the location of the crack tip would not produce large errors in either r_i or θ_i. The exact origin of the crack tip could not be identified in the photographs; however, the fringe loop closes at the edge of the groove (see Fig. 9) locating the X-coordinate of the crack tip. The center of the groove was taken for the Y-coordinate locating the crack tip. While exact comparisons cannot be made to verify the accuracy of this approach, it is believed that individual determinations of K are within ± 10 percent. When curves are drawn through several individual K determinations, the curve represents an averaging process and the accuracy should be improved.

Reading of the data processing was performed with the use of a digitizer (Talso, Inc. Model BL 611-B) interfaced with a programmable calculator (HP-9815A). The values of K_{I}, K_{II}, and σ_{ox} were printed out after every iteration and the calculation was terminated when convergence was observed (normally after about five iterations).

The second step in the process is to convert the K-value in the birefringent

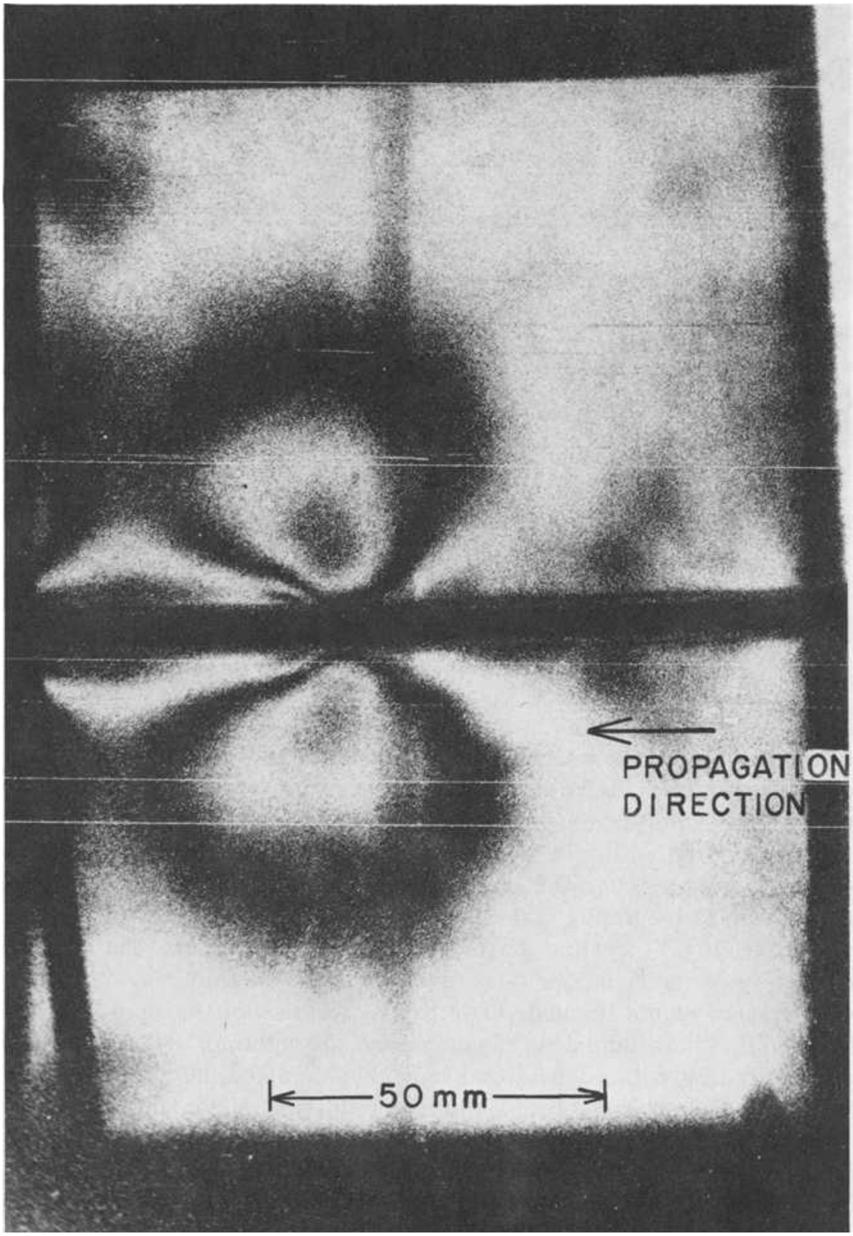

FIG. 7—*Isochromatic fringe loops obtained with the birefringent coating.*

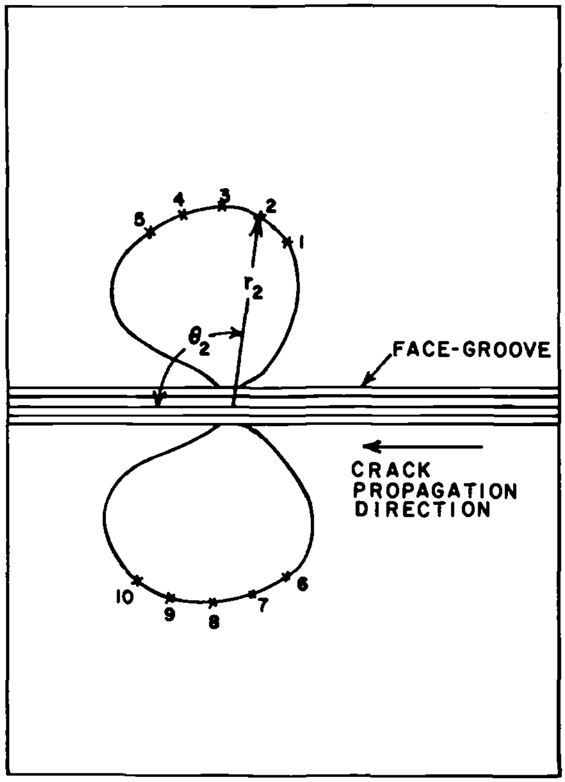

FIG. 8—*Typical data extraction from the isochromatic loops.*

coating to the K-value in steel. This was accomplished by relating the stresses in the steel to stresses in the coating, as described in Ref *14*, to obtain

$$K^s = \frac{E^s}{E^c} \frac{1 + \nu^c}{1 + \nu^s} K^c \tag{1}$$

where E is the modulus of elasticity and ν is Poisson's ratio. The superscripts s and c refer to steel and coating, respectively.

Der et al [*11*] examined the validity of Eq 1 by mounting the birefringent coating on one side of the crack path of Homalite 100 specimens. The comparison of K obtained using Eq 1 to analyze isochromatic loops in the coating with K determined directly from isochromatic fringes in the Homalite 100 indicated a good agreement.

The third step in the analysis was to account for the effect of face grooves on the determination of K from the specimens employed in this study. Pre-

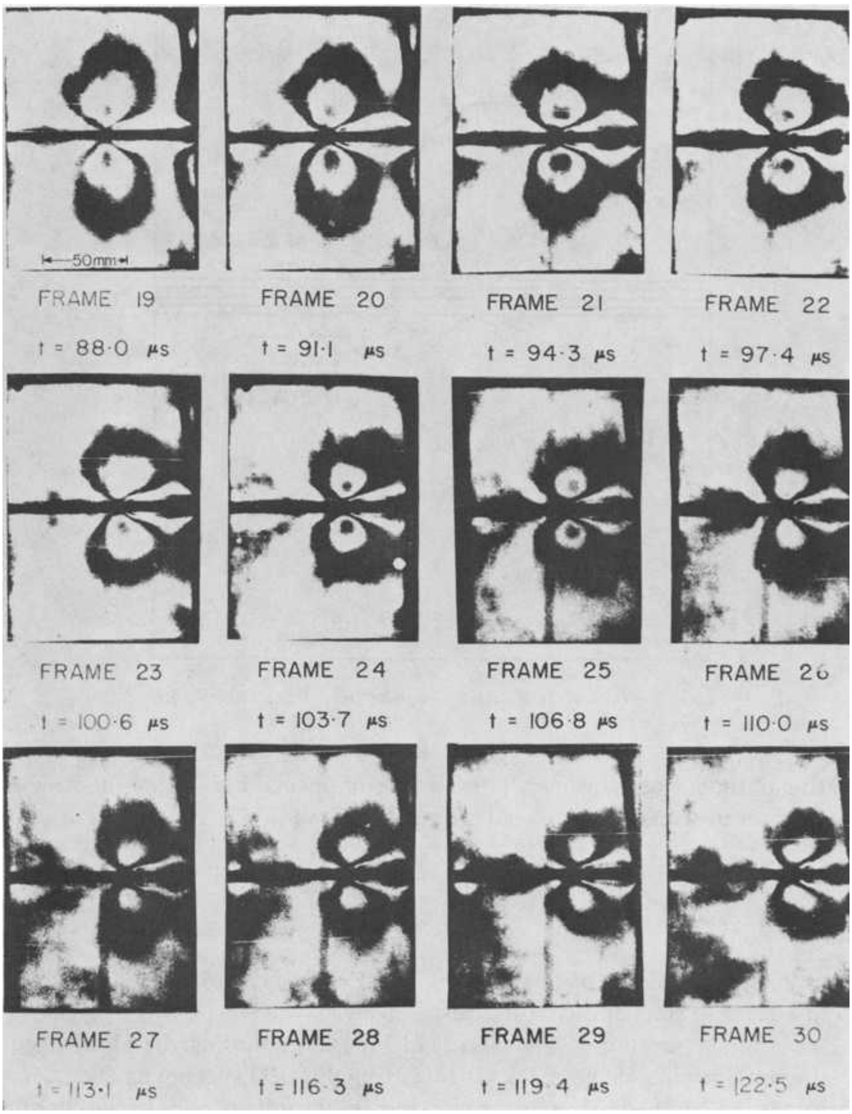

FIG. 9a—*Sequence of isochromatic fringe patterns during propagation period (crack propagation from left to right).*

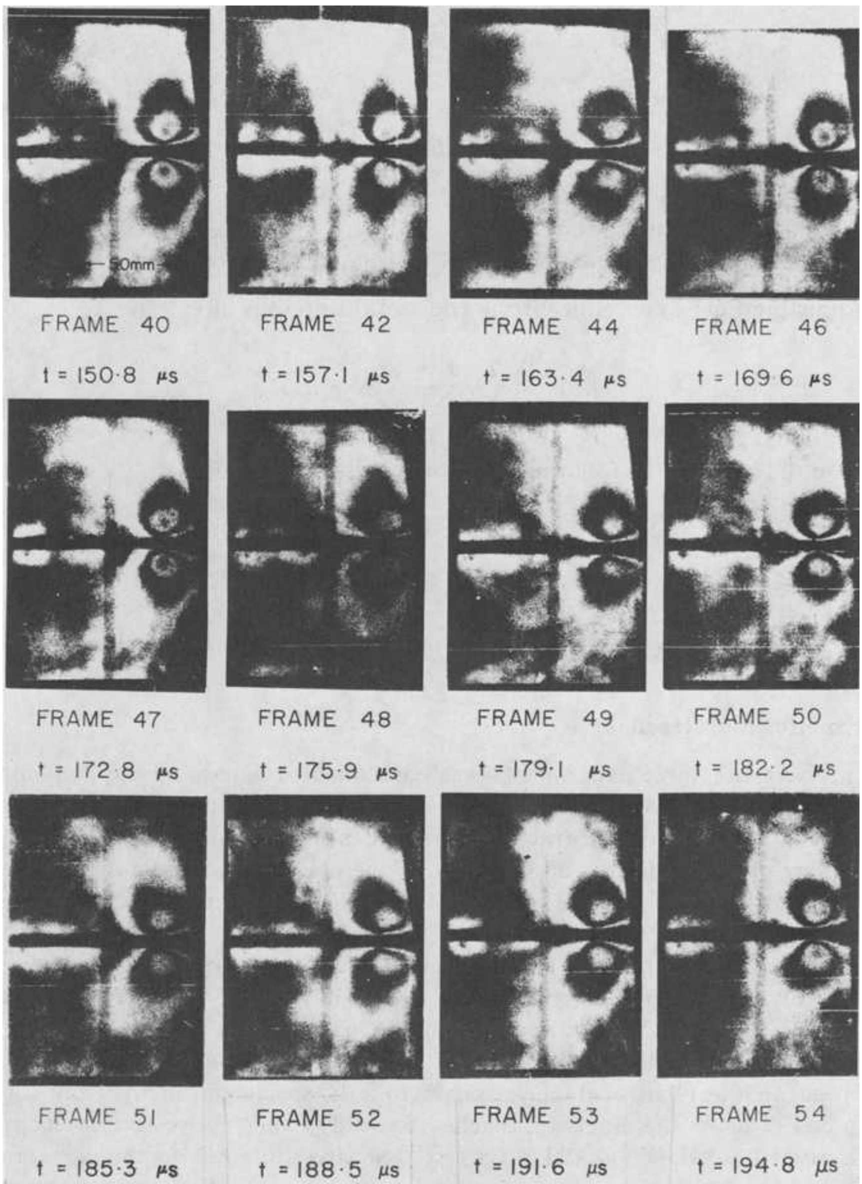

FIG. 9*b*—*Sequence of isochromatic fringe patterns during crack arrest phase (crack arrest at Frame 48).*

vious studies with face-grooved Homalite 100 specimens showed that the effect of the grooves was to increase K by a factor F so that

$$K^G = FK \tag{2}$$

where

$$F = \sqrt{B/B_N}, \tag{3}$$

B = specimen thickness,
B_N = net thickness, and
G = superscript identifying the K associated with grooved specimens.

Adjusting Eq 1 to account for the effect of the grooves gives

$$(K^s)^G = \frac{E^s}{E^c}\frac{1+\nu^c}{1+\nu^s}K^c\sqrt{B/B_N} \tag{4}$$

In the analysis the following material constants were used

E^s = 206.9 KPa,
E^c = 2.48 KPa,
ν^s = 0.30,
ν^c = 0.36, and
[3]f_σ = 6.69 MPa-mm/fringe.

Experimental Results

A series of three experiments was conducted to determine the dynamic behavior of the crack propagating in 4340 steel. Typical photoelastic results showing the isochromatic fringe patterns for the run arrest event in Specimen 362 are given in Figs. 9*a* and 9*b*. The fringe patterns in Fig. 9*a* are for the propagating crack and the patterns in Fig. 9*b* for the arrested crack. The crack position a and the isochromatic fringe data (N_i, r_i, θ_i) were measured from each of these frames. The results of the data analysis showing the stress-intensity factor K and the crack length a as a function of time are presented in Figs. 10, 11, and 12 for Specimens 348, 362, and 375, respectively.

Examination of the results for Specimen 348, Fig. 10, shows that the crack propagated at relatively high velocity across the specimen ranging from 730 to 664 m/s. As the crack approached the end of the specimen, its velocity decreased but the crack did not arrest. The stress-intensity factor shows an oscillation about a monotonically decreasing mean value. While scatter exists in the experimental determination of K, it is believed that the oscillations are

[3]Note that the static material fringe value for polycarbonate has been used because no data are available on the dynamic value.

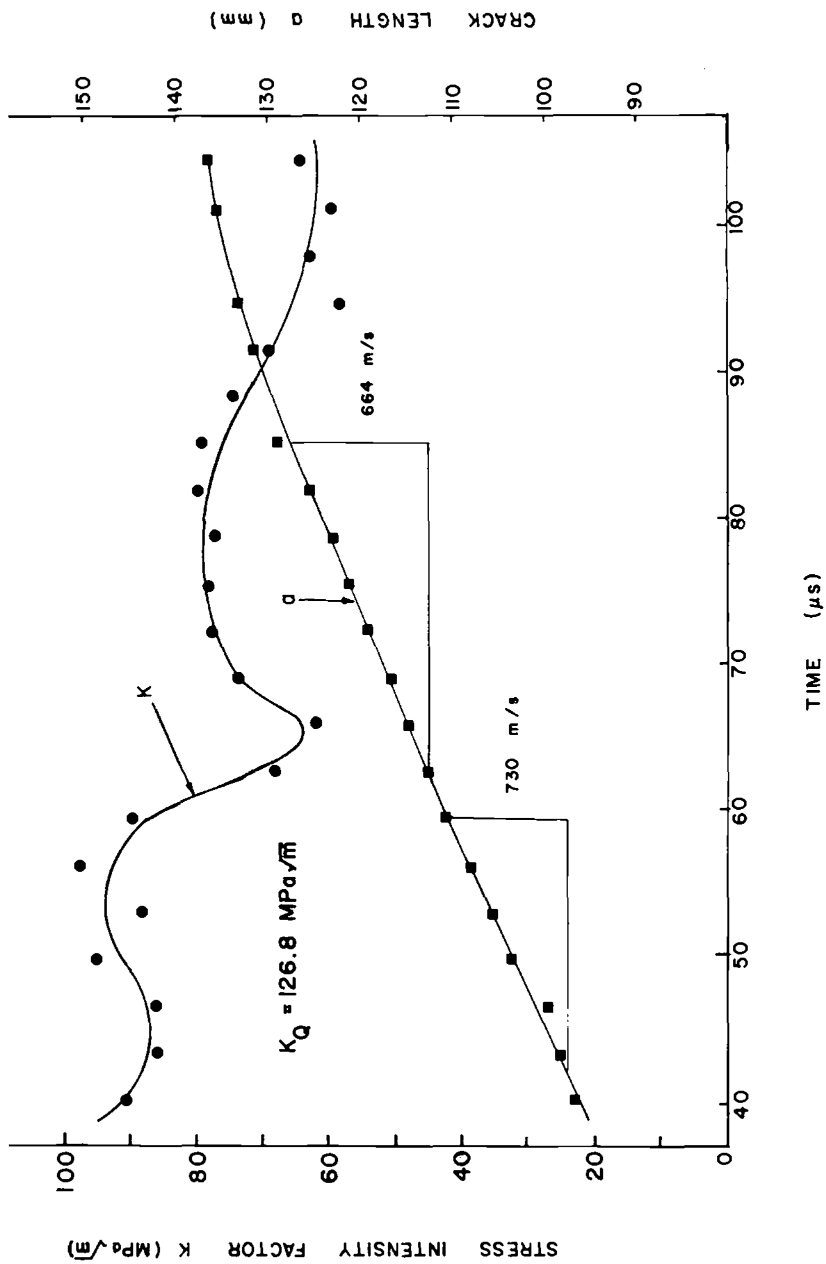

FIG. 10—*Stress-intensity factor* K *and crack length* a *as a function of time for Specimen 348.*

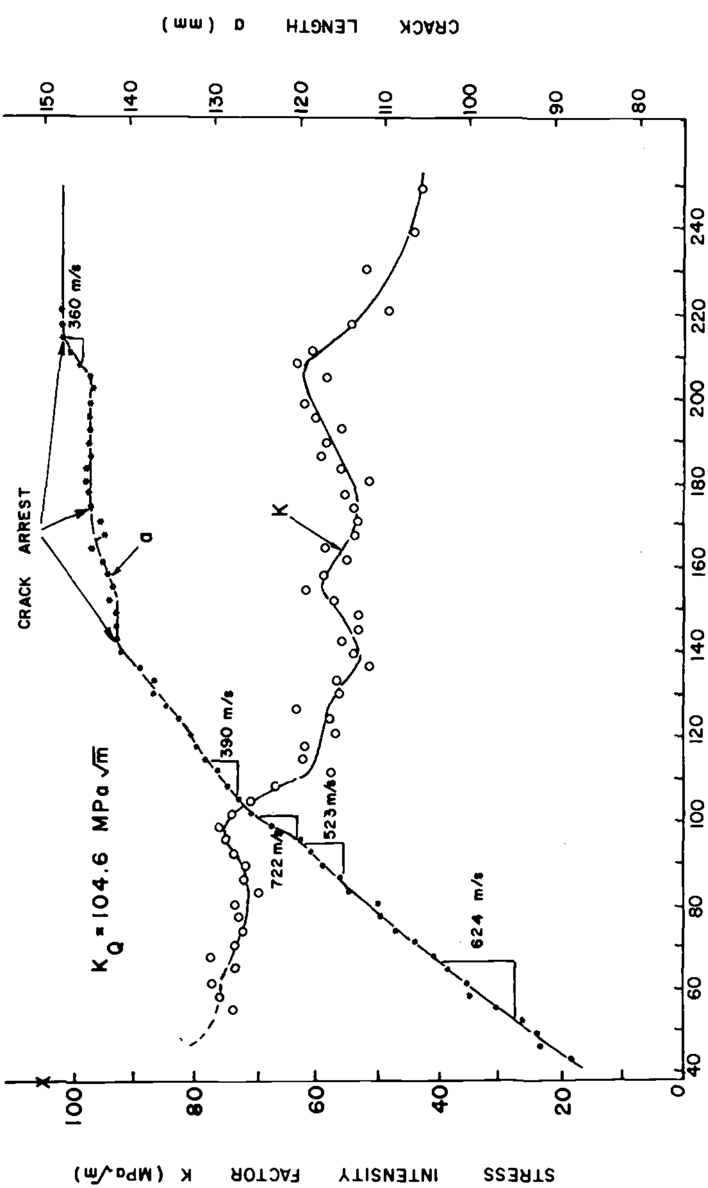

FIG. 11—*Stress-intensity factor* K *and crack length* a *as a function of time for Specimen 362.*

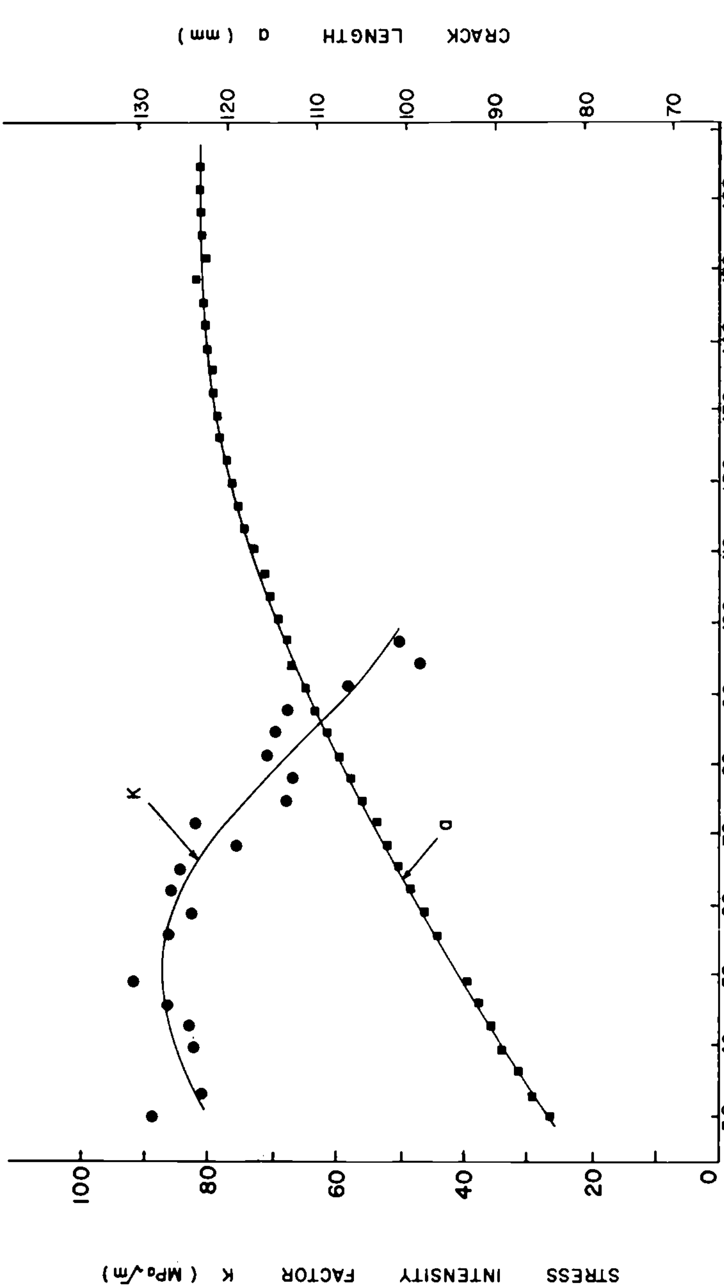

FIG. 12—*Stress-intensity factor* K *and crack length* a *as a function of time for Specimen 375.*

real. Apparently, at high velocity, the changes in K do not markedly affect the crack-tip velocity.

Results from Specimen 362, Fig. 11, show many additional features of the dynamic crack behavior. Early in the observation period, the crack propagated at a constant velocity of 600 m/s while K decreased from $K_Q = 104.6$ MPa$\sqrt{m}$ to about $K_Q = 72$ MPa$\sqrt{m}$. After declining to $K = 72$ MPa$\sqrt{m}$, K then increased with a corresponding increase in $\dot{a}$. In this time period, from $t = 88$ to 135 μs, the crack-tip velocity varied between 720 and 250 m/s as K varied. Finally, in the third region for $t > 140$ μs, the crack repeatedly arrested and reinitiated with increasing time duration at each arrest. When the crack arrested, the stress-intensity factor increased as the kinetic energy in the specimen was converted to strain energy. The instantaneous stress-intensity factor at arrest, $K_{Im} = 52$ MPa$\sqrt{m}$, was the same at each of the three occurrences of arrest. Reinitiation of the crack occurred at $K_{Id} = 60$ to 62 MPa$\sqrt{m}$.

The results from the third specimen, Fig. 12, indicate that the initial velocity of the crack was 450 m/s and the velocity decreased monotonically to zero. The stress-intensity factor exhibited one minor oscillation early in the propagation phase and then decayed monotonically. Analysis of the isochromatics loops in the last half of the event was not performed due to the development of Mode II loading, which occurred when the crack turned and ran out of the groove.

Discussion

Data from Figs. 10-12 were used to obtain the $\dot{a}$-K relation for 4340 steel shown in Fig. 13. Results from Specimens 348 and 362 are in good agreement and provide a sufficient number of points to establish the vertical stem and the beginning of the transition region of the $\dot{a}$-K curve. This relation indicates arrest when $K_{Im} = 52$ MPa$\sqrt{m}$ and velocity increases of 31 m/s for a unit increase in K above K_{Im}.

Comparison of the $\dot{a}$-K relation between Homalite 100 (see Fig. 1) and that of steel shows the similarity in the vertical stem; however, the slope of the stem is higher for Homalite 100 than for steel. The slope of the $\dot{a}$-K curve is related to fracture surface roughness, with the slope decreasing as the surface becomes rougher for a given specimen.

The $\dot{a}$-K relation for Specimen 375 is also shown in Fig. 13, and significant differences with respect to the results from Specimens 348 and 375 are noted. Inspection of the fracture surfaces as shown in Fig. 14 indicate the reason for this difference. The fracture surface for Specimens 348 and 362 show approximately equivalent surface roughness, whereas Specimen 375 is much smoother. Apparently the heat treatment of No. 375 was different, resulting in a material with a lower terminal velocity and apparently a material with a lower K_{Im}.

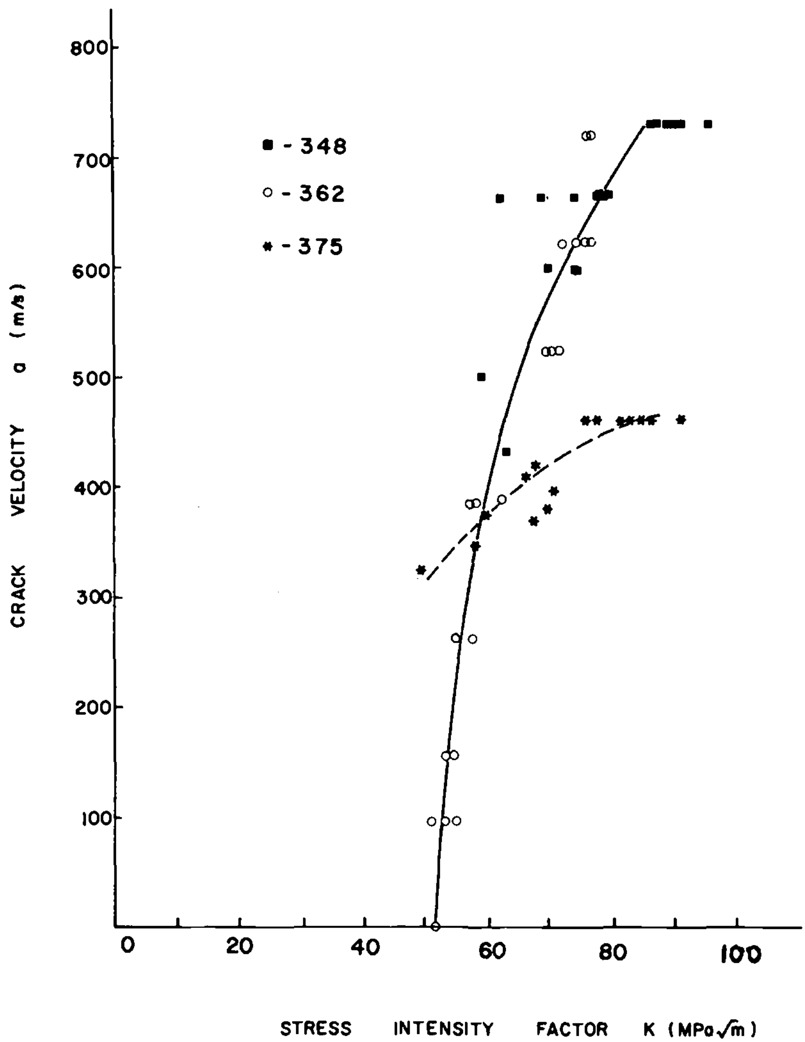

FIG. 13—*Crack velocity* $\dot{a}$ *as a function of stress-intensity factor* K *for 4340 steel.*

The photoelastic determination of the arrest toughness K_{Im} was compared with a prediction of K_{Ia} based on the MRL procedure. With this method, the crack-opening displacement Δ is measured at a position 0.25 W removed from the load line, and K_Q or K_{Ia} is given by

$$K = \frac{YE}{W}\sqrt{\frac{B}{B_N}}\,\Delta \tag{5}$$

where Y is a dimensionless factor which is a function of a/W.

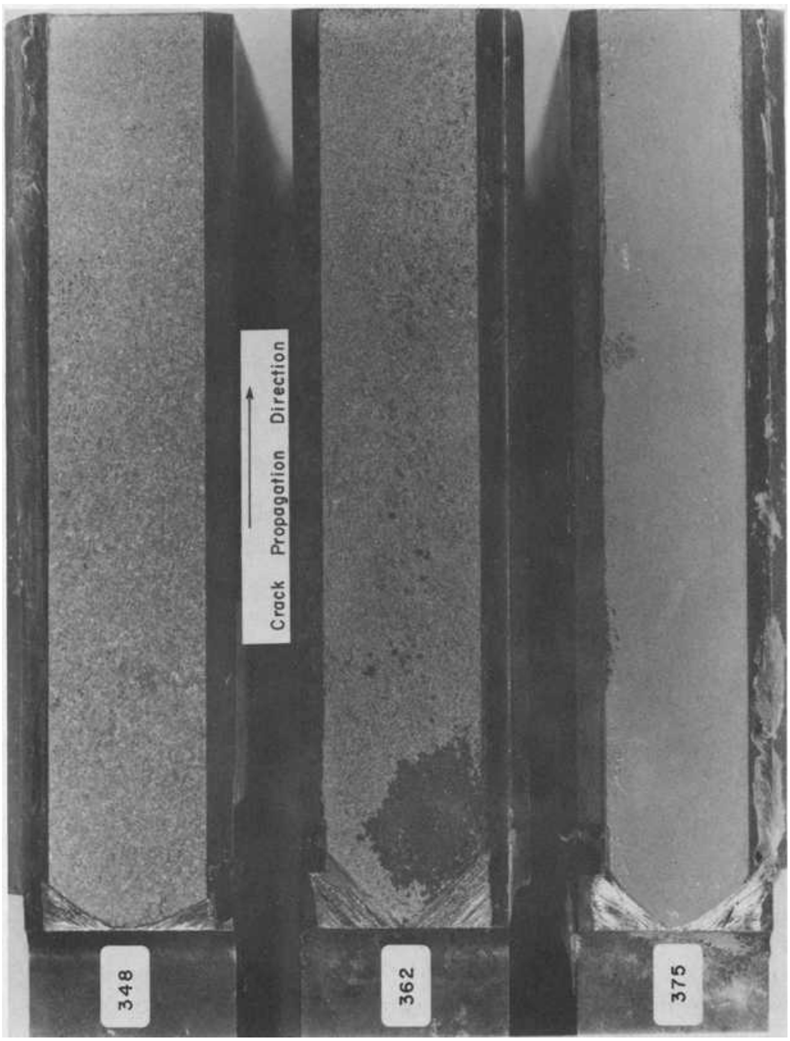

FIG. 14—*Appearance of fracture surfaces for the three specimens.*

Results of the MRL procedure applied to Specimen 362 with $W = 170$ mm are

Initial conditions

$$a_0 = 60 \text{ mm}, \Delta_0 = 0.85 \text{ mm} \qquad K_Q = 104.6 \text{ MPa}\sqrt{\text{m}}$$

Arrest conditions

$$a_f - 148 \text{ mm}, \Delta_f = 1.26 \text{ mm} \qquad K_{Ia} = 59.3 \text{ MPa}\sqrt{\text{m}}$$

The comparison shows reasonably good agreement between the $K_{Im} = 52$ MPa$\sqrt{\text{m}}$ from photoelastic analysis and the $K_{Ia} = 59.3$ MPa$\sqrt{\text{m}}$ from the MRL procedure.

Conclusions

A method has been developed for determining instantaneous stress-intensity factors from steel compact tension specimens by means of split birefringent coatings and dynamic photoelasticity. While the method requires further refinement such as dynamic calibration and optimizing the coating thickness, it does provide an excellent means for observing the dynamic characteristics of the run arrest event.

The $\dot{a}$-K relation for oil-quenched and tempered 4340 is similar in shape to the $\dot{a}$-K relation for Homalite 100. The value of $K_{Im} = 52$ MPa$\sqrt{\text{m}}$ was determined as the arrest toughness for 4340 with $R_c = 46$.

Results from the photoelastic measurements, $K_{Im} = 52$ MPa$\sqrt{\text{m}}$, compared favorably with the results from the MRL procedure, where $K_{Ia} = 59.3$ MPa$\sqrt{\text{m}}$.

Acknowledgments

This research program was sponsored by the U.S. Nuclear Regulatory Commission, Contract No. NRC-04-76-172. The authors would like to thank C. Z. Serpan for his support and encouragement, Dr. G. R. Irwin for his advice and guidance, and Mr. Nutter for his work in the laboratory.

References

[1] Kobayashi, A. S. in *Experimental Techniques in Fracture Mechanics*, Society for Experimental Stress Analysis, Iowa State Press, Ames, Iowa, Chapter 6, Monograph No. 1, 1973, pp. 126-145.

[2] Bradley, W. B. and Kobayashi, A. S. in *Proceedings*, Society for Experimental Stress Analysis, Vol. 27, No. 1, 1970, pp. 106-113.

[3] Kobayashi, A. S., Wade, B. G., and Bradley, W. B. in *Deformation and Fracture of High Polymers*, H. H. Kansch, J. A. Haselle, and R. I. Taffer, Eds., Plenum Press, New York, 1973, pp. 487-500.

[4] Kobayashi, T. and Dally, J. W. in *Fast Fracture and Crack Arrest, ASTM STP 627,* G. T. Hahn and M. F. Kanninen, Eds., American Society for Testing and Materials, 1977, pp. 257-273.
[5] Kobayashi, A. S., Emery, A. F., and Mall, S. in *Fast Fracture and Crack Arrest, ASTM STP 627,* G. T. Hahn and M. F. Kanninen, Eds., American Society for Testing and Materials, 1977, pp. 257-273.
[6] Irwin, G. R., Dally, J. W., Kobayashi, T., Fourney, W. L., and Etheridge, J. M., "Photoelastic Studies of Crack Propagation and Crack Arrest," NUREG-0342, NRC-5, U.S. Nuclear Regulatory Commission, Sept. 1977.
[7] Kobayashi, T., Dally, J. W., and Fourney, W. L., "Influence of Specimen Geometry on Crack Propagation and Arrest Behavior," a paper presented at the 6th International Conference on Experimental Stress Analysis, Sept. 1978, Munich, Germany.
[8] Irwin, G. R. in *Fast Fracture and Crack Arrest, ASTM STP 627,* G. T. Hahn and M. F. Kanninen, Eds., American Society for Testing and Materials, 1977, pp. 7-18.
[9] Van Elst, H. C., *Dynamic Crack Propagation,* G. C. Sih, Ed., Noordhoff International Publishing, Leyden, The Netherlands, 1972, pp. 283-332.
[10] Daniel, I. M. and Rowlands, R. E., *Experimental Mechanics,* Vol. 15, Dec. 1975, pp. 449-457.
[11] Der, V. K., Barker, D. B., and Holloway, D. C., *Mechanics Research Communications,* Vol. 5, No. 6, 1978, pp. 313-318.
[12] Crosley, P. B. and Ripley, E. J., "Guidelines for Measuring K_{Ia} with a Compact Specimen" in *Prospectus for a Cooperative Test Program on Crack Arrest Toughness Measurement* under the auspices of ASTM Committee E24.0304.
[13] Sanford, R. J. and Dally, J. W., *Engineering Fracture Mechanics,* Vol. 11, 1979, pp. 621-633.
[14] Zandman, F., Redner, S., and Dally, J. W., *Photoelastic Coatings,* Society for Experimental Stress Analysis Monograph No. 3, Iowa State University Press, Ames, Iowa, 1977.

P. B. Crosley[1] *and E. J. Ripling*[1]

Comparison of Crack Arrest Methodologies

REFERENCE: Crosley, P. B. and Ripling, E. J., **"Comparison of Crack Arrest Methodologies,"** *Crack Arrest Methodology and Applications, ASTM STP 711,* G. T. Hahn and M. F. Kanninen, Eds., American Society for Testing and Materials, 1980, pp. 211-227.

ABSTRACT: The ASTM Cooperative Test Program data are used to compare the static (K_{Ia}) and dynamic (K_{Id}, K_{Idm}) approaches to crack arrest. It is shown that K_{Ia} is not dependent on K_Q. This is consistent with the requirements of the static approach, but not the dynamic one, which requires that K_{Ia} decrease with K_Q if K_{Id} ($=K_{Idm}$) is a constant. K_{Id} increases systematically with K_Q at a rate that is consistent with calculations based on the use of a constant value for K_{Ia} which is equal to its measured mean value. Only in the limiting case of very short crack jumps (associated with very-low-average crack speeds) can K_{Id} be identified as a minimum value at which $K_{Id} = K_{Idm}$. In this case $K_{Idm} \approx K_{Ia} \approx K_{Im}$. The latter is the idealized minimum value of K that will support the continued propagation of a running crack.

KEY WORDS: fracture toughness, crack arrest, A533B-1 steel, running cracks

Both the static (K_{Ia}) and the dynamic (K_{Id}, K_{Idm}) crack arrest methodologies are based on the assumption that there is a material property, K_{Im},[2] which is the lowest value of the stress-intensity factor which will support the continued propagation of a running crack. Indeed, both methods are aimed at obtaining an experimental approximation of K_{Im}.

The K_{Ia} approach asserts that the stress-intensity factor observed in the static condition following arrest—which is, by definition, K_{Ia}—is a reasonable approximation to K_{Im}.

The dynamic approach is somewhat more involved. It is based on a dynamic analysis which allows values of crack speed and of running crack toughness, K_{Id}, to be inferred from a laboratory test. By obtaining K_{Id}

[1]Associate director of research and president, respectively, Materials Research Laboratory, Inc., Glenwood, Ill. 60425.

[2]In this paper the distinction between K_{Idm}, the value inferred from tests, and K_{Im}, the idealized value, will be preserved. Some authors appear to use K_{Idm} and K_{Im}, and even K_{Id}, interchangeably.

values as a function of velocity, the minimum value, K_{Idm}, on a K_{Id}-velocity plot, may be found and taken as an approximation to K_{Im}. The quantity measured in an individual test, however, is K_{Id}.

When a test is run, the crack starts to propagate from a static condition with which is associated an initial value of the formally calculated stress-intensity factor, K_Q. In the static condition following the crack's arrest, the stress-intensity factor has the value K_{Ia}. For the intervening time, a value K_{Id} may be inferred from the dynamic analysis and applied to the running crack. The dynamic analysis, which in effect defines K_{Id}, states that $K_Q \geq K_{Id} \geq K_{Ia}$. At a higher value of K_Q the crack is expected to run at a higher average velocity and to propagate a greater distance. Also, the ratio K_{Id}/K_{Ia} is expected to increase. There is no question, therefore, that K_{Ia} and K_{Id} must be measuring different things and that, except possibly for very short crack jumps (where other problems may arise), they cannot be comparable approximations to K_{Im}. This fact, which is not in dispute, appears to be accepted sometimes as proof that the K_{Ia} methodology is no good. It is in reality nothing more than a statement of what the particular dynamic model predicts.

It should be recognized, of course, that the dynamic model which serves as the basis for obtaining an experimental K_{Id} measurement says nothing about whether a particular value is K_{Idm} and hence to be considered as an approximation to K_{Im}. In general, K_{Id} is velocity-dependent, and, presumably, there is no way of knowing beforehand how K_{Id} depends on crack speed in a particular material. If, however, there is a reason for identifying K_{Id} as K_{Idm}, a reason such as experimental evidence that K_{Id} is insensitive to crack velocity in a class of material, then this K_{Id} can be compared with K_{Ia} to see which is a more meaningful approximation to K_{Im}.

In the cooperative program on crack arrest being carried out under ASTM Committee E24.01.07, a large number of tests are being run on both Battelle Columbus Laboratories (BCL) and Materials Research Laboratory (MRL) types of compact specimens. The test reports from the different participating laboratories provide values (or the data from which to calculate values) of K_{Ia} and of K_{Id} from both types of test specimens, and the results available so far may be looked at to see how K_{Ia} and K_{Id} are affected by different test variables and, it is hoped, to provide insight into the relative merits of the conflicting methodologies.[3]

Analysis of Cooperative Program Data

The data discussed here are ASTM Cooperative Test Program results available in time to be included in this paper. Room temperature data on

[3]Throughout this paper the toughness parameter obtained from the BCL procedure[4] will be denoted K_{Id}, with no judgment being made as to whether or not any of them should be designated as K_{Idm} or taken as an approximation to K_{Im}.

stress-relieved AISI 1018 steel and on A533 Grade B Class 1 steel are considered. On the latter material, test results from both the BCL and the MRL specimens are represented. For the former, only MRL specimen data are available.

All of the K_Q- and K_{Ia}-values (with the exception of one obviously miscalculated K_{Ia}-value on a BCL specimen) are taken from the submitted test reports. The participants in the Cooperative Test Program did not calculate K_{Id} for the MRL specimens, and many of the early results on the BCL specimens were incorrectly calculated; therefore, all K_{Id}-values reported here were calculated anew. The formulas used were, for the BCL specimen

$$K_{Id}/K_Q = 2.336 - 14.17\,x + 49.2\,x^2 - 78.1\,x^3 + 45.5\,x^4$$

and for the MRL specimen

$$K_{Id}/K_Q = 1 - 0.92\,x + 0.33\,x^2$$

where $x = \Delta a/W$, that is, the total crack jump distance divided by the specimen width.

The preceding expressions are polynomial fits to the curves shown in Fig. 1, which is taken from the BCL test procedure.[4]

Another BCL analysis result which proves useful in examining the test results is shown in Fig. 2. This plot of K_{Ia}/K_{Idm} versus K_Q/K_{Idm} will be used to relate K_{Ia} to K_Q on the assumption that K_{Idm} is a constant.

Figure 3*a* shows K_{Ia} plotted against K_Q for the stress-relieved AISI 1018 steel. For all of the data the mean K_{Ia} is 85.6 MPa $m^{1/2}$ with a standard deviation of 12.7 MPa $m^{1/2}$. A least-squares linear fit, which has a positive slope and a standard deviation of 12.3 MPa $m^{1/2}$, does not fit the data appreciably better than the constant line through the mean. According to the BCL dynamic analysis, the K_{Ia}-K_Q plot has a negative slope, and the expected dependence of K_{Ia} on K_Q, based on Fig. 2, and taking $K_Q = K_{Ia}$ ($= K_{Im}$) to occur at 86 MPa $m^{1/2}$, is also shown in Fig. 3*a*.

Figure 3*b* shows K_{Id} plotted against K_Q for the stress-relieved AISI 1018 steel. For all of the data the mean K_{Id} is 92.9 MPa $m^{1/2}$ with a standard deviation of 12.2 MPa $m^{1/2}$. The least-squares linear fit has a positive slope and the standard deviation of K_{Id} about this line is 6.1 MPa $m^{1/2}$; that is, the positive sloping straight line is a much better fit to the data than the mean value. The expected dependence of K_{Id} on K_Q for a constant K_{Ia} equal to its mean value of 86 MPa $m^{1/2}$ is also shown in Fig. 3*b*.

Whereas the data on AISI 1018 steel just discussed included test results

[4]"Prospectus for a Cooperative Test Program on Crack Arrest Toughness Measurement," Subcommittee on Dynamic Testing, Dynamic Initiation, Crack Arrest Task Group, American Society for Testing and Materials, 1977.

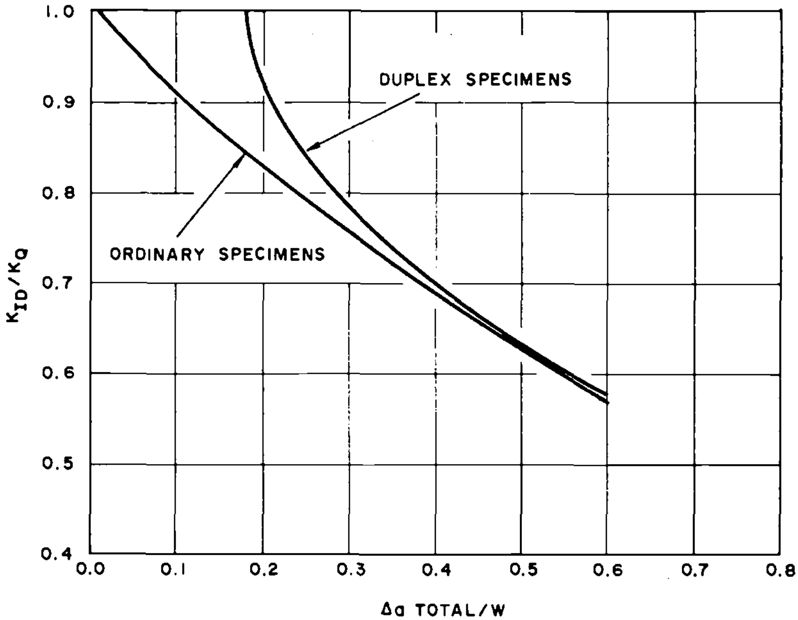

FIG. 1—*Reference curves for ordinary and duplex compact tension test specimens showing the relation between* $\Delta\bar{a}/W$ *and* K_{Id}/K_Q *(footnote 4).*

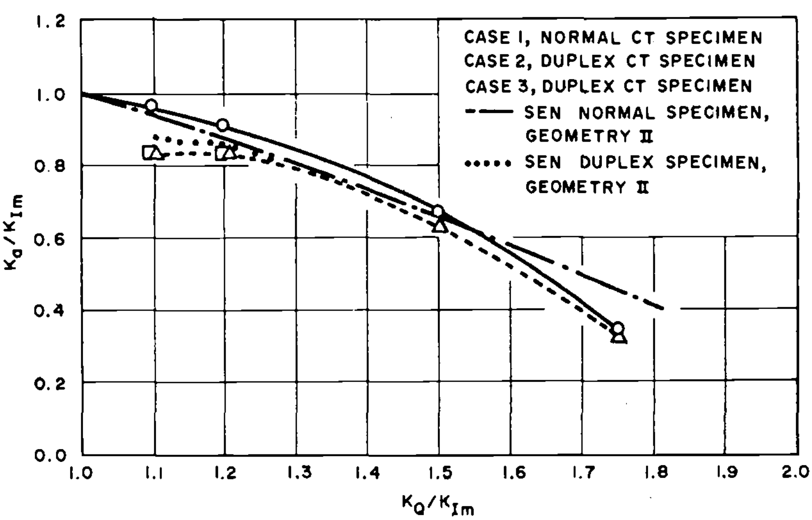

FIG. 2—*Influence of the relative initiation stress-intensity level on the* K_{Ia}/K_{Idm} *ratio.*[5]

[5]Hahn, G. T. et al, Third Annual Progress Report (Oct. 1976-Sept. 1977), NUREG/CR-0057, BMI-1995, Battelle Memorial Institute, Columbus, Ohio, 1978.

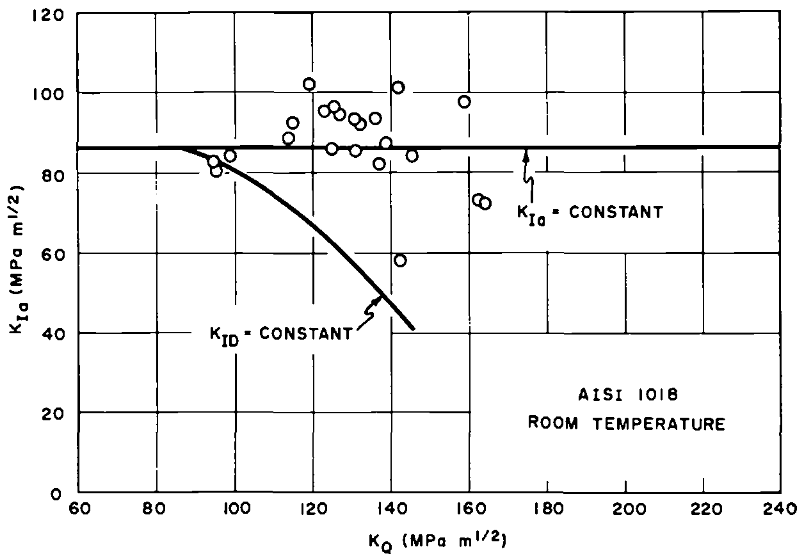

FIG. 3a—*Dependence of* K_{Ia} *on* K_Q *for AISI 1018 steel. Cooperative Test Program data.*

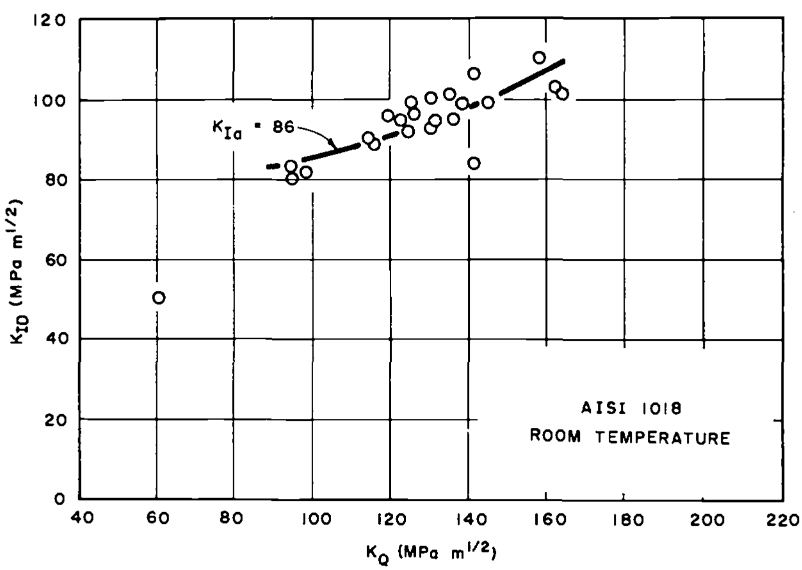

FIG. 3b—*Dependence of* K_{Id} *on* K_Q *for AISI 1018 steel. Cooperative Test Program data.*

from only the MRL specimens, room temperature test results on the A533 Grade B Class 1 steel are available from both specimen types. Consequently, the range in K_Q is larger. Figure 4*a* shows K_{Ia} from both tests plotted against K_Q, with K_Q varying from about 100 MPa $m^{1/2}$ to about 260 MPa $m^{1/2}$. For all of the data, the mean value of K_{Ia} is 109.6 MPa $m^{1/2}$ with a standard deviation of 10.8 MPa $m^{1/2}$. The least-squares straight line would have K_{Ia} increasing from 101.4 to 121.4 MPa $m^{1/2}$ as K_Q increases from 110 to 260 MPa $m^{1/2}$. The standard deviation of K_{Ia} about this line is 9.1 MPa $m^{1/2}$, in contrast to the standard deviation of 10.8 MPa $m^{1/2}$ about the mean. Again, if K_{Id} were constant, K_{Ia} would be expected to decrease, not increase, with increasing K_Q; this expected behavior, taken from Fig. 2, is also plotted in Fig. 4*a*.

Figure 4*b* shows K_{Id} plotted against K_Q. The mean value of K_{Id} is 127.4 MPa $m^{1/2}$ with a standard deviation of 26.8 MPa $m^{1/2}$. The least-squares straight line has a strong positive slope according to which K_{Id} would increase from 90.8 to 179.5 MPa $m^{1/2}$ as K_Q increases from 110 to 260 MPa $m^{1/2}$. The standard deviation about this line, 6.5 MPA $m^{1/2}$, indicates that the line is a distinctly better fit to the K_{Id} data than the assumption of a constant K_{Id}. The least-squares straight line, however, makes little physical sense, especially at low values of K_Q, where the line

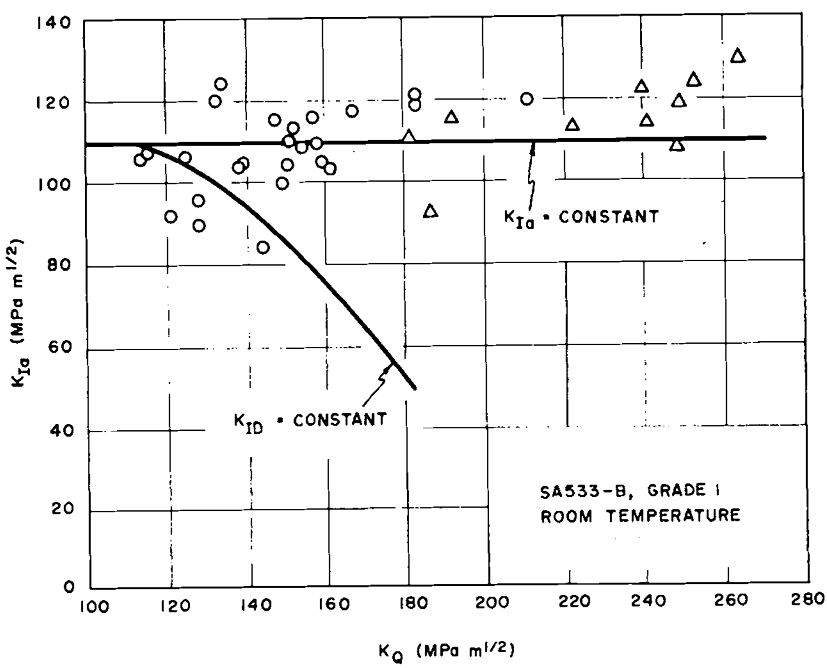

FIG. 4*a*—*Dependence of* K_{Ia} *on* K_Q *for SA533B Grade 1 steel. Cooperative Test Program data.*

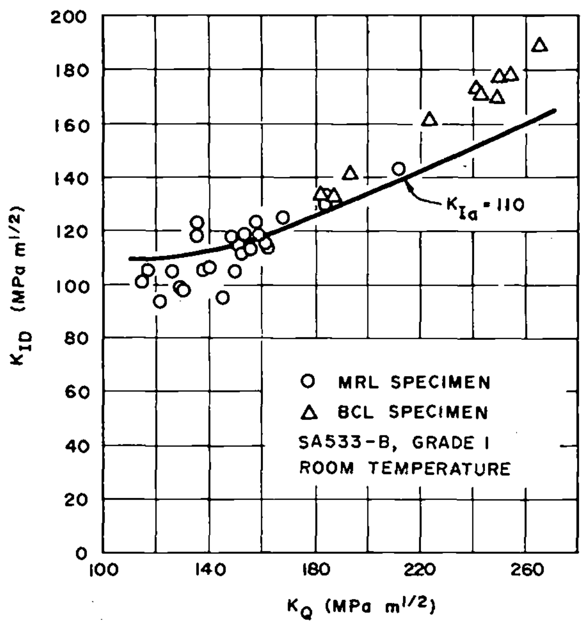

FIG. 4*b*—*Dependence of* K_{Id} *on* K_Q *for SA533B Grade 1 steel. Cooperative Test Program data.*

would suggest that K_{Id} is less than K_{Ia}. A calculated curve which assumes that K_{Ia} is constant and equal to the mean value, 110 MPa m$^{1/2}$, is shown in Fig. 4*b*. For this curve $K_{Ia} = K_{Id} = K_Q$ at $K_Q = 110$ MPa m$^{1/2}$, and K_{Id} does not increase appreciably with K_Q until K_Q exceeds about 150 MPa m$^{1/2}$. The calculated curve for constant K_{Ia} is not a good fit to the BCL specimen data. This is probably a result of the fact that the MRL machine compliance was used for the calculations. The BCL method uses a 50-mm wedge and split-pin assembly, while the MRL procedure uses a 25-mm assembly. The compliance of the former is expected to be less than that of the latter.

It is evident in Fig. 4*b* that the range of K_{Id}-values measured with the two different specimen types is rather distinct. While the plot suggests that this is the result of a systematic dependence of K_{Id} on K_Q, it may be that although the specimens yield similar K_{Ia}-values, one or the other may not give correct K_{Id} results. If the two specimen types are considered separately, the MRL specimen gives a mean K_{Id} value of 113.4 MPa m$^{1/2}$ with a standard deviation of 12.2 MPa m$^{1/2}$. A least-squares straight-line fit gives $\Delta K_{Id}/\Delta K_Q = 0.454$ and the standard deviation about the line is 6.7 MPa m$^{1/2}$. Taking the results from the BCL specimens by themselves, the mean K_{Id} is 162.5 MPa m$^{1/2}$ with a standard deviation of 19.9 MPa m$^{1/2}$. The standard deviation about the least-squares straight line, which has a slope of $\Delta K_{Id}/\Delta K_Q = 0.647$, is 2.6 MPa m$^{1/2}$. For these data the value of K_Q ranges from about 180 to 260 MPa m$^{1/2}$. Thus, each set of data considered separately, as well as the combined results, shows a distinct trend of K_{Id} increasing with K_Q.

Discussion

All the data generated in the cooperative program to date show K_{Ia} to be independent of K_Q, while K_{Id} increases with increasing K_Q. The latter is not unexpected; the larger K_Q is, the greater the expected average crack velocity, and hence the greater the expected value of K_{Id} for rate-dependent materials.

The fact that $K_{Id} = f(K_Q)$ does not necessarily suggest that the analysis on which K_{Id} is based is wrong. Nor, of course, does it say anything about the validity of K_{Ia} as an approximation of K_{Im}. As stated earlier, the BCL dynamic analysis only defines a value of K_{Id} associated with a particular average crack velocity; it does not suggest that any specific value of K_{Id} is a minimum one. So long as K_Q is not much higher than K_{Id}, the average crack velocity is low, and K_{Id} approaches its minimum value, at which point $K_{Id} \approx K_{Idm}$ ($\approx K_{Ia}$), as shown in Figs. 3*b* and 4*b*. This conformity of the BCL and MRL approach to crack arrest becomes more apparent in plots of relative crack velocity as a function of K_{Id}. The Cooperative Test Program data can be readily represented this way by using the BCL reference curves shown in Fig. 5. The data on AISI 1018 steel, Fig. 6, are

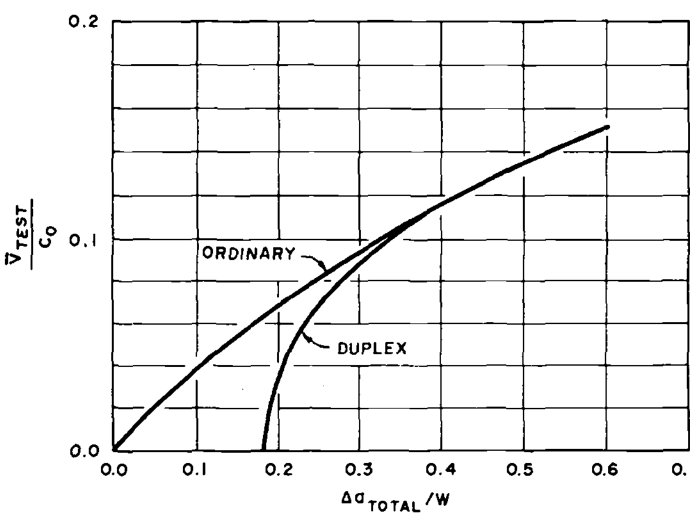

FIG. 5—*Reference curves for ordinary and duplex compact tension test specimens showing the relation between* Δa *total/W and* V/C$_0$ (*footnote 4*).

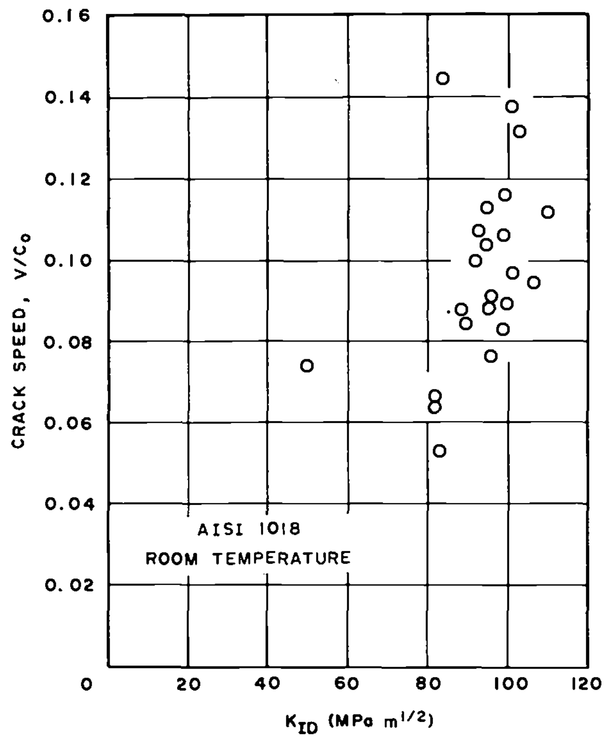

FIG. 6—*Dependence of crack speed on* K_{Id} *for AISI 1018 steel. Cooperative Test Program data.*

limited to a small range of K_{Id}-values so that K_{Id} seems to be only moderately dependent on crack speed. If data had been collected on specimens having higher values of K_Q, higher average crack speeds would have been expected, and the curve would have had a horizontal branch, which is typical of this relationship.[6,7] Nevertheless, an extrapolation of the data to zero speed gives a value of $K_{Id} \approx 86$ MPa $m^{1/2}$, and for this value $K_{Id} = K_{Idm}$ ($\approx K_{Ia} \approx K_{Im}$). The dependence of crack speed on K_{Id} for the SA533-B Grade 1 steel, Fig. 7, covers a wider range of K_{Id}'s and the curve has the typical shape of an inverted "L." Again, an extrapolation of the data to zero speed gives a value of about 110 MPa $m^{1/2}$, so that, at this point, $K_{Id} = K_{Idm}$ ($\approx K_{Ia} \approx K_{Im}$).

[6]Mostovoy, S., Crosley, P. B., and Ripling, E. J. in *Cracks and Fracture, ASTM STP 601*, American Society for Testing and Materials, 1976.

[7]Kobayashi, T. and Dally J. W. in *Fast Fracture and Crack Arrest, ASTM STP 627*, American Society for Testing and Materials, 1977.

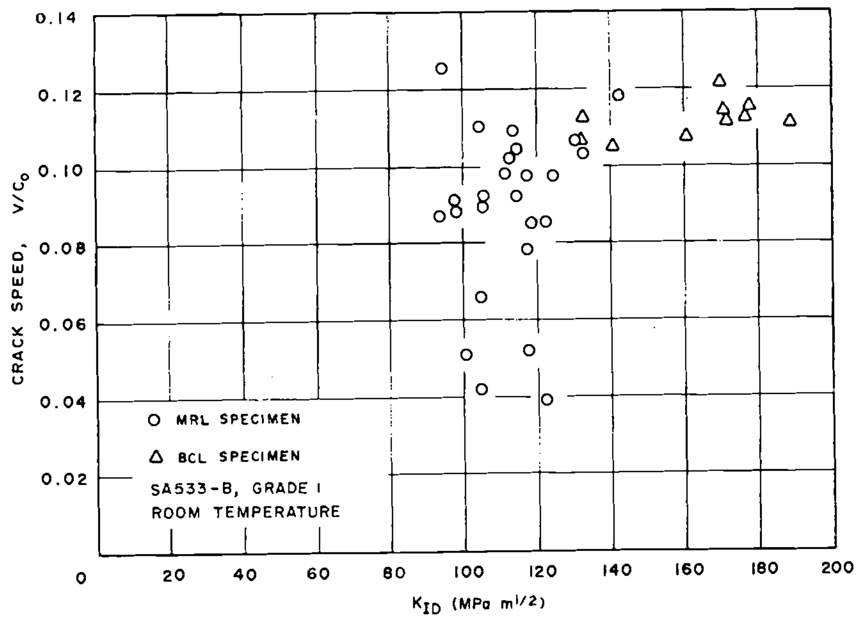

FIG. 7—*Dependence of crack speed on* K_{Id} *for SA533B Grade 1 steel. Cooperative Test Program data.*

Acknowledgments

The authors are grateful to the Electric Power Research Institute, who funded this study, and to Dr. T. U. Marston and Dr. K. Stahlkopf for their continuing interest and many helpful suggestions.

DISCUSSION

G. T. Hahn,[1] *A. R. Rosenfield,*[1] and *R. G. Hoagland*[1] (*written discussion*)—In this paper the authors set out to examine how K_{Ia} and K_{Id} are affected by different test variables "to provide insight into the relative merits" of the static and dynamic methods of interpreting crack arrest tests. They find that the K_{Id}-values of the Cooperative Test Program data set show a systematic increase with K_Q while K_{Ia}-values do not. On this basis they propose first that the K_{Id}-values are crack velocity-dependent and, second, that the minimum value of K_{Id} (either K_{Im} or K_{Idm}) occurs at zero velocity and corresponds to K_{Ia} in the particular steels. Implicit in

[1]Battelle Columbus Laboratories, Columbus, Ohio.

the second proposal is their view that dynamic effects in the compact specimen at arrest are negligible.

We believe the authors are correct in noting that the K_{Id}-values derived with the dynamic method of analysis correspond to the average velocity attained by the crack during the event. The dynamic calculations we have performed show that both the crack velocity and Δa, the size of the crack jump, increase with K_Q. Consequently, K_{Id} is expected to vary with both K_Q and Δa when a velocity dependence exists. The Cooperative Test Program data show that K_{Id}-values are independent of Δa. In view of this we are not convinced that the authors' first proposal is correct.

It should also be noted that after the authors presented this paper two discrepancies in the evaluation of load-line displacement of the Cooperative Test Program data were identified (see Addendum to the discussers' paper in this volume[2]). These corrections have the effect of altering the K_{Id}-values for weld-embrittled specimens and duplex specimens by about 20 and −10 percent, respectively. With these corrections the results are altered to the extent that they no longer support the authors' second proposal or its implications. We do agree that a trend of K_{Id} increasing with K_Q remains and is puzzling under the circumstances, but it would be premature to call upon this dependence to invalidate the dynamic method until an understanding of its origins provides a basis for discounting dynamic effects at arrest.

It is also necessary to draw attention to the results in Fig. 8 which show that K_{Ia} from both types of test specimens trends with Δa. It is consistent with a growing dynamic contribution analogous to the one in DCB specimens,[3] and could be viewed as evidence of dynamic effects in the compact specimen. Recent measurements of load and load-line displacement in wedge-loaded, weld-embrittled compact specimens performed at Battelle may have a bearing on the observations. The measurements show significant departures from linear elastic behavior for weld-embrittled specimens of A533B steel for $K_I \gtrsim 120$ MPa $m^{1/2}$. We believe that the dependence of K_{Ia} on Δa would be accentuated in the absence of the departures. Figure 8 shows this to be the case for results from duplex specimens which do not depart from linearity.

A more detailed analysis of the Cooperative Test Program data that incorporates the dependencies of K_Q and Δa simultaneously is shown in Fig. 9. This analysis shows to what extent it is possible to distinguish between the static and dynamic method of analysis on the basis of the Cooperative Test Program data and in the absence of an independent

[2] Hahn, G. T., Hoagland, R. G., Rosenfield, A. R., and Barnes, C. R., this publication, pp. 248-269.

[3] Kalthoff, J. F., Beinert, J., and Winkler, S. in *Fast Fracture and Crack Arrest, ASTM STP 627,* American Society for Testing and Materials, 1977, p. 161.

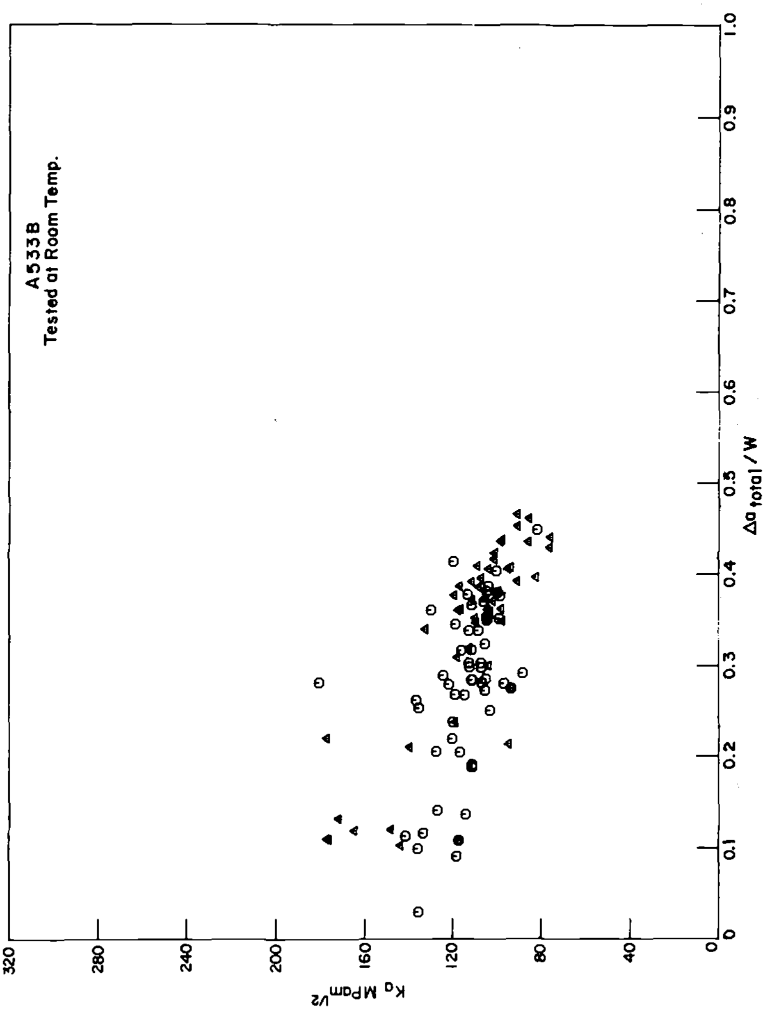

FIG. 8a—*Effect of crack jump length on the* K_{Ia} *results from the Cooperative Test Program.* (Δ) *and* (○) *denote data obtained by the BCL and MRL procedures, respectively. Test temperatures greater than 14°C.*

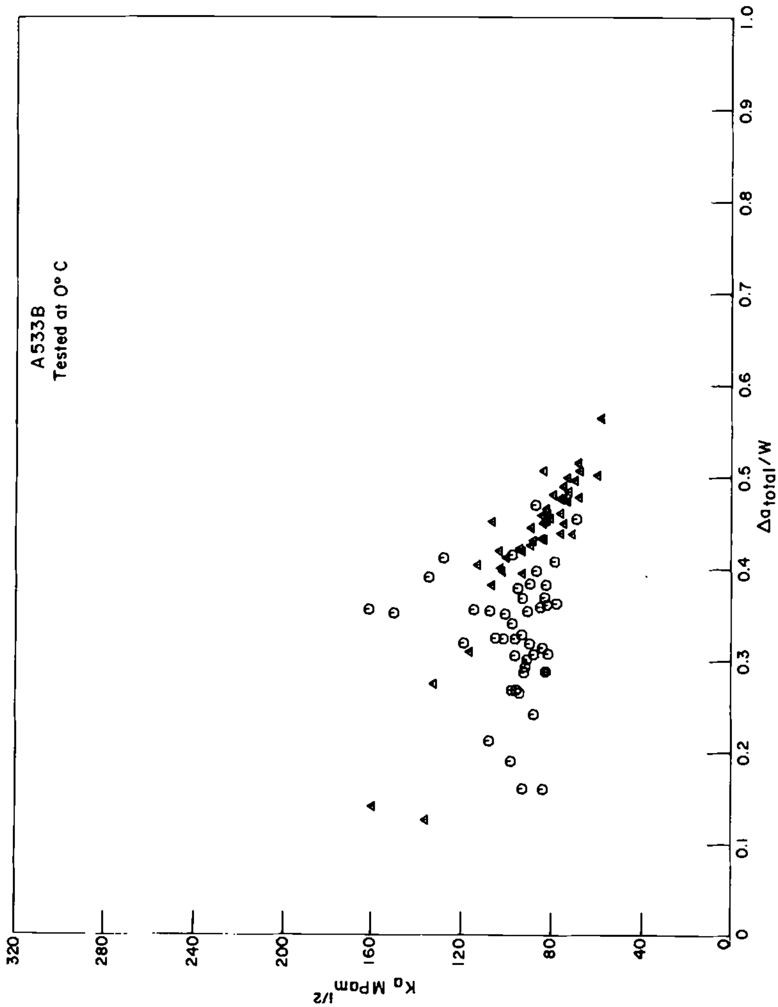

FIG. 8b—*Effect of crack jump length on the K_{Ia} results from the Cooperative Test Program. (Δ) and (○) denote data obtained by the BCL and MRL procedures, respectively. Test temperatures less than 14°C.*

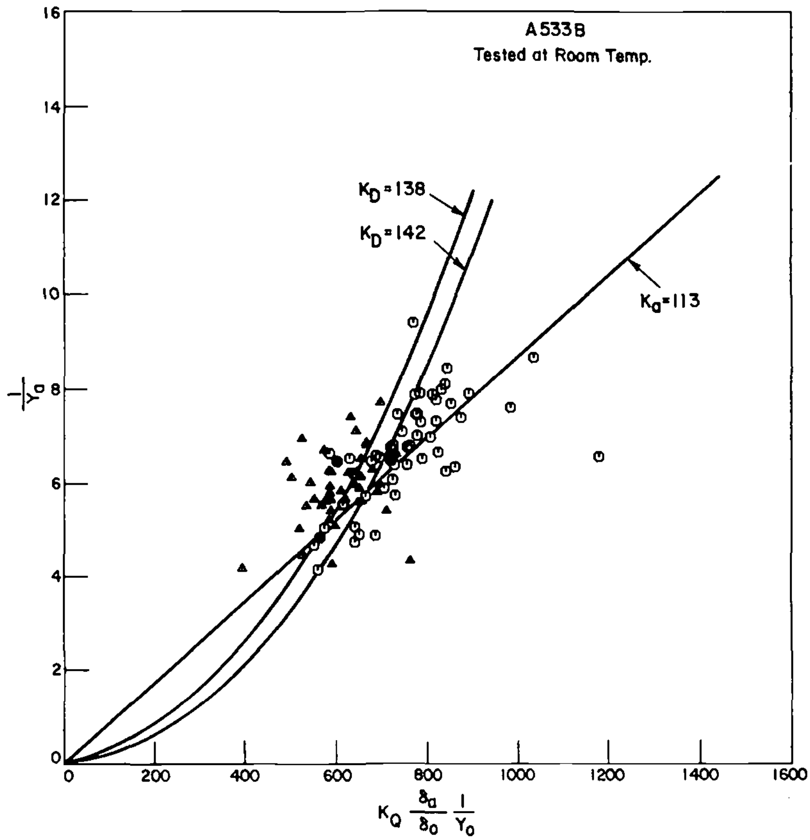

FIG. 9—*Parametric representation of the room temperature, A533B data according to Eq 3.* (Δ) *and* (○) *denote data obtained by the BCL and MRL procedures, respectively.*

measurement of K_{Im}. This type of plot derives from the following considerations. Since K can be computed according to

$$K = \frac{E\delta}{W^{1/2}} Y \tag{1}$$

then K_a can be expressed as

$$K_a = K_Q \left(\frac{\delta_a}{\delta_0}\right)\left(\frac{Y_a}{Y_0}\right) \tag{2}$$

where

δ = displacement measurement.

Y = dimensionless function of a/W, and

$0, a$ = subscripts referring to initiation and arrest conditions, respectively.

It should be noted that the function Y used in the MRL procedure is different from that employed in the BCL procedure because in the former case displacement is measured at $0.25W$ from the load line while in the latter case displacement is measured on the load line.

Equation 2 may be rearranged to give

$$\frac{1}{Y_a} = \frac{1}{K_a}\left[K_Q \left(\frac{\delta_a}{\delta_0}\right)\frac{1}{Y_0}\right] \tag{3}$$

which, if K_a is a constant, is the equation of a straight-line relation between the dependent variable $1/Y_a$ and the independent variable

$$K_Q \frac{\delta_a}{\delta_{0a}} \frac{1}{Y_0}$$

The straight line through the data in Fig. 9 is based on taking K_a = 113 MPa m$^{1/2}$, which is very close to the means of 114 MPa m$^{1/2}$ for the weld-embrittled results and 112 MPa m$^{1/2}$ for the duplex results. On the other hand, the reference curves in the BCL procedure predict a nonlinear relation between $1/Y_a$ and

$$K_Q \frac{\delta_a}{\delta_0} \frac{1}{Y_0}$$

The two curves in Fig. 9 depict this relation derived from the BCL reference curves, taking K_d to be constant and equal to 138 MPa m$^{1/2}$ and 142 MPa m$^{1/2}$ for the weld-embrittled and duplex results, respectively. Both ways of representing the data pass through the center of gravity of the data cluster as they must.

Unlike the authors' Fig. 3*a* and 4*a*, which give an erroneous impression, we find the scatter in the data is too large to distinguish between the static and dynamic method of analysis. This lack of definition holds even though the static and dynamic treatments lead to distinctly different estimates of crack arrest toughness; for example, $K_{Id} \simeq$ 140 MPa m$^{1/2}$ and $K_{Ia} \simeq$ 113 MPa m$^{1/2}$. Consequently, we look to more direct measurements of the crack-tip stress intensity coupled with numerical modeling that provide a more complete description of the run-arrest event to define the contribution of dynamic effects. The direct observations reported in this volume by Kobayashi and Dally[4] and by Kalthoff et al[5] point to relatively small

[4] Kobayashi, T. and Dally, J. W., this publication, pp. 189-210.
[5] Kalthoff, J. F., Beinert, J., Winkler, S., and Klemm, W., this publication, pp. 109-127.

dynamic effects at arrest in the compact specimens. More recent dynamic photoelastic measurements and finite-element calculations by Kobayashi et al[6] with Homalite-100 and polycarbonate show a substantial kinetic energy return prior to arrest. A resolution of these differences is now called for.

P. B. Crosley and E. J. Ripling (authors' closure)—The authors appreciate the discussion prepared by Drs. Hahn, Rosenfield, and Hoagland, but wish to point out that the discussion does not alter the original observations. The Cooperative Test Program results showed that K_{Ia} was independent of K_Q while K_{Id} increased systematically with K_Q. Revising, as the discussers have done, the method of calculating K_Q and, hence, K_{Id}, brings the results from the two specimen types into closer correspondence, but does not change the dependence of K_{Ia} or of K_{Id} on K_Q. These dependencies are wholly consistent with the authors' static approach to crack arrest, and inconsistent with the discussers' dynamic one.

The discussers' present curves which show that K_{Ia} decreases systematically with crack jump distance, Δa. It should be pointed out that a random specimen-to-specimen variation in K_{Ia} will show up as a systematic dependence of K_{Ia} on Δa. Actually, it is Δa that depends on K_{Ia}; cracks will run farther in specimens with lower crack arrest toughness. The authors discuss this in more detail in another paper in this volume.[7] The point is that the observed correlation between K_{Ia} and Δa is not evidence of a "growing" dynamic contribution; dynamic effects should be looked for in the dependence of K_{Ia} and K_{Id} on K_Q, not on Δa. Here, as well as in the dependence on Δa, the results are wholly consistent with the authors' static approach.

In their Fig. 9, the discussers plot the results in a somewhat more complex way to eliminate the "erroneous impression" given by the authors' simple plots of K_{Ia} and K_{Id} versus K_Q. At first sight, it appears that the discussers' representation has succeeded in losing any distinction between the two methodologies within the scatter in the data. It is the authors' opinion, however, in looking closely at the discussers' Fig. 9, that, despite the scatter, the results there are noticeably better represented by the straight-line corresponding to $K_a = 113$ than to either of the curves corresponding to constant K_{Id}.

Finally, the discussers "do agree that a trend of K_{Id} increasing with K_Q remains ... but it would be premature to call upon this dependence to invalidate the dynamic method. ..." This is certainly not the only bit of

[6]Kobayashi, A. S., Seo, K., Jou, J. Y., and Urabe, Y., "Dynamic Analyses of Homalite-100 and Polycarbonate Modified Compact-Tension Specimens," ONR Technical Report No. 35, Department of Mechanical Engineering, University of Washington, Seattle, Wash., March 1979.

[7]Crosley, P. B. and Ripling, E. J., this publication, pp. 321–337.

datum that supports the static rather than their dynamic approach. The following has also been shown:

1. The static approach described the crack jump length in a thermally shocked pressure vessel better than the dynamic approach.[8]
2. By using a static analysis, data collected on fatigue precracked tapered DCB specimens were able to predict whether or not a running crack would arrest in an SEN specimen.[9]
3. K_{Ia} data collected with tapered DCB specimens and compact specimens gave the same scatterband as a function of test temperature.[10]
4. The use of a static analysis was also shown to be justified on the basis of crack velocity and strain measurements made over the course of a run-arrest segment of crack extension.[11]

[8]Crosley, P. B. and Ripling, E. J., "Crack Arrest Studies," Final Report for Electric Power Research Institute Project RP-303-1, March 1979.

[9]Crosley, P. B. and Ripling, E. J. in *Proceedings*, Third International Conference on Pressure Vessel Technology, Part II, Materials, Fabrication and Inspection, San Antonio, Tex., 1973, pp. 995–1005.

[10]Ripling, E. J., Crosley, P. B., and Marston, T. U., in *Proceedings*, American Society of Mechanical Engineers/Canadian Society of Mechanical Engineers, Pressure Vessel and Piping Conference, Montreal, Que., Canada, 25–30 June 1978.

[11]Crosley, P. B. and Ripling E. J. in *Proceedings*, International Conference on Dynamic Fracture Toughness, London, England, June 1976.

C-Lun Chow[1] *and S. J. Burns*[1]

K_{Id}-Values Deduced from Shear Force Measurements on Double Cantilever Beam Specimens

REFERENCE: Chow, C-Lun and Burns, S. J., "**K_{Id}-Values Deduced from Shear Force Measurements on Double Cantilever Beam Specimens,**" *Crack Arrest Methodology and Applications, ASTM STP 711,* G. T. Hahn and M. F. Kanninen, Eds., American Society for Testing and Materials, 1980, pp. 228–239.

ABSTRACT: Time-varying shear force measuring techniques have been used to investigate the dynamic critical stress-intensity factor versus crack propagation velocity curve. The product of the shear force at the loading end times the square root of the loading time on a rapidly wedged double cantilever beam specimen is uniquely related to the critical bending moment at the crack tip. Static compliance measurements on side-grooved specimens were incorporated into a Bernoulli-Euler beam model for calibration purposes and to eliminate the inappropriate built-in beam assumption. The compliance calibration shows a crack length shift from a measured crack length to a beam model length at a fixed compliance value. This shift does not affect the magnitude of the calculated critical bending moment at the crack tip when the load and the load-point displacement are measured quantities. The effective crack length is calculated from the beam model length with the length shift correction. The K_{Id}-values (calculated from the critical bending moment) versus crack velocity have been investigated at several test temperatures for a low-carbon steel. K_{Id}-values show a generally decreasing trend when crack velocity increases. K_{Ic} at fast fracture initiation is larger than the corresponding K_{Id}-value for all tests recorded.

KEY WORDS: cantilever beams, crack propagation, fracture properties, critical stress intensity, crack velocity

A series of K_{Id} versus crack velocity data for AISI 1018 cold-rolled steel, tested at different temperatures, is presented in this paper. K_{Id} versus crack velocity values are calculated from a directly measurable quantity—the time-varying shear force at the loading end of the rapidly wedged double cantilever beam (DCB) specimen.

The fracture initiates from a sharp starting crack in the DCB specimen

[1] Research assistant and professor, respectively, University of Rochester, Rochester, N.Y. 14627. Coauthor Chow is presently at De Havilland Aucraft of Canada, Ltd., Downsview, Ont., Canada.

with rapid wedge loading. Energy is continuously supplied to the test specimen by the time-varying loading force. The slender beam-shaped test specimen has a critical bending moment, M^*, at the crack tip [1,2].[2] M^* is related to the specific fracture surface energy, R, by $M^* = (RwEI)^{1/2}$, where w is the width of the crack path, E is Young's modulus, and I is the moment of inertia of one arm of the beam about the neutral axis. For the constant displacement rate loading DCB, the product of the shear force across the loading end times the square root of the loading time is proportional to M^* [3,4]. Therefore, R can be deduced by measuring the time-varying shear force across the loading end of a DCB specimen. K_{Id} is assumed to be related to R by a simple static relation, $R = K_{Id}^2/E(1 - \nu^2)$, where E is Young's modulus and ν Poisson's ratio.

V-shaped side grooves were machined into all DCB specimens tested in the present work. Because of these grooves, the specimen was softer than beam model predictions. A static compliance measurement incorporated into a Bernoulli-Euler beam model uses a crack length shift at a fixed compliance value. Since $\mathcal{G}$ is proportional to the slope of the compliance versus crack length curve, the length shift correction does not affect the magnitude of the K-value. Therefore, the length shift does not affect the magnitude of the calculated critical bending moment at the crack tip when the load and the load-point displacement are the measured quantities. However, crack lengths obtained through beam models must be shift-corrected. The time derivative of the crack length gives the crack propagation velocity, $\dot{l}$.

In this paper, the test scheme used is briefly described in the first section. Static compliance measurements which lead to corrections to the beam theory are then presented. The K_{Id} versus crack velocity curves are described in a section on experimental results. Comparison of K_{Ic}- and K_{Id}-values at the fracture propagation point are then discussed. Finally, general conclusions are summarized.

Test Scheme

All the DCB specimens are machined to have the longitudinal direction coincide with the rolling direction of the AISI 1018 cold-rolled steel plate. The DCB specimen, which is designed to be a slender beam and to remain essentially elastic throughout the fracture test, has the nominal dimensions of 2.54 by 5.08 by 42 cm. A more detailed description of the design of the DCB specimens has been reported elsewhere [5,6]. A pair of 60-deg V-shaped side-crack guiding grooves were introduced in the thickness direction of each side of the beam. The width of the fractures varies from 0.64 to 1.27 cm by increments of approximately 0.32 cm. The fracture is initiated

[2] The italic numbers in brackets refer to the list of references appended to this paper.

from a short machined starting crack, about 3 cm long, with a swallow-tail cut and fatigued to be totally about 6 cm long. The specimen is fractured by inserting a 30-deg wedge which is attached to a massive, 300-kg hammer that free falls from a wedge drop machine from a height of approximately 2 m. The energy in the wedge is orders of magnitude larger than the energy in the fracture event. The wedge applies an essentially constant deflection rate of about 1.6 m/s on each arm of the DCB specimen. The loading machine has been described in detail in Refs. *5* and *6*.

A 90-deg strain-gage rosette is mounted, close to the loading point, on the neutral axis of one of the DCB arms. The rosette monitors the time-varying shear force across the beam during fracture propagation. The time-varying shear force is recorded for calculating K_{Id}-versus-l values. The gage and recording instruments used for fracture test are experimentally shown to be adequate for the specified DCB specimen [*4*].

Static Compliance Calibration

The side grooves for guiding the crack propagation direction have a significant effect on the deformation of the precracked part of the DCB specimen [*4, 7, 8*]. A detailed description of static compliance measurements on the specified fracture specimen is reported in Ref *4*. The measured compliance values at different simulated crack lengths are shown in Fig. 1. The compliance, C, when plotted as $C^{1/3}$ versus the beam length is a straight line as beam models predict (Curve S). Curve D is based on the dynamic analysis [*2*] and the experimentally measured total fracturing time [*3*] of a specimen with this specified geometry.

The measured compliance value increases monotonically with respect to the simulated crack length, l, and increases rapidly when the crack tip is 1½ beam heights from the free end of the beam. The measured compliance values are a reasonable straight line (Curve E) that does not go through the origin.

Figure 1 shows that the compliance values of the beam models are lower than the measured values for the same crack length. This comparison indicates that the beam length predicted by the simple beam model is longer than the crack length for the same compliance value. Figure 1 also shows that by keeping the compliance value fixed and shifting curve E a distance Δl to Curve S, then both curves will match each other almost perfectly. For any simulated crack length, l, the compliance value is calculated from the simple beam equation in Fig. 1. For this compliance value, a corresponding beam length, $l_m = l_{model}$, of the built-in beam model can be obtained.

$$l = l_m - \Delta l \tag{1}$$

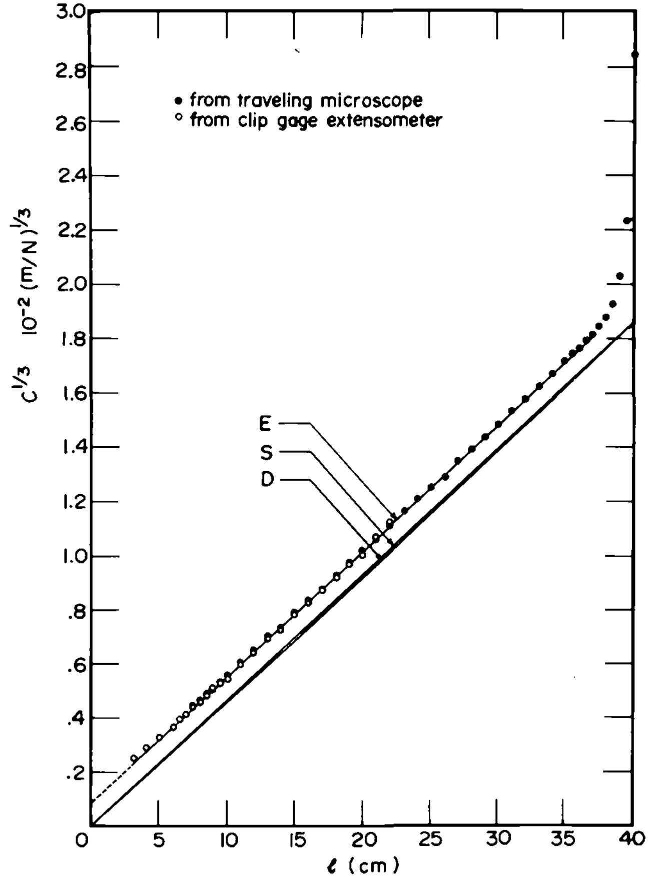

FIG. 1—*Measured compliance values and beam model compliances versus crack lengths. Curve E is a fitted curve of measured values. Curve S is a Bernoulli-Euler beam on a rigid foundation with V-shaped side-grooved cross section. Curve D is a dynamic Bernoulli-Euler beam on a rigid foundation with a V-shaped side-grooved cross section.*

Δl depends on specimen geometry including the side grooves and may depend on elastic moduli as well. Figure 2 is a plot of l versus l_m from the measured compliance. The curve is fitted linearly to have a slope of 1 and the Δl-value is found to have an average value of 1.84 cm with at most -8 percent deviation at the initial crack length and less than ± 2 percent for $l > 8$ cm. Equation 1 is the calibration that relates the crack length to a simple beam crack model.

Fracture Test Data

Typical recorded fracture test data of the time-varying shear force, $Q(t)$, which is monitored by a 90-deg strain-gage rosette, are shown in Fig. 3. A

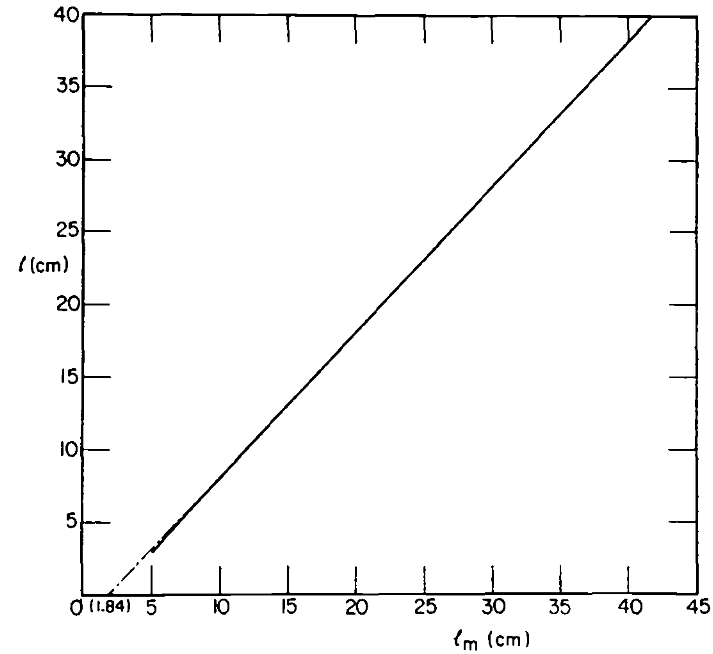

FIG. 2—*Corresponding beam model crack length* l_m *at a fixed compliance value versus the measured length,* l.

detailed description of these data have been reported in Ref *4*. The $Q(t)$ trace is digitized to form $Q(t)t^{1/2}$, which is proportional to the critical bending moment at the crack tip, M^*. However, a smoothed $Q(t)t^{1/2}$ curve is used to calculate $R(t)$ since the oscillations that appear on $Q(t)$ and $Q(t)t^{1/2}$ are believed to be from stress waves producing complex beam vibrations. The numerically smoothed $Q(t)t^{1/2}$ curve is constructed from only three constants: the first gives the average K_{Id}-values; the second specifies if K_{Id} increases or decreases with velocity; and the last looks for a minimum in the curve. The smoothed $Q(t)t^{1/2}$ curve is used to provide, first, R (t), and thus $K_{Id}(t)$, as mentioned earlier, and second, $l_m(t)$ by the built-in beam model [*2-4*]. $l_m(t)$ is corrected by Eq 1 to provide an effective crack length $l(t)$. The derivative of $l(t)$ gives the crack propagation velocity, $\dot{l}(t)$. At each instant of time there is a K_{Id} and a corresponding $\dot{l}$-value. Thus, K_{Id} versus $\dot{l}$ from a single test can be obtained.

Experimental Results

K_{Id}-versus-$\dot{l}$ curves are the final results from the rapid wedging dynamic fracture test. The test temperatures used in this study were −196, −140, −78, −60, −40, and 0°C.

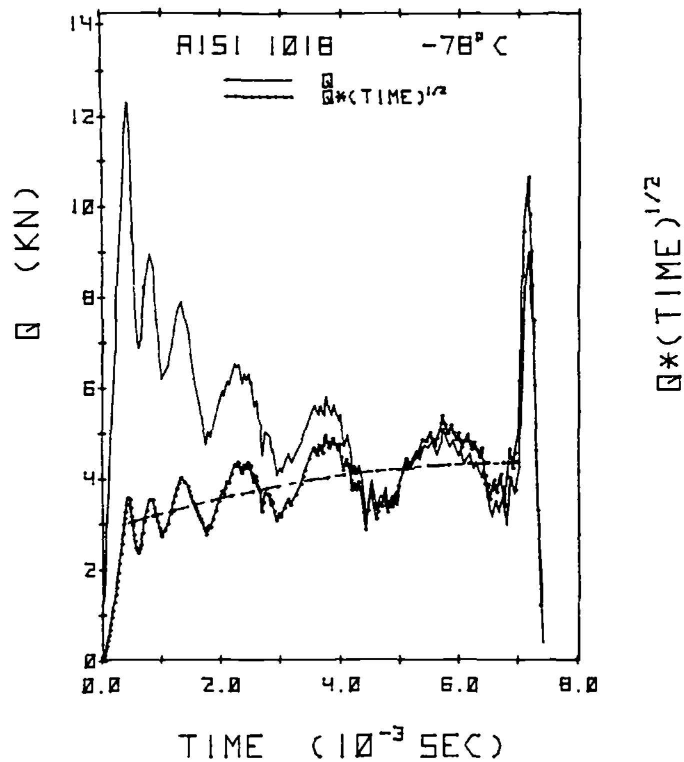

FIG. 3—*Scaled and smoothed* Q(t) *and* $Q(t)t^{1/2}$ *traces for the test at* $-78°C$. *The peaks shown on* Q(t) *are also shown on* $Q(t)t^{1/2}$.

The fracture surfaces of the specimens tested at $-196°C$ are reasonably flat. In addition to the flat fracture, there are only very small shear lips. The thickness of the specimen satisfies the static requirement for plane-strain conditions. Thus, the dynamic stress-intensity values are presumably plane strain. Figure 4 shows the summary of these tests. K_{Id} decreases as $\dot{l}$ increases when $\dot{l}$ is below about 50 m/s. K_{Id} reaches a minimum value versus $\dot{l}$ in the range of 50 to 80 m/s. As $\dot{l}$ becomes higher than 80 m/s, K_{Id} increases slightly as $\dot{l}$ increases. The upper three curves, (i), (ii), and (iii), show higher K_{Id}-values at high $\dot{l}$ values. This may be due to a slight temperature gradient occurring throughout the specimen. The temperature close to the crack initiation end is slightly higher than the temperature at the far end of the specimen. The specimen from the two lower curves, (iv) and (v), have been very carefully controlled to give a uniform temperature. The slightly increasing trend of the K_{Id}-versus-$\dot{l}$ plot on the high $\dot{l}$ side may also be due to overestimating the resistance to fracture initiation because the starting crack, which is saw-cut, is not sharp enough—although it is dovetailed.

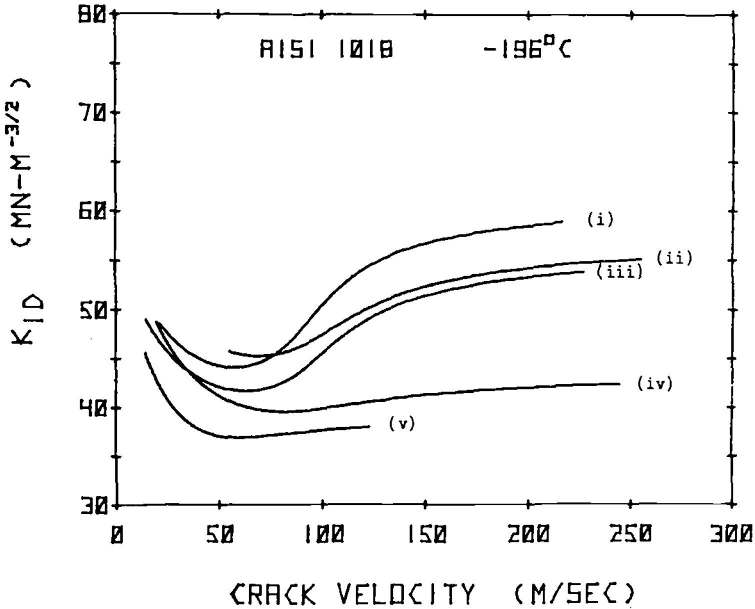

FIG. 4—K_{Id} versus $\dot{l}$ *for a series of tests at −196°C.*

The fracture surface for the −140°C test is reasonably flat and is similar to tests at −196°C. The starting crack on this specimen is also saw-cut. K_{Id} versus $\dot{l}$ behaves the same as for the −196°C tests; see Fig. 5.

The fracture surface for the test at −78°C is flat for the most part and appears rough near the very end of the specimen. A fatigue precrack is the starting crack. K_{Id} decreases monotonically as $\dot{l}$ increases in the tested $\dot{l}$ range as Fig. 6 shows. K_{Id}-values from both Curves (i) and (ii) have good reproducibility although the $\dot{l}$-range changes quite a bit.

K_{Id} vs $\dot{l}$ for the −60°C tests is shown in Fig. 7. All three specimens broke only halfway down the beam. The fracture surfaces were still quite flat. Curve (i) of K_{Id} versus $\dot{l}$ shows a minimum around $\dot{l}$ = 50 m/s. This minimum may be due mostly to a temperature gradient (as mentioned early in this section) throughout the specimen, and partly due to the bluntness of the starting crack. Specimens for Curves (ii) and (iii) have been carefully temperature controlled and have fatigued precracks. The low-end $\dot{l}$ values may deviate quite a bit from the true $\dot{l}$, yet K_{Id}-values show nice reproducibility.

Both specimens tested at −40 and 0°C have fractured over 30 cm and then have broken off. A fatigue precrack is used as the starting crack. The fracture path is quite flat at the beginning part and then turns rough in the latter part of the specimen. In addition to the roughness of the fracture path, there are a lot of broken ligaments on the fracture surfaces. These

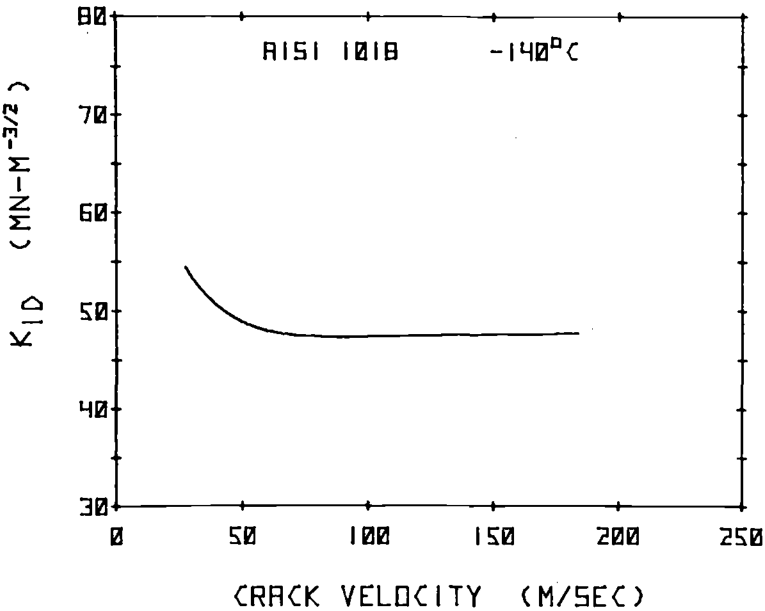

FIG. 5—K_{Id} *versus* $\dot{l}$ *for the test at* $-140°C$.

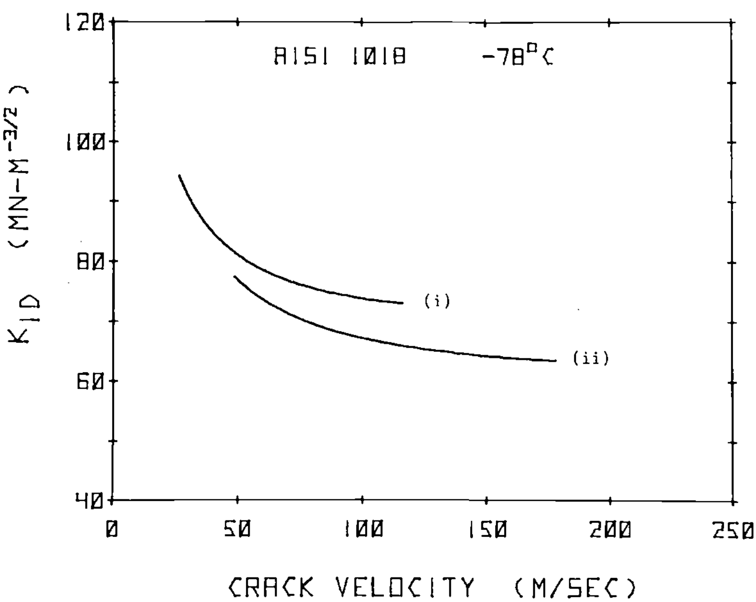

FIG. 6—K_{Id} *versus* $\dot{l}$ *for the tests at* $-78°C$.

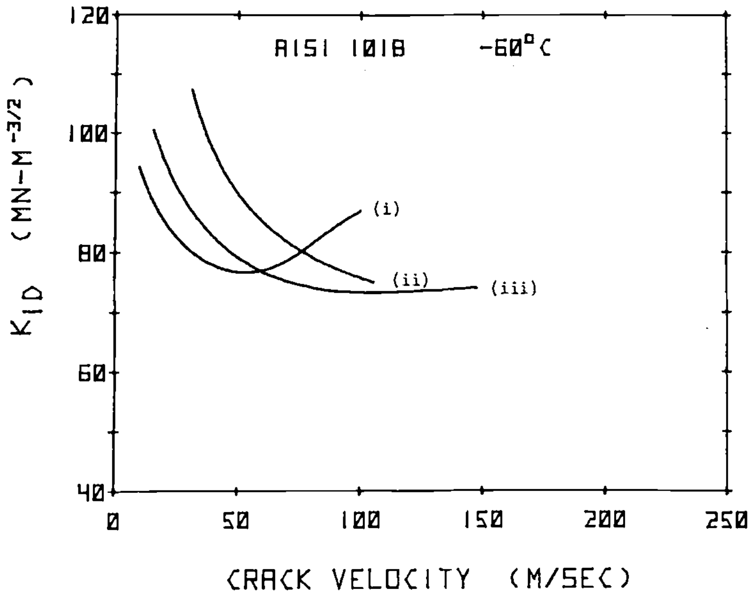

FIG. 7—K_{Id} *versus* $\dot{l}$ *for the tests at* $-60°C$.

effects cause the crack to propagate quite slowly, and K_{Id} is very high at low $\dot{l}$-values; see Figs. 8 and 9. Figure 10 is a plot of $Q(t)$ and $Q(t)t^{1/2}$ versus t for the 0°C specimen. The stress wave oscillations on $Qt^{1/2}$ are significantly smaller than the absolute change in the value of $Qt^{1/2}$ during the test. It follows that at higher temperatures the rate dependence of crack propagation is a significantly stronger effect than the stress wave oscillations.

For all specimens with either swallow-tailed starting cracks or fatigue precracks, the peak-load K_{Ic}-values are higher than the K_{Id}-values at the highest crack velocities. A typical example is shown in Fig. 3. K_{Ic} corresponds to the first peak in the $Q(t)t^{1/2}$ trace. Physically, this point indicates the onset of fast fracture propagation as discussed in Ref *4*. K_{Id} is the corresponding point at the same time value on the smoothed $Q(t)t^{1/2}$ curve. The peak point is always higher (higher value in $Qt^{1/2}$ scale) than the corresponding point on the smoothed curve. The higher $Qt^{1/2}$-value gives a higher stress-intensity value, $\dot{K}$-values for all the K_{Ic} tests reported vary from 1.2×10^5 to 5×10^5 (MN m$^{-3/2}$)/s.

Conclusions

Time-varying shear force measurements have been applied to double cantilever beam specimens for studying dynamic crack propagation. This technique is based on the theory that the shear force across the loading end

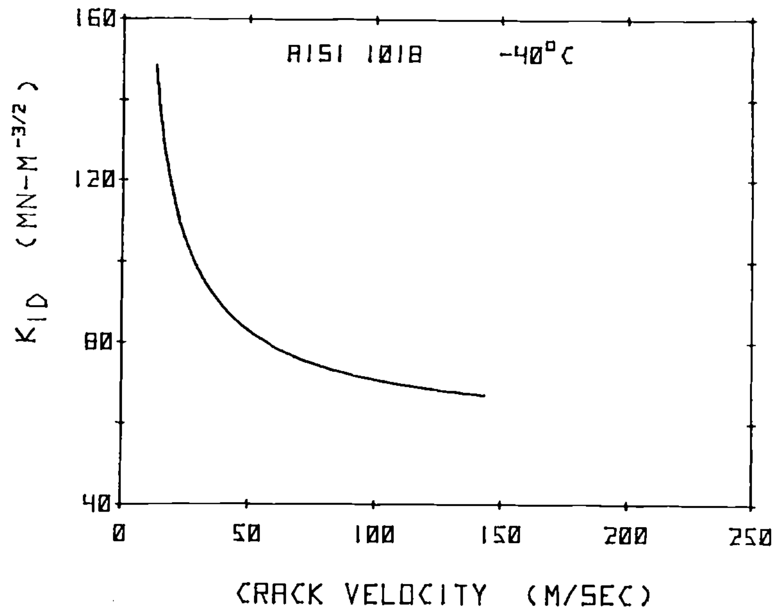

FIG. 8—K_{Id} versus $\dot{l}$ *for the test at −40°C.*

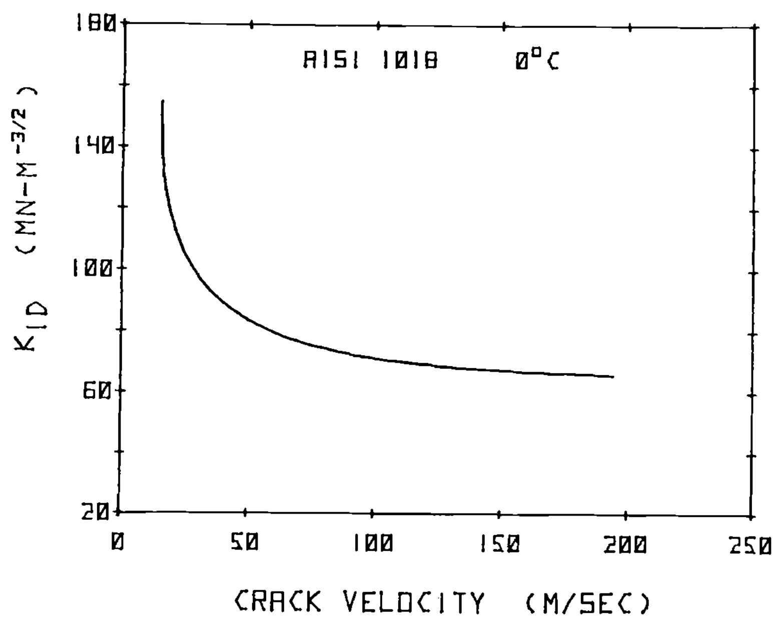

FIG. 9—K_{Id} versus $\dot{l}$ *for the test at 0°C.*

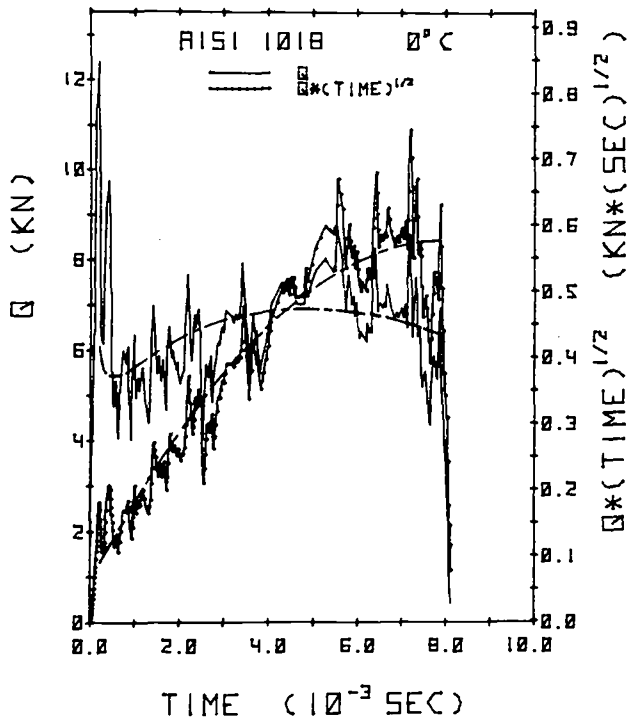

FIG. 10—*Scaled and smoothed* Q(t) *and* Q(t)t$^{1/2}$ *races for the test at 0°C. The rate effect is large since the value of* Q(t)t$^{1/2}$ *changes dramatically in the test.*

of a rapidly wedged slender DCB specimen times the square root of the loading time is proportional to the critical bending moment at the crack tip, M^*. Static compliance measurements were used to incorporate the built-in beam model to the side-groove effects on the DCB specimen. The constant length shift correction will not affect the magnitude of M^* and gives an effective crack length after correction. This correction is valid even for more-sophisticated beam models [*9,10*] with side grooves [*4*]. $Q(t)t^{1/2}$ is numerically smoothed to eliminate stress wave oscillations and this smoothed curve then provides the information for calculating $K_{\text{Id}}(t)$ and $\dot{l}(t)$. K_{Id} versus $\dot{l}$ has a generally decreasing trend as $\dot{l}$ increases, and $|\partial K_{\text{Id}}/\partial|$ increases as temperature increases. For a single test, $\dot{l}$ usually varies by a factor of 10.

This rapidly wedged DCB specimen test is unique in that the crack velocity starts at a high value and decreases throughout the test. The test has stability when K_Q at initiation is approximately the same value as K_{Id} and $\partial K_{\text{Id}}/\partial \dot{l}$ is negative. This keeps the crack's K-value during the fracture event continually increasing. Crack propagation-arrest test specimens, however, seem to dominantly test where $\partial K_{\text{Id}}/\partial \dot{l}$ is positive. Since

$\partial K_{\text{Id}}/\partial \dot{l}$ is negative in the low range of crack speeds, slow crack velocities are typical of the rapidly wedged DCB test. Occasionally a test specimen breaks an "arm" during testing. This phenomenon is associated with the lack of stability of the fracture plane remaining on the symmetry plane of the slender DCB specimen. When the crack leaves the symmetry plane, the K-values tabulated are suspect. The reproducibility of the fracture tests was shown in the previous section. For achieving good reproducibility, a stiff wedge, a fatigued starting crack, and a well-controlled temperature environment are recommended. K_{Ic}-values at the onset of fast fracture propagation are also noted. These values are higher than the corresponding K_{Id}-values for all the tests at different temperatures for this low-carbon steel.

Acknowledgments

This work was supported by the U.S. Department of Energy through Contract EY-76-S-02-2422 at the University of Rochester.

References

[1] Gurney, C. and Hunt, J. in *Proceedings*, Royal Society of London, Vol. A299, 1967, p. 508.
[2] Bilek, Z. J. and Burns, S. J.: *Journal of the Mechanics and Physics of Solids*, Vol. 22, 1974, p. 85.
[3] Burns, S. J. and Chow, C-L., in *Fast Fracture and Crack Arrest, ASTM STP 627*, American Society for Testing and Materials, 1977, p. 228.
[4] Chow, C-Lun and Burns, S. J., *International Journal of Fracture*, Vol. 15, 1979, p. 457.
[5] Burns, S. J., Air Force Materials Laboratory Technical Report "Crack Arrest in Titanium," AFML-TR-75-101, Wright-Patterson Air Force Base, Dayton, Ohio, July 1975.
[6] Burns, S. J. in *Proceedings*, 12th Annual Meeting of Society of Engineering Science, University of Texas, Austin, Tex., Oct. 1975, p. 121.
[7] Berry, J. P., *Journal of Applied Physics*, Vol. 34, 1963, p. 62.
[8] Hoagland, R. G., *Journal of Basic Engineering*, Vol. 89, 1967, p. 525.
[9] Kanninen, M. F., *International Journal of Fracture*, Vol. 10, 1974, p. 415.
[10] Malluck, J. F. and King, W. W., *International Journal of Fracture*, Vol. 13, 1977, p. 655.

Z. Bílek[1]

Some Comments on Dynamic Crack Propagation in a High-Strength Steel

REFERENCE: Bilek, Z., "**Some Comments on Dynamic Crack Propagation in a High-Strength Steel,**" *Crack Arrest Methodology and Applications, ASTM STP 711,* G. T. Hahn and M. F. Kanninen, Eds., American Society for Testing and Materials, 1980, pp. 240–247.

ABSTRACT: The dependence of the dynamic plane-strain fracture toughness, K_{Id}, on crack velocity was measured for propagating cracks in SAE4340 steel at room temperature. It has been shown that K_{Id} for SAE4340 steel in the quenched-and-tempered condition increases slowly for increasing crack velocity up to $\dot{a} \approx 100$ m/s and then increases sharply above 100 MNm$^{-3/2}$ at $\dot{a} > 1000$ m/s.

KEY WORDS: crack propagation, crack velocity, dynamic fracture toughness, double cantilever beam specimen, high-strength steel, axial force

Nomenclature

a	Crack length
$\dot{a}$	Crack-tip velocity
A	Cross-sectional area of one arm of specimen
C_L	Longitudinal wave velocity
C_S	Shear wave velocity
DCB	Double cantilever beam
E	Modulus of elasticity
F_k	Generalized dissipative force
G	Shear modulus
h	Half height of the specimen, Fig. 1
I	Moment of inertia of one arm of beam
K_{Ic}	Static fracture toughness
K_{Id}	Dynamic fracture toughness for a running crack
M	Applied bending moment

[1]Senior research scientist, Department of Mechanical Properties, Institute of Physical Metallurgy, Czechoslovak Academy of Sciences, 616 62 BRNO Zizkova 22, Czechoslovakia; formerly with Brown University, Providence, R.I.

q_k Generalized coordinate
Q Shear force
t Time
T Kinetic energy
u Displacement of neutral axis of beam, Fig. 1
V Potential energy
V_e Constant end loading velocity of beam
W Specimen thickness
x, y Rectangular coordinates, Fig. 1
γ Effective specific surface energy
γ_o Reversible specific surface energy
γ_p Irreversible specific surface energy
ψ Mean angle of rotation of cross section about neutral axis
ν Poisson's ratio
ρ Density
σ_{ys} Static uniaxial yield stress

The fracture failure of pressurized pipelines, bridge girders, or ship hulls can be prevented by stopping propagating cracks before the structural integrity of the unit is completely lost. Crack arrest in a structure requires that the dynamic stress-intensity factor in the structure be less than the material's dynamic fracture toughness K_{Id}. This paper is concerned with dynamic crack propagation in the commercially important SAE4340 steel. The discussion consists of (1) a description of the DCB specimen model being used for experimental data analysis at the Institute of Physical Metallurgy, and (2) a brief summary of the most important results on K_{Id} measurements by two independent experimental procedures. It is the author's hope that the research results reported here will provide further insight into dynamic fracture and will be of use in the improvement of K_{Id} measurements.

A Model of the DCB Specimen Using a Timoshenko Beam on a Rigid Foundation

The geometry of the DCB specimen loaded by a time-dependent force $Q(t)$ and a bending moment $M(t)$ is schematically illustrated in Fig. 1. The loading causes a horizontal crack to propagate from left to right. In elaborating the mathematical model, because of symmetry we shall consider only the upper half of the specimen in the rectangular coordinate system x, y. The origin for this system is at the loaded end of the specimen, as shown in Fig. 1. The motion of the crack at any time must be in agreement with Hamilton's principle for nonconservative systems

$$\int \left[\delta(T - V) + \sum_{k=1}^{m} F_k \delta q_k \right] dt = 0 \tag{1}$$

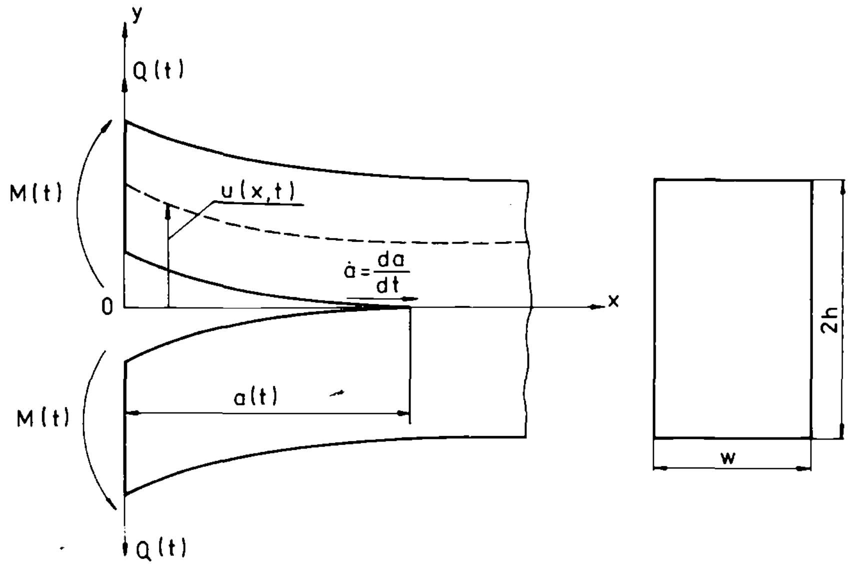

FIG. 1—*Schematic illustration of a DCB specimen opened by a force* Q(t) *and a bending moment* M(t), *including the notation used to describe the specimen geometry and the coordinate system.*

where

T = kinetic energy,
V = potential energy of system,
F_k = kth generalized dissipative force, and
q_k = kth generalized coordinate.

According to the Timoshenko theory of elastic beams, the kinetic energy is

$$T = \frac{1}{2}\int_0^{a(t)} \left[\rho A \left(\frac{\partial u(x,\ t)}{\partial t}\right)^2 + \mathrm{I}\rho \left(\frac{\partial \psi(x,\ t)}{\partial t}\right)^2\right] dx \qquad (2)$$

where

$A = wh$ = cross-sectional area,
ρ = mass density, and
$u(x,\ t),\ \psi(x,\ t)$ = average deflection of cross section and mean angle of rotation of cross section about the neutral axis, respectively.

The potential energy arises from strain energy of the bent part of the beam, the reversible surface energy calculated by integrating the reversible specific surface energy γ_0 over the fracture area, and from work done by the applied shear force $Q(t)$ and the applied bending moment $M(t)$

$$V = \frac{1}{2}\int_0^{a(t)} \left[EI\left(\frac{\partial\psi(x, t)}{\partial x}\right)^2 + GA\left(\frac{\partial u(x, t)}{\partial x} - \psi(x, t)\right)^2\right]dx$$
$$+ \gamma_o wa(t) - Q(t)u(0, t) - M(t)\psi(0, t) \quad (3)$$

where

E = Young's modulus,
ν = Poisson's ratio,
$G = E/2(1 + \nu)$, and
$I = wh^3/12$ = moment of inertia for a rectangular beam of height h.

The irreversible part of the surface energy γ_p gives a generalized dissipative force

$$F_1 = w\gamma_p \quad (4)$$

By inserting Eqs 2-4 into Hamilton's principle, Eq 1, we obtain, following some variational manipulations [12][2]

$$\frac{\partial^2 u(x, t)}{\partial x^2} - \frac{\partial\psi(x, t)}{\partial x} = \frac{1}{C_S^2}\frac{\partial^2 u(x, t)}{\partial t^2}, \qquad C_S^2 = \frac{G}{\rho}, \qquad C_L^2 = \frac{E}{\rho}$$
$$\frac{\partial^2\psi(x, t)}{\partial x^2} + \frac{A}{I}\frac{C_S^2}{C_L^2}\left(\frac{\partial u(x, t)}{\partial x} - \psi(x, t)\right) = \frac{1}{C_L^2}\frac{\partial^2\psi(x, t)}{\partial t^2} \quad (5)$$

$$GA\left(\frac{\partial u(x, t)}{\partial x} - \psi(x, t)\right) - Q(t), \qquad EI\frac{\partial\psi(x, t)}{\partial x} = M(t) \quad (6)$$

for $x = 0$, and for $x = a(t)$

$$\left(\frac{\partial u(a, t)}{\partial x}\right)^2 \frac{C_S^2}{C_L^2}\frac{A}{I}\left[1 - \left(\frac{\dot{a}(t)}{C_S}\right)^2\right]$$
$$+ \left(\frac{\partial\psi(a, t)}{\partial x}\right)^2\left[1 - \left(\frac{\dot{a}(t)}{C_L}\right)^2\right] = \frac{2\gamma w}{EI}, \quad (7)$$

where γ is specific fracture surface energy and is given by the sum of the reversible and irreversible specific fracture surface energies

$$\gamma = \gamma_o + \gamma_p \quad (8)$$

In addition, the symmetry of the problem and the assumed rigid support of

[2]The italic numbers in brackets refer to the list of references appended to this paper.

the beams at the crack tip specify the deflection and the rotation of the deflected beam at the crack tip [that is, $x = a(t)$] as zero

$$u[a(t), t] = 0, \qquad \psi[a(t), t] = 0 \tag{9}$$

The Timoshenko beam equations, Eqs 5, represent a special case of the more general equations, derived by Kanninen [*1*], for a beam on an elastic foundation. Equation 7 gives the fracture criterion at the crack tip. For long slender DCB specimens, such as used in Refs *2-4*, Eqs 5 may be reduced to one equation of Bernoulli-Euler beam motion, and the fracture criterion, Eq 7, then yields the condition on the bending moment at the crack tip

$$EI\frac{\partial^2 u(a, t)}{\partial x^2} = (2\gamma wEI)^{1/2} \tag{10}$$

recently derived by Bílek and Burns [*5*]. It is interesting to point out that Eq 7 restricts maximum crack velocity in the DCB specimen to C_L although the less-general expression, Eq 10, allows virtually unlimited $\dot{a}(t)$.

Equations 5 represent a hyperbolic system which is readily solvable numerically, with the boundary and initial conditions corresponding to the current experimental procedures, by using a least-squares or a finite-difference technique. In particular, for fixed displacement loading [$u(0, t) =$ constant] or constant opening rate loading [$u(0, t) = V_e t$], the specific fracture energy γ (and hence K_{Id}) may be calculated from the recorded crack length dependence on time. Also, the crack velocity profile may be found if the function $\gamma(\dot{a})$ [or $K_{Id}(\dot{a})$] is specified.

Dependence of Fracture Toughness of SAE4340 Steel on Crack Velocity

Studies of unstable and stable crack propagation over a wide range of crack velocities were carried out [*6*] in order to establish the $K_{Id} - \dot{a}$ dependence in SAE4340 high-strength steel in the quenched-and-tempered condition: oil-quenched at 870°C and tempered at 385°C for 1 h ($\sigma_{ys} = 1367$ MNm^{-2}). The unstable crack propagation study employed DCB specimens which were slowly wedge-loaded as described in Refs *7-9*. Essentially, the identical specimen geometry used recently to investigate SAE4340 steel properties [*10,11*] was applied, the only difference being that the specimen thickness was increased to 25 mm to meet the ASTM Test for Plane-Strain Fracture Toughness of Metallic Materials (E 399-74) requirements at high crack velocities. The crack velocity was varied by changing the root radius of the starting notch from 0.2 to 1 mm; crack velocities were measured using crack propagation gages of Type MM CPC 03. During a typical test, a steady-state velocity was maintained from the start until shortly before arrest. Only for $\dot{a} > 1000$ m/s did the crack velocity vary somewhat between fracture initiation and crack arrest. This behavior is consistent with earlier results on PMMA [*12*] and it is obviously related to a strong increase of K_{Id} with crack velocity [*13*]. The effect of vertical compressional force was eliminated with the help of the tie-down device proposed in Ref *7*. The dynamic fracture toughness values, K_{Id}, calculated by the model proposed in the previous section are shown in Fig. 2 for 20 specimens successfully fractured (from 25 specimens tested).

Rapidly wedged DCB specimens were used to produce a stable crack propagation with crack velocities $\dot{a}$ < 150 m/s. Rigid loading of the test specimen was achieved by using a 25-deg wedge firmly mounted on the bottom of the moving carriage of a drop-weight fracture machine used for NDT testing. Specimens of outside dimensions 55 mm high by 25 mm wide by 380 mm long, with deep side grooves similar to the specimens designed in Refs *3* and *6* were used. The thickness of 12.5 mm across the grooved section was sufficient to provide valid plane-strain K_{Id} data. The R.F. current technique developed by Carlsson [*14*] was applied to measure crack length versus time. The crack velocity in DCB specimens that are opened at a constant rate varies continuously throughout the test; it decreases as the crack length increases, so that K_{Id} may be recorded as a function of $\dot{a}$ in a single test. The

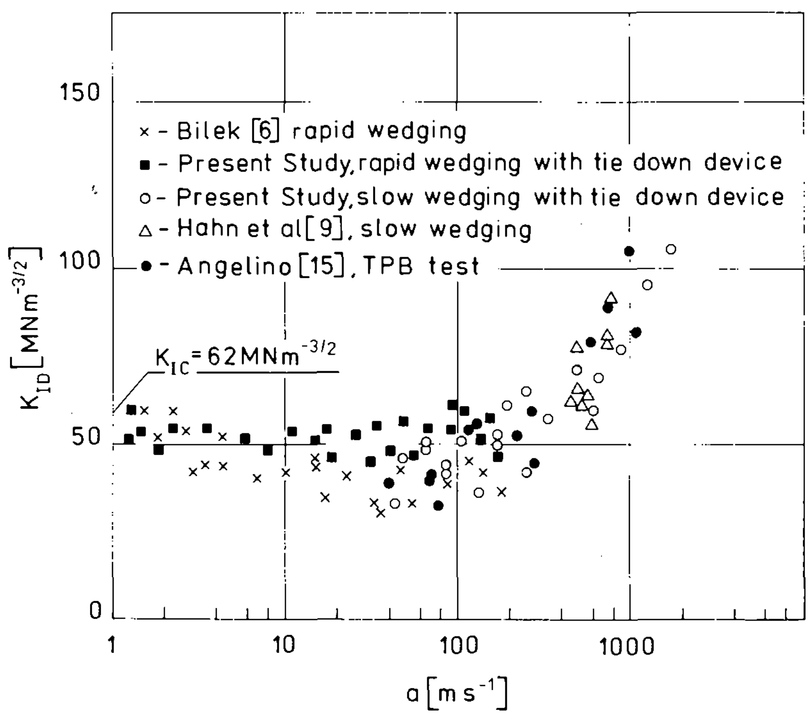

FIG. 2—*Velocity dependence of* K_{Id} *values for SAE4340 steel. A logarithmic abscissa is used because of the wide range of* $\dot{a}$.

K_{Id} data are calculated numerically from a Timoshenko beam model were nearly identical, within numerical errors, to data obtained directly from the analytic Bernoulli Euler beam model [*5*]. The foregoing analyses tacitly assume a DCB specimen ideally wedged at a constant rate and ignore the effect of axial force produced by wedging. The K_{Id} data for SAE4340 steel [*6*] were not properly treated from this point of view. In the course of this work we removed completely the influence of axial force, using the tie-down device similar to the device used in slow wedging tests. The K_{Id} results are plotted in Fig. 2. In the same figure, the Battelle data [*9*] and recent data by Bílek [*6*] on the same steel are plotted, as well as the data derived by Angelino [*15*] from three-point bend (TPB) tests for a similar steel, UCN-100. Figure 2 clearly indicates the influence of axial force on rapid wedging K_{Id} data and consequently on the interpretation of the $K_{Id} - \dot{a}$ curve. The K_{Id}-values are somewhat higher in their dependence on crack velocity when the tie-down device is used. Within the experimental error the K_{Id}-values are a constant or slightly increasing function of up to $\dot{a} \approx 100$ m/s and then increase sharply in accordance with the results of Refs *9* and *15*. This conclusion is also consistent with the results from photoelastic coating on 4340, obtained by Kobayshi in this symposium, which had a minimum K_{Id} at zero velocity. In addition, the K_{Id} data determined from stable (rapid wedging) and unstable (slow wedging) measurements correspond well in the velocity range $\dot{a} = 60 \div 150$ ms^{-1}, demonstrating a significant similarity in these two experimental methods discussed already by Malluck and King [*16*].

The preliminary fractographic measurements revealed the predominantly intergranular fracture with secondary cracks at high crack velocities ($\dot{a} >$ 100 m/s). In specimens fractured at relatively low velocity, the fracture is intergranular; however, some well-developed cleaved areas are observed, and the transition between intergranular and cleaved areas is often marked by dimpled regions.

Conclusion

The concepts of the slowly and rapidly wedged DCB specimens have proven to be useful tools for dynamic fracture toughness measurements for a wide range of crack velocities. The K_{Id} data presented in this paper are self-consistent and the agreement with other values in the literature is good. Both experimental techniques are extensively used to study $K_{Id} - \dot{a}$ dependence for various steels at different temperatures [*17*]. With the help of the tie-down device proposed in Ref *7*, the effect of vertical compressive force was eliminated in slow and rapid wedging experiments. However, further investigations of this effect on crack dynamics in rapidly wedged specimens are necessary. Specifically, a detailed numerical analysis is desirable that takes into account the influence on crack propagation of the stress waves generated by the wedge impact.

Acknowledgment

The research summarized here was carried out with support from U.S. National Academy of Sciences and the Materials Research Laboratory at Brown University. It is a pleasure to acknowledge the helpful discussions I had with Drs. G. T. Hahn, M. Kanninen, A. Rosenfield, and P. Gehlen, the assistance of Sara Mancino in the manuscript preparation, and communications with Professors S. J. Burns, J. R. Rice and L. B. Freund.

Finally, I would like to dedicate this paper to Academician P. Rys, director of the Institute of Physical Metallurgy, on the occasion of his 60th birthday, as an expression of my thanks for his many years of help and encouragement.

References

[*1*] Kanninen, M. F., *International Journal of Fracture*, Vol. 10, 1974, p. 415.
[*2*] Burns, S. J. and Bílek, Z., *Metallurgical Transactions*, Vol. 4, 1973, p. 975.
[*3*] Burns, S. J. and Chow, C. L. in *Fast Fracture and Crack Arrest, ASTM STP 627*, American Society for Testing and Materials, 1976, p. 228.
[*4*] Bílek, Z. and Burns, S. J. in *Proceedings*, International Conference on Dynamic Crack Propagation, Bethlehem, Pa., 1972, p. 371.
[*5*] Bílek, Z. and Burns, S. J., *Journal of the Mechanics and Physics of Solids*, Vol. 22, 1974, p. 85.
[*6*] Bílek, Z., *Scripta Metallurgica*, Vol. 12, 1978, p. 1101.
[*7*] Hoagland, R. G. et al in *Fast Fracture and Crack Arrest, ASTM STP 627*, American Society for Testing and Materials, 1977, p. 177.
[*8*] Hahn, G. T. et al in *Fracture Mechanics*, N. Perrone et al, Eds., 1978, p. 205.
[*9*] Hahn, G. T. et al, "Critical Experiments, Measurements, and Analyses to Establish a Crack-Arrest Methodology for Nuclear Pressure Vessel Steels," Reports to the U.S. Nuclear Regulatory Commission, Battelle Columbus Laboratories, Columbus, Ohio, 1974-1976.
[*10*] Hahn, G. T. et al, *Metallurgical Transactions*, Vol. 5, 1974, p. 475.
[*11*] Hahn, G. T. et al, *Metallurgical Transactions*, Vol. 7, 1976, p. 43.
[*12*] Bílek, Z. and Kysclák, P. in *Proceedings*, International Conference on Materials Behaviour Under Impulsive Loading, Brno, Czechoslovakia, 1978, p. 34.
[*13*] Freund, L. B., *Journal of the Mechanics and Physics of Solids*, Vol. 25, 1977, p. 69.
[*14*] Carlsson, J., *Transactions*, Royal Institute of Technology, Vol. 189, 1962, p. 1.
[*15*] Angelino, G. C. in *Fast Fracture and Crack Arrest, ASTM STP 627*, American Society for Testing and Materials, 1977, p. 392.
[*16*] Malluck, J. F. and King, W. W., *International Journal of Fracture*, Vol. 13, 1977, p. 655.
[*17*] Bílek, Z., "The Dynamic Crack Propagation in Structural Steels," Research Report, Institute of Physical Metallurgy, Brno, Czechoslovakia, 1979 (in Czech).

G. T. Hahn,[1] *R. G. Hoagland,*[1] *A. R. Rosenfield,*[2] *and C. R. Barnes*[2]

A Cooperative Program for Evaluating Crack Arrest Testing Methods

REFERENCE: Hahn, G. T., Hoagland, R. G., Rosenfield, A. R., and Barnes, C. R., **"A Cooperative Program for Evaluating Crack Arrest Testing Methods,"** *Crack Arrest Methodology and Applications, ASTM STP 711,* G. T. Hahn and M. F. Kanninen, Eds., American Society for Testing and Materials, 1980, pp. 248-269.

ABSTRACT: Early and incomplete results of a multilaboratory test program examining two procedures for measuring crack arrest toughness are presented. The program involves 30 laboratories, with each participant conducting 10 tests, including eight of a common heat of A533B steel. The preliminary results are encouraging. No special difficulties in applying the test procedures have been encountered and the test specimens are performing satisfactorily. The results appear to be quite reproducible. Crack arrest toughness values derived from the two procedures with a static analysis agree closely, but values calculated using a dynamic analysis differ by about 50 percent. A possible source of this discrepancy is identified.

KEY WORDS: Cooperative Test Program, crack arrest toughness, A533B steel

The details of two new sets for measuring crack arrest toughness were presented by Crosley and Ripling [*1*][3] and Hoagland et al [*2*] on 23 March 1977 at the meeting of the ASTM Dynamic Initiation-Crack Arrest Task Group (now E-24.01.07). Following discussions, the Task Group approved a suggestion by W. F. Brown, Jr. to carry out a multilaboratory cooperative testing program designed to acquaint potential users with the two test procedures. Representatives of nine U.S. laboratories at the meeting expressed interest in participating, and G. T. Hahn agreed to serve as the program's coordinator. Further, T. U. Marston on behalf of Electric Power Research Institute (EPRI) offered to supply a large piece of

[1]Professor of metallurgical engineering and research professor of material science, respectively, Vanderbilt University, Nashville, Tenn. 37235.

[2]Senior researcher and researcher, respectively, Battelle Columbus Laboratories, Columbus, Ohio 43205.

[3]The italic numbers in brackets refer to the list of references appended to this paper.

A533B steel to serve as the common test material. Additional support was subsequently provided by both EPRI and the Nuclear Regulatory Commission (NRC).

Since that meeting, the program has grown into a multinational effort, involving the 30 laboratories listed in Table 1. Test pieces have been produced from the common plate, distributed, and testing has begun. This paper describes the program and presents early but incomplete findings which are encouraging. They show that the measurements themselves are reproducible and identify a number of questions about their interpretation that remain to be resolved.

Crack Arrest Test Procedures

The aim of the ASTM Cooperative Test Program is to examine the two test procedures for measuring the crack arrest toughness. This quantity is regarded as the minimum in the variation of the fast fracture with crack velocity [*3*] and is designated K_{Im}. The two procedures are very similar. They both employ specimens, shown in Figs. 1 and 2, adapted from the compact tension specimen design of the ASTM Test for Plane-Strain

TABLE 1—*Participants in cooperative program on crack arrest toughness measurements.*

United States	Italy
Babcock and Wilcox	Centro Sperimentale Metallurgico
Battelle	
Combustion Engineering	Japan
General Electric	IHI
Materials Research Laboratory	Kawasaki Steel
Naval Research Laboratory	Mitsubishi Heavy Industries
Oak Ridge National Laboratory	Nippon Kokan
U.S. Army Material and Mechanics Research Center	
University of Maryland	The Netherlands
Westinghouse Electric Corp.	Koninklike/Shell-Laboratories
	Metals Research Institute (TNO)
Denmark	Norway
RISØ National Laboratory	Norsk Veritas
Finland	South Africa
Technical Research Centre of Finland	Atomic Energy Board
France	Sweden
Centre d' Etude de Bruyère le Chatel of Commissariat à l'Energie Atomique	Royal Institute of Technology
	United Kingdom
Germany	British Welding Institute
Bundesanstalt Für Materialprufung	Central Electricity Generating Board
Institut Für Festkorpermechanik	U.K. Atomic Energy Authority
Kraftwerk Union	
Slaatlichen Material Prüfungsanstalt	

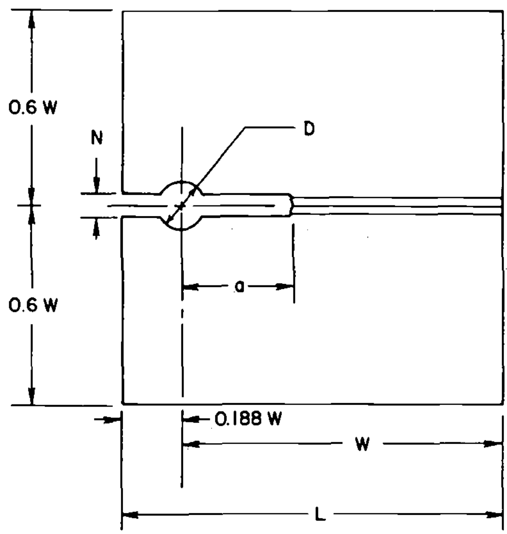

FIG. 1—*Weld-embrittled crack arrest test specimen:* W = *169.4 mm,* N = *12.7 mm (0.075W),* a = *59 mm (0.35W),* B = *50.8 mm,* D = *25.4 mm (0.15W),* B_N = *0.75B.*

Fracture Toughness of Metallic Materials (E 399-74). Both specimens incorporate a blunt starter slot and a starter section to facilitate crack initiation. The overall dimensions are not very different: W = 169 mm for the Crosley and Ripling design; W = 208 mm for the other. The specimen thickness is 51 mm in both cases. Both procedures load the specimen by relatively slow, transverse-wedge loading illustrated in Fig. 3. The two basic measurements called for are also nearly the same. One measurement, the crack length at arrest, is common to both procedures. The other measurement seeks to evaluate the load-line displacement, and while this is done at two different stages (at the onset of fracture [*2*], and after arrest in the other [*1*]) the results obtained should be nearly the same because fracture proceeds with almost constant load-line displacement for stiff wedge loading.

The two procedures do differ in several respects:

Starter Section—To facilitate initiation of a run-arrest event in relatively tough steels, Crosley and Ripling deposit a thin, ~3-mm layer of brittle weld bead at the tip of the wide starter slot. In contrast, the Hoagland et al specimen employs a massive, hardened AISI-4340 steel starter section which is electron beam welded to the test section. In this case, the narrow slot is cut into the 4340 steel after welding. The two specimen types are referred to as the "weld-embrittled" specimen and the "duplex" specimen in this paper.

Initiation of Run-Arrest Event—To facilitate initiation of the fracture,

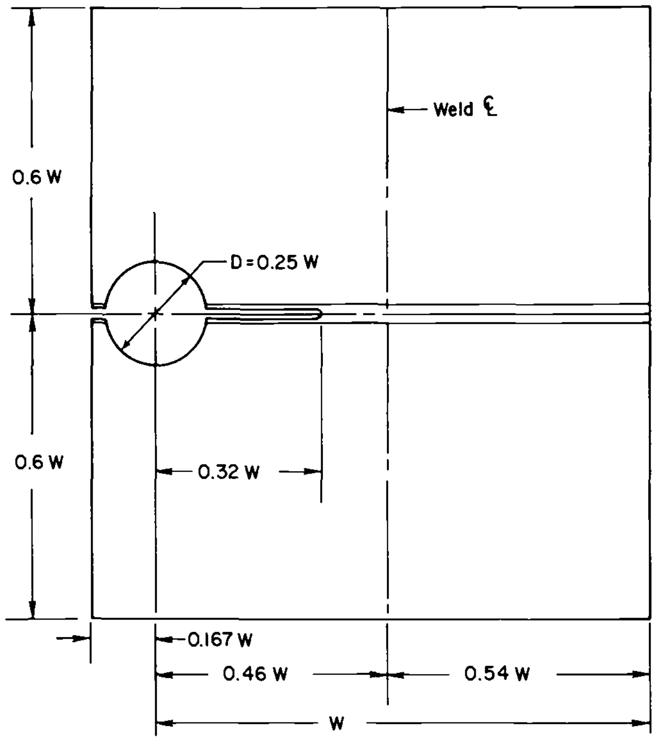

FIG. 2—*Duplex crack arrest test specimen:* W = *208 mm,* B = *50.8 mm,* B_N = *0.75B.*

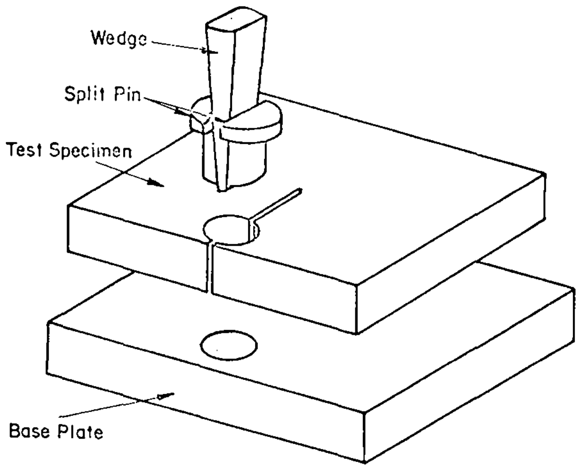

FIG. 3—*Transverse loading arrangement.*

a high *compressive* preload of about 450 KN is applied to the weld-embrittled specimen before it is loaded in tension. Initiation in the duplex specimen is controlled by adjusting the slot root radius and by load cycling, that is, unloading and reloading the specimen in the event it fails to break at the desired K_Q-level.

Instrumentation—The displacement gage in the weld-embrittled specimen is located near the crack mouth a distance $0.25W$ from the load line. The load-line displacement is then inferred from a correlation reported by Roberts [*4*]. In the duplex specimen the displacement is measured directly at the load line.

Analysis—Crosley and Ripling apply a static analysis which neglects the kinetic energy in the specimen at the instant of arrest. Hoagland et al use a dynamic analysis which accounts for kinetic energy but neglects damping prior to arrest [*5*]. In principle, both analyses can be applied to either procedure.

Cooperative Test Program Scope and Schedule

The program provides for the conduct of 10 crack arrest tests by each participating laboratory:

1. Test 4 weld-embrittled specimens of A533B following the Crosley and Ripling [*1*] procedure.
2. Test 4 duplex specimens of the same plate of A533B following the Hoagland et al [*2*] procedure.
3. Test 2 "practice" specimens of AISI-1018 steel. The practice specimens are of the weld-embrittled type and are intended to allow each laboratory to check out procedures and instrumentation.
4. Two tests on A533B are to be performed with each procedure at room temperature, and two at 0°C. The AISI 1018 specimens will be tested at room temperature.

The program provides for a total of 300 tests by the 30 participating laboratories. Both the static and the dynamic analyses are being applied to each set of test results.

To minimize variability connected with specimen fabrication and advance the program's schedule, all of the weld-embrittled specimens were fabricated by the Materials Research Laboratory (MRL) and all the duplex specimens by Battelle Columbus Laboratories (BCL), and were supplied to the participants with appropriate loading wedges. Specimens were shipped in July and August of 1978. The schedule called for communication of the test results to the program coordinator before 30 Jan. 1979, and the completion of a final report in time for presentation at the March 1979 ASTM E-24 meeting in Atlanta.

Description of the Common Plate of A533B Test Material

The test specimens for the Cooperative Test Program were cut from a plate 2.529 by 5.607 by 0.246 m which was given the following heat treatments prior to testing:

1. Austenitized for 4 h at 871°C and water-quenched.
2. Tempered for 4 h at 663°C and air-cooled.
3. Stress-relieved for 40 h at 593 to 649°C and furnace-cooled at 55 deg C per hour to 316°C.

The chemical analysis and the conventional mechanical properties of the plate are given in Tables 2-4. These show that the material falls within the specification for A533 Grade B plate. The drop-weight measurements conducted at Battelle indicate a nil-ductility transition (NDT) of −40°C.

TABLE 2—*Chemical analysis of A533B steel.*

Element	A533B Specification		Actual
	Basic Requirement	Residuals[a]	
C (max)	0.25	...	0.22
Mn	1.06 to 1.62	...	1.56
P (max)	0.035	0.015	0.011
S (max)	0.040	0.018	0.011
Si	0.13 to 0.32	...	0.26
Mo	0.41 to 0.64	...	0.54
Ni	0.37 to 0.73	...	0.60
Cu (max)	...	0.12	0.111
V (max)	...	0.06	0.009
Sn	...	...	0.011
Cr	...	...	0.099
Al	...	...	0.024
Nb	...	...	0.009
Zr	...	...	0.003
Ti	...	...	0.002
B	...	...	0.0003
Co	...	...	0.019
W	...	...	0.003

[a]Nuclear reactor beltline considerations (Paragraph X2 of A533B).

TABLE 3 *Tensile properties of A533B steel.*

Test Temperature, °C	Yield Strength, MPa (ksi)	Tensile Strength, MPa (ksi)	% Reduction in Area
23	473 (68.6)	628 (91.2)	55.1
−18	486 (70.5)	646 (93.8)	54.3
−40	497 (72.2)	663 (96.2)	56.9

TABLE 4—*Drop-weight results.*

1. −12°C (+10°F)	no break
2. −23°C (−10°F)	no break
3. −34°C (−30°F)	no break
4. −50°C (−58°F)	break (out of notch)
5. −46°C (−50°F)	no test
6. −46°C (−50°F)	break
7. −40°C (−40°F)	break
8. −34°C (−30°F)	no break
NDT = −40°C (−40°F)	

NOTE: Head weight = 27 kg (60 lb); drop = 1.524 m (5 ft); assumed minimum strength = 425 MPa (60 000 lb/in.^{2})

However, the Charpy data (see Figs. 4 and 5) are the deciding factor in determining the RT_{NDT} of −20°C. The two test temperatures RT and 0°C are therefore ~40 and 20 deg C above the RT_{NDT}, respectively. Determinations of slow loading and rapid loading fracture toughness values of the test plate are planned.

Results of the Cooperative Test Program

Incomplete results from 14 of the participating laboratories received

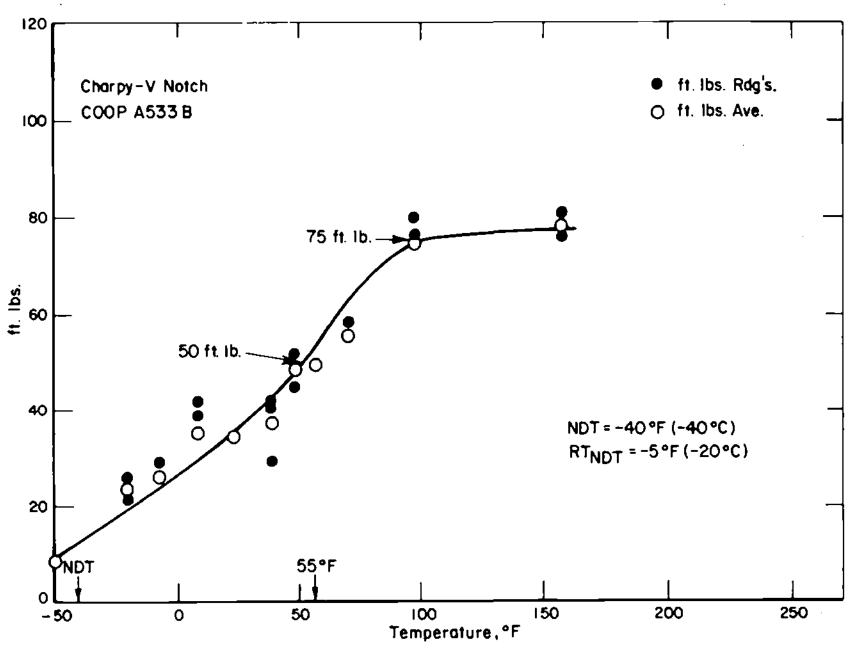

FIG. 4—*Charpy V-notch energy values for Cooperative Test Program A533B steel (1 ft-lb = 1.356J).*

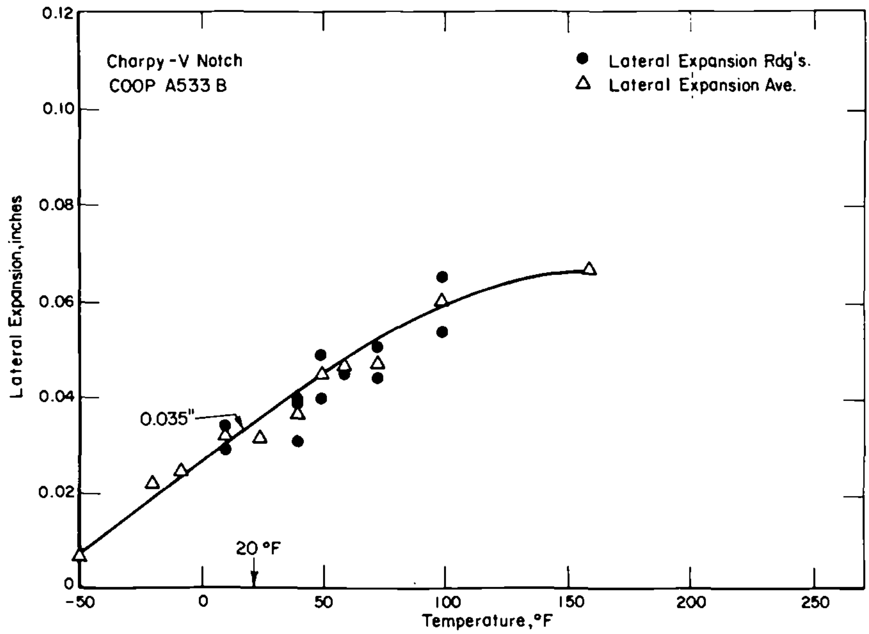

FIG. 5—*Charpy V-notch lateral expansion values for Cooperative Test Program A533B steel (1 in. = 25.4 mm).*

before 27 Oct. 1978 are summarized in Tables 5 and 6. Note that the laboratory numbering system is intended to preserve the anonymity of the participants and does *not* correspond to the listing in Table 1. Also, the symbol K_{Ia} is used to identify crack arrest toughness values derived with the static analysis using measurements of both test procedures, and K_{Im} is used to identify values derived with the dynamic analysis from both procedures. K_{Ia} and K_{Im} are regarded as different estimates of the crack arrest toughness.

The results obtained so far are very encouraging. None of the laboratories has reported any special difficulties in applying the two test procedures, and the test specimens are performing as intended. Photographs of an entire set of fractured and heat-treated specimens provided by Laboratory 19 are shown in Fig. 6. These are reasonably typical of the photographs received to date. The different crack front profiles for the A533B steel specimens tested at room temperature shown in Fig. 6 are common to both duplex and weld-embrittled specimens. The appearance of the crack front in the 1018 specimen also is quite characteristic. Battelle's experience is that the crack tends to lead at the top face of the AISI 1018 specimens.

TABLE 5—*Summary of crack arrest toughness values derived with the static analysis, using measurements obtained from both test procedures.*

			K_{Ia}, MPa m$^{1/2}$							
			Weld-Embrittled Specimens[a]				Duplex Specimens[b]			
			A533B							
Laboratory	1018 RT		RT		0°C		RT		0°C	
2	84	101	118	103	...	...	110	115	...	...
3	86	93	104	125	...	...	120	113	...	...
7	84	82	117	113	84	91	...	...	...	...
8	98	93	102	119	94	86	...	...	...	...
9	92	82	104	96	77	94	...	...	...	...
10	72[c]	81[c]	130	131	...	...	112	124	...	...
14	73	58	83/108	99/120	...	...	122	105	...	...
16	95	95	103	121	...	...	114	108	...	...
17	98	...	92	115	...	...	...	...	...	...
19	87	73	110	109	93	89	92	130	100	95
23	50	92	107	109	83	83	...	...	...	...
24	92	86	...	...	88	...	153	126	100	107
26	96[c]	85[c]	119[c]	105[c]	97[c]	88[c]	115[c]	124[c]	94[c]	85[c]
27	81/67	97	106	89	...	...	113	...	...	...

[a] Weld-embrittled specimens tested following the Crosley and Ripling procedure.
[b] Duplex specimens tested following the Hoagland et al procedure.
[c] Received too late to be included in the graphical presentation.

TABLE 6—*Summary of crack arrest toughness values derived with the dynamic analysis, using measurements of both test procedures.*

	K_{Im}, MPa m$^{1/2}$											
			Weld-Embrittled Specimens[a]				Duplex Specimens[b]					
			A533B									
Laboratory	1018 RT		RT		0°C		RT		0°C			
2	99	107	132	107	...	...	133	141	...	...		
3	93	101	117	123	...	...	175	162	...	...		
7	83	80	125	119	94	101	...	...	...	...		
8	98	101	116	132	101	101	...	...	...	...		
9	94	95	112	99	83	88	...	...	...	...		
10	86[c]	85[c]	120	138	...	...	169	171	...	...		
14	85	84	116/104	114/105	...	...	172	174	...	...		
16	95	97	115	132	...	...	168	167	...	...		
17	111	95	...	118	...	...	...	...	...	...		
19	99	108	115	118	100	95	131	186	149	144		
23	49	88	106	106	81	90	...	...	...	...		
24	96	87	...	103	...	73	192	180	153	158		
26	100[c]	87[c]	123[c]	117[c]	114[c]	83[c]	152[c]	163[c]	148[c]	131[c]		
27	83/108	99	103	98	...	...	...	...	...	...		

[a] Weld-embrittled specimens tested following the Crosley and Ripling procedure.
[b] Duplex specimens tested following the Hoagland et al procedure.
[c] Received too late to be included in the graphical presentations.

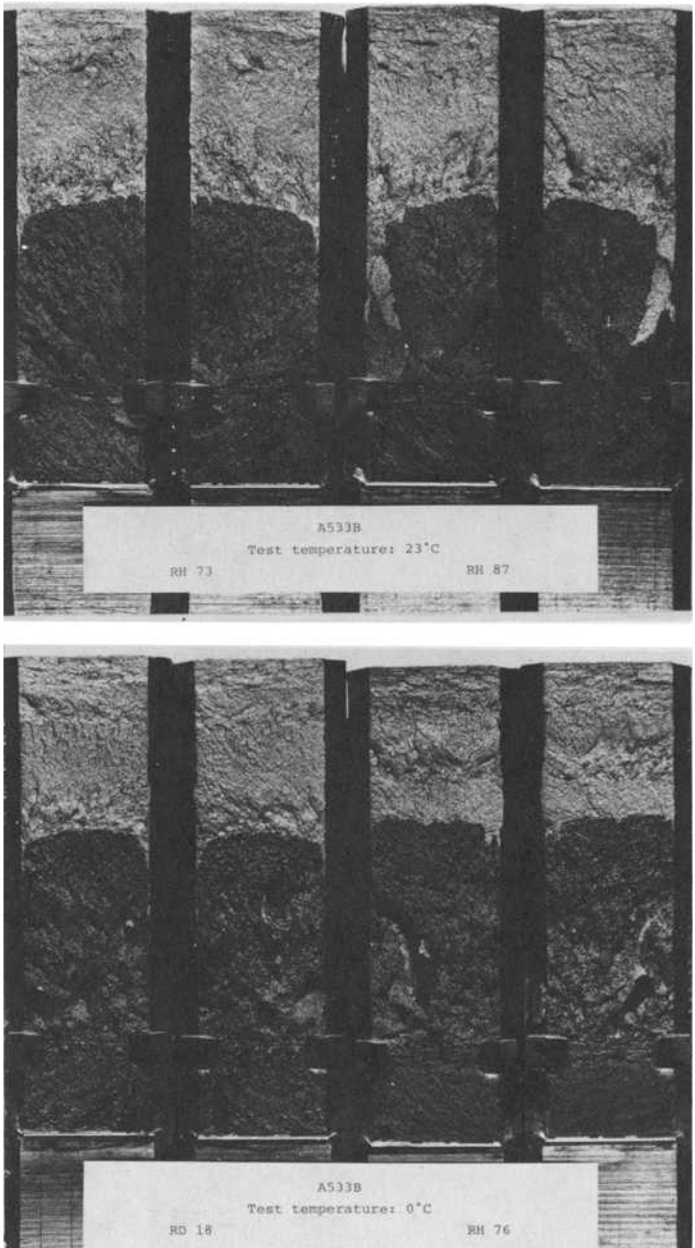

FIG. 6—*Photographs of a set of fractured and heat-tinted crack arrest specimens supplied by Laboratory 19.*

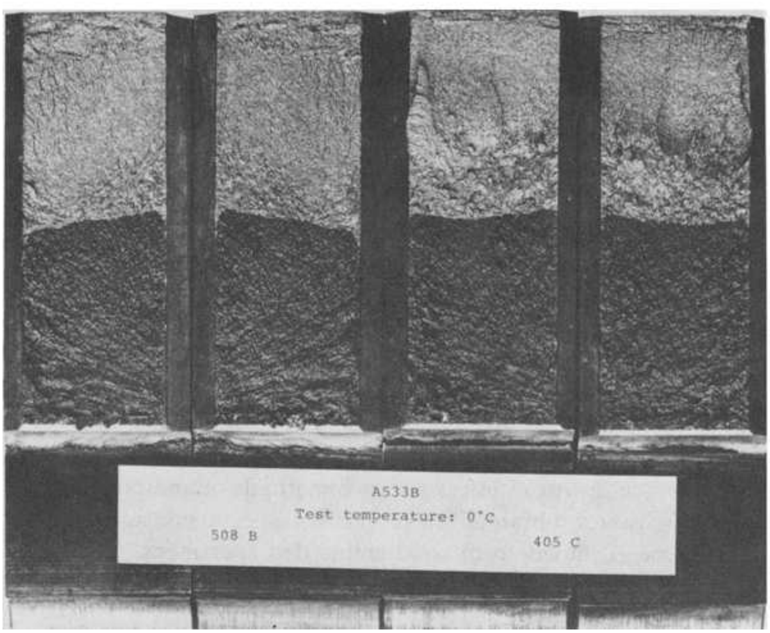

FIG. 6—(*Continued.*)

FIG. 6—(*Continued.*)

The available results are presented in the form of histograms in Figs. 7-11, and as a function of the size of the crack jump in Figs. 12-16. Statistical analyses are summarized in Table 7. These show that the results are quite reproducible. In fact, the variability of measurements may be smaller than indicated in Table 7. This is brought out by Fig. 12, which contains evidence of dependencies of K_{Ia} and K_{Im} on the size of the crack jump. Both K_{Ia}- and K_{Im}-values in this figure fall with decreasing crack jump size for $\Delta a \lesssim 30$ mm, and K_{Ia}-values with increasing crack jump for $\Delta a \gtrsim 75$ mm. Since such a crack jump size dependence will alter the interpretation and statistical analysis of the data, the results in Table 7, which do not recognize a crack jump size dependence, should be regarded as highly tentative. Possible origins of the crack jump size dependence are discussed by Hahn et al [*6*] in a symposium note not included in this volume.

The data reveal the following similarities and differences among the results of the two test procedures and two methods of analysis:

1. The K_{Ia}-values obtained from duplex specimens agree reasonably well with those obtained from weld-embrittled specimens. The K_{Ia}-values from duplex specimens are about 10 percent larger than the ones from weld-embrittled specimens.

2. In contrast, there is a large difference in the K_{Im}-values derived from the two specimens. The K_{Im}-values from duplex specimens are 50 percent larger than the ones calculated from weld-embrittled specimens.

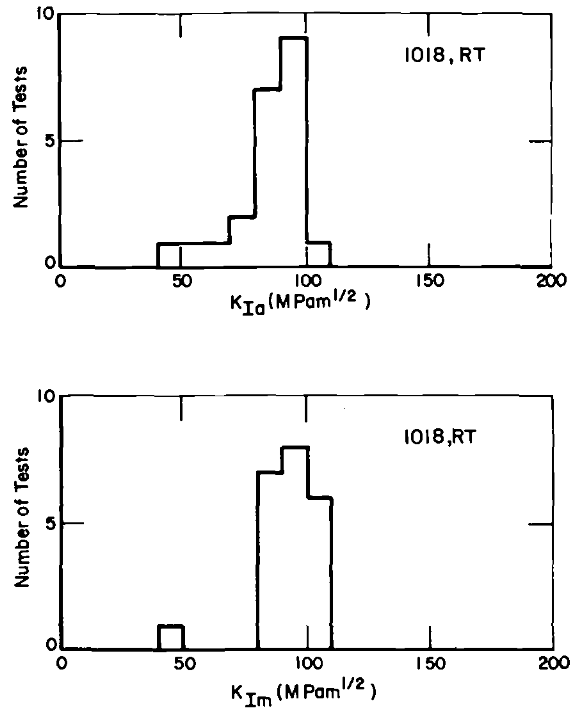

FIG. 7—*Histograms of crack arrest toughness values of cold-worked 1018 steel derived from weld-embrittled specimens at room temperature.*

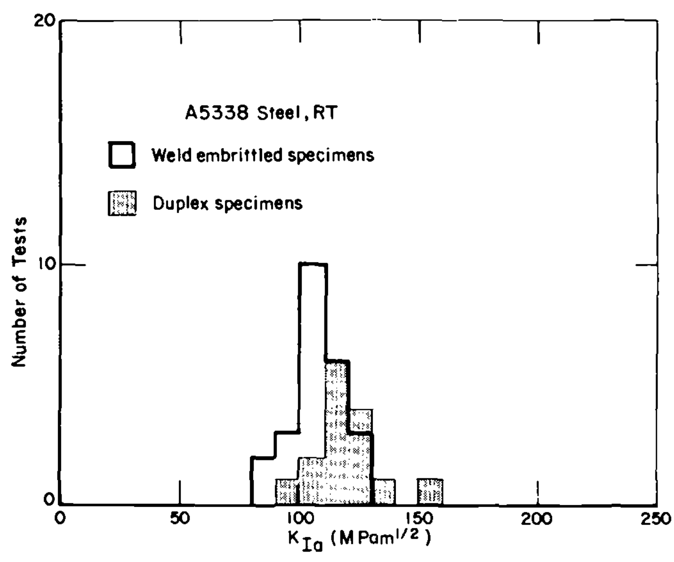

FIG. 8—*Histograms of crack arrest toughness values from the static analysis for A533B steel specimens tested at room temperature.*

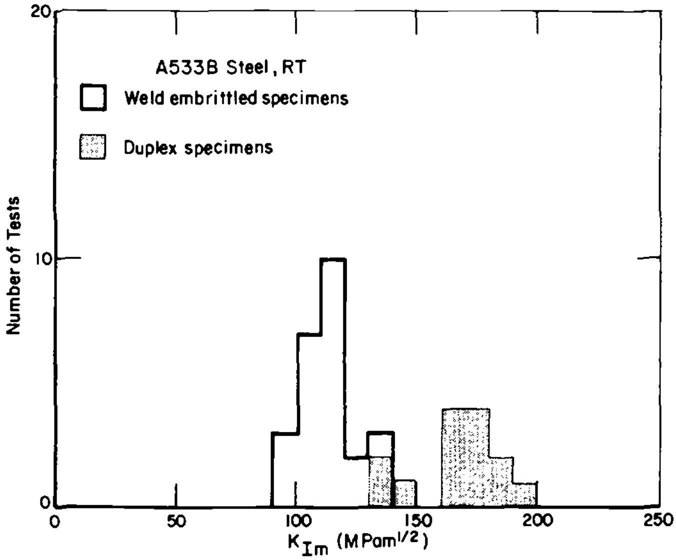

FIG. 9—*Histograms of crack arrest toughness values from the dynamic analysis for A533B steel tested at room temperature.*

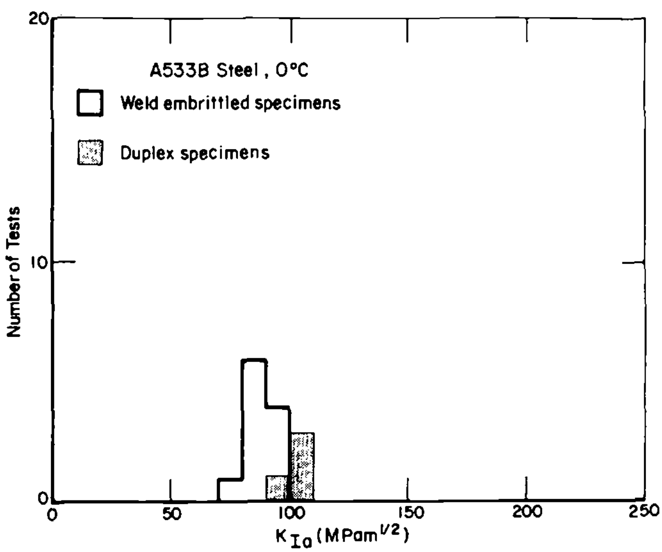

FIG. 10—*Histograms of crack arrest toughness values derived from the static analysis for A533B steel specimens tested at 0°C.*

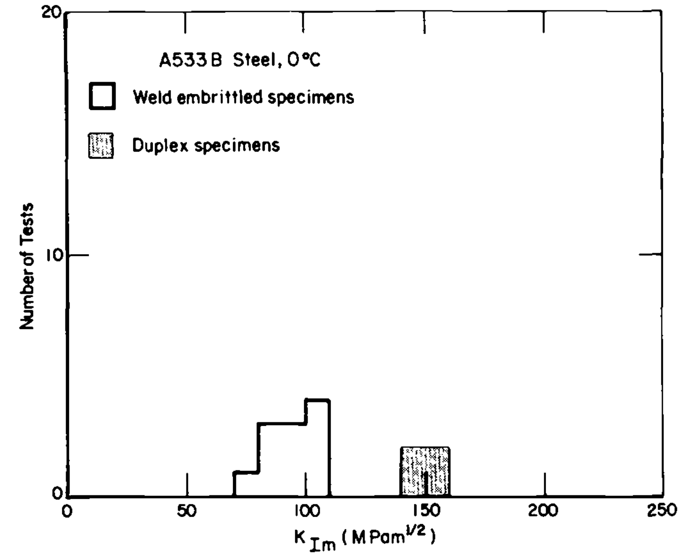

FIG. 11—*Histograms of crack arrest toughness values derived from the dynamic analysis for A533B steel specimens tested at 0°C.*

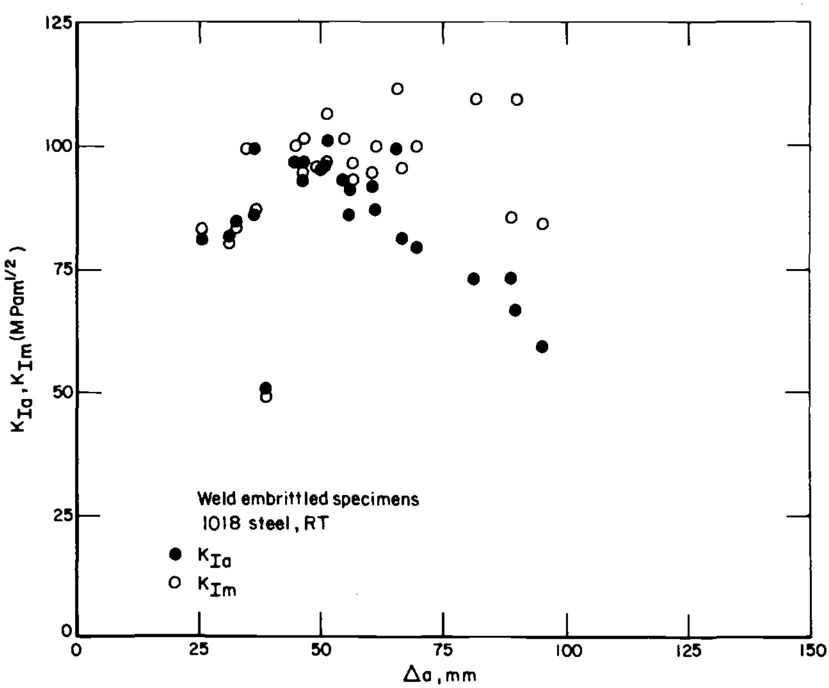

FIG. 12—*Variation with the size of the crack jump of* K_{Ia}*-and* K_{Im}*-values derived from the weld-embrittled 1018 practice specimens.*

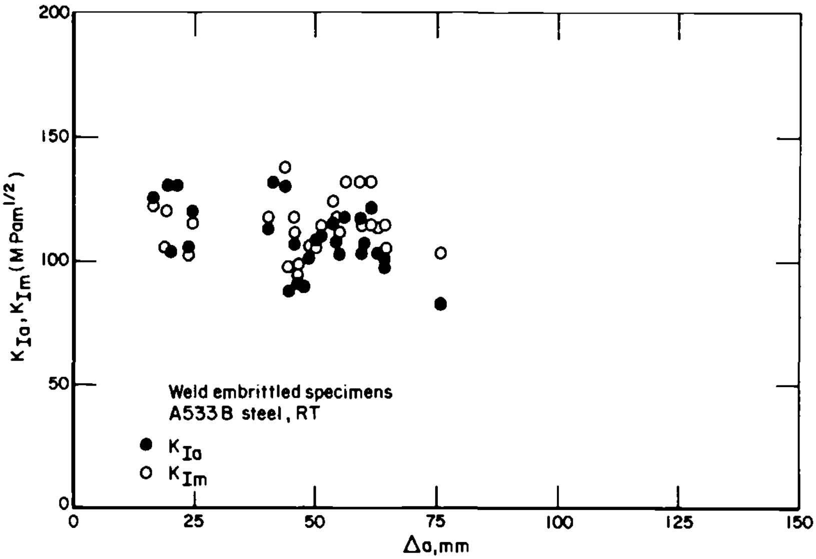

FIG. 13—*Variation with the size of the crack jump of K_{Ia}- and K_{Im}-values derived from weld-embrittled A533B steel specimens tested at room temperature.*

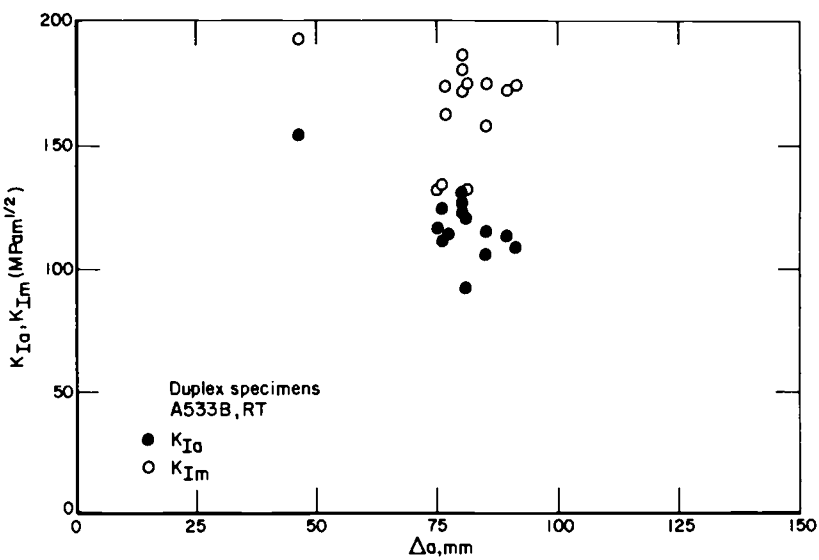

FIG. 14—*Variation with the size of the crack jump of K_{Ia}-and K_{IM}-values derived from duplex specimens of A533B steel tested at room temperature.*

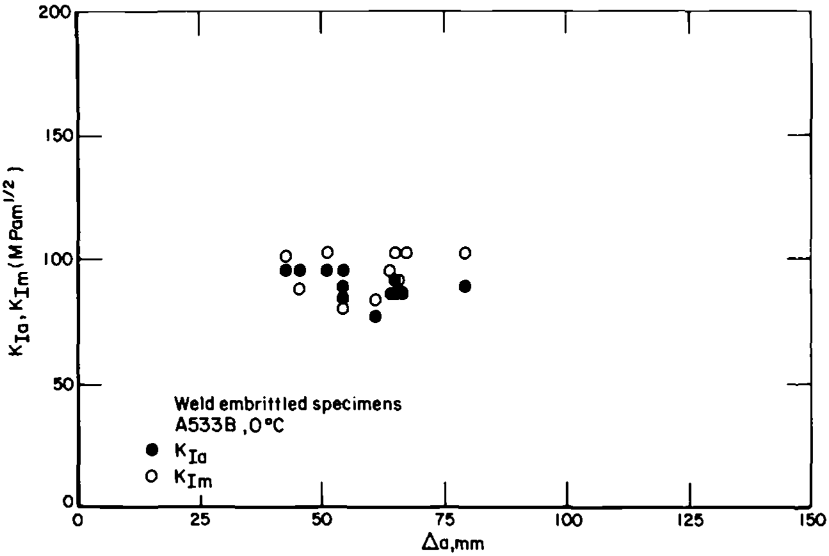

FIG. 15—*Variation with the size of the crack jump of* K_{Ia}*-and* K_{Im}*-values derived from weld-embrittled specimens of A533B steel tested at 0°C.*

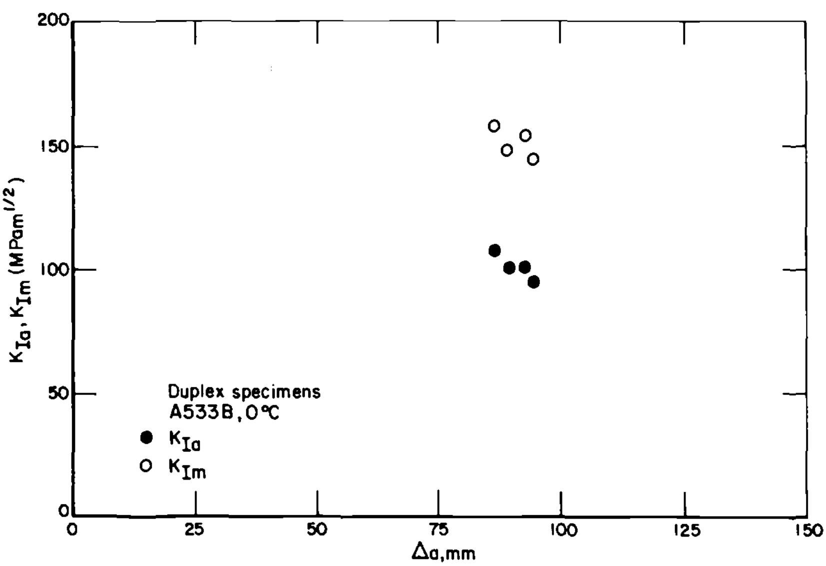

FIG. 16—*Variation with the size of the crack jump of* K_{Ia}*- and* K_{Im}*-values derived from duplex specimens of A533B steel tested at 0°C.*

TABLE 7—*Statistical analyses results.*

Test Specimen	Test Condition	Mean	Standard Deviation
	A. Static Analysis—K_{Ia}, MPa m$^{1/2}$		
Weld-embrittled	1018-RT	84.75	12.36
Weld-embrittled	A533B-RT	109.17	11.67
Weld-embrittled	A533B-0°C	88.23	5.61
Duplex	A533B-RT	117.4	12.86
Duplex	A533B-0°C	96.83	7.41
	B. Dynamic Analysis—K_{Im}, MPa m$^{1/2}$		
Weld-embrittled	1018-RT	92.76	12.12
Weld-embrittled	A533B-RT	114.75	10.99
Weld-embrittled	A533B-0°C	92.61	11.04
Duplex	A533B-RT	164.75	17.56
Duplex	A533B-0°C	147.16	9.24

3. The static and dynamic analyses lead to about the same crack arrest toughness values when applied to weld-embrittled specimens. The K_{Im}-values are about 10 percent larger in this case.

4. Again, in contrast, the two methods of analysis do not agree well when applied to duplex specimens; K_{Im}-values are about 50 percent larger than K_{Ia} here.

A large part of these discrepancies may be connected with the correlation of Roberts [*4*] which Crosley and Ripling [*1*] employ to calculate the load line displacement, V, from the measurements of displacement across the slot mouth a distance 0.25W from the load line, Δ. Simultaneous measurements of these two displacements performed on weld-embrittled 1018 and A533B steel specimens show that the correlation underestimates the load-line displacement at the onset of fracture and particularly for short cracks. A comparison of the calculated and measured correction factors is given in Table 8. These new corrections would serve to, first, increase the small discrepancy between the K_{Ia}-values from the two tests; second, eliminate about half the discrepancy between K_{Im}-values noted in Item 1 of the foregoing; and, third, introduce a greater difference between K_{Im}- and K_{Ia}-values for the weld-embrittled specimen (see Items 3 and 4 of the preceding). Confirmation of the corrections in Table 8 from other participants is desirable.

TABLE 8—*Correction factors for displacement values.*

Crack Length, mm	V/Δ Calculated	Measured
a = 59 (a_0)	0.612	0.733
a = 138 (arrest)	0.776	0.747

Conclusions

1. Early and incomplete results of the Cooperative Test Program are encouraging. No special difficulties in applying the test procedures have been encountered, and the test specimens are performing satisfactorily.
2. The results appear to be quite reproducible. Crack arrest toughness values derived from two procedures with a static analysis agree closely, but values calculated using a dynamic analysis differ by about 50 percent.
3. The correlation between load-line displacement and crack mouth displacement is identified as one possible source of the discrepancy. Confirmation from other participants is desirable.
4. The statistical analysis of the variability may be complicated by a systematic dependence of certain arrest toughness values on the size of the crack jump. This should become clearer when more results are available.

Acknowledgments

The authors wish to thank the participating laboratories for making these results available in time for the symposium. They are indebted to T. U. Marston of the Electric Power Research Institute (EPRI) for providing the very large plate of testing material. They also wish to acknowledge the substantial support provided by the late E. K. Lynn, T. U. Marston, and both the U.S. Nuclear Regulatory Commission and EPRI, who have made this program possible.

ADDENDUM

Between the time the paper was prepared and the writing of this Addendum, the data collection portion of the Cooperative Test Program has been virtually completed. In addition, certain errors in both procedures have been identified and corrected. These modifications produced significant changes in the results, bringing K_{ID} and K_{Im} data from both procedures into closer agreement. Therefore, it is the purpose of this addendum to expedite the reporting of the now-completed results of this program with an analysis of the significance of the results to be reported at a later date.

Table 9 is the updated version of Table 6, containing the means and standard deviations of the K_{ID} and K_{Ia} results. These data have been recomputed from the raw data supplied by the various participants. The recalculations were necessary because (1) the Crosley-Ripling procedure used a compliance relation (at $0.25W$ from the load line) derived by Roberts [7] which leads to underestimates of K for short crack lengths in their

TABLE 9—*Computed results of Cooperative Test Program.*[a]

Test Specimen	Material and Test Condition	Number of Data	Mean	Standard Deviation
		A. K_{Ia} Results		
Weld embrittled	1018-RT	52	88.8	12.4 (13.9%)
Weld embrittled	A53313-RT	55	114.0	15.2 (13.3%)
Weld embrittled	A533B-OC	44	97.0	18.0 (18.6%)
Weld embrittled	A533B-OC	40[b]	92.3	9.9 (10.8%)
		40[b]	92.3	9.9 (10.8%)
Duplex	A533B-RT	49	112.0	25.3 (22.5%)
Duplex	A533B-OC	44	87.4	20.4 (23.3%)
		40[b]	85.8	20.3 (23.6%)
		B. K_{ID}, K_{Im} Results		
Weld embrittled	1018-RT	52	112.1	14.1 (12.6%)
Weld embrittled	A533B-RT	55	138.7	16.0 (11.5%)
Weld embrittled	A533B-OC	44	122.1	24.6 (20.2%)
		40[b]	115.3	12.3 (10.6%)
Duplex	A533B-RT	46	142.2	23.6 (16.6%)
Duplex	A533B-OC	43	132.0	13.7 (10.3%)
		39[b]	131.2	13.9 (10.6%)

[a]Data from weld-embrittled specimens computed using compliance data derived by Newman. All stress-intensity data from duplex specimens decreased by 11.4 percent to account for bending of split pin.
[b]Data from Laboratory 5 excluded.

specimen, and (2) the testing method in the Hoagland et al procedure called for measurements of load-line displacements on the split pin which introduce errors, producing an overestimate of K. The first source of error is reduced by replacing the Roberts compliance relation with a relation computed by Newman [*8*] which has been shown to be accurate for a crack-line, wedge-loaded compact specimen [*9*]. This correction increases the average K_Q of the weld-embrittled results by about 21 percent with a corresponding increase in K_{ID}. The second correction is based on measurements comparing the relative displacement of the two halves of the split pin with the load-line displacement on one face of specimen. These measurements indicate that the split pin displacement is 11.4 percent larger than the actual load-line displacement, probably because of bending of the pins. It should also be noted that this correction contains an element of uncertainty because it may vary from specimen to specimen.

One particular set of data, that from Laboratory 5, was unusually large and judged to be atypical. For this reason, Table 9 lists the means of K_{Ia} and K_{ID}, K_{Im} exclusive of Laboratory 5 data as well as for the entire data set. It is now apparent from this more complete compilation of results that there exists fairly good agreement in both crack arrest toughness parameters between the two procedures. On the basis of these findings, the ASTM E-24 Crack Arrest Task Group is proceeding in the design of a round-robin program to evaluate a recommended practice on crack arrest.

References

[1] Crosley, P. B. and Ripling, E. J., "Guidelines for Measuring K_{Ia} with a Compact Specimen," presented to the Dynamic Initiation-Crack Arrest Task Group, American Society for Testing and Materials, 23 March 1977.

[2] Hoagland, R. G., Gehlen, P. C., Rosenfield, A. R., Kanninen, M. F., and Hahn, G. T., "Proposed Tentative Method of Test for Fast Fracture Toughness and Crack Arrest Toughness," presented to the Dynamic Initiation-Crack Arrest Task Group, American Society for Testing and Materials, 23 March 1977, and revised 19 Oct. 1977.

[3] Hahn, G. T. and Kanninen, M. F., in *Fast Fracture and Crack Arrest, ASTM STP 627*, American Society for Testing and Materials, 1977, p. 413–414.

[4] Roberts, E., Jr., *Materials Research and Standards*, Vol. 9, Feb. 1969, p. 27

[5] Hahn, G. T., Corten, H. T., Debel, C. P., Gehlen, P. C., Hoagland, R. G., Kanninen, M. F., Kim, K. S., Marschall, C. W., Popelar, C., Rosenfield, A. R., and Simon, R. "Critical Experiments, Measurements and Analyses to Establish A Crack Arrest Methodology for Nuclear Pressure Vessel Steels," NUREG/CR-0057, BMI-1995, Battelle Memorial Institute, Columbus, Ohio, May 1978.

[6] Hahn, G. T., Hoagland, R. G., and Rosenfield, A. R., "Effects of Residual Stresses on the Weld-Embrittled Crack Arrest Test Specimen," presented at the Symposium on Crack Arrest Methodology and Applications, Philadelphia, Pa., May 1978.

[7] Roberts, E., *Metals Research and Standards*, Vol. 9, 1969, p. 27.

[8] Newman, J. C., "Crack-Opening Displacements in Center-Crack, Compact, and Crack-Line Wedge-Loaded Specimens," NASA Technical Note TN D-8268, National Air and Space Administration, 1976.

[9] McCabe, D. E. and Sha, G. T. in *Developments in Fracture Mechanics Test Methods Standardization, ASTM STP 632*, American Society for Testing and Materials 1977, p. 82.

W. L. Fourney[1] *and Takao Kobayashi*[1]

Critical Examination of Battelle Columbus Laboratory Crack Arrest Toughness Measurement Procedure

REFERENCE: Fourney, W. L. and Kobayashi, Takao, **"Critical Examination of Battelle Columbus Laboratory Crack Arrest Toughness Measurement Procedure,"** *Crack Arrest Methodology and Applications, ASTM STP 711*, G. T. Hahn and M. F. Kanninen, Eds., American Society for Testing and Materials, 1980, pp. 270–288.

ABSTRACT: Two procedures to characterize crack arrest toughness have been proposed to the ASTM E24.03.04 Committee for possible adoption as a testing standard. One of the procedures, proposed by Battelle Columbus Laboratory (BCL), uses results from a dynamic computer code based on an energy balance criterion. This computer code is utilized to construct two reference curves which relate K_{ID}/K_Q or K_{IDm} with $\Delta a/a_0$ and V/c_0 with $\Delta a/a_0$. Here K_{ID} represents the plane-strain fast fracture toughness, K_{IDm} the minimum value of plane-strain fast fracture toughness or plane-strain crack arrest toughness, K_Q the initial stress intensity, V the crack velocity, c_0 the bar wave velocity, Δa the crack jump distance, and a_0 the initial crack length.

With these two reference curves for a given specimen geometry and a knowledge of K_Q, c_0, and $\Delta a/a_0$, not only is the determination of the crack arrest toughness K_{IDm} proposed but also the characterization of the stress-intensity factor and crack velocity relationship.

The authors have utilized a one-dimensional version of the computer code developed by BCL to examine the predicted crack behavior in Homalite 100 and have made comparisons with experimentally observed crack behavior. This paper discusses the following aspects:

1. Comparison of the predicted crack positions with experimentally observed positions for rectangular double cantilever beam (R-DCB) models.
2. Influence of the shape of the K versus crack velocity ($\dot{a}$) relationship on the reference curves generated for the R-DCB geometry.
3. Examination and comparison of the BCL code-generated K-versus-$\dot{a}$ curve with the experimental curve for R-DCB and crack line loaded (CLL) compact specimens.
4. K levels and velocities predicted by the reference curves compared on a test-by-test basis with experimentally observed values.

[1] Professor and associate professor, University of Maryland, College Park, Md. 20742.

KEY WORDS: stress intensity factor, battelle columbus laboratory procedure, crack arrest toughness, *K-versus-$\dot{a}$* relationship, crack velocity, dynamic photoelasticity

The Battelle Columbus Laboratory (BCL) approach to measuring crack arrest toughness was examined by comparing predictions made by utilizing the suggested procedure with experimental results. The BCL procedure bases the determination of arrest toughness on measurements of crack jump length and stress intensity measured at the instant of crack initiation. These values are used along with provided reference curves to determine the arrest toughness.

The reference curves are generated by a finite-difference computer code which uses an energy balance criterion to determine crack speed and propagation distance. This program is described in more detail by Hahn et al [*1,2*].[2] The reference curves plot the ratios of K_{ID}/K_Q or K_{IDm}/K_Q and V/C_0 versus the ratio of crack jump length to original crack length ($\Delta a/a_0$). Curves are provided for rectangular double cantilever beam (R-DCB) and compact tension (CT) specimen geometries of both ordinary (single material) and duplex composition. Knowing the value of crack jump distance, one can determine not only K_{Id} but the velocity of propagation as well.

The reference curves provided have been generated for a material such that K_{Id} is not a function of crack speed ($\dot{a}$). In the prospectus for the Cooperative Test Program [*3*] it is stated that the same reference curves should work well even for a material with a highly dependent K-versus-$\dot{a}$ relationship since changes in this particular parameter have been shown to have little effect on the reference curves.

This paper presents an examination of the proposed BCL procedure. The following aspects are considered:

1 Crack position for a Homalite 100 R-DCB model as predicted by the BCL computer code is compared with experimental results obtained at the University of Maryland.

2 Changes in the BCL reference curves as a result of inputting the photoelastically determined K-versus-$\dot{a}$ relationship for Homalite 100 are determined for the R-DCB geometry.

3 Experimental data are used as specified by the procedure to determine K-versus-$\dot{a}$ relationships for three different materials (Homalite 100, Araldite B, and 4340 steel). Where possible, modified reference curves (those generated by input of the photoelastically determined K-versus-$\dot{a}$ relationship) are used to yield the predicted K-versus-$\dot{a}$ functions. These generated curves are then compared with experimentally determined values.

[2] The italic numbers in brackets refer to the list of references appended to this paper.

4 Finally, K and velocity values predicted by the BCL procedure are compared with the experimentally determined ones on a test-by-test basis.

Critical Examination of Proposed BCL Procedure

Prediction of Crack Position as a Function of Time

The computer code used to generate the BCL reference curves was used also to study crack propagation behavior in a wedge-loaded R-DCB fabricated from Homalite 100. The program input was matched to the initial conditions of a similar experiment conducted at the University of Maryland.

The geometry of the model was similar to the BCL specimen and is presented in Fig. 1. The model had an initial crack length of 77 mm and unstable crack propagation began with a wedge load of 343 N. The corresponding value of K_Q was 0.667 MPa$\sqrt{\text{m}}$ and the crack ran 119 mm before arresting. Details of the experiment are presented in Refs *4* and *5*.

The K-versus-$\dot{a}$ curve determined from tests of six such models was

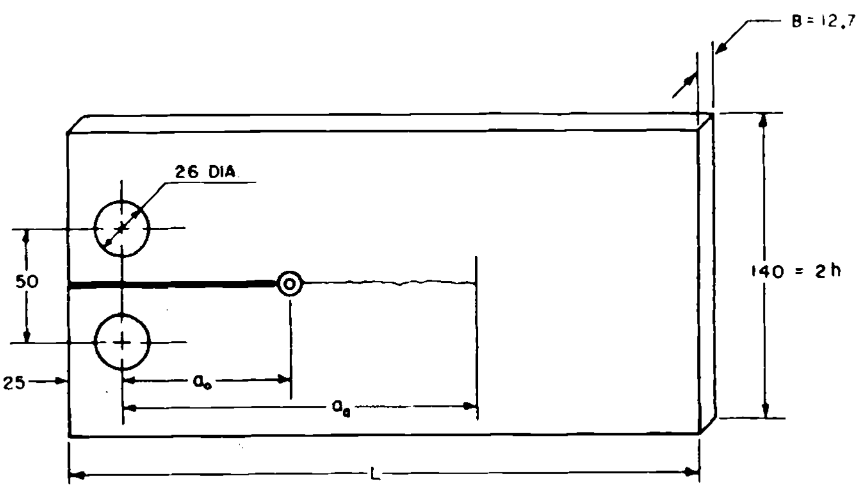

Test No.	Model No.	a_0 (mm)	L (mm)	P_W (lbs)/N	a_a (mm)	$\dot{a}$ (in./sec/m/sec)
59	1	48	300	- / -	256	15,500/394
63	2	74	276	160/712	-	14,500/368
64	3	53	278	48/214	109	8,070/350
65	4	77	278	77/343	196	11,700/297
66	5A	77	276	62/275	101	3,700/95
124	6	65	276	56/249	90	1,700/43

FIG. 1—*Geometry of R-DCB models (1 lb. = 0.45 kg).*

utilized along with specimen geometry and other properties of the Homalite 100 material as input for the BCL one-dimensional computer code.

Figure 2 gives the *a*-versus-*t* values obtained from both the experimental test and the computer output. Note that the computer input for K_Q was 0.7 MPa$\sqrt{m}$ rather than the experimentally measured value of 0.67 MPa$\sqrt{m}$. This was done since the particular version of the computer code that was available did not have an accurate routine for calculating K_Q. The routine used did not give the required pin displacement of 0.19 mm for a K_Q of 0.667 MPa$\sqrt{m}$. Hence the value of K_Q was raised slightly in order to have the proper pin displacement prior to crack initiation. The code predicted first arrest at 188 mm, which was in reasonably close correspondence with the first experimentally observed arrest at 196 mm. The computer predicted a velocity of 325 m/s, which is 9.5 percent higher than the optically measured value of 297 m/s.

Effect of K-*Versus*-$\dot{a}$ *on Reference Curves.*

The K-versus-$\dot{a}$ relationship for Homalite 100 has been determined by Dally and Kobayashi [6]. Figure 3 is the curve determined for R-DCB's by dynamic photoelasticity [2]. The subroutine depicting a constant K-value was removed from the BCL computer code and replaced by one which uses the hyperbolic function indicated in Fig. 3 to approximate the K-versus-$\dot{a}$ behavior for the material.

A one-dimensional version of the BCL program was used by Gehlen of BCL to generate the reference curves given in Fig. 4. These reference curves are for R-DCB's and are valid for the geometry given in Fig. 1.

In Fig. 4, three different curves are presented. The solid curve is the reference curve presented in the Cooperative Test Program procedure and is for a material with K independent of $\dot{a}$. The curve denoted by solid circles was generated with the Γ-shaped K relationship from an analytic model which contained torsional springs along the crack line as well as typical elastic springs. The curve denoted by open circles represents results from using the Γ relationship with an analytical model without the torsional springs along the crack line.

From viewing Fig. 4*a* it is seen that the published reference curve falls between the results obtained with and without torsional springs. The maximum deviation occurs at large jump distances. The BCL curve tends to overpredict K-values by about 11.0 percent at a $\Delta a/a_0$ value of 1.7 when compared with the curve containing torsional springs. It tends to underpredict by about 8.0 percent at the same $\Delta a/a_0$ ratio when no torsional springs are used in the analytical model. In both cases, the prediction using the BCL curve with regard to K-level appears to be sufficient (being well within 10 percent of the reference curves for the case of nonconstant K).

The curves for velocity given in Fig. 4*b* do not agree quite as well. The

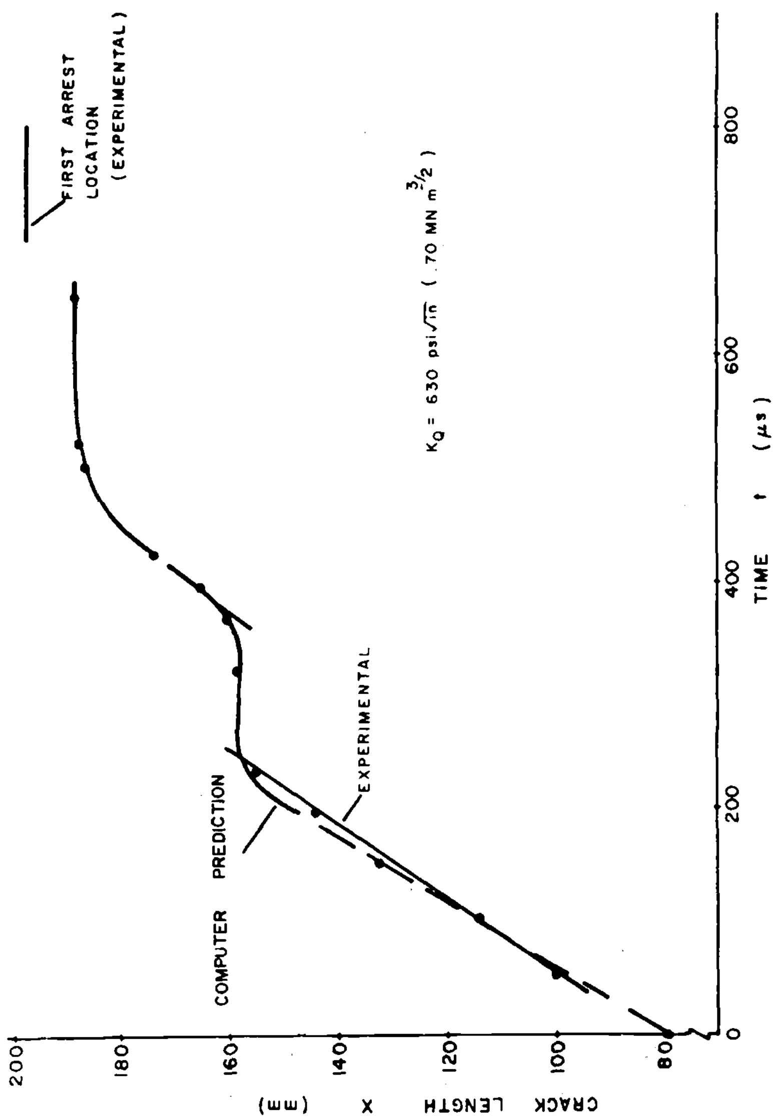

FIG. 2—*Crack position as a function of time for Test 65.*

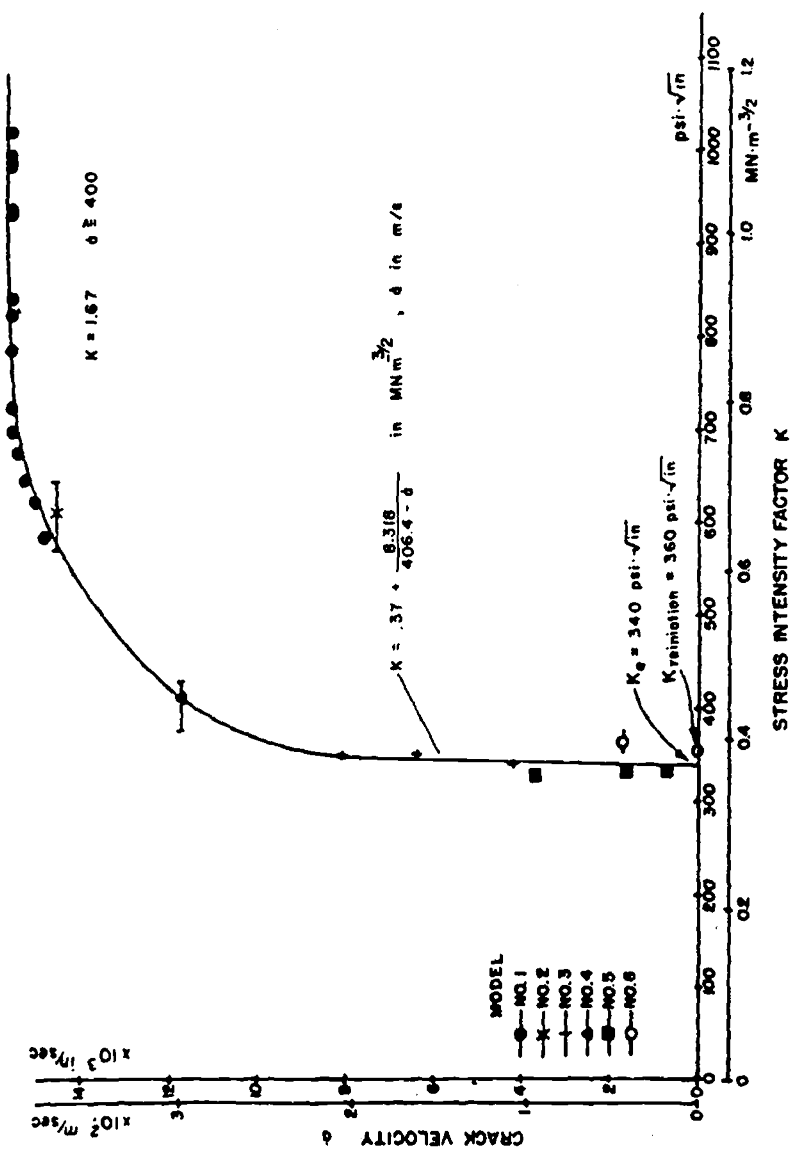

FIG. 3—*Crack velocity ȧ as a function of stress-intensity factor* K *for Homalite 100 (determined with a uniform-height R-DCB specimen).*

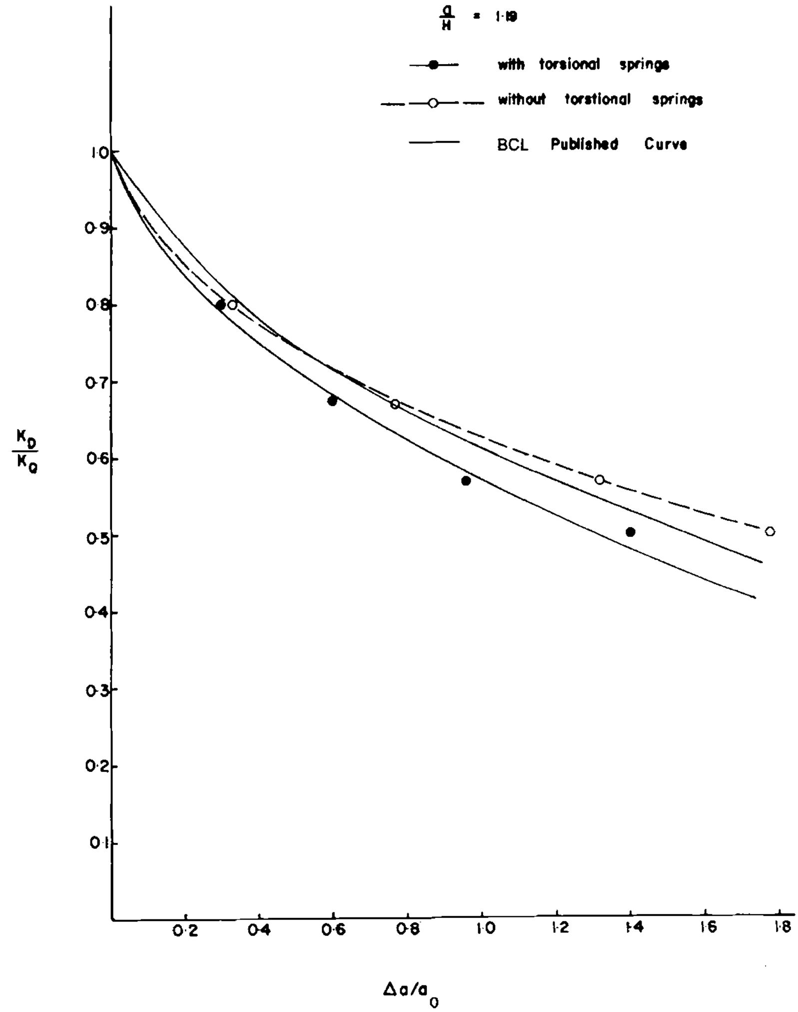

FIG. 4a—*Reference curves for determining stress intensity* K_{Id} *for R-DCB geometry.*

published BCL curve (solid line) overestimates velocities up to 10 percent for the case with torsional springs and up to 29.0 percent for the case with no torsional springs at higher values of $\Delta a/a_0$. Just as in the case with K reference curves, the differences decrease as the value of $\Delta a/a_0$ decreases, giving identical results for jump distances less than 40 percent of the original crack length.

The question of which of the two corrected curves (with or without torsional springs) best fits the experimental data is addressed in a later section.

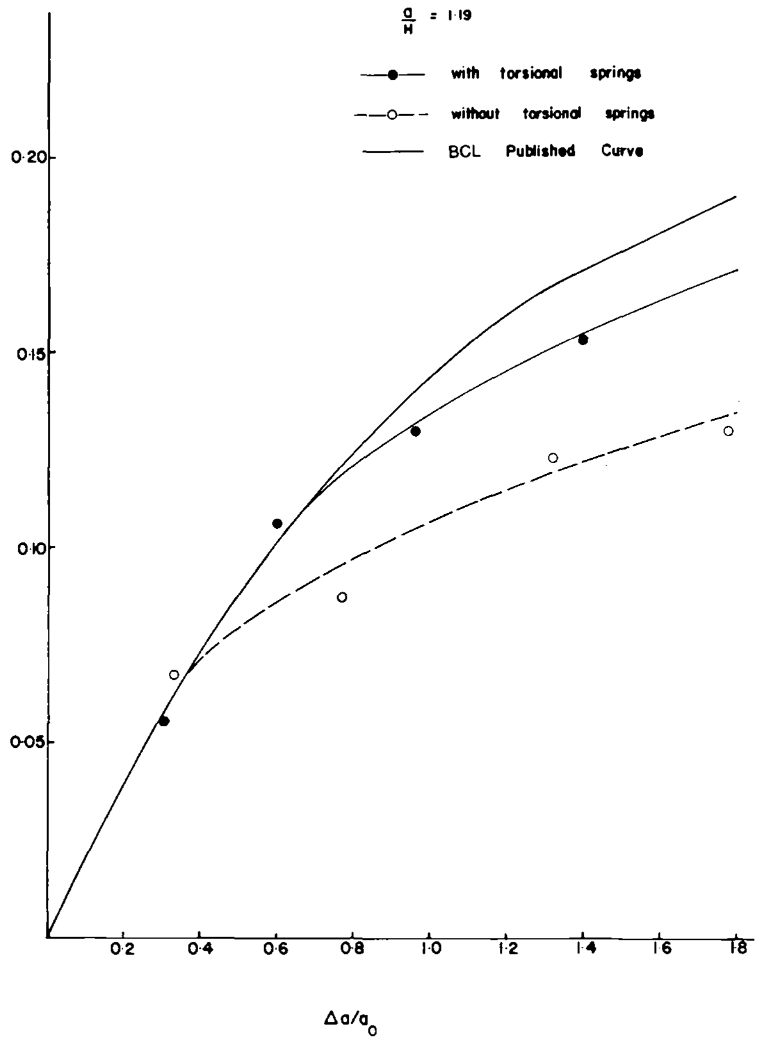

FIG. 4*b*—*Reference curves for determining velocity for R-DCB geometry.*

Prediction of K-*Versus*-$\dot{a}$ *from BCL Procedure*

In addition to the R-DCB reference curves, the BCL compact tension reference curves published in the Cooperative Test Program procedure [*3*] were used as follows to determine points on the K-versus-$\dot{a}$ curve for Homalite 100 and Araldite B materials. Crack-opening displacement at load line was recorded during loading of modified CT specimens with the geometry given in Fig. 5. The value at the onset of rapid fracture was used to calculate K_Q. This and the crack jump distance were used with

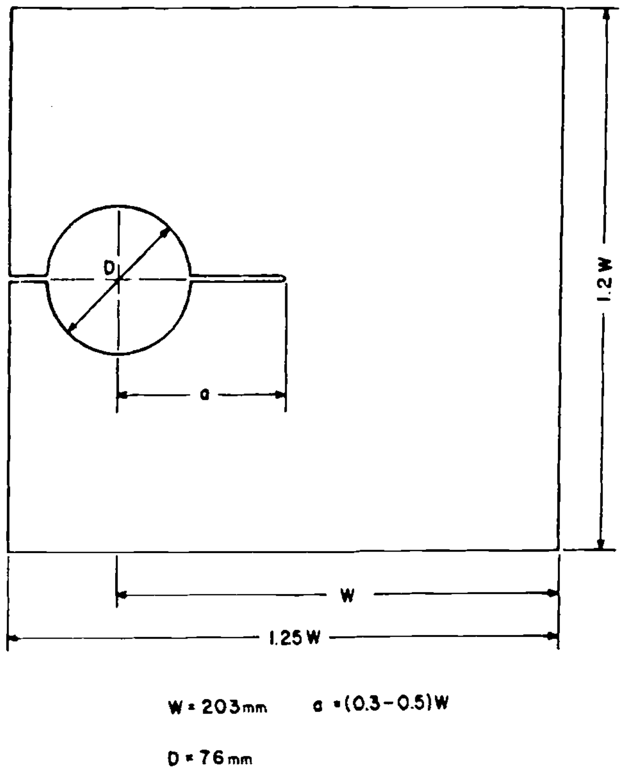

FIG. 5—*Modified compact tension model geometry.*

the reference curves to determine a value of K_{ID} and velocity for the test. These points were plotted so a comparison of K-versus-$\dot{a}$ as predicted by the BCL procedure could be made with the photoelasticity-determined relationship.

Figure 6 shows the results obtained for three Homalite 100 tests utilized in postarrest tests at the University of Maryland. The three predicted points are in reasonable agreement with the experimentally generated curve. Modified curves reflecting an experimental K-versus-$\dot{a}$ relation input were not available for the CT geometry, but trends obtained from the R-DCB curve can probably be applied. Hence, the largest $\dot{a}$-value shown could be high by about 10 percent. Such a correction would make the agreement in Fig. 6 somewhat better.

Figure 7 presents similar results obtained for modified compact tension (M-CT) specimens made from Araldite B material. Again, as in the case of the Homalite 100, the agreement is good at small jump lengths but becomes worse as larger K_Q-values are utilized. The experimentally determined curve in Fig. 7 is for specimens tested at Maryland and the

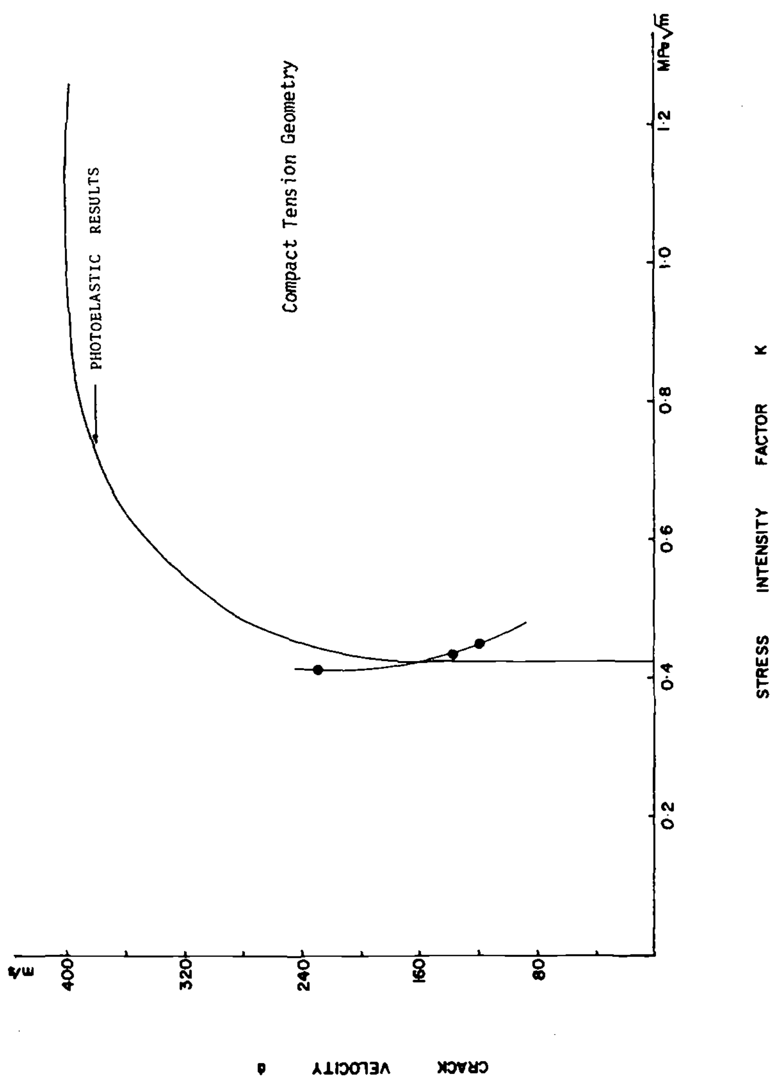

FIG. 6—*Comparison of BCL predicted K-versus-ȧ relationship for Homalite 100.*

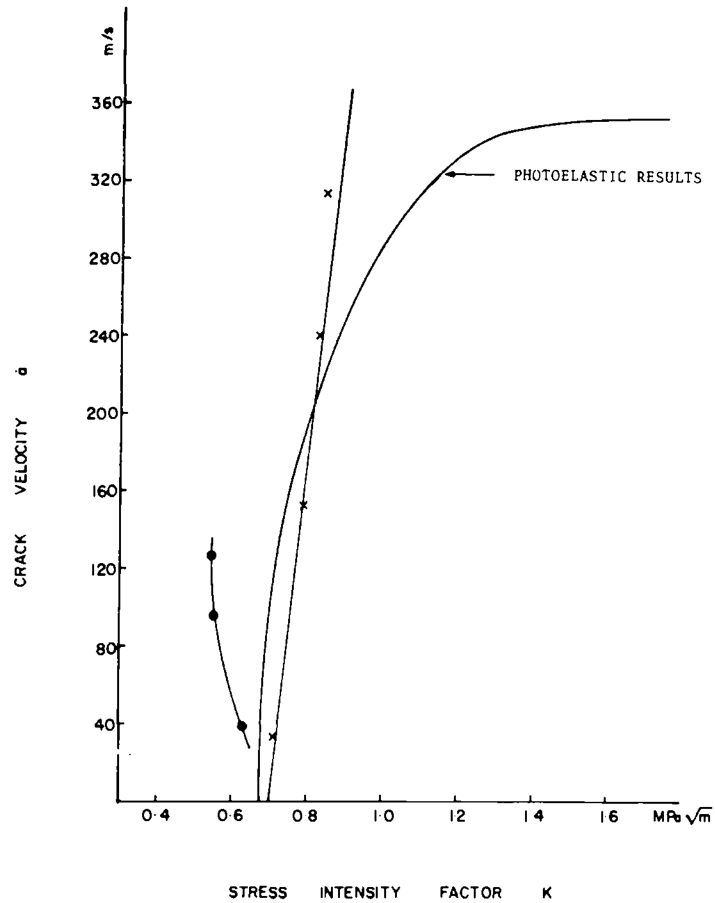

FIG. 7—*Comparison of BCL predicted* K*-versus-*$\dot{a}$ *relationship for Araldite B—R-DCB and M-CT geometries.*

detailed results are the subject of another paper in this volume [7]. Also shown in Fig. 7 are R-DCB results from data published by Kalthoff et al [7]. The agreement is better for the R-DCB geometry, but again at higher velocities the predicted curve falls to the left and in this case above the experimentally determined reference curve.

Results for R-DCB specimens made from Homalite 100 are shown in Fig. 8. The solid curve in Figs. 8*a*, 8*b*, and 8*c* is the same and was obtained from photoelastic experiments. Figure 8*a* shows results from applying the BCL published reference curve to seven different tests. Figure 8*b* shows a comparison which utilized reference curves from the analytical model with torsional springs. Finally, Fig. 8*c* is a comparison of the results obtained by assuming no torsional springs. The best comparison in this

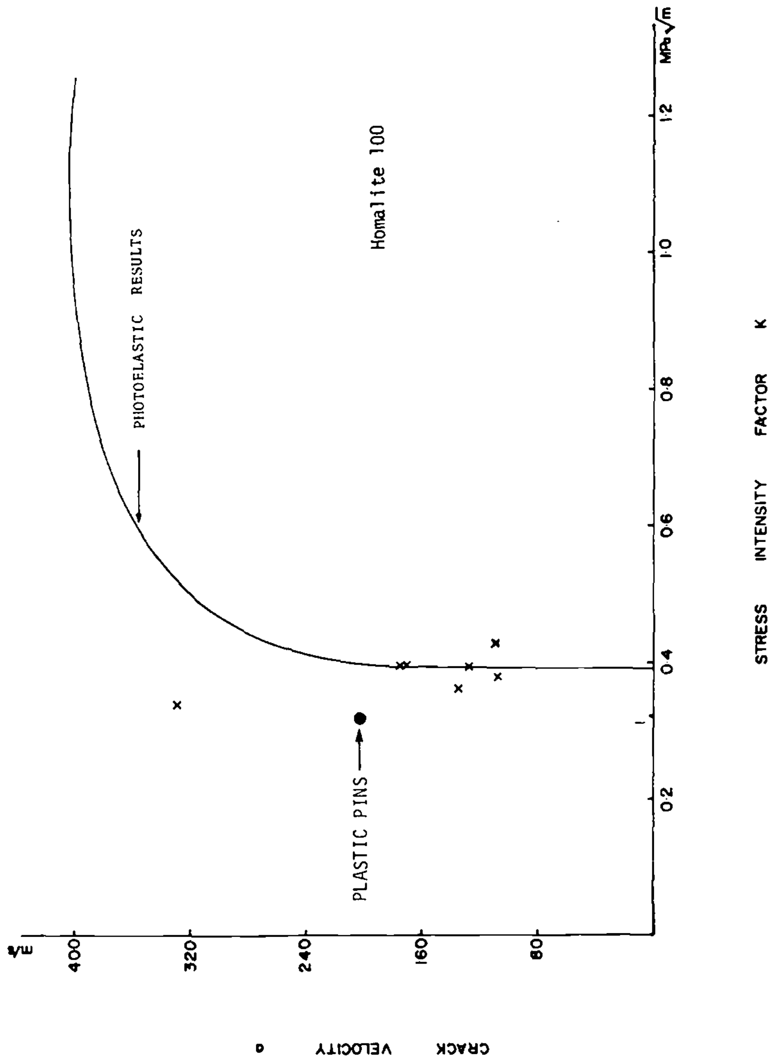

FIG. 8a—*Relationship for R-DCB geometry and points predicted by BCL procedure.*

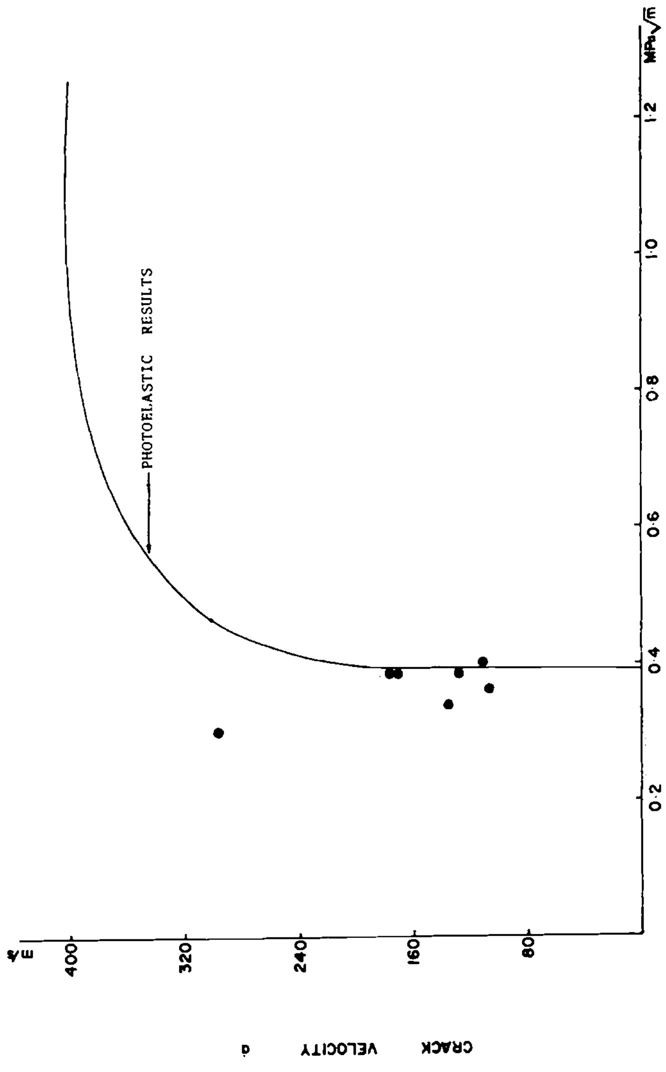

FIG. 8b—*Comparison of Homalite 100* K*-versus-ȧ relationship generated by assuming torsional springs.*

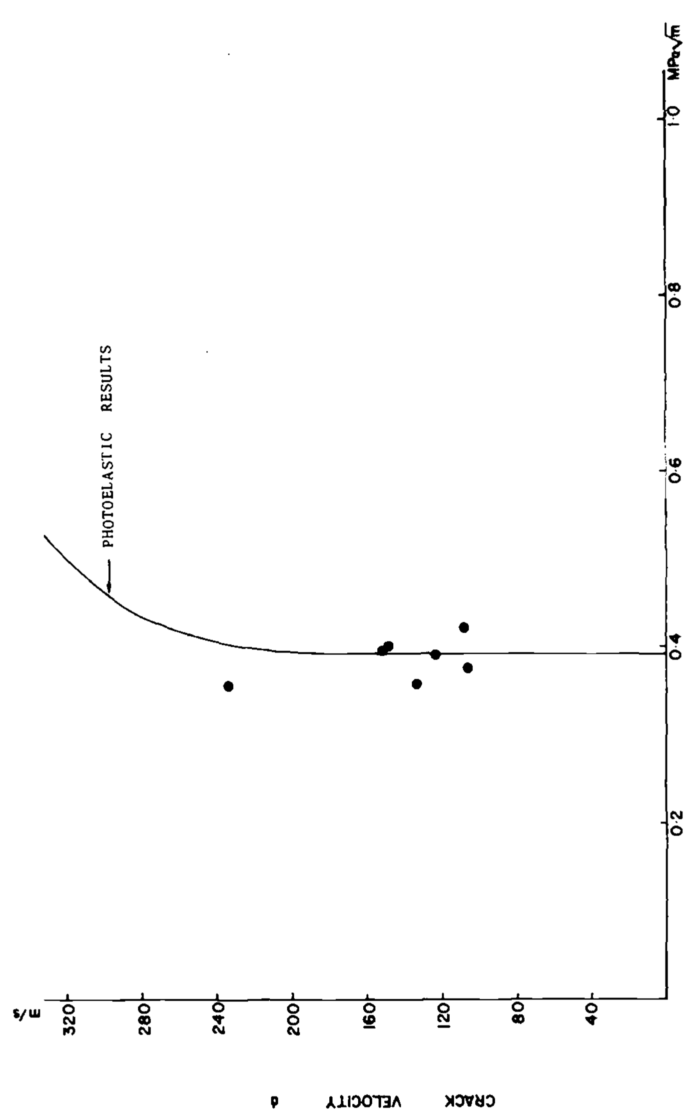

FIG. 8c—*Comparison of Homalite 100 K-versus-ȧ relationship generated by assuming no torsional springs.*

particular case is clearly obtained with the reference curve that assumes no torsional springs along the crack line. It is noted that the value of Δa corresponding to the highest velocity point in Figs. 8*a* through 8*c* is slightly too large (Δa = 119 mm: a_{max} = 106 mm) to meet the criterion for a valid test as presented in the BCL procedure [*3*]. The results from this same test have been compared in detail earlier in this paper with the BCL procedure and have shown excellent agreement from the standpoint of propagation distance and crack speed.

As a matter of interest, the result from Test 259 [*9*] for a R-DCB specimen loaded with a relatively compliant system (plastic pins and wedges) is also shown in Fig. 8*a*. The BCL code assumes a rigid loading system and the prediction for the compliant model by the BCL procedure is well to the left of the correct K-versus-$\dot{a}$ relationship.

Some of the test results reported in Fig. 8 are from experiments in which crack opening was not recorded but where K_Q-values were determined from the readings of the load on the wedge taken just prior to crack initiation. It was difficult to account accurately for the friction present in those tests. In order to increase the data available for comparative purposes and to achieve more accuracy, another series of R-DCB experiments was conducted in which actual crack opening was measured. The results from the BCL prediction procedure as applied to this new series of test are presented in Fig. 9.

It is noted that the specimen material for this series of tests was from a different shipment of Homalite 100 and the K-versus-$\dot{a}$ relationship determined photoelastically was found to be shifted considerably to the right (K_{Im} = 0.52 MPa$\sqrt{m}$ as compared to 0.38 MPa$\sqrt{m}$ for the first three shipments). The solid line in Fig. 9 represents the photoelastically determined function. The points plotted represent the prediction made from the BCL published reference curves. The predicted "curve" falls to the right of the photoelastically determined K-versus-$\dot{a}$ relationship. Since the relationship of stress-intensity factor to velocity is not the same as used in generating the corrected reference curves, they are not strictly applicable in this case. The trends are more than likely to be the same. The no-torsional-spring model would decrease velocity values and increase K-levels predicted. The model with springs would likewise lower velocities and at the same time lower K-levels.

The lowermost predicted point in Fig. 9 is just barely considered a valid test since the crack jump that occurred was only slightly larger than the specimen thickness (Δa = 13.08 mm compared with B = 12.7 mm).

The two points identified with darkened circles in Fig. 9 represent the results of the BCL procedure as applied to two tests in which the crack propagation occurred under "fixed grip" conditions. In these tests

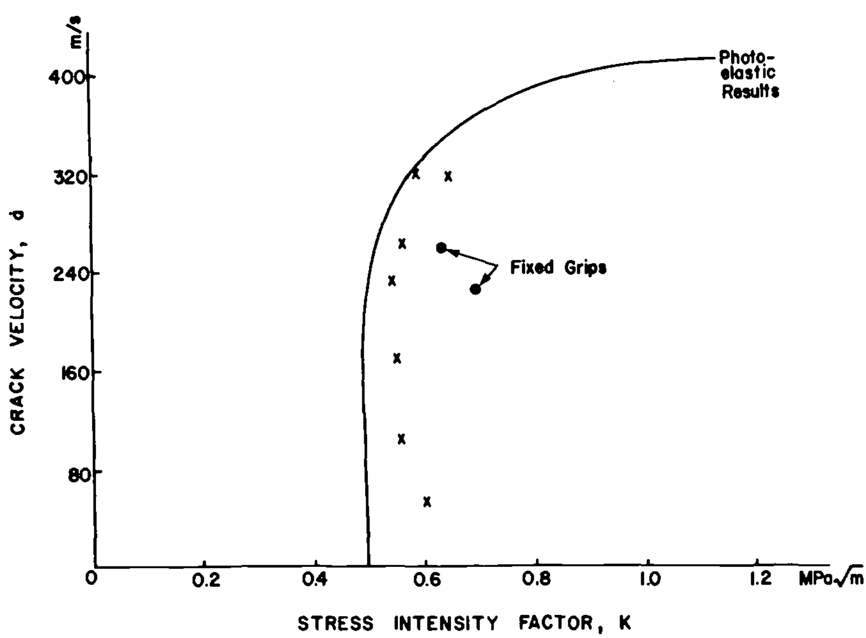

FIG. 9—*Comparison of R-DCB* K*-versus-*$\dot{a}$ *relationship for new shipment of Homalite 100.*

a displacement was applied to the pins and they were rigidly locked in place so that no change in displacement could occur during propagation. This rigid loading system is more in line with the assumptions made by the BCL code. The points are shifted to the right when compared with results for nonfixed conditions.

Figure 10 shows predictions made for 4340 steel CT specimens of the Materials Research Laboratory (MRL) design. The details of the tests are described in a separate paper by Kobayashi and Dally [*10*] in this volume. A split photoelastic coating was applied to the surface of the 4340 specimens and a K-versus-$\dot{a}$ function was determined by reflection photoelastic techniques. A large number of steel specimens were used to determine the stress-intensity factor as a function of crack speed. Only three resulted in arrest sufficiently far from the end of the specimen to be considered valid from the BCL criterion for a valid test. Of these three, the uppermost one, is borderline valid. The crack jump length was 76.45 mm and the crack jump length permitted by the BCL procedure was 75.44 mm. As has been the case with all the predictions presented, the points determined from the BCL procedure lie to the left of the curve determined photoelastically, with the deviation increasing at the higher velocity values.

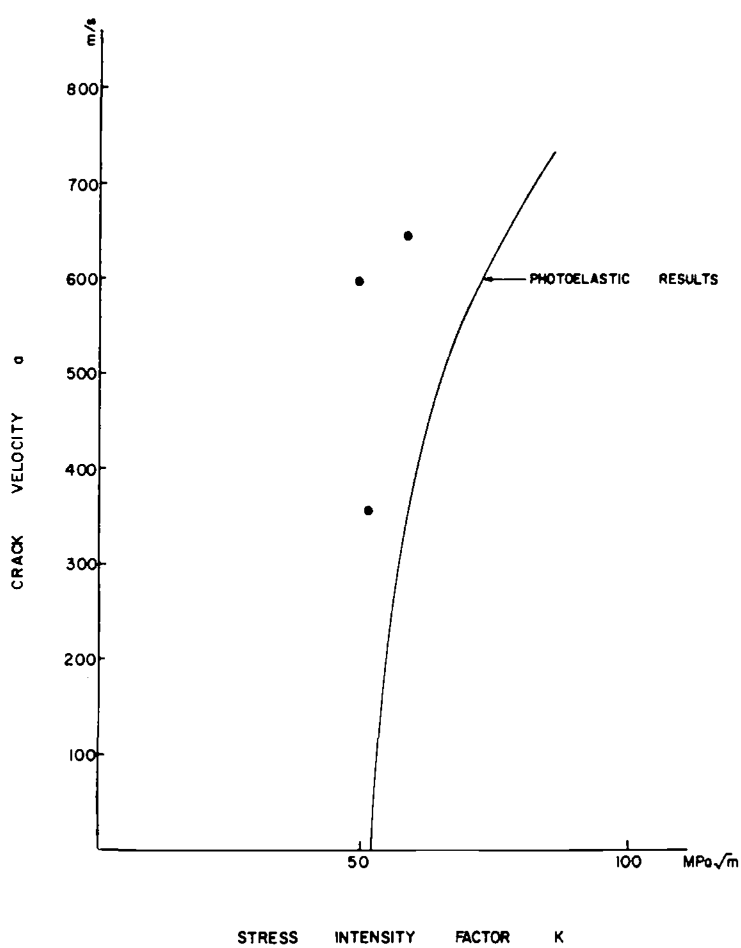

FIG. 10—*Comparison of* ȧ-K *relation obtained using BCL reference curve with results from birefringent coating experiments—4340 steel compact tension geometry.*

K *and Crack Velocity Levels*

The K-levels predicted from the BCL procedure are normally lower than those determined photoelastically. This is especially true at the higher crack velocity values. Comparisons presented have shown that for the R-DCB geometry K-values are better predicted from the use of the corrected (for proper K-versus-$\dot{a}$ input) BCL reference curve that assumes no torsional springs.

Table 1 presents values of velocities—actual and predicted—from various tests conducted at the University of Maryland. When possible all three predicted velocities (BCL published curves, torsional spring reference curves, and no-torsional-spring reference curves) are presented. It is

TABLE 1—*Comparison of Predicted Velocity (m/s) with Experimentally Measured Values.*

Test	Actual	No Torsional Springs	Torsional Springs	BCL
354	214	...	...	261
65	297	232	294	325
66	66	108	109	109
124	43	133	133	133
258	97	106	105	105
352	92	...	...	104
357	285	...	...	316

apparent from the table that the published BCL curves result in predicted velocities that are too large (Test 354, for example, had a velocity of 214 m/s compared with a predicted value of 261 m/s). The analytical model with no torsional springs, which was found to predict the K-level most accurately, appears to underestimate the velocities at higher values. The analytical model with torsional springs seems to predict the actual velocities closer than the other two reference curves examined.

Summary

Comparisons have been made between experimental values and predictions utilizing the BCL procedure for determining crack arrest toughness.

For the one model examined in detail the BCL predictions of arrest distance and crack velocity were good.

The reference curves published are in disagreement by as much as 10 percent at high jump distances when compared with curves generated by using a correct K-versus-$\dot{a}$ relationship as computer input.

The K-versus-$\dot{a}$ curves determined from the procedure show a backward lean which is not observed in the experimental results.

Velocities as predicted from BCL published reference curves appear to be larger by approximately 10 percent than values determined experimentally.

K_{Im}—if determined by averaging a significant number of separate K_{Im}-values as predicted by the procedure—appears to give a good estimate of the experimentally determined value. The values utilized in the averaging must be from a number of tests which cover the entire range of crack speeds.

References

[1] Hahn, G. T. et al, "Critical Experiments, Measurements and Analyses to Establish a Crack Arrest Methodology for Nuclear Pressure Vessel Steels," Battelle Report, BMI-1937, Battelle Memorial Institute, Columbus, Ohio, Aug. 1975.

[2] Hahn, G. T. et al, "Critical Experiments, Measurements and Analyses to Establish a Crack Arrest Methodology for Nuclear Pressure Vessel Steels," Battelle Report, BMI-NUREG-1959, Battelle Memorial Institute, Columbus, Ohio, Oct. 1976.
[3] "Prospectus for a Cooperative Test Program on Crack Arrest Toughness Measurement," Subcommittee on Dynamic Testing/Dynamic Initiation—Crack Arrest Task Group, American Society for Testing and Materials, 9 Dec. 1977.
[4] Irwin, G. R. et al, "A Photoelastic Characterization of Dynamic Fracture," Nuclear Regulatory Commission Report NUREG-0072, Dec. 1976.
[5] Irwin, G. R. et al, "Photoelastic Studies of Crack Propagation and Crack Arrest," Nuclear Regulatory Commission Report NUREG-0342, Sept. 1977.
[6] Kobayashi, Takao and Dally, J. W. in *Fast Fracture and Crack Arrest, ASTM STP 627*, American Society for Testing and Materials, 1976, p. 257.
[7] Metcalf, J. T. and Kobayashi, T., this publication, pp. 128–145.
[8] Kalthoff, J. F., Beinert, J., and Winkler, S. in *Fast Fracture and Crack Arrest, ASTM STP 627*, American Society for Testing and Materials, 1976, p. 161.
[9] Fourney, W. L. and Kobayashi, Takao, in *Fracture Mechanics Applied to Brittle Material, ASTM STP 678*, American Society for Testing and Materials, 1979, pp. 47–59.
[10] Kobayashi, T. and Dally, J. W., this publication, pp. 189–210.

G. T. Hahn,[1] *R. G. Hoagland,*[1] *J. Lereim,*[2] *A. J. Markworth,*[3] *and A. R. Rosenfield*[3]

Fast Fracture Toughness and Crack Arrest Toughness of Reactor Pressure Vessel Steel

REFERENCE: Hahn, G. T., Hoagland, R. G., Lereim, J., Markworth, A. J., and Rosenfield, A. R., "**Fast Fracture Toughness and Crack Arrest Toughness of Reactor Pressure Vessel Steel,**" *Crack Arrest Methodology and Applications, ASTM STP 711,* G. T. Hahn and M. F. Kanninen, Eds., American Society for Testing and Materials, 1980, pp. 289–320.

ABSTRACT: Crack propagation and arrest measurements have been made using six pressure vessel steels and a submerged-arc weldment. The base-metal crack arrest toughness, K_{Im}, is found to increase linearly with temperature above nil-ductility transition (NDT), and between NDT and (NDT + 100°C) is substantially greater than K_{IR}. NDT is found to be a more consistent reference temperature than room temperature NDT (RT_{NDT}). It is suggested that the absolute value of K_{Im} at any temperature is composed of cleavage and dimpled-rupture contributions, with regions of dimpled rupture being contained in shear walls normal to the crack plane and parallel to the direction of crack travel. Shear walls which do not completely fracture are the source of unbroken ligaments observed on the fracture surface. The arrest toughness of the weldment is significantly lower than that of the baseplate and displays little evidence of unbroken ligaments or shear walls.

KEY WORDS: crack propagation, crack arrest toughness, reactor pressure vessel steels, submerged-arc weldment, fractography.

Nomenclature

a	Crack length
a_a	Crack length at arrest
a_0	Crack length at initiation
A_t	True areal fraction of ductile fracture
H	Height of shear wall
J_{Ic}	Path-independent integral associated with crack initiation

[1]Professors of materials, Vanderbilt University, Nashville, Tenn. 37235; formerly Battelle Columbus Laboratories, Columbus, Ohio.
[2]Research engineer, Det norske Veritas, Oslo, Norway.
[3]Principal researchers, Battelle Columbus Laboratories, Columbus, Ohio 43205.

K_{Ia} Static stress intensity following crack arrest
K_{Ic} Plane-strain fracture toughness
K_{ID} Propagating crack toughness
K_{Id} Dynamic loading value of K_{Ic}
K_{Im} Crack arrest toughness, minimum fast fracture toughness
K_{IR} Reference toughness curve [*8*]
NDT Nil-ductility temperature (ASTM E-208)
RT_{NDT} Reference nil-ductility temperature [*8*]
S_y Standard error of estimate
t Extent of heavy slip in vicinity of shear wall
V_t Volume of plastic material per unit of projected crack area
w Dimension from centerline of loading pin to far end of compact specimen
W_p Plastic work per unit volume
δ_a Load-line displacement at crack arrest
δ_a Load-line displacement at crack initiation
ϵ_f Fracture strain associated with a shear wall
$\bar{\sigma}$ Flow stress

Interest in crack arrest centers around situations where a rapidly propagating crack encounters tougher material. The postulated loss-of-coolant accident in reactor pressure vessels is an example. In this case a crack will grow into increasingly warmer and less radiation-embrittled steel. Because of the need for making improved predictions, increasing interest has been focused on methods for measuring the toughness associated with crack arrest.

ASTM Committee E24.01.07 is evaluating procedures for measuring arrest toughness, denoted K_{Im}. Two methods are under consideration and a Cooperative Test Program (CTP) utilizing both is in progress as discussed in a companion paper [*1*].[4] The present paper reports a crack arrest data base, material variability, and a fractographic interpretation of K_{Im}. It describes the results obtained in crack arrest experiments on several heats of reactor pressure vessel steels and of a submerged-arc weldment. The procedure includes the use of the duplex compact specimen and a dynamic analysis of the test data [*2*]. Each experiment yields a value of K_{ID}, the propagating crack toughness. In turn, K_{Im}, the arrest toughness, is the minimum value of K_{ID} at the particular test temperature. The experimental data also yield values of K_{Ia}, the static stress intensity after crack arrest, which is also being considered as a measure of K_{Im} by ASTM E24.01.07.

Methods of applying K_{Im} data in a computer model of crack arrest in a cylinder under thermal shock conditions are discussed in a second com-

[4]The italic numbers in brackets refer to the list of references appended to this paper.

panion paper [3]. Taken together, the procedures and results of the three papers offer the prospect of improved predictive capability of crack arrest in structures of practical interest.

Procedure

Data Base Materials

Four plates of A533B steel, two pieces of A508-2 steel forgings, and a submerged-arc weldment were received from various sources. Mechanical properties, mostly provided by the suppliers, are given in Table 1. The K_{Ic}-values were estimated using either J_{Ic} or equivalent energy, while the other data are obtained from standardized tests. Chemical analyses, heat treatments, and more mechanical property data of these materials are given in detail elsewhere (Heat CTP: Ref *1*; other A533B heats plus the weld: Ref *4*; A508 heats: Ref *5*). With the exception of a low chromium content in the Battelle Columbus Laboratories (BCL) heat, all of the chemical contents are within specification. The heat treatments are all based on commercial practice. Figure 1 shows the static fracture toughness levels of these heats where available. Most of the values above 200 MPa $m^{1/2}$ are suspect since they were obtained using the equivalent-energy method [6]. These are reported only for completeness.

Experimental Methods

All tests were performed using duplex specimens with stiff wedge loading. The procedures have been reported previously [2, 7] and will not be repeated in detail here. Briefly, the specimen consists of a starter section of high-strength low-toughness steel which is electron-beam welded to a block of the material being tested. The two specimen designs and sizes are given in Fig. 2 along with the transverse wedge loading arrangement currently being used. In the earlier parts of this research the double cantilever beam specimen was used. More recently the compact specimen has been adopted. The former design has better crack-arresting capability, while the latter does not need deep side grooves. The starter section contains a blunt notch so that excess strain energy is stored in the specimen and is used to drive the crack once it is initiated. The load-point displacement and crack length at arrest are measured. These quantities are then used to calculate propagating-crack toughness with the aid of reference curves derived from finite-difference computations. These computations also allow one to determine crack velocity. While the K_{Im}-values reported are actually K_{ID}-values, little error is introduced since the K_{ID}/velocity curve has a broad flat minimum [2] and our data lie in this range. It should also be pointed out that the K_{Im} data are ob-

TABLE 1—*Data Base Materials.*

Alloy	Heat	Nil-Ductility Temperature, °C	Reference Nil-Ductility Temperature, °C	Yield Strength at NDT, MPa	Plane-Strain Fracture Toughness, K_{Ic} at NDT, MPa $m^{1/2}$	Charpy Shelf Energy, J
A533B	(BCL)	−12	−12	453	120	182
A533B	(CBI)	−29	−12	>438	<160	~125
A533B	(CE)	−12	−12	471	102	160
A533B	(CTP)	−40	−20	497	...	102
A508	(BW/B)	−7	−7	>488 <528	170	163
A508	(BW/D)	4	4	>454 <498	122	201
SA weldment	(CEW)	−57	−57	576	130	176

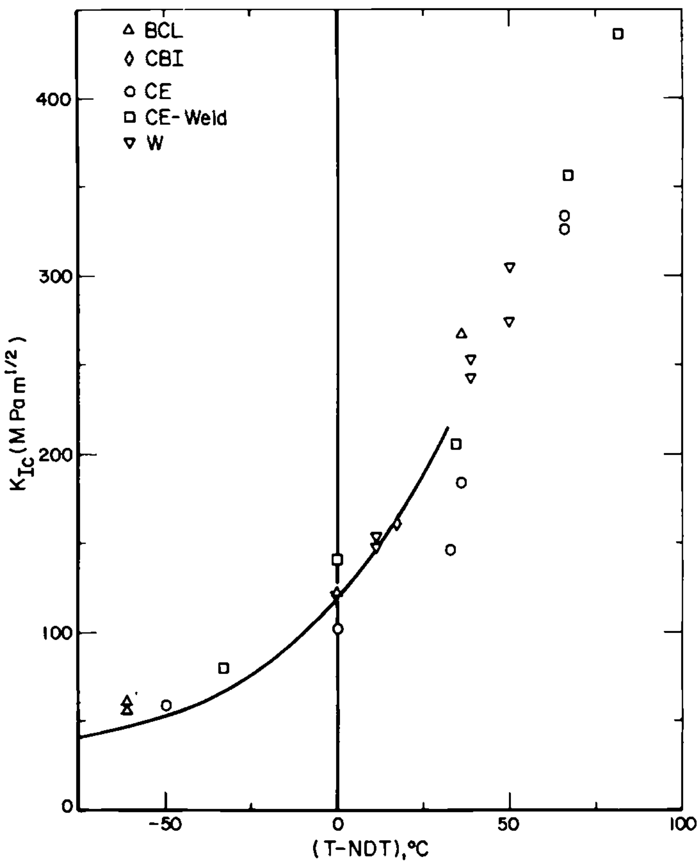

FIG. 1—*Temperature dependence of plane-strain fracture toughness of some reactor pressure vessel steels and a submerged-arc weldment.*

tained using the load-point displacement at initiation while K_{Ia} measurement involves displacement after crack arrest.

Experimental Results

K_{Im} *and* K_{Ia} *Measurements*

The results of the crack arrest toughness evaluations for the different heats of A533B, A508, and the weldment are summarized in Figs. 3-6. Detailed tabulation of these data are provided in Table 2. The graphs make use of two common indexing temperatures, the RT_{NDT} and NDT [*8*], to facilitate comparisons for the different materials on a single graph. The spread in the data therefore reflects (1) material variability from specimen to specimen within a heat, (2) heat-to-heat variability, (3) variability arising from the approximate

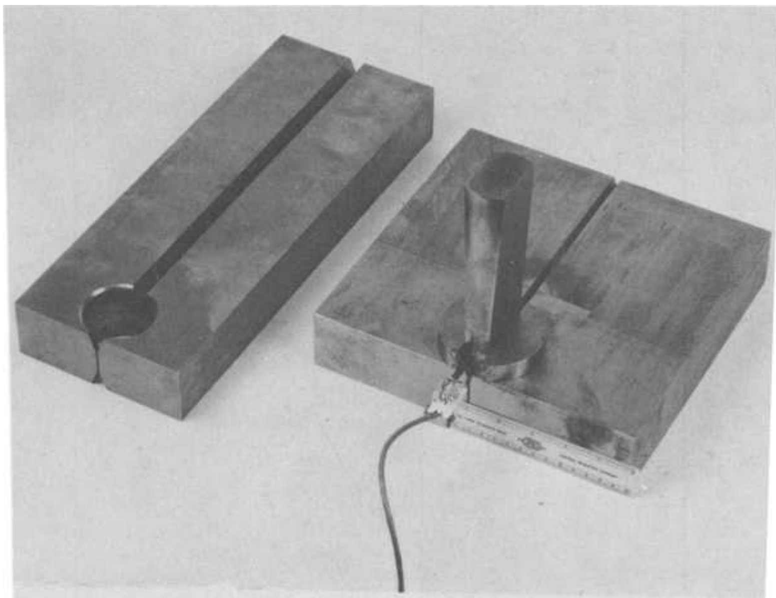

	DCB	CT
Height (mm)	140	250
Length (mm)	400	250
Thickness (mm)	50	50

FIG. 2—*The double cantilever beam and compact tension crack arrest test specimens and transverse wedge loading arrangement.*

nature of the concept of a single indexing temperature (for example, NDT or RT_{NDT}), and (4) the possibility of variability arising from use of differing specimen designs. Of these, materials variability is most pronounced and the heat-to-heat variability is influenced by the choice of indexing temperature.

These four variabilities are not differentiated in the statistical analysis discussed in the next section. The crack arrest toughness values are in each case compared with (1) the average trend of (slow loading) K_{Ic}-values for these heats (see Fig. 1), (2) the K_{IR}-curve, and (3) the upper bound of the original K_{Id}-K_{Ia} data set which was used to establish the K_{IR}-curve [*8*].

The K_{Im}-values for the plate and forging materials in the range RT_{NDT} to $RT_{NDT} + 70°$ generally fall in the band between K_{Ic} and the upper bound of the original K_{Id}-K_{Ia} set, well above the K_{IR}-curve. The K_{Im}-values are about equal to K_{Ic} at the RT_{NDT} but are less temperature-dependent than K_{Ic} above RT_{NDT}. The K_{Im}-values for the submerged-arc weldment are significantly

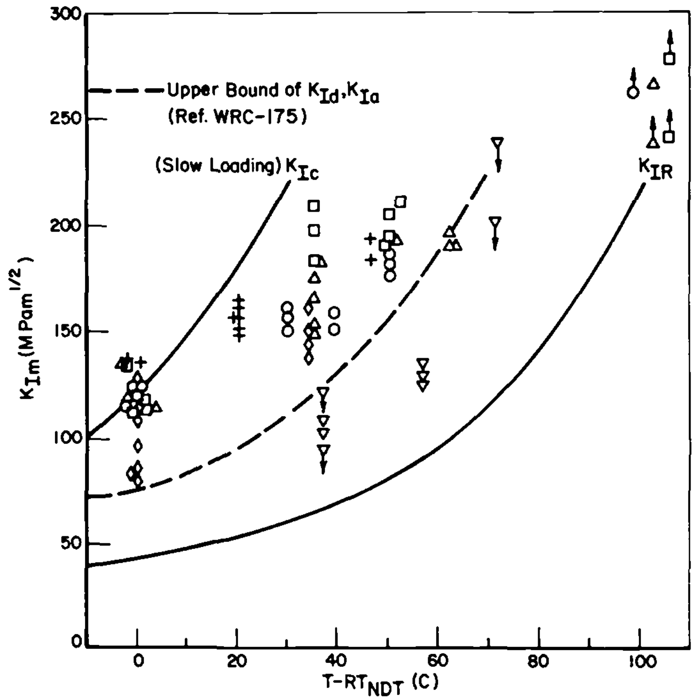

FIG. 3—*Results of crack arrest toughness measurements on data base materials derived from the dynamic analysis approach and indexed on RT_{NDT}. (Key to material symbols in Fig. 4.)*

lower and, while falling in the band between the K_{IR}-curve and the upper bound of the K_{Id}-K_{Ia} set, are still significantly above the K_{IR}-curve.

The K_{Ia}-values obtained from the same test specimens are on average 32 percent smaller than the corresponding K_{Im}-values. For the base materials, the K_{Ia}-values tend to fall into the band between the K_{IR}-curve and the upper bound of the K_{Ia} set. They also display less temperature dependence than K_{Ic} or K_{IR}. The K_{Ia}-values for the weldment straddle the K_{IR}-curve. The present K_{Ia} measurements are compared with the data collection for A533B plate recently reported by Ripling et al [*9*], represented by the shaded band in Fig. 5. The Ripling et al values display essentially the same temperature dependence but are approximately 20 percent lower than the present results.

Statistical Analysis

Results of the linear regression analysis of crack arrest toughness measurements for the A508 and A533B base materials are summarized in Table 3 and in Figs. 7-10. The results for the weldment were not included because the data clearly represent a different population. As discussed in the

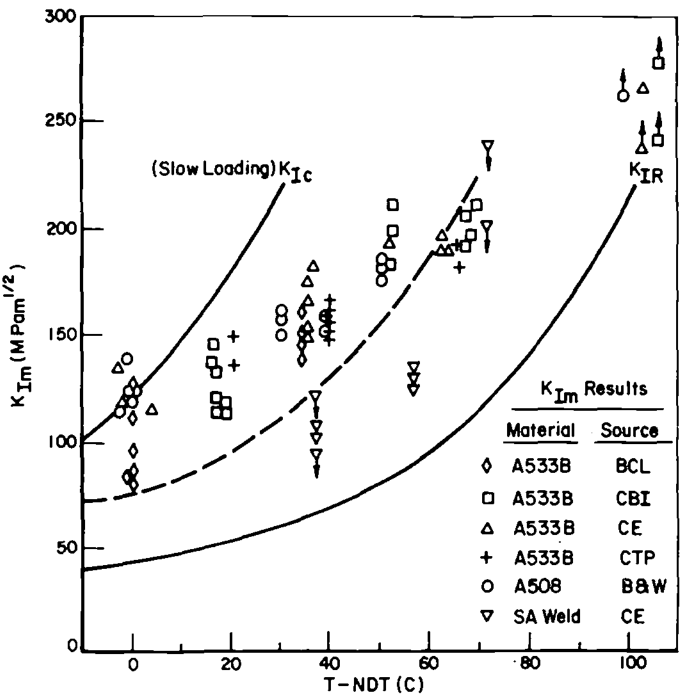

FIG. 4—*Results of crack arrest toughness measurements on data base materials derived from the dynamic analysis approach and indexed on NDT.*

following, the different fracture surface morphology of the weldment supports this exclusion. More information about the statistical analysis is presented in the Appendix. Note that to the extent the data are normally distributed about the regression line, the probabilities that a data point lies above the $2s_y$ and $3s_y$ lower bound are 0.9773 and 0.9987, respectively.

The analyses show that both the K_{Im}- and K_{Ia}-values for the plates and forgings fall significantly above the K_{IR}-curve. The tabulation of s_y-values in Table 3 also shows that the variability of the data is smaller when the NDT is used as the indexing temperature as opposed to the RT_{NDT}. The s_y-values for K_{Im} and K_{Ia} are comparable, and about 16 MPa m$^{1/2}$.

Comparison of K_{Im}*-Values from the Two Specimen Designs*

For some of the steels reported in this paper, both double cantilever beam (DCB) and compact tension (CT) specimen designs (Fig. 2) were tested at identical temperatures. These data obtained permit a comparison of the results from the two specimens to determine whether the K_{Im} results contain a geometry dependence. Referring to the summary of the test results con-

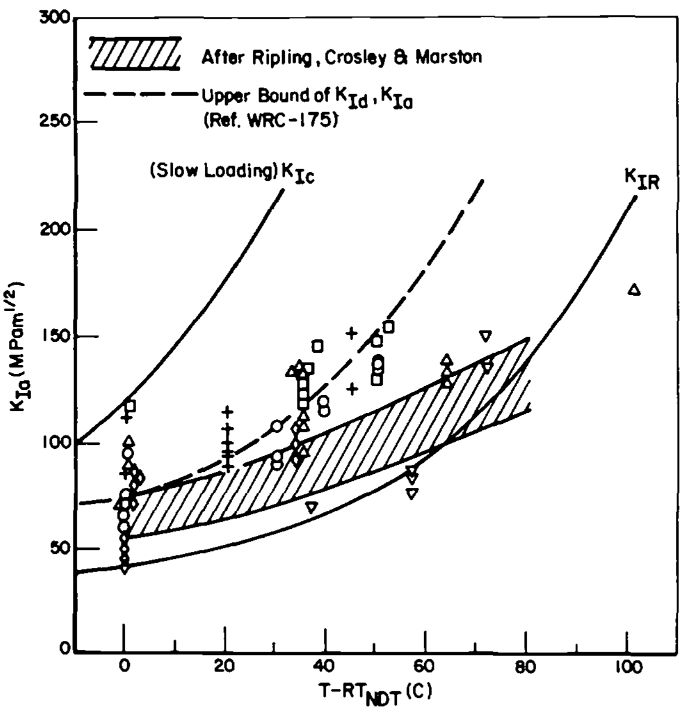

FIG. 5—*Results of crack arrest toughness measurements on data base materials derived from the static analysis approach and indexed on RT_{NDT}. (The shaded band represents the K_{Ia} data collection of Ripling, Crosley and Marston* [9]).

tained in Table 2, there are three instances where both designs were used under the same conditions: CBI steel tested at 35°C, CE tested at 35°C, and BW steel tested at 0°C. (These temperatures are relative to the RT_{NDT}.) Averages of the results for each specimen type have been plotted one against the other in Fig. 11.

Although the amount of data is insufficient for a sound statistical interpretation, examining Fig. 11 shows that the agreement between the two specimen types is good. There is some trend of the DCB results to exceed the CT results although the discrepancy is of the order of 10 percent or less.

Effect of Crack Jump Length on K_{ID} and K_{Ia}

In previous papers [*7,10*] we have reported systematic variations of the stress intensity at arrest, K_{Ia}, with the length of crack jump. These data are, however, subject to criticism since they were obtained using earlier procedures. In particular, sources of excess energy supply in the loading system were present [*4*], with the result that the crack propagated farther than it

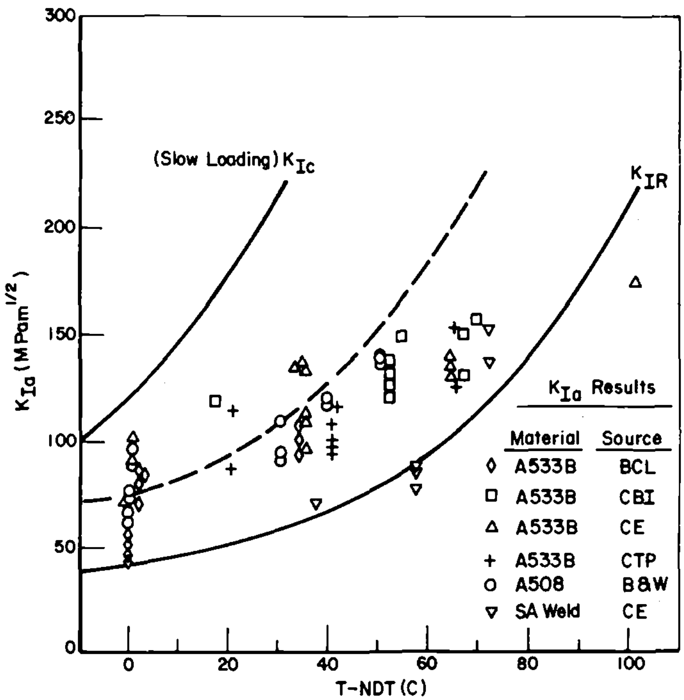

FIG. 6—*Results of crack arrest toughness measurements on data base materials derived from the static analysis approach and indexed on NDT.*

would have under fixed-grip conditions. The use of transverse wedge loading has almost completely eliminated this problem. There has also been a change in our measurement technique; we now use the displacement after crack arrest to calculate K_{Ia}, in accord with the procedure of Ripling et al [*9*].

Figure 12 shows the variation of K_{ID} and K_{IA} with crack jump for two nuclear pressure vessel steels tested at NDT and for one steel tested at slightly differing temperatures. Similar results are obtained at other temperatures. The systematic decrease of K_{Ia} with crack jump length, reported previously [*7,10*], persists. On the other hand, K_{ID}-values show no systematic crack jump length dependence. Since larger crack jumps correspond to larger crack velocities, this observation further demonstrates that the K_{ID}/velocity curve has a broad shallow minimum at these temperatures, facilitating determination of K_{Im}.

Fractography

The crack propagation mechanism constitutes an important issue in interpreting the K_{Im} measurements reported here. It has been shown by the

TABLE 2—*Summary of Crack Arrest Toughness Measurement Conditions and Results.*

Specimen Identification	Specimen Type	Notch Root Radius, mm	Relative Temperature $T-RT_{NDT}$, °C	δ_o, mm	δ_a, mm	a_o, mm	a_a, mm	K_Q MPa $m^{1/2}$	K_{ID} MPa $m^{1/2}$	K_{Ia} MPa $m^{1/2}$
					BCL A533B					
AR-1	DCB	1.85	0	1.65	1.88	82.6	139.5	171	128	87
AR-2	DCB	1.85	0	1.80	1.98	82.8	168.9	185	116	81
AQ-1	DCB	1.85	0	1.40	1.65	82.3	185.7	145	83	55
AQ-2	DCB	1.88	0	1.65	1.91	82.8	156.5	170	114	85
AO-2	DCB	1.83	0	2.90	4.19	81.5	251.7	303	135	76
AV-1	DCB	1.88	0	1.57	1.65	83.8	205.0	154	82	52
AU-2	DCB	1.85	0	1.63	2.06	82.0	221.7	174	86	49
DD-1	DCB	1.91	0	1.98	3.28	83.1	253.8	205	94	47
AU-1	DCB	1.85	34	1.60	1.77	82.0	135.4	181	139	107
DD-2	DCB	1.91	34	2.13	3.00	83.3	178.1	219	144	93
DD-3	DCB	3.61	34	1.80	2.49	83.1	147.6	186	150	101
DD-4	DCB	3.53	34	2.01	2.36	84.6	143.5	203	162	116
					CBI A533B					
DA-88	DCB	3.56	52	2.05	2.10	83.7	128.4	259	212	156
DA-89	DCB	2.79	49	1.96	1.96	84.6	136.7	244	190	137
DA-91	DCB	2.84	35	2.13	2.15	86.7	135.0	258	209	124
DA-93	DCB	3.30	110	2.21	2.24	84.4	107.1	274	>274[a]	...[a]
DA-94	DCB	3.30	110	1.94	1.98	86.0	110.1	236	>236[a]	...[a]
DA-96	DCB	2.84	35	2.19	2.21	85.0	143.9	272	197	118
DA-98	DCB	3.56	50	2.09	2.16	85.0	135.5	259	205	148
DA-104	DCB	2.36	35	1.88	1.92	84.0	135.8	235	183	132
DA-107	CT	2.34	35	1.17	1.17	68.8	119.6	216	183	137
DA-110	CT	2.79	0	0.85	0.93	68.0	148.5	158	112	83
DA-111	CT	2.79	0	1.12	1.22	69.5	149.7	205	143	118
DA-86	DCB	3.22	19	1.96	1.97	78.6	158.1	263	168	113
DA-95	DCB	3.25	21	1.95	2.00	83.7	169.4	248	156	105
DA-97	DCB	3.28	3	1.73	1.78	83.2	164.5	220	143	97

TABLE 2—*Continued.*

Specimen Identification	Specimen Type	Notch Root Radius, mm	Relative Temperature $T-RT_{NDT}$, °C	δ_o, mm	δ_a, mm	a_o, mm	a_a, mm	K_Q MPa $m^{1/2}$	K_{ID} MPa $m^{1/2}$	K_{Ia} MPa $m^{1/2}$
					CE A533B					
EA-1	DCB	3.25	35	1.95	2.03	82.7	156.3	251	168	119
EA-7	DCB	3.30	35	1.96	2.03	82.3	179.6	251	151	97
EA-8	DCB	3.30	35	1.96	2.04	82.4	163.2	254	165	113
EA-9	DCB	3.25	62	2.00	2.12	82.8	138.7	258	196	134
EA-10	DCB	3.30	102	2.18	2.24	82.7	113.9	278	264	207
EA-12	DCB	3.30	102	1.84	1.88	82.4	108.1	236	>236[a]	...[a]
EA-13	DCB	3.30	62	1.86	1.92	83.4	131.2	237	189	131
EA-14	DCB	3.30	63	1.80	1.93	82.9	126.9	230	188	138
EA-15	DCB	2.95	35	1.78	1.83	82.9	131.4	228	182	136
EA-16	DCB	3.30	35	2.18	2.31	82.2	167.5	282	181	109
EA-29	CT	3.33	0	1.03	1.12	68.7	145.7	188	136	102
EA-30	CT	3.25	1	0.89	1.04	68.5	150.5	163	114	84
EA-31	CT	3.25	−1	0.96	0.96	68.7	164.7	176	116	69
EA-32	CT	3.05	35	0.95	0.96	68.5	117.0	175	148	118
					CTP A533B					
RD-44	CT	1.29	0	1.33	1.41	68.7	164.2	245	136[b]	86[b]
RH-88	CT	1.27	2	1.38	1.67	69.5	167.3[c]	252	146	113
RH-79[d]	CT	1.03	20	1.24	1.33	69.2	164.2	230	153	97
RD-2	CT	1.27	20	1.44	1.58	69.7	176.1[c]	263	165	91
RH-55	CT	1.26	20	1.27	1.32	71.2	152.3	229	163	113
RH-46[d]	CT	1.16	20	1.25	1.33	70.0	162.7	229	153	100
RH-53[d]	CT	1.04	20	1.27	1.34	69.5	167.5[c]	231	150	96
RD-38[d]	CT	1.08	20	1.25	1.31	70.0	156.2	229	158	107
RD-43	CT	1.47	46	1.21	1.26	69.7	116.2[c]	221	192	153
RG-136[d]	CT	1.12	44	1.48	1.56	76.3	156.6	254	180	126

					B&W A508					
BW-11	DCB	3.15	0	1.63	1.68	81.7	155.3	210	141	96
BW-12	DCB	3.20	0	1.78	1.83	84.2	204.1	229	123	71
BW-15	CT	3.18	39	1.09	1.21	66.7	138.6	205	151	119
BW-16	CT	3.28	39	1.17	1.25	67.7	143.1	215	157	118
BW-18	CT	3.40	98	1.41	1.46	67.6	95.0	261	>261[a]	...[a]
BW-19	CT	3.30	50	1.27	1.42	67.7	140.1	236	174	138
BW-20	CT	3.18	50	1.31	1.38	67.8	136.7	241	181	138
BW-21	CT	3.38	50	1.38	1.43	69.2	142.1	247	185	135
BW-22	CT	2.82	0	1.24	1.35	70.2	181.5	225	137	64
BW-23	CT	2.92	30	1.24	1.36	70.7	154.1	225	157	114
BW-24	CT	2.90	0	1.06	1.17	68.0	171.3	196	124	72
BW-26	CT	2.92	30	1.28	1.41	70.7	168.5	231	150	95
BW-27	CT	2.92	0	1.07	1.33	66.9	188.6	196	114	60
BW-28	CT	3.20	30	1.37	1.49	67.7	172.3	253	160	92
					CE Weldment					
EP-6	CT	1.40	37	1.27	...	70.5	...	230	<122[c]	...[c]
EP-9	CT	1.52	37	0.98	1.58	69.7	194	180	<103[c]	...[c]
EP-10	CT	1.02	37	0.96	...	70.7	...	173	<90[c]	...[c]
EP-12	CT	1.96	57	1.08	1.13	71.5	161.1	200	136	85
EP-14	CT	1.02	37	0.89	0.94	66.7	162.6	167	110	70
EP-19	CT	1.88	57	1.04	1.22	70.7	172.3	187	120	77
EP-20	CT	1.78	57	1.00	1.05	67.4	154.6	186	127	87
EP-22	CT	3.61	71	1.38	1.52	72.3	148.5	248	<201[e]	136
EP-25	CT	3.68	71	1.37	1.46	73.5	132.5	242	<231[e]	152

[a]Crack stopped at weld.
[b]Crack branched and ran out of plane and out of the side groove in the test section.
[c]Tentative bounds for the crack extension increment for this test specimen (63 mm < Δa < 97 mm) where exceeded.
[d]Specimen has 12.5-mm-deep side groove segments at the weld.
[e]Arrested crack front not straight.

TABLE 3—*Results of linear regression analysis of crack arrest toughness measurements.*

Variables	Intercept[a] A, MPa $m^{1/2}$	Coefficient[a] B, MPa $m^{1/2}$/°C	Standard Error[b] of Estimate, MPa $m^{1/2}$	Correlation Coefficient
K_{Im} versus T-NDT	116.1	1.28	16.8	0.8737
K_{Im} versus T-RT_{NDT}	126.9	1.19	21.3	0.7871
K_{Ia} versus T-NDT	73.9	1.07	16.4	0.8382
K_{Ia} versus T-RT_{NDT}	82.5	1.01	19.2	0.7694

[a] $K_{Ix} = A + Bx$, where x is either T-NDT or T-RT_{NDT}.
[b] See Appendix.

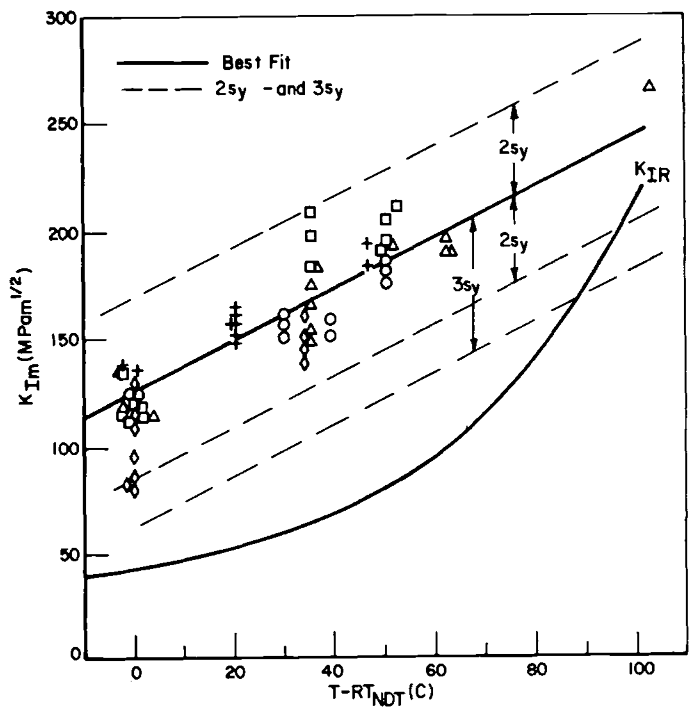

FIG. 7—*Results of linear regression analysis of crack arrest toughness measurements on data base materials derived from the dynamic analysis approach and indexed on RT_{NDT}.*

authors [*11,12*] and others [*13,14*] that, when crack propagation in medium-strength ferritic steels occurs by cleavage and ductile tearing, the cleavage precedes tearing. As a consequence, near the crack tip the fracture surface partitions into areas where separation has occurred by cleavage and ductile tearing and into unbroken regions in which eventual failure will occur by ductile tearing. This behavior commonly manifests itself in the nuclear pressure vessel steels as large unbroken ligaments on the fracture surfaces of

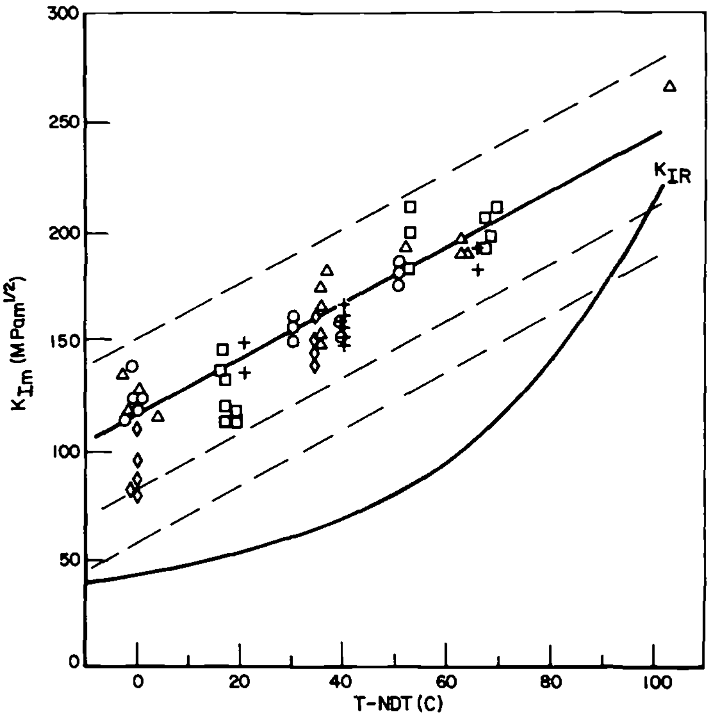

FIG. 8—*Results of linear regression analysis of crack arrest toughness measurements on data base materials derived from the dynamic analysis approach and indexed on NDT.*

specimens tested at the NDT or above [*15*]. Ligaments as large as 10 to 20 mm in length are sometimes observed. For example, the three broken pairs of fracture surfaces shown in Fig. 13 display prominent unbroken ligaments. All three specimens are of A508 and tested at NDT + 30°C. In one case, Specimen BW23, the ligament is along the edges of the fracture surface. In this case the K_{ID}-value is in close agreement with the values obtained from the other two specimens which had much straighter crack fronts. Considering questions which have been raised with regard to the effect of crack front profile on crack arrest toughness measurements, this result suggests that some allowance for crack front irregularity and tunneling is appropriate.

Smaller ligaments visible to the naked eye are always observed. Under microscopic examination, areas of ductile dimples can be observed in a spectrum of sizes. Typical examples of this fracture appearance showing the ductile areas interspersed with cleavage in these steels are provided in Fig. 14. A portion of these ligaments which failed in a ductile fashion did so before crack arrest. Indeed the authors have shown [*13*] that the total areal density of unbroken ligaments is greatest near the arrested crack tip and decreases

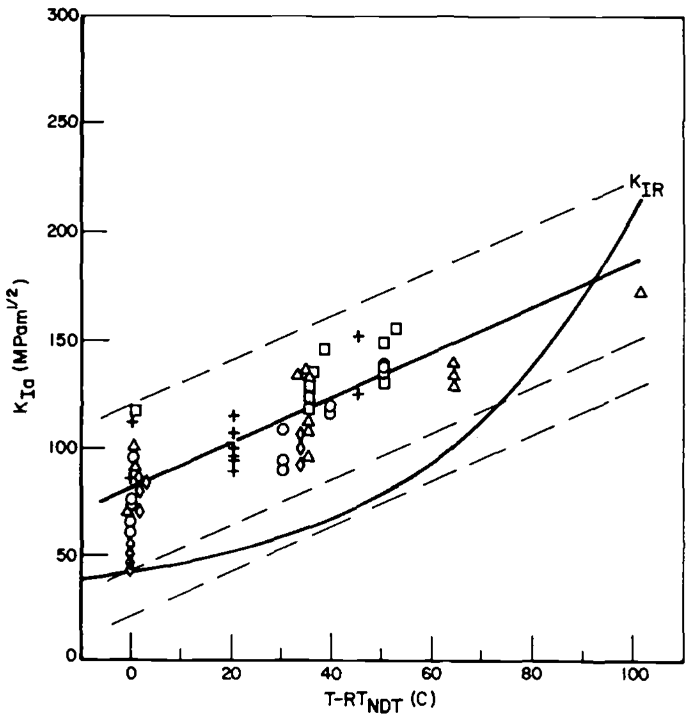

FIG. 9—*Results of linear regression analysis of crack arrest toughness measurements on data base materials derived from the static analysis approach and indexed on RT_{NDT}.*

gradually away from the crack tip, with larger ligaments surviving farther back from the crack tip than the smaller ones.

There is evidence that a substantial part of the energy dissipated during crack propagation in these steels is consumed by the plastic deformation and rupture of the ductile ligaments. In Fig. 15, for example, very large shear strains are visible adjacent to the failed ligament which joined two non-coplanar sheets of cleavage. The distortion of the microstructure suggests strains on the order of 2 to 3 in a band approximately 50 to 100 μm on either side of the failure plane. The eventual failure of the ligament is brought about by the formation of and linking of voids originating on cementite particles (See Fig. 14).

The shear walls of the size shown in Fig. 15 tend to be oriented nearly perpendicular to the crack plane. Furthermore, the length of the walls generally is much greater than their height, with their length oriented parallel to the direction of crack propagation. These characteristics give rise to the familiar river pattern which always points back to the fracture origin. The schematic in Fig. 16 shows in a simplified way how certain ligaments and shear walls are believed to form as a result of uncoordinated extension of the

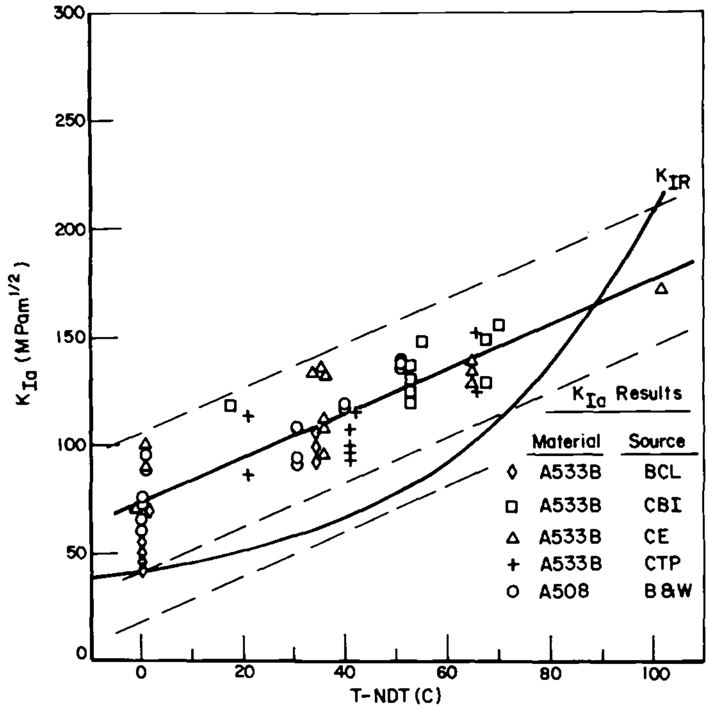

FIG. 10—*Results of linear regression analysis crack arrest toughness measurements on data base materials derived from the static analysis approach and indexed on NDT.*

crack front by cleavage. This uncoordinated crack extension leads to non-coplanar sheets of cleaved areas which eventually join by shear of the connecting ligament.

Because of the nearly perpendicular orientation of the shear walls, an observation of the fracture surface in a view normal to the crack plane may tend to create the impression that the total areal fraction of ductile rupture is considerably less than the true value. In Fig. 17, for example, two areas are shown with one view normal to the surface and another with the crack plane tilted 26 deg. From the change in the projected width of the shear wall due to tilt, we estimate that the shear walls evident in these two views are tilted approximately 70 deg with respect to the crack plane. In this case a normal view understates the areal fraction of ductile rupture by a factor of 3. It is also noteworthy that upon tilting the specimen in the microscope new areas of ductile rupture are observed. It should also be noted that the not uncommon observations of the dependence of the areal fraction of cleavage on temperature from normal-view microscopic observation of fracture surfaces probably overestimate the amount of cleavage.

It is possible to estimate the amount of energy dissipated in the plastic

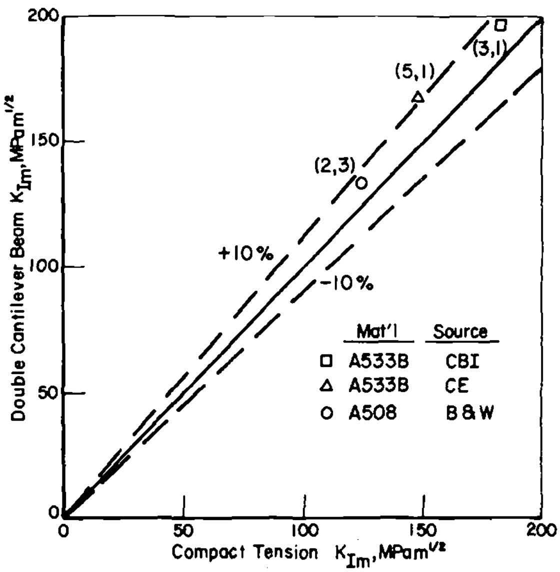

FIG. 11—*A comparison of* K_{Im} *results obtained from compact tension and DCB test specimens. Each point represents an average of one or more results from each specimen type at the same temperature. The number of specimens involved in the average is identified in parentheses, the first being the number of DCB specimens, and the second the number of compact tension specimens.*

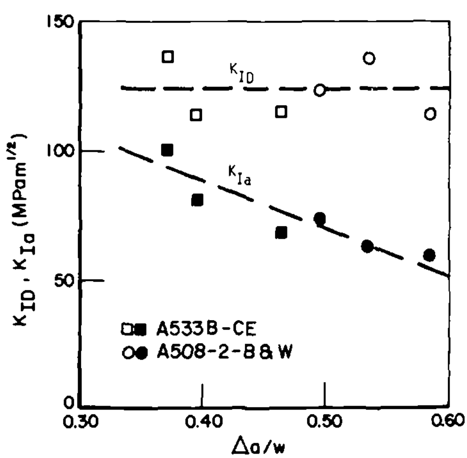

FIG. 12a—*Variation of fast fracture toughness and stress intensity at crack arrest,* K_{Ia}, *with length of crack jump: compact tension specimens. (Two steels tested at NDT. Open symbols =* K_{ID}*; closed symbols =* K_{Ia}*.)*

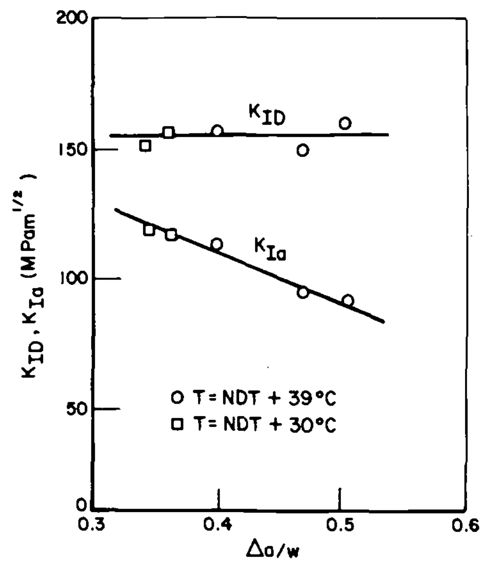

FIG. 12b—*Variation of fast fracture toughness and stress intensity at crack arrest,* K_{Ia}, *with length of crack jump: compact tension specimens. (A508-2 tested above NDT.)*

deformation and rupture of the ligaments per unit area of fracture surface. This in turn provides an estimate of the contribution of ductile rupture processes to the K_{Im} measurements. The work done in the the plastic deformation of an element of volume to failure is approximately

$$W_p = \int_0^{\epsilon_f} \bar{\sigma} d\bar{\epsilon} \simeq \bar{\sigma}\epsilon_f$$

where $\bar{\sigma}$ is an average flow stress consistent with the strain range, constraint, and strain hardening occurring in the element, and ϵ_f is the plastic strain at failure. At room temperature the yield strengths of the nuclear pressure vessel steels in this study are typically 450 MPa with ultimate strengths on the order of 620 MPa. For the average stress in a ligament we estimate 750 MPa.[5] If the average strain in the ligament at fracture is taken as 2, the plastic work done per unit volume is 1500 MJ/m^3.

In order to gain an estimate of the thickness of the deformed region adjacent to the shear walls, a number of sections perpendicular to the crack plane

[5]Reasonable estimates of the strain rates in a ligament during crack propagation are in the range of 10^3 to 10^4 s^{-1}. According to Hahn et al [*16*], these strain rates would elevate the yield stress by at least 280 MPa. In addition, the deformation of the ligament is likely to occur under primarily plane-strain conditions, which accounts for an additional 15 percent elevation of the yield strength. The contribution due to strain hardening is uncertain and therefore an average increment in flow stress of 300 MPa above the conventional uniaxial tensile yield strength should be conservative.

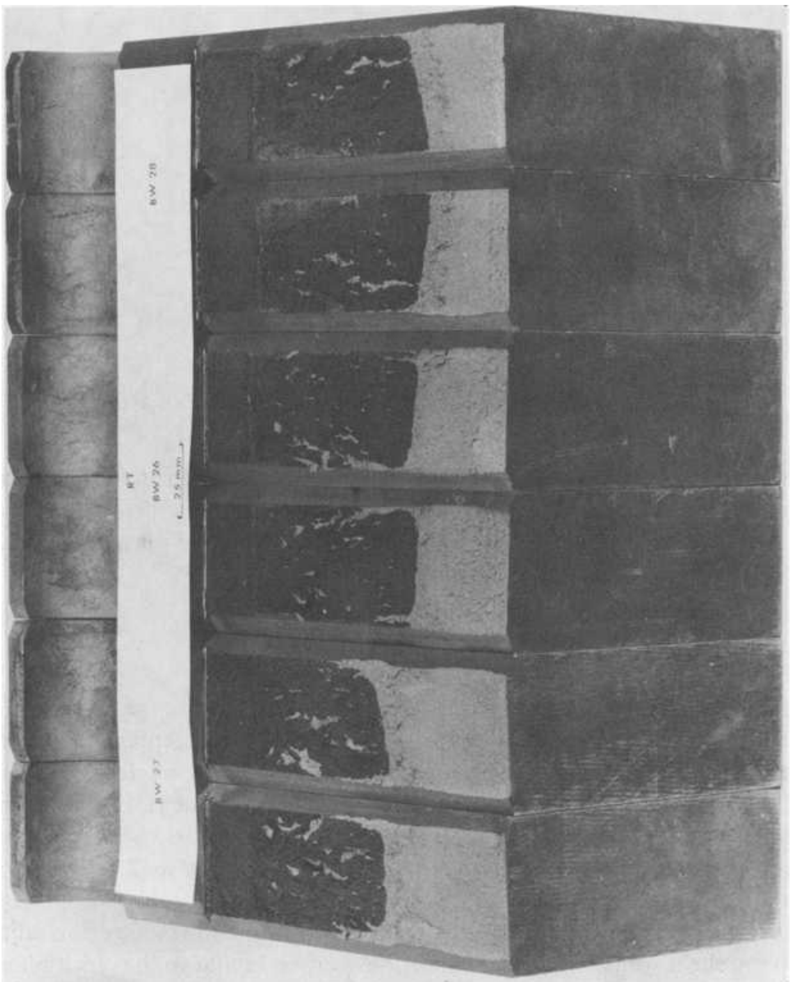

FIG. 13—*Mating fracture surfaces from three specimens of A508 forging steel tested at 22°C.*

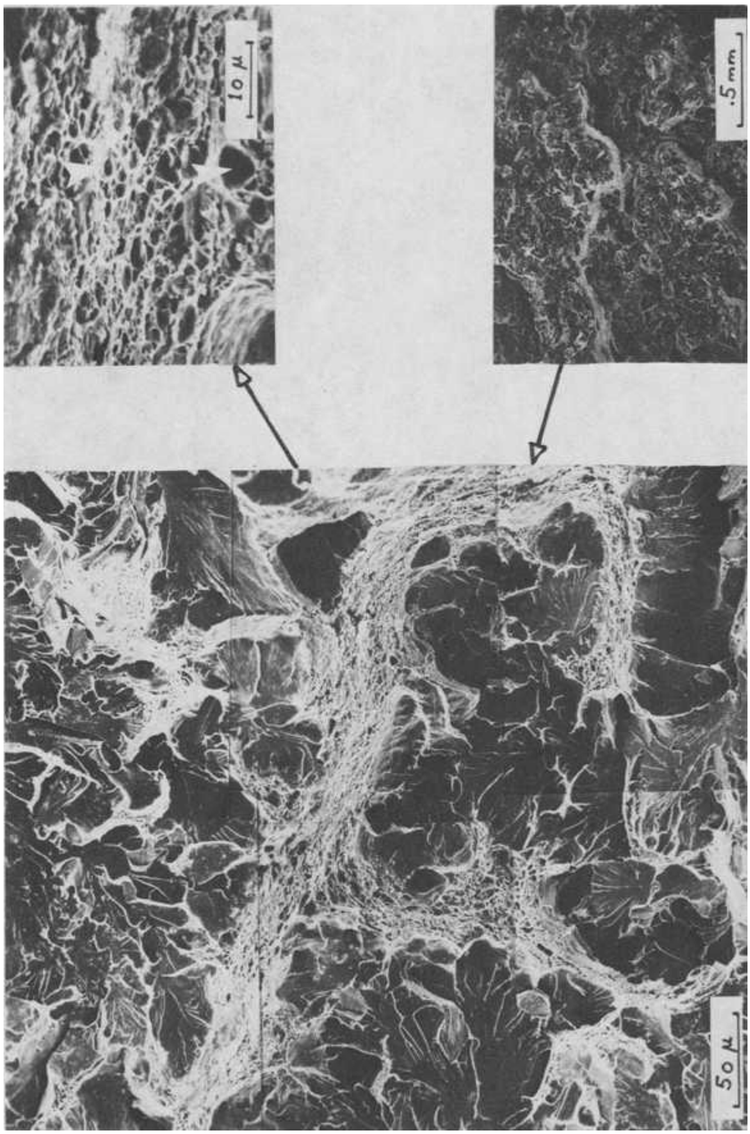

FIG. 14—*An area of a fracture surface of A508 tested at 50°C above RT_{NDT} showing regions of ductile fracture surrounding cleavage areas. At the highest magnification the ductile fracture surface is revealed as a high density of small voids, some of which contain visible particles.*

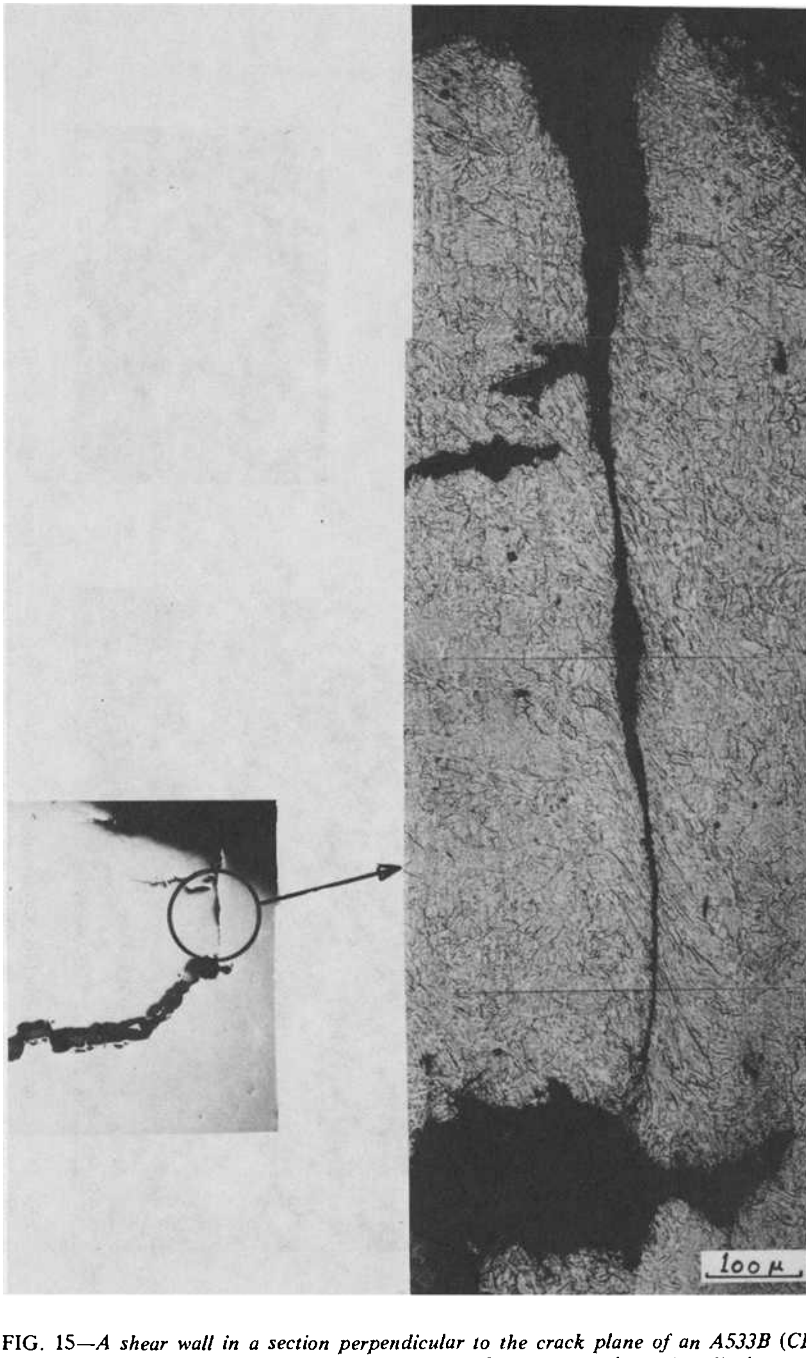

FIG. 15—*A shear wall in a section perpendicular to the crack plane of an A533B (CBI) specimen. Test temperature was 19°C above RT_{NDT}. The section is also perpendicular to the crack propagation direction.*

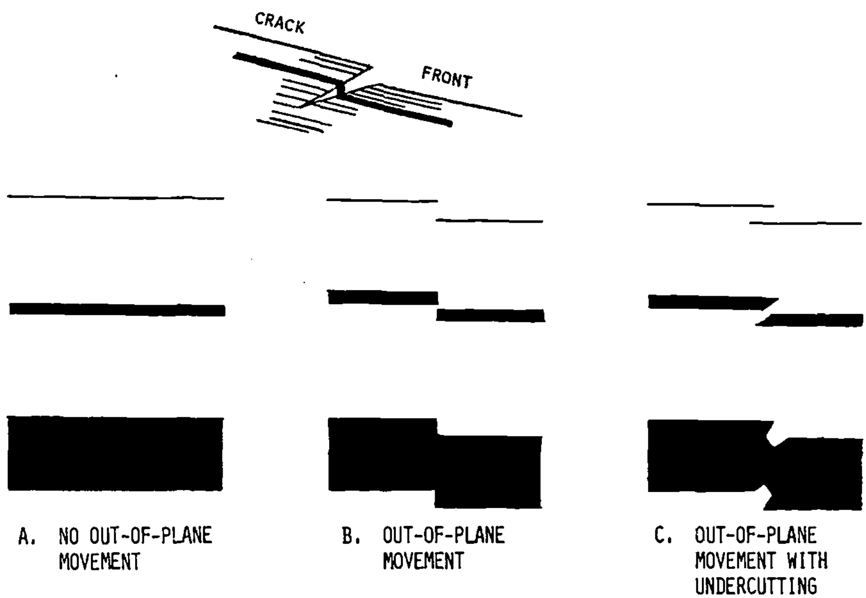

FIG. 16—*Schematic showing a possible mechanism for generating shear walls by shear of the ligament joining two noncoplanar crack segments.*

were examined quantitatively. Figure 15 is a section of this type on a broken A533B steel specimen. From a series of sections on broken A508 steel specimens, the thickness of recognizable deformation was found to correlate with the height of the shear wall as shown in Fig. 18. The average shear wall height in these sections was found to be in the range of 100 to 300 μm. From Fig. 18 this indicates that the thickness of the deformed zone bounding the shear walls will, on average, be of the order of 100 μm.

Table 4 summarizes a set of measurements of the areal fraction of ductile fracture on A508 specimens tested at -7, 22, and 43°C. These measurements were taken from several photomicrographs of the fracture surfaces viewed perpendicular to the crack plane. In accordance with the measurements described in the preceding, this areal fraction was corrected by a factor of 3 to approximate the true areal fraction of ductile fracture and then further multiplied by 100 μm to provide the volume of plastically deformed material in the shear walls per unit of projected crack area.

We can arrive at a value for K_{Im} if we assign a value to the toughness of the cleavage portion of the fracture surface of approximately 35 MPa $m^{1/2}$. This value is consistent with the toughness of this class of steels at very low temperatures where the fracture is nearly 100 percent cleavage [*11,17,18*]. The plastic work term together with the cleavage toughness give the crack arrest toughness values at each of the three test temperatures in Table 4.


25 μ

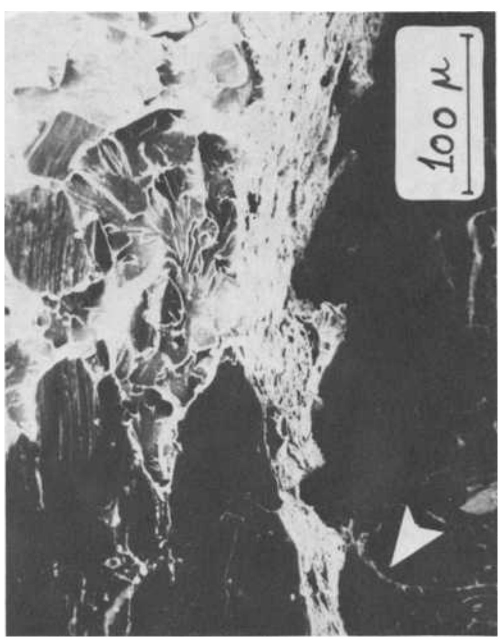
100 μ

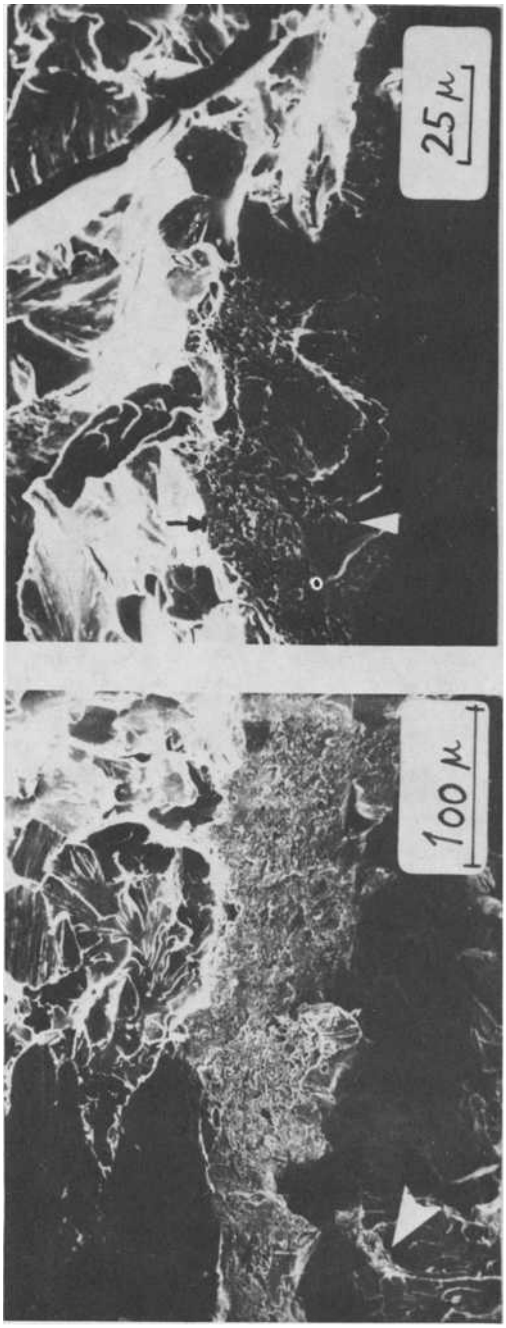

FIG. 17—*Two views of ductile fracture areas on the fracture surface of an A533B specimen. In* (a) *the viewing direction is perpendicular to the crack plane, while in* (b) *the specimen has been tilted 26 deg to determine the true ductile fracture area.*

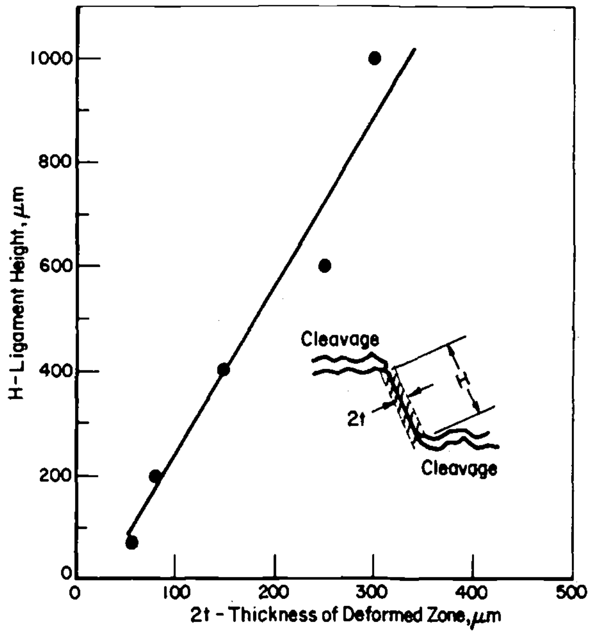

FIG. 18—*Results of measurements from cross section of fracture surfaces of A508 steel specimens correlating the height of the shear wall,* H, *with the thickness of recognizable deformation,* 2t.

TABLE 4—*Summary of fractographic analysis of A508 specimens showing the relation between ligament formation and* K_{Im}.

Test temperature, °C	−7	22	43
Areal fraction of ductile fracture[a]	0.14	0.17	0.22
True areal fraction,[b] A_T	0.42	0.51	0.66
Volume of plastic material per unit projected crack area,[c] V_T, mm/m[3]	0.042	0.051	0.066
Plastic work per unit projected crack area, kJ/m[2] [d]	63	76	98
Estimated K_{Im},[e] MPa m$^{1/2}$	123	139	157
Measured K_{Im}, MPa m$^{1/2}$	124	157	174

[a]Determined from scanning electron microscopy fractographs with projected crack area perpendicular to the viewing direction.

[b]Per unit of projected crack area and assuming that the true ductile fracture area is three times the projected area on the fractograph.

[c]Assuming that an average thickness of deformation adjacent to the shear walls is 100 μm.

[d]For $W_p = 1500$ MJ/m^3.

[e]Based on a cleavage toughness of K_{Im} (cleavage) = 35 MPa m$^{1/2}$ and computing

$$K_{Im} = \left[K_{Im}^2 \text{(cleavage)} + \frac{E W_p V_T}{(1 - \nu^2)} \right]^{1/2}$$

The agreement between the calculated toughness and measured toughness values is surprisingly good, in view of the approximations involved. Nevertheless, the results indicate that the formation of ligaments and their eventual failure as shear walls is the dominant energy dissipating mechanism during crack propagation. A further, although indirect, confirmation of this point appears when the fracture surfaces of the weldment material are compared with the base materials as in Fig. 19. In contrast to the A508 steel, the weldment displays a much smoother surface with little macroscopic evidence of unbroken ligaments or shear walls. This is consistent with the low K_{Im}-levels of the weldment. The increasing K_{Im} with increasing temperature also correlates reasonably well with the areal percentage of ductile fracture. Extrapolating these estimates to fully ductile fracture (taking the true area to be three times the projected area, as before), a crack arrest toughness of 320 MPa $m^{1/2}$ is predicted. This would correspond to a K_{Im}-value for a running crack expected at upper shelf. It is interesting to note that the highest baseplate values of K_{Ic} (Fig. 1) are on this order. For the dimpled rupture mechanism, K_{Im} is likely to occur at zero crack velocity and is likely to equal K_{Ic} [*19*]. The K_{Ic}-values in Fig. 1, however, were obtained mostly by an approximate method, and a more thorough investigation of this point is required.

Discussion

This paper has concentrated on reporting a K_{Im} data base, providing a statistical analysis of it, and suggesting a physical basis for the observed K_{Im}-values. The data show clearly that K_{Im} is significantly larger than either of the alternative arrest toughness parameters, K_{Ia} or K_{IR} (which is partially based on K_{Ia} data). K_{Im} has been used because it is based on first principles and because it can be related to physical features on the fracture surface. The K_{Im} methodology provides a means of assigning a dynamically determined quantity to a dynamic event: crack propagation and arrest.

In reporting the results, we have included a statistical analysis of the data which contains the realistic assumption that no reference toughness curve (such as K_{IR}) can be an absolute lower limit but can represent only a very small but finite probability of failure. Further development of safety analysis should take this point into account.

As pointed out in the Appendix, part of the scatter in the data is probably due to heat-to-heat variations in dynamic toughness. The metallographic results suggest that the reason for such variation may lie in differing tendencies for ligament formation and shear wall rupture, and also provide a physical basis for dynamic fracture toughness. The most important implication of these fractographic observations and toughness estimates is that K_{Im}, as derived by the BCL test procedure, represents a real physical quantity: the toughness associated with a rather complex mix of crack propagation

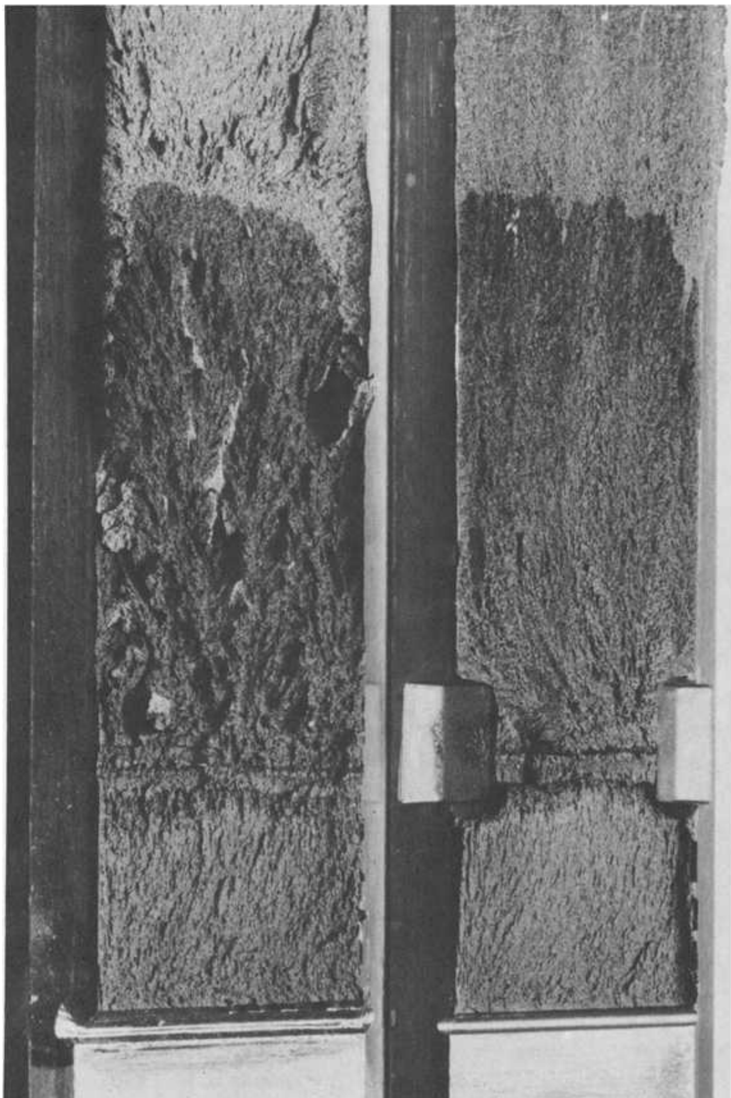

FIG. 19—*Appearance of fast fracture surface of* (top) *A508 tested at* RT_{NDT} + *30°C and* (bottom) *SA-weldment tested at* RT_{NDT} + *57°C. For the weldment,* K_{Im} = *127 MPa* $m^{1/2}$, *and for the A508,* K_{Im} = *157 MPa* $m^{1/2}$.

mechanisms. The crack tip extends rapidly by cleavage but is retarded by the rupture of intervening ligaments. These rupture processes eventually absorb most of the fracture energy after the crack has traveled some distance and the cleavage path has generated the ligaments. In fracture toughness testing, the standard methods employ a sharp, flat fatigue crack as a crack starter. Crack initiation is the instability due to the onset of cleavage propagation. At this point ligaments play little or no role in determining the local conditions which trigger the instability. It is currently believed, therefore, that K_{Im} contains a measure of a mechanism not occurring in initiation tests, and that mechanism is ligament deformation and rupture.

In contrast to K_{Im}, no physical basis for K_{Ia} has been suggested. Indeed, the crack-jump dependence of K_{Ia} as illustrated in Fig. 12 suggests that it is not possible to specify a unique value of this parameter. An apparently constant value will be observed if the specimen-to-specimen difference in jump length is small, and it is this observation that gives greatest support to the idea that K_{Ia} is a material property. A corollary point is that K_{Ia} will approach K_{Im} if the crack jump length is reduced to a sufficiently small value.

With regard to the K_{IR}-based procedures, the data suggest that they seriously underestimate the actual arrest toughness, that the introduction of the RT_{NDT} reference temperature increases the scatter in the data, and that NDT is probably the more consistent parameter. In addition, by including data on the weldment we have provided a clear indication that the toughness/temperature relation depends on the material being investigated. Finally, the K_{IR} curve for base material does not appear to exhibit the correct temperature dependence for baseplate and forgings, being too flat at lower temperatures and too steep at higher temperatures.

Conclusions

Within the temperature range from NDT to (NDT + 100°C):

1. Crack arrest toughness, K_{Im}, increases linearly with temperature and exhibits significantly higher values than the stress intensity after arrest, K_{Ia}.

2. The value of K_{Im} is determined to a large extent by the process of formation and rupture of shear walls normal to the crack plane.

Acknowledgments

We are grateful to the U. S. Nuclear Regulatory Commission for support of this work, and to Mr. P. Albrecht, the project manager. The energy and dedication of the late E. K. Lynn of that agency were a particular inspiration. We also wish to thank our colleagues C. R. Barnes and P. N. Mincer for their excellent performance of the experiments. The plates, forgings, and weldment were generously provided by R. Bruscato, T. U. Marston, and W. A. Van Der Sluys.

References

[1] Hahn, G. T. et al, this publication, pp. 248-269.
[2] Hoagland, R. G., Gehlen, P. C., Rosenfield, A. R., and Hahn, G. T., "Analysis of Crack Arrest in Reactor Pressure Vessels," ASME Paper 78-Mat-16, American Society of Mechanical Engineers, 1978.
[3] Gehlen, P. C., Hahn, G. T., Cheverton, R. D., and Iskander, S. K., this publication, pp. 392-421.
[4] Hahn, G. T. et al, "Critical Experiments, Measurements, and Analyses to Establish a Crack Arrest Methodology for Nuclear Pressure Vessel Steels," Third Annual Progress Report, NUREG/CR-0057, BMI-1995, Battelle Memorial Institute, Columbus, Ohio, 1977.
[5] Hahn, G. T. et al, "Critical Experiments, Measurements, and Analyses to Establish a Crack Arrest Methodology for Nuclear Pressure Vessel Steels," Thirteenth Quarterly Progress Report, BMI-2010, Battelle Memorial Institute, Columbus, Ohio, 1978.
[6] Witt, F. J., "A Procedure for Determining Bounding Values on Fracture Toughness K_{Ic} at Any Temperature," Heavy Section Steel Technology Program, 5th Annual Information Meeting, Paper No. 13, 1971.
[7] Hoagland, R. G., Rosenfield, A. R., Gehlen, P. C., and Hahn, G. T. in *Fast Fracture and Crack Arrest ASTM STP 627,* American Society for Testing and Materials, 1977, pp. 177-202.
[8] "PVRC Recommendations on Toughness Requirements for Ferritic Materials," Welding Research Council Bulletin 175, 1972.
[9] Ripling, E. J., Crosley, P. B., and Marston, T. U. in *Proceedings*, Joint American Society of Mechanical Engineers/Canadian Society of Mechanical Engineers Pressure Vessels and Piping Conference, Montreal, Que., Canada, June 1978.
[10] Hahn, G. T., Hoagland, R. G., and Rosenfield, A. R. in *Proceedings*, SMIRT-4 Paper G1/6, 1977.
[11] Hoagland, R. G., Rosenfield, A. R., and Hahn, G. T., Metallurgical Transactions, Vol. 3, 1972, p. 123.
[12] Hahn, G. T., Gehlen, P. C., Hoagland, R. G., Kanninen, M. F., Popelar, C., Rosenfield, A. R., and de Campos, V. S., "Critical Experiments, Measurements, and Analyses to Establish a Crack Arrest Methodology for Nuclear Pressure Vessel Steels," First Annual Report to U.S. Nuclear Regulatory Commission, BMI-1937, Battelle Memorial Institute, Columbus, Ohio, 1975.
[13] Eftis, J. and Krafft, J. M., *Transactions*, American Society of Mechanical Engineers, Vol. 87, 1967, p. 525.
[14] Dvorak, J. in *Proceedings*, "Fracture 1969," P. L. Pratt, et al, Eds., Chapman and Hall, London 1969, pp. 338-349.
[15] Hahn, G. T., Rosenfield, A. R., Marschall, C. W., Hoagland, R. G., Gehlen, P. C., and Kanninen, M. F. in *Fracture Mechanics*, N. Perrone, et al, Eds., University of Virginia, Charlottesville, Va., 1978, pp. 205-227.
[16] Hahn, G. T., Kanninen, M. F., and Rosenfield, A. R. in *Proceedings*, "Fracture 1969," P. L. Pratt, et al, Eds., Chapman and Hall, London, 1969, pp. 905-906.
[17] Wessel, E. T., Clark, W. G., Jr., and Pryle, W. H. in *Proceedings*, "Fracture 1969," P. L. Pratt, et al, Eds., Chapman and Hall, London, 1969, pp. 825-850.
[18] Hoagland, R. G., *Transactions*, American Society of Mechanical Engineers, Vol. 89D, 1967, pp. 525-532.
[19] Hahn, G. T., Hoagland, R. G., and Rosenfield, A. R., *Metallurgical Transactions*, Vol. 7A, 1976, pp. 49-54.

APPENDIX

Statistical Analysis of Data

A statistical analysis of the data for K_{Im} and K_{Ia} as functions of T-NDT or T-RT_{NDT} was carried out using regression-analysis techniques. The reasons for conducting this analysis were (1) to determine functional relations between the dependent variables (K_{Im}, K_{Ia}) and each of the independent variables (T-NDT, T-RT_{NDT}), and (2) to estimate an approximate lower limit for each of the dependent variables as functions of each of the independent variables.

Before discussing results obtained from the statistical studies, attention must be drawn to an important point, namely, that the least-squares analysis we have carried out is based on the following assumptions: (1) Data for the independent variable are known exactly. (2) Data for the dependent variable are normally distributed—for any given value of the independent variable, the standard deviation of this normal distribution, remaining constant as the independent variable changes. However, consideration of the data being analyzed indicates that, not only are values for the independent variable not precisely known,[6] but, in addition, values for the dependent variable are not normally distributed as postulated. For example, the data gathered from the various different heats appear generally to be members of different data populations instead of the same population. We did analyze one subset of data (the K_{Ia} data for $-1°C \leq$ T-$RT_{NDT} \leq 2°C$) and found that a rough fit could be obtained to either a normal or a log-normal distribution; but this is really a moot point in view of the fact that the data contained within the subset represent different populations. Nevertheless, with these facts in mind, we proceeded to carry out regression-analysis studies using a procedure by which the sum of squares of deviations of the data from the regression curve, measured along the ordinate axis, was minimized. In this sense, the functional relations thus obtained do represent "best fits" to the data; but interpretations based on calculated values for "standard errors," associated with measurement of the dependent variable, must be viewed with caution.

Data were initially fitted to a quadratic equation of the form $y = a + bx + cx^2$, where y and x are, respectively, the dependent and independent variables, and a, b, and c are the regression coefficients to be calculated. However, it was found that the term which was quadratic in x contributed only to a relatively small extent; that is, the statistically predicted variation of y with x was predominantly linear. Consequently, the analyses were repeated with the quadratic term deleted, so that y was taken to have a purely linear dependence upon x. All results described herein are based on that assumed linear dependence.

The approximate lower limit for the dependent variable was calculated, as a function of the independent variable, using a parameter known as the "standard error of the estimate," s_y, which, for a linear fit to the data of the form $y = a + bx$, is given by

$$s_y = \left(\frac{S}{N-2}\right)^{1/2}$$

where S is the sum of squares of deviations (measured along the ordinate axis) of the data from the regression line and N is the number of data points (60 in this case). If the data were normally distributed about the regression line, the estimated probability, P_{ns_y}, that a data point lies above $y - ns_y$, where y is the value calculated from the regression equation for a given value of x, is as indicated in Table 5 for selected values of n.

Provided the assumptions used in the analyses do not introduce significant errors in Figs. 7-10, the $-2s_y$ lines represent the lower limit of toughness for all but ~2.28 percent of plates while the $-3s_y$ lines lie below all but ~0.13 percent of the total population. It should be recalled, however, that the data under analysis here were *not* members of a single, normally distributed population along the y-axis, for given values

[6]NDT is itself a statistical quantity determined by an approximate sensitivity analysis.

TABLE 5—*Variation of* P_{ns_y} *with* n.

n	P_{ns_y}
1	0.8413447
2	0.9772499
3	0.9986501
4	0.9999683

of x, and, also, values for the independent variable x were not precisely known for these data. Consequently, values calculated for P_{ns_y} using these data should be regarded only as rough estimates.

P. B. Crosley[1] *and E. J. Ripling*[1]

Significance of Crack Arrest Toughness (K_{Ia}) Testing

REFERENCE: Crosley, P. B. and Ripling, E. J., "**Significance of Crack Arrest Toughness (K_{Ia}) Testing,**" *Crack Arrest Methodology and Applications, ASTM STP 711,* G. T. Hahn and M. F. Kanninen, Eds., American Society for Testing and Materials, 1980, pp. 321-337.

ABSTRACT: The statically calculated value of crack arrest toughness, K_{Ia}, is shown to be specimen-insensitive. The values of K_{Ia} fall within the same scatterband when the quantity is measured with tapered double cantilever beam (T-DCB) specimens, single-edge notched specimens, or modified compact specimens.

The large amount of data collected from the ASTM Cooperative Test Program made it possible to statistically describe the dependence of K_{Ia} on crack jump length and K_Q In a collection of data in which both K_Q and K_{Ia} scatter, K_{Ia} will decrease in systematic fashion with increased crack jump length, and decreasing K_Q, because of an ordering of the scattered data. This trend was found in the cooperative program data.

Probably the most unequivocal method to determine the invariance of K_{Ia} is to examine it as a function of K_Q. Thirty-five data points obtained by 12 different laboratories on two different types of compact specimens were available at the time this report was written. The standard deviation in K_{Ia} was less than 10 percent even though K_Q varied by a factor of almost 2.5 to 1.

Measurements of crack velocity and strains on T-DCB specimens justified the use of a static analysis for calculating K_{Ia}. Most of the time required for a run-arrest segment of crack extension is used in slowly decelerating the crack toward zero velocity. The strain measurements during this decelerating period are close to statically calculated values.

The Reference Stress Intensity Factor, K_{IR}, is conservative relative to K_{Ia} for SA533B Grade 1 steel at temperatures near and below the reference nil-ductility temperature (RT_{NDT}). At mildly elevated temperatures, the curve appears to be nonconservative.

KEY WORDS: crack arrest, stress-intensity factor, pressure vessel steel, compact (K_{Ia}) specimen, wedge loading, brittle weld, crack jump, fracture toughness

Some 10 years ago, while investigating the effect of strain rate on the fracture toughness of a pressure vessel steel, Crosley and Ripling [*1*][2] noted that a quantity which they called *crack arrest toughness* and identified

[1]Associate director of research and president, respectively, Materials Research Laboratory, Inc., Glenwood, Ill. 60425.

[2]The italic numbers in brackets refer to the list of references appended to this paper.

by the symbol K_{Ia} showed less variability than crack initiation toughness measured in the same set of experiments. When the crack initiation toughness was high, the crack would jump a greater distance before arresting, and the increased crack jump was such as to preserve a reasonably constant value of the load measured immediately after arrest. Because the specimens were of the contoured double cantilever beam (C-DCB) type in which the proportionality between the load and the stress-intensity factor is independent of the crack length, this constancy of arrest load implied a reproducibility of K_{Ia}, the stress-intensity factor calculated from that load. Out of this experience emerged a formal definition of K_{Ia} as the value of the stress-intensity factor measured a short time (of the order of one millisecond) after a run-arrest segment of crack extension. It was assumed that K had essentially the same value shortly after arrest as it had at the moment of arrest.

The original intent was not specifically to address the problem of arresting a running crack, but rather to obtain a fracture toughness measurement which would account as fully and fairly as possible for very high strain-rate effects. Even with very large specimens and rapid rates of loading, K_{Ic}-values consistent with the size requirements of the ASTM Test for Plane-Strain Fracture Toughness of Metallic Materials (E 399-74) could not be measured at temperatures very much above the nil-ductility transition (NDT). Measurements of K_{Ia} were restricted to about the same temperature range, and here K_{Ia} seemed to be in generally good agreement with the lower bound of static and dynamic crack initiation toughness measurements. The K_{IR} reference fracture toughness curve of the American Society of Mechanical Engineers (ASME) Boiler and Pressure Vessel Code, Section III, Appendix G, uses K_{Ia} data in this spirit; that is, K_{Ia}-values were part of the aggregate of data used in establishing the K_{IR} curve even though the application does not involve consideration of crack arrest. On the other hand, Appendix A of Section XI of the Code is explicitly concerned with crack arrest. Here the K_{Ia} curve is used in a manner which parallels the procedure used in defining K_{Ia}. A statically calculated stress-intensity factor is compared with a crack arrest toughness value to assess whether or not crack arrest will occur.

Since rapid crack propagation is a dynamic phenomenon, there is a natural concern about characterizing crack arrest in a manner which involves only a static analysis. In an infinite plate with a single advancing crack front, there is a one-to-one correspondence between the stress-intensity factor at a moving crack tip and the static value for the same crack-tip position [*2*]. A real structure, however, is finite, and stress waves reflect off boundaries and interact with the moving crack. Dynamic effects exist; the K_{Ia} approach, like any other engineering practice, is an oversimplification. Should it therefore be abandoned? One way to address this question is to determine experimentally the degree to which K_{Ia} is influenced by dynamic effects. This paper is concerned with whether or not K_{Ia} measured on a particular type of specimen shows systematic variations with different test parameters and with whether or not the same value of K_{Ia} is measured when different types of specimens are employed.

Tapered DCB Specimen

Over the years the linear compliance change DCB specimen has undergone a succession of modifications to enhance its suitability for crack arrest studies, but the basic test procedure has not changed [3].

While other specimen types provide a faster decrease of K with crack length under fixed grip conditions, crack arrest can be obtained in the tapered DCB (T-DCB) specimen in the presence of a sizeable load train compliance. Pin-and-clevis loading, therefore, can be used, and the arrest load from which K_{Ia} is calculated can be read from a load cell included in the load train. A drawback of this arrangement is that initiation toughness, K_Q, cannot be too much higher that the arrest toughness, K_{Ia}, without the crack's extending too far for a K_{Ia} measurement to be made.

Face grooves are used to suppress the formation of shear lips. A fatigue crack is normally used as a crack starter, and the fact that no welding is involved in specimen fabrication does away with concern over residual stresses from this source.

A troublesome feature of DCB-type specimens is a tendency for the crack to veer out of the desired plane of extension. The tendency for such behavior can be reduced by making the specimen larger or by otherwise shaping it so as to reduce the bending stresses in the cantilever beam arms.

Until quite recently, almost all of the K_{Ia} measurements with which the authors have been concerned were obtained on C-DCB or T-DCB specimens. A substantial amount of data were collected on heavy-section steel technology (HSST) Plate 02, a 0.3-m plate of SA533 Grade B Class 1 steel. K_{Ia} was defined as a function of temperature as shown in Fig. 1. In these tests, particularly at temperatures above NDT, there was a tendency for cracks to depart from the minimum section defined by the face grooves. Such behavior is almost invariably associated with abnormally high K_{Ia}-values, and, in Fig. 1, tests where the departure at the arrest position was more than 2.5 mm are not included.

Since the work done on HSST Plate 02, a limited number of tests have been run on three other heats of SA533 Grade B Class 1 steel. The newer K_{Ia} results are in good agreement with the measurements made on the HSST material [4].

Measurements made at Materials Research Laboratory (MRL) on T-DCB specimens have continued to show the same behavior which first attracted

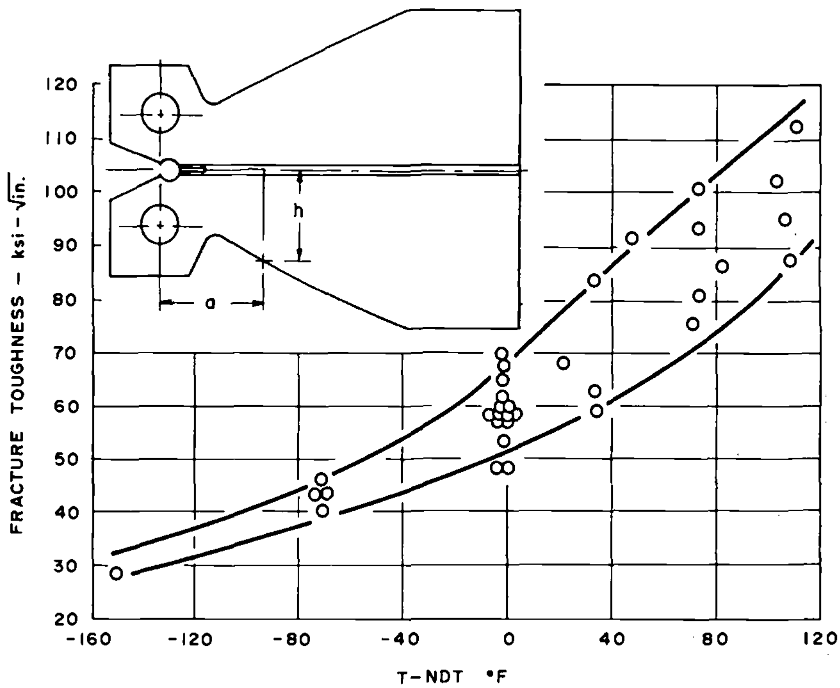

FIG. 1—*Crack arrest toughness versus test temperature for HSST plate of SA533 Grade B Class 1 steel, using the T-DCB specimen* [5].

attention to K_{Ia}; namely, the measured value of K_{Ia} has proven to be insensitive to the crack initiation toughness or crack jump length. Dynamic effects are not showing up as a systematic variation of K_{Ia}. It might be argued, of course, that the T-DCB is a peculiar type of specimen, that it does not permit high enough K_Q's or long enough crack jumps for dynamic effects to show up strongly, or that there is some defect in the K_{Ia} measurement procedure.

Single-Edge Notch Specimen Experiments

To determine whether or not K_{Ia}-values measured on C-DCB specimens could be applied to crack arrest in a different structure, experiments were conducted with single-edge notch (SEN) specimens. These were chosen because they differed greatly from the DCB specimen. Whereas crack arrest occurs in the DCB specimen because K decreases as the crack runs, in the SEN specimen, K increases as the crack runs, and carrying out the experiments required that a crack be initiated in and run through a low-toughness crack starter section before encountering the tougher base-plate material.

The experimental details have been described elsewhere [5]; the main features were as follows. Specimens were made from HSST Plate 02; the starter section was a zone which had been melted in an electron beam (EB) welder; and cracking could be initiated at a preselected load level by hydrogen charging the EB weld. When the hydrogen charging was successful in producing crack initiation, the crack either ran to the end of the EB weld zone and arrested, or it ran completely through the specimen. The idea was that if K were less than the K_{Ia} of the baseplate when the crack reached the weld/baseplate interface, then the crack should arrest there. If not, the crack should run the full width of the specimen without arresting.

The results are shown in Fig. 2. The plotted points are statically calculated K-values corresponding to a crack position at the end of the weld zone in cases where the crack did not arrest, or to the measured crack length, which coincided with the end of the weld zone, when the crack did arrest. The K-level which divides arrest behavior from no-arrest behavior was reasonably well defined and corresponds with K_{Ia} results which were measured with C-DCB specimens, as can be seen in Fig. 1.

These results were encouraging to the view that K_{Ia} might have a fairly

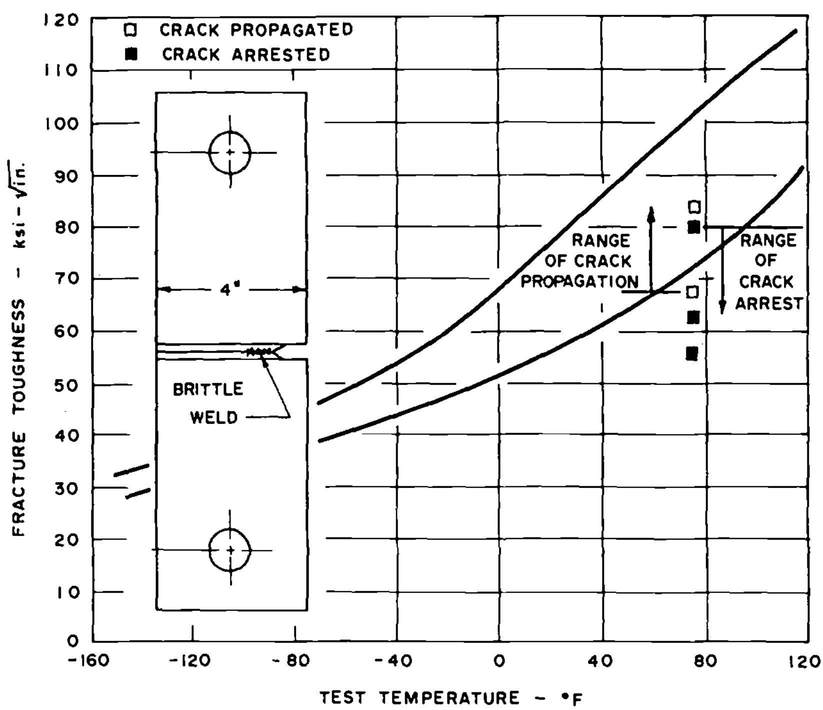

FIG. 2—*Crack arrest and propagation values obtained on an SEN specimen compared with scatterband obtained on T-DCB specimens, HSST plate of SA533 Grade B Class 1 steel.*

general applicability, and additional tests with more elaborate instrumentation were planned. Unfortunately, the hydrogen charging technique of initiating cracks could not be made to work on subsequent batches of SEN test specimens, and the project was abandoned. The findings remained open to the criticisms that only a few tests were run, that there were uncertain effects of residual stresses associated with EB welding, etc.

Compact K_{Ia} Specimen

While it was hoped that the compact geometry might be developed into a practical K_{Ia} test specimen, the main motivation in developing this test method was, once again, to measure K_{Ia} in a structure distinctly different from the T-DCB. In the beam-type specimen the boundaries nearest the crack are the top and bottom surfaces; at the arrest position the crack front is still far from the back end of the specimen. Since the opposite is true with the compact geometry, it was thought that this specimen would present the crack with a wholly different dynamic environment, and hence provide a test of the applicability of the K_{Ia} approach in different structural configurations. Also, the compact geometry simulates better the propagation of a crack across a pressure vessel wall.

Several changes in testing practice were involved. Transverse wedge loading was adopted at the outset because it seemed fairly certain that a pin loading arrangement would be too compliant. As a consequence, the K_{Ia}-value would be inferred from a displacement measurement rather than a load measurement. Wedge loading made fatigue precracking impractical, but, because the value of K_{Ia} was not supposed to be sensitive to how fracture was initiated, it seemed permissible to abandon the fatigue precrack in favor of the simplest and cheapest alternative. Following as much as possible the ASTM practice, Conducting Drop-Weight Test to Determine Nil-Ductility Transition Temperature of Ferritic Steels (E 208-69), for making drop-weight NDT specimens, a machine-notched brittle weld deposit was used. When this gave K_Q-values that were too high, the specimens were precompressed to make crack initiation easier.

The experimental program was discontinued before the test procedure could be refined, but a few tests were run on SA533 Grade B Class 1 steel. These results are plotted, along with the scatterband from the old tests on HSST Plate 02, in Fig. 3. Taken at face value, they seem to indicate that K_{Ia} being measured on the wedge-loaded compact specimens with precompressed, machine-notched brittle weld crack starters is pretty much like K_{Ia} measured on pin-loaded T-DCB specimens with fatigue precracks.

Cooperative Crack Arrest Program

In 1978 the authors' involvement turned from making tests to making specimens to be tested elsewhere. The MRL compact specimen, in the

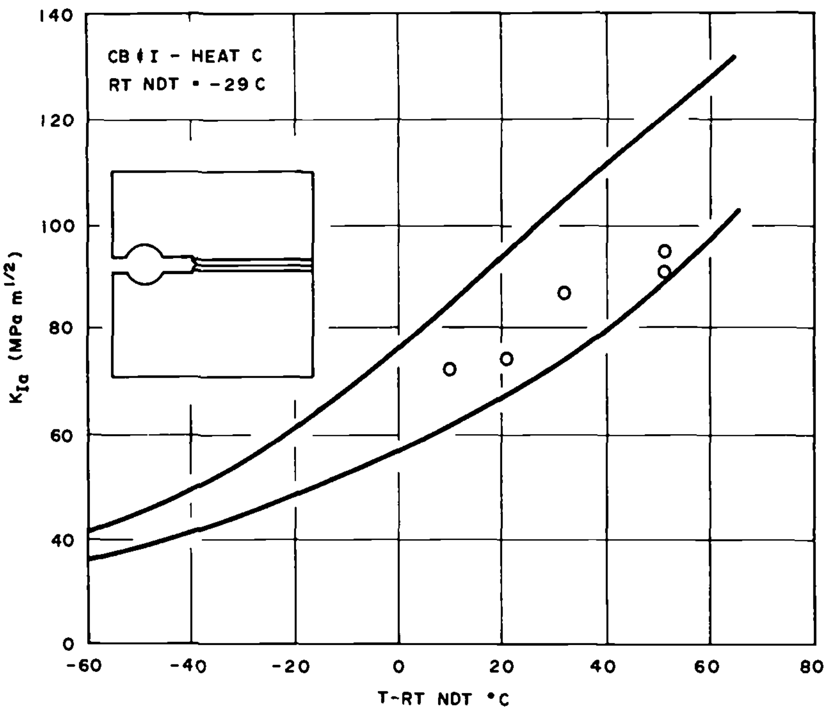

FIG. 3—*Crack arrest toughness versus reference test temperature. SA533 Grade B Class 1 steel, using compact specimens* [4].

stage of development described in the preceding, was included in the ASTM Cooperative Crack Arrest Program, and a test procedure was written and submitted for publication [*6*]. Sixty specimens of AISI 1018 steel and 120 specimens of SA533 Grade B Class 1 steel were made and distributed to 30 program participants. The specimens of 1018 steel were to be tested at room temperature to give the laboratories experience with the test procedure before tests on the pressure vessel steel were undertaken. The SA533-B specimens were to be tested at room temperature and at 0°C. Twenty-three test results on the AISI 1018 steel and 25 room temperature test results on the A533-B steel were available to the authors in time to be included herein. (Too few of the lower-temperature test results had been submitted to warrant their being considered here.) Although these results constitute only a fraction of all the results expected from the program, there are enough data at this point to see whether or not there is a systematic variation of K_{Ia} with K_Q or crack jump distance as might be produced by dynamic effects. Also, it may be judged whether or not the K_{Ia}-values measured in the different laboratories on the MRL compact K_{Ia} specimen are consistent with the earlier results on SA533

Grade B Class 1 steel, which results, as discussed in the foregoing, were derived mainly from tests on T-DCB specimens.

Load-Train Compliance

Figure 4 shows data from 48 tests run with the MRL compact specimen on the cooperative test program. The ratio K_{Ia}/K_Q is plotted as a function of a_f/W, the arrested crack length divided by the specimen width. It was thought that a useable range of crack jump might be such that $0.55 < a_f/W < 0.8$. Clearly, the data sample an even wider range than this. Also plotted in Fig. 4 is calculated behavior assuming an initial crack length corresponding to $a_0/W = 0.35$, which is representative of the specimens,

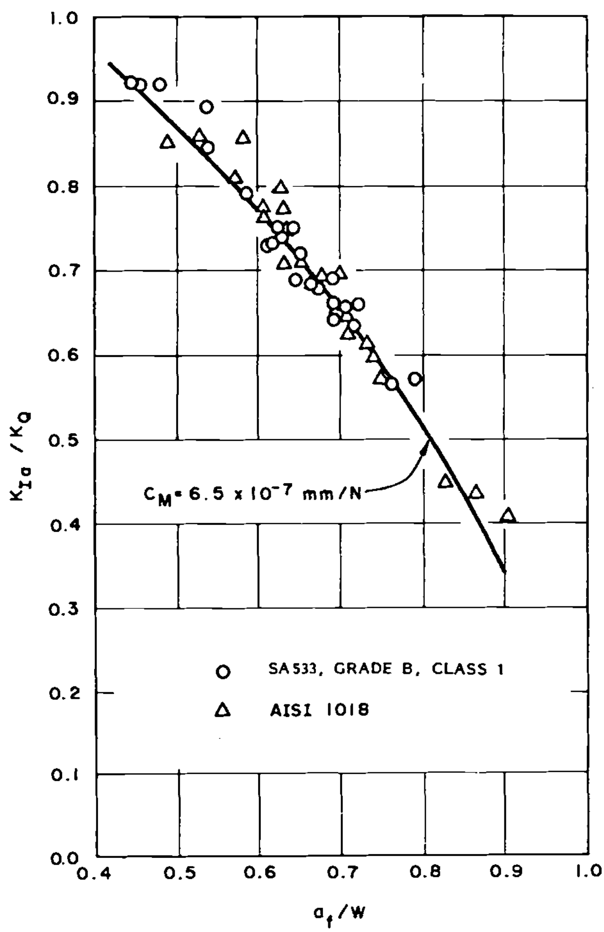

FIG. 4—*Ratio of* K_{Ia}/K_Q *to* a_f/W *for all available data on cooperative program on MRL specimens.*

and assuming a load-train compliance corresponding to $EB\ C_M = 6.66$, where E is Young's modulus (206 800 MPa), B is the specimen thickness (50.8 mm), and C_M is the load-train compliance (deflection per unit of specimen opening load). This load-train compliance, C_M or EBC_M, is a formally calculated quantity which serves as a measure of the departure from fixed-grip conditions [6]. Under fixed-grip conditions, $EBC_M = 0$, and for the compact specimen at $a/W = 0.35$, $EBC = 18.4$, where C is the specimen compliance. Thus the load-train compliance is small with respect to the specimen compliance, but not negligible. As Fig. 4 shows, the value of $EBC_M = 6.66$ (which corresponds to $C_M = 6.5 \times 10^{-7}$ mm/N) represents all of these cooperative test program results quite well, and this value is used in subsequent calculations which involve load-train compliance.

Dependence of K_{Ia} on Crack Jump Length

In looking for systematic dependencies of K_{Ia} on test parameters, it seems natural to look first for a dependence on crack jump distance, or on the final crack length in a group of tests where the initial crack size is the same. If K_{Ia} is exactly constant, it clearly cannot depend on the crack length at arrest. In reality K_{Ia}, like any other measurement, will show some scatter, and random specimen-to-specimen variation can show up as systematic dependence on crack jump distance simply because cracks will generally run farther when K_{Ia} is lower. Consider, for example, a series of K_{Ia}-values that scatter as shown in Fig. 5*a*. If these points were all obtained on specimens having identical values of K_Q, the specimens with low values of K_{Ia} would exhibit long crack jumps and those with high values of K_{Ia} would exhibit short crack jumps, as shown schematically by Curve B in Fig. 5*b*. If in a second series of tests a constant, but higher, value of K_Q were used, and the same K_{Ia}-values were sampled, the K_{Ia}-versus-a_f/W curve would move to the right as shown by Curve A in Fig. 5*b*. This demonstration implies that if the variation in K_Q is small with respect to the variation of K_{Ia} in a particular set of tests, then random variations in K_{Ia} will appear as a systematic crack length dependence. If a large range of K_Q is sampled and the scatter in K_{Ia} is relatively small, K_{Ia} will appear to be independent of crack length. Thus, a dependence of K_{Ia} on crack length in a given set of experiments is not, in and of itself, evidence that K_{Ia} is an inappropriate crack arrest characterization parameter.

Figure 6 shows K_{Ia} measured on the 23 MRL compact K_{Ia} specimens of AISI 1018 steel plotted against a_f/W. The mean value of K_{Ia} was 85.6 MPa $m^{1/2}$ with a standard deviation of 12.7 MPa $m^{1/2}$. The three points for which $a_f/W > 0.8$ give the impression of a downward trend in K_{Ia} with a_f/W, but this is quite consistent with expected behavior assuming a

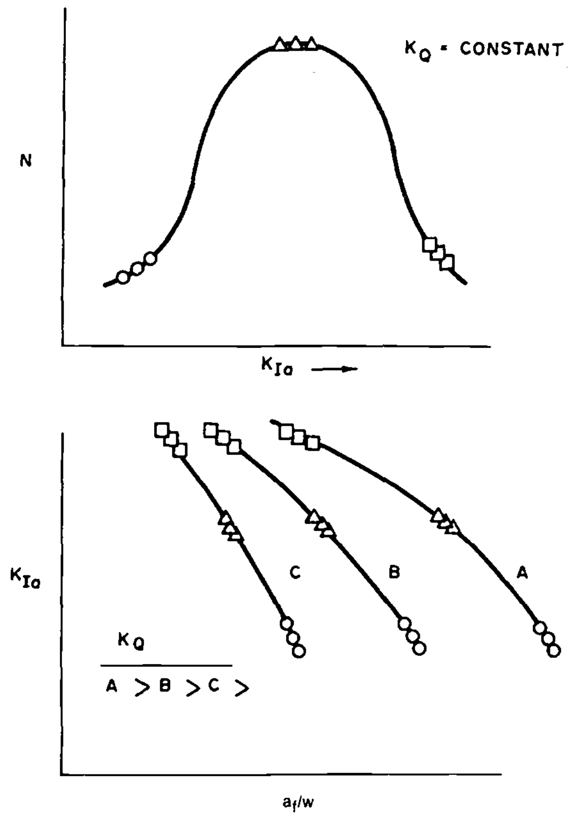

FIG. 5—*Schematic representation of the dependence of* K_{Ia} *on* a_f/W.

random specimen-to-specimen variation of K_{Ia}. The broken curves in the figure indicate how K_{Ia} is expected to vary with crack length for two values of K_Q, the mean value plus and minus the standard deviation for this set of tests. These curves were calculated using the load-train compliance value given earlier. Most of the data would be expected to lie between these two curves, as they do, and, hence, exhibit a downward sloping trend. (One test result was substantially different from all the others: the crack initiated at $K_Q = 62$ MPa $m^{1/2}$, but nevertheless ran a reasonable distance ($a_f/W = 0.57$) before arresting with $K_{Ia} = 50$ MPa $m^{1/2}$.)

Figure 7 shows K_{Ia} measured on the 25 MRL compact K_{Ia} specimens of SA533 Grade B Class I steel tested at room temperature. The mean K_{Ia} was 107.6 MPa $m^{1/2}$; the standard deviation was 10.4 MPa $m^{1/2}$. When plotted against a_f/W, K_{Ia} does not appear to show a strong trend with crack jump length, because most of results cluster around the mean K_{Ia}. However, when one considers the data points that are further removed

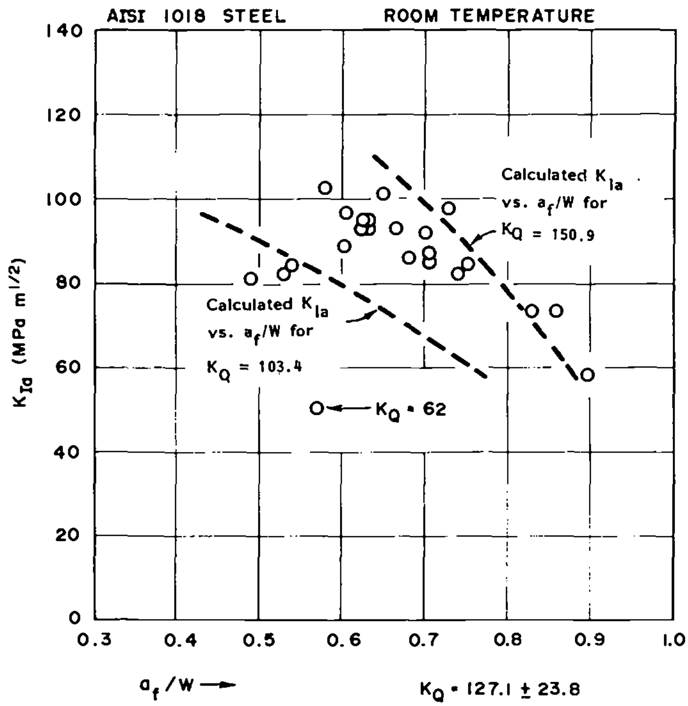

FIG. 6—*Dependence of* K_{Ia} *on* a_f/W *for the AISI 1018 steel specimens tested in the cooperative program.*

from the mean, a downward trend is noticeable. This is exactly what is expected, as indicated by the broken curves which were calculated here in the same manner as above.

Each of the sets of data just discussed constitutes many more test results from a single specimen type on a single material at a single temperature than are normally available. Yet, as has been shown, drawing inferences from the correlation between K_{Ia} and crack jump length involves some subtleties which may not always be appreciated. This should be borne in mind when analyzing smaller data sets in which K_{Ia} shows a substantial variability.

Dependence of K_{Ia} on K_Q

Another and better way to look for a systematic dependence of K_{Ia} is to correlate the measured values of K_{Ia} with K_Q, which, for convenience, we call the crack initiation toughness. For the compact specimen with the brittle weld crack starter, in contrast to the fatigue-cracked DCB, it is not really proper to speak of a crack initiation toughness in terms of a stress-

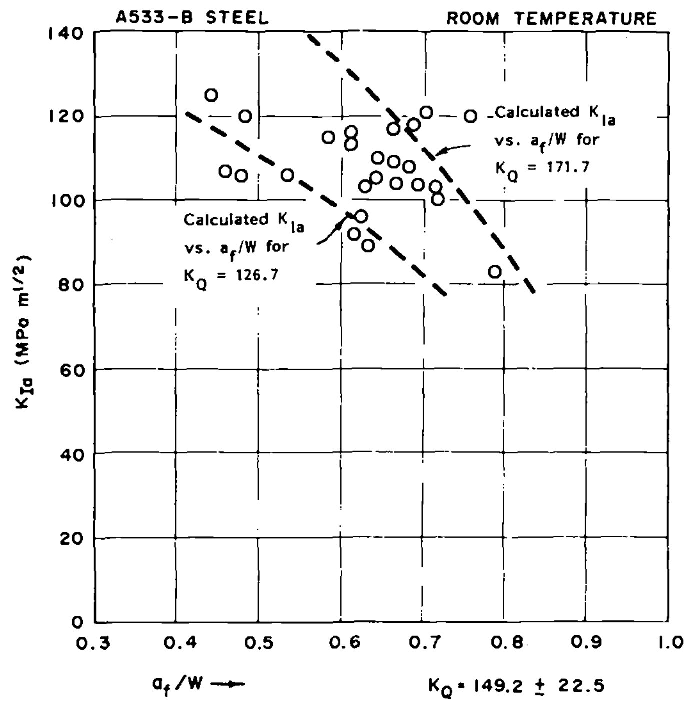

FIG. 7—*Dependence of* K_{Ia} *on* a_f/W *for SA533 Grade B Class 1 steel specimens tested in the cooperative program.*

intensity factor. There is no sharp crack; hence, K_Q is not a stress-intensity factor. K_Q is strictly a formally calculated value equal to the stress-intensity factor which would exist if there were an initial crack with a length corresponding to the machined notch depth. Nonetheless, while it is not a toughness measurement, K_Q is a convenient test parameter to reference. The crack is, of course, expected to jump farther, the higher the value of K_Q. The question is whether the crack jump is such that K_{Ia} remains constant, or is there, rather, a systematic change, presumably a decrease in K_{Ia} with increasing K_Q.

The data obtained on the 23 MRL compact K_{Ia} specimens of AISI 1018 steel are presented in Fig. 8; K_{Ia} is plotted against K_Q. A least-squares linear fit to the data gives a positive slope, $\Delta K_{Ia}/\Delta K_Q = 0.14$, but the standard deviation about the line (12.3 MPa m$^{1/2}$) is scarcely different from the deviation about the mean (12.7 MPa m$^{1/2}$). Two tests gave distinctly lower values of K_{Ia} than the remainder, and, while there is no reason at this time to reject these test results, it may be that they have an undue influence on the fitted line. Eliminating these points, the average K_{Ia} is 88.8 MPa m$^{1/2}$ with a standard deviation of 8.2 MPa m$^{1/2}$.

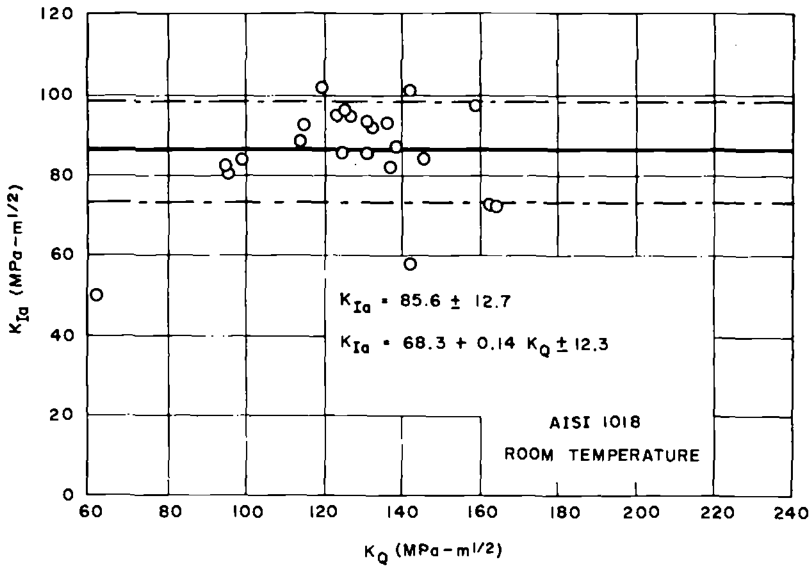

FIG. 8—*Dependence of* K_{Ia} *on* K_Q *for AISI 1018 steel; cooperative program test data.*

The fitted straight line has a slight negative slope, $\Delta K_{Ia}/\Delta K_Q = 0.052$; the standard deviation about the line is 8.1 MPa $m^{1/2}$. Clearly, the assumption that K_{Ia} is independent of K_Q is consistent with the data.

Figure 9 includes data from 25 MRL compact K_{Ia} specimens and also from 10 Battelle Columbus Laboratories (BCL) duplex compact specimens, all from tests of the SA533 Grade B Class 1 steel at room temperature. As already noted for the 25 tests on MRL specimens, the average K_{Ia} was 107.6 MPa $m^{1/2}$ with a standard deviation of 10.4 MPa $m^{1/2}$. For the 10 tests on the BCL specimens, the mean K_{Ia} was 114.7 MPa $m^{1/2}$ with a standard deviation of 10.5 MPa $m^{1/2}$. When the two sets of data are combined, the mean K_{Ia} is 109.6 MPa $m^{1/2}$, and the standard deviation about the mean is 10.8 MPa $m^{1/2}$. When straight lines are fitted to the data from the MRL specimens, the data from the BCL specimens, and the combined data, the slopes $\Delta K_{Ia}/\Delta K_Q$ are 0.218, 0.237, and 0.133, respectively. The respective standard deviations about the line are 9.2, 7.5 and 9.1 MPa $m^{1/2}$. The two individual data sets each suggests an upward trend of K_{Ia} with increasing K_Q. One would expect dynamic effects to produce the opposite behavior. When the two sets are combined, and a very large range of K_Q/K_{Ia} is represented, the upward trend is less pronounced. The statistics seem to bear out the impression one gets from Fig. 9: K_{Ia} is independent of K_Q.

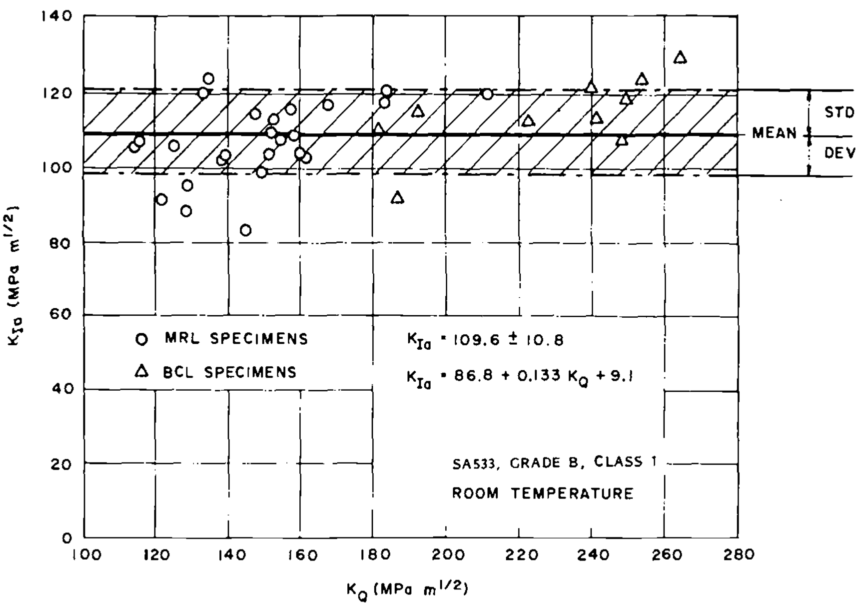

FIG. 9—*Dependence of* K_{Ia} *on* K_Q *for SA533 Grade B Class 1 steel: cooperative program test data.*

Comparison with Earlier Results

For the plate of SA533 Grade B Class 1 steel being tested in the cooperative program, the NDT and reference nil-ductility (RT_{NDT}) temperatures have been reported as −40°C and −20°C, respectively [7]. The room temperature K_{Ia} data just discussed are compared against the scatterband from the old data on HSST Plate 02 in Fig. 10. The data from the cooperative program are shown by a horizontal arrow indicating the mean, and a vertical arrow indicating the standard deviation. Two vertical bars are plotted representing the two ways (NDT and RT_{NDT}) of matching up the temperature axis. With either match, the data obtained by the different laboratories on MRL- and BCL-type compact specimens are in good agreement with the earlier data established on T-DCB specimens. The compact specimen has made it easier to test at higher temperatures; the cooperative program is producing many test results at a temperature where tests could barely be run with T-DCB specimens. Indeed, if NDT is regarded as furnishing the right temperature match-up, the new data are near the upper temperature limit of the older test results. The K_{IR} curve, also shown on Fig. 10, rises more steeply than the trend of K_{Ia} with temperature. Already at NDT + 63°C, K_{IR} is one standard deviation below the mean of the 35 K_{Ia}-values so far available. Some measurements are falling below K_{IR}. The lowering of K_{Ia} with respect to the K_{IR} curve

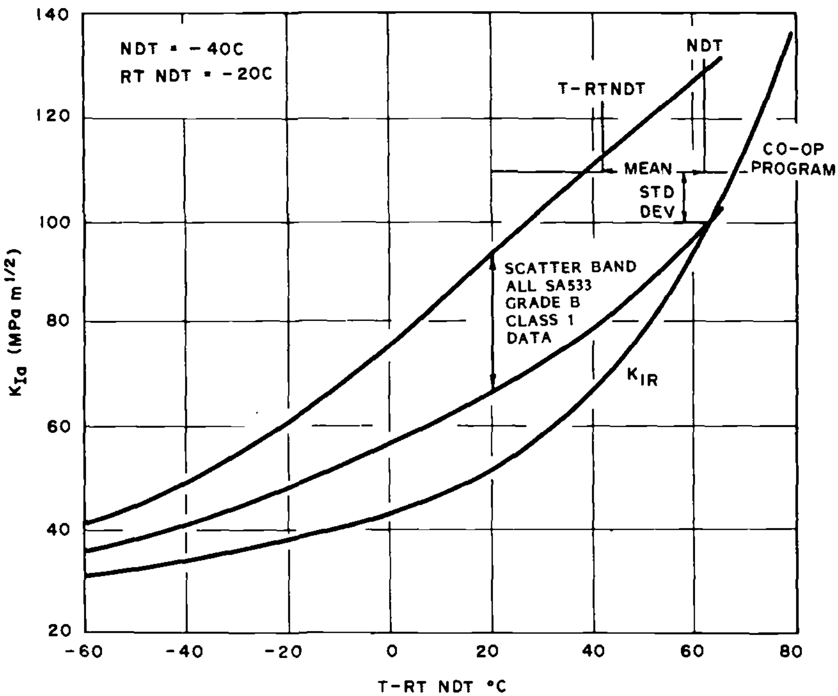

FIG. 10—*Relationship between* K_{IR}- and K_{Ia}-*values collected in the cooperative program for SA533 Grade B Class 1 steel.*

appears as though it would be more pronounced with further increase in temperature, so that K_{IR} will cease to be reasonably interpretable as a lower-bound curve if K_{Ia} results are maintained in the corpus of data from which the curve is to be defined.

Dynamic Versus Static Aspects of a Run-Arrest Segment of Crack Extension

In the first section of this paper, rapid crack propagation was said to be a dynamic phenomenon so that K_{Ia} must, at least to some extent, be an oversimplified description of K at the moment of arrest. Yet, all of the data discussed in the preceding not only support the view that K_{Ia} is an adequate description of crack arrest, but the uncertainty in defining the quantity is small compared with other fracture properties—the standard deviation being less than 10 percent for tests run by 12 different laboratories on two different types of specimens, with K_Q varying by a factor of almost 2.5 to 1.

A rationale for this consistency of K_{Ia} has been proposed on the basis of crack-tip velocity and specimen strain measurements made over the course of a run-arrest segment of crack extension [8]. These data, obtained only on T-DCB specimens, are typified by the results shown in Fig. 11. Shortly after initiation the crack attains a velocity of about 550 m/s, Fig. 11*b*. It maintained this high velocity for about 60 μs of the approximately 200 μs required for the total event. During this time interval, the strains experienced by the shear gage, Fig. 11*c*, are quite close to statically calculated shear strains for this position. The bending strains on the arm of the specimen cannot be represented by a static calculation, however, until later in the event; Fig. 11*d*. This difference in the two gages is probably a result of the fact that the bending gage is closer to the load line than the shear gage. Nevertheless, the difference between the bending gage values and values calculated statically probably is a result of the rapid acceleration of the crack tip from zero velocity to 500 m/s. Over most of the time of the event, the last 100 to 150 μs, the crack slowly decelerated toward zero velocity, and over this long time interval the specimen tends toward a condition of static equilibrium. During this deceleration period, a static calculation of K is justified which would explain the invariance of K_{Ia}.

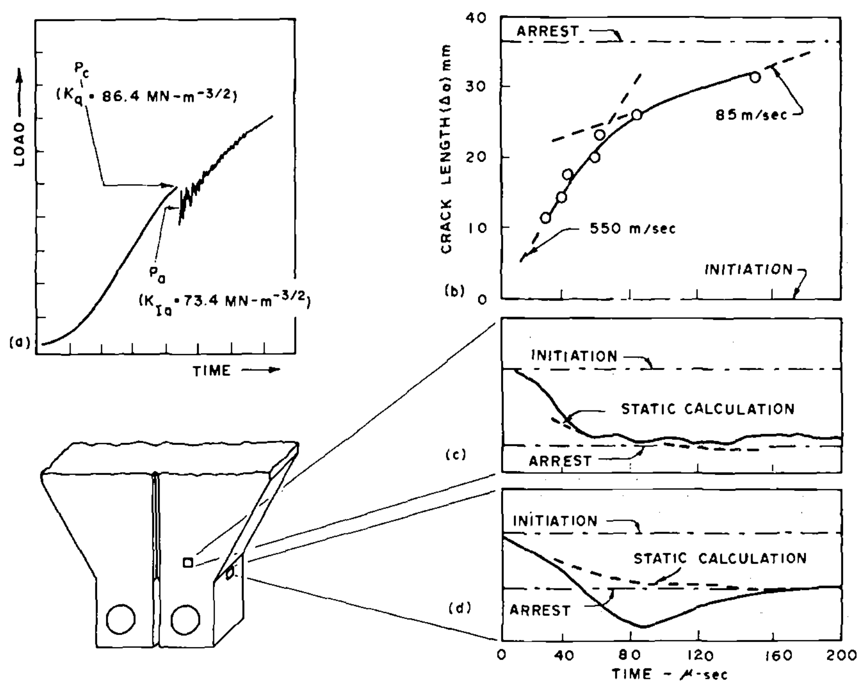

FIG. 11—(a) *In-line load cell-time oscilloscope trace.* (b) *Ladder gage position-time curve.* (c) *Shear strain-time curve.* (d) *Arm strain-time curve* [8].

Summary

About 10 years ago, Crosley and Ripling began measuring a postarrest toughness value that they identified as K_{Ia}, and suggested that it might be a convenient measurement for accounting for high rate effects. As more data were collected, K_{Ia} was thought to define the minimum toughness of rate-sensitive materials as a function of test temperature. This characteristic of K_{Ia} led to its use for defining the Reference Stress Intensity Factor above NDT in Section III, Appendix G, of the ASME Boiler and Pressure Vessel Code.

Since K_{Ia} was being promulgated as a material property, it was necessary to demonstrate that it was not specimen-sensitive. This was done by making measurements on tapered DCB specimens, SEN specimens, and modified compact specimens, all of which yielded the same range of values of K_{Ia} for SA533B Grade 1 steel.

The ASTM Cooperative Test Program produced a large amount of K_{Ia} data on two types of compact specimens taken from a single plate of SA533B-1 steel, and tested by a number of laboratories. These data showed K_{Ia} to be essentially constant even when K_Q varied over a range of about 2.5 to 1. K_{Ia} was also shown to vary systematically with a_f/W in a manner that is a reflection of the scatter found in K_Q and K_{Ia}.

The use of a static analysis for calculating K_{Ia} was also shown to be justified on the basis of crack velocity and strain measurements made over the course of a run-arrest segment of crack extension.

Finally, on the basis of data available at present, it appears that the Reference Stress Intensity Factor, K_{IR}, may be nonconservative at temperatures above about T-RT_{NDT} = 65°C.

References

[1] Crosley, P. B. and Ripling, E. J., *Journal of Basic Engineering, Transactions*, American Society of Mechanical Engineers, Vol. 91, Series D, No. 3, Sept. 1969.

[2] Freund, L. B., *Journal of the Mechanics and Physics of Solids*, Vol. 20, 1972, Part 1, p. 129 and Part 2, p. 141.

[3] Crosley, P. B. and Ripling, E. J. in *Fast Fracture and Crack Arrest, ASTM STP 627*, American Society for Testing and Materials, 1977, p. 203-227.

[4] Ripling, E. J., Crosley, P. B., and Marston, T. V. in *Proceedings*, Joint American Society of Mechanical Engineers/Canadian Society of Mechanical Engineers, Pressure Vessel and Piping Conference, Montreal, Que., Canada, 25-30 June 1978.

[5] Crosley, P. B. and Ripling, E. J. in *Proceedings*, Second International Conference on Pressure Vessel Technology, Part II, Materials, Fabrication and Inspection, San Antonio, Tex., 1973, pp. 995-1005.

[6] Crosley, P. B. and Ripling, E. J., "Guidelines for Measuring K_{Ia} with a Compact Specimen," to be published in ASTM *Journal of Testing and Evaluation*.

[7] Hahn, G. T., Hoagland, R. G., Rosenfield, A. R., and Barnes, C. R., this publication, pp. 248-269.

[8] Crosley, P. B. and Ripling, E. J., "Crack Arrest Studies," Second Annual Report for Electric Power Research Institute, Project RP303-1, Sept. 1976.

Application of Dynamic Fracture Mechanics to Crack Propagation and Arrest in Pressure Vessels and Pipelines

P. A. McGuire,[1] *S. G. Sampath,*[1] *C. H. Popelar,*[2] *and M. F. Kanninen*[1]

A Theoretical Model for Crack Propagation and Crack Arrest in Pressurized Pipelines

REFERENCE: McGuire, P. A., Sampath, S. G., Popelar, C. H., and Kanninen, M. F., **"A Theoretical Model for Crack Propagation and Crack Arrest in Pressurized Pipelines,"** *Crack Arrest Methodology and Applications, ASTM STP 711,* G. T. Hahn and M. F. Kanninen, Eds., American Society for Testing and Materials, 1980, pp. 341-358.

ABSTRACT: The further development of a mathematical model for steady-state crack propagation in a pressurized pipeline is described. A key parameter in the model—the location of the plastic yield hinge relative to the moving crack tip—was determined by forcing agreement with crack speeds observed in the full-scale line pipe tests. The maximum crack driving force predicted by the model was then taken as a measure of the minimum fracture toughness value required for crack arrest. Comparisons with existing empirical formulations derived by Battelle, the American Iron and Steel Institute, British Steel, and the British Gas Council for the minimum required toughness values for crack arrest were made to demonstrate the reasonableness of this approach.

KEY WORDS: crack arrest, pipelines, arrest toughness, crack speeds

A mathematical model for crack propagation in a pressurized pipeline has been developed in a series of papers [*1-3*].[3] The objective has been to develop a theoretical basis for predicting the speed of axial crack propagation and the conditions for crack arrest that would be independent of full-scale pipe experiments. While exhibiting some degree of success, the model has not been completely adequate for these purposes. The present work was undertaken to improve some known deficient aspects of the

[1] Researcher, principal researcher, and research leader, respectively, Battelle Columbus Laboratories, Columbus, Ohio 43201.

[2] Professor, Department of Engineering Mechanics, The Ohio State University, Columbus, Ohio 43210.

[3] The italic numbers in brackets refer to the list of references appended to this paper.

model in order to provide a reliable prediction of pipeline crack arrest requirements.

Specific attention in this work has been placed on the determination of a key parameter of the model: the location of a plastic yield hinge relative to the moving crack tip. In contrast to other features of the model, it has not been possible to derive this parameter from basic mechanics considerations. In this work, a pragmatic approach was taken. Previously, primary emphasis was placed on the accurate computation of the speed of crack propagation. In contrast, the work reported here has sought to determine the yield hinge location empirically to match the observed crack speeds as nearly as possible. In this way, it is believed that the maximum crack driving force for various specified pipe sizes and operating conditions can be reliably predicted. This is the key result of the model. It provides an estimate of the minimum fracture toughness of the pipe material required for crack arrest.

Development of an Analysis Model for Crack Propagation in Pressurized Pipelines

Application of Dynamic Fracture Mechanics to Pipes

In applying dynamic fracture mechanics to analyze crack propagation and arrest in pipelines, it is necessary to consider the following specific aspects:

1. Kinetic energy contribution to crack growth.
2. Work done by pressurized gas on pipe walls.
3. Inertia of deforming pipe walls.
4. Pressure decay due to escaping gas and pipe deformation.
5. Large-scale plastic deformation behind crack tip.
6. Constraint of backfill on deformation of pipe.

The approach adopted here is one that attempts to minimize mathematical complexity while retaining all the necessary ingredients of a fundamentally correct solution. This has led to a "one-dimensional" representation for steady-state crack propagation, developed from an energy balance standpoint. The major simplification involved in this approach is that the pipe is taken to be linear elastic in the vicinity of the crack tip. The crack driving force, or dynamic energy release rate, is a generalization of the static strain energy release rate that includes contributions due to inertial forces and kinetic energy. It is assumed that the inelastic processes associated with crack growth are contained within an infinitesimally small neighborhood of the crack tip. Then, the dynamic energy release rate G for a through-wall crack can be expressed as

$$G = \frac{1}{h}\left\{\frac{dW}{da} - \frac{dU}{da} - \frac{dT}{da}\right\} \tag{1}$$

where

W = work done by external forces acting on the pipe walls,
U = strain energy of the pipe,
T = kinetic energy of the pipe,
h = pipe wall thickness, and
a = crack length.

Because $\mathcal{R}$ is a function of the crack speed V, the energy balance criterion for crack propagation is stated most generally as

$$G(a, t) = \mathcal{R}(V) \tag{2}$$

where t denotes time. If $G < \mathcal{R}$, crack propagation is not possible. This is the condition both prior to crack growth initiation and at the arrest of unstable crack propagation. At this time the fracture toughness of the pipeline material has been assumed to be independent of the crack speed and equal to the energy absorbed in a drop weight tear test (DWTT).[4]

The transient conditions accompanying crack growth initiation in a pressurized pipeline are extremely complex. Crack arrest presents similar difficulties. To avoid the necessity of modeling these processes, the model development has been restricted to a state of "steady-state" crack propagation. Physically, this represents the situation long enough after the initiation of crack growth[5] that the influence of the origin of the crack growth process is negligible. In this context, crack arrest is predicted by the model when, for given operating conditions and pipe properties, steady-state crack propagation is not possible.

For the special case of steady-state crack propagation considered here, a simplification can be made in Eq 2 since G then becomes a function of crack speed only. By choosing an origin attached to the moving crack tip, the new axial coordinate is defined by

$$\xi = x - Vt \tag{3}$$

where

x = stationary axial coordinate of the pipe,
V = crack speed, and
t = time.

Then, Eq 2 becomes

$$G(V) = \mathcal{R} \tag{4}$$

[4]The DWTT energy is the total energy imparted to a specimen of pipe steel to fracture it by impact. It therefore includes the kinetic energy and energy dissipated in the inelastic deformation of the fractured pieces. In addition, the test gives an average toughness over an (unknown) range of crack speeds.

[5]This may be only one or two pipe diameters.

where the crack speed dependence of R has been omitted in recognition of the fact that DWTT energies cannot provide this information.

Equation of Motion for Steady-State Axial Crack Propagation

An equation of motion for steady-state axial crack propagation in a pressurized pipeline by which G can be evaluated has been given in Refs *1-3*. In essence, four basic assumptions on the pipe behavior are made: (1) the axial displacement and in-plane forces are negligible; (2) the circumferential variations in pressure are insignificant; (3) the deformation is elastic everywhere ahead of a fully plastic yield hinge that develops a distance l behind the crack tip; and (4), in the cracked region, the pipe deformation is inextensional in the circumferential direction. The model conforming to these assumptions is shown in Fig. 1.

The approach followed is, starting from the elastic equations of motion for the displacements of a circular cylindrical shell, that of introducing integral operators to transform each displacement component into its circumferentially integrated value. Then, consistent with the foregoing assumptions, it follows that $\bar{w}$, the circumferentially integrated value of the radial displacement, becomes the dominant variable in the analysis. As shown in Ref *1*, in this way the governing equation for the problem reduces to a single ordinary linear differential equation. Incorporating a backfill term developed in later work [*3*] then gives

$$\frac{d^4\bar{w}}{d\xi^4} + 12(1-\nu^2)\frac{V^2}{h^2C_0{}^2}\frac{d^2\bar{w}}{d\xi^2} + \left\{\frac{12(1-\nu^2)}{R^2h^2}H(\xi) + \frac{12(1-\nu^2)k}{Eh^3}\right\}\bar{w} = 24\pi\frac{1-\nu^2}{Eh^3}p(V,\xi) - \frac{2}{3R^4}\delta(\xi) \quad (5)$$

where

R = pipe radius,
h = wall thickness,

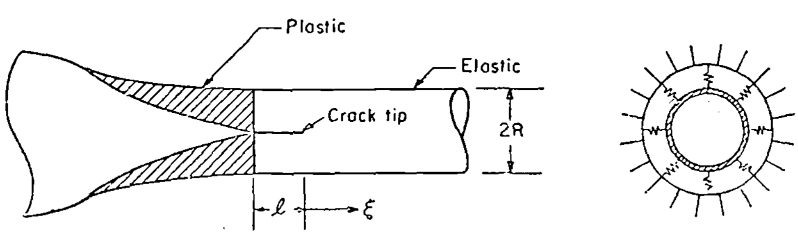

FIG. 1—*Theoretical model for steady-state crack propagation in a pipeline with backfill.*

k = foundation modulus for a pipe with backfill,
$C_0 = \sqrt{E/\rho}$ = elastic bar wave speed in the material [C_0 = 5000 m/s (16 400 ft/s) in steel],
p = pressure acting in the pipe,
δ = crack-opening displacement,
H = Heaviside step function, and

$$\bar{w}(\xi) = \int_0^{2\pi} w(\phi, \xi)d\phi \tag{6}$$

where ϕ denotes the circumferential coordinate in the pipe.

To evaluate the crack-opening displacement, it was assumed that the cracked portion of the pipe is essentially in a state of plane strain with respect to the axial coordinate. Subject to this assumption, it is readily found from the equations of shell theory that

$$\delta(\xi) = \bar{w}(\xi)H(-\xi) \tag{7}$$

Subsequent work by Emery et al [*4*] using a two-dimensional finite-difference computation verified that Eq 7 is quite accurate, even in the close proximity of the crack tip.

As in modeling pipeline behavior, it is convenient to characterize the soil by a Winkler foundation, and to neglect its inertia in comparison with that of the pipe. As described in Ref *3*, the foundation modulus k is determined by representing the pipe-soil system as an expanding circular cylindrical hole under uniform pressure in an infinite elastic medium. The plane-stress solution to this problem gives

$$k = 2G_s/R \tag{8}$$

where G_s is the shear modulus of the soil. Due to the difficulty in obtaining exact measurements of G_s and the fact that the solution is not particularly sensitive to the value chosen, a representative value of G_s = 7 MPa (1000 psi) has been used throughout this work.

Steady-State Pressure Distribution

As shown in Ref *2*, starting with the result given by Maxey et al [*5*] for the gas pressure at a propagating crack tip, the relation for the pressure behind the crack tip can be obtained by combining the two-dimensional shell deformation equations and the one-dimensional gas dynamics equations. In this approach each pipeline section is treated as a circular cylindrical shell in a state of plane strain with respect to the axial direction. It is further assumed that the gas flow in any cross-sectional plane does not disturb the axial flow pattern and that the gas leakage can be represented as choked flow from an infinite reservoir.

Ahead of the crack tip it is assumed that changes in pipe area and shape can be neglected. In the region behind the crack tip, however, the formulation must be generalized to account for large-scale deformation as well as for the loss of gas through the crack. In both regions, the formulation leads to a pressure distribution that is a function of the crack speed V, the line pressure p_L, the speed of decompression waves in the gas V_g, and the specific heat ratio γ of the gas. The decompressed pressure level p_0 at the crack tip is given by the relation [5]

$$p_0 = p_L \left\{ \frac{2}{\gamma + 1} + \frac{\gamma - 1}{\gamma + 1} \frac{V}{V_g} \right\}^{2\gamma/(\gamma-1)} \tag{9}$$

This is assumed to apply everywhere ahead of the crack tip. The leakage of gas behind the crack tip couples the shell deformation and gas dynamics equations. Solution (by finite-difference integration) of these equations indicates that, qualitatively, the decay is exponential. Therefore, to have an explicit statement for the pressure distribution, an exponential function is used. Whereupon the pressure distribution at any cross section in the pipeline is expressed as

$$p(\xi) = \begin{cases} p_0 & 0 \leq \xi \\ p_0 e^{b\xi/R} & -d \leq \xi \leq 0 \\ 0 & \xi \leftarrow d \end{cases} \tag{10}$$

where ξ is the coordinate fixed to the moving crack tip—see Eq 3—and d is the length in which a choked condition at the crack tip is expected to occur. The coefficient b for pressure decay is a function of crack speed that is determined numerically. Typical results of the finite-difference integration for p are shown in Fig. 2. Using such results, the exponential decay is matched to the calculated pressure at a point one pipe radius behind the crack tip to determine b.

Equations for Determination of the Crack Driving Force

By substituting Eqs 7, 8, and 10 into Eq 5, steady-state crack propagation is found to be governed by

$$\frac{d^4\overline{w}}{d\xi^4} + 12(1 - \nu^2)\frac{V^2}{h^2C_0^2}\frac{d^2\overline{w}}{d\xi^2} +$$

$$\left\{\frac{12(1-\nu^2)k}{Eh^3} + \frac{2H(-\xi)}{3R^4} + \frac{12(1-\nu^2)}{R^2h^2} H(\xi)\right\}\bar{w}$$

$$= \frac{24\pi(1-\nu^2)}{Eh^3} p_0[e^{b\xi/R}H(-\xi) + H(\xi)] \quad (11)$$

The solution of Eq 11 which gives bounded displacements ahead of the crack tip (that is, as $\xi \to \infty$) is

$$\frac{\bar{w}}{h} = \{C_1 \cos[(1+\mu^2)^{1/2}\omega\xi/R] + C_2 \sin[(1+\mu^2)^{1/2}\omega\xi/R]\}$$

$$\cdot \exp[-(1-\mu^2)^{1/2}\omega\xi/R] + 2\pi \frac{\alpha^4}{\omega^4}\frac{R^2}{h^2}\frac{p_0}{E}, \qquad \xi \geq 0 \quad (12)$$

where α, β, ω, and μ are dimensionless parameters defined as

$$\alpha^4 = 3(1-\nu^2)\frac{R^2}{h^2} \qquad \beta^4 = 3(1-\nu^2)\frac{kR^4}{Eh^3}$$

$$\omega^4 = \alpha^4 + \beta^4 \qquad \mu = \frac{\alpha^2 V}{\omega C_0}$$

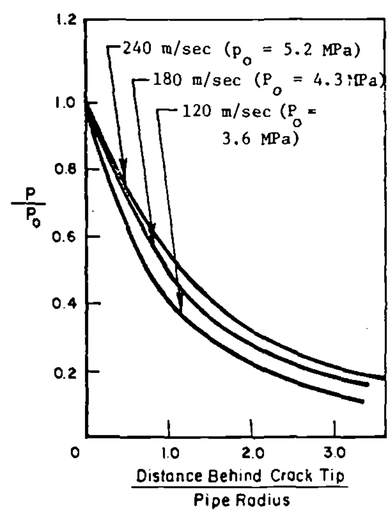

FIG. 2—*Calculated values of the pressure behind the crack tip for various crack speeds* (P_L = *8.0 MPa*).

There are two possible solutions for the region between the plastic hinge and the crack tip. These are

$$\frac{\bar{w}}{h} = C_3 \sin \lambda_1 \xi/R + C_4 \cos \lambda_1 \xi/R + C_5 \sin \lambda_2 \xi/R + C_6 \cos \lambda_2 \xi/R + \frac{8\pi\alpha^4 R^2 p_0 e^{b\xi/R}}{(4\beta^4 + 4\omega^2\mu^2 b^2 + b^4)h^2 E} \qquad \frac{\beta}{\omega} \leq \mu \leq 1 \quad (13)$$

where

$$\lambda_{1,2} = \mu\omega\sqrt{2}\left\{1 \mp \left[1 - \frac{\beta^4}{\mu^4\omega^4}\right]^{1/2}\right\}^{1/2}$$

and

$$\frac{\bar{w}}{h} = [C_7 \cos \lambda_4 \xi/R + C_8 \sin \lambda_4 \xi/R] \cosh \lambda_3 \xi/R + [C_9 \cos \lambda_4 \xi/R + C_{10} \sin \lambda_4 \xi/R] \sinh \lambda_3 \xi/R + \frac{8\pi\alpha^4 R^2 p_0 e^{b\xi/R}}{(4\beta^4 + 4\omega^2\mu^2 b^2 + b^4)h^2 E} \qquad 0 \leq \mu \leq \beta/\omega \quad (14)$$

where

$$\lambda_{3,4} = [\beta^2 \mp \mu^2\omega^2]^{1/2}$$

The constants of integration appearing in Eq 12–14 are determined by requiring that the deflection, slope, moment, and shear force be continuous across $\xi = 0$ and that a fully plastic yield hinge exist at $\xi = -l$. The plastic hinge is represented by zero transverse shear and a fully plastic moment of magnitude $Yh^2/4$ where Y is the yield stress of the pipeline material. The resulting constants of integration are rather lengthy and will not be reproduced here. They can be found in Ref 7.

The final step is to express G in terms of $\bar{w}$ and the known parameters in the problem. This result was derived in Ref *2* as

$$G = \frac{R}{2h}\left\{[p\bar{w}]_{\xi=-l} - [p\bar{w}]_{\xi=\infty} + \frac{Yh^2}{4}\left(\frac{d^2w}{d\xi^2}\right)_{\xi=-l} + 2\int_{-l}^{0} \bar{w}\frac{dp}{d\xi}d\xi + \frac{1.044}{2\pi}\frac{EhV^2}{C_0{}^2}\left[\left(\bar{w}\frac{d^2\bar{w}}{d\xi^2}\right)_{\xi=-l} - \left(\frac{d\bar{w}}{d\xi}\right)_{\xi=-l}\right]\right\} \quad (15)$$

where the point $\xi = -l$ denotes the position of the plastic yield hinge. This was derived in the previous work in the form $l = l(V, R, h)$ but it has since been decided that the formulation was not satisfactory. Subsequent work has concentrated on this parameter in an effort to improve the model.

Determination of the Plastic Yield Hinge Location

The preceding discussion has given the essential features of a mathematical model capable of predicting crack speeds and conditions for crack arrest in pipelines. Of key importance, in order to keep the model tractable, the pipe and the surrounding soil are considered to behave elastically everywhere ahead of the crack tip and behind the tip to some distance l. At $\xi = -l$, a fully plastic yield hinge appears. (This location may be viewed as the average location of the gross yielding which exists behind the crack tip.) Investigation of this parameter has indicated that G is extremely sensitive to the location of the yield hinge. Hence, a study was conducted to establish a relation between the various pipeline properties and the value of l that would give the best possible agreement with experimental measurements.

Measured crack speeds are available from the results of the full-scale pipeline fracture experiments [5,6].[6] It was possible to find the l needed for exact agreement by ignoring any possible functional relationship between l and the pipeline properties and recasting the formulation to yield $G = G(l)$ for $V =$ constant. In each full-scale test, V was set equal to the measured crack speed and G was calculated for a range of yield hinge locations. The value of l needed for exact agreement is denoted as l_e. This was determined graphically, locating the point at which $G(l_e) = \mathcal{R}$. Several possible functional relationships between l_e and the pipeline parameters (that is, R, h, Y, p_L) were evaluated. The most successful correlation was achieved by allowing l_e to depend only on h and V. As shown in Fig. 3, l_e/h tends to decrease linearly with increasing crack speed with differing slopes for the nonbackfill and for the backfill cases. The lines in the figure are completely empirical, but do provide a reasonable fit to the data. The equations are given by

$$\frac{l}{h} = \pi^2 - \frac{V}{V_0} \tag{16}$$

where $V_0 = 34.6$ m/s (113.6 ft/s) for backfill and 95.6 m/s (313.6 ft/s) without backfill. This formulation was adopted for use in the analysis.

For the pipelines with backfill, Fig. 3 includes five cases where the

[6] These data are also summarized in Ref 3.

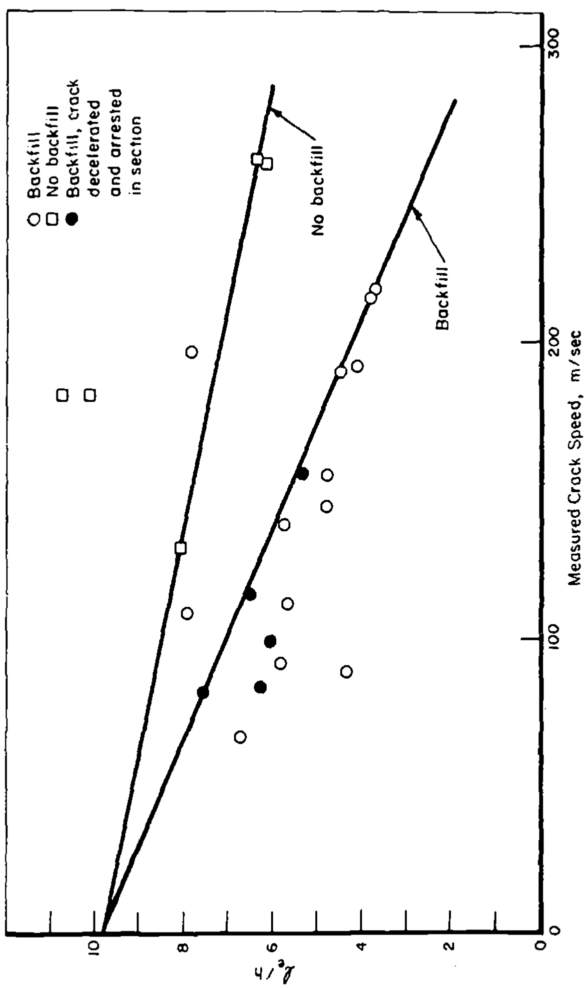

FIG. 3—*Location of plastic hinge for exact agreement between predicted and measured crack speeds using* h *as a trial correlation parameter.*

cracks actually arrested within the section. These cracks are treated as propagating, however, and a representative crack speed was selected as the steady-state speed. Choosing to include these tests results in an equation with a somewhat higher slope and intercept. This, in turn, will result in more conservative estimates of G since larger values of l generally yield larger values of G. The prime consideration in computing G for these cases is that crack arrest is never predicted for a pipeline where crack propagation actually occurred in the full-scale experiments.

Computational Results on Crack Propagation and Crack Arrest in Pipelines

Comparison of Predicted and Measured Crack Speeds

Typical results of calculations made using the pipeline crack propagation model described in the preceding section are illustrated by the $G = G(V)$ curves shown in Figs. 4 and 5. These show that for, both backfill and non-backfill conditions, G initially increases with crack speed, reaches a maximum, then decreases monotonically. Not revealed in the figures is the fact that G actually becomes zero at a geometry-dependent crack speed V_{lim} given approximately by

$$V_{\text{lim}} = \frac{(E/\rho)^{1/2}}{[3(1 - \nu^2)]^{1/4}} \left(\frac{h}{R}\right)^{1/2} \tag{17}$$

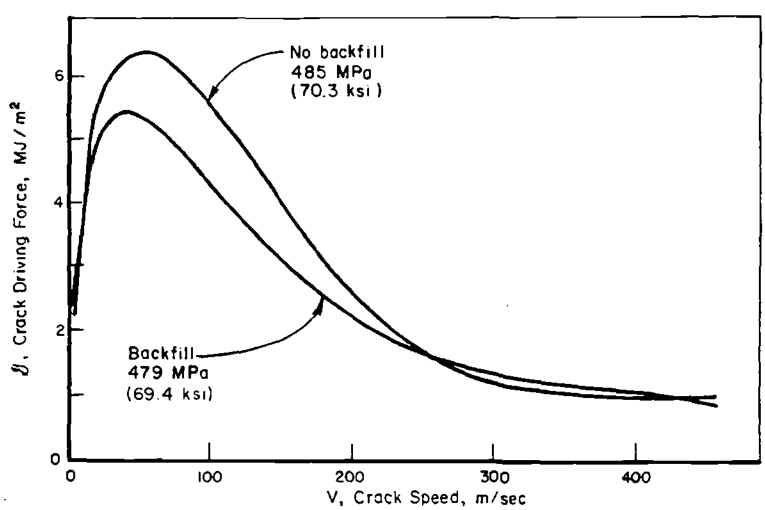

FIG. 4—*Calculated dynamic energy release rate as a function of crack speed for pipelines with and without backfill, based on Battelle full-scale experiment No. A31* (R = *0.457 m*, h = *8.4 mm*, P_L = *8.0 MPa*).

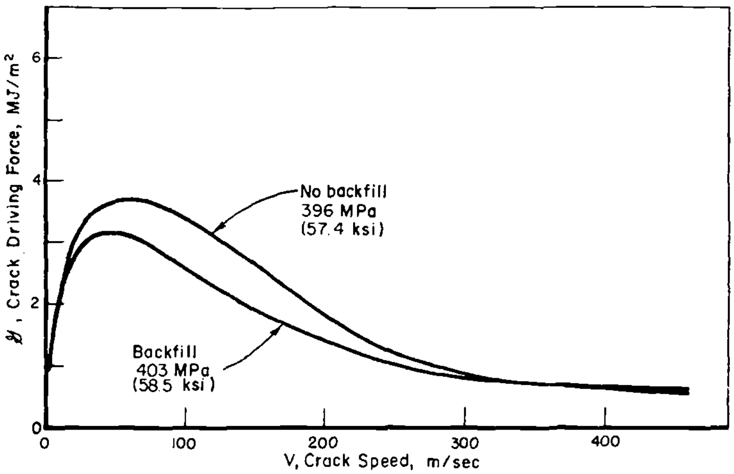

FIG. 5—*Calculated dynamic energy release rate as a function of crack speed for pipelines with and without backfill, based on Battelle full-scale experiment No. A35* (R = *0.33 m*, h = *7.9 mm*, P_L = *8.0 MPa*).

which serves as an upper bound on the crack speeds for which the model is valid; *nota bene*, for steel, $(E/\rho)^{1/2} = 5000$ m/s (16 400 ft/s). Computational results for each test in the large body of full-scale experimental results compiled by Maxey et al [*5,6*] have been obtained for comparison with these data.

First, for the same pipe geometry, material properties, and operating conditions, it can be seen from Figs. 4 and 5 that G for a pipeline without backfill is generally higher than for one with backfill.[7] Thus, for the same toughness, the predicted crack speeds will be lower for pipes with backfill. Also, there will be conditions where backfill could arrest a crack where crack propagation would be possible without backfill. These predictions are qualitatively consistent with the test results.

To use the theoretical model to predict crack speeds, some measure of the dynamic fracture toughness is needed. Since there is no other means of finding the fracture energy of a material as tough as pipe steel, this quantity, as in previous work, is approximated by the energy absorbed in the drop weight tear test (DWTT). Using $\mathcal{R}$-values obtained in this way, predicted crack speeds corresponding to each full-scale test were determined graphically by locating the point at which $G(V) = \mathcal{R}$ on a plot typified by Figs. 4 and 5. These speeds are compared in Fig. 6 with the crack speeds measured in the full-scale tests.

All predicted speeds are taken from the descending, that is, $(dG/dV < 0)$,

[7] As noted in Figs. 4 and 5, the pipes used in the backfill and nonbackfill cases had slightly different yield stress values.

branch of the curves because only these speeds represent stable crack growth. In many of the full-scale test results used for comparison with the model predictions, nearly constant crack speeds were observed. However, in five of the full-scale tests included in the comparison, the crack speeds decreased and arrested within the pipe section. Because the deceleration rate was small, these cracks have been considered as propagating, with a representative crack speed chosen for comparison purposes. In other tests, where there was a considerable range in the measured crack speeds, the average value was taken.

In previous work [*2,3*] comparisons like that of Fig. 6 served as an independent verification of the model predictions. In this work, however, the crack speeds were forced toward agreement with the measured values in order to set the yield hinge position. Nevertheless, such a comparison does provide an important check because it is not likely that good agreement could be obtained over such a wide range of conditions[8] by setting a single parameter if the model were not fundamentally correct. When the

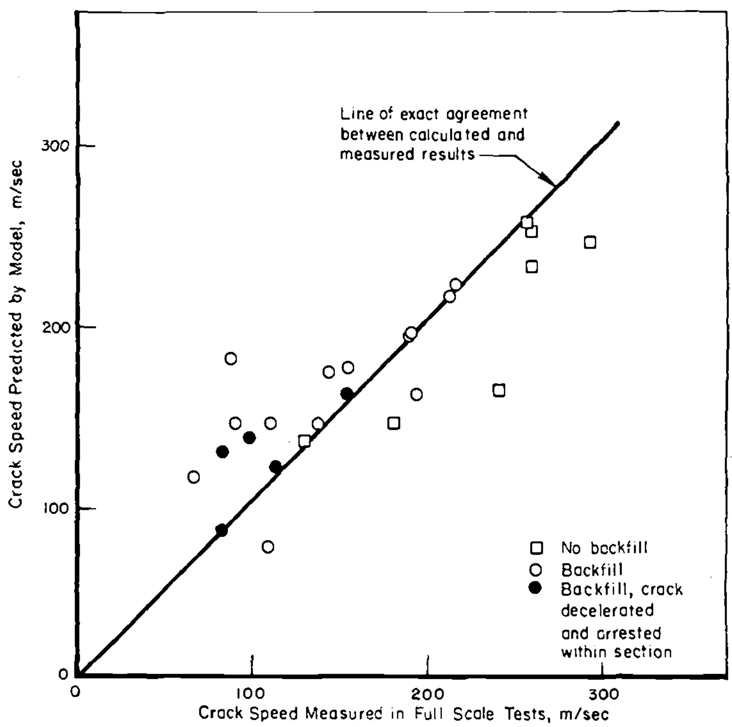

FIG. 6—*Comparison of predicted crack speeds and full-scale pipeline tests results.*

[8] A complete summary of the properties of the pipes used in the full-scale tests can be found in Ref *3*.

difficulty in establishing an exact value for $\mathcal{R}$ is considered along with the lack of a definitive measure of crack speed, it is felt that the theoretical results agree remarkably well with the measured crack speeds.

Comparison of Predicted and Empirical Crack Arrest Criteria

The most important result that can emerge from the analysis of pipeline crack propagation is a criterion for crack arrest. For given pipeline conditions, the results typified by Figs. 4 and 5 show that the model predicts a minimum level of fracture toughness above which crack propagation is not possible. In terms of the function $G = G(V)$, this corresponds to the maximum value of the crack driving force, G_{max}. Numerical results obtained with the theoretical model can be used to derive an empirical relationship for G_{max}. Then, for ease of comparison with the predictions of other empirical formulations, it is convenient to relate G_{max} to a minimum upper-shelf two-thirds-thickness Charpy energy for crack arrest, $(C_V)_{min}$.

To determine an approximate simple relation for $(C_V)_{min}$, an average pipe radius of 0.447 m (17.6 in.), wall thickness of 10.4 mm (0.4104 in.), and yield stress of 483 MPa (70 ksi) were first chosen. These values represent average values for all of the pipes used in the full-scale experiments [*5,6*]. A line pressure of 9.65 MPa (1400 psi) was taken to give a hoop stress of 415 MPa (60 ksi), a value somewhat higher than average. The effect of each of these four quantities was evaluated by varying them individually, by ± 10 percent, keeping all other parameters constant, and analyzing the resulting effect. A dependence on all four quantities was observed. The corresponding relations are

$$(C_V)_{min} = \begin{cases} 300\, p_L{}^{5/4} Y^{3/4} R^{19/12} h^{-1/3}/E & \text{Backfill} \\ 500\, p_L{}^{4/3} Y^{2/3} R^{19/12} h^{-1/4}/E & \text{No backfill} \end{cases} \tag{18}$$

The quantities p_L, Y, and E are in units of ksi, R and h in inches, and $(C_V)_{min}$ in ft-lb for two-thirds-thickness specimens to facilitate comparison with the relations developed by the pipeline industry.[9]

Empirical relations that have been developed for the minimum Charpy energy for crack arrest work include the results obtained by Maxey et al [*6*] at Battelle for the American Gas Association. This is

$$(C_V)_{min} = \begin{cases} 0.0072\, \sigma_0{}^2 (Rh)^{0.333} & \text{Backfill} \\ 0.0098\, \sigma_0{}^2 (Rh)^{0.284} & \text{No backfill} \end{cases} \tag{19}$$

[9] Appropriate conversion factors are: 1 ksi = 6.895 MPa; 1 in. = 0.254 m; and 1 ft · lb = 1.356 J.

where $\sigma_0 = pR/h$, the hoop stress. Next, work on behalf of the American Iron and Steel Institute [8] gives

$$(C_V)_{\min} = 0.021\ \sigma_0^{3/2} R^{1/2} \quad \text{Backfill} \tag{20}$$

A result obtained by the British Gas Council [9] is[10]

$$(C_V)_{\min} = 0.021\ \sigma_0^{1} R/h^{1/2} \quad \text{Backfill} \tag{21}$$

Finally, a result obtained both by British Steel [10] (see footnote 9) and by Sumitomo [11] is

$$(C_V)_{\min} = 0.00079\ \sigma_0^{2} R \quad \text{Backfill} \tag{22}$$

It should be recognized that these equations are valid only in a pressure range of 60 to 80 percent of the pressure that would cause yielding of the pipe. Note also that, despite their apparent dissimilarity, all of these relations are based on essentially the same data base.

Since the empirical formulations involve only factors of σ_0, R, and h, Eq 18 is recast into this form. For pipeline steels, E is 2.0×10^5 MPa (29 000 ksi) and the operating conditions are usually such that σ_0 is equal to 72 percent of the yield stress. Setting $\sigma_0 = 0.72Y$ in Eq 18 to eliminate the yield stress then gives

$$(C_V)_{\min} = \begin{cases} 0.0132\ \sigma_0^{2} R^{1/3} h^{2/3} & \text{Backfill} \\ 0.0215\ \sigma_0^{2} R^{1/4} h^{3/4} & \text{No backfill} \end{cases} \tag{23}$$

for the predictions of the model. Table 1 summarizes the coefficients in the various relations to facilitate comparison between this result and the empirical correlations.

Discussion and Conclusions

For given pipe materials, pipe sizes, and specified operating conditions, the minimum fracture toughness required to preclude a long-running unstable fracture can be predicted from the mathematical pipe fracture model described in this paper. If a value of the dynamic fracture toughness of the pipe material is supplied that is less than the value for crack arrest, the model can also provide an estimate of the crack propagation speed. A simple relation is also derived from the model to estimate the minimum arrest toughness value. This relation compares reasonably well with the

[10] This result is an approximation of a more complicated formulation—see Ref *6*.

TABLE I—*Comparison of the exponents in the empirical and theoretical relations for the minimum toughness required to arrest unstable crack propagation in a pressurized pipeline.*

Developer	Exponent of Hoop Stress	Exponent of Pipe Radius	Exponent of Wall Thickness
	PIPES WITH BACKFILL		
Battelle [6]	2.0	0.333	0.333
AISI [8]	1.5	0.5	0
British Gas Council [9]	1.0	1.0	−0.5
British Steel [10]	2.0	1.0	0
This paper	2.0	0.33	0.667
	PIPES WITHOUT BACKFILL		
Battelle [6]	2.0	0.284	0.284
This paper	2.0	0.25	0.750

various empirical relations that have been developed from the full-scale pipe tests results, although it is somewhat conservative.

Previous work on the model development proceeded entirely from fundamental mechanics considerations, with full-scale test results used only to check the progress being made. However, because it was not possible to set a key internal parameter in this way, the current work departed from this approach. The point of view that the crack arrest prediction of the model was of paramount importance was adopted. Then, the measured and predicted crack speeds were forced into correspondence by an optimum choice of this parameter. It is believed that this makes the model offer a reliable, albeit conservative, crack arrest prediction.

The major shortcoming of the theoretical model is its highly idealized treatment of plastic deformation in the pipe. While the use of an axisymmetric plastic yield hinge produces qualitatively correct behavior, as might be expected, the experimental results of Shoemaker et al [12,13] indicate that plasticity also engulfs the crack tip. However, attempts to improve this aspect of the model would inevitably lead to a much more complicated solution. For example, using a bilinear stress-strain curve and allowing some plastic deformation ahead of the crack tip causes the governing differential equation to have variable coefficients. A closed-form solution is then no longer possible. While it is possible to integrate the equation numerically, the computer solution time would become large, thus losing the essential simplicity of the approach. However, there may be applications where this would nevertheless be a useful approach; for example, in the use of the model to treat sleeves and other mechanical crack arrestor devices that perform by constraining the pipe wall deformation.

Alternative pipeline fracture models also exist [14-18]. In most of these, it appears that a somewhat more realistic account is taken of plastic deformation and other aspects of the problem than was done in the development of the model described in this paper. In particular, the pronounced pipe ovalization and resulting longitudinal plastic strain induced ahead of the crack tip observed in the experiments conducted by Shoemaker et al [*12,13*] have been neglected here. However, it is also true that none of the competing approaches has yet demonstrated any predictive capability—either with regard to crack speeds or to practical measures to assure crack arrest. With all its idealizations, the model given here can make useful predictions with a quite reasonable degree of accuracy.

Acknowledgments

This paper is based on research sponsored under Project NG-18 by the Pipeline Research Committee of the American Gas Association. The authors would like to thank Robert Eiber and Willard Maxey of Battelle for their assistance in understanding and interpreting the pipeline experimental results.

References

[*1*] Kanninen, M. F. and Sampath, S. G., *Journal of Pressure Vessel Technology*, Part II, Vol. 95, 1973, p. 971.

[*2*] Kanninen, M. F., Sampath, S. G., and Popelar, C., *Journal of Pressure Vessel Technology*, Vol. 98, 1976, p. 56.

[*3*] Popelar, C., Rosenfield, A. R., and Kanninen, M. F., *Journal of Pressure Vessel Technology*, Vol. 99, 1977, p. 112.

[*4*] Emery, A. F., Love, W. J., and Kobayashi, A. S. in *Fast Fracture and Crack Arrest, ASTM STP 627*, G. T. Hahn and M. F. Kanninen, Eds., American Society for Testing and Materials, 1977, p. 142.

[*5*] Maxey, W. A., Kiefner, J. F., Eiber, R. J., and Duffy, A. R. in *Proceedings*, 12th World Gas Conference, International Gas Union, Paris, 1973.

[*6*] Maxey, W. A., Kiefner, J. F., and Eiber, R. J., NG-18 Report No. 100, Battelle Memorial Institute, Columbus, Ohio, 12 Dec. 1975.

[*7*] McGuire, P. A., Sampath, S. G., Popelar, C. H., and Kanninen, M. F., "A Theoretical Model for Crack Propagation and Arrest in Pressurized Pipelines," NG-18 Report No. 115, Battelle Memorial Institute, Columbus, Ohio, 1 March 1978.

[*8*] "Running Shear Fracture in Line Pipe," AISI Technical Report, Sub-Committee of Large Diameter Line Pipe Producers, American Iron and Steel Institute, 1 Sept. 1974.

[*9*] Poynton, W. A. in *Proceedings*, Symposium on Crack Propagation Pipelines, Institute of Gas Engineers, Newcastle-upon-Tyne, England, March 1974.

[*10*] Dick, J. A., Jamieson, P. McK., and Walker, E. F. in *Proceedings*, Symposium on Crack Propagation in Pipelines, Institute of Gas Engineers, Newcastle-upon-Tyne, England, March 1974.

[*11*] Podlasek, R., private communication, 1978.

[*12*] Shoemaker, A. K. and McCartney, R. F., *Journal of Engineering Materials Technology*, Vol. 96, 1974, p. 318.

[*13*] Ives, K. D., Shoemaker, A. K., and McCartney, R. F., *Journal of Engineering Materials Technology*, Vol. 96, 1974, p. 309.

[*14*] Freund, L. B., Parks, D. M., and Rice, J. R. in *Mechanics of Crack Growth, ASTM STP 590*, American Society for Testing and Materials, 1976, p. 243.

[15] Abou-Sayed, I. and Freund, L. B. in *Proceedings*, Eighth Southeastern Conference on Theoretical and Applied Mechanics, Blacksburg, Va., 1976.
[16] Parks, D. M., and Freund, L. B., *Journal of Pressure Vessel Technology*, Vol. 100, 1978, p. 13.
[17] Mimura, H. in *Proceedings*, 16th Japan Congress on Materials Research, 1973, p. 101.
[18] Owen, D. R. J., *International Journal of Fracture*, Vol. 13, 1977, p. 821.

L. B. Freund[1] *and D. M. Parks*[2]

Analytical Interpretation of Running Ductile Fracture Experiments in Gas-Pressurized Linepipe

REFERENCE: Freund, L. B. and Parks, D. M., "**Analytical Interpretation of Running Ductile Fracture Experiments in Gas-Pressurized Linepipe,**" *Crack Arrest Methodology and Applications, ASTM STP 711,* G. T. Hahn and M. F. Kanninen, Eds., American Society for Testing and Materials, 1980, pp. 359–378.

ABSTRACT: Ductile crack propagation in pneumatically pressurized pipelines is an extremely complex process, involving interactions between the fracturing pipe, the escaping gas, the covering backfill, and mechanical crack arresters, if any are present. In order to extend the experience gained through testing programs to the design of pipelines, it appears to be necessary to develop theoretical models of the process based on simplifying assumptions which are consistent with the available experimental data. Over the past several years, the American Iron and Steel Institute has conducted a full-scale test program on propagating shear fractures in pneumatically pressurized linepipe, and many measurements have been made of crack motion, pipe wall deformation, pressure loading, fracture toughness, etc. The relevant data are reviewed, and some implications for modeling pipe wall plasticity, gas flow and escape, and backfill resistance are considered. Pipe wall deformations are assumed on the basis of test data, and the contributions to an overall energy balance equation due to individual deformation components are computed in the spirit of upper-bound calculations of plastic limit load analysis. It is concluded that for ductile materials the resistance of the pipe wall material to axial in-plane stretching near the crack tip is a major contribution to the total structural and inertial resistance to the gas pressure driving force, and relative magnitudes of other resistance terms are also estimated for the case of no backfill. The capacity for soil backfill to dissipate the work of the driving force is also considered, and it is concluded that for soils with low cohesion the inertial resistance of the backfill is much greater than the resistance due to soil strength.

KEY WORDS: crack propagation, fracture mechanics, pipelines, plastic deformation, ductile fracture, gas dynamics, soil backfill

[1]Professor of engineering, Division of Engineering, Brown University, Providence, R. I. 02912.
[2]Assistant professor, Department of Mechanical Engineering, Massachusetts Institute of Technology, Cambridge, Mass. 02139.

Ductile shear fractures can propagate in the axial direction over long distance at very high rates in large-diameter pressurized linepipe, such as that used in natural gas transmission lines. With a view toward developing an understanding of this phenomenon and establishing pipeline design criteria, several organizations have sponsored testing programs to determine the propagation and arrest characteristics of running ductile fractures. Experimental results obtained through the program sponsored by the American Iron and Steel Institute (AISI) are summarized by Ives et al [*1*][3] and Shoemaker and McCartney [*2*]; results of the program sponsored by the American Gas Association are summarized by Maxey et al [*3,4*]; and results of the British Gas Council program are summarized by Poynton et al [*5,6*]. The present discussion is based primarily on the experimental results obtained in the AISI program. In these tests, long sections of steel pipe with capped ends were pressurized with air to simulate pipeline operating conditions. Typically, the length of the test section was greater than 100 pipe diameters, the wall thickness was less than 1/65 of a diameter, and the initial equilibrium line pressure was 60 to 80 percent of the plastic limit load pressure based on the initial tensile yield stress of the pipe wall material. Axial crack growth was then initiated from an artificially induced flaw at the center of the test section. In each test the pipe was instrumented with crack detectors, strain gages, and pressure transducers. The electronically recorded data which were obtained are summarized in Refs *1* and *2*.

In order to extend the experience gained through these testing programs to the design of pipelines, it is necessary to develop theoretical models of the process. A brief listing of just the principal features of the process as observed in the experiments illustrates the complicated nature of the process and suggests numerous complexities which might be encountered in attempts at modeling. For example, the process typically involves thinning and plane-stress ductile fracture of the pipe wall at the crack tip, general three-dimensional deformation of the pipe wall, large-scale plastic flow of the pipe wall material, inertial resistance of the material to motion, gas flow along the fracturing pipe and escape through the opening crack, and the resistance to crack growth due to soil backfill and mechanical crack arresters when either are present. Because of this complexity, therefore, models intended to describe all details of the process are hopelessly complicated. Instead, the development of tractable models must be based on simplifying assumptions which are consistent with the available experimental data. If the results of the analysis are to be used for system parameters outside the range of parameters used in the testing programs, it is essential that all important aspects of the process be taken into account in the model so that the model provides a true characterization of the process.

On the basis of the observations drawn from the full-scale test data

[3] The italic numbers in brackets refer to the list of references appended to this paper.

reported in Refs *1* and *2*, an analytical model was recently developed [*7*] for ductile crack propagation in an initially pressurized long cylindrical shell. The analysis was directed toward the ductile range of material behavior, for which extensive yielding occurs in the pipe walls, and the material was represented as being rigid-ideally plastic. Further, to obtain a tractable model, the shell deformation was assumed to be steady as seen by an observer moving with the crack tip, and, on the basis of strain-time data in Ref *1*, kinematic assumptions were made so that the deformation was expressed in terms of a single function of position along the shell axis which is determined in accordance with a variational statement of the equation of motion. Separation of material was represented by a Dugdale zone of localized yielding in which a critical opening displacement is attained for fracture. With these approximations, which are discussed at some length in Ref *7*, the pressure distribution decay length required to drive the crack is estimated. In a separate study concerned with the dynamics of gas escape [*8*], the pressure decay profile was estimated for the case of a widely opening crack. Other analytical models have been considered by Kanninen et al [*9,10*], Hahn et al [*11*], and Poynton et al [*6*]. Numerical studies of the problem have been described by Emery et al [*12*] and Owen and Shantaram [*13*],

The purpose of the present discussion is to review various aspects of the experimental results and to consider the implications of these results in the development of analytical models of the process. The driving force for this ductile crack propagation process is the gas pressure acting on the pipe wall. Various contributions to resistance of crack growth can be identified; for example, inertial resistance of the pipe material to motion, resistance of the wall material to deformation, and fracture resistance. On the basis of the available data, quantitative estimates are made of the *relative* magnitudes of the crack driving force and the various contributions to crack growth resistance involved in the process. From such results, the relative importance of each contribution identified in analytical modeling can be inferred. Because of the complexity of the process, some fairly wide-ranging assumptions must be made in meeting this objective. However, the work-energy procedure to be followed is quite general and the special assumptions can be easily adjusted to suit individual tastes. An important point is that the general conclusions to be drawn are quite insensitive to the details of the assumptions made because global energy-work terms, rather than point-wise stress and deformation fields, are compared. Of course, it is precisely this feature which makes energy methods so useful in continuum mechanics.

The data [*1,2*] indicate that after the crack tip has moved about four pipe diameters from the initiator, the crack length no longer has an influence and, therefore, a semi-infinite crack is assumed. Furthermore, it was observed that the crack extended at a fairly constant rate in each uniform test section. Therefore, it is assumed that the semi-infinite crack extends at a constant rate along a generator of the cylindrical pipe, and the deformation field is time-independent as seen by an observer moving with the crack tip. The pipe is considered to be a thin cylindrical shell, and the small-deflection strain-displacement relations are employed. Typical pipe material yields plastically at extensional strains of about 0.2 percent in simple tension, whereas extensional strains in excess of 2 percent have been observed in the tests. Thus, elasticity effects are neglected and the material is considered to be ideally plastic.

The present calculations are based on an overall energy balance which, for the problem at hand, requires that the rate of work of all loads or tractions on the surface of a material volume equals the rate of increase of kinetic energy of the material plus the rate at which energy is irreversibly dissipated through plastic flow. If such an energy balance is enforced for all kinematically admissible deformation fields, the balance is normally called the principle of virtual work, and standard procedures of variational calculus lead to the field equations of motion as a necessary condition for the balance to hold. In this study the work balance is examined only for a restricted class of deformation fields and no attempt is made to derive field equations. Instead, deformations are assumed on the basis of the full-scale test data and the contributions to the energy balance equation due to individual deformation components are computed in the spirit of upper-bound calculations of plastic limit load analysis. In the following section, individual contributions are estimated and compared for the case of steady-state ductile crack propagation in a pipeline with neither soil backfill nor mechanical crack arresters. The capacity for soil backfill to dissipate the work of the driving force is discussed in a subsequent section. Crack arresters are not considered here, but a discussion of the wire-wrapped mechanical arrester was recently presented elsewhere [*14*].

Steady-State Crack Propagation: No Backfill

An important observation in making assumptions concerning the deformation is that, generally, thin shells tend to deform predominantly by bending, and they have large relative resistance to stretching or shear of the middle surface. For the opening of an axial fracture in a cylindrical shell, the deformation cannot be accommodated simply by bending, and some middle surface stretching must accompany the outward flaring of the shell walls near the tip of an advancing crack. Study of the shell strain-displacement relations suggests that the observed flaring of the walls must be accompanied by stretching of the middle surface in the axial direction, as shown in Fig. 10 of Ref *1*. As can be seen from Figs. 10 and 11 of Ref *1*, the extensional strains in the circumferential direction are much smaller than those in the axial direction, except very near the fracture path. Thus, the in-plane shear strain and the extension in the circumferential direction are taken to be zero, except for the latter within a Dugdale zone of plastic separation ahead of the tip.

Spatial coordinates on the shell middle surface are defined in Fig. 1. The mean radius of the undeformed shell is a, the wall thickness is h, the circumferential coordinate is θ, and the axial coordinate is ξ, measured from the moving crack tip. Because of the assumption of steady-state fields, the operation of time differentiation is replaced by $V\partial/\partial\xi$ where V is the crack-tip speed. The length of the Dugdale zone of the plastic separation is R. Finally, the axial, circumferential, and radial components of displacement of a point initially at (ξ,θ) are denoted by u, v, and w, respectively.

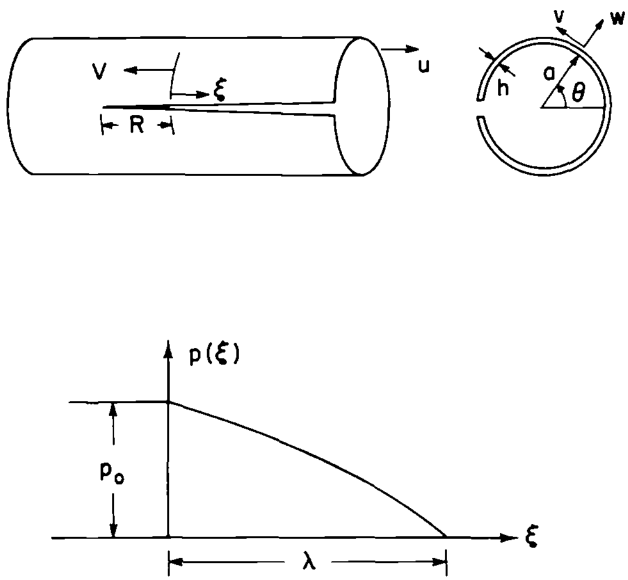

FIG. 1—*Geometry and coordinate system for analysis of steady-state crack propagation.*

Resistance to the Driving Force

The driving force for the ductile fracture process is the gas pressure on the pipe walls, and the modeling of the gas flow process is described in the next subsection. The energy balance is considered for the axial interval between the leading edge of the plastic zone at $\xi = -R$ and the point behind the crack tip at which the applied internal pressure has been reduced to essentially atmospheric pressure, say at $\xi = \lambda$. The strain and velocity fields must therefore be specified for the interval $-R < \xi < \lambda$ in a manner consistent with any kinematical constraints. The displacement field is assumed to be

$$w = \delta_t(1 + \xi/R)^2/2\pi \tag{1}$$

$$v = -\theta\delta_t(1 + \xi/R)^2/2\pi \tag{2}$$

$$u = a\delta_t(\theta^2 - \pi^2/4)(1 + \xi/R)/2R\pi \tag{3}$$

This displacement field was constructed by assuming that each circular cross section deforms into a concentric circle, that the radial acceleration of the pipe wall material is uniform over the interval, and that the circumferential and shear strains of the middle surface vanish. The length scale of the deformation field is set by the crack-tip opening displacement δ_t. The crack progresses with a fixed value of δ_t, a value which characterizes the resistance of the material to ductile fracture. The pipe wall is undeformed for $\xi < -R$ and Eqs 1, 2, and 3 satisfy continuity of displacement at $\xi = -R$. The net rate of kinetic energy uptake, of plastic dissipation, and of fracture energy dissipation over the interval $-R < \xi < \lambda$ are now computed for the deformation (Eqs 1, 2, and 3) under the assumption that the material is rigid-perfectly plastic with tensile flow stress σ_0.

1. Energy dissipated in fracture D_1: The region of progressive wall thinning directly ahead of the tip leading up to the predominantly shear fracture described in Ref *1* is idealized as a one-dimensional cohesive zone of length R with the cohesive stress-resisting opening being σ_0. The rate of energy absorption within this plastic zone is

$$D_1 = 2 \int_{-R}^{0} \sigma_0 h \dot{v}(\xi, \pi) d\xi = V \sigma_0 \delta_t h \tag{4}$$

where the superposed dot denotes time derivative. It is convenient to express all energy rates as multiples of the reference value $\sigma_0 haV \equiv D$, where the multiplier depends only on the dimensionless quantities representing fracture toughness (δ_t/h), yield zone extent (R/a), geometrical configuration (h/a), material inertia $(\rho V^2/\sigma_0)$, and pressure loading $(ap_0/h\sigma_0$ and $\lambda/a)$. Thus

$$\frac{D_1}{D} = \left(\frac{\delta_t}{h}\right)\left(\frac{h}{a}\right) \tag{5}$$

It is common to assume that an estimate of the critical crack-tip opening displacement δ_t may be obtained from standard Charpy tests by assuming that the energy absorbed per unit fracture surface area in the Charpy specimen is equal to the product of the yield stress of the material times δ_t. This estimating procedure ignores the effect of the plane-strain type of constraint which is operative in the crack-tip region in the center portion of the Charpy specimen, an effect which could lower the estimate by as much as 50 percent.

2. Kinetic energy rate D_2: Inertial effects in the axial direction appear to be much less than those in the radial and circumferential directions, and the axial contribution to kinetic energy is therefore neglected. The net rate of kinetic energy uptake by the pipe wall material in the interval $-R < \xi < \lambda$ is then

$$D_2 = \frac{\partial}{\partial t} \int_{-R}^{\lambda} \int_{-\pi}^{\pi} \frac{1}{2} \rho h(\dot{v}^2 + \dot{w}^2) a d\theta d\xi \tag{6}$$

where ρ is the mass density of the pipe material. The result of evaluating Eq 6 for the deformation field (Eqs 1, 2, and 3) is

$$\frac{D_2}{D} = \frac{1}{\pi}\left(1 + \frac{\pi^2}{3}\right)\left(\frac{\rho V^2}{\sigma_o}\right)\left(\frac{\delta_t}{h}\right)^2\left(\frac{h}{a}\right)^2\left(\frac{a}{R}\right)^2\left(1 + \frac{\lambda}{R}\right)^2 \tag{7}$$

3. Dissipation through axial in-plane stretching D_3: The in-plane axial strain $\epsilon_\xi = \partial u/\partial \xi$ is uniform within the interval $-R < \xi < \lambda$ according to Eq 3. The strain rate $\dot{\epsilon}_\xi$, and therefore the plastic dissipation associated with this strain component, is zero. However, ϵ_ξ is discontinuous across the line $\xi = -R$, $-\pi < \theta < \pi$ so that this line represents a traveling plastic hinge in the terminology of plastic structural analysis. The energy dissipation in the hinge is simply the discontinuity in ϵ_ξ times the operative flow stress integrated over the hinge line times V, that is

$$\begin{aligned} D_3 &= \int_{-\pi}^{\pi} \sigma_o h |\epsilon_\xi(-R, \theta)| \, a d\theta \\ &= D \frac{\pi^2}{4}\left(\frac{a}{R}\right)^2\left(\frac{h}{a}\right)\left(\frac{\delta_t}{h}\right) \end{aligned} \tag{8}$$

This is the energy dissipation associated with the relatively large axial in-plane strains which have been observed [*1*] adjacent to the fracture path upon approach of the crack tip. As can be seen from Eq 3 and the strain-displacement relation $\epsilon_\xi = \partial u/\partial \xi$, the axial strain is indeed maximum along the crack line $\theta = \pm\pi$. The fact that the axial plastic strain develops within a discrete hinge according to Eq 3 poses no problem for the present work rate calculation, because the net dissipation depends only on the final axial plastic strain and it is independent of the length interval over which this strain develops. A maximum measured axial in-plane strain of 1 to 2 percent is reported in Ref *15*, and this provides a useful check on the assumed deformation field. From Eq 3

$$(\epsilon_\xi)_{\max} = \frac{3\pi}{8} \frac{a\delta_t}{R^2} \tag{9}$$

The value of $(\epsilon_\xi)_{\max}$ can be determined from test data, a is a known geometrical parameter, and δ_t may be inferred from independent Charpy fracture tests on the wall material. The relation (Eq 9) thus provides an estimate of R

directly from the data. For example, for available data, relevant parameters in Eq 9 fall within the ranges $30 < a/h < 60$, $0.05 < \delta_t/h < 0.33$, and $0.01 < (\epsilon_\xi)_{\max} < 0.02$ so that R/a is in the range $0.22 < R/a < 1.15$. Although no direct measure of R is available, values of R/a in the upper part of this range appear to be consistent with observations, and the value $R/a = 0.75$ is used in all calculations.

4. Dissipation through circumferential bending D_4: As the pipe walls flare open behind the crack tip, the cross-sectional curvature continuously decreases, resulting in the dissipation of work through plastic flow. According to a common idealization in the plastic analysis of cylindrical shells, the internal stress resisting the change in curvature is the fully plastic bending moment per unit length in the ξ-direction $\sigma_0 h^2/4$ [7]. The curvature in the circumferential direction is derived from the displacement field according to $\kappa_\theta = (\partial v/\partial\theta - \partial^2 w/\partial\theta^2)/a^2$, and the rate of plastic work is

$$D_4 = \int_{-R}^{\lambda} \int_{-\pi}^{\pi} -\frac{1}{4}\sigma_0 h^2 \dot{\kappa}_\theta \, a d\theta d\xi \tag{10}$$

Substitution of the displacement field (Eqs 1 and 2) and evaluation of the integral (Eq 10) yields the estimate

$$\frac{D_4}{D} = \frac{1}{4}\left(\frac{\delta_t}{h}\right)\left(\frac{h}{a}\right)^2\left(1 + \frac{\lambda}{R}\right)^2 \tag{11}$$

Other contributions to the overall structural resistance to crack growth could be estimated in the same manner, such as those due to axial bending, middle surface twist, or axial kinetic energy. It seems, however, that the dominant contributions are included among the preceding four and these suffice for present purposes.

Estimate of the Driving Force

The driving force for ductile crack propagation in a gas-pressurized linepipe is provided by the large amount of energy stored in the compressed gas at normal operating pressures. Depending on pipe geometry and material strength levels, typical operating pressures for large-diameter transmission pipelines may be of the order of 80 to 100 atm. The gas flow accompanying the initiation and subsequent ductile propagation of cracks requires a gas dynamics analysis of the process in order to assess the crack-tip region pressure distribution $p(\xi, \theta)$ associated with the often-observed constant-velocity crack propagation. This pressure distribution, once determined, in conjunction with the normal component $\dot{w}$ of velocity field (Eq 1) of the shell, provides the input (driving) work rate

$$\dot{W}_0 = \int_{-R}^{\lambda} \int_{-\pi}^{\pi} p(\xi, \theta)\dot{w}ad\theta d\xi \tag{12}$$

The mechanics of the actual cracking process is of coupled fluid/solid interaction, and the pressure distribution of the escaping gas is not truly independent of the deformation of the structure [7]. In order to obtain tractable models, however, the solid mechanics and gas dynamics subsystems have often been decoupled and separately analyzed, as discussed in the following. Justification for such decoupling is provided by the extent of agreement of the resulting analyses with observations; however, there are important not-well-understood aspects of the process, discussed in a later section, which seem to require a more explicit treatment of the solid/fluid interactions.

Maxey et al [4] noted that a nominal gas pressure in the vicinity of a steadily running crack tip, p_0, was less than the initial line pressure, p_L, for crack velocities V less than the sound speed of initially pressurized gas, C_L. They modeled the crack by considering a semi-infinite duct initially pressurized with a perfect gas at a pressure p_L substantially greater than exterior (for, example, atmospheric) pressure. At a certain instant, gas is suddenly allowed to escape from the end of the duct and, simultaneously, the end of the duct begins to recede at velocity V. If the boundary condition at the open end is that the local particle velocity, relative to the moving end, equals the local sonic speed, it can be shown that for transient, adiabatic duct flow, the local pressure p_0 at the moving end is given by

$$p_0 = p_L \left[\frac{2}{\gamma + 1} + \frac{(\gamma - 1)V}{(\gamma + 1)C_L}\right]^{2\gamma/(\gamma-1)} \tag{13}$$

where γ is the ratio of specific heat at constant pressure to specific heat at constant volume for the gas. For air, $\gamma \approx 1.4$. Maxey et al [4] found that Eq 13 agreed closely with the experimentally observed pressures in the crack-tip region, and the AISI experiments [1,2] also obtained pressures immediately ahead of the running crack tip in good agreement with Eq 13.

This pressure magnitude has been taken as an upstream boundary condition for modeling the gradual pressure decay associated with gas exit through a flaring crack opening [8,9]. Experiments [1] suggest only small circumferential pressure variation at cross sections downstream from the crack tip, so that the pressure in $-R < \xi < \lambda$ may be taken as circumferentially uniform. Parks and Freund [8] critically discussed existing one-dimensional models of gas flow which account for mass and momentum loss from the pipe and change in duct cross-sectional area due to flaring. They also provided a two-dimensional model of gas exit from a widely flaring crack profile (as is observed for ductile pipe materials) which gives an essentially universal relationship for normalized average pressure $p(\xi)/p_0$ in the region downstream from the crack tip. In particular, the pressure decays to about 0.20 p_0 within about two diameters from the crack tip. This decay pattern is consistent with full-scale tests [*1*] and with model experiments [*16–18*].

The results of Ref *8* are not strictly in agreement with a linear pressure decay from p_0 to 0 over some distance λ but, for present purposes, it can be approximated sufficiently well by such a relationship if λ is taken to be about $4a$. Thus an estimate of $p(\xi, \theta)$ is

$$p(\xi, \theta) = \begin{cases} p_0 & -R \leq \xi \leq 0 \\ p_0(1 - \xi/\lambda) & 0 \leq \xi \leq \lambda \end{cases} \tag{14}$$

with p_0 given by Eq 13.

When this field is inserted into Eq 12, along with Eq 1, the driving force work rate is

$$\dot{W}_0 = D\left(\frac{p_0 a}{\sigma_0 h}\right)\left(\frac{h}{a}\right)\left(\frac{\delta_t}{h}\right)\left(1 + \frac{\lambda}{R} + \frac{\lambda^2}{3R^2}\right) \tag{15}$$

The perfect gas idealization which has been used in the models discussed here may not always be an entirely appropriate model for the behavior of hydrocarbon mixtures in natural gas transmission pipelines. The most important such nonideal effect would seem to be that spontaneous condensation into atomized droplets can occur at constant pressure during rapid expansion. One-dimensional solutions of the receding semi-infinite duct problem have been obtained by King [*19*] using a realistic thermodynamic characterization of methane. The main difference between these results and the ideal gas is that in Eq 13, p_0 is a monotone decreasing function of crack velocity. Due to condensation, however, there can exist a velocity range roughly between 180 and 275m/s (within the range of observed ductile crack velocities V) in which crack-tip pressure p_0 remains essentially constant. It is likely that this effect on the velocity dependence of driving force (Eq 12) would tend more to sustain steady growth. King [*19*] has also considered other nonideal gas dynamics aspects of ductile crack propagation in pipelines.

Comparison of Work Rates

For comparison of the relative magnitudes of the various work rates, numerical values of system parameters for two particular tests are considered. Values given in Table 1 are data for Test No. A31(CA4) as reported by Maxey et al [*3*] and Test No. SF-12W as reported by Ives et al [*1*]. For the first case, the values of the dimensionless parameters involved are h/a = 0.0183, $\rho V^2/\sigma_0$ = 1.075, R/a = 0.75, δ_t/h = 0.138, λ/a = 4, and $ap_0/h\sigma_0$ = 0.600. In calculating these parameters, ρ was taken to be 7770 kg/m^3, δ_t

TABLE 1—*Typical system parameters for full-scale tests from sources shown. Crack speed V was taken as the median speed for the process.*

	a, cm	h, cm	σ_0, MPa	p_L, MPa	CVN, J/cm^2	V, m/s
A31(CA4) [3]	46	0.84	484	7.92	56	260
SF-12W [1]	53	0.95	531	6.41	56	244

was computed as the Charpy energy divided by σ_0 without use of a constraint factor, and p_0 was computed from p_L using Eq 13 for $\gamma = 1.3$ with $V/C_L = 260/396$. Likewise, for the second case, the values of the dimensionless parameters are $h/a = 0.0179$, $\rho V^2/\sigma_0 = 0.869$, $R/a = 0.75$, $\delta_t/h = 0.111$, $\lambda/a = 4$, and $ap_0/h\sigma_0 = 0.474$, where p_0 was here computed from p_L using Eq 13 for $\gamma = 1.4$ and $V/C_L = 244/341$.

For purposes of comparison, work rates normalized with respect to D_1, the fracture work rate given in Eq 5, are computed. The results of the calculations are given in Table 2. Several general observations can be made on these results. For example, the rate of work of the gas pressure exceeds each of the individual dissipation rates, as it must if an energy balance is to be strictly enforced. Also, the dissipation due to axial in-plane stretching of the pipe wall is about four times larger than the dissipation of energy in the fracture process and an order of magnitude larger than either the kinetic energy uptake rate by the pipe wall or the dissipation in circumferential bending. Some implications of these observations are made in the concluding section.

Finally, an estimate of the rate of elastic energy release is included. The elastic energy density in the pipe wall material ahead of the crack tip is $(ap_0/h)^2/2E$, where E is Young's modulus, and the elastic energy density far behind the crack tip is essentially zero. Thus the rate of elastic energy release is V times the energy stored per unit length in the pipe wall ahead of the tip, which may conveniently be expressed as

$$F = D\pi\left(\frac{\sigma_0}{E}\right)\left(\frac{ap_0}{h\sigma_0}\right)^2$$

The ratio F/D_1 is also given in Table 2.

TABLE 2—*Comparison of work rates for the data in Table 1, normalized with respect to the fracture work rate* D_1.

	D_2/D_1	D_3/D_1	D_4/D_1	$\dot{W}_0/D_1$	F/D_1
A31(CA4)	0.264	4.39	0.184	9.49	1.05
SF-12W	0.168	4.39	0.180	7.50	0.912

The material volume for which the energy measures are being computed is that part of the pipe instantaneously between the cross sections at $\xi = -R$ and $\xi = \lambda$. Thus, in an overall energy balance for this volume, the rate of work of the tractions at $\xi = -R, \lambda$ arising from the internal stresses must be included. Because the pipe material at these sections is not being strained, except for circumferential bending at $\xi = \lambda$, the internal stresses cannot be determined from the deformation field (Eqs 1, 2, and 3). At $\xi = -R$ all particles have zero velocity and rotation rate and, therefore, the work rate of the tractions at this section is zero. At $\xi = \lambda$, the particle velocities and rotation rates which are work-rate conjugate to the stress resultants are not zero, and within the framework of the present discussion are given by suitable derivatives of the displacements (Eqs 1, 2, and 3). Because all of the applied loads have been reduced to zero at the section $\xi = \lambda$ and remain zero beyond, it is anticipated that the rate of work of the tractions will be small at $\xi = \lambda$, with the exception of the in-plane axial traction. The reason for this exception is that, if the pipe wall is to begin decelerating and ultimately come to rest at some point far behind the crack tip, then the wall must experience some reversed axial in-plane straining to accommodate the deceleration. If the reversed straining is simply reversed plastic flow, then the axial in-plane stress at $\xi = \lambda$ is at (or near to) σ_0 for $|\theta| < \pi/2$ and $-\sigma_0$ elsewhere on the section, and the work rate of this traction is

$$\begin{aligned} \dot{W}_1 &= -\int_{-\pi}^{\pi} \sigma_0 h |\dot{u}(\lambda, \theta)| a d\theta \\ &= -D \frac{\pi^2}{4} \left(\frac{a}{R}\right)^2 \left(\frac{h}{a}\right) \left(\frac{\delta_t}{h}\right) \end{aligned}$$

where the minus sign reflects the fact that the traction is opposed to the velocity and tends to decelerate the walls. The result that $-\dot{W}_1 = D_3$ reflects the fact that, in order to bring the outward acceleration of the walls to zero, the reversed axial plastic straining must exactly cancel the previous axial plastic straining which took place near the crack tip. To result in a deceleration in the outward motion of the wall, $-\dot{W}_1$ should be larger than D_3. However, the deceleration appears to be very small in magnitude compared with the rapid acceleration in the crack-tip region, and the anticipated slight difference between $-\dot{W}_1$ and D_3 is ignored. Finally, evidence of the reversed axial straining just mentioned is apparent in photographs of fractured pipe in Fig. 4 of Ref *6*, in Fig. 4 of Ref *15*, and in Fig. 3 of Ref *20*, which show a wavy or scalloped pipe wall adjacent to the fracture path after crack propagation. The waviness arises from the fact that the reversed deformation is not entirely accommodated by reversed in-plane plastic strain, but also by buckling under in-plane compressive stress of the previously stretched wall material. Furthermore, it is interesting to note that if all of the reversed axial straining is accommodated by buckling, then an estimate of the prior plastic stretching can be made from observation of the amplitude and the wavelength of the waves in the pipe wall after crack propagation. For example, an amplitude-to-wavelength ratio along the fracture path of 1:10 implies an incompatible plastic stretch of about 2 percent.

The Effect of Backfill

When gas transmission pipelines are buried in soil, the presence of the backfill material affects the propagation of ductile fracture. From Fig. 3 of Ref *20*, it can be seen that a pipe which was initially buried at some depth below the surface is apparently resting at the bottom of a V-shaped trench after the crack has propagated past. This indicates that the soil above and on either side of the pipe acquired considerable kinetic energy as the crack tip passed. This kinetic energy uptake, especially for the soil on the *sides* of the pipe, must be accounted for because part of the work rate of the pressure on the pipe walls (Eq 12) is transferred through the wall directly into deforming the soil. Furthermore, the resistance of the soil material to plastic deformation must also be included, although the rather small shear strength of dry, cohesionless granular media under the low confining pressures near a free surface would seem to render the magnitude of the plastic dissipation of the soil much smaller than its kinetic energy uptake, as will be shown. Finally, the possible effects of backfill on gas escape and resulting pressure distribution and hence driving force will be noted.

Resistance Effects: The Rectangular Trench Model

The resistance to steady crack propagation due to backfill can be evaluated by integrating the work of the "back pressure" tractions on the *exterior* of the deforming pipe wall. If the soil/pipe wall friction is assumed small, then the effective back pressure of the soil is a normal, inward-directed traction distribution $p_s(\xi, \theta)$ and the total energy absorption of the soil due to uptake of kinetic energy and plastic dissipation is

$$D_5 = \int_{-R}^{\lambda} d\xi \int_{-\pi}^{\pi} p_s(\xi, \theta)\dot{w}(\xi)d\theta \qquad (15)$$

where $\dot{w}$ is obtained from Eq 1. For the present, rather than carrying out the calculations implied in Eq 15 for detailed kinematical models of backfill deformations, we choose to examine the simplified model shown in Fig. 2. In this idealization the pipe is taken to rest in a rectangular trench of depth H, a parameter intended mainly to account for the depth of burial of the pipe.

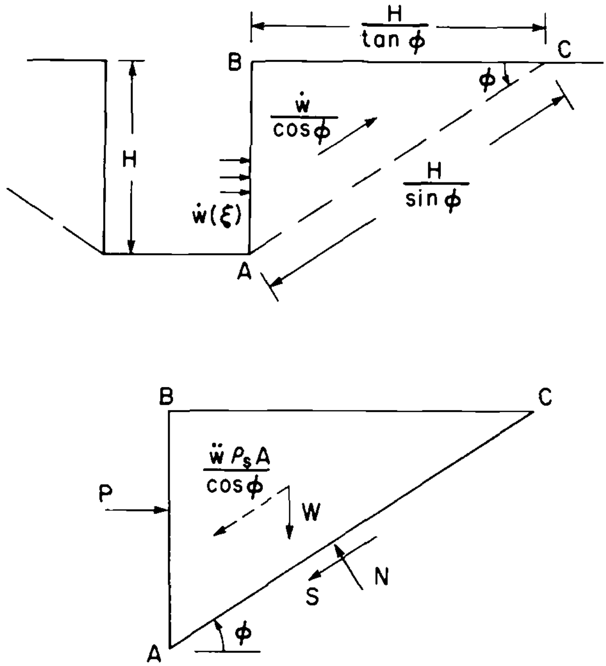

FIG. 2—*Rectangular trench model for calculation of backfill resistance to pipe wall deformation.*

At a given ξ location along the pipe, the vertical boundaries are subject to a uniform velocity normal to themselves equalling the local radial velocity of pipe wall at that section, $\dot{w}(\xi)$ from Eq 1. The triangular block of soil ABC slides as a rigid body along a straight slipline at an angle ϕ from the horizontal. Thus, the velocity of the block along slipline AC is $\dot{w}/\cos\phi$. This model can be treated in the spirit of Coulomb's analysis of the stability of soil masses by equilibrating the resultant forces, including, by D'Alembert's principle, the body forces due to acceleration, acting on the triangular block. The free-body diagram for this is shown in Fig. 2, where the force P is meant to characterize the total force per unit length applied to one half of the soil by the pipe wall, so that the numerical value of Eq 15 is given by

$$D_5 = \int_{-R}^{\lambda} 2P(\xi)\dot{w}(\xi)d\xi \tag{16}$$

It remains to calculate P at a given cross section in terms of N and S, the resultant normal and shear tractions acting across the slipline, and the body forces due to gravity and acceleration of the soil, $W = Ag\rho_s$ and $\ddot{w}\rho_s A/\cos\phi$, respectively. Here ρ_s is the mass density of the backfill, g the acceleration of gravity, and $A = \frac{1}{2}H^2/\tan\phi$ the area of the triangle ABC. Dynamic equilibrium in the N and S directions, respectively, gives

$$N = P\sin\phi + W\cos\phi \tag{17a}$$

$$S = P\cos\phi - W\sin\phi - \frac{\rho_s A\ddot{w}}{\cos\phi} \tag{17b}$$

Now, for frictional cohesionless materials, the linear Mohr-Coulomb condition for localized deformation along a band is that the normal and shear forces acting on the band be proportional, that is, $S = fN = \tan\omega N$ where f is the friction coefficient of the interface and is equal to the tangent of ω, the angle of the Mohr-Coulomb yield surface. By incorporating this relationship into Eq 17, one can obtain P as

$$P = \frac{\rho_s H^2}{2\sin\phi}\frac{[\ddot{w} + g\cos\phi(\sin\phi + f\cos\phi)]}{[\cos\phi - f\sin\phi]} \tag{18}$$

It is now worth comparing the relative sizes of the two bracketed terms in the numerator. For dry sand, $f \approx 1/2$ and the second term is therefore roughly of size g. The first term is equal to $V^2\delta_t/\pi R^2$; values for the parameters V, δ_t, and R must be chosen for comparison. As was noted earlier, the plastic zone size R is typically equal to the pipe radius, a. For toughness, let $\delta_t \simeq h/3$. Then, for thin-wall pipe geometries with $h/a = 1/50$, and for large-diameter gas transmission pipe radii of $a = 61$ cm, we find that $\ddot{w} = g$ when $V \approx 54$ m/s. However, typical crack velocities observed in backfilled tests are usually three to five times this large. Consequently, because of the V^2 term in $\ddot{w}$, it can be expected that at actual crack velocities the term $\ddot{w}$ is much larger than $g\cos\phi(\sin\phi + f\cos\phi)$. By neglecting the latter term, then, with $P \approx \ddot{w}\rho_s H^2/2\sin\phi(\cos\phi - f\sin\phi)$, we can minimize the resistance force P with respect to slipline inclination ϕ to obtain $\phi_{\text{optimal}} = (\pi/4) - (\omega/2)$ or, equivalently, $f = \cot 2\phi$. Finally, this optimal ϕ-value can be substituted into the relationship for P, which can be simplified to give

$$P = \frac{\rho_s H^2 V^2 \delta_t}{\tan\phi\pi R^2} \tag{19}$$

When this is substituted into Eq 16, there results

$$D_5 = D\frac{1}{\pi^2\tan\phi}\left(\frac{V^2\rho_s}{\sigma_0}\right)\left(\frac{\delta_t}{h}\right)^2\left(1 + \frac{\lambda}{R}\right)^2\left(\frac{h}{a}\right)\left(\frac{H}{a}\right)^2\left(\frac{a}{R}\right)^2 \tag{20}$$

This treatment has ignored the shearing of the backfill due to nonuniform deformation along the pipe axis. This would, in general, provide an additional resistance term from the backfill of the form

$$D_6 = D\left(\frac{\tau_s}{\sigma_0}\right)\left(\frac{\delta_t}{h}\right)\frac{1}{\pi \tan \phi}\left(\frac{H^2}{a^2}\right)\frac{\dot{a}}{R}\left(1 + \frac{\lambda}{R}\right)$$

where τ_s is a representative shear strength of the unconfined backfill near the free surface. An estimate for the strength of a dry cohesionless sand backfill might be, say, half of the average overburden stress, $\tau_s \approx \frac{1}{2}H\rho_s g$. With this estimate it is seen that D_5 is considerably greater than D_6 for reasonable velocities V, if the trench depth parameter H is taken to be of order 1 m. Because of the smallness of the D_6 term, it will be neglected subsequently.

With D_5 calculated, we can, if desired, compare the relative magnitudes of the energy uptake of the backfill due to kinetic energy uptake and due to the plastic deformation along the shear band AB. The kinetic energy uptake is the more important term at observed crack velocities.

The only new parameter is this trench model of backfill deformation is the trench depth H. As was noted before, H is meant to characterize backfill depth. Common practice for large-diameter linepipe is to place 76 cm of sand over the pipe. Consequently, it would seem reasonable in such situations to choose a value for H of about $76 + 2a$ cm. (Recall the original V-shaped trench of Ref *20* which motivated the model; H should be roughly the burial depth of the bottom of the pipe.)

In unpublished work by the authors and V. C. F. Li, this simple model of backfill kinematics has been supplemented by more realistic two-dimensional slipline fields of circular cylinders expanding in the neighborhood of a free surface, taking the soil to be incompressible. In every case, we find that the kinetic energy uptake of the soil dominates plastic dissipation for observed crack speeds. Furthermore, all of the alternative kinematic fields seem to give similar energy uptake rates for reasonable values of the parameters. The latter is likely true because in each model roughly equivalent masses are accelerated by essentially the same amount.

This modeling of backfill resistance contributions is mainly directed at the case of dry sand backfill. Additional factors which would modify the conclusions drawn could include the presence of pore fluid in the soil. Clearly, saturated material would have a higher effective mass density, but the rapid soil deformation (as compared with pore fluid diffusion times) would also result in undrained backfill behavior, and higher strength. Also, in possible cold-climate applications, frozen backfill would have a significantly larger strength contribution, and the backfill itself might be more likely to "fracture" rather than to flow.

Discussion and Conclusions

According to the present model calculations, the main resistance to the gas pressure on the pipe wall during ductile crack propagation without backfill is the resistance of the wall material to in-plane axial stretching. For the assumed deformation field, this contribution is four times larger than the fracture energy and an order of magnitude larger than the other computed contributions. It is quite possible that the resistance of the pipe wall to axial stretching has been overestimated through the various approximations which have been made. The effect is so large, however, that it must be concluded that axial pipe wall stretching must be taken into account in the development of theoretical models of the process.

The fracture resistance of the material, as measured by δ_t, enters the energy balance in an indirect way. All terms are proportional to δ_t except the kinetic energy rate, which is proportional to $(\delta_t)^2$. Thus, the relative magnitudes of the dominant terms, namely, the rate of work of the gas and the rate of plastic dissipation in axial stretching, are not influenced by changes in δ_t. On the other hand, the ratio of the kinetic energy rate to the driving force rate is proportional to $\delta_t V^2$, so that a modest variation in δ_t for fixed driving force could lead to significant variations in V, or a small change in driving force at fixed δ_t could also lead to significant variations in V, and so on. This observation is qualitatively consistent with the results of full-scale tests on pipe without backfill where large variations in crack-tip propagation speed were found within test sections of uniform fracture resistance or Charpy energy. Conversely, because of this sensitivity of V to slight variations in system parameters, simple models of the type being considered here cannot be expected to lead to crack speed predictions which are always close to measured values.

As was stated in the preceding, the crack is assumed to propagate with a fixed value of crack-tip opening displacement δ_t in this analysis, and the actual value of δ_t was taken to be the Charpy energy per unit area of the specimen ligament divided by the yield stress of the wall material. This estimate could be doubled through an alternative interpretation of the Charpy energy. In the case of Charpy tests above the transition temperature for pipeline steels, large plastic displacement normally precedes crack extension. The net Charpy energy CVN then includes mainly the energy dissipated up to extension of the crack, and the value of the fracture-characterizing parameter J at the onset of crack extension is essentially $2 \times CVN \div A$ where A is the specimen ligament area [*21*]. On the other hand, the near crack-tip value of the same parameter J is $\sigma_0 \delta_t$ where, as before, the influence of lateral constraint is ignored. Thus, assuming monotonic proportional loading and invoking the path-independence of J as expressed through its well-known representation as a line integral around the crack tip, the two expressions for J are equated to yield $\delta_t = 2 \times CVN \div (\sigma_0 A)$. Although the kinetic energy rate term in Table 2 is doubled through this alternative interpretation of δ_t, the main conclusions of the analysis are unaffected.

In the calculation of the fracture energy rate D_1 it was assumed that the strength of the wall material was given by the yield stress σ_0 from the onset of flow up to shear separation. The pipeline steels used in the AISI program [1] did show some strain-hardening, and perhaps it would be more appropriate to use the ultimate tensile strength rather than σ_0 in calculating the fracture energy. If this is done, however, it has no effect on the relative magnitudes of the terms in Table 2. It is also noted that reasonable variations of R/a, for which no direct measurements are available, and σ_0, which might vary with V to account for rate sensitivity of the flow stress, have little influence on the relative magnitudes of the terms in Table 2.

The elastic energy release rate F appearing in Table 2 was calculated under the assumption that elastic energy was stored in the pipe wall ahead of the crack tip as hoop strain due to the pressure p_0. The pressure p_0 was used for this calculation rather than the line pressure p_L because the pipe wall elastic energy release associated with reduction of the pressure from p_L to p_0 goes into accelerating the gas, and the driving force of the gas is subsequently taken into account explicitly. Only the elastic energy due to the pressure p_0 is available in the pipewall near the crack tip to drive the fracture process. In view of the extensive plastic flow which occurs during this crack propagation process, the relative magnitude of the elastic energy release rate is surprisingly large, and this result suggests that perhaps elasticity effects should be included in attempts at developing more refined models.

The various energy rate estimates in Table 2 were computed for the pipe material instantaneously between the leading edge of the plastic zone and the section at which the pressure on the pipe wall has decayed to zero, that is, in the interval $-R < \xi < \lambda$. At the section $\xi = \lambda$ the pipe wall still has kinetic energy due to its outward motion, and it appears that this kinetic energy is dissipated through plastic circumferential bending in $\xi > \lambda$. For $\xi > \lambda$, the pipe wall is decelerating, and the kinetic energy rate and circumferential bending dissipation rate have opposite sign.

Finally, it is noted from Eq 20 that the resistance provided by backfill increases as the depth of burial, reflected in H, becomes large. Consequently one may speculate that if pipe were buried sufficiently deeply, the energy required to deform the backfill would become so large that a long-running steady fracture of the type modeled could not be sustained. However, the presence of the backfill also retards the escape of gas from the running fracture, with the result that the local pressure decay distance λ will be increased. The resulting increase in the driving force $\dot{W}_0$ could conceivably offset the increasing resistance terms D_5, thus sustaining crack growth at increased burial depths. Until suitable models for the mechanics of gas escape through a surrounding granular backfill material are developed, the question of dominance of the increase in resistance of driving force with increasing burial depth would seem to remain open.

It is interesting, however, to note the results of calculations which were made using the equation of motion derived in Ref 7, including the effects of pipe wall and backfill inertia. The pressure decay was again taken to be linear over some (to-be-determined) distance λ. It was found that, in this gas dynamics-uncoupled model, for a material toughness given by δ_t, there was a maximum attainable velocity of crack propagation. For any velocity less than this values, a solution could be obtained for some λ-value. This uncoupled calculation reveals that the *required* pressure decay length necessary to drive the assumed crack propagation in this backfilled condition is of the order 7 to $8a$. This required decay length is somewhat greater than the apparently maximum obtainable decay length of roughly $4a$ both predicted and observed in the no-backfill case. Presumably the presence of backfill material then does inhibit gas escape, resulting in longer pressure decay profiles. Of course, the actual pressure decay profile need not be linear, and must be determined from experiments and a coupled gas dynamics/solid mechanics analysis. We conclude that the topic of backfill effects on gas escape would seem to merit further examination both experimentally and in the formulation of models of the processes.

Acknowledgment

This work was supported in part by a grant from the National Science Foundation (NSF), Solid Mechanics Program, to Brown University.

Some of the calculations on soil backfill were carried out by Mr. Victor Li as part of the NSF-sponsored 1976 summer Undergraduate Research Participation Program at Yale University. Participation in the program was made possible through a grant from the AISI Committee of Large Diameter Line Pipe Producers.

Finally, we are grateful to A. K. Shoemaker, U. S. Steel Research Laboratories, and J. E. Hood, The Steel Company of Canada, for helpful discussions on portions of this work.

References

[1] Ives, K. D. Shoemaker, A. K., and McCartney, R. F., *Journal of Engineering Materials and Technology*, Vol. 96, 1974, pp. 309-317.

[2] Shoemaker, A. K. and McCartney, R. F., *Journal of Engineering Materials and Technology*, Vol. 96, 1974, pp. 318-322.

[3] Maxey, W. A., Kiefner, J. F., Eiber, R. J., and Duffy, A. R. in *Proceedings*, 12th World Gas Conference, International Gas Union, Nice, France, 1973.

[4] Maxey, W. A., Kiefner, J. F., Eiber, R. J., and Duffy, A. R. in *Fracture Toughness, ASTM STP 514*, American Society for Testing and Materials, 1972, pp. 70-81.

[*5*] Poynton, W. A. and Fearnehough, G. D. in *Dynamic Crack Propagation*, G. C. Sih, Ed., Noordhoff, 1974, pp. 183-196.

[*6*] Poynton, W. A., Shannon, R. W. E., and Fearnehough, G. D., *Journal of Engineering Materials and Technology*, Vol. 96, 1974, pp. 323-329.

[*7*] Freund, L. B., Parks, D. M., and Rice, J. R. in *Mechanics of Crack Growth, ASTM STP 590*, American Society for Testing and Materials, 1976, pp. 243-262.

[*8*] Parks, D. M. and Freund, L. B., *Journal of Pressure Vessel Technology*, Vol. 100, 1978, pp. 13-17.

[*9*] Kanninen, M. F., Sampath, S. G., and Popelar, C., *Journal of Pressure Vessel Technology*, Vol. 98, 1976, pp. 56-65.

[*10*] Popelar, C., Rosenfield, A. R., and Kanninen, M. F., Vol. 99, 1977, pp. 112-121.

[*11*] Hahn, G. T., Sarrate, M., Kanninen, M. F., and Rosenfield, A. R., *International Journal of Fracture*, Vol. 9, 1973, pp. 209-222.

[*12*] Emery, A. F., Love, W. J., and Kobayashi, A. S. in *Fast Fracture and Crack Arrest, ASTM STP 627*, American Society for Testing and Materials, 1977, pp. 143-158.

[*13*] Owen, D. R. J. and Shantaram, D., *International Journal of Fracture*, Vol. 13, 1977, pp. 821-837.

[*14*] Freund, L. B., Li, V. C. F., and Parks, D. M., *Journal of Pressure Vessel Technology*, Vol. 101, 1979, pp. 51-58.

[*15*] Shoemaker, A. K., McCartney, R. F., and Ives, K. D., "Mechanical Crack-Arrester Concepts for Line-Pipe Applications," presented at the Conference on Materials Engineering in the Arctic, St. Jovite, Que., Canada, 1976.

[*16*] Alder, G. M., "The Flow Through a Propagating Shear Fracture in a High Pressure Gas Main," University of Edinburgh, Department of Mechanical Engineering Report, Edinburgh, U.K., Aug. 1972.

[*17*] Alder, G. M., "The Pressure Loading on the Walls of a Propagating Shear Fracture in a High Pressure Gas Main," University of Edinburgh, Department of Mechanical Engineering Report, Edinburgh, U.K., Sept. 1973.

[*18*] Alder, G. M., "Gas Discharge Through Propagating Ductile Fractures in High Pressure Pipelines," University of Edinburgh, Department of Mechanical Engineering Report, Edinburgh, U.K., May 1974.

[*19*] King, G. G., "Decompression of Gas Pipelines During Longitudinal Ductile Fractures," presented at American Society of Mechanical Engineers, Energy Technology Conference, Houston, Tex., 1978.

[*20*] Eiber, R. J. and Maxey, W. A., "Full-Scale Experimental Investigation of Ductile Fracture Behavior in Simulated Arctic Pipeline," presented at the Conference on Materials Engineering in the Arctic, St. Jovite, Que., Canada, 1976.

[*21*] Rice, J. R., Paris, P. C., and Merkle, J. G. in *Progress in Flaw Growth and Fracture Toughness Testing, ASTM STP 536*, American Society for Testing and Materials, 1973, pp. 231-245.

A. F. Emery,[1] *A. S. Kobayashi,*[1] *W. J. Love,*[1]
and P. K. Neighbors[2]

An Analysis of the Dynamic Propagation of Elastic and Elastic-Plastic Circumferential Cracks in Pressurized Pipes

REFERENCE: Emery, A. F., Kobayashi, A. S., Love, W. J., and Neighbors, P. K., "**An Analysis of the Dynamic Propagation of Elastic and Elastic-Plastic Circumferential Cracks in Pressurized Pipes,**" *Crack Arrest Methodology and Applications, ASTM STP 711,* G. T. Hahn and M. F. Kanninen, Eds., American Society for Testing and Materials, 1980, pp. 379-391.

ABSTRACT: The dynamic motion of a circumferential through-crack in an axially stressed pipe was examined with a finite-difference shell code to determine the crack opening shapes and speed of extension of elastic-plastic crack propagation. Calculations were also performed with an additional hoop stress to examine the effect of earlier plastic deformation due to a biaxial stress state.

The results were compared with those obtained for elastic propagation of the circumferential crack and those obtained in a study of pressure-driven axially oriented cracks. As previously noted, in the study of the elastic fracture, the crack characteristics are primarily functions of the ratio of the dynamic crack intensity factor developed for a crack of fixed length to the crack initiation stress-intensity factor, K_{IQ}. Elastic-plastic circumferential cracks propagate slower than their elastic counterparts but substantially faster than comparably loaded axial cracks. Although slower moving, the crack openings are much larger. No effect of shell thickness was noted, and no edge flaps were found to exist.

KEY WORDS: crack propagation, pipes, fracture properties, stresses, strains, plastic deformations

Nomenclature

a Radius of shell
C_2 Elastic shear wave velocity

[1] Professors of mechanical engineering, University of Washington, Seattle, Wash. 98195.
[2] Staff member, Sandia Laboratories, Livermore, Calif. 94550.

h	Half thickness of shell
K_I	Plane-strain Mode I stress-intensity factor
K_{Ic}	Plane-strain Mode I critical static stress-intensity factor
K_{max}	Maximum dynamic stress-intensity factors observed for fixed-length cracks
K_{IQ}	Mode I crack initiation stress-intensity factor
M	Moment resultants
N	Force resultants
Q	Shear resultants
r	Radius
S_{ij}	Stresses
t	Time
T	Surface loads
u	Axial displacement
v	Circumferential displacement
w	Radial displacement
x	Axial coordinate
z	Radial coordinate
α	Axial rotation
β	Circumferential rotation
Δ	Increment
θ	Angular coordinate
ρ	Density
δ	Half central crack opening

Piping system components are designed to meet a number of criteria, among which is the loss of fluid postulated to be caused by a rupture of the piping system. The worst case is presumed to occur when the piping fractures instantaneously by propagation of a circumferential through-crack which, upon severance of the pipe, permits the fluid to escape and to propagate fluid pressure waves throughout the piping.

Although the crack cannot circumscribe the pipe instantly, the propagation, for design purposes, is assumed to occur in zero time. Emery et al [*1*][3] have analyzed the behavior of an elastic circumferential crack, propagating in an axially stressed pipe, to determine its opening shape and speed for a range of initial stresses and crack initiation stress-intensity factors. These results were compared with those obtained in the studies of comparably stressed axial through-cracks. No hoop stresses due to internal pressurization were considered because of the linear nature of the problem and the absence of crack edge flaps, which are the only components of the pipe strongly affected by the fluid pressure forces. Fluid leakage was also estimated to be small because of the small crack openings and because no flaps were ob-

[3]The italic numbers in brackets refer to the list of references appended to this paper.

served to exist. Previous studies [*1-5*] of axially oriented cracks had demonstrated that such flaps were of prime importance in affecting the motion of the crack. However, their absence suggested that the pressure forces, which cause crack propagation and which created the flaps in the axial case, but which do not, in themselves, cause circumferential crack growth, are of little importance in the latter case.

On the other hand, the pressure-generated hoop stresses do affect yielding and thus are of importance in the examination of elastic-plastic crack propagation.

A more complete analysis of this biaxial state of stress would require that the structure-fluid interaction be considered in the manner that the axial crack has been studied by Kanninen [*2*], Freund [*3*] and Emery [*4,5*]. These studies have indicated the conditions under which the fluid pressure calculations may be decoupled from the structural calculations.

In this paper we examine the behavior of a propagating elastic-plastic circumferential through-crack. Pipes with axial stresses only and with both axial stresses and internal pressure are considered. The elastic-plastic crack behavior is compared with that of a comparable elastic circumferential crack and axial crack growth. Both small and large deflections are considered. Fluid-structure interactions are not considered because of the small crack openings encountered.

Structural Analysis

Consider a cylindrical shell of thickness $2h$ and midsurface radius a as shown in Fig. 1, where u and v are the midsurface deflections in the x and θ directions, respectively, w is the radial deflection, and α and β are the rotations of lines, originally perpendicular to the midsurface, in the x and θ direc-

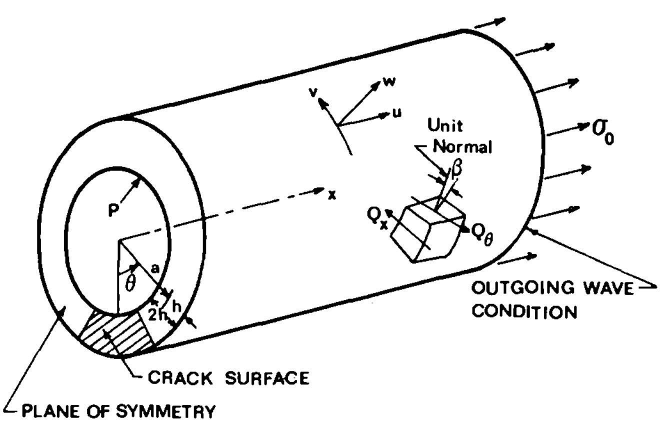

FIG. 1—*Fracturing cylindrical shell.*

tions. The dynamic equations of motion with the assumption of plane sections remaining plane, and of small strains but large deflections, are

$$A\ddot{u} + B\ddot{\alpha} = a\frac{\partial \overline{N}_{xx}}{\partial x} + \frac{\partial \overline{N}_{\theta x}}{\partial \theta} + a\,\overline{T}_x{}^N \tag{1a}$$

$$B\ddot{u} + C\ddot{\alpha} = a\frac{\partial \overline{M}_{xx}}{\partial x} + \frac{\partial \overline{M}_{\theta x}}{\partial \theta} + ah\,\overline{T}_x{}^M - a\overline{Q}_x \tag{1b}$$

$$\left(A + \frac{B}{a}\right)\ddot{v} + B\ddot{\beta} = a\frac{\partial \overline{N}_{x\theta}}{\partial x} + \frac{\partial \overline{N}_{\theta\theta}}{\partial \theta} + a\,\overline{T}_\theta{}^N + \overline{Q}_\theta \tag{2a}$$

$$\left(B + \frac{C}{a}\right)\ddot{v} + C\ddot{\beta} = a\frac{\partial \overline{M}_{xx}}{\partial x} + \frac{\partial \overline{M}_{\theta\theta}}{\partial \theta} + a\,\overline{T}_\theta{}^M - a\,\overline{Q}_\theta \tag{2b}$$

$$A\ddot{w} = a\frac{\partial \overline{Q}_x}{\partial x} + \frac{\partial \overline{Q}_\theta}{\partial \theta} - \overline{N}_{\theta\theta} + a\,\overline{T}_z \tag{3}$$

where

$$[A,B,C] = \int_{-h}^{h} \rho r\,[1,z,z^2]\,dz \tag{4}$$

The force and moment resultants, $\overline{N}$, $\overline{M}$, and $\overline{Q}$, and the surface tractions $\overline{T}$ for large deflections are defined in terms of those for small deflections N, M, Q, and T by

$$\begin{bmatrix}\overline{N}_{xx}, & \overline{N}_{\theta x}\\ \overline{M}_{xx}, & \overline{M}_{\theta x}\end{bmatrix} = \left(1 + \frac{\partial u}{\partial x}\right)\begin{bmatrix}N_{xx}, & N_{\theta x}\\ M_{xx}, & M_{\theta x}\end{bmatrix} + \frac{1}{a}\frac{\partial u}{\partial \theta}\begin{bmatrix}N_{x\theta}, & N_{\theta\theta}\\ M_{x\theta}, & M_{\theta\theta}\end{bmatrix} + \alpha\begin{bmatrix}Q_x, & Q_x\\ 0, & 0\end{bmatrix} \tag{5a}$$

$$\begin{bmatrix}\overline{N}_{x\theta} & \overline{N}_{\theta\theta}\\ \overline{M}_{x\theta} & \overline{M}_{\theta\theta}\end{bmatrix} = \frac{\partial v}{\partial x}\begin{bmatrix}N_{xx}, & N_{\theta x}\\ M_{xx}, & M_{\theta x}\end{bmatrix} + \left(1 + \frac{1}{a}\frac{\partial v}{\partial \theta} + \frac{\partial w}{\partial a}\right)\begin{bmatrix}N_{x\theta}, & N_{\theta\theta}\\ M_{x\theta}, & M_{\theta\theta}\end{bmatrix} + \alpha\begin{bmatrix}Q_\theta, & Q_\theta\\ 0, & 0\end{bmatrix} \tag{5b}$$

$$[\overline{Q}_x, \overline{Q}_\theta] = \frac{\partial w}{\partial x}[N_{xx}, N_{\theta x}] + \left(\frac{1}{a}\frac{\partial w}{\partial \theta} - \frac{v}{a}\right)[N_{x\theta}, N_{\theta\theta}] + [Q_x, Q_\theta] \tag{5c}$$

$$\begin{bmatrix}\overline{T}_x{}^N\\ \overline{T}_x{}^M\end{bmatrix} = \alpha\begin{bmatrix}p\\ p\end{bmatrix} - \frac{1}{h}\begin{bmatrix}0\\ \dfrac{\partial u}{\partial x}Q_x + \dfrac{1}{a}\dfrac{\partial u}{\partial \theta}Q_\theta + \dfrac{\partial w}{\partial x}N_{xx} + \left(\dfrac{1}{a}\dfrac{\partial w}{\partial \theta} - \dfrac{v}{a}\right)N_{x\theta}\end{bmatrix} \tag{6a}$$

$$\begin{bmatrix}\overline{T}_\theta{}^N\\ \overline{T}_\theta{}^M\end{bmatrix} = \beta\begin{bmatrix}p\\ p\end{bmatrix} + \frac{1}{h}\begin{bmatrix}0\\ -\dfrac{\partial v}{\partial x}Q_x - \left(\dfrac{1}{a}\dfrac{\partial v}{\partial \theta} + \dfrac{w}{a}\right)Q_\theta + \dfrac{\partial w}{\partial x}\left(N_{\theta x} + \dfrac{M_{\theta x}}{a}\right)\end{bmatrix} + \begin{bmatrix}0\\ \dfrac{1}{h}\left(\dfrac{1}{a}\dfrac{\partial w}{\partial \theta} - \dfrac{v}{a}\right)\left(N_{\theta\theta} + \dfrac{M_{\theta\theta}}{a}\right)\end{bmatrix} \tag{6b}$$

$$\overline{T}_z = p \tag{6c}$$

where

$$\begin{bmatrix}N_{xx}, & N_{x\theta}\\ M_{xx}, & M_{x\theta}\end{bmatrix} = \frac{1}{a}\int_{-h}^{h} r\begin{bmatrix}S_{xx}, & S_{x\theta}\\ zS_{xx}, & zS_{x\theta}\end{bmatrix}dz \tag{7a}$$

$$\begin{bmatrix}N_{\theta x} & N_{\theta\theta}\\ M_{\theta x} & M_{\theta\theta}\end{bmatrix} = \int_{-h}^{h}\begin{bmatrix}S_{\theta x}, & S_{\theta\theta}\\ zS_{\theta x}, & zS_{\theta\theta}\end{bmatrix}dz \tag{7b}$$

$$Q_x = \frac{1}{a}\int_{-h}^{h} r\,S_{xz}\,dz \qquad Q_\theta = \int_{-h}^{h} S_{\theta z}\,dz \tag{7c}$$

where S's represent the Piola-Kirchoff stresses, which are related to the strains by the Hookean linear elastic relationships [*6*] with the necessary adjustments to ensure the correct shear wave velocities [*7*]. The stresses during elastic-plastic deformations are computed by using the von Mises yield condition and incremental plastic strain theory. In performing the elastic-plastic calculations, it is usual to use several iterations for each loading step to ensure that the final state lies on the yield surface and is in agreement with the flow rule. Because the calculations, using large deflection theory, are very time-consuming and because no dynamic plastic effects were included, no iterations were made. Instead, it was assumed that any small error generated during one time step would be compensated for during the next time step. Although this is not generally true for arbitrary time steps, the time increments used herein were one-fifth to one-tenth the normal size, and comparisons made with dynamic finite-element codes showed the assumption to be satisfactory [*8*].

Finite-Difference Algorithm

The pipe was modeled by a thin shell subdivided into a series of mesh points and uniform spatial regions by the mesh illustrated in Fig. 2. The force and moment resultants were defined at the edges of each element as shown, and the displacements and rotations were specified at the element center. An explicit finite-difference algorithm was used to solve for the displacements and rotations at time $t + \Delta t$ in terms of values at time t and $t - \Delta t$ in the form

$$\Delta w(t + \Delta t) - 2\Delta w(t) + \Delta w(t - \Delta t) = F(t) \tag{8}$$

where $F(t)$ represents the right-hand side of Eq 3. The time step was restricted by

$$C_0 \Delta t < 2h \tag{9}$$

which is $2h/a\Delta\theta$ or $2h/\Delta x$ smaller than the usual value used in shell computations. Larger values of Δt require an implicit solution plus an iteration for the plastic deformation.

Dynamic Fracture of a Steel Pipe

A steel cylindrical shell with an internal radius of $a = 0.076$ m (3 in.) and wall thicknesses of $h/a = 1/120$, $1/60$, $1/30$, and $1/15$ was divided into a finite-difference mesh of $\Delta\theta = 9$ deg and $x/a\Delta\theta = 1/2$. The shell was taken to be three radii long with an outgoing wave condition applied at the end at which the axial stress was applied. The material was A533B steel with a modulus of 1.97×10^5 MPa (28.8×10^6 lb/in.^{2}), a Poisson's ratio of 0.28, and a yield stress of 505 MPa (74 000 lb/in.^{2}). The fracture toughness was assumed to be $K_{\mathrm{Ic}} = 65.4$ MPa $\sqrt{\mathrm{m}}$ (60 ksi $\sqrt{\mathrm{in.}}$). Weiss's [*9*] notch-strength theory of ductile static fracture for mildly ductile material was extended to the dynamic fracture without modification. (Tough ductile materials should be handled by the net section yielding method of Ref *10*.) This criterion states that fracture occurs when the dynamic axial strain, ϵ_{xx}, at a distance of $r_p = K_{\mathrm{Ic}}^2/2\pi\sigma_{\mathrm{ys}}^2$ ahead of the moving crack tip, is equal to the yield strain of the material. For these calculations, the yield strain was assumed to be $\epsilon_{ys} = 0.002569$, which was prescribed at a distance of $r_p =$ 2.67 mm (0.1053 in.) ahead of the crack tip. The elastic and elastic-plastic crack extensions occur when the stress resultant N_{xx} or the axial strain ϵ_{xx} satisfies the respective criterion of

$$N_{xx} = \frac{K_{\mathrm{I}} 2h}{\sqrt{2\pi a \Delta\theta/2}}, \; \epsilon_{xx} = \frac{\epsilon_{ys}}{a\Delta\theta/2} \frac{K_{\mathrm{I}}^2}{2\pi\sigma_{ys}^2} \tag{10}$$

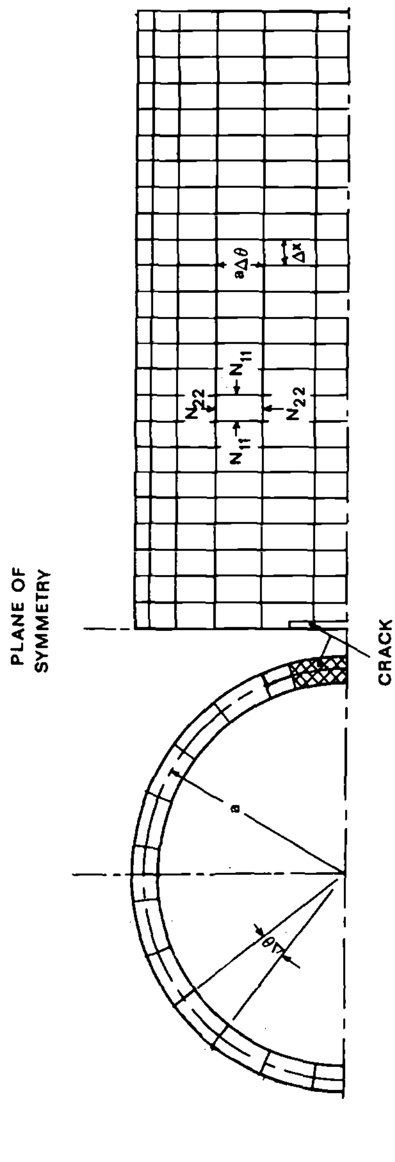

FIG. 2—*Finite-difference mesh for the circumferential crack.*

Both N_{xx} and ϵ_{xx} are evaluated at a point, called the critical point, one-half mesh distance, $a\Delta\theta/2$, ahead of the crack tip. Care must be taken in establishing the mesh to ensure that in the elastic-plastic calculations the strain ϵ_{xx} at the critical point, at which propagation is presumed to occur, is larger than the largest possible elastic strain generated at an equal time. To ensure that small oscillations in the computed values of N_{xx} and ϵ_{xx} did not affect the results, without requiring a finer mesh, the value of crack initiation stress-intensity factors K_{IQ} was taken to be 1.5 K_{Ic} or 105 MPa $\sqrt{m}$ (97 ksi $\sqrt{in.}$).

Figure 3 illustrates the dynamic stress-intensity factor, K_I, calculated using Eq 10 for circumferential and axial cracks of the same length and the same static elastic stress-intensity factors. Dynamic crack propagation was initiated after the crack surface was suddenly released and permitted to open and the crack initiation stress-intensity factor reached it's prescribed K_{IQ}-value. For the axial crack, the stress-intensity factor increases slowly and the crack opening stress wave propagates around the circumference and impacts the crack tip at a time near 140 μs. The stress-intensity factor for the elastic circumferential crack increases very quickly and shows a high percentage of high-frequency oscillation. The highly loaded elastic-plastic circumferential crack, on the other hand, rises continuously until a time of approximately 90 μs, at which point it is about 14 times the critical value. For larger times, the value oscillates, but generally remains constant. With the axial stress of 205 MPa (30 000 lb/in.^{2}), the final plateau is much more evident. In an actual piping situation, reflected waves would cause unloading and a reduction in the crack tip strain, thus leading to a well-defined maximum value of ϵ_{xx}. During the rise, some small oscillations exist, but in general it may be said that for a sufficiently high loading, given enough time and the lack of reflected unloading waves, the ductile crack will always propagate since there is no well-defined maximum as exists for the elastic crack. For the pressurized axial crack, the outward-oriented surface force coupled with the long times associated with the slow crack growth permits a substantial amount of local bending of the crack edges (the flaps). This deformation has been shown to be a dominant feature of such axial cracks in that a substantial energy is absorbed by it and because of the effect it has upon the direction of the resulting force.

Elastic circumferential cracks, on the other hand, tend to propagate at higher speed, and the natural rigidity of the cylinder to crack edge bending inhibits the flap motion and forces the energy to be absorbed in crack-tip movement. Consequently, the elastodynamic details of the fracture process and its history tend to be considerably different from those of the axial crack. Furthermore, stress waves which emanate from the crack tip are passed out of the system by the outgoing wave condition, and, unless a reflection mechanism exists downstream in the pipe, do not return to affect the crack motion as they do for the axial crack. There is an effect due to reflection at

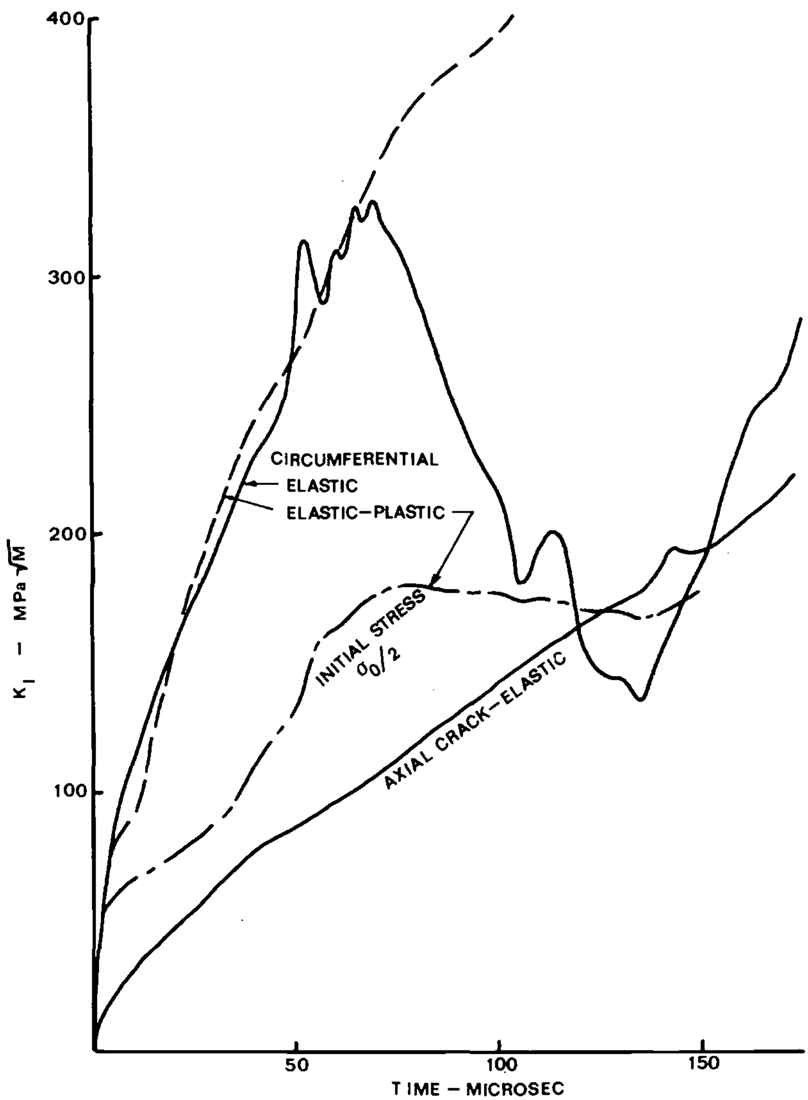

FIG. 3—*Stress-intensity factors developed by a crack of fixed length whose edges are suddenly released (initial stress = σ_O).*

$\theta = 180$ deg from the crack center, but because these waves do not intersect the crack at right angles to its direction of motion, the effect is slight.

Crack-Tip Motion

The crack-tip motion was computed by permitting the crack to extend one mesh interval whenever the criterion $K_I = K_{IQ}$ was satisfied. Calculations were done for thicknesses of $h/a = 1/120$, 1/60, 1/30, and 1/15. No appreciable effect of thickness was observed even though the moment of inertia $\rho h^3/12$ changed by a factor of 512, indicating that there was no significant flap formation and suggesting that computations can be successfully made without considering rotatory inertia or transverse shear. For the axial crack, large and small deformation calculations differed because of the flap deformation. For the circumferential crack, however, less than 1 percent differences in results were noted between large and small deformation computations.

Figure 4 illustrates the time history of the crack-tip position for several values of K_{max}/K_{IQ} for circumferential and axial cracks. Only the elastic case was considered in the latter case since the elastic and elastic-plastic axial crack results are very similar. K_{max} is defined as the maximum dynamic stress-intensity factor developed by a crack of fixed length in the absence of yielding since A533B is only mildly ductile. For very ductile materials, the elastic-plastic value of K_I would depend upon the nature and extent of the stress waves reflected from the boundaries of the pipe, and the crack-tip movement may not be adequately represented by the results shown in Fig. 4.

Figure 5 illustrates the calculated maximum crack speeds expressed in terms of the ratio K_{max}/K_{IQ}. These maximum crack speeds are linearly related to this ratio over the range of 1.1 to 6 provided that there is no static net section yielding in the absence of a crack. For all values of K_{max}/K_{IQ}, the elastic-plastic crack speeds (for both axial and circumferential cracks)

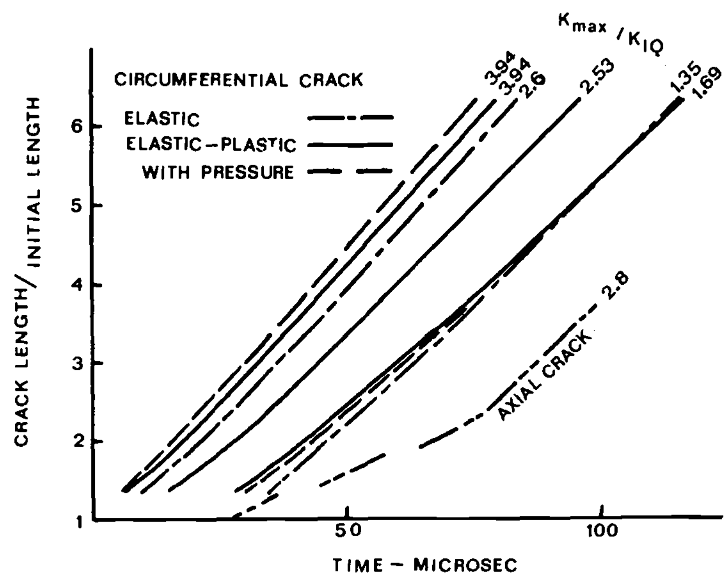

FIG. 4—*Crack-tip movement for circumferential crack for different values of* K_{max}/K_{IQ}.

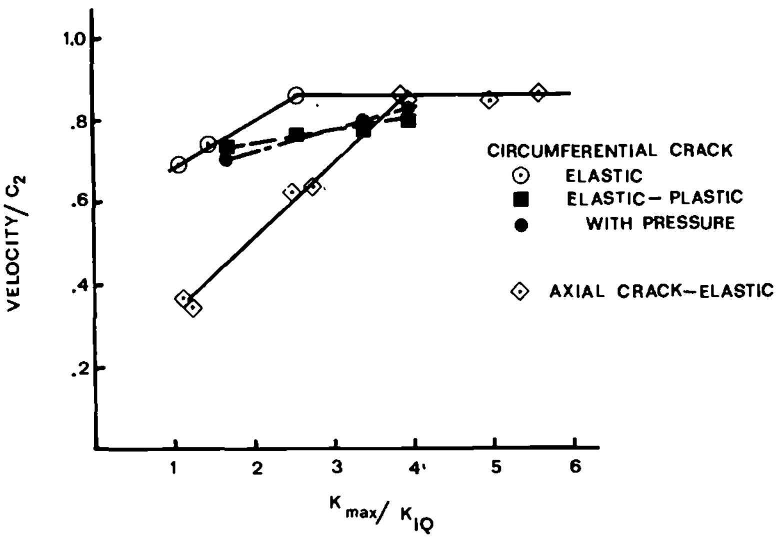

FIG. 5—*Maximum crack-tip velocities as a function of* K_{max}/K_{IQ}.

are slightly lower than those determined for the elastic case, but with about the same upper limit.

Calculations were also made for cases in which the effects of plasticity were enhanced by the addition of a hoop stress of 207 MPa (30 000 lb/in.^{2}) due to a pressure of 3.45 MPa (500 lb/in.^{2}). For small axial stresses, the crack moves a little later than in the absence of the pressure because the stress is slightly reduced by the enhanced plastic deformation. For high axial loads, the yielding is so widespread that a critical strain is reached earlier and the crack moves markedly earlier. On the other hand, the propagation velocity is unaffected by the pressure at the low axial load, but reduced by 5 percent for the higher axial load.

Crack Opening Shapes

Figure 6 shows the crack opening shapes for the different cases for strongly overdriven cracks and illustrates that the elastic-plastic crack shapes are significantly different near the crack tip. At the center of the crack, the elastic-plastic circumferential crack openings are much larger than the elastic circumferential crack openings because of the longer times needed to propagate the former. If the circumferential crack shapes are normalized by the value at the center of the crack, the opening shapes for all the circumferential cracks are almost identical. The opening shapes for elastic-plastic cracks with no internal pressure and with internal pressure were found to differ by only about 10 percent. This small difference is primarily due to the nearly equal crack propagation velocities and tip histories.

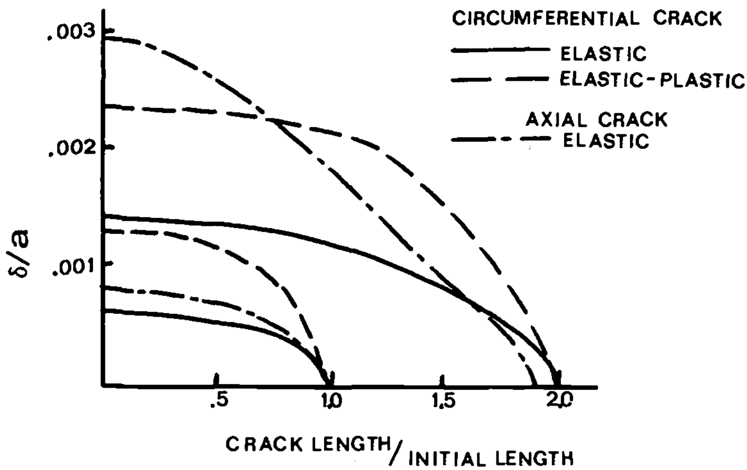

FIG. 6—*Crack opening shapes for a strongly overdriven crack* (K_{max}/K_{IQ} = *2.6*).

Conclusions

The calculations have shown that for elastic and elastic-plastic circumferential uniaxial states of stress, for elastic-plastic circumferential cracks with biaxial states of stress, and for pressurized axial cracks, the propagation is primarily determined by the ratio of $K_{\max}/K_{\mathrm{IQ}}$ where $K_{\max}$ is the maximum brittle stress-intensity factor developed by a crack of fixed length. For equal values of overdriving, the circumferential crack speeds are substantially higher than the velocity of the axial crack. Both types of cracks appear to have equal limiting velocities for both elastic and elastic-plastic cracks, with the latter being slightly lower than that of the former. In all of the circumferential crack results, the severance velocity is so high that substantial fluid loss and critical fluid pressure waves are unlikely—especially in comparison with the axial crack case.

The results and conclusions for the elastic-plastic case are based upon the observation that A533B is only mildly ductile. Obviously, different materials would act differently. In particular, the crack speeds would be much lower for more ductile materials, elapsed times would be longer, crack openings would be larger, and fluid losses greater. Furthermore, it might not be possible to correlate the results in terms of the ratio $K_{\max}/K_{\mathrm{IQ}}$. For these materials, calculations would have to be performed for each specific loading of interest.

Acknowledgments

The work reported in this paper is sponsored by the Electric Power Research Institute under Contract No. RP-231-1-1. The authors wish to thank Drs. C. Chan and J. Carey of the Institute for their encouragement throughout the course of this research program.

References

[1] Emery, A. F., Kobayashi, A. S., and Love, W. J., "An Analysis of the Propagation of a Brittle Circumferential Crack in a Pipe Subjected to Axial Stresses," ASME Paper 78-PVP-101, presented at the Joint American Society of Mechanical Engineers/Canadian Society of Mechanical Engineers Pressure Vessel and Piping Conference, Montreal, Que., Canada, 1978.

[2] Kanninen, M. F., Sampath, S. G., and Popelar, C., *Journal of Pressure Vessel Technology, Transactions*, American Society of Mechanical Engineers, Vol. 98, Feb. 1976, pp. 56-65.

[3] Freund, L. B., Parks, D. M., and Rice, J. R. in *Mechanics of Crack Growth, ASTM STP 590*, American Society for Testing and Materials, 1976, pp. 243-262.

[4] Emery, A. F., Love, W. J. and Kobayashi, A. S., *Journal of Pressure Vessel Technology, Transactions*, American Society of Mechanical Engineers, Vol. 99, Series J., No. 1, Feb. 1977, pp. 122-136.

[5] Emery, A. F., Love, W. J., and Kobayashi, A. S., *Journal of Pressure Vessel Technology, Transactions*, American Society of Mechanical Engineers, Vol. 98, Feb. 1976, pp. 2-8.

[6] Novoshilov, V. V., *Foundations of the Nonlinear Theory of Elasticity*, Graylock Press, 1953.

[7] Hermann, G. and Mirsky, I., *Journal of Aerospace Science*, Vol. 25, 1958, pp. 451-458.

[8] Emery, A. F. and Cupps, F. J., "The Finite Difference Computations of the Dynamic Motion of Cylindrical Shells Including the Effect of Rotary Inertia," Sandia Laboratory Report SCL-73-0071, Sandia Laboratories, Livermore, Calif.

[9] Weiss, V. and Sengupta, M. in *Mechanics of Crack Growth, ASTM STP 590*, American Society for Testing and Materials 1977, pp. 194-207.

[10] Kanninen, M. F., Sampath, S. G., Broek, D., Marshall, C. W., McGuire, P., and Wilkowski, G. M., *Transactions*, 4th Structural Mechanics in Reactor Technology Conference, San Francisco, Calif., Aug. 1977.

R.D. Cheverton,[1] *P.C. Gehlen,*[2] *G.T. Hahn,*[3]
and S.K. Iskander[4]

Application of Crack Arrest Theory to a Thermal Shock Experiment

REFERENCE: Cheverton, R. D., Gehlen, P. C., Hahn, G. T., and Iskander, S. K., **"Application of Crack Arrest Theory to a Thermal Shock Experiment,"** *Crack Arrest Methodology and Applications, ASTM STP 711,* G. T. Hahn and M. F. Kanninen, Eds., American Society for Testing and Materials, 1980, pp. 392–421.

ABSTRACT: This paper presents evaluations of the onset of fracture and crack arrest in a thick-walled A508 steel cylinder (530-mm outside diameter, 240 mm inside diameter and 910 mm long) for thermal shock loading conditions similar to those postulated for a nuclear reactor vessel. The evaluations include static finite-element as well as static and dynamic finite-difference analyses of the flawed cylinder. The calculated values of the stress-intensity factor at initiation and at arrest are compared with the fracture toughness (K_{Ic}) and crack arrest toughness (K_{Im}) values obtained from small specimens tested at the same temperatures. The stress-intensity factor at initiation agrees with K_{Ic}, while the stress-intensity factor at arrest is less than K_{Ic} and consistent with estimates of K_{Im}. Dynamic effects (such as inertial effects) at arrest are negligible, and the static and dynamic analyses give the same result for the rather small (12 mm) crack extension experienced by the vessel. However, a dynamically calculated large (93 mm) crack extension for a hypothetical brittle steel is 52 percent longer than predicted by the static analysis. It follows that dynamic effects may not be negligible for very deep penetrations of the vessel wall.

KEY WORDS: crack arrest, thermal shock, pressurized water reactor vessel, loss-of-coolant accident, A508 steel, crack arrest toughness, fracture toughness, cylinder, finite element, finite difference, dynamic analysis

Nomenclature

- a Crack length
- a_0 Initial crack length

[1]Senior development specialist, Oak Ridge National Laboratory, Oak Ridge, Tenn. 37830.
[2]Associate professor, Department of Mechanical Engineers, University of Tulsa, Tulsa, Okla.
[3]Professor of metallurgy, Vanderbilt University, Nashville, Tenn. 37235.
[4]Section head, Solid Mechanics Section, Computer Sciences Division, Union Carbide Corp., Nuclear Division, Oak Ridge, Tenn. 37830.

a_a	Crack length at arrest
$\dot{a}$	Crack velocity
BCL	Battelle's Columbus Laboratories
δ_i	Displacement at initiation of run-arrest event
δ_a	Displacement at arrest
FE	Finite element
FD	Finite difference
K_I	Stress-intensity factor
$(K_I)_{max}$	Value of K_I where $dK_I/dt = 0$
K_{Ia}	Estimate of crack arrest toughness derived from a static analysis of K_I at arrest
K_{Ic}	Fracture toughness
K_{ID}	Fast fracture toughness
K_{Im}	Minimum in the variation of K_{ID} with crack velocity; also crack arrest toughness
K_Q	Stress intensity for onset of crack extension from blunted starting slot
L	Work of external loads + kinetic energy − internal strain energy
ORNL	Oak Ridge National Laboratory
PWR	Pressurized water reactor
r	Radius
t	Time
TSE	Thermal shock experiment
TSV	Thermal shock vessel
u	Displacement
W	Cylinder wall thickness
ϕ	Angle between adjacent nodes

Several fracture mechanics analyses of crack arrest have been proposed, including the static, dynamic, and energy conservation approaches [*1*].[5] Critical evaluations of these analyses have been confined mainly to run-arrest events in small laboratory test specimens [*2-5*]. This paper presents evaluations for crack arrest in a relatively large cylinder (530-mm outside diameter, 240-mm inside diameter, and 910 mm long) that was subjected to thermal shock loading. The experiment is one of a series conducted at ORNL [*6*] to investigate crack initiation and arrest under thermal shock loading conditions similar to those encountered by a pressurized water reactor (PWR) vessel during hypothetical loss-of-coolant and steamline-break accidents. Such accidents would be followed by the injection of low-temperature coolant that would pass over the relatively hot inner surface of the vessel wall to produce the following effects (refer to Fig. 1):

1. A steep positive temperature gradient through the wall.

[5] The italic numbers in brackets refer to the list of references appended to this paper.

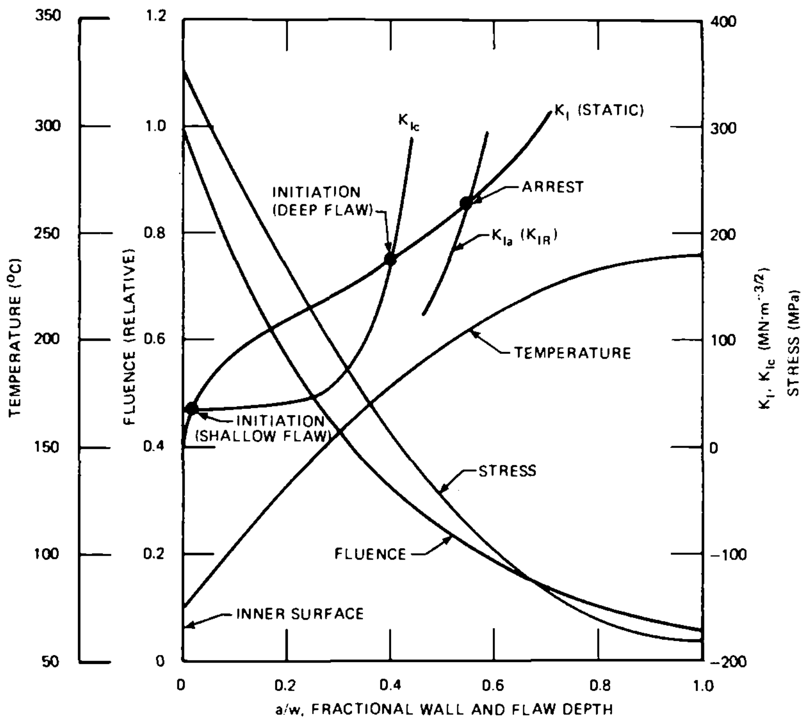

FIG. 1—*Typical instantaneous temperature, stress, fluence, stress-intensity factor and fracture and arrest toughness (high-copper material) for a PWR vessel subjected to a loss-of-coolant accident thermal shock (maximum fluence = 4 × 10^{19} neutrons (n)/cm^2.*

2. High, thermally induced tensile stresses and thus an appreciable stress-intensity factor (K_I) for flaws extending from the inner surface.

3. A reduction in fracture toughness (K_{Ic}) corresponding to the reduction in temperature.

The combined effect of the high stress-intensity factor for a preexisting flaw and the low fracture toughness induced by the cooling and by radiation damage may result in propagation of the flaw. However, because of the sensitivity of fracture toughness to temperature and fluence, the positive gradient in temperature, and the attenuation of the fluence, there is a net positive gradient in toughness in the vessel wall, as shown in Fig. 1, that tends to provide a mechanism for crack arrest.

Four thermal shock experiments were conducted at ORNL on the large cylinders. Data retrieved from the experiments included the temperature distribution through the wall as a function of time, and indications of crack initiation and arrest as detected by crack-opening-displacement gages and acoustic emission instrumentation. At the completion of an experiment, the temperature distributions were used as the thermal loadings for the calculation of the stress-intensity factors.

In one of the experiments (TSE-4), the cylinder initially contained an 1 1-mm-deep, long axial crack that propagated in a single jump to a depth of 23 mm, under the influence of the thermal shock, and arrested. Test conditions for this experiment are given in Table 1.

One of the objectives of TSE-4 was to compare calculated values of the stress-intensity factor corresponding to the arrest event with laboratory measurements of the crack arrest toughness for the same material. Calculations of the stress-intensity factor were performed by ORNL and BCL, and static fracture toughness and arrest toughness values for the TSE-4 test cylinder material were obtained at both laboratories. This paper presents an analysis of the TSE-4 initiation-arrest event using this information. The results of the analysis indicate that dynamic effects at arrest are negligible for the rather small (12 mm) crack extension experienced in TSE-4, and thus the static and dynamic analyses of the arrest event agree with each other and with the experiment.

A dynamic calculation for a hypothetical temperature-invariant crack arrest toughness reveals a crack penetration of 93 mm, which is 52 percent deeper than predicted by the static analysis. It follows that dynamic effects may not be negligible for very deep penetrations of the vessel wall.

Analysis of Crack Arrest

The various analytical approaches adopt essentially the same linear elastic fracture mechanics (LEFM) criterion for crack arrest: crack propagation must stop when the instantaneous value of the stress-intensity factor is less

TABLE 1—*Test conditions and material properties for TSE-4.*

Test specimen dimensions, m	
OD	0.53
ID	0.24
length	0.91
Test specimen material	A508 steel, Class 2 chemistry
Heat treatment	quench only from 871°C
Flaw	long axial crack
initial depth, mm	11 ± 1
final (arrested) depth, mm	23 ± 2
Temperatures, °C	
wall (initial)	291
sink (initial)	−25
Coolant	40 weight % methyl alcohol, 60 weight % water
Material properties	
Young's modulus, 6Pa	193
Poisson's ratio	0.3
bar wave speed, m/s	5000
coefficient of thermal expansion, $10^{-6}\,°C^{-1}$	11.7
density, g/cm^3	7.86

than the crack arrest toughness, or $K_I < K_{Im}$ [*7*]. The crack arrest toughness is defined as the minimum in the variation of the propagating crack toughness (K_{ID}) with respect to crack speed [*8*]. As shown schematically in Figs. 2*a* and 2*b*, K_{Im} can be equal to or less than K_{Ic}, depending on the nature of the K_{ID}-versus-$\dot{a}$ curve.

Differences among the analytical approaches can arise from the way K_I is evaluated. The static analysis approach [*9*] evaluates K_I in the conventional way; that is, it assumes static equilibrium conditions and neglects the kinetic energy in the structure or test specimen at the instant of crack arrest. In contrast, the dynamic analysis approach [*10*] seeks to account for the kinetic energy and inertia in the calculation of K_I but neglects

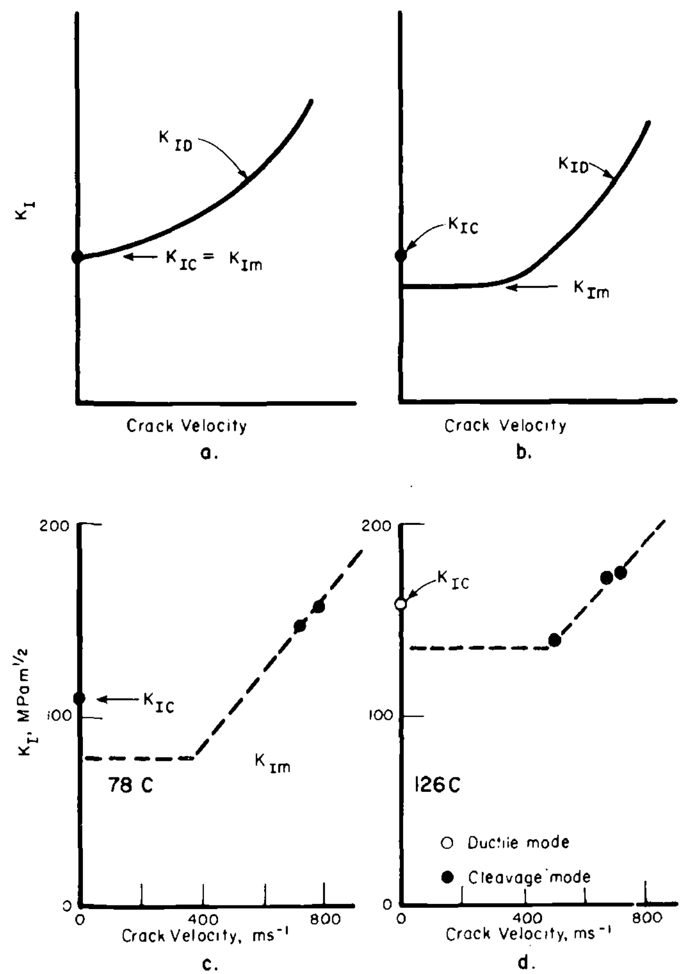

FIG. 2—K_{ID} *versus* $\dot{a}$: (a) *and* (b) *schematic;* (c) *and* (d) *quenched-only A508 steel.*

damping. In effect, the dynamic approach allows for conversion of kinetic energy to fracture energy in the latter stages of propagation event, while the static analysis does not. The results of the static and dynamic analyses will agree when kinetic energy return is negligible, such as for small crack jumps (small relative to the body dimensions). The energy conservation approach [*1*] assumes that all of the kinetic energy is utilized as fracture energy before arrest. This approximation makes it possible to estimate K_I-values at arrest from the conventional static calculations.

It should be noted that Crosley and Ripling [*11*] have developed test procedures that employ the static analysis approach to evaluate crack arrest toughness. Values obtained in this way are designated K_{Ia} by these workers. Similar procedures devised by Hoagland et al [*12*] use the dynamic analysis approach. In this case, the crack arrest toughness in designated K_{Im}.

Material Characterization for TSE-4

Two test cylinders (TSV-1) and TSV-2) were used in the series of thermal shock experiments at ORNL, with TSV-2 being used for TSE-4. To simulate postulated PWR fracture conditions as closely as possible, the two test cylinders were fabricated from pressure vessel grade A508 steel and were given a quench-only heat treatment.[6] This treatment reduces the toughness and increases the yield strength relative to the standard quenched-and-tempered condition—changes which simulate irradiation effects to some extent.

The ORNL characterizations were performed on prolongations of the two test cylinder forgings, and included tensile, Charpy-V, and static fracture toughness (precracked Charpy and compact tension) data. Characterizations conducted at BCL were carried out on material taken from TSV-1 after completion of the thermal shock experiments. These included static fracture toughness tests (1T compact tension specimens) and crack arrest toughness measurements.

The yield and ultimate strengths of the A508 material in the quench-only condition are nearly independent of temperature in the range −73 to 260°C and have average values of 970 and 1170 MPa, respectively. Charpy-V impact data from ORNL are presented in Table 2, and static fracture toughness data from the two laboratories are presented in Fig. 3. No systematic differences between the results for TSV-1 and TSV-2 or with distance from the outer surface are apparent. Values of the various toughness parameters at approximately 77 and 131°C have special significance because these temperatures correspond to the TSE-4 initiation and arrest events, respectively.

[6]Quenched in water from 870°C.

TABLE 2—*Charpy-V impact values from CA[a]-oriented specimens from thermal shock vessel TSV-1 and TSV-2 prolongations after aging for 24 h at 288°C and cooling in air.*

		Charpy-V Impact	
Depth[b]	Test Temperature, °C	Energy, J	Lateral Expansion, mm
	TSV-1		
0.58	23	...	...
	66	13	0.08
	79	...	...
	93	27	0.25
	149	43	0.61
	204	48	0.61
0.69	38	...	...
	66	...	...
	93	...	...
	149	...	...
0.77	23	...	...
	66	10	0.05
	93	22	0.30
	149	49	0.64
	204	59	0.86
0.86	23	...	...
	66	15	0.03
	93	25	0.2
	149	38	0.51
	204	43	0.61
	TSV-2		
0.57	−46	8	0
	−17	14	0
	10	9	0.08
	38	11	0.13
	66	23	0.18
	93	23	0.30
	121	38	0.43
	177	47	0.66
	232	42	0.48
0.76	−46	12	0
	−17	14	0
	10	11	0.13
	38	18	0.18
	66	15	0.15
	81	...	...
	93	22	0.25
	121	40	0.61
	177	43	0.58
	232	44	0.61

[a]Specimen oriented circumferentially (tangentially), and crack propagates axially relative to test cylinder.
[b]Depth from outer surface/wall thickness.

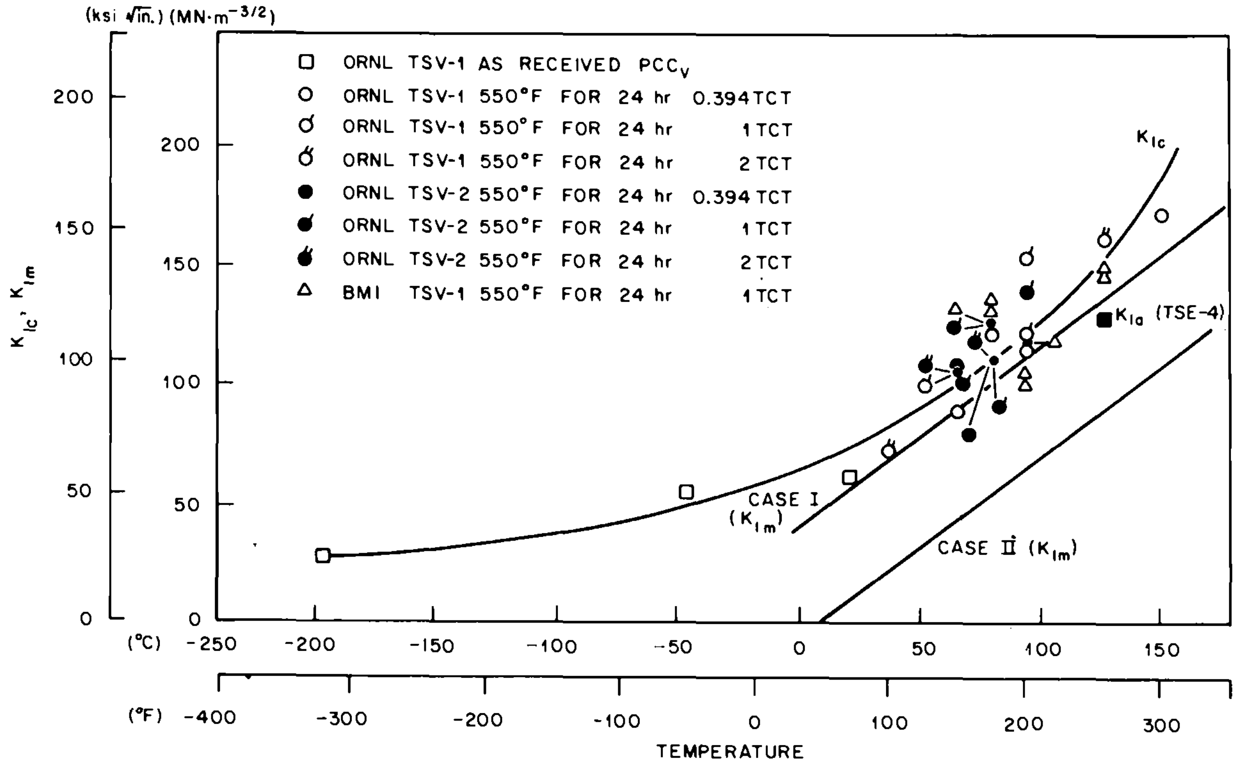

FIG. 3—K_{Ic} *versus temperature for TSV-1 and TSV-2 material (A508 quench-only) with assumed* K_{Im} *curves superimposed.*

Scanning electron micrographs (SEM's) of two BCL compact tension specimens are shown in Figs. 4*a* and 4*b* for test temperatures of 93 and 126°C, respectively. These SEM's reveal that the onset of crack extension proceeds by the cleavage mode at temperatures $\leq$93°C and by the ductile, fibrous (void nucleation and growth) mode at 126°C. In contrast, micrographs of the actual TSE-4 fracture show that the crack in the cylinder propagated and arrested by cleavage (Fig. 4*d*).

Crack arrest measurements were performed on wedge-loaded, duplex, rectangular double cantilever beam (DCB) specimens [*13*] (140-mm wide, 400-mm long, and 50-mm thick). Broken and heat-tinted specimens are illustrated in Fig. 5, and the results obtained at two temperatures are summarized in Table 3. The tests provide K_{ID}-values at essentially one crack velocity, ~700 ms^{-1}, at each temperature. SEM's of these fractures show that fast fracture and arrest in the DCB specimens proceed with the cleavage mode[7] at both 78 and 126°C (Fig. 4*c*). It is important to note that the DCB specimens tested at 78 and 126°C reproduced the mode of propagation and arrest observed in the cylinder (compare Figs. 4*c* and 4*d*).

The K_{Ic}-value can be regarded as a measure of both K_{ID} (for very low crack velocity) and K_{Im}, provided the fracture proceeds by the ductile mode (Fig. 2*a*). However, the K_{Im} value tends to fall below K_{Ic} for propagation involving cleavage (Fig. 2*b*) [*14*]. Since fast fracture and arrest in the DCB specimens (and presumably in TSE-4) proceed by cleavage at 77 and 126°C, neither the K_{Ic}- nor K_{ID}-values measured are acceptable estimates of K_{Im} at these temperatures. Rough estimates of K_{Im} for 77 and 126°C (77 and 134 MPa m$^{1/2}$, respectively) were deduced from run-arrest events (pop-ins), which proceeded by cleavage in two 1*T* compact specimens tested at 93°C.[8] The resulting K_{ID} crack velocity curves for the two temperatures are shown in Figs. 2*c* and 2*d*. The curves are similar to one reported by Bilek [*15*] for a quenched-and-tempered steel, which also involves propagation by cleavage.

The K_{Ia}-values in Table 3 were deduced from the same experiments, using the displacement values measured after arrest, according to the practice followed by Crosley and Ripling [*11*]. These values are 7 to 20 percent lower than the average values of K_{Ic}. In the presence of dynamic effects, the value of K_{Ia} is expected to be less than the value of K_{Im}. This is indeed observed at 126°C, but not at the lower temperature. This dis-

[7] Clevage fractures at different levels are connected by vertical ductile shear failures [*14*], but the fracture surfaces at 77 and 126°C are predominantly clevage.

[8] The onset of crack extension occurred with pop-ins involving 3.8- and 5.0-mm crack extensions accompanied by a drop in load. The values of the stress-intensity factor at arrest ($K_I = K_{Im}$ = 94 and 96 MPa m$^{1/2}$ at 93°C) were obtained directly, assuming crack-extension at constant displacement and negligible dynamic effects for the small crack extensions. The values at 77 and 126°C were obtained by applying the linear temperature coefficient for K_{Im} (1.19 MPa m$^{1/2}$ per deg C), which was obtained for this material in a different heat-treated condition [*14*].

crepancy probably is connected with specimen-to-specimen variability and the approximate nature of the temperature coefficient (see footnote 8).

Methods of Analysis for Calculating K_I

The elastic plane-strain stress-intensity factors were obtained by numerical analysis using either a finite-element (FE) or a finite-difference (FD) technique. The FE technique was applied by ORNL to the static analysis of TSE-4, while BCL used the FD technique for both static and dynamic events.

Two approaches were used in the static FE technique. One approach is based upon the so-called energy release rate method [*16*], and a typical FE model used is shown in Fig. 6*a*. The other approach is based upon the classical relationship between the displacements near the crack tip and the stress intensity-factor K_I, and for our analysis an eight-noded, 1/4-point singularity element was used in the vicinity of the crack [*17,18*]. A typical model for this approach is shown in Fig. 6*b*.

The Battelle FD scheme used to analyze fast fracture events in two-dimensional structures such as compact tension and single edge notch specimens is described elsewhere [*18*]. Conceptually, the two-dimensional scheme used to analyze TSE-4 is identical to that in Ref *18*, although the numerical details differ. Details required to familiarize the reader with the method are discussed briefly in this paper, and a complete description is given in Ref *19*.

Within the usual assumptions of two-dimensional LEFM, the FD analysis for TSE-4 was performed by first modeling the test specimen with a grid similar to that shown in Fig. 7. The stress-intensity factor is calculated by means of the strain energy release rate technique, which requires knowledge of the displacements. These displacements are obtained by solving Lagrange's equation, which for the radial and circumferential directions is

$$\frac{d}{dt}\left(\frac{\partial L}{\partial \dot{u}_{ijk}}\right) - \frac{\partial L}{\partial u_{ijk}} = 0, \qquad k = 1,2 \tag{1}$$

where u_{ij1} and u_{ij2} are the radial and circumferential strains at node ij, and L is the sum of the work done by the external loads and the kinetic energy of the system, less the internal strain energy.

The initial conditions for the dynamic problem are obtained by solving a static problem for the initial crack configuration. The dynamic analysis then commences by releasing the node nearest the crack tip, and the equations of motion are solved. The stress-intensity factor is then computed and compared with the dynamic crack toughness K_{ID}. If K_I is equal to or larger than K_{ID}, the next node is released. The procedure is continued until $K_I < K_{ID}$. At that time the crack is considered to be arrested.

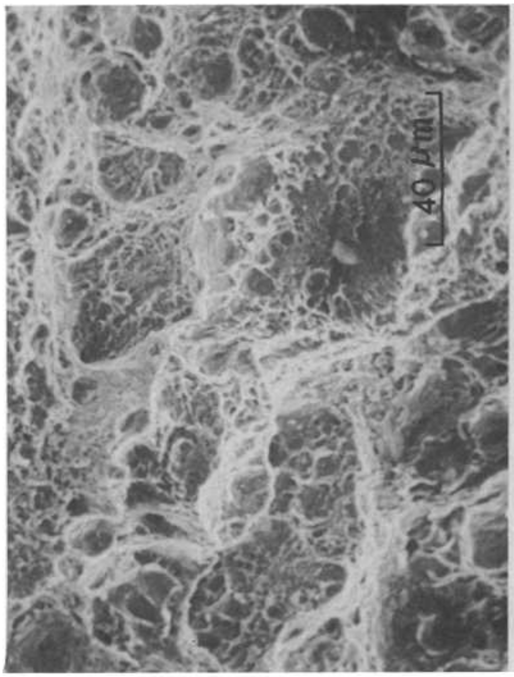

(b) CT specimen, 126°C, K_{Ic}=150 MPa$m^{1/2}$

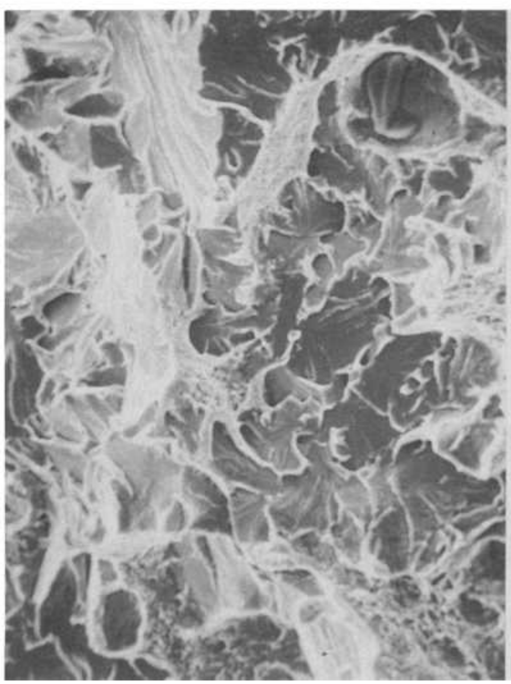

(a) CT specimen, 93°C, K_{Ic}=116 MPa$m^{1/2}$

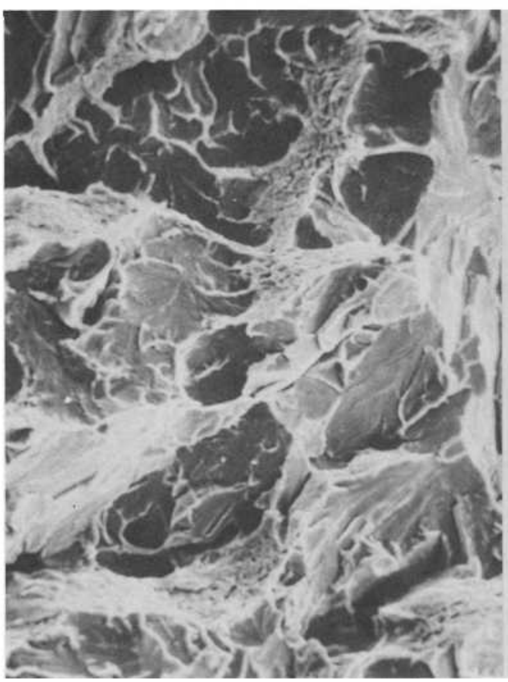

(c) Duplex DCB crack arrest toughness specimen, 126°C, K_{Id} = 172 MPam$^{1/2}$

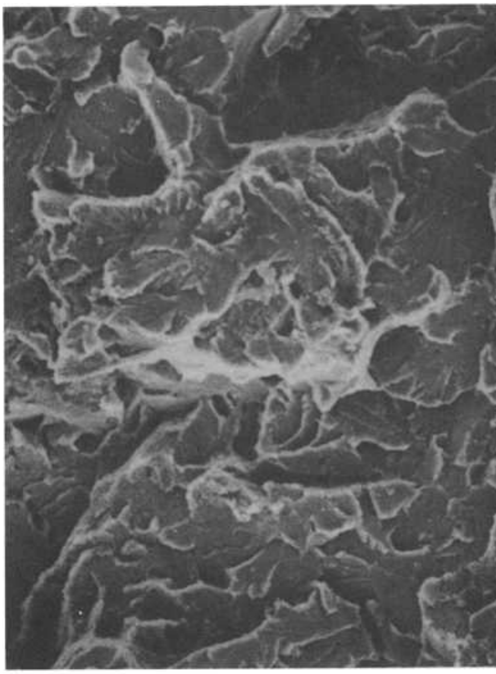

(d) TSE-4 fracture surface intermediate between initial flaw and crack arrest

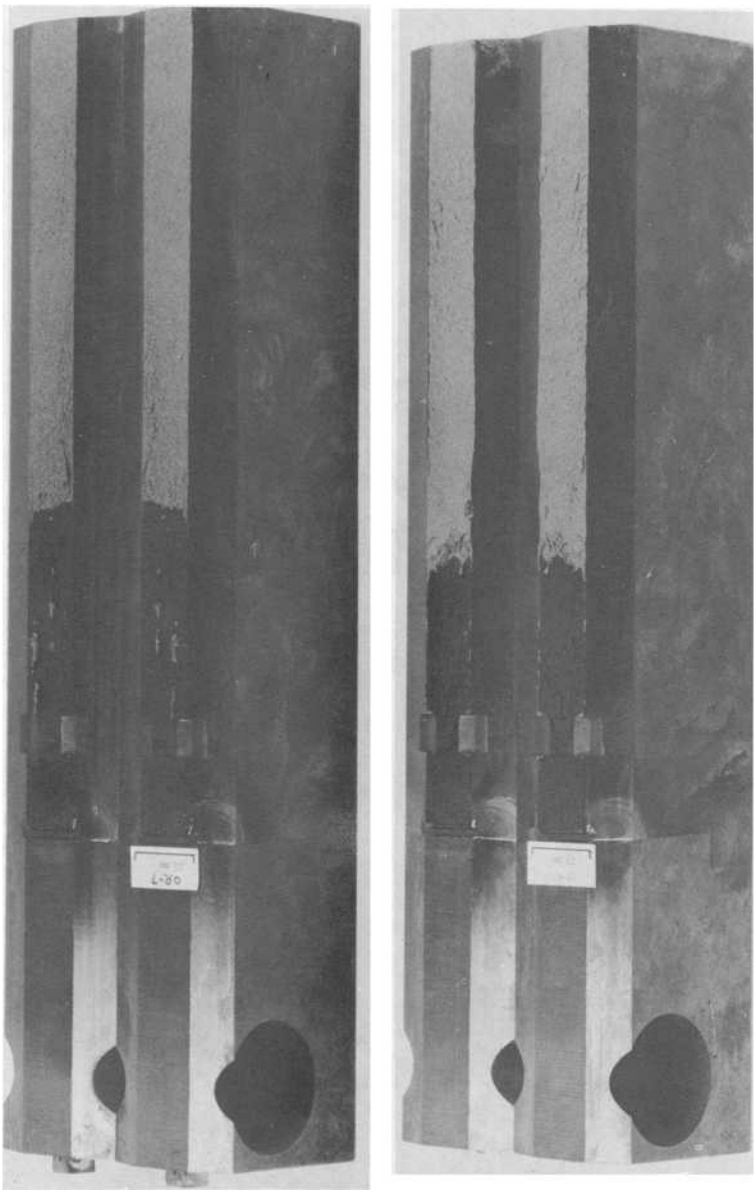

FIG. 5—*Rectangular-DCB crack arrest specimens broken open after heat tinting to reveal the position of the crack front at arrest.*

TABLE 3—*Results of crack arrest toughness measurements on TSV-1 material.*

Specimen	Test Temperature, °C	a_0, mm	a_a, mm	δ_i, mm	δ_a, mm	K_Q, MPa $m^{1/2}$	K_{Ia}, MPa $m^{1/2}$	K_{ID}, MPa $m^{1/2}$	Estimated Velocity, m/s	$K_{Im}{}^{a}$, MPa $m^{1/2}$
OR-5	126	84.5	168.3	2.78	2.81	264.7	122	172	670	
OR-6	126	83.7	175.4	3.01	3.02	289.0	125	173	700	134
OR-9	127	80.1	123.6	1.42	1.42	188.1	113	139	475	
OR-7	78	83.4	192.1	2.90	...	281.0	106	157	780	77
OR-8	78	84.7	181.7	2.51	2.51	240.6	100	149	710	

[a] These results were estimated from pop-in observations (short crack growth) as discussed in footnote 8 of the text.

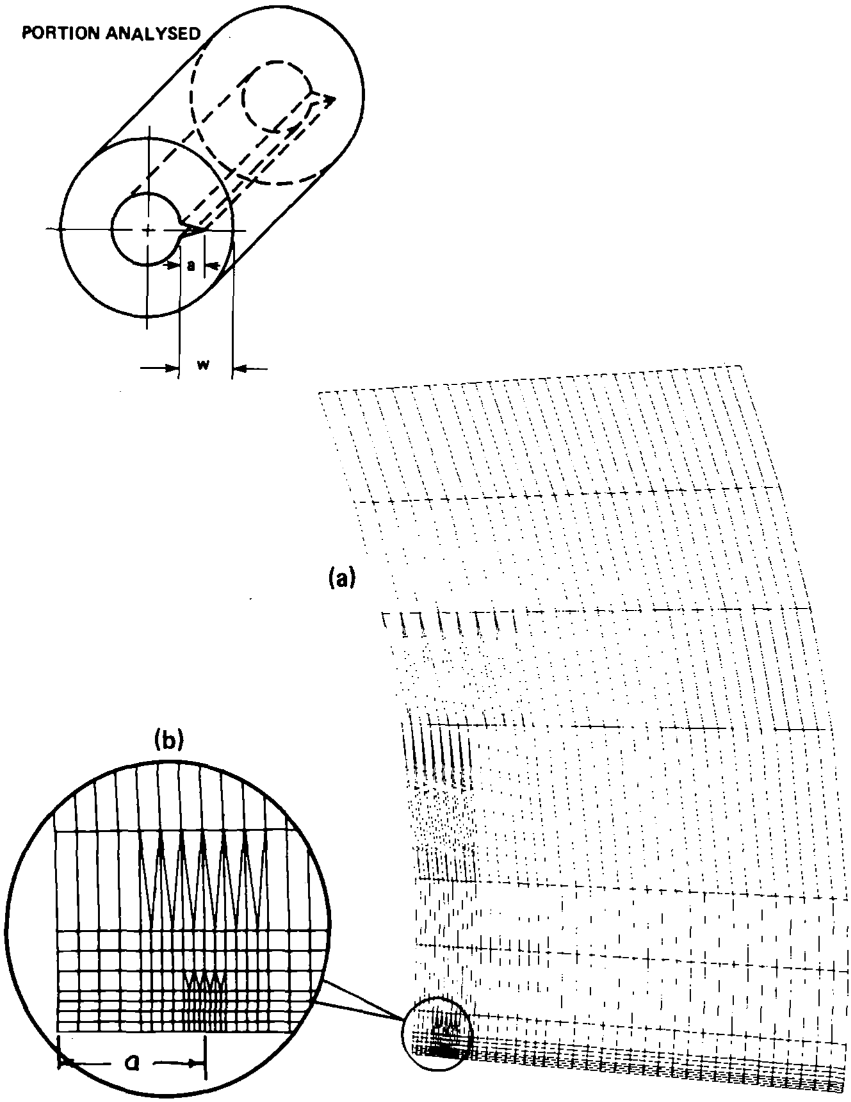

FIG. 6a—*Finite-element idealization of the longitudinal crack:* (a) *15-deg segment of the mesh used to model one half of the cylinder;* (b) *details of the crack region.*

The sudden release of a node in the FD analysis introduces additional dynamic effects that are peculiar to the numerical analysis technique. As discussed in Ref *18*, the magnitude of the effect depends on the ratio of the nodal spacings in the r- and ϕ-directions and is negligible for ratios < 0.06. Typical values of Δr and $\Delta\phi$ for the TSE-4 analysis are 2.92 mm and 25.7 deg.

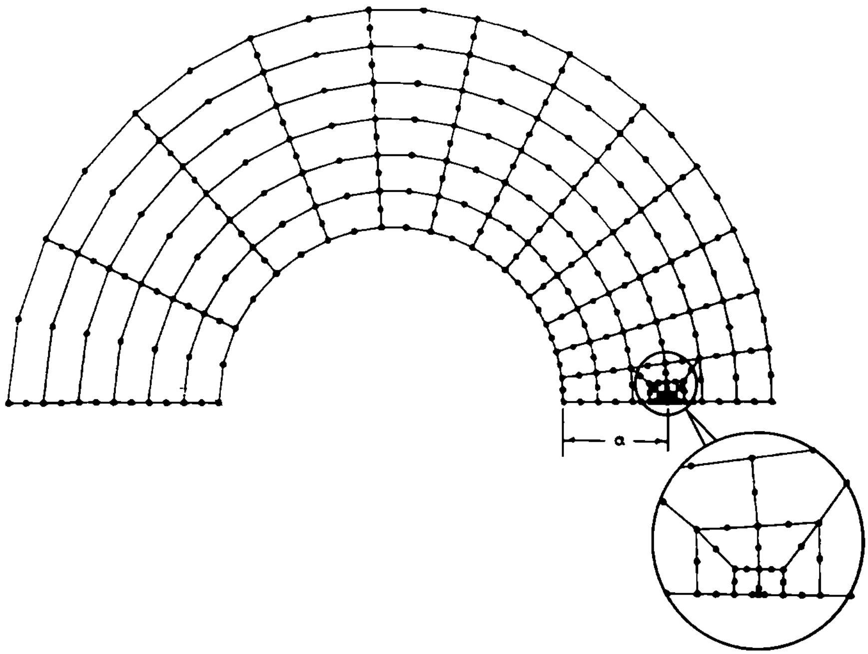

FIG. 6*b*—*Finite-element model using ¼-point, 8-noded element.*

Considerable efforts were expended to ensure convergence of all numerical techniques. This was accomplished by means of mesh and time-step refinement studies, comparisons with closed-form solutions, and comparisons between the three different numerical analysis approaches for the static case. For the actual TSE-4 conditions the FE and FD static K_I-values agree within 2 percent, but for assumed deeper flaws in the test specimen the agreement between the FE and FD results was not as good [for $a/w = 0.5$, K_I(FD) > K_I(FE) by ~30 percent]. Based on the results of numerous accuracy tests conducted on the particular FE method of analysis, it is believed that the FE K_I-values are accurate within ±10 percent.

With regard to the time-step convergence studies, it was determined that for the TSE-4 analysis a satisfactory time step was ~0.2 μs (from a stability point of view the maximum allowable time step is proportional to the smallest nodal spacing).

As a check on the accuracy of the dynamic aspects of the FD analysis, a run-arrest experiment conducted by Kalthoff et al [*2*] with an Araldite-B DCB specimen was calculated by BCL. The crack speed and K_{ID}-values occurring during the dynamic event were calculated correctly, and the calculated crack length at arrest was within 10 percent of the actual value [*18*].

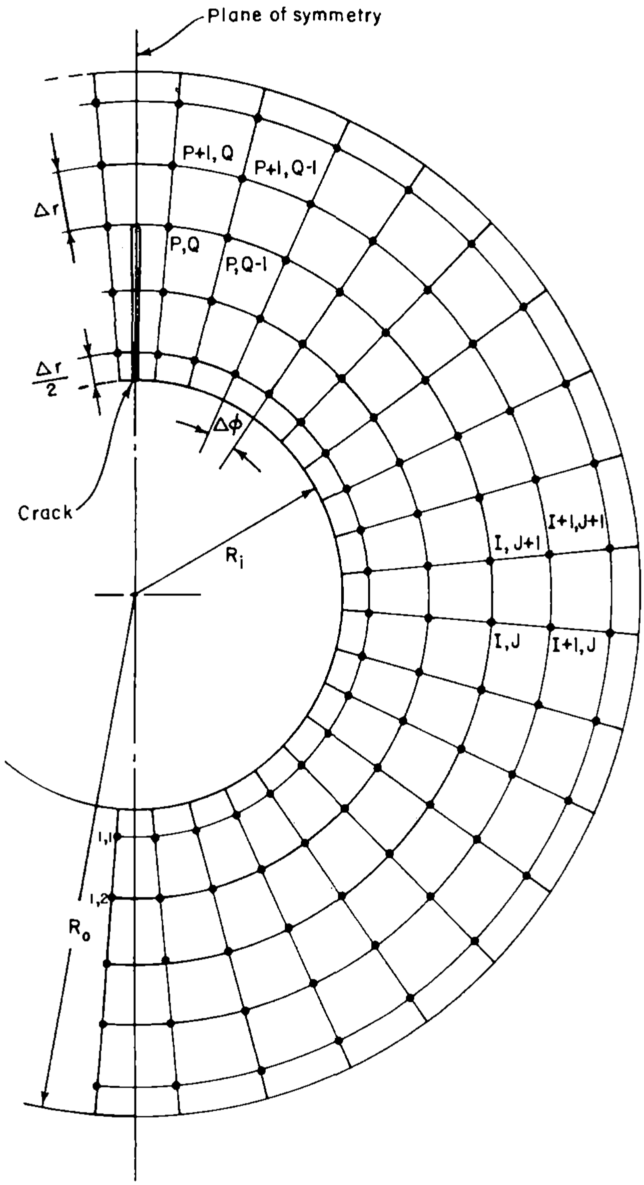

FIG. 7—*A finite-difference net for a cracked thick-wall cylinder.*

Analysis of TSE-4

During the TSE-4 thermal transient, crack initiation and arrest took place along the entire crack front at a time of 150 s. The measured radial temperature distribution at this time was used in the static calculation of K_I for both the initial crack depth and the final crack depth (depths determined post-test by destructive means). These K_I-values constituted the static fracture toughness and static arrest toughness for the temperatures occurring at that time (150 s) at the two crack tips. The measured radial temperature profile, the calculated K_I distribution (assuming various crack depths), and the nominal K_{Ic} radial distribution (based on the K_{Ic}-versus-temperature curve in Fig. 3), all corresponding to 150 s, are shown in Fig. 8. Tabulated values of K_I and temperature at 150 s for the two actual crack depths and the corresponding material toughness values are presented in Table 4. It is observed in this table that the K_I-values calculated by ORNL and BCL agree within 2 percent, and that the nominal value of K_I (calculated by ORNL) corresponding to crack initiation (114 MPa $m^{1/2}$) and the average value of K_{Ic} taken from Fig. 3 (108 MPa $m^{1/2}$) agree within 6 percent, which is well within the uncertainty in both numbers. The K_I-value corresponding to crack arrest (127 MPa $m^{1/2}$) is 11 percent greater than that corresponding to crack initiation and is reasonably close to the aforementioned rough estimate of K_{Im} (134 MPa $m^{1/2}$).

A static interpretation of the TSE-4 initiation-arrest event is displayed graphically in Fig. 9, which is a plot of fractional crack depth (a/w), corresponding to $K_I = K_{Ic}$, $K_I = K_{Ia}$, and $(K_I)_{max}$[9] versus time in the transient. This plot is constructed using the $(K_I)_{max}$-value and the intersections of the K_I curve with the K_{Ic} and K_{Ia} curves, similar to those shown in Fig. 8, for different times in the transient. Points 1 and 2 in Fig. 9 represent the measured time and crack depths corresponding to the actual initiation and arrest events, respectively, and thus the vertical distance between Points 1 and 2 represents the crack jump. Curve b in Fig. 9 is based on the best pre-TSE-4 estimate of the K_{Ic}-versus-temperature curve (K_{Ic} curve in Fig. 3), while Curves a and c are based on assumed K_{Ic}- and K_{Ia}-versus-temperature curves normalized to the experimental results at Points 1 and 2.

The difference between Curves a and b could be explained by the initial flaw being blunted to some extent. However, photomicrographs of test flaws prepared in an identical manner indicate that the TSE-4 initial flaw was sharp. Thus the difference is attributed to the uncertainty in K_{Ic} or to a bias between the relatively small laboratory test specimens used to obtain the curve in Fig. 3 and the TSE-4 test specimen, or to both.

It is of interest to note that following the arrest event (Point 2), reinitia-

[9] $(dK_I/dt) = 0$.

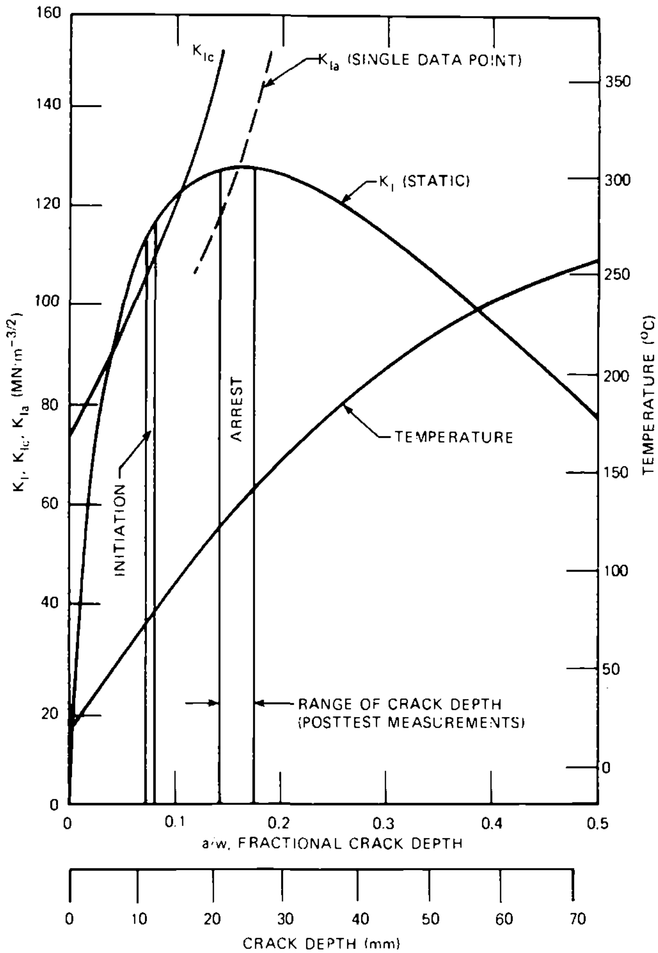

FIG. 8—*Measured radial temperature distribution and corresponding calculated* K_I *distribution at 150 s in TSE-4 transient. Initiation and arrest events are indicated.*

TABLE 4a—*TSE-4 initiation and arrest data.*

Event	Crack Depth, mm	Temperature, °C	ORNL Static Analyses, K_I[a] MPa m$^{1/2}$	BCL Analyses, K_I MPa m$^{1/2}$
Initiation	11 ± 1	77 ± 3	114 ± 2	112 ± 11[b]
Arrest	23 ± 2	131 ± 9	127 ± 1	124 ± 15[c]

[a] Variation associated with uncertainty in crack depth; does not include uncertainty in K_I calculation, which is ~ ± 10 percent.
[b] Static.
[c] Dynamic.

TABLE 4b—*TSV-1 and TSV-2 toughness data.*

Event	Temperature, °C	K_{Ic}[a]	K_{Im}	K_{Ia}
Initiation	77[b]	108 ± 3	77 ± 15	103 ± 12
Arrest	131[b]	158 ± 10	134 ± 20	120 ± 15

[a] Variation associated with uncertainty in crack depth in TSV-2 and thus temperature. Uncertainty in K_{Ic} data (Fig. 3) is ~ ±20 percent.
[b] K_{ID} and K_{Ia} measurements were performed at 78 and 126°C, respectively (BCL data).

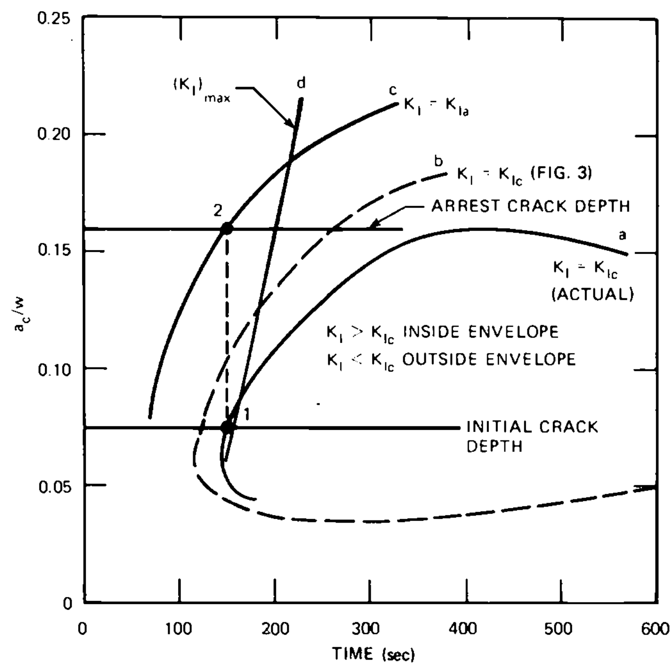

FIG. 9—*Fractional crack depth corresponding to* $K_I = K_{Ic}$, $K_I = K_{Ia}$, *and* $(K_I)_{max}$ *versus time in transient for TSE-4.*

tion could take place only after Curve d had been crossed. By this time, however, K_I was decreasing with time, and thus even though K_I/K_{Ic} might eventually increase to unity or beyond, reinitiation presumably could not take place [*21*]. It is also possible, as indicated in Fig. 9, that $(K_I/K_{Ic})_{max}$ for the arrested crack depth was less than unity, in which case reinitiation could not take place even if K_I were increasing with time. In any event, reinitiation did not take place, and unfortunately the accuracy with which K_I/K_{Ic} is known for the final crack depth is not sufficient to permit a determination of which mechanism, if not both, prevented reinitiation.

Several dynamic calculations pertaining to TSE-4 were made by BCL.

For each case, the initial crack depth and the stress-intensity factor at the time of initiation (K_Q) were taken to be 11 mm and 112 MPa $m^{1/2}$, respectively; it was assumed that $K_{ID} \neq f(\dot{a})$, and thus $K_{Im} = K_{Id}$. (Other applicable data are given in Table 1). For the first calculation and as a first approximation, it was further assumed that K_{Im} was only slightly less than K_{Ic} at the initiation temperature, and the K_{Im}-versus-temperature curve was approximated by the linear relation identified as Case I[10] in Fig. 3. Results of this calculation indicated a crack jump of 6 mm compared with the actual jump of 12 mm. As shown in Fig. 10, the dynamic stress-intensity factor at the instant of arrest is nearly equal to the static value, indicating that dynamic effects for a 6-mm crack jump in TSE-4 are small; the propagation time for this crack jump was 125 μs.

The calculated crack jump can be increased by decreasing K_{Im}, and thus for the second calculation the K_{Im}-curve in Fig. 3 (Case I) was shifted to the right an arbitrary amount (~58°C); this K_{Im}-versus-temperature curve is referred to as Case II[11] in Fig. 3. The result of this calculation was a crack jump of 19 mm with a propagation time of 30 μs. Once again, as shown in Fig. 10, the dynamic stress-intensity factor at the instant of arrest is nearly equal to the static value, indicating small dynamic effects for the 19-mm jump as well.

The results of these two calculations show that the actual crack jump of 12 mm had essentially no dynamic effect associated with it, and thus K_{Im} would be nearly equal to the static arrest toughness (K_{Ia}) calculated for TSE-4. For the given set of assumptions mentioned in the preceding, the value of K_{Im} at 131°C required for a dynamically calculated crack jump of 12 mm is 124 MPa $m^{1/2}$, which agrees very well with the static value obtained from an analysis of TSE-4 (127 MPa $m^{1/2}$) and with the average of the three K_{Ia}-values measured at BCL, after correcting for the 5 K temperature difference between lab measurement and TSE-4 (125 MPa $m^{1/2}$).

Certainly all of the preceding analyses are subject to the effects of uncertainties in the calculations and experimental data. Most-probable values were used in the analyses, and no attempt was made to conduct a sensitivity analysis. The estimated uncertainties pertaining to the initiation and arrest events in TSE-4 and to the DCB data are included in Table 4.

Analysis of a Deep Flaw Under Modified TSE-4 Conditions

As illustrated in the preceding section, the shallow flaw associated with TSE-4 exhibited essentially no dynamic effects. Under a different set of circumstances, however, the flaw could extend farther and might have

[10] K_{Im} (MPa $m^{1/2}$) $= 0.78T$ (°C) $+ 41.2$.
[11] K_{Im} (MPa $m^{1/2}$) $= 0.78T$ (°C) $- 4.7$.

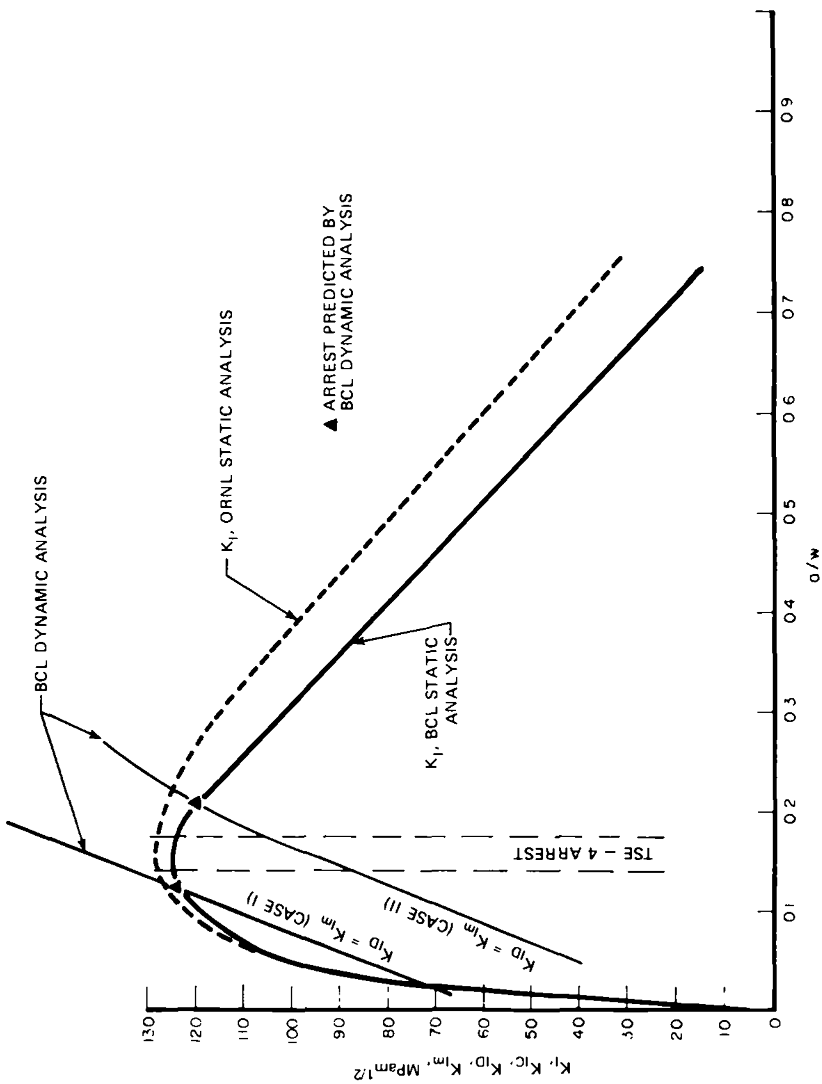

FIG. 10—*Analyses of run arrest event in TSE-4.*

substantial dynamic effects. In order to examine analytically the dynamic effects associated with a "long" crack jump in TSV-2 under TSE-4 loading conditions, a hypothetical material was considered for which the toughness was independent of temperature and crack velocity, and $K_{Im} = K_{ID} = K_{Ic} = 62$ MPa $m^{1/2}$. As shown in Fig. 11, the static-analysis approach predicts, that the crack will extend from 11 to 73 mm ($a/w = 0.5$), assuming that $K_{Ia} = K_{Im}$.

A dynamic analysis of this hypothetical problem indicates that the flaw would extend to 93 mm ($a/w = 0.64$), stop for ~ 100 μs, and extend an additional 11 mm for a total penetration of 104 mm ($a/w = 0.72$). This is illustrated in Fig. 12, which is a plot of crack growth versus time, and also in Fig. 11, which shows that K_{Ia} would have to be reduced to ~ 23 MPa $m^{1/2}$ for the static analysis to result in the same total crack growth. This comparison of the dynamic and static approaches indicates a very significant difference in the predicted crack growth for this particular set of conditions.

Discussion

The application of the particular dynamic method of analysis to TSE-4 indicates that the run-arrest event in TSE-4 was essentially void of dynamic effects at arrest. Thus the stress-intensity factor at arrest calculated using the static and dynamic models should agree, and indeed they do; furthermore, this stress-intensity factor can be interpreted as K_{Im}, the crack arrest toughness of the cylinder material. The particular value obtained (~ 127 MPa $m^{1/2}$) is associated with a temperature of 131°C and is 20 percent less than the K_{Ic}-value from Fig. 3 at the same temperature.

A precise value of K_{Im} was not determined from the laboratory testing of the DCB specimens because of insufficient K_{ID} data, and this prevented an accurate comparison of K_{Im}-values obtained from DCB specimens and deduced from TSE-4. However, the rough estimate of ~ 134 MPa $m^{1/2}$ based on the DCB specimen cleavage pop-ins is consistent with $K_{Im} < K_{Ic}$ and is reasonably close to the TSE-4 value (~ 127 MPa $m^{1/2}$).

The dynamic analyses of the DCB specimens used in this study indicate that substantial dynamic effects were present. The relative values of K_{ID} and K_{Ia} for a temperature (126°C) close to the arrest temperature of TSE-4 (131°C) are consistent with experience on other reactor pressure vessel steels [22]. The three K_{Ia}-values obtained at 126°C vary with crack jump distance in a manner consistent with a material for which K_{ID} increases substantially with crack velocity. However, the variation is not large (122, 125, 113 MPa $m^{1/2}$), and the average, corrected for the 5 K temperature difference between lab test and TSE-4 (125 MPa $m^{1/2}$) agrees well with the K_{Ia}-value obtained from the static analysis of TSE-4 (127 MPa $m^{1/2}$).

The absence of significant dynamic effects in TSE-4 at arrest is not

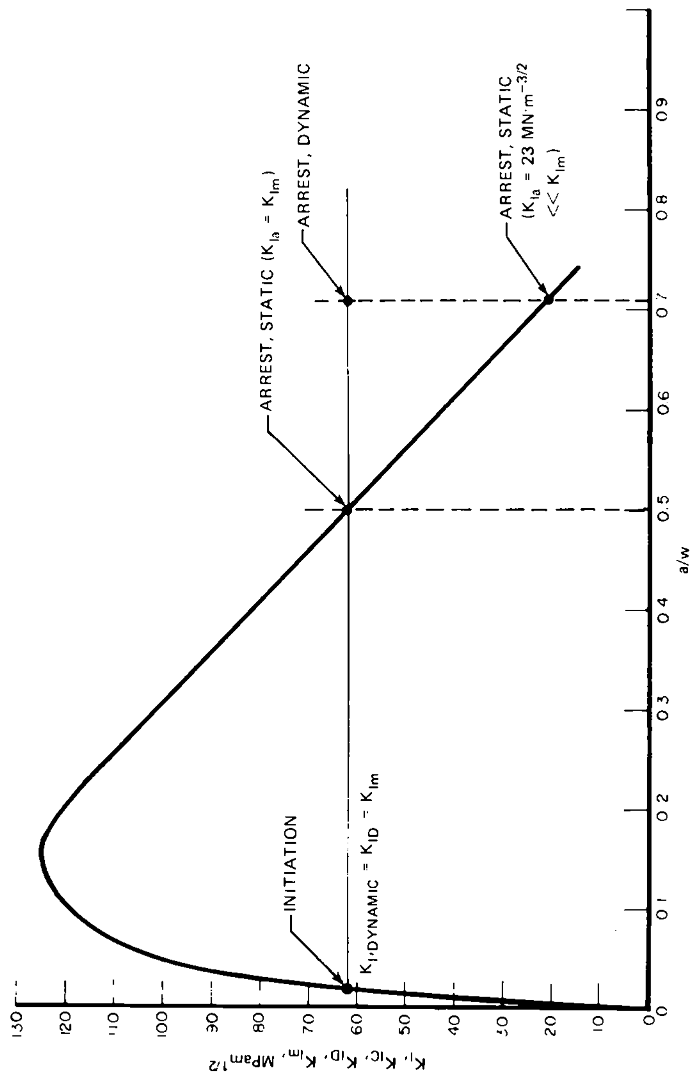

FIG. 11—*Analysis of hypothetical long-jump (run arrest) event under TSE-4 conditions.*

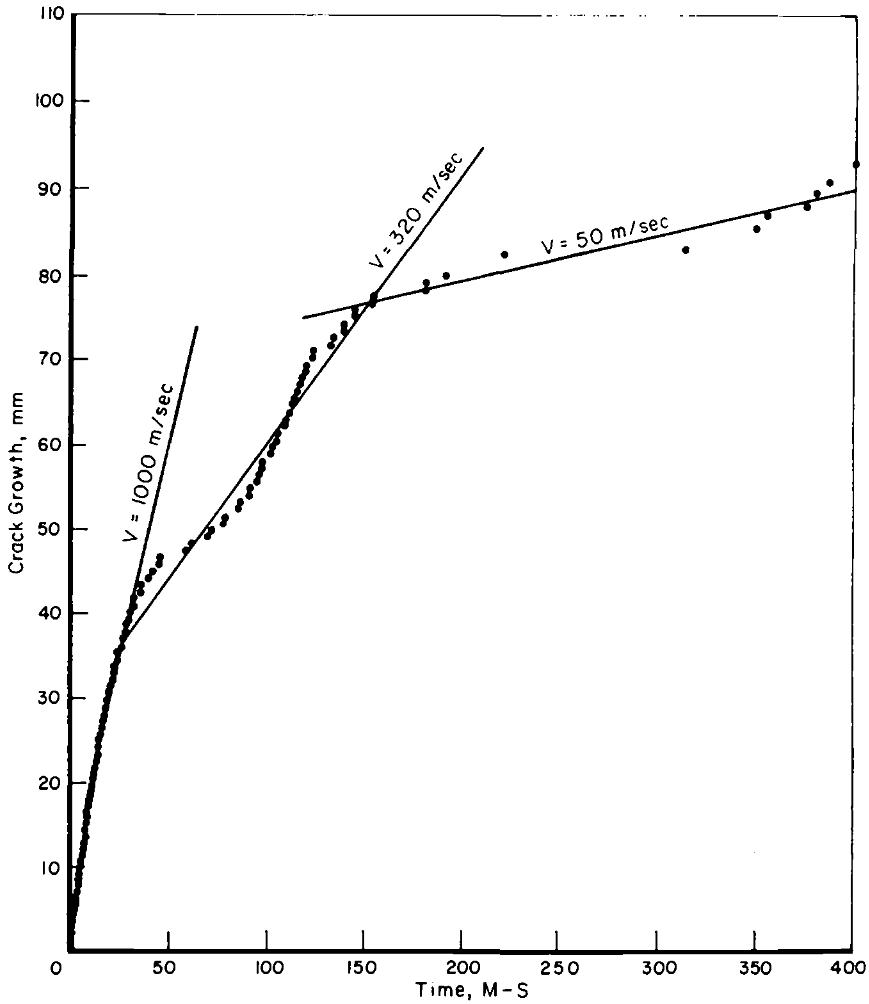

FIG. 12.—*Crack growth versus time for hypothetical long-jump (run arrest) event under TSE-4 conditions.*

surprising considering that (1) the distance the crack propagated was only 9 percent of the uncracked ligament, and (2) dynamic effects at arrest vanish in the limit of infinitesimal crack jumps [*1*]. The dynamic calculation also failed to reveal a significant dynamic contribution for Case II, where the crack jump was 15 percent of the uncracked ligament. However, the indications of large dynamic effects were evident for the one calculation which produced a large jump, fracturing 69 percent of the remaining ligament. In this case, the crack propagated 52 percent farther than the static analysis approach predicted. This result suggests that under some circumstances involving a large crack jump in a heavy-wall cylinder dynamic effects may not be negligible. It is difficult to generalize from these results. More experiments and dynamic analyses are desirable both to validate the computational procedures and to examine run arrest in the geometry and gradients of full-scale vessels to permit conclusions about the PWR vessel.

Acknowledgments

This research was sponsored by the Office of Nuclear Regulatory Research, U.S Nuclear Regulatory Commission (NRC), under Interagency Agreements 40-551-75 and 40-552-75 with the U.S. Department of Energy under Contract W-7405-eng-26 with the Union Carbide Corp.

The authors wish to thank the NRC for supporting the research. They are grateful for the assistance provided by the late E. K. Lynn, who encouraged the ORNL-BCL collaboration. They also wish to thank their respective colleagues M. F. Kanninen, C. Popelar, R. G. Hoagland, A. R. Rosenfield, C. R. Barnes, P. N. Mincer, and S. E. Bolt, who contributed to the analytical and experimental work reported in the paper, and C. Pepper for help with the manuscript.

References

[*1*] Hahn, G. T., Rosenfield, A. R., Marschall, C. W., Hoagland, R. G., Gehlen, P. C., and Kanninen, M. F. in *Fracture Mechanics*, N. Perrone, H. Liebowitz, D. Mulville, and W. Pilkey, Eds., University Press of Virginia, Charlottesville, Va., 1978, p. 205.

[*2*] Kalthoff, J. F., Beinert, J., and Winkler, S. in *Fast Fracture and Crack Arrest, ASTM STP 627*, American Society for Testing and Materials, 1977, p. 161.

[*3*] Kalthoff, J. F., Beinert, J., Winkler, S., and Klemm, W., this publication, pp. 109–127.

[*4*] Fourney, W. L. and Kobayashi, Takao, this publication, pp. 270–288.

[*5*] Kobayashi, T. and Dally, J. W., "Photoelastic Evaluation of the Method of Measuring Crack Arrest Toughness with a Tapered-DCB Specimen," presented at America Society of Mechanical Engineers/Canadian Society of Mechanical Engineers Pressure Vessel and Piping Conference, Montreal, Que., Canada, 25–29 June 1978.

[*6*] Cheverton, R. D., Iskander, S. K., and Bolt, S. E., "Applicability of LEFM to the Analysis of PWR Vessels Under LOCA-ECC Thermal Shock Conditions," NUREG-CR-0107, ORNL/NUREG-40, Nuclear Regulatory Commission, Oct. 1978.

[*7*] Irwin, G. R. in *Fast Fracture and Crack Arrest, ASTM STP 627*, American Society for Testing and Materials, 1977, p. 7.

[8] Hahn, G. T. and Kanninen, M. F. in *Fast Fracture and Crack Arrest, ASTM STP 627*, American Society for Testing and Materials, 1977, p. 411.
[9] Kraftt, J. M. and Irwin, G. R. in *Symposium on Fracture Toughness and Its Applications, ASTM STP 381*, American Society for Testing and Materials, 1965, pp. 114-129.
[10] Kanninen, M. F., Popelar, C., and Gehlen, P. C. in *Fast Fracture and Crack Arrest, ASTM STP 627*, American Society for Testing and Materials, 1977, p. 19.
[11] Crosley, P. B. and Ripling, E. J. in *Fast Fracture and Crack Arrest, ASTM STP 627*, American Society for Testing and Materials, 1977, p. 372.
[12] Hoagland, R. G. et al, "Proposed Tentative Method of Test for Fast Fracture Toughness and Crack Arrest Toughness," prepared in support of the work of ASTM Committee E24.03.04 toward a test method for crack arrest, American Society for Testing and Materials, Oct. 1977.
[13] Hoagland, R. G. in *Fast Fracture and Crack Arrest, ASTM STP 627*, American Society For Testing and Materials, 1977, p. 177.
[14] Hahn, G. T., et al, this publication, pp. 289-320.
[15] Bilek, Z., this publication, pp. 240-247.
[16] Iskander, S. K., "The Calculation of Stress Intensity Factors in Thick Cylinders Subjected to Transient Temperature Gradients by the Finite Element Method," K/SCD/TM-2, Union Carbide Corp., Nuclear Division, Oak Ridge, Tenn., April 1976.
[17] Barsoum, R. S., *International Journal of Numerical Methods in Engineering*, Vol. 10, 1976, pp. 25-37.
[18] Iskander, S. K. in *Heavy-Section Steel Technology Program Quarterly Progress Report*, ORNL/NUREG/TM-120, Oak Ridge National Laboratory, Oak Ridge, Tenn., Jan-Mar. 1977, pp. 97-101.
[19] Popelar, C. H. and Gehlen, P. C., *International Journal of Fracture Mechanics*, Vol. 15, No. 2, April 1979, pp. 169-177.
[20] Third Annual Progress Report to the U.S. Nuclear Regulatory Commission [Contract No. AT(49-24)-0293], BMI-1995, Battelle Memorial Institute Report, Columbus, Ohio, May 1978.
[21] Loss, F. J., Gray, Jr., R. A., and Hawthorne, J. R., "Significance of Warm Prestress to Crack Initiation During Thermal Shock," NRL/NUREG-8165, Naval Research Laboratory, Washington, D. C., Sept. 1977.
[22] Hahn, G. T. Gehlen, P. C., Hoagland, R. G., Marschall, C. W., Kanninen, M. F., Popelar, C. H., and Rosenfield, A. R., "Second Annual Progress Report to NRC on Critical Experiments, Measurements and Analyses to Establish a Crack Arrest Methodology for Nuclear Pressure Vessel Steels," BMI/NUREG-1959, Battele Memorial Institute, Columbus, Ohio, 1976.

DISCUSSION

P. B. Crosley[1] *and E. J. Ripling*[1] (*written discussion*)—This is the second paper that two of the four authors wrote on this thermal shock experiment. The authors' Fig. 8 is a copy of a figure one of the present discussers gave as a discussion to their earlier paper.[2] It shows that a static analysis of the experiment, used in conjunction with K_{Ia} measurements on the test vessel material, is in exact agreement with the TSE-4 test

[1]Materials Research Laboratory, Glenword, Ill.

[2]Hoagland, R. G., Gehlen, P. C., Rosenfield, A. R., and Hahn, G. T., "Analysis of Crack Arrest in Reactor Pressure Vessels," presented at the Joint American Society of Mechanical Engineers/Canadian Society of Mechanical Engineers Pressure Vessel and Piping Conference, Montreal, Que., Canada, June 1978.

results. The same thing is shown in Table 4, where the material value of K_{Ia} and the static analysis results of K_I at arrest are posted.

Their analysis shows that for this vessel test there were no dynamic effects, so they allow that a static approach (involving K_{Ia}) should work as well as the dynamic approach. It is apparent that the static approach worked extremely well; but how well does the dynamic approach work? The material toughness values, measured by the authors, by use of their fully dynamic methodology, namely, $K_{ID} = 173$ MPa $m^{1/2}$ at 126°C and 153 MPa $m^{1/2}$ at 78°C, are stated to be not applicable to the TSE-4 experiment. Since they are above K_{Ic}, they indicate that no unstable cracking should have occurred. This is explained away by the authors by asserting that the crack in TSE-4 propagated at a velocity at which a lower K_{ID} value pertained. What value? The authors make a circuitous argument to arrive at a value of K_{Im} (more properly K_{IDm}) $\approx K_{Ia}$, that is, $K_{IDm} = 77$ MPa $m^{1/2}$ at 77°C and $K_{IDm} = 134$ MPa $m^{1/2}$ at 126°C. If one is willing to accept these values, which show no relationship to their measured ones, then the dynamic analysis gives reasonable results.

One must conclude that the purpose of the first parts of this paper is to show that a static analysis, using the measured values of K_{Ia}, is in excellent agreement with the vessel post-test measurements; and if one is willing to accept the authors' implied values of K_{IDm}, rather than measured values of K_{ID}, then the dynamic analysis is also reasonable.

In the last part of the paper, "Analysis of a Deep Flaw Under Modified TSE-4 Conditions," the hypothetical experiment seems wholly unrelated to the real experiment. The material properties put into the analysis to show dynamic effects are totally unrealistic: the assumption of velocity independence, $K_{ID} = K_{Im} = K_{Ic} = 62$ MPa $m^{1/2}$, is questionable; to assume that this same toughness value, 62 MPa $m^{1/2}$, pertains over the range of temperatures from 25 to 250°C, is ridiculous. What seems to have been demonstrated is that, with an appropriate assignment of hypothetical material properties, the authors' analysis predicts dynamic effects. This is nothing new. Their analyses have regularly predicted dynamic effects. What has still not been demonstrated is the occurrence of dynamic effects in the real experiment.

A likely place to look for dynamic effects in crack arrest is in laboratory specimens, specimens which are smaller than the TSE-4 structure and should, then, offer more opportunity for stress wave reflections. Two of the four authors have shown how K_{Ia} should vary with K_Q according to their dynamic analysis.[3] As shown in Fig. 13, the dependence of K_{Ia} on K_Q is quite similar for a large number of shapes. This proposed behavior for the normal compact specimen is compared with actual specimen data

[3] Hahn, G. T., et al, "Third Annual Progress Report, Oct. 1976-Sept. 1977," NUREG-CR-0057, BMI-1995, Battelle Memorial Institute, Columbus, Ohio, May 1978.

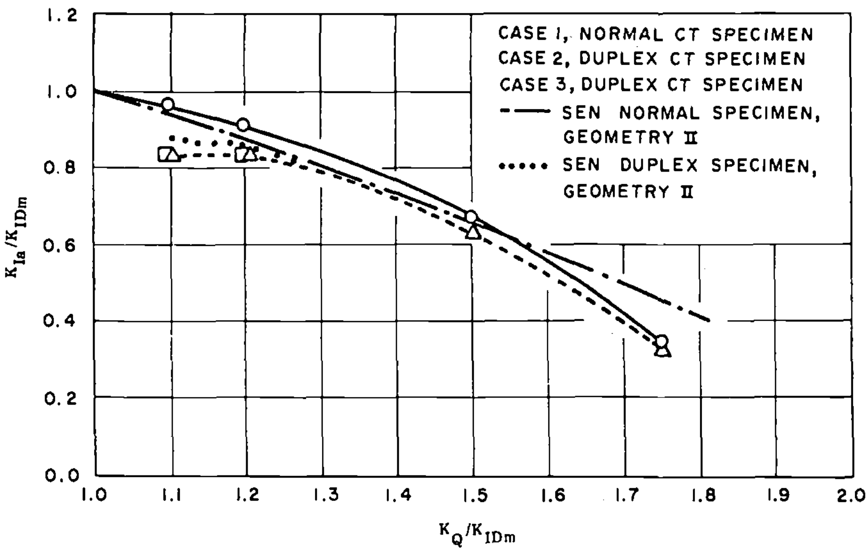

FIG. 13—*Influence of the relative initiation stress-intensity level on the* K_{Ia}/K_{IDm} *ratio according to BCL dynamic analysis.*

in Fig. 14. Obviously, static and dynamic analyses lead to pronounced differences for large crack jumps (that is, hihg K_Q-values), and the specimen data are in good agreement with the static approach, which, of course, means that the BCL dynamic analysis must be wrong.

R. D. Cheverton, P. C. Gehlen, G. T. Hahn, and S. K. Iskander—The discussers and reader are referred to Kalthoff et al[4] for direct observations of large dynamic effects[5] in DCB specimens, and to Kobayashi[6] for both direct observations and *independent* dynamic analyses showing comparable dynamic effects in the compact tension specimen. The results of these studies are in good agreement with the BCL dynamic analysis, as in the work of Fourney and Kobayashi in this volume. The discussers' comment that the BCL dynamic analysis "regularly" predicts dynamic effects is at odds with the work under discussion; that is, the dynamic effect of the TSE-4 event is found to be negligible by the BCL dynamic analysis. Furthermore, systematic calculations of run arrest events performed with the BCL

[4]Kalthoff, J. F., Beinert, J., and Winkler, S. in *Fast Fracture and Crack Arrest, ASTM STP 627*, American Society for Testing and Materials, 1977, p. 161.

[5]The term "dynamic effect" is used here to denote that the stress-intensity value at the instant of crack arrest is larger than the value calculated for the remote application of load or displacement using conventional static LEFM analyses.

[6]Kobayashi, A. S. in *Nonlinear and Dynamic Fracture Mechanics*, AMD Vol. 35, American Society of Mechanical Engineers, 1979, p. 19.

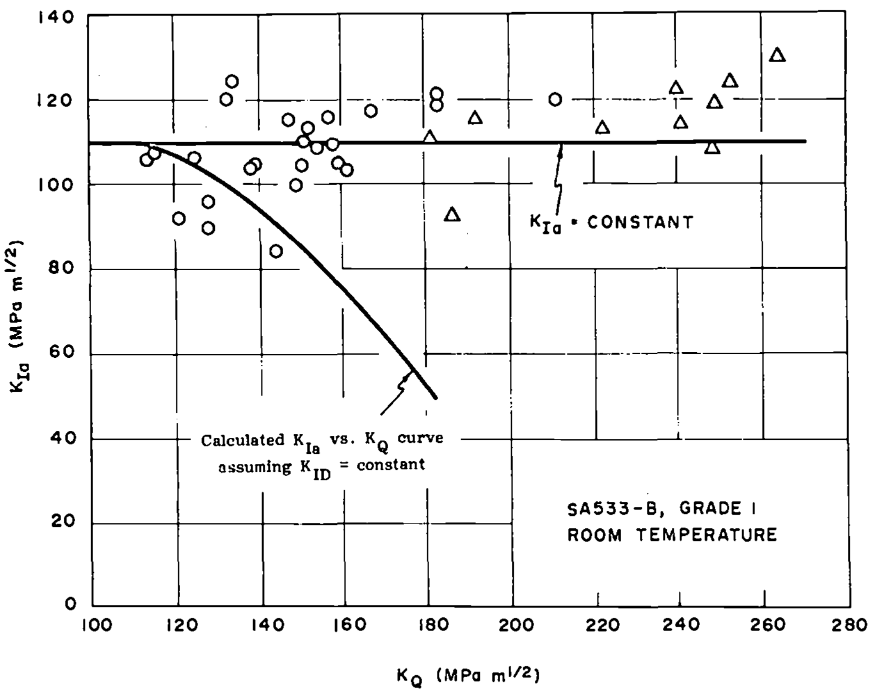

FIG. 14—*Dependence of* K_{Ia} *on* K_Q *for SA533-B, Grade 1 steel. Cooperative Test Program data. "*K_{ID} *= constant" curve shows expected dependence from dynamic analysis.*

dynamic analysis[7] show clearly that K_{Ia} can be *independent* of K_Q when the K_{ID}-crack velocity curve displays a strong upswing of the type reported in the present paper.

The discussers are correct in sensing that the dynamic calculation of the long crack jump reported in the paper does not relate to the actual TSE-4 event. This calculation was performed because Section XI, Article A5000 of the ASME Pressure Vessel Code provides for crack penetrations up to 75 percent of the wall thickness. The calculation was designed to examine the general validity of the static analysis approach for deep penetrations advocated by the discussers and contained in Article A5000. It was performed for the TSE-4 vessel geometry and the TSE-4 thermal stress gradient simply for convenience. Under these conditions, it is necessary to employ a (hypothetical) relatively low material toughness value to achieve a deep penetration. Consequently, the calculation sheds light on the method of analysis, but *not* on the likelihood of a deep penetration in a full-scale vessel.

[7] Hahn, G. T., Gehlen, T. C., Hoagland, R. G., Kanninen, M. F., Popelar, C., Rosenfield, A. R., and de Campos, V. S., "*Critical Experiments, Measurements and Analyses to Establish* a Crack Arrest Methodology for Nuclear Pressure Vessel Steel," Report to the Nuclear Regulatory Commission, BMI-1937, Aug. 1975.

T. U. Marston,[1] *E. Smith,*[2] *and K. E. Stahlkopf*[1]

Crack Arrest in Water-Cooled Reactor Pressure Vessels During Loss-of-Coolant Accident Conditions

REFERENCE: Marston, T. U., Smith, E., and Stahlkopf, K. E., **"Crack Arrest in Water-Cooled Reactor Pressure Vessels During Loss-of-Coolant Accident Conditions,"** *Crack Arrest Methodology and Applications, ASTM STP 711,* G. T. Hahn and M. F. Kanninen, Eds., American Society for Testing and Materials, 1980, pp. 422-431.

ABSTRACT: The current American Society of Mechanical Engineers Code procedure for crack arrest in a reactor vessel is based on a static linear elastic fracture mechanics analysis and the assumption that arrest occurs when the crack-tip stress intensification, K_I, equals some critical value, K_{Ia}—the so-called crack arrest toughness. The paper argues that the conditions for crack arrest in a nuclear pressure vessel, when it is subjected to thermal stresses resulting from a hypothetical loss of coolant accident, can be demonstrated with the current Code method, provided that an appropriate value for K_{Ia} can be obtained from laboratory tests. The difficulties in selecting the appropriate value of K_{Ia} for this component analysis are highlighted, particular attention being given to the effect of test specimen geometry, crack jump length, and material variability. Against this background, the paper outlines a possible procedure for obtaining the appropriate K_{Ia}-value. It is emphasized that the viability of the approach may be highly dependent on the structure's characteristics, and an approach considering kinetic (dynamic) effects may be necessary for other crack arrest problems.

KEY WORDS: fracture mechanics, ASME Code, warm prestressing, crack propagation

One postulated emergency condition for the pressure vessel of a water-cooled nuclear reactor is a loss-of-coolant accident (LOCA), which might be the result of a large break in a main coolant line to the reactor vessel. The LOCA is followed by operation of the emergency core cooling system (ECCS), when introduction of the relatively cold ECCS water subjects the hot pressure vessel to high thermal stresses in the vicinity of the inner surface. If this surface contains a crack-like defect, the stress intensity at the crack tip increases

[1]Project manager and program manager, respectively, Electric Power Research Institute, Nuclear Power Division, Systems and Materials Department, Palo Alto, Calif. 94303.

[2]Professor, University of Manchester, Manchester, U. K.

with time to a maximum, and then decays as the temperature gradient through the wall becomes smaller. Additionally, with highly irradiation-sensitive materials, neutron bombardment can cause a lowering of the fracture toughness, K_{Ic}, at a given temperature. If the embrittlement is sufficiently severe, K_{Ic} could be low enough that the rising K_I due to the emergency condition will exceed K_{Ic} and the crack will extend. Because the primary objective is to retain a coolable core configuration after an emergency condition, it is essential to guard against the possibility of the crack penetrating the vessel wall.

Article A-5300, which deals with flaw evaluation for emergency and faulted conditions, of Section XI of the American Society of Mechanical Engineers (ASME) Boiler and Pressure Vessel Code [*1*],[3] which provides rules for in-service inspection of nuclear power plant components, states that each postulated incident should be considered in the following manner:

1. Determine the maximum end-of-life fluence profile through the wall thickness at the flaw location.
2. Determine the temperature and stress profiles through the thickness of the component at the flaw location.
3. Using irradiated fracture toughness data, determine the crack arrest (K_{Ia}) and crack initiation (K_{Ic}) fracture toughness profiles through the thickness of the component as a function of time following the postulated incident.
4. Calculate the stress-intensity factors for various penetration depths of the assumed flaw.
5. The crack penetration at which the calculated stress-intensity factor exceeds the K_{Ic} profile corresponds to the critical size for initiation (a_i), and the penetration at which the stress-intensity factor goes below the K_{Ia} curve corresponds to the critical crack size for arrest (a_a). This comparison is illustrated in Fig. 1 for both an arrest and a nonarrest situation.
6. Curves such as Fig. 1 should be prepared for a number of selected times following each postulated accident to establish the critical time and the smallest a_i,

The smallest value of a_i determined by the foregoing procedure, and for which the crack penetration (p) is greater than 75 percent of the wall thickness after all postulated accidents have been considered, represents the minimum critical initiation flaw size for emergency and faulted conditions at the flaw location. The flaw evaluation procedure is explained in detail in Ref *12*.

The vaidity and usefulness of the approach depend on two points:

1. Can static crack arrest K_{Ia} procedures be used for nuclear pressure vessel analysis?
2. Can appropriate K_{Ia}-values be measured in suitable laboratory tests?

[3]The italic numbers in brackets refer to the list of references appended to this paper.

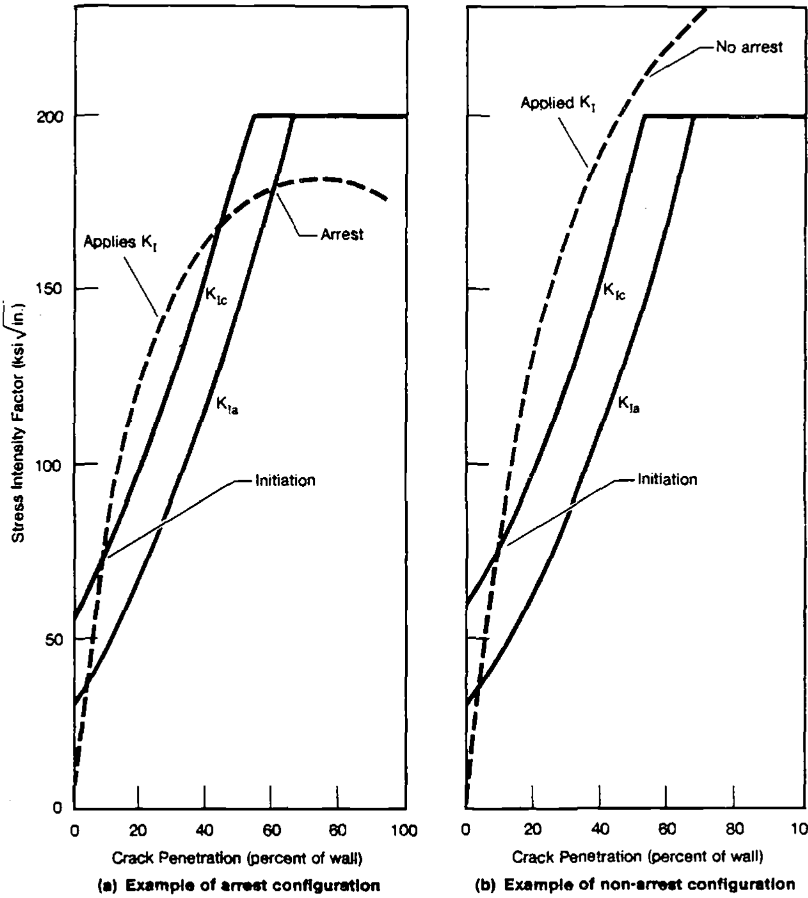

FIG. 1—*Determination of critical flaw sizes for postulated condition* [1].

The K_{Ia} crack arrest procedure essentially depends on a static linear elastic fracture mechanics (LEFM) analysis for the structure, where dynamic effects associated with the crack propagation event are not considered. This simplified static procedure [*2,3*] has been questioned in recent years as to its accuracy and, more importantly, as to the conservatism of its predictions. Accordingly, dynamic approaches to crack propagation and arrest have been developed (see for example Ref *4*); these approaches are significantly more complicated than K_{Ia} static approach.

It is against this background that the present paper addresses the problem of crack propagation and arrest in the pressure vessel of a water-cooled reactor subject to a LOCA. The crack arrest procedure that can be employed in the light of present ASME Code rules is discussed, as well as an approach for obtaining K_{Ia}-values for use in the arrest analyses. It should be emphasized that the authors do not assert that the Code and K_{Ia} procedures can be used satisfactorily for all crack arrest problems, since attention in this paper is concentrated merely on one specific, albeit very important, crack arrest problem where dynamic effects are minimal.

Outline of Problem and Demonstration of Validity of K_{Ia} Crack Arrest Procedures

Various theoretical analyses have been performed for the potential for crack extension during a LOCA of a pressurized-water reactor vessel. To illustrate the general problem, however, the present discussion will be based on the theoretical analysis conducted by Cheverton [5] for a typical vessel. The following assumptions were made in modeling the vessel:

1. Wall thickness = 216 mm (8.5 in.).
2. Inner wall fluence = 4×10^{19} neutrons (n)/cm^2 $E > 1$ MeV (corresponding to a 40-year operation period).
3. High-impurity copper level (>0.25 percent, corresponding to severe predicted irradiation embrittlement).
4. Preirradiation K_{Ic} versus temperature as defined by Westinghouse [6, 7] for SA533-B1 steel.
5. Vessel not pressurized during the LOCA due to loss of coolant.

As described earlier, decreasing fluence and increasing temperature toward the outside wall surface provide a mechanism for the arrest of a running crack that might start to propagate from the highly stressed material of relatively low toughness near the inner wall surface. Arrest is assumed to occur when the K_{Ia}-value exceeds the K_I-value at the crack tip, the K_{Ia}-versus-temperature behavior for reactor pressure vessel material being defined in Section XI, Appendix A, of the ASME Boiler and Pressure Vessel Code. While other trend curves are available, the degradation in K_{Ia} due to neutron irradiation through the wall has been characterized in Cheverton's subject analysis according to the procedures of Regulatory Guide 1.99 [8]. This guide predicts the K_{Ia} and K_{Ic} versus relative temperature trends for irradiated material by a simple temperature translation of the unirradiated properties based on the fluence level and residual copper and phosphorus content of the steel. In Cheverton's reference calculational model, the K_{Ic}-versus-temperature trend for the irradiated material has been obtained in a similar manner by the identical temperature translation.

Figure 2 gives K_I as a function of the crack-tip position for a long axial flaw 450 s after the LOCA. The curves show that an axial crack with a depth-to-wall thickness ratio (a/W) of 0.03 will initiate at this time. This crack will then propagate to a relative depth of $a/W = 0.35$ before it arrests. The arrest occurs at a K_I-level greater than the K_{Ic} associated with initiation, because the crack extends into a region of increasing temperature which provides significantly higher values of K_{Ia} that arrest the crack. It is important to ap-

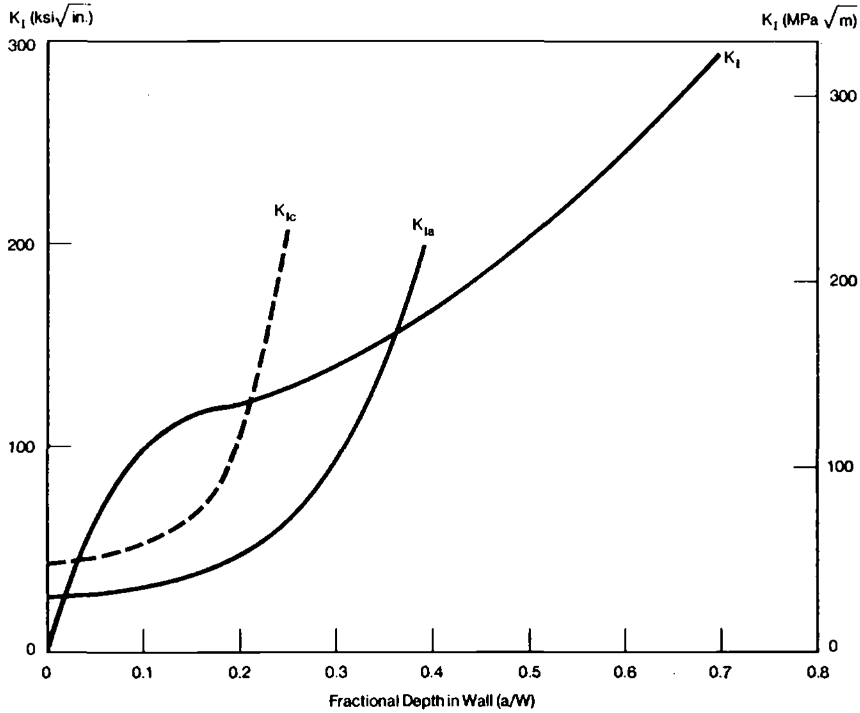

FIG. 2—*Critical levels for initiation* K_{Ic} *and arrest* K_{Ia} *of a crack, as defined by the intersection of these curves with the* K_I *curve. The curves refer to the behavior of a long axial flaw 450 s after the LOCA* [9].

preciate that flaws of different sizes can initiate at different times after the LOCA; Fig. 2 represents the conditions only after a time of 450 s. Figure 3 shows a crossplot of the intersections of the K_I curve with the K_{Ic} and K_{Ia} curves at various times, the dashed line illustrating the progressive initiation, arrest, and reinitiation behavior of a shallow crack; this description suggests that the crack could penetrate deep into the wall, and extend beyond the 75 percent penetration limit that is set by the Code.

Figure 4 depicts the behavior of K_I with time for a family of long axial flaws, and the dashed curve represents the locus of points for which K_I/K_{Ic} is unity. The intersection of the K_I and K_{Ic} curves occurs with decreasing K_I for flaws of depth (a/W) greater than 0.2. This means such cracks will have been warm prestressed [9] (that is, although K_I may attain its maximum early in the transient, the critical-level K_{Ic} is not reached unitl sometime later). Such cracks should therefore not extend. Nevertheless, it is possible to predict crack propagation to relative depths greater than 0.2. Thus, for example, consider a crack whose relative depth is 0.1. This crack will not be subject to warm prestressing; according to Fig. 3 it will start to propagate at a time of

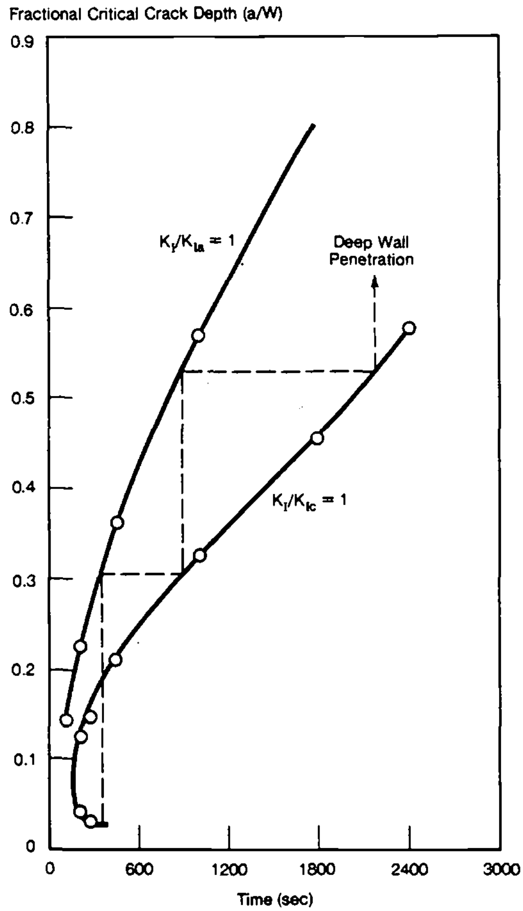

FIG. 3—*Crossplot of the intersection of the* K_I *curve with the* K_{Ic} *and* K_{Ia} *curves at various times* [9].

180 s and will penetrate to a relative depth of 0.2. Since only cracks whose relative depth is grater than 0.2 will be subject to warm prestressing, this crack will reinitiate at a time of 420 s and then extend to a relative depth of 0.34. Because of warm prestressing, farther extension is unlikely at 1080 s into the event, whereas reinitiation would normally be predicted in the absence of warm prestressing.

The preceding arguments, which are developed in Ref *9*, lead to the conclusion that although warm prestressing cannot prevent crack initiation from shallow cracks, the amount of crack extension can be limited by this phenomenon. The central problem regarding crack arrest is therefore to guarantee that a shallow crack will not penetrate deep into the vessel wall, the likely situation where deep penetration is most likely being that for which

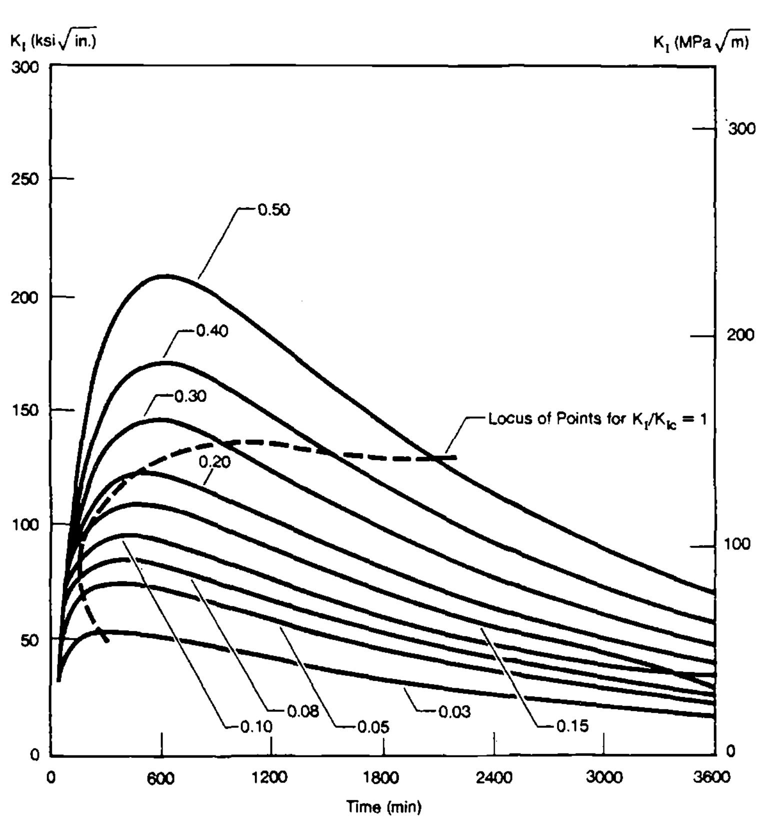

FIG. 4—*Stress-intensity factor* K_I *versus time for different crack depths* a/W. *The dashed curve represents the locus of points at which the critical level* K_{Ic} *for initiation would be attained in the absence of warm prestressing* [9].

$a/W = 0.2$, where the K_{Ia} approach shows that propagation will occur to a relative depth of $a/W = 0.34$.

It is important that the K_{Ia} approach should therefore be valid for a crack jump of this magnitude. In considering the problem, it should be emphasized that the crack is penetrating normally into the vessel wall. Unlike the situation with the common double cantilever beam (DCB) test, for example, surfaces in the vessel parallel to the crack are so remote that only the effect of reflections from the outer wall need be considered. Propagation of a crack from a/W 0.20 to 0.34 in a vessel 215.9 mm (8.5 in.) thick implies a crack jump length of 30.48 mm of (1.2 in.), while the outer surface is 142.24 mm (5.6 in.) away at the hypothetical arrest point. It is difficult to rationalize the outer surface having any effect in such a situation, and therefore its effect may also be ignored. In addition, there is negligible motion of the vessel as a result of crack extension. Thus it would seem proper to use the K_{Ia} approach for this crack propagation and arrest event. This view is supported by

Kalthoff's experimental observations [10] on wedge-loaded single-edge notch (SEN) specimens of Araldite B. The difference between the statically K_{Ia}-and dynamically $K_{Ia}{}^{dyn}$-determined fracture thoughness values is considerably smaller, by a factor of 2, than for DCB specimens for equivalent crack jump distances and crack propagation velocities, and Kalthoff has concluded that dynamic effects are small in SEN than in DCB specimens. (Surfaces parallel to the crack are farther away in the SEN specimen than in the DCB specimen.)

The general conclusion emerging from this section's considerations is that certainly for crack jump lengths of the order of 25.4 mm (1 in.) through the vessel wall, the K_{Ia} arrest procedure will be adequate; it may be adequate even for larger crack jumps, but this point requires further investigation. However, beacuse of warm prestressing effects associated with long cracks, the long-crack behavioral situation may not be relevant. Of course, the approach developed in this section depends on reliable K_{Ia} data being available; this point will be considered in the next section.

Determination of K_{Ia} via Laboratory Experiments

In principle, one requires to know the value of K_{Ia} in a nonreflecting situation where there are no wave reflections from surrounding surfaces, that is ideally for a situation where there is a small crack jump length in an infinite body. Clearly this is an impossible situation to attain in practice, since all laboratory experimental specimens have finite boundaries which introduce dynamic effects. Consequently, as has been emphasized in the extensive series of papers generated by the Battelle Columbus group (see for example Ref 4), a crack will propagate farther than is predicted by the K_{Ia} approach. This is due to kinetic energy generated within the specimen, during the early stage of propagation, which is available to allow the crack to propagate farther than if no such energy is generated. The magnitude of the dynamic effects clearly depends on the specimen configuration, with some geometries exhibiting more dynamic effects than others. For example, as indicated in the preceding section, the SEN specimen displays fewer dynamic effects than the DCB specimen; this is because surfaces parallel to the crack plane are farther away in the SEN specimen and the effect of reflected stress waves is thereby diminished.

The presence of boundaries, particularly those parallel to the crack plane, lead to crack arrest at K_{Ia}-values that are lower than the value appropriate to the nonreflecting situation. This means that laboratory test measurements of K_{Ia} will be conservative with respect to the pressure vessel application discussed in the preceding section. It should be appreciated, however, that there will be a scatter in K_{Ia}-values due to material variation, although this is not expected to be as great compared with K_{Ic} measurements. On the one hand, a high K_{Ia}-value is required to simulate the nonreflecting situation, while on the other hand a low value is required to be conservative from the material variability aspect; these objectives are conflicting.

To proceed against this background, the authors suggest that the results of the SA533-B1 round-robin test program be considered; in this program both compact tension specimens of the Battelle design [4] are being tested. Assuming that one of these specimens is shown to be preferable, as a result of the round-robin program, a possible procedure is to test three specimens at a given temperature and use the lowest of the three K_{Ia}-values as input to the pressure vessel assessment procedure described in the preceding section; in other words, the data base for the earlier considerations should be secured.

Discussion and Conclusions

It should be strongly emphasized that the present paper has discussed only one specific crack propagation and arrest problem, namely that of crack propagation and arrest in a pressure vessel during a hypothetical LOCA in a water-cooled nuclear reactor. For this particular situation it has been argued that, in view of the geometrical factors, K_{Ia} arrest procedures in accord with the ASME Code provisions should be adequate for assessing the propagation of cracks whose initial depths are less than 20 percent of the vessel's thickness. As indicated in the paper, deeper cracks will be subject to warm-prestressing effects that should prevent them from extending farther into the vessel. Even in the unlikely event of the warm-prestressing argument being invalid, it is expected, again because of geometrical factors, that the propagation and arrest of cracks whose lengths are somewhat greater than $0.2W$ can still be considered via the K_{Ia} procedure. If support is required for this view, it might be desirable to conduct a dynamic analysis along the Battelle Columbus lines [4], although it should be recognized that long cracks may be associated with plasticity effects. For other practical crack propagation and arrest situations, particularly where there are surfaces parallel to the direction of crack propagation, the dynamic approach might indeed be necessary.

Arising from this brief survey of the LOCA problem, the areas that might be worth considering in the future, in order to secure the position outlined in this paper, are as follows.

1. Propagation of long cracks using an appropriate dynamic approach to confirm that a static analysis is sufficiently accurate; warm prestressing then will not be a necessary part of the safety argument.

2. Sensitivity study of the parameters in the model problem discussed herein to see whether this paper's approach can be applied to a wider range of LOCA conditions.

Otherwise, it may be concluded that the K_{Ia} procedure based on the ASME Code provisions should be adequate for discussing the LOCA problem.

References

[*1*] ASME Boiler and Pressure Vessel Code, Section XI, Article A-5300, American Society of Mechanical Engineers, 1975.

[*2*] Krafft, J. M. and Irwin, G. R. in *Fracture Toughness Testing and its Application, ASTM STP 381*, American Society for Testing and Materials, 1965, p. 114.

[*3*] Crosley, P. B. and Ripling, E. J. in *Fast Fracture and Crack Arrest, ASTM STP 627*, American Society for Testing and Materials, 1977, p. 203.

[*4*] Hoagland, R. G., Rosenfield, A. R., Gehlen, P. C. and Hahn, G. T. in *Fast Fracture and Crack Arrest, ASTM STP 627*, American Society for Testing and Materials, 1977, p. 177.

[*5*] Cheverton, R. D., ORNL/NUREG/TM-31, Oak Ridge National Laboratory, Sept. 1976.

[*6*] Shabbits, W. O., WCAP-7623, Westinghouse R&D Center, Pittsburgh, Pa., Dec. 1970.

[*7*] Shabbits, W. O., Pryle, W. H., and Wessel, E. T., WCAP-7414, Westinghouse R&D Center, Pittsburgh, Pa., Dec. 1969.

[*8*] Regulatory Guide 1.99, U.S. Nuclear Regulatory Commission, Office of Standards Development, Washington, D.C.

[*9*] Loss, F. J., Gray, R. A., and Hawthorne, J. R., NRL/NUREG Rep. 8165, Naval Research Laboratory, Washington, D.C., Sept. 1977.

[*10*] Kalthoff, J.F. in *Proceedings*, Joint American Society of Mechanical Engineers/Canadian Society of Mechanical Engineers Pressure Vessel and Piping Conference, Montreal, Que., Canada, June 1978.

[*11*] Crosley, P. B. and Ripling, E. J. in *Fast Fracture and Crack Arrest, ASTM STP 627*, American Society for Testing and Materials, 1977, p. 372.

[*12*] "Flaw Evaluation Procedures—Background and Application of ASME Section XI Appendix A," T. U. Marston, Ed. Report NP-719-SR, Electric Power Research Institute, Palo Alto, Calif., Aug. 1978.

Summary

Summary

While more time must pass to fully appreciate the contributions in this volume, some of their implications for testing, analysis, and material response are already evident. The deliberations of the ASTM Crack Arrest Task Group, E24.01.06, in Atlanta five months after the symposium, were strongly influenced by the results of the Cooperative Test Program previewed in this volume. These indicated that the two test specimen configurations: duplex and weld embrittled, yield essentially the same K_{Ia}-values and similar K_{ID}-values (see addendum to the paper by *Hahn, Hoagland, Rosenfield, and Barnes*). The task group, therefore, selected the weld embrittled design advanced by Crosley and Ripling for a round robin scheduled to get underway in 1980. This specimen will be called the "compact crack arrest specimen." It has the virtue that it can be fabricated at lower cost and in thicker sections because it does not require electron beam welding, which proved troublesome for the duplex specimen.

Several problems with the design of the compact crack arrest specimen are receiving further attention. In the absence of a hardened starter section, large-scale plastic deformation can be expected prior to crack initiation when the specimen is loaded to the high K-levels of practical interest. Appropriate specimen size requirements or corrections for the plastic component of displacement need definition. A more convenient method of controlling the K-value at the onset of the run-arrest event is also desirable. The pre-compression loading presently employed requires a large testing machine and introduces residual stresses whose effects are not well understood. There are also indications that the variation of K_{ID}-values with K_Q, noted by Crosley and Ripling, may reflect a strong velocity dependence of the resistance to crack propagation. The possible influence of this dependence on the behavior of the test specimen and the interpretation of the results—particularly the connections between K_{Ia}, K_{ID}, and K_{Im} (the minimum resistance to penetration)—should be examined in more detail.

The best method of analyzing run-arrest events in test specimens and in large structural components remains an unsettled issue. At the time of the earlier symposium, there was general agreement that precise treatments for the arrest of a rapidly propagating crack must be based upon dynamic analyses of the propagation even itself. However, as noted in the summary to that volume, there was considerable disagreement in evidence on the extent to which the not inconsiderable computational and experimental complexity required for a fundamentally correct analysis is necessary for practical applications. Indeed, for small crack jump lengths, a dynamic fracture mechanics treatment will be indistinguishable from a simpler quasi-static analysis. But, when the two approaches differ, it must be that the dynamic approach is more nearly correct. And, because it generally predicts that the crack will propagate faster and further than will a static analysis, it may be dangerous to assume *a priori* that quasi-static conditions prevail in any given circumstance.

The papers contained in this volume indicate that, while the schism between the dynamic and quasi-static approaches to crack arrest still exists, substantial accommodation appears to have been reached. This has been done on a pragmatic basis. Crosley and Ripling note in their paper that, because dynamic effects exist in crack arrest, the quasi-static approach is an oversimplification. Nevertheless, as they assert, reasonably constant statically determined arrest values can be determined experimentally that will suffice for practical purposes.

This same point of view was adopted in the paper by Marston et al. They applied a quasi-static approach to assess crack propagation and arrest in a nuclear pressure vessel subjected to thermal stresses in a hypothetical loss-of-coolant accident (LOCA). They concluded that, while dynamic analyses may in general be necessary for crack arrest problems, because of the geometry of the vessel and the anticipated short jump length, a quasi-static analysis should suffice. This assumption is corroborated by the dynamic analysis of the short-jump LOCA event reported in the paper by Cheverton et al. But, as Cheverton et al also point up, for a hypothetical long crack jump, a dynamic analysis predicts a much deeper penetration than would a quasi-static analysis. This conclusion would seem to be reinforced by Dally et al who proposed a thick-walled ring specimen for mechanically simulating crack propagation under a thermal stress that might occur in a LOCA event. Their results also indicate that quasi-static stress analyses will generally not be applicable for dynamic crack propagation.

It can be perhaps concluded that the dynamic-quasi-static crack arrest controversy is no longer a critical issue. A perusal of the papers contained in this volume will indicate the field has advanced and, in doing so, new critical issues have emerged. Of most prominence is the growing realization that the applicability of even the most rigorous analysis procedures that have been developed may be much more limited than was previously realized. That is, virtually all mathematical solutions and interpretations of experimental results are now made in terms of linear elastic fracture mechanics (LEFM) treatments. (Dynamic fracture mechanics, which uses elastodynamic analyses, are no less subject to this than are quasi-static treatments.) However, most work is done on either ductile tough materials like the nuclear pressure vessel stress A533B or on viscoelastic polymeric materials. These materials do not satisfy the basic assumptions of LEFM. Moreover, all materials—even those which satisfy LEFM requirements at the initiation of crack growth—will leave a wake of residual plasticity behind the propagating crack tip. While this has been always ignored, there may be reason to question the propriety of neglecting it, as follows.

The basic assumption in elastodynamic analyses of crack propagation has been that the dynamic fracture toughness is a unique geometry-independent material property that can, at most, depend upon crack speed, temperature, and plate thickness. However, results presented by several of the contributors to this volume are beginning to seriously question the legitimacy of this assumption. Some investigations indicate that the external dimensions of the component can affect values inferred for the toughness property. Dahlberg et al point up that, even if K dominance of the inelastic region around the crack tip exists, a dependence of the dynamic fracture toughness on higher order derivatives of crack speed cannot be excluded by theoretical means. If so, geometry-dependence and incorporation of higher order derivatives of the crack speed must be accepted in linear elastic dynamic fracture mechanics. Whether or not residual plasticity or other nonlinear effects could play a key role in mollifying this lack of uniqueness cannot be presently determined. What does seem clear is that a growing lack of confidence exists in the fundamental soundness of the LEFM-based procedures for analyzing fast fracture and crack arrest. In fact, it may be that this has become the most critical issue in the field.

An important fact that cannot be overlooked in any use of experimental observations to assess the basis of mathematical analysis procedures is that no direct measurement of the stress intensity factor is possible. While observations of fringe and shadow patterns associated with a propagating crack can be made, the relation of these measurements to fracture mechanics parameters always requires the use of some mathematical model. And, any such model must be based upon a constitutive relation and other presumptions about the interaction between the propagating crack and the component that contains it. (Most often, it is tacitly assumed that the near crack tip region can be treated as if it were in a quasi-static linear elastic infinite medium.) To assess such approaches, Popelar and Kanninen have devised a dynamic viscoelastic representation for polymer DCB test specimens. Freund and Parks have begun the development of an elastic-plastic analysis model for ductile crack propagation in pressurized pipelines. Clearly, other such nonlinear treatments will be required to resolve the questions that are yet unanswered in the subject covered by this volume.

While the applicability of linear elastic crack arrest treatments may well be the most outstanding issue at the time of the second symposium, it is clear from the many papers devoted to it in this volume that such treatments still can be quite useful. The paper by McGuire et al showed how such an approach was applied successfully for an assessment of pipeline safety. Mall et al used an elastodynamic finite element model to determine dynamic initiation toughness in impact loaded three-point bend specimens. Emery et al were similarly successful in studying dynamic circumferential crack propagation in an axially stressed pipe.

There is considerable work in progress in refining both the analysis and experimental procedures needed for crack arrest assessments evidenced by the papers in this volume. Shmuely and Perl have developed an improved two-dimensional dynamic finite difference code that simulates a continuous rather than a discrete movement of the crack tip. Malluck and King have compared two different methods for relaxing the restraining reaction force at the crack tip to permit a similar effect for finite element models. As they point up, much work must yet be done in developing numerical analysis methods for fast fracture and crack arrest. Hence, it is fortunate that closed form solutions such as that of Popelar for the double torsion test specimen also are being pursued.

Advances in experimentation are also in evidence in this volume. In addition to those already mentioned, Kobayashi and Dally describe a dynamic photoelastic method for the direct determination of the instantaneous stress intensity factor for running cracks by use of a split birefringent coating applied to the surface of a compact tension test specimen. By using the shadow optical method of caustics in both a photoelastic material (by transmission) and in steel (by reflection), Kalthoff et al have investigated crack arrest and post arrest behavior. They find that the dynamic effect (that is, the difference between the dynamic stress intensity factor at the instant of crack arrest and the static value that exists long after arrest) is strongly affected by specimen geometry and material type. They conclude that these differences must be taken into account in establishing a physically correct, generally applicable, crack arrest methodology.

When direct observation of the tip of a propagating or arresting crack is not appropriate, analysis methods are needed to interpret the experimental results. Work at Battelle has provided a set of reference curves for this purpose. In their paper, Fourney and Kobayashi describe a critical examination of these and report that they do have a reasonably good basis. In other work of this general type, Gates had independently studied the effects of specimen geometry and loading conditions for crack propagation in steel and found that his results are in general agreement with other analyses. Chow and Burns have employed a shear force measurement technique in a rapidly wedged DCB specimen to deduce dynamic toughness values for 1018 steel. Bilek presents results from both slow and rapid loading of a DCB specimen to obtain values for 4340 steel.

Contributions to the important task of material characterization and the origins of fracture toughness are also contained in this volume. Metcalf and Kobayashi have made an intensive study of the two commonly used photoelastic materials, Homalite 100 and Araldite B, to better understand dynamic crack propagation and arrest results in these materials. Hahn et al present a crack arrest data base from crack propagation and arrest measurements on six pressure vessel steels and a submerged-arc weldment. A fractographic interpretation of the arrest toughness is also given. Finally, Burns has made an interesting effort to connect the rate-controlling mechanisms for slow crack growth with those of rapid crack propagation by replacing the isothermal condition applicable to the former with an adiabatic condition. While incomplete for lack of key experimental data, this kind of approach is clearly needed for an increased understanding of the subject.

The toughness values generated by the Cooperative Test Program (see addendum of the paper by Hahn, Hoagland, Rosenfield, and Barnes) are most important, since they represent the most extensive and up-to-date collection of crack arrest measurements on a nuclear pressure vessel steel. The K_{Ia}-values measured at room temperature, NDT + 60°C, straddle the K_{IR}-curve of Section III of the ASME boiler and Pressure Vessel Code. This curve was originally drawn to represent lower bound toughness behavior. It would appear that the improvements in crack arrest test methodology will require a downward revision of the K_{IR}-curve, at least for crack arrest considerations.

In conclusion, it can be said that the study of dynamic crack propagation and crack arrest is one with very important practical applications. In accord with this, the subject is receiving the attention of a highly capable and energetic group of researchers. Clear progress has been made since the time of the earlier symposium in this field. While some of the issues that existed at that time have been resolved, new issues have emerged that are now being addressed. This is natural in the study of a complex problem area. Hence, it can be taken as evidence of the healthy progress that is being made towards the eventual reduction of crack arrest considerations to routine engineering practice.

G. T. Hahn

Vanderbilt University, Nashville, Tenn. 37235; editor.

M. F. Kanninen

Battelle Memorial Institute, Columbus Laboratories, Columbus, Ohio; 43201; editor.

Index